

Getting wired

Citation for published version (APA):

De Botelho Ferreira Braga Malheiro, A. (2021). *Getting wired: strategies to develop peripheral nerve, innervated tissue and neurovascular in vitro platforms*. [Doctoral Thesis, Maastricht University]. Maastricht University. <https://doi.org/10.26481/dis.20210611am>

Document status and date:

Published: 01/01/2021

DOI:

[10.26481/dis.20210611am](https://doi.org/10.26481/dis.20210611am)

Document Version:

Publisher's PDF, also known as Version of record

Please check the document version of this publication:

- A submitted manuscript is the version of the article upon submission and before peer-review. There can be important differences between the submitted version and the official published version of record. People interested in the research are advised to contact the author for the final version of the publication, or visit the DOI to the publisher's website.
- The final author version and the galley proof are versions of the publication after peer review.
- The final published version features the final layout of the paper including the volume, issue and page numbers.

[Link to publication](#)

General rights

Copyright and moral rights for the publications made accessible in the public portal are retained by the authors and/or other copyright owners and it is a condition of accessing publications that users recognise and abide by the legal requirements associated with these rights.

- Users may download and print one copy of any publication from the public portal for the purpose of private study or research.
- You may not further distribute the material or use it for any profit-making activity or commercial gain
- You may freely distribute the URL identifying the publication in the public portal.

If the publication is distributed under the terms of Article 25fa of the Dutch Copyright Act, indicated by the "Taverne" license above, please follow below link for the End User Agreement:

www.umlib.nl/taverne-license

Take down policy

If you believe that this document breaches copyright please contact us at:

repository@maastrichtuniversity.nl

providing details and we will investigate your claim.

Getting wired:
Strategies to develop peripheral nerve, innervated
tissue and neurovascular in vitro platforms

Afonso Malheiro



Maastricht University



MERLN Institute

ISBN/EAN: 978-94-6423-296-7
Cover art by Observ (Pedro Pereira)

Getting wired:
Strategies to develop peripheral nerve, innervated tissue
and neurovascular in vitro platforms

To obtain the degree of Doctor at Maastricht University,
on the authority of the Rector Magnificus Prof. dr. Rianne M. Letschert
in accordance with the decision of the Board of Deans,
to be defended in public on Friday 11th June at 14.00 hours

by

Afonso Malheiro

Supervisor:

Prof. Dr. Lorenzo Moroni

Co-supervisor:

Dr. Paul Wieringa

Assessment committee:

Prof. Dr. Roman Truckenmüller, chairman

Prof. Dr. Anthony Metcalfe, University of Birmingham

Prof. Dr. Marc van Zandvoort

Prof. Dr. Martijn van Griensven

Prof. Dr. Martijn Malessy, Leiden University MC

Table of contents

Chapter	Page
1. General introduction	7
2. Patterning vasculature: the role of biofabrication to achieve a multicellular ecosystem	31
3. A three-dimensional biomimetic peripheral nerve model for drug testing and disease modelling	71
4. 3D culture platform of human iPSCs-derived nociceptors for peripheral nerve modelling and tissue innervation	121
5. Investigating the effect of phosphodiesterase-4 (PDE4) inhibitors on Schwann cells myelination in a 3D regeneration model and in a hyperglycemia model	169
6. Development of a human model of innervated skin for <i>in vitro</i> testing	203
7. Exploring the neurovascular axis: endothelial cell interactions within a biomimetic <i>in vitro</i> platform	233
8. General discussion	279
9. Valorization	289
Other	
Summary	297
Acknowledgements	300
Biography	302
Publications related to this thesis	303

Chapter 1

General Introduction

Afonso Malheiro, Paul Wieringa, Lorenzo Moroni

Department of Complex Tissue Regeneration, MERLN Institute for Technology-Inspired Regenerative Medicine, Maastricht University, The Netherlands

Abstract

Nerves and blood vessels (BVs) establish extensive arborized networks to innervate tissues and deliver oxygen/metabolic support. Developmental cues direct the formation of these intricate and often overlapping patterns, which reflect close interactions within the peripheral neurovascular (NV) system. Besides the mutual dependence to survive and function, nerves and BVs share several receptors and ligands, as well as principles of differentiation, growth and pathfinding. NV interactions are maintained in adult life and are essential for certain regenerative mechanisms, such as wound healing. In pathological situations, e.g. diabetes mellitus type II, the NV system can be severely perturbed and become dysfunctional. Unwanted neural growth and vascularization is also associated with the progression of some pathologies, such as cancer and endometriosis. In this review, we describe the fundamental NV interactions in development, highlighting the similarities between both networks and wiring mechanisms. We also describe the vascular and neural network contributions to regenerative processes and potential pathological dysfunctions. Finally, we provide an overview of current *in vitro* models used to replicate and investigate the NV ecosystem, addressing present limitations and future perspectives.

The peripheral neurovascular system

With the evolution of ever larger multicellular organisms, distinct tissues began to form with increasing complexity, eventually creating distinct organs that were capable of performing highly specialized tasks. Throughout this process, the development and evolution of the vascular and nervous system was key. The vascular network covered the organs, providing oxygen and nutrient supply and removing the metabolic waste. Similarly, the nervous system extended branches that connected target organs to the central nervous system (CNS), establishing communication and permitting coordination of tasks^{1,2}. The result was the formation of extensive and arborized patterns of nerves and blood vessels (BVs), with significant overlap between the two networks (fig. 1a-c). The mutual dependence of nerves and blood vessels (BVs) also contributed to this neurovascular (NV) alignment, since nerves require vascularization to ensure oxygen and metabolic support (fig. 1d), whereas large BVs need innervation to regulate vasodilation and vasoconstriction^{3,4}.

This chapter will cover the peripheral NV system, highlighting developmental aspects, interactions during regeneration and NV dysfunction in pathological situations. Finally, current *in vitro* models of peripheral NV units will be discussed.

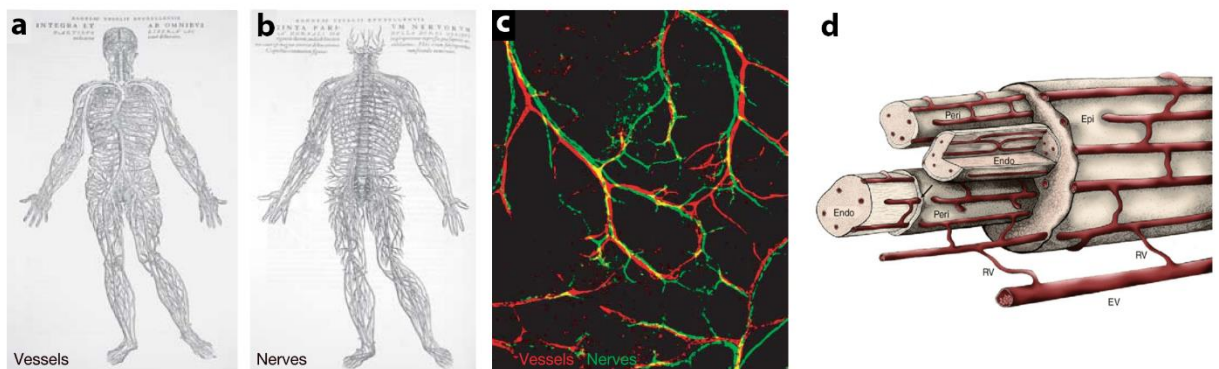


Figure 1. The neurovascular network. Illustrations of the vessel (a) and nerve (b) network drawn by Andreas Vesalius, a 16th-century Flemish anatomist and physician. (c) Example of vessels (red) and nerves (green) following a similar path. (d) Illustration of the vasa nervorum, showing how vessels cover the peripheral nerves. (a,b,c) were extracted from Carmeliet et al. (2005)¹ and (d) was extracted from Mizisin et al. (2011)⁵.

Reaching the target

The formation of both vascular and nervous system is tightly controlled by a series of developmental cues that ensure the formation of a complex and highly stereotypical mature network. In the evolutionary history, BVs arose later than nerves, but co-adopted the same architectural principals and molecular mechanisms as those responsible to wire up the nervous system⁶. As a consequence, both tissues share several signaling pathways and principles of growth, differentiation, organization and pathfinding^{6,7}. During embryonic development, vasculature is formed at an earlier stage than nerves, when mesoderm-derived angioblasts differentiate and coalesce to form the primary vascular plexus, in a process termed vasculogenesis⁸. Subsequent vessel formation occurs mainly via sprouting angiogenesis, as the vascular network extends and remodels to cover avascular regions⁹. The peripheral nerve system (PNS) arises from the trunk neural crest, as neurons of different subtypes send neurite projections in a spatially and temporally orchestrated manner¹⁰. Arising from the CNS, parasympathetic nerve fibers project towards most organs to innervate them. From the dorsal root ganglia and sympathetic ganglia, sensory and sympathetic neurons, respectively, extend axons towards their targets, while motor neurons from the ventral spinal cord send projections to the periphery¹¹. To vascularize and innervate tissues, BVs and nerves make use of similar pathfinding mechanisms. Sprouting BVs designate a specialized endothelial cell as “tip cell” to sense the environment and pave the way, while trailing “stalk cells” proliferate and form capillary lumens to allow blood flow. In a similar fashion, neuron growth cones project numerous filopodia that actively extend and retract in response to the environment^{4,7}. Both tissues manage to travel to distant targets by dividing their path into smaller segments bounded by intermediate targets, thus simplifying the navigational task^{1,6}. To help in this, and to promote growth and survival, there is a plethora of signals and respective receptors that are shared between BVs and nerves (table 1). These signals can act at a short range when matrix-bound or at a long range when freely soluble, and can either provide an attractive or a repulsive cue^{2,7,9} (fig. 2). As an example of common signals, nerve growth factor (NGF) is a known neurotrophic factor but can also exert a positive influence on endothelial cell (EC) proliferation, survival and migration^{12,13}. Similarly, the vascular endothelial growth factor (VEGF) family is a well-characterized inducer of vasculogenesis and angiogenesis, but evidence has shown it can also promote neurogenesis, neuroprotection and neural growth¹⁴. Furthermore, four families of classic axonal guidance cues — ephrins, netrins, slits and semaphorins — were discovered to induce vessel guidance as well (table 1). These cues can stimulate attraction or repulsion, depending on receptor configuration or activity of secondary messengers^{7,9}. Besides this developmental stereotypical configuration of larger BVs and nerves, target tissues also regulate vessel sprouting and axonal arborization. Hypoxic tissues secrete VEGF to recruit

vascular supply, whereas target tissues devoid of synaptic input secrete neurotrophic factors, such as NGF, to attract innervation. In both cases, once the target tissue is sufficiently supplied with oxygen or electrically stimulated, the production of growth factors (GFs) by the target tissue subsides¹.

Ligand	Form	Receptor	Type of cue	
			<i>Nerves</i>	<i>Blood vessels</i>
<i>Ephrin</i>	Cell membrane-bound	<ul style="list-style-type: none"> ▪ Eph 	Attractant ¹⁵ / Repellent ¹⁶	Attractant ¹⁷ / Repellent ¹⁸
<i>Netrin</i>	Matrix-bound	<ul style="list-style-type: none"> ▪ Deleted in Colorectal Cancer (DCC) ▪ Unc5 	Attractant ^{19,20} / Repellent ^{19,20,21}	Attractant ²² / Repellent ²³
<i>Slit</i>	Matrix-bound	<ul style="list-style-type: none"> ▪ Roundabout (Robo) 	Attractant ²⁴ / Repellent ^{25,26}	Attractant ²⁷ / Repellent ²⁴
<i>Semaphorin</i>	Diffusible	<ul style="list-style-type: none"> ▪ Plexin ▪ Neuropilin (Nrp) 	Attractant ²⁸ / Repellent ²⁸	Attractant ²⁹ / Repellent ^{29,30}

Table 1. Common signals and receptors shared by nerves and blood vessels and their influence on pathfinding (attraction or repulsion).

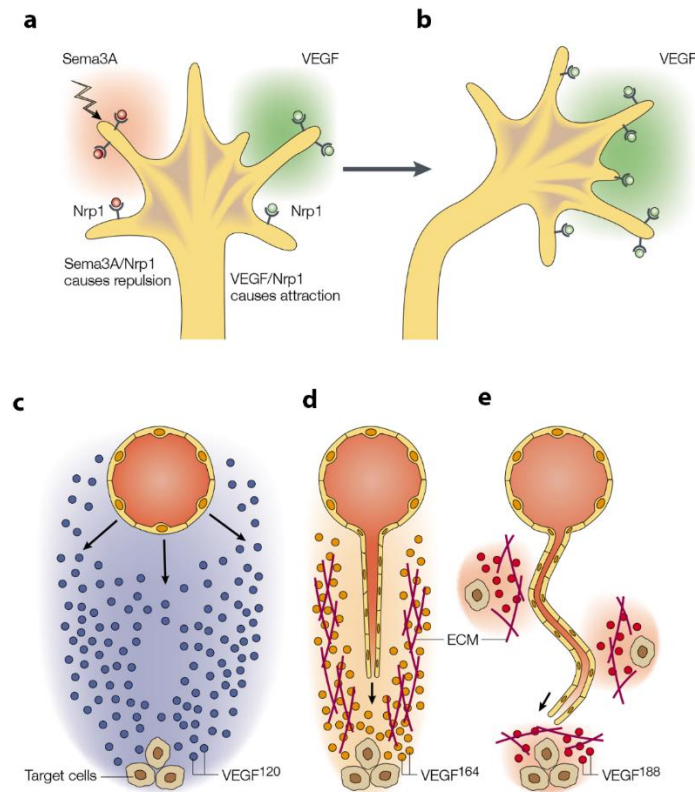


Figure 2. Pathfinding mechanisms of nerves and BVs. (a,b) Attractive and repulsive cues determine the direction of axons and sprouting vessels. (a) Both axons and endothelial cells (ECs) express Nrp1 at their filopodia, to which Sema3A and VEGF bind. Sema3A causes repulsion whereas VEGF attracts the filopodia. (b) As a result, axons or ECs move towards the VEGF gradient. (c-e) Role of VEGF signaling in vessel branching. (c) The soluble VEGF120 does not bind to the matrix and consequently fails to provide long-range guidance. (d) The VEGF164 isoform provides both short-range matrix guideposts and long-range attraction gradients that allow the sprouting vessel to reach the target efficiently. (e) The VEGF188 isoform bind only to matrix and thus does not provide any long-range attraction, causing the sprout to be misguided over short distances. (a-e) were extracted from Carmeliet et al. (2003)² after permission.

The NV wiring

From embryonic development to adulthood, the NV networks maintain an ordered configuration, where nerves and BVs often follow a convergent path. To arrive at this composition, two distinct mechanisms are known to be in place. One is the existence of a central mediator that attracts and directs nerves and BVs organization³¹. This is observed in the mouse whisker pad, which displays a double ring structure around each follicle, composed

of nerves (inner ring) and BVs (outer ring). In mutant mice, lacking trigeminal neurons and thus lacking nerve rings, vessel rings still form normally. Similarly, in mice with deformed vessel rings, nerve rings are able to form normally. These findings indicate the existence of a central and independent patterning mechanism³². The other patterning mechanism results from the direct influence of a tissue on the other. A well-characterized example of this occurs in the developing limb skin, where cutaneous nerves invade the primary capillary plexus and induce nerve-vessel alignment^{33,34}. The recruitment of vessels to the vicinity of nerves, occurs via secretion of Cxcl12 by Schwann cells (SCs) and neurons, which attracts Cxcr4⁺ ECs. Following NV alignment, VEGF-A secreted by the SCs and neurons induces arteriogenesis, marked by upregulation of ephrinB2 and Nrp1. Nrp1 upregulation further leads to increased sensitivity to VEGF-A, which helps to maintain this nerve-artery congruency (fig. 3a-d and f-m). In mutant mice lacking sensory and motor nerves, the vessels exhibited an altered pattern and defective arterial differentiation. Furthermore, in mutants with abnormal nerve patterns, remodeled arteries aligned with these nerves and could undergo arterial differentiation¹¹. Taken together, these observations indicate a direct influence of nerves on BVs. Conversely, a direct influence of BVs on nerve patterning also occurs. This is the case for sympathetic nerve alignment with arteries, as observed in the skin. Smooth muscle cells cover the arteries and secrete artemin, which acts as a neurotropic factor, attracting sympathetic fibers to ride along the arterial (and sensory fiber) template (fig. 3e). Because artemin secretion gradually shifts distally, a local growth factor gradient is perpetuated to guide sympathetic fibers as they grow towards the target organ, resulting in NV alignment^{2,11,35}.

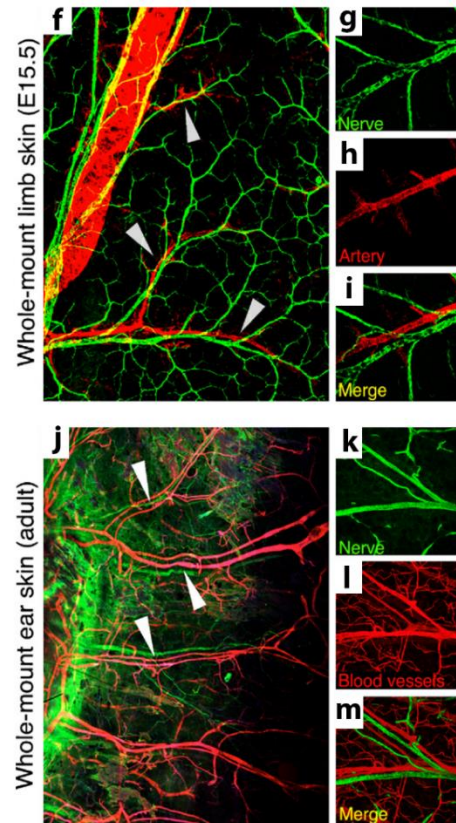
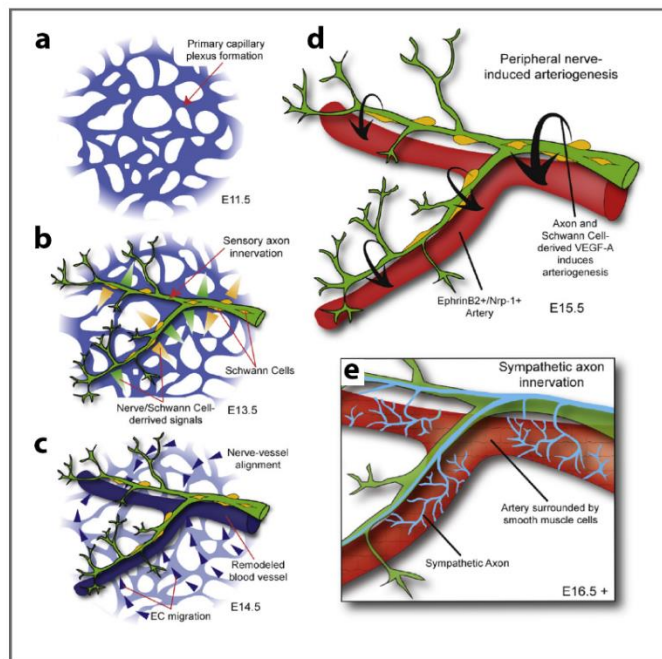


Figure 3. a-e: Mechanisms of NV patterning within the developing limb skin. a) Formation of a primary capillary plexus via vasculogenesis at E11.5. b) Sensory axons accompanied by Schwann cells invade the vascular plexus at E13.5 and secrete signals (e.g. Cxcl12) to pattern the vessels. c) In response to those signals, the vessels align with the nerves. d) BVs aligned with the nerves undergo arteriogenesis in response to nerve and Schwann cell-derived VEGF-A, upregulating ephrinB2 and Nrp-1. e) Sympathetic axons innervate the limb skin, using the BVs and sensory nerves as a template for migration. Sympathetic innervation of the arteries is necessary to regulate vessel tone. f-m: NV congruency in the embryonic and adult skin. f-i: NV alignment on E15.5 mouse embryo skin. Whole-mount immunofluorescence micrograph showing the alignment of nerves (green) and arteries (red). j-m: NV alignment is maintained in the adult phase. Whole-mount ear skin preparations from an adult mouse, showing nerves (green) and BVs (red) following parallel paths. All images were extracted from James et al. (2011)¹¹, after permission.

NV dysfunctions

Damage to the PN tissue can occur in diverse situations, from localized traumatic insults (nerve crush, compression, stretching or transection)³⁶, to systemic disorders, such as in Guillain-Barré syndrome or diabetes mellitus type II³⁷. Because of the close interlink between nerves and BVs, peripheral neuropathies often result in NV dysfunctions.

The PN contains an abundant and redundant vascular supply (fig. 1d). Thus, if the blood flow is partially interrupted due to an artery block (e.g. atherosclerosis, thrombosis, etc.), ischemia can still be prevented³⁸. However, in the eventuality of complete blood flow interruption, ischemia ensues and can provoke axonal conduction block and distal axonal degeneration. Ischemia can also arise after nerve damage if regeneration is incomplete, resulting in chronically denervated nerve stumps. In these situations, blood flow is typically reduced as a result of poor vascular regeneration due to an unfavorable environment (e.g. scarring or fibrosis) or due to lower metabolic demands because of axonal loss³⁸. Traumatic injuries, however, account only for a small fraction of neuropathy cases. In diabetes mellitus type II (DM), 50 % of individuals develop a neuropathy within time^{37,39}. DM can lead to profound alterations in the vascular, glial and neuronal components, with potential severe consequences affecting not only the PNs but also other organs such as kidneys (diabetic nephropathy), eyes (diabetic retinopathy) and skin (fig. 4a)⁴⁰. The most common pathogenic insults are dyslipidemia, hypertension, impaired insulin signaling, and most frequently hyperglycemia^{40,41}. Increased intracellular glucose levels activate the polyol pathway, which converts glucose to sorbitol via aldose reductase activity. Sorbitol accumulation leads to elevated osmotic pressure, oxidative stress and mitochondrial dysfunction that results in cellular damage^{41,39,42}. Myelinating SCs express aldose reductase and are consequently affected by hyperglycemia, which is manifested by de-differentiation to an immature phenotype, denoted by reduced myelin protein synthesis. Due to this, the myelin layer can reduce in thickness (demyelination) and develop morphological aberrations, such as infoldings, outfoldings and layer decompaction (fig. 4c), ultimately leading to lower nerve conduction velocities^{39,42,43}. Furthermore, SC dysfunction also includes reduced secretion of trophic factors, such as ciliary neurotrophic factor (CNTF) and desert hedgehog, which support neurons and ECs⁴¹. Similarly, ECs also express aldose reductase and suffer behavioral alterations. Most notably, the polyol pathway flux activates the proinflammatory and prothrombotic pathways, potentially leading to capillary membrane thickening and pericyte/smooth muscle cell dysfunctions that can result in loss of BV coverage (fig. 4e-l)^{41,44,45}. The end result is vessel leakage and reduced blood flow, which decreases the trophic and oxygen support to neurons and SCs, causing cellular damage.

Neural and vascular growth can also be directly associated to pathologies and provoke unwanted consequences. A major example is the role that vascularization and innervation play in the onset and development of tumors. The dependence of vascularization for tumor growth has been known for long, because as in any other tissue, cells that are farther than 200 μm from a BV will suffer hypoxia. Therefore, for tumors to grow beyond 1-2 mm, they need to recruit BVs, which is done through the secretion of angiogenic factors, such as VEGF, fibroblast growth factor (FGF), epidermal growth factor (EGF), hepatocyte growth factor (HGF) and platelet-derived growth factor (PDGF)⁴⁶. There are several mechanisms for tumor vascularization, including not only the classical sprouting angiogenesis, but also intussusception, vessel co-option, vasculogenesis, vasculogenic mimicry and lymphangiogenesis⁴⁷. The vascular network that is formed within tumors is vastly different from the one in normal tissues and that formed during wound healing. Normal BVs display an ordered, hierarchical and uniform architecture and appropriate mural cell coverage. Conversely, BVs in tumors exhibit a tortuous and irregular shape and their density is heterogeneous. Moreover, these BVs are leaky and lack appropriate pericytes/smooth muscle cell coverage^{8,46}. To prevent tumor growth, several strategies have been deployed, but most research has focused in inhibiting VEGF signaling^{46,47}. To this matter, anti-VEGF antibodies (e.g. bevacizumab) have been used clinically in combination with chemotherapy or cytokine therapy, but produced only a small increase in patient's survival^{8,46}. This resistance to VEGF inhibitors stems from the adaptation of tumors to other forms of vascularization, such as vasculogenic mimicry and vessel co-option from surrounding tissues⁴⁶. Additionally, other non-targeted angiogenic factors such as FGF and HGF can also attract BV ingrowth⁸. More surprisingly, nerves were also discovered to play a preponderant role in tumor initiation and progression. In various examples, such as in prostate, gastric and pancreatic cancer, nerves were found to stimulate tumor development, and tumor denervation via surgical or pharmacological techniques was effective in suppressing further growth⁴⁸. This influence of nerves derives from the release of neuropeptides (e.g. substance P) and neurotransmitters (e.g. acetylcholine) from nerve fibers surrounding the tumor and in the tumor, which are able to modulate metastatic cascades⁴⁹. Another important aspect of nerve-cancer relationship is that tumor cells also release neurotrophic factors. These signals lead to the activation of cancer cell survival, proliferation and invasion, but also stimulate the outgrowth of nerves into the tumor⁴⁸. Secretion of NGF, either in final or precursor (proNGF) form, has been detected in various forms of cancer (e.g. breast and prostate). Because of this, tumor suppression strategies using anti-NGF antibodies have been explored, with success in preventing tumor growth, metastasis and angiogenesis in breast cancer⁵⁰. Furthermore, the expression of axon guidance molecules, including different semaphorin and slit isoforms have also been detected in solid tumors, although their role in axonogenesis is still unclear.

Cancer is not the only pathology whose progression and symptoms are directly linked to NV tissue development. In endometriosis, an inflammatory condition affecting 5-10 % of women in reproductive age, whose exact origin is still unknown, a heavily vascularized and innervated ectopic tissue resembling the endometrium, develops in pelvic area sites (e.g. ovaries, ligaments, peritoneal surfaces, etc.). The formation of this tissue can lead to severe pain, the most common symptom⁵¹. Similarly to tumor vascularization, endometrial implant vascularization is proportionally related to its size and is triggered by an angiogenic switch from its hypoxic cell mass⁵². This angiogenic switch is denoted by the large release of angiogenic factors, such as VEGF, FGF and angiopoietin (Ang-1) by the endometrial implant but also by recruited activated macrophages and other inflammatory cells, including neutrophils, dendritic cells and regulatory T cells⁵³. Hormone stimulation, namely estrogen, is also responsible to stimulate vascularization. Again, sprouting angiogenesis is not the only vascularization mechanism, since vasculogenesis from circulating endothelial progenitor cells (EPCs) and inosculation of pre-established vascular networks can also provide a vascular supply to endometriotic lesions⁵³. In women without endometriosis, the functional layer of endometrium is absent of innervation. However, endometriotic lesions display a rich innervation of mainly sympathetic and sensory fibers, particularly nociceptors expressing the transient receptor vanilloid subtype 1 (TRPV-1)^{3,54}. Both the endometrial cells and the immune cells — macrophages, mast cells and neutrophils — establish an inflammatory environment rich in neurotrophic factors, containing NGF, brain derived growth factor (BDNF) and neurotrophin-3 (NT-3) that attract nerve fibers. These fibers are thought to contribute to the inflammatory environment by secreting pro-inflammatory molecules. At the same time, nociceptor fibers surrounding and infiltrated in the endometriotic implant become sensitized by this inflammatory milieu and convey this information to the CNS, where a pain sensation will be perceived^{3,55}. To alleviate pain, treatments must focus in targeting and arresting NV tissue development. Currently, there is no effective therapy for endometriosis-associated pain, and most research has focused in inhibiting angiogenesis, via VEGF blockers and receptor tyrosine kinase inhibitors³.

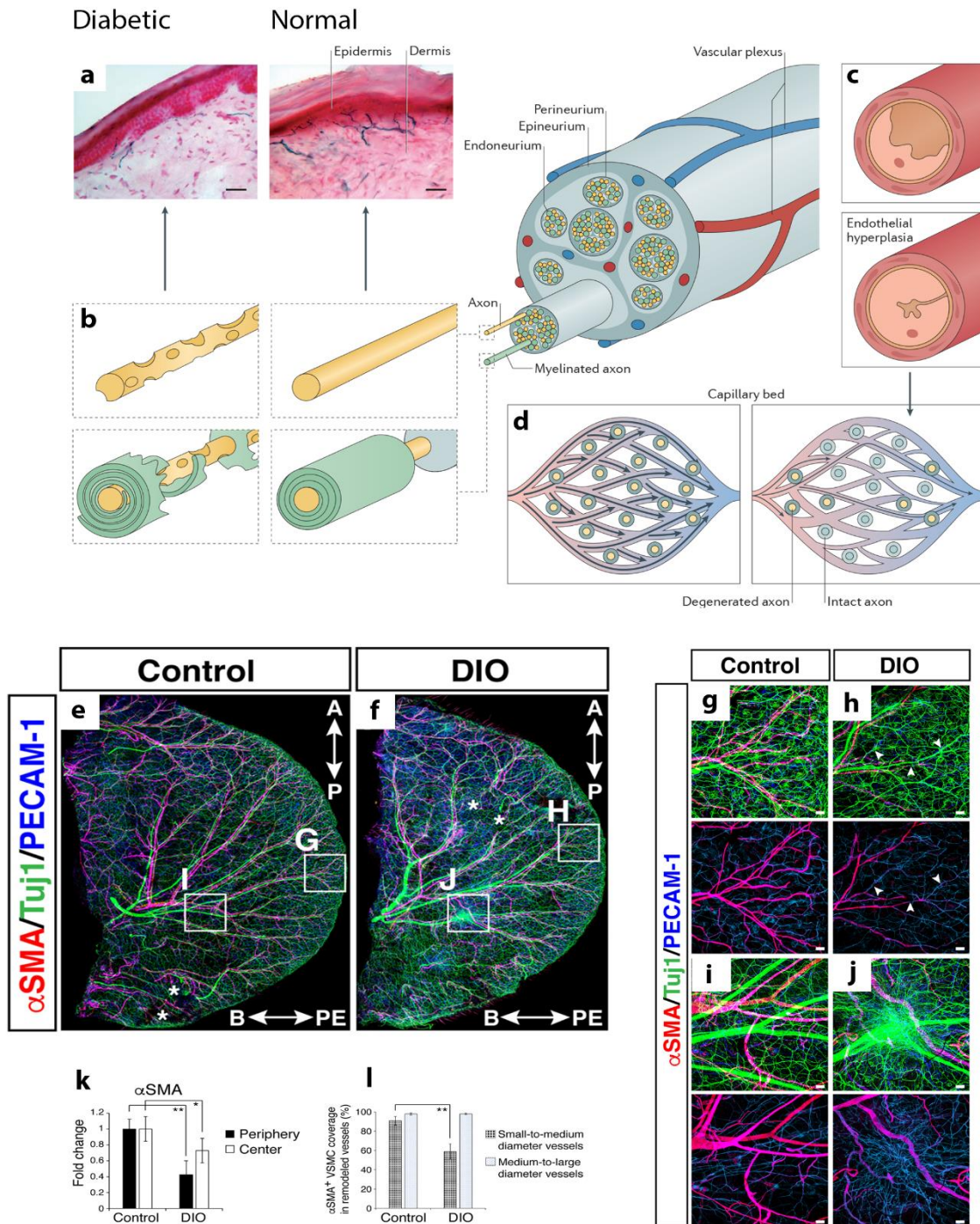


Figure 4. NV dysfunctions in DM. (a-d) Illustration of the different types of damage in DM neuropathies, involving axonopathy, schwannopathy and microvasculopathy. (a) Skin section showing epidermal nerve fiber loss in a diabetic patient (left panel) compared to a healthy one (right panel). Scale bar is 40 μ m. (b) Axonal and myelin degeneration resulting in nerve fiber loss. (c) Endoneurial capillaries from patients with DM. Top panel shows a capillary from a patient without DM neuropathy, and bottom panel shows a capillary from a patient with DM, in

which endothelial cell hyperplasia and basement membrane thickening led to capillary lumen size reduction. d) Narrowing of individual capillaries might not prevent blood from passing through the endoneurial capillary bed per se, but the resulting increase in velocity of blood prevents efficient oxygen extraction, causing hypoxia. (e-j) NV abnormalities in the ear skin of an adult mice with DM. Whole-mount immunostaining to BVs (blue, PECAM-1), axons (green, Tuj1) and vascular smooth muscle cells (α SMA) on control (e) and diabetic (f) mice. (g-j) Magnification of the box regions shown in (e,f) showing axonal abnormalities and lack of vascular smooth muscle cells coverage in diabetic mice. Asterisks indicate skin damage from the dissection and/or staining procedure and scale bar is 100 μ m. (k,l) Quantification of α SMA presence shows reduced mural cell cover in diabetic specimens. (a-d) was extracted and modified from Gonçalves et al. (2017)⁴¹ and (e-j) was extracted from Yamakazi et al. (2018)⁴⁵ after reprinting permission.

NV interactions in regeneration

Both the neural and vascular system possess the ability to react to damage and engage in a repair process to restore functionality. By sensing the environment, neural and vascular cells can alter their phenotype and enter in a regenerative mode that encompasses remodeling and regrowth until homeostasis is achieved. Understanding these repair mechanisms is critical for the development of smart therapies that can harness and potentiate the natural healing ability of tissues.

The events following a PN injury have been thoroughly investigated, and it is now clear that BVs play a crucial role in the success of PN regeneration. After a traumatic injury, damaged axons secrete the neuropeptides substance P (SP) and calcitonin gene-related peptide (CGRP) that promote enlargement of intraneurial BVs⁵⁶. Vasodilation coupled with the release of monocyte chemoattractant protein-1 (MCP-1) by SCs prompts the recruitment of resident and circulating macrophages⁵⁷. The arrival and differentiation of these cells is crucial for PN regeneration, as activated macrophages phagocytose the axonal and myelin debris that inhibit axonal regrowth (Wallerian degeneration)⁵⁸. Moreover, macrophages also secrete VEGF-A in response to hypoxia to induce neovessel formation, and secrete IL-1 to stimulate SC secretion of NGF and SC proliferation⁵⁹. The newly formed vessels are critical to ensure oxygen and metabolic support to proliferating SCs that organize in cellular tracks, termed bands of Büngner, to act as conduits for regrowing axons⁵⁶. In the situation of full nerve transection, BVs can also act as templates for Bands of Büngner. In a study by Cattin et al.⁶⁰, the authors discovered that macrophages invade the regenerating bridge, formed between the nerve stumps, and secrete VEGF-A in response to hypoxia. The latter is responsible for EC attraction and formation of a network of anisotropic vessels that span the bridge. Following

this, SCs use these vessels as tracks to proliferate and cross the bridge, taking regrowing axons along. In mice with an absent or compromised PN vasculature, nerve repair was compromised, confirming the dependence of nerve growth on vasculature.

These discoveries have propelled the development of new therapies that can improve the PN regeneration potential. Hobson et al. have demonstrated that supplementation of VEGF in a silicon nerve guide enhances vascularization, axonal regeneration and SC migration, in a dose-dependent manner⁶¹. In a different strategy, Fang et al.⁶² used a gene-delivery system to introduce plasmid DNA encoding for NGF and VEGF in rats with a crushed sciatic nerve, and observed a synergistic effect of both GFs compared to individual dosages. Furthermore, VEGF-only doses led to higher sciatic function index and thicker myelin sheaths than NGF-only doses. Because VEGF is also a neurotrophic factor, it is not clear whether the improvement of neural regeneration seen in both studies is a direct consequence of neovessel presence or VEGF-stimulation. Nevertheless, the pre-establishment of vascularization prior to nerve growth is now regarded as a critical and necessary step for effective PN repair. Due to this, several nerve grafts have been designed to stimulate vascularization⁶³. Earlier strategies included the use of nerve grafts with intact vasculature⁶⁴ or the use of artificial guides that were pre-vascularized *in vivo*⁶⁵. However, such strategies are limited due to the need of autologous transplantation. More recently, tissue engineering approaches have incorporated ECs within biomaterial nerve guides, and shown successful vascular and neural regeneration⁶⁶. Whether the nerve guide is pre-vascularized or permits a rapid *in vivo* vascularization, future repair strategies are now regarding vascularization as a central concern for efficient PN regeneration.

NV regeneration is not only important in the context of PN repair, but also to restore function to other organs. In the wound healing process, the precise and regulated participation of BVs and nerves is essential for an appropriate tissue regeneration. The first phase of this process is hemostasis, where BVs become constricted and a fibrin clot is formed in order to stop bleeding. The clot and the surrounding wound tissue releases pro-inflammatory cytokines and GFs, such as FGF, EGF and transforming growth factor (TGF)- β to attract inflammatory cells, thus commencing the inflammatory phase. During this phase, infiltrating neutrophils, lymphocytes and macrophages are responsible for clearing wound debris and inducing a reparative state that promotes vascularization, extracellular matrix (ECM) formation and re-epithelialization⁶⁷. In the hypoxic wound site, ECM fragments and activated macrophages release a myriad of angiogenic GFs, including VEGF, FGF (1 and 2) and TGF- β that trigger an angiogenic response⁶⁸. Recruited ECs become activated and secrete proteolytic enzymes (e.g. matrix metalloproteinases) that degrade the surrounding ECM in order to proliferate, migrate and form new capillaries^{69,70}. Following this, BVs are stabilized via mural cell recruitment and ECM deposition. Once the oxygen levels are restored, a remodeling phase

begins to promote vessel regression and replacement of the provisional ECM with a collagen type I-rich matrix^{68,70}.

The participation of nerves is also determinant for a successful and quick wound healing process. The skin is richly innervated by sensory and sympathetic fibers and defective innervation in neuropathies such as spinal cord injury or DM, can result in impaired wound healing⁷¹. Both the sensory and sympathetic fibers secrete several neurotransmitters and neuropeptides that have been shown to play vital roles and enhance the wound healing process⁷². For instance, the vasoactive intestinal peptide (VIP) and NGF stimulate re-epithelialization and angiogenesis; while the first promotes collagen deposition, the second promotes collagen maturation and remodelling⁷³. Sensory neurons, in particular, have been shown to accelerate skin re-epithelization in a wound healing model, via SP mediation⁷⁴. In animal models denervated of sensory fibers, wound healing was delayed and incomplete^{73,75}. SCs also aid in the regenerative process by differentiating to a repair phenotype and providing trophic support via paracrine signaling to non-neural cells at the wound site⁷⁶. The secretome of nerve fibers can directly influence skin cells, for instance by promoting proliferation of keratinocytes and fibroblasts. However, it can also indirectly contribute to the wound healing, by enhancing the angiogenesis process. As an example, SP stimulates vasodilation, vascular permeability and EC proliferation. Similarly, CGRP is a potent vasodilator and stimulates EC proliferation and wound contraction⁷¹. In sum, nerves and BVs interact with each other and directly with skin tissue to drive the wound healing mechanisms.

Contrary to amphibians, the ability to regenerate limbs is absent in adult mammals, with the exception of the distal digit^{77,78}. If the digit tip is removed distal to the nail bed, tissue regeneration is still possible via a process deeply influenced by nerves. Using a murine digit tip regeneration model, Johnson et al.⁷⁷ proposed that after damage, axons degenerate and their associated SCs undergo dedifferentiation. Dedifferentiated SCs localize to the regenerating blastema and start secreting GFs, particularly oncostatin M (OSM) and platelet-derived growth factor AA (PDGF-AA), which promote the proliferation of the blastema mesenchymal precursor cells. Blastema cell expansion is essential for the regeneration of tissues such as bone and dermis, and in the absence or dysregulation of SC activity, blastema expansion is insufficient to drive full multi-tissue regeneration. Once regeneration is complete, axons regrow into the newly formed tissue and associate with dedifferentiated SCs, which either differentiate to a mature phenotype or maintain their regenerative program.

In some situations, often related to disease-induced neuropathies, NV regeneration is not possible and the damage can be irreversible. If the underlying cause of neuropathy is not removed, spontaneous regeneration cannot occur and treatments are rendered futile⁷⁹. Despite the worldwide prevalence of diabetic neuropathy (DN), leading to nerve function loss, there is yet no cure for this disease⁷⁹. In DN, the skin is often affected and shows reduced

density of epidermal nerve fibers (ENFs), which causes loss of sensorial ability and impaired wound healing^{80,81}. Some research has focused in promoting functional recovery of denervated skin by stimulating the regrowth of ENFs. For this, therapies aim to protect intact neurons and induce the regrowth of previously pruned ENFs towards the right targets⁷⁹. Due to the chance of off-targets, systemic drug delivery systems have been abandoned in favor of localized therapies. For instance, local insulin treatments have shown improved skin innervation and conduction velocities in diabetic rodents^{82,83}. Similarly, transdermal delivery of GFs have also demonstrated potential in promoting re-innervation^{84,85}.

***In vitro* NV models**

The current understanding of NV interactions in a healthy or pathological state is still limited. As knowledge expands, it will be possible to develop new therapies and further improve existing ones.

To date, most research has relied on the use of animal models, mainly rodent models. These offer a great tool to observe the intricate NV patterns (fig. 3) and their dysfunctions in a disease context (fig. 4). However, the complexity of animal models, their high cost and their innate divergence from human anatomy/physiology, limits the translational potential of the findings^{86,87}. In this regard, *in vitro* NV platforms might be able to offer a better research tool that will allow to unlock the current enigmas. At the same time, the cell culture platform should allow to precisely control physiological conditions and perform controlled experiments, such as drug testing. However, the task of recreating a human 3D microenvironment with functional and mature nerves and BVs is not a simple one. At present, most research models have aimed to recreate the NV unit of the CNS⁸⁸, and only a few peripheral NV models have been reported. In the work of Grasman et al.⁸⁹, the authors established a two-dimensional (2D) co-culture of rat/chicken dorsal root ganglia (DRGs) with human umbilical vein endothelial cells (HUVECs), and showed that EC-derived BDNF enhances axonal growth (fig. 5a). Because HUVECs originate from the umbilical cord, a non-innervated tissue, this model relevance is limited. Yuan et al.⁹⁰ described a similar system, but containing human microvascular endothelial cells (HMVECs) as a vascular population instead. These cells originate from the skin, a richly innervated tissue, and thus constitute a more relevant cell source. The authors reported that co-cultures of HMVECs and DRGs led to higher overall cell viability and higher mRNA levels and secretion of VEGF and NGF, compared to single cultures. Both these models consisted of planar cultures not representative of the native architecture of nerves and BVs. While axons can still elongate in 2D, ECs require a 3D cell adhesive and degradable matrix (e.g. collagen or fibrin hydrogel) to form capillaries with lumens. Therefore, the upgrade to 3D cell cultures is essential for proper NV tissue engineering. Additionally, alternative sources of neurons, of

human origin instead (from stem cell populations), are preferred over animal-derived DRGs, which require recurrent animal sacrifice. Besides this, DRGs correspond to only one neuronal phenotype (sensory) and are composed of a heterogeneous cell population that needs to be purified to obtain pure neuron cultures. To overcome this, several stem cell differentiation protocols have been established to obtain functional and phenotypically distinct neuron populations^{91,92}. Aiming to address current limitations, the work of Osaki et al.⁹³ describes a NV microfluidic platform containing embryonic stem cell-derived motor neurons (ESC-MNs) and induced pluripotent stem cell (iPSC)-derived ECs within a collagen gel (fig. 5b-c). The presence of ECs was shown to improve neuron differentiation, axonal elongation and activity (measured by Ca^{2+} oscillation). On the other hand, neurons were able to influence vascular networks and promoted vessel enlargement. Still, this model presented some limitations regarding the fidelity of the engineered tissue. First, the absence of glial and mural cells is an oversimplification of the cellular milieu, precluding the formation of myelinated nerves and mature BVs. These support cells are indispensable for NV tissue function, participate in several biological processes (e.g. regeneration mechanisms), and are affected in diverse pathological situations. Second, the size of the generated tissues is only a small scale representation of the actual structures, which in their actual dimensions are subjected to different physical forces/parameters (e.g. oxygen tension).

Future efforts in modelling the peripheral NV unit must focus in achieving mature tissue morphologies and architectures representative of the complexity and dimensions of the human body. To date, most strategies report disorganized and sometimes flat neuron cultures with no glial cell support and vascular networks with immature morphologies, i.e. closed vessels and lacking mural cell stabilization. NV biofabrication improvements entail the generation of 3D neural tissues with anisotropic and myelinated axons emanating from a neuron cluster to replicate the peripheral nerve morphology and a 3D vascular network with open vessels stabilized by mural cells. Because the full replication of a whole PN is a demanding and impractical task due to its large size (can reach 1 meter), smaller segments can be reproduced as long as the individual unit sizes are attained.

Because the PN tissue is composed of phenotypically different populations, the generation of distinct and representative neuron models and evaluation of their properties and signaling pathways is also necessary. The ECM also plays a role in mediating or directly influencing tissue interactions, and thus the use of an ECM-like matrix that recapitulates *in vivo* chemical interactions and mechanical forces is crucial. The combination of NV models with perfusable systems that can deliver nutrients and drugs at physiological fluid flow conditions will also enhance the clinical potential of the model. This will permit the distribution of chemicals through the vessel network at native shear stress rates to defined regions, which will also allow a localized analysis of the tissue response. Besides this, microfluidic platforms can be coupled

to detectors for on-line measurements, such as oxygen detectors, and even connected to other microfluidic organ platforms of interest (e.g. liver model to investigate drug metabolism⁹⁴). Finally, due to the precise environmental control that is possible to exert on *in vitro* models, pathologies with multiple physiological imbalances such as DM that can produce simultaneously hyperglycemia and dyslipidemia, can be better studied by individually assessing each parameter's influence.

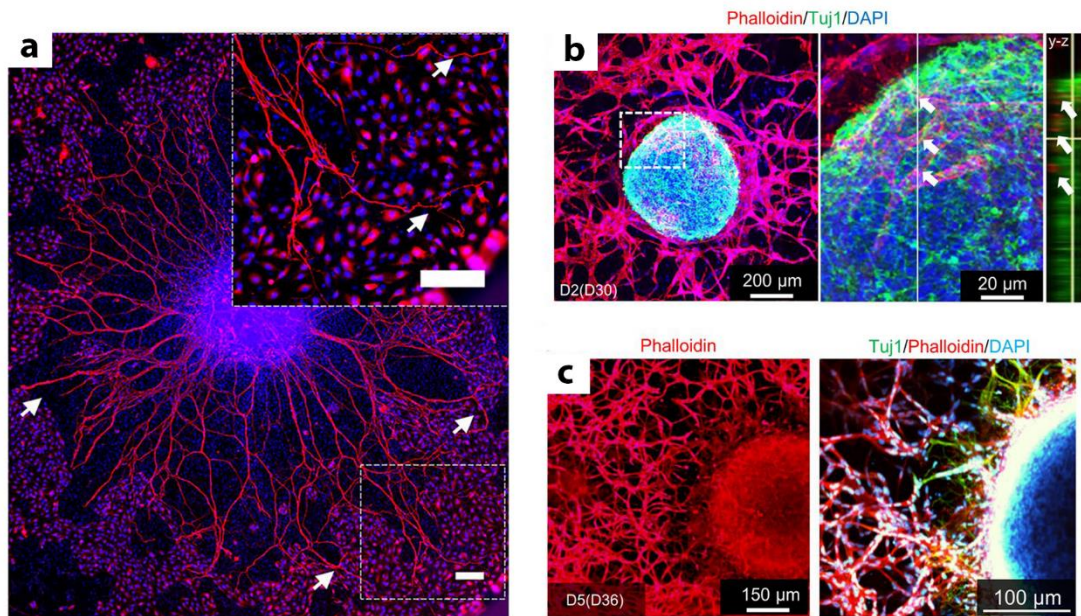


Figure 5. *In vitro* models containing NV tissue. a) 2D co-culture of HUVECs and a DRG. Axonal elongation was enhanced in the presence of HUVECs compared to samples without the vascular component. Immunostaining to Tuj1 (red). DAPI is shown in blue. Scale bar is 200 μm. Image extracted from Grasman et al.⁸⁹. b) 3D co-culture of ESC-MNs and HUVECs in a collagen gel. b) After 2 days of co-culture, the HUVECs formed well-connected microvascular networks surrounding the spheroid. c) After 5 days of culture, neurites begun to elongate and establish connections with the existing vasculature. Immunostaining to Tuj1 (green). Phalloidin is shown in red and DAPI in blue. (b,c) were extracted from Osaki et al⁹³.

Conclusion

Nerves and BVs establish intricate and convergent patterns throughout the body, as they provide support to most organs. Alterations of normal physiology can affect both tissues simultaneously and produce adverse and serious consequences. Currently, several outstanding questions remain regarding NV interactions: what control is exerted to orchestrate the spatiotemporal presence and quantity of guidance molecules that direct nerves and BVs growth and stereotypical pattern formation? Can this knowledge be harnessed to promote NV tissue regeneration? What about for tissue engineering? How are NV interactions maintained in adulthood? Are there other unknown cooperation mechanisms? What strategies can be

devised to selectively inhibit pathological NV tissue development? How can NV tissue damage be prevented or mitigated in disorders such as DM? To unravel these mysteries and develop therapies against currently untreatable maladies, much work is still needed. The use of functional and humanized 3D *in vitro* NV models are a promising tool to decode these complex interactions and improve preclinical research, but further development is still required to fully replicate the native organ complexity.

Outline of this thesis

In this chapter, **chapter 1**, we have provided a review about the peripheral neurovascular system, discussing biological interactions, associated disorders and the state-of-the-art of representative *in vitro* models. In **chapter 2**, we review the biofabrication techniques to include vascularization within tissue engineered constructs and discuss the current challenges in representing an organ's complexity. In **chapter 3**, the first experimental chapter, we lay the foundational bricks of this thesis and show the development of a 3D *in vitro* model of a peripheral nerve based on a neural cell line (PC12 cells) and demonstrate its applications in modelling axonal growth, assessing a compound neurotoxicity and recreating a diabetes scenario (hyperglycemia-induced damage), in which therapeutic drugs can be investigated. This 3D model was improved by substituting PC12 cells with iPSCs-derived nociceptors, and the establishment of this second version is described in **chapter 4**. Here, we also demonstrate neuron functionality testing and show again the ability to mimic hyperglycemia-induced damage and to conduct drug testing. In **chapter 5**, we used the previously established biomaterial platform and a SC model to evaluate the influence of PDE4 inhibitors, a class of drugs with shown benefits in CNS remyelination but never investigated for PN applications, on the myelination phenotype of Schwann cells in different contexts (regeneration and disease). Using the knowledge obtained in previous chapters, we developed a fabrication method to produce a fully human *in vitro* innervated skin model where drug testing via topical delivery can be performed, which is displayed in **chapter 6**. In the last experimental chapter, **chapter 7**, we combined the knowledge gathered in the first review chapters and via experimental findings (mainly chapters 3 and 4) to develop of a 3D *in vitro* model of peripheral neurovascular tissue. Additionally, we demonstrate a role for SCs as cells that can promote and stabilize vascular networks. In **chapter 8**, we provide a general overview of *in vitro* models within the research context and discuss the contents of this thesis and how they fit within the general panorama. Finally, in **chapter 9**, we discuss the potential valorization of this work regarding its societal impact and commercialization opportunities.

References

1. Carmeliet, P. & Tessier-Lavigne, M. Common mechanisms of nerve and blood vessel wiring. *Nature* 436, 193–200 (2005).
2. Carmeliet, P. Blood vessels and nerves: common signals, pathways and diseases. *Nat. Rev. Genet.* 4, 710–720 (2003).
3. Morotti, M., Vincent, K., Brawn, J., Zondervan, K. T. & Becker, C. M. Peripheral changes in endometriosis- associated pain. *Hum. Reprod. Update* 20, 717–736 (2014).
4. Eichmann, A. & Thomas, J. L. Molecular parallels between neural and vascular development. *Cold Spring Harb. Perspect. Med.* 3, 1–16 (2013).
5. Mizisin, A. P. & Weerasuriya, A. Homeostatic regulation of the endoneurial microenvironment during development, aging and in response to trauma, disease and toxic insult. *Acta Neuropathol.* 121, 291–312 (2011).
6. Zacchigna, S., Almodovar, C. R. De & Carmeliet, P. Similarities Between Angiogenesis and Neural Development: What Small Animal Models Can Tell Us. *Curr. Top. Dev. Biol.* 80, 1–55 (2008).
7. Raab, S. & Plate, K. H. Different networks, common growth factors: Shared growth factors and receptors of the vascular and the nervous system. *Acta Neuropathol.* 113, 607–626 (2007).
8. Potente, M., Gerhardt, H. & Carmeliet, P. Basic and therapeutic aspects of angiogenesis. *Cell* 146, 873–887 (2011).
9. Eichmann, A., Makinen, T. & Alitalo, K. Neural guidance molecules regulate vascular remodeling and vessel navigation. *Genes Dev.* 19, 1013–1021 (2005).
10. Newbern, J. M. Molecular Control of the Neural Crest and Peripheral Nervous System Development. *Curr Top Dev Biol.* 1–27 (2015)
11. James, J. M. & Mukoyama, Y. suke. Neuronal action on the developing blood vessel pattern. *Semin. Cell Dev. Biol.* 22, 1019–1027 (2011).
12. Troullinaki, M. et al. Nerve growth factor regulates endothelial cell survival and pathological retinal angiogenesis. *J. Cell. Mol. Med.* 23, 2362–2371 (2019).
13. Emanuelli, C. et al. Nerve growth factor promotes angiogenesis and arteriogenesis in ischemic hindlimbs. *Circulation* 106, 2257–2262 (2002).
14. Rosenstein, J. M., Krum, J. M. & Ruhrberg, C. VEGF in the nervous system. *Organogenesis* (2010)
15. Conover, J. C. et al. Disruption of Eph/ephrin signaling affects migration and proliferation in the adult subventricular zone. *Nat. Neurosci.* 3, 1091–1097 (2000).
16. Drescher, U. et al. In vitro guidance of retinal ganglion cell axons by RAGS, a 25 kDa tectal protein related to ligands for Eph receptor tyrosine kinases. *Cell* 82, 359–370 (1995).

17. Nakagawa, S. et al. Ephrin-B regulates the ipsilateral routing of retinal axons at the optic chiasm. *Neuron* 25, 599–610 (2000).
18. Füller, T., Korff, T., Kilian, A., Dandekar, G. & Augustin, H. G. Forward EphB4 signaling in endothelial cells controls cellular repulsion and segregation from ephrinB2 positive cells. *J. Cell Sci.* 116, 2461–2470 (2003).
19. Huber, A. B., Kolodkin, A. L., Ginty, D. D. & Cloutier, J. F. Signaling at the growth cone: Ligand-receptor complexes and the control of axon growth and guidance. *Annu. Rev. Neurosci.* 26, 509–563 (2003).
20. Barallobre, M. J., Pascual, M., Del Río, J. A. & Soriano, E. The Netrin family of guidance factors: Emphasis on Netrin-1 signalling. *Brain Res. Rev.* 49, 22–47 (2005).
21. Goodman, C. S. & Shatz, C. J. Developmental mechanisms that generate precise patterns of neuronal connectivity. *Neuron* 10, 77–98 (1993).
22. Kye, W. P. et al. The axonal attractant Netrin-1 is an angiogenic factor. *Proc. Natl. Acad. Sci. U. S. A.* 101, 16210–16215 (2004).
23. Lu, X. et al. The netrin receptor UNC5B mediates guidance events controlling morphogenesis of the vascular system. *Nature* 432, 179–186 (2004).
24. Kuan, H. W. et al. Biochemical purification of a mammalian slit protein as a positive regulator of sensory axon elongation and branching. *Cell* 96, 771–784 (1999).
25. Brose, K. et al. Slit proteins bind robo receptors and have an evolutionarily conserved role in repulsive axon guidance. *Cell* 96, 795–806 (1999).
26. Kidd, T., Bland, K. S. & Goodman, C. S. Slit is the midline repellent for the Robo receptor in *Drosophila*. *Cell* 96, 785–794 (1999).
27. Tong, M., Jun, T., Nie, Y., Hao, J. & Fan, D. The role of the SLIT/Robo signaling pathway. *J. Cancer* 10, 2694–2705 (2019).
28. Nakamura, F., Kalb, R. G. & Strittmatter, S. M. Molecular basis of semaphorin-mediated axon guidance. *J. Neurobiol.* 44, 219–229 (2000).
29. Sakurai, A., Doci, C. & Gutkind, J. S. Semaphorin signaling in angiogenesis, lymphangiogenesis and cancer. *Cell Res.* 22, 23–32 (2012).
30. Bagnard, D. et al. Semaphorin 3A-vascular endothelial growth factor-165 balance mediates migration and apoptosis of neural progenitor cells by the recruitment of shared receptor. *J. Neurosci.* 21, 3332–3341 (2001).
31. Andreone B, Lacoste B, G. C. Neuronal and Vascular Interactions. *Annu Rev Neurosci* 38, 25–46 (2015).
32. Oh, W. J. & Gu, C. Establishment of Neurovascular Congruency in the Mouse Whisker System by an Independent Patterning Mechanism. *Neuron* 80, 458–469 (2013).
33. Mukoyama, Y.-S., Gerber, H.-P., Ferrara, N., Gu, C. & Anderson, D. J. Peripheral nerve-derived VEGF promotes arterial differentiation via neuropilin 1-mediated positive feedback. *Development* 132, 941–52 (2005).

34. Li, W. et al. Peripheral nerve-derived CXCL12 and VEGF-A regulate the patterning of arterial vessel branching in developing limb skin. *Dev. Cell* 24, 359–371 (2013).
35. Honma, Y. et al. Artemin is a vascular-derived neurotropic factor for developing sympathetic neurons. *Neuron* 35, 267–282 (2002).
36. Menorca, R. M. G., Fussell, T. S. & Elfar, J. C. Peripheral Nerve Trauma: Mechanisms of injury and recovery. *Hand Clin.* 29, 317–330 (2013).
37. Feldman, E. L. et al. Diabetic neuropathy. *Nat. Rev. Dis. Prim.* 5, (2019).
38. Zochodne, D. W. & Zochodne, D. W. Regeneration and the vasa nervorum. *Neurobiol. Peripher. Nerve Regen.* 153–169 (2009)
39. Vægter, C. B. Peripheral Glial Cells in the Development of Diabetic neuropathy. *Front. Neurol.* 9, 1–9 (2018).
40. Rajchgot, T. et al. Neurons and microglia; a sickly-sweet duo in diabetic pain neuropathy. *Front. Neurosci.* 13, 1–17 (2019).
41. Gonçalves, N. P. et al. Schwann cell interactions with axons and microvessels in diabetic neuropathy. *Nat. Rev. Neurol.* 13, 135–147 (2017).
42. Hao, W. et al. Hyperglycemia promotes Schwann cell de-differentiation and demyelination via sorbitol accumulation and Igf1 protein down-regulation. *J. Biol. Chem.* 290, 17106–17115 (2015).
43. Cermenati, G. et al. Diabetes-induced myelin abnormalities are associated with an altered lipid pattern: Protective effects of LXR activation. *J. Lipid Res.* 53, 300–310 (2012).
44. Yan, C. et al. Dysfunction of the neurovascular unit in diabetes-related neurodegeneration. *Biomed. Pharmacother.* 131, 110656 (2020).
45. Yamazaki, T. et al. Whole-Mount Adult Ear Skin Imaging Reveals Defective Neuro-Vascular Branching Morphogenesis in Obese and Type 2 Diabetic Mouse Models. *Sci. Rep.* 8, 1–11 (2018).
46. Katayama, Y. et al. Tumor neovascularization and developments in therapeutics. *Cancers (Basel).* 11, (2019).
47. Hillen, F. & Griffioen, A. W. Tumour vascularization: Sprouting angiogenesis and beyond. *Cancer Metastasis Rev.* 26, 489–502 (2007).
48. Boilly, B., Faulkner, S., Jobling, P. & Hondermarck, H. Nerve Dependence : From Regeneration to Cancer. *Cancer Cell* 31, 342–354 (2017).
49. Kuol, N., Stojanovska, L., Apostolopoulos, V. & Nurgali, K. Role of the nervous system in cancer metastasis. *J. Exp. Clin. Cancer Res.* 37, 1–12 (2018).
50. Adriaenssens, E. et al. Nerve growth factor is a potential therapeutic target in breast cancer. *Cancer Res.* 68, 346–351 (2008).
51. Zondervan, K. T. et al. Endometriosis. *Nat. Rev. Dis. Prim.* 4, (2018).

52. Groothuis, P. G., Nap, A. W., Winterhager, E. & Grümmer, R. Vascular development in endometriosis. *Angiogenesis* 8, 147–156 (2005).
53. Laschke, M. W. & Menger, M. D. Basic mechanisms of vascularization in endometriosis and their clinical implications. *Hum. Reprod. Update* 24, 207–224 (2018).
54. Miller, E. J. & Fraser, I. S. The importance of pelvic nerve fibers in endometriosis. *Women's Heal.* 11, 611–618 (2015).
55. Morotti, M., Vincent, K. & Becker, C. M. Mechanisms of pain in endometriosis. *Eur. J. Obstet. Gynecol.* 209, 8–13 (2017).
56. Caillaud, M., Richard, L., Vallat, J. M., Desmoulière, A. & Billet, F. Peripheral nerve regeneration and intraneural revascularization. *Neural Regen. Res.* 14, 24–33 (2019).
57. Tofaris, G. K., Patterson, P. H., Jessen, K. R. & Mirsky, R. Denervated Schwann cells attract macrophages by secretion of leukemia inhibitory factor (LIF) and monocyte chemoattractant protein-1 in a process regulated by interleukin-6 and LIF. *J. Neurosci.* 22, 6696–6703 (2002).
58. Fansa, H., Schneider, W. & Keilhoff, G. Revascularization of Tissue-Engineered Nerve Grafts and Invasion of Macrophages. *Tissue Eng.* 7, 519–524 (2001).
59. Lindholm, D., Heumann, R., Meyer, M. & Thoenen, H. Interleukin-1 regulates synthesis of nerve growth factor in non-neuronal cells of rat sciatic nerve. *Nature* 330, 658–9 (1987).
60. Cattin, A. L. et al. Macrophage-Induced Blood Vessels Guide Schwann Cell-Mediated Regeneration of Peripheral Nerves. *Cell* 162, 1127–1139 (2015).
61. Hobson, M. I., Green, C. J. & Terenghi, G. VEGF enhances intraneural angiogenesis and improves nerve regeneration after axotomy. *J. Anat.* 197 Pt 4, 591–605 (2000).
62. Fang, Z. et al. Enhancement of sciatic nerve regeneration with dual delivery of vascular endothelial growth factor and nerve growth factor genes. *J. Nanobiotechnology* 18, 1–14 (2020).
63. Muangsanit, P., Shipley, R. J. & Phillips, J. B. Vascularization Strategies for Peripheral Nerve Tissue Engineering. *Anat. Rec.* 301, 1657–1667 (2018).
64. D'Arpa, S. et al. Vascularized nerve 'grafts': just a graft or a worthwhile procedure? *Plast. Aesthetic Res.* 2, 183 (2015).
65. Yapici, A. K., Bayram, Y., Akgun, H., Gumus, R. & Zor, F. The effect of in vivo created vascularized neurotube on peripheric nerve regeneration. *Injury* 48, 1486–1491 (2017).
66. Gao, H. et al. The use of fiber-reinforced scaffolds cocultured with schwann cells and vascular endothelial cells to repair rabbit sciatic nerve defect with vascularization. *Biomed Res. Int.* 2013, (2013).
67. Guo, S. & DiPietro, L. A. Factors affecting wound healing. *J. Dent. Res.* 89, 219–229 (2010).

68. Sorg, H., Tilkorn, D. J., Mirastschijski, U., Hauser, J. & Kraemer, R. Panta Rhei: Neovascularization, angiogenesis and nutritive perfusion in wound healing. *Eur. Surg. Res.* 59, 232–241 (2018).
69. Kumar, P. et al. Role of angiogenesis and angiogenic factors in acute and chronic wound healing. *Plast. Aesthetic Res.* 2, 243 (2015).
70. Tonnesen, M. G., Feng, X. & Clark, R. A. F. Angiogenesis in wound healing. *J. Investig. Dermatology Symp. Proc.* 5, 40–46 (2000).
71. Kiya, K. & Kubo, T. Neurovascular interactions in skin wound healing. *Neurochem. Int.* 125, 144–150 (2019).
72. Emmerson, E. Efficient Healing Takes Some Nerve: Electrical Stimulation Enhances Innervation in Cutaneous Human Wounds. *J. Invest. Dermatol.* 137, 543–545 (2017).
73. Article, R. The Role of Neuromediators and Innervation in Cutaneous Wound Healing. *Acta Derm Venereol* 2016; 587–594 (2016)
74. Blais, M. et al. Sensory Neurons Accelerate Skin Reepithelialization via Substance P in an Innervated Tissue-Engineered Wound Healing Model. *Tissue Eng. Part A* 20, 2180–2188 (2014).
75. Smith, P. G. & Liu, M. Impaired cutaneous wound healing after sensory denervation in developing rats: Effects on cell proliferation and apoptosis. *Cell Tissue Res.* 307, 281–291 (2002).
76. Parfejevs, V. et al. Injury-activated glial cells promote wound healing of the adult skin in mice. *Nat. Commun.* 9, 1–16 (2018).
77. Johnston, A. P. W. et al. Dedifferentiated Schwann Cell Precursors Secreting Paracrine Factors Are Required for Regeneration of the Mammalian Digit Tip. *Cell Stem Cell* 19, 433–448 (2016).
78. Farkas, J. E. & Monaghan, J. R. A brief history of the study of nerve dependent regeneration. *Neurogenesis* 4, e1302216 (2017).
79. Landowski, L. M., Dyck, P. J. B., Engelstad, J. & Taylor, B. V. Axonopathy in peripheral neuropathies : Mechanisms and therapeutic approaches for regeneration Axonopathy in peripheral neuropathies : Mechanisms and therapeutic approaches for regeneration. *J. Chem. Neuroanat.* (2019)
80. Intraepidermal nerve fiber density as a marker of early diabetic neuropathy. *Muscle Nerve* 35, 591–598 (2007).
81. Cadau, S. et al. Invitro glycation of an endothelialized and innervated tissue-engineered skin to screen anti-AGE molecules. *Biomaterials* 51, 216–225 (2015).
82. Greenberg, D. a & Jin, K. From angiogenesis to neuropathology. *Nature* 438, 954–959 (2005).
83. Singhal, A., Cheng, C., Sun, H. & Zochodne, D. W. Near nerve local insulin prevents conduction slowing in experimental diabetes. *Brain Res.* 763, 209–214 (1997).

84. Zheng, L. et al. TAT-Mediated Acidic Fibroblast Growth Factor Delivery to the Dermis Improves Wound Healing of Deep Skin Tissue in Rat. 1–13 (2015)
85. Benson, H. A. E. Transdermal Drug Delivery : Penetration Enhancement Techniques. 23–33 (2018).
86. Low, L. A., Mummery, C., Berridge, B. R., Austin, C. P. & Tagle, D. A. Organs-on-chips: into the next decade. *Nat. Rev. Drug Discov.* (2020)
87. Xiong, Z. Y. and H.-R. In vitro, Tissue-Based Models as a Replacement for Animal Models in Testing of Drugs at the Preclinical Stages. *Intech* 13 (2016).
88. Potjewyd, G., Moxon, S., Wang, T., Domingos, M. & Hooper, N. M. Tissue Engineering 3D Neurovascular Units: A Biomaterials and Bioprinting Perspective. *Trends Biotechnol.* 36, 457–472 (2018).
89. Grasman, J. M. & Kaplan, D. L. Human endothelial cells secrete neurotropic factors to direct axonal growth of peripheral nerves. *Sci. Rep.* 7, 1–12 (2017).
90. Yuan, Q., Li, J. J., An, C. H. & Sun, L. Biological characteristics of rat dorsal root ganglion cell and human vascular endothelial cell in mono- and co-culture. *Mol. Biol. Rep.* 41, 6949–6956 (2014).
91. Chambers, S. M. et al. Combined small-molecule inhibition accelerates developmental timing and converts human pluripotent stem cells into nociceptors. *Nat. Biotechnol.* 30, 715–720 (2012).
92. Osaki, T., Uzel, S. G. M. & Kamm, R. D. Microphysiological 3D model of amyotrophic lateral sclerosis (ALS) from human iPS-derived muscle cells and optogenetic motor neurons. *Sci. Adv.* 4, 1–16 (2018).
93. Osaki, T., Sivathanu, V. & Kamm, R. D. Engineered 3D vascular and neuronal networks in a microfluidic platform. *Sci. Rep.* 8, 1–13 (2018).
94. Deng, J. et al. Engineered liver-on-a-chip platform to mimic liver functions and its biomedical applications: A review. *Micromachines* 10, 1–26 (2019).

Chapter 2

Patterning vasculature: the role of biofabrication to achieve an integrated multicellular ecosystem

Afonso Malheiro[§], Paul Wieringa[§], Carlos Mota, Matthew Baker, Lorenzo Moroni

Department of Complex Tissue Regeneration, MERLN Institute for Technology-Inspired Regenerative Medicine, Maastricht University, The Netherlands

[§] These authors contributed equally to this manuscript.

Abstract

In regenerative medicine (RM), creating engineered tissues with functionally relevant vasculature is a critical goal. Recent technological advances in biofabrication and bioprinting have been reported which present significant steps toward achieving this aim. While many approaches to address this challenge derive from microfabrication techniques, progress in the material science field and 3D printing technologies fields have introduced exciting new possibilities for the creation of increasingly complex and functional vascularized tissues. Here, we provide a brief overview of the process of vascularization and its importance within the fields of RM and tissue engineering (TE). We give a brief synopsis of various strategies that have been reported to induce cell patterning for a designed vascular network within a TE construct, including material-based strategies, structural molding approaches, and direct cell-patterning techniques. As well as highlighting advances in the field, we discuss possible areas for further development; in particular, we advocate a combination of strategies to successfully overcome current limitations in developing functional artificial tissues. Overall, the technological innovations in new bioprinting approaches and complementary progress in materials development are recognized as having critical roles as TE matures towards broadly applicable, clinically relevant applications.

Keywords: Tissue Engineering, Vascularization, Multicellular Architectures, Bioprinting, Multi-scale Patterning

Introduction

The development and improvement of biofabrication techniques have enabled substantial advances in the field of RM. Three-dimensional (3D) biomimetic and patient-specific constructs can now be designed with the aim to fully restore a damaged tissue's functionality¹. While progress towards larger tissue replacements has been made, the inclusion of functional vasculature within these constructs to maintain cell viability is still a great challenge facing the biofabrication/TE field. For this reason, the clinical translation of lab-grown tissues remains limited to thin tissues, such as skin and bladder^{2,3,4,5}, which can survive through avascular diffusion of nutrients and oxygen. To transplant thick tissues, the engineered construct must be prevascularized to remain viable, functional, and quickly integrate with the host⁶.

Biofabrication technologies is a promising avenue to address the challenge of prevascularization⁷⁻⁹. Methods such as 3D printing of solid polymers, electrospinning, and stereolithography depend on scaffolds, from natural or synthetic origin, to serve as temporary support for seeded cells while the tissue is forming and maturing. Engineering vascularization within such TE constructs is complicated by the random manner in which cells are seeded and populate the scaffolds. Alternate approaches develop a modular construct by controlled assembly of smaller tissue building blocks. The motivation of these techniques is to mimic the native tissue architecture by directing cell organization, for instance through structures designed to guide cellular self-assembly. Examples of such technologies include 3D bioprinting, inkjet printing, and live cell lithography. Approaches that achieve vascular tissue patterning enable the creation and study of vascular networks through the spatial control over vessel formation.

Patterning capability is an asset not only for improved vascularization but also as we progress towards multicellular systems that can yield functional tissues or complex organ models. Constructs composed of functional cells, the parenchyma, and supporting cells, the stroma, can be sequentially assembled together with the endothelium in order to achieve the multilayered architectural context of an organ¹⁰. Additionally, nerve tissue could also be supplied to the construct, which would permit the study of neurovascular interactions. Considering that a full functional tissue is only achieved when innervated¹¹, the combination of a vascular and neural network in a single platform is a significant advance towards a true representation of an organ microenvironment.

Likewise, organoids can also greatly benefit from the presence of vasculature. These miniaturized versions of organs provide accurate anatomical replicas and constitute powerful tools for *in vivo* simulations, such as drug response. However, perfusion is required to emulate the dynamic mechanistic environment of cells¹². Furthermore, the maturation of progenitor cells used to generate organoids often requires blood flow for the transportation of biochemical

cues, such as paracrine signals, which are responsible for establishing communication between cells. In the case of renal organoids, for example, sustained circulation allows the cells to mature and gain functionality in terms of absorption, secretion, and filtration^{13,14}.

With these potential applications, strategies to engineer vascularization are a major research focus in the field of biofabrication. Advances in this area may thus address the current limitations of TE¹⁵, unlocking the viable fabrication of complex and large implants and contributing to our understanding of synergistic multicellular systems. Here we provide an overview of biofabrication approaches to create vascular networks as well as discuss the latest developments with a focus on patterning techniques. As summarized in Figure 1, we have categorized approaches to control the development of vascular networks as:

- **Material-induced patterning** — guidance of vessel growth through the selective presentation of physicochemical cues, such as cell adhesion peptides, growth factors, protease-sensible crosslinks and/or crosslinking density, to cells within a biomatrix;
- **Structure-induced patterning** — two-step biofabrication processes that consist of the construction of vessel-like architectures through additive or subtractive manufacturing and further lining with endothelial cells
- **Direct cell patterning** — use of micromolding or printing techniques to assemble vessels by deposition of vascular-specific cells into defined locations.

We also consider the limitations inherent to the abovementioned strategies and discuss recent research that aims at tackling these. Finally, some prospects regarding vascular integration within a multicellular ecosystem, multiple length scales needed for functional vascularization, and future expectations of organ development are also discussed.

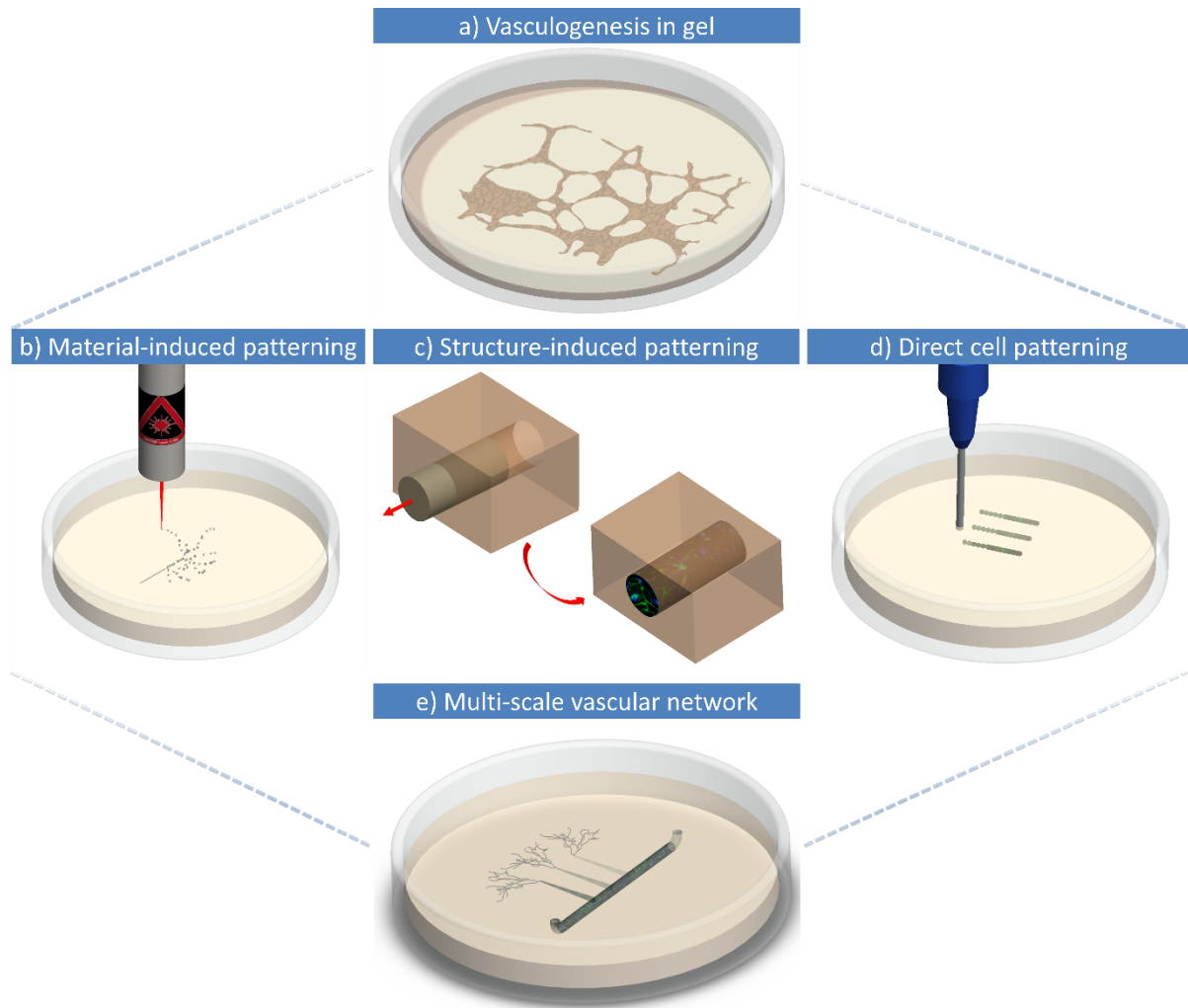


Figure 1. Overview of the classical biofabrication approaches to achieve and pattern vasculature in a TE construct. **a)** Spontaneous and uncontrolled self-assembly of vessels from randomly seeded endothelial cells within a bulk hydrogel. **b)** Photo-patterning of physicochemical cues, for instance, cell adhesion peptides (e.g. RGD), growth factors (e.g. VEGF) and protease-sensible crosslinks (e.g. MMP-sensible crosslinks) for vessel growth guidance. **c)** Vascular channel formation through the removal of a channel template within a hydrogel and subsequent endothelialization (e.g. perfusion with endothelial cells). **d)** Bioprinting of cellular spheroids into a biocompatible support (e.g. collagen hydrogel). The spheroids will fuse automatically and self-assemble into vascular structures. **e)** Combination of biofabrication approaches to produce a vascular network with multi-scale dimensions and clear perfusion accesses. The larger vessel with an inlet/outlet could be fabricated through structure-induced patterning techniques. Smaller vessels emanating from the parent vessel could be produced by direct cell patterning techniques and would provide a bridge to a microvessel pattern achieved through material-induced patterning strategies.

Biological Processes and Requirements

In the absence of a capillary network, an implant will rely on diffusional processes for the supply of oxygen and nutrients as well as the removal of metabolites. However, implants of clinically relevant size normally exceed the diffusion limit (approximately 200 μm), leading to the development of a necrotic core and failure to integrate with the host tissue^{16,17,8}. Therefore, the long-term survival of an avascular cell-laden construct strongly depends on rapid neovascularization, the formation of new blood vessels¹⁸. An alternative approach is to engineer a vascular network within the tissue implant, which requires a deep understanding of the well-orchestrated natural processes that lead to vessel formation and remodeling. A thorough description of these processes can be found in literature^{19,20,21,22}.

During early embryonic development, *de novo* formation of blood vessels is achieved through the differentiation of mesodermal progenitor cells in a process termed vasculogenesis. Initially, hemangioblasts located on the yolk sac form focal aggregations designated by blood islands. Within these structures, cells located in the periphery will differentiate into angioblasts, while those in the center will originate hematopoietic cells. Migrating angioblasts self-assemble into aggregates, proliferate, and finally differentiate to form the primary vascular plexus^{22,23}. Post-natal vasculogenesis can also occur during tumor growth or revascularization of damaged tissue, via circulating endothelial progenitor cells (EPCs). This subtype of CD34/VEGFR-2-positive bone marrow-derived angioblasts can be recruited to specific areas and differentiate for *in situ* vessel growth, in a process promoted by vascular endothelial growth factor (VEGF) and basic fibroblast growth factor (bFGF)^{22,24}.

In another neovascularization process, angiogenesis forms blood vessels from pre-existing ones; it is the main mechanism during embryogenesis (following creation of the vascular plexus) and adult life. New vessels can be formed from sprouting endothelial cells (sprouting angiogenesis) or through the splitting of other vessels (intussusceptive angiogenesis)^{23,24}. We focus on the former process here because it is more relevant to the integration of implants within the host vasculature. Sprouting angiogenesis initiates in response to pro-angiogenic signals that are secreted by local tissues according to their oxygen and nutrient demands. In hypoxic conditions, cells are induced to secrete VEGF, leading to endothelial cell activation and liberation from their matrix support via proteolytic degradation (through secretion of matrix metalloproteinases, MMPs)^{25,19}. Subsequently, the Notch pathway controls the specification of endothelial cells into tip or stalk cells via a Notch/DLL4 feedback loop¹⁹. Tip cells will lead the sprouting process by sensing their surroundings with filopodia, guiding the sprout via attractive or repulsive signals²⁶. Endothelial cells in close contact will then form a lumen by coalescence of intracellular vacuoles, and new vascular cords are created as soon as migrating neighbor tip cells fuse together. These new vessels remain immature and need to undergo further stabilization steps to become functional. First, perfusion

begins by re-establishing a quiescent endothelial phenotype and reshaping the new vessels connections, which are further strengthened by the formation of adherent and tight junctions. Next, maturation steps involve mural cell recruitment and extracellular matrix (ECM) deposition. Pericytes, attracted by the endothelial platelet-derived growth factor (PDGF), are recruited to capillaries and adhere to them via the angiopoietin 1 (ANG1) action¹⁹. For arteries and veins, smooth muscle cells (SMCs) are the stabilization effectors in a process promoted by transforming growth factor β (TGF- β)²⁷. To complete maturation, vessels are remodeled as a consequence of fluid flow shear stress, which leads to increased diameter and wall thickness (arteriogenesis)²⁴.

Due to this intricate sequence of events, both vasculogenesis and angiogenesis are slow processes. Thus, host endothelial cell invasion is often not fast enough to promote vascularization within a large implant before its failure¹⁸. For this reason, efforts have been made to initiate these vascularization processes within TE constructs prior to implantation to maintain viable tissue of a clinically relevant size. These endeavors, however, require a veritable source of endothelial cells. Mature cells, such as human umbilical vein endothelial cells (HUVECs) or human microvascular endothelial cells (HMVECs), have been widely researched for this purpose^{25,28,29,30}. These cells can be easily collected from the umbilical cord or by skin biopsy, respectively, and are relatively simple to culture, forming vascular networks both *in vitro* and *in vivo*³⁰. However, expansion of mature cells to sufficient quantity can be a limiting factor due to their low proliferation rate. In comparison, EPCs exhibit an increased proliferation potential and survival rate when compared to their mature counterparts^{30,31}. Late-outgrowth EPCs, also known as endothelial colony-forming cells (ECFCs), participate in tubulogenesis *in vitro* and have been shown to lead to an accelerated anastomosis in a co-culture with fibroblasts when compared to HUVECs³². Large expansion of these cells is a drawback, however, due to the high incidence of cytogenetic alteration³⁰. The other EPCs subtype, the early EPCs, do not form vascular networks but can also contribute to neovascularization through paracrine signals^{18,31}.

Vessel maturation and long-term stability are dependent on the addition of supporting cells to the system. Pericytes and SMCs are obvious cell choices, but others such as mesenchymal stem cells (MSCs) and fibroblasts, have been reported to display pericyte-like behaviour^{33,34}. Fibroblasts, mostly of dermal origin, have already been successfully co-cultured with HUVECs²⁵, HMVECs²⁹, and EPCs³², demonstrating their versatility. In comparison with SMCs and MSCs, fibroblasts (derived from human dermis and mouse 10T1/2 cell line) promoted the formation of a denser vascular network over a 28-day culture period with HUVECs³⁵.

Prior Art: Standard Approaches

To better understand vascular formation, numerous *in vitro* models have been developed (for a review, see Goodwin³⁶). Endothelial cells were initially grown on flat substrates of either tissue-culture plastic or on hydrogel surfaces and served to highlight important factors that simulate vasculogenesis and vascular morphogenesis, such as ECM components (i.e., laminins) and the pro-vascularization factors VEGF and bFGF³⁶. In lieu of the presence of growth factors, co-cultures with suitable mural cells have also been able to stimulate endothelial cells to form vascular networks³⁷.

Because two-dimensional (2D) substrates intrinsically limit the formation of 3D vascular structures, researchers began to encapsulate cells within hydrogels of reconstituted ECM proteins to better approximate the protein composition and 3D environment found *in vivo* (Figure 1, top panel). Proteinaceous gels made from collagen, fibrin, or Matrigel (a tumor-derived ECM) have been critical in initiating the vascularization processes within a 3D context. Synthetic hydrogels can also support vessel formation, but they must emulate natural ECM materials in terms of being cell adhesive, sufficiently soft, and susceptible to cellular remodeling to allow for cell migration and self-assembly of vasculature³⁸.

When *in vitro* vascularization is initiated with appropriate 3D environments, vascular formation is more comparable to that of the *in vivo* state³⁹. Furthermore, endothelial cells grown in 3D exhibit enhanced matrix-remodeling capabilities, a critical mechanism in angiogenesis⁴⁰. Compared to 2D substrates, 3D environments can also stimulate endothelial cells from a wider variety of sources to form capillaries⁴¹, and the resulting networks are stable for a longer period of time. However, similar to the 2D culture systems, endothelial monocultures undergo a more efficient capillary formation in the presence of angiogenic factors. Studies have shown that VEGF-releasing hydrogels⁴², hydrogels with covalently bound VEGF⁴³, and hydrogels with covalently bound VEGF peptide mimetics⁴⁴ are all capable of inducing vascularization in otherwise inert polyethylene glycol (PEG)-based systems. Strategies such as these, along with adhesive properties and MMP sensitivity, have been recently thoroughly reviewed⁴⁵.

Alternatively, vascular networks will spontaneously form when endothelial cells and appropriate mural cells are cultured together within the hydrogel, with the mural cells providing both angiogenic factors and, crucially, integrating with newly formed vessels to stabilize and further mature nascent vasculature^{33,46}. In addition to dissociated cells, the culturing of aggregates of cells or explanted tissues within hydrogels has enabled the study of angiogenesis, whereby vessels extend from the aggregate into the surrounding gel^{36,47}. Known as the sprouting assay, this is also used to study the process of anastomosis where sprouting vessels connect with one another. Again, the successful formation of sprouts requires either the addition of growth factors or the presence of other supporting cells types. These techniques to create 3D vascular *in vitro* models have also been applied to the vascularization of tissue

scaffolds as a means to improve the viability of implanted constructs^{48,49} or as cell-based angiogenic therapies for treatment of tissues that have become ischemic, such as the myocardium⁵⁰.

Similar to the 3D culture platforms described above, implantable tissues have been embedded within carrier hydrogels in combination with supporting cells, such as HUVECs and hMSCs, to encourage prevascularization and promote anastomosis^{51,52}. However, this approach lacks control over the size and distribution of vessel formation, risking delayed anastomosis of the tissue and reduction in delivery of oxygen and nutrients within the implant.

Importance of Cell Patterns

The strategies described above rely on the uncontrolled addition of endothelial and supporting cells as a way to induce vascularization within a TE construct, which poses some limitations. With all cells having a random starting position, vascular morphogenesis will be dependent on the spontaneous self-organization of endothelial cells²⁴. Under this condition, neovascularization seems to occur initially via the formation of endothelial clusters in a vasculogenic-like process, followed by extensive sprouting. Subsequently, vascular networks are formed as a combination of sprout anastomoses or cluster thinning²⁵. Although this results in vasculature, this is a time-consuming process that might prove too slow to supply the demands of a thick implant. Moreover, network formation occurs in a random manner and is characterized by non-uniform rate, length, diameter, and tubule orientation, which results in a network with a tortuous morphology, dense interconnectivity, and possibly distanced more than 200 μm from tissue-specific cells⁵³. This random network also does not offer any clear location for natural or surgical anastomosis, which may result in delayed perfusion²⁴. Finally, in a natural setting, the blood flows from macro- to microvessels, which allows the conservation of shear rate at bifurcations, as described by Murray's law. If the shear rate falls below a certain threshold, which can occur when parent and daughter vessels have the same diameter, thrombus formation can occur and perfusion is lost. This problem has been reported in a prevascularization strategy using unpatterned cell-embedded hydrogels⁵⁴.

To address some of these problems, recent efforts have focused on controlling cell localization as a strategy to improve neovascularization within a TE construct. Cell-patterning techniques bring several advantages. First, vessels can be assembled faster. Second, patterning can direct vessels to resemble the natural vascular tree in order to maintain a shear rate above the thrombogenesis onset. Third, patterning can recapitulate native vessel-tissue architecture (e.g., liver microarchitecture) and to ensure its distribution complies with the diffusion limit^{53,8}. Larger patterned structures, forming macrovessels, may provide clear locations for surgical anastomosis, thus leading to a faster perfusion of the implant and good host integration. Lastly, patterning techniques facilitate the combination of a bioreactor with a

TE construct, in which an inlet/outlet can be employed to dynamically seed cells, provide fluid flow within the construct (essential step for vessel maturation), and/or administer drugs until the point of implantation^{55,10}. The following sections will review different strategies to induce vessel patterning through materials modification, structural guidance, and direct cell deposition.

Material-Induced Patterning

The development of new materials has been pursued to direct and to spatiotemporally control the formation of vascular networks. Materials-based control of the vascular ingrowth at a molecular level remains one of the most promising patterning strategies. Towards this aim, several prominent materials-based strategies have been successfully employed to guide and direct vasculature formation in 2D and 3D space as depicted in Figure 2.

Currently, spatiotemporal control of vascularization is most commonly effected through patterns of growth factors, adhesive peptides (e.g., RGD), crosslink density and/or patterns of MMP-degradable crosslinks (Figure 1b)). As already discussed, growth factors such as VEGF have a direct influence on both vasculogenic and angiogenic processes. Therefore, their presentation to cells in pre-defined patterns can potentially provide control for region-specific cell differentiation and over sprouting direction. Sprouting angiogenesis anisotropy could also be harnessed with patterning of cell adhesion peptides and MMP-sensible crosslinks, which are both required for endothelial cell migration. For example, Leslie-Barbick and coworkers⁵⁶ demonstrated that the photo-patterning of covalently bound VEGF and RGD within a PEG diacrylate (DA) hydrogel network directed the formation of tubular-like endothelial cell organization with significant upregulation of angiogenic genetic markers. Exhibiting the ability of this approach to recapitulate complex architectures, Culver and coworkers⁵⁷ recorded the vasculature of several model tissues (retina, cerebral cortex, and heart) via confocal imaging and patterned into 3D hydrogels. Within an MMP-cleavable PEGDA network, covalently bound RGD was patterned via two-photon polymerization to match the architecture of the tissue vasculature. When this patterning of RGD was effected in hydrogels laden with HUVECs and 10T1/2s fibroblast-like cells, the co-culture organized into complex tubule-like networks that overlaid remarkably well with the biomimetic patterns (Figure 2a). In another work utilizing RGD patterning, Lee and co-workers⁵⁸ successfully transferred a VEGF-containing hydrogel capable of inducing vasculogenesis⁴² into a photo-patternable system capable of directing vasculogenesis *in vivo*. Utilizing a caged RGD sequence (photolabile 3-(4,5-dimethoxy-2-nitrophenyl)-2-butyl ester (DMNPB)), they were able to exhibit spatial control over the presentation of RGD and direct the migration of cells within the biomaterial (Figure 2b). This system allows real-time modification of the biomaterial; consequently, they showed that spatiotemporal regulation of RGD presentation within VEGF-containing hydrogels was able to

direct vascularization to specific locations of the hydrogel when implanted subcutaneously in mice.

In addition to the patterning of cell-adhesive molecules and growth factors, spatial control over the degradation of the material can also be utilized to guide vessel formation. In a study by Hanjaya-Putra and coworkers⁵⁹, acrylated hyaluronic acid (HA) was crosslinked with MMP-sensitive crosslinks and functionalized with RGD. In the absence of photopolymerization, cell-remodelable hydrogels were formed that allowed vasculogenesis, while photopolymerization created a non-degradable network that blocked vasculogenesis in both *in vitro* and *in vivo* models. Both hydrogels allowed vacuole and lumen formation; however, the photocrosslinked hydrogel did not allow branching, sprouting, or network formation. By photopolymerizing sections of a hydrogel in the presence of a mask, controlled and directed angiogenesis from ECFCs seeded on top of the hydrogels was demonstrated (Figure 2c). In a step towards selectivity of hydrogel remodeling for vascularization, research to determine the effect of MMP cleavage-site specificity on vascular ingrowth has shown promising results *in vitro*, yet all materials showed similar results *in vivo*⁶⁰.

While the “off/on” patterning of materials has been shown to enable directional vascularization within hydrogels, the utilization of gradients within materials is less explored. In a telling example, Turturro and coworkers⁶¹ fabricated PEGDA hydrogels with concurrent gradients of stiffness, susceptibility to MMP cleavage, and RGD density via a gradient polymerization technique. When compared to bulk polymerized hydrogels, those formed via gradient polymerization showed increased directionality of formed vascular networks when populated with HUVEC and human umbilical artery smooth muscle cell (HUASMC) aggregates (Figure 2d). Interestingly, in areas with the highest network density and highest concentration of RGD, vascularization was affected along the gradient of the material – vascularization occurred bidirectionally from high-to-low and low-to-high density areas. The exact mechanisms of this polarization are currently unknown, but follow-up research has shown that stable gradients of VEGF within hydrogels can consistently increase vascularization depth in *in vivo*-implanted hydrogels relative to non-gradient hydrogels⁶². Using multiphoton laser patterning, Aizawa et al. created a covalently bound gradient of VEGF within a hydrogel to direct angiogenic activity⁶³. In addition, it is well known that gradients of oxygen concentration are able to direct vascularization towards the hypoxic area⁶⁴. Gradients have consistently been shown to affect the vascularization propensity of hydrogels, but remain an underexplored and promising variable to consider when engineering instructive materials for tissue regeneration.

Much work remains to be done towards the spatiotemporal control of vascularization within tissue-engineered constructs and biomaterials. While the above approaches have made significant progress, specificity and selectivity are needed when attempting to recreate vasculature within complex tissue with multiple cell types. In this regard, gradients and/or

patterning of VEGF- or MMP-cleavable sites specific for vascularization may be the most promising, since vascularization networks will be competing with other cell types for adhesion and proliferation.

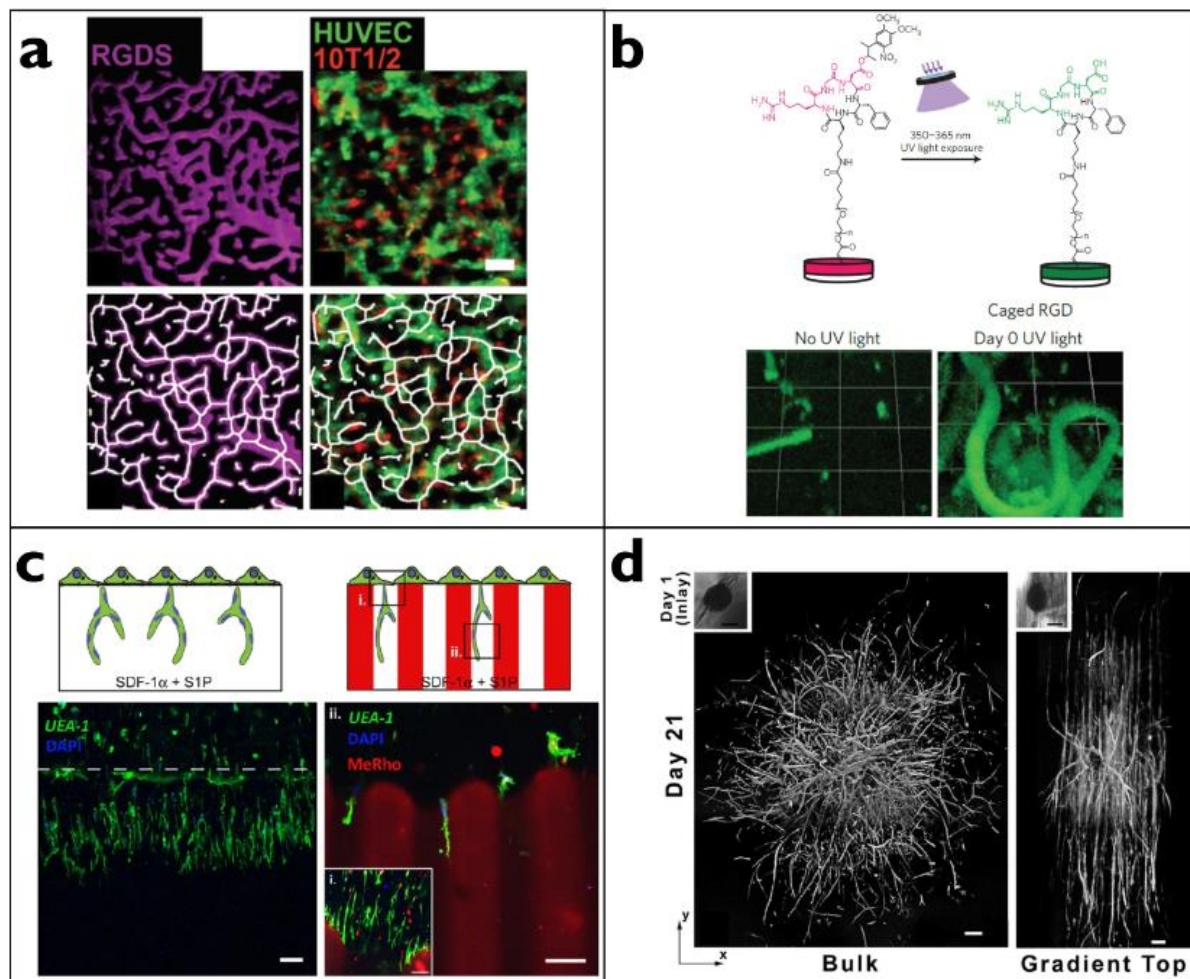


Figure 2. Shown are leading examples of materials based patterning of vascularization. **a)** Control over the covalent photopatterning of RGD within a degradable PEGDA based hydrogel has been shown to recapitulate biomimetic networks of vascularization⁵⁷. **b)** Through judicious use of photolabile protecting groups, the patterning of RGD sites within a hydrogel can be effected after fabrication of the hydrogel with success in directing vascular formation subcutaneously in mice⁵⁸. Additionally, patterning of MMP cleavable hydrogels **c)** with networks that are “permissive” and “non-permissive” to cellular remodelling has shown to be an effect strategy for the directing the vascularization of ECFC clusters⁵⁹. In an interesting example, complex gradients **d)** of MMP cleavable crosslinks, RGD concentration, and VEGF concentration have been shown to provide directionality to the growth of vascular networks in hydrogel materials. Surprisingly, these vessels are formed bidirectionally along the gradient i.e. high-to-low and low-to-high directionality⁶¹. Scale bars: **a)** 50 μm ; **c)** 100 μm ; **d)** 200 μm .

Structure-Induced Patterning

In order to engineer a vascular pattern, a number of techniques have evolved that produce structural patterns of microchannels, which provide a designed 3D architecture to localize endothelial cells and direct self-assembly of microvessel networks. The beginning of this 'structural patterning' can be traced to the field of microfluidics, which employs rigid microfabricated molds to transfer microchannel structures to softer polymeric materials and create well-defined microchannels; a brief review by Kim et al. provides an overview of the field⁶⁵. While microfluidic devices are attractive tools for vascularization studies (reviewed by Smith et al.⁶⁶), they are typically fabricated from polymers that do not mimic the native biological environment. This has prompted the integration of cell-laden hydrogels within microfluidic devices for an improved *in vivo* approximation. Initial strategies relied on vasculogenesis to create perfusable vessel networks⁶⁷⁻⁶⁹, enabling the study of nutrient transport⁷⁰ and also revealing that the application of flow itself can induce formation of vasculature⁷¹. Because these microvessels take time to develop and are random in nature, various techniques aim to accelerate the formation of designed vascular networks by incorporating guiding microchannel structures within biomimetic hydrogels. Such structures resemble the vessel lumens and once they are populated with an endothelial cell layer, a vascular network microarchitecture can be achieved much faster than through random cell self-assembly. Figure 3 provides an overview of these structure-induced patterning techniques, classified into three main categories in the discussion below: layer-by-layer film casting; removable template molding; sacrificial templating.

Layer-by-Layer Film Casting

The layer-by-layer approach casts a polymer solution onto microfabricated molds to produce a biocompatible hydrogel layer with microchannel structures. These layers are then placed on top of a flat substrate to form an enclosed, perfusable channel network. Numerous hydrogel materials have been used to create microfluidic devices, ranging from the bioinert alginate⁷² and agarose⁷³ (Figure 3a) to the intrinsically cell-adhesive fibrin and collagen⁷⁴. These studies report microchannel sizes from 20 μm ⁷⁴ to 1000 μm ⁷³, all of which have been shown to maintain the viability of cells encapsulated within the bulk of the hydrogel. This technique is particularly promising to recreate the *in vivo* setting of endothelialized vessels surrounded by mural cells. Starting with fibrin or collagen gels laden with mural cells, it has been shown that such microchannel systems can be seeded with endothelial cells to form a structurally patterned vessel-like organization.

Whereas traditional microfluidic materials can be bonded to a substrate to create a sealed perfusable system, hydrogel films must be either placed in a specialized apparatus that mechanically maintains a seal⁷⁵ or two gel surfaces must undergo localized depolymerization,

placed against one another, and then repolymerized to form a bond⁷²⁻⁷⁴. By employing a microfabricated mold, precise and intricate designs can be achieved of interconnected networks of microchannels with a wide range of dimensions. However, this micro-molding approach intrinsically limits this technique to planar microchannels designs, in contrast to the arborized 3D vessel structures observed in vivo. Furthermore, the cumbersome assembly and sealing of such a layer-by-layer hydrogel device restricts the broader application of this approach.

Removable Template Molding

Microchannels were first formed within a monolithic hydrogel construct by forming the gel around removable channel templates, such as wires or needles (Figure 1c). Acellular collagen gels formed in this way have been used as nutrient beds, with emulated blood flow to support multiple layers of cultured cells⁷⁶. This improved the viability of thick (~100 μm) layers of cells; endothelial cells from the cell layer were shown to migrate and surround the microchannels in a manner reminiscent of vasculature. Similar devices made of gelatin methacrylate (GelMA), a photo-crosslinkable collagen derivative, were shown to support both the encapsulation of fibroblasts within the gel and the seeding of endothelial cells within the microchannels for a more direct recreation of vascular structures⁷⁷.

The need to physically remove templates from fragile hydrogels typically requires these molding structures to be non-adherent, to be sufficiently large and strong enough to be manually extracted. To preserve the integrity of the encasing structure, most reported strategies employ channel templates with a straight shape such as rigid wires or needles with diameters ranging from 76 to 300 μm ^{77,78}. In place of a novel approach encapsulates flexible agarose 'wires', 250 to 1000 μm in diameter, within GelMA⁷⁹ (Figure 3b). Agarose does not adhere to the gelatin and, at these diameters, has sufficient strength to be manually extracted. Furthermore, channels with slight curvatures are also possible. In this system, osteoblasts were encapsulated within the GelMA and perfused endothelial cells formed a monolayer on the microchannel wall. José et al. recently reported vessels with 45°-angled bifurcations can also be patterned, by pulling out flexible polydimethylsiloxane (PDMS) rods from a collagen medium. These materials do not adhere to one another, permitting template removal and formation of an open channel network that can be further endothelialized.⁸⁰

While the formation of microchannels via the methods described can create endothelialized microchannel within a single, monolithic segment of hydrogel, this cannot easily realize an intricately designed, interconnected microchannel networks as achieved through film casting. Furthermore, the need to extract the removable molds restricts channel size and limits design complexity.

Sacrificial Molding

A versatile alternative molding strategy using a sacrificial template to create complex microchannel networks. In this approach, the template structure is fabricated, embedded within a hydrogel precursor, and later dissolved after the hydrogel is crosslinked. Bellan et al. reported on the formation of microchannels within a biocompatible gelatin hydrogel construct, achieved by embedding Shellac microfibers and later removing them via degradation in an ammonia bath⁸¹. A more recent example employs water-soluble polyvinyl alcohol (PVA) cast in a PDMS mold to form well-defined sacrificial templates⁸². This template was embedded within a non-aqueous hydrogel precursor to prevent premature PVA dissolution, followed by thorough washing with water and PBS after crosslinking to extract any non-aqueous solvents and the PVA template. A novel method of creating suitable sacrificial template was reported by Huling et al.⁸³, where the preserved vascular tissue of a mouse kidney was used to cast a polycaprolactone (PCL) template. This template was later coated with a layer of crosslinked collagen and the PCL was dissolved with acetone. While unique in its recreation of the arborized and multiscale vascular pattern, the final hollow 3D structure of thin collagen restricted cell seeding to the outside of the microchannel structures. In general, these approaches require harsh conditions to form the microarchitecture, limiting the introduction of cells to when device fabrication is complete.

To make sacrificial templates resilient to the aqueous conditions of cell-laden hydrogels, a few studies have taken water-soluble structures and coated them with a biocompatible water-insoluble layer of poly(DL-lactide-co-glycolide) (PDLGA)^{82,84}. Miller et al., in particular, have elegantly combined this approach with the 3D printing of an organized lattice of carbohydrate glass microfilaments, ranging in size from 150 to 750 μm ⁸⁴. While this study produced microchannels in cell-laden hydrogels and reported angiogenesis as endothelial cells within the channels invaded the surrounding hydrogel, a major drawback of this approach is the residual barrier of the PDLGA sheath on the microchannel perimeter. To create microchannel structures without the use of protective polymer layers or harsh dissolving agents, alginate can be used as the sacrificial material. In a recent report, a crosslinked alginate template was created, then disrupted using either sodium citrate or alginate lyase, resulting in 40- μm channels within a fibrin gel⁸⁵. This process retained the viability of embedded cells dissociated from cardiac tissue, with the endothelial cells of this mixed population observed to migrate and populate the lumen of the microchannels. Ethylenediaminetetraacetic acid (EDTA) has also been used to liquefy alginate and form microchannels from 20 to 500 μm in diameter with collagen, gelatin, or agarose⁸⁶ (Figure 3c). While this approach is capable of multilayered 3D microchannel architecture and supports the seeding of endothelial cells within the microchannels to form vascular-like structures, compatibility with embedded cells has not been shown.

Solubilizing agents are avoided altogether by using sacrificial templates that liquefy in response to temperature changes. One study formed and embedded a gelatin template at room temperature, later raising the temperature to 37°C to liquefy the gelatin and form microchannels⁸⁷. The embedding matrices reported include collagen, Matrigel, and fibrinogen, with fibroblasts hosted within the gels and endothelial cells perfused within the channels. The gelatin templates were fabricated with a PDMS mold, leading to microchannels ranging from 6 to 50 µm in width. Lee et al. have alternatively devised a poly(N-isopropylacrylamide) (PNIPAM) template strategy that requires cooling from 37°C to 32°C to liquefy and remove the template⁸⁸. This permits faster gelation at 37°C for hydrogels such as collagen or Matrigel, ensuring the viability and homogeneous distribution of encapsulated cells. While this work reported microchannels ranging from 35 to 100 µm in diameter and maintains the viability of encapsulated fibroblasts, no seeding of endothelial cells was described. This could be attributed to the highly random organization of the microchannel network produced, which could have hampered cell seeding.

To achieve a more designed capillary network, thermoresponsive materials such as Pluronic F-127 can be printed directly to fabricate a custom-designed sacrificial pattern with high-fidelity. These patterns can also be printed in combination with other cell-laden bioinks and further embedded within cell-adhesive hydrogels, such as GelMA⁸⁹. Upon cooling to 4°C, the pluronic material undergoes gel-to-fluid transition, resulting in an empty channel networks that offers precise locations for perfusion with endothelial cells. Applying this strategy, Kolesky et al. demonstrated its potential by fabricating a large and vascularized tissue construct. Here, the authors used 3D printing to pattern hMSCs in a lattice that was intercalated with Pluronic F-127. These structures were further encapsulated in a gelatin/fibrinogen mixture carrying human fibroblasts, followed by fugitive ink removal and endothelialization of the network (Figure 3d). To assess the vasculature functionality and develop a bone-like construct, osteogenesis-inducing biomolecules were perfused and the resulting expression of bone markers evaluated. The vascularized scaffolds stained positively for collagen type I and osteocalcin, and showed a much denser formation of mineralized matrix compared to the avascular control¹⁰.

Overall, sacrificial molding methods present a versatile approach to create microchannel structures, but are generally restricted to either planar or completely random networks. For this reason, advances in bioprinting techniques hold great promise in terms of improved 3D design capabilities and integration with additional tissues

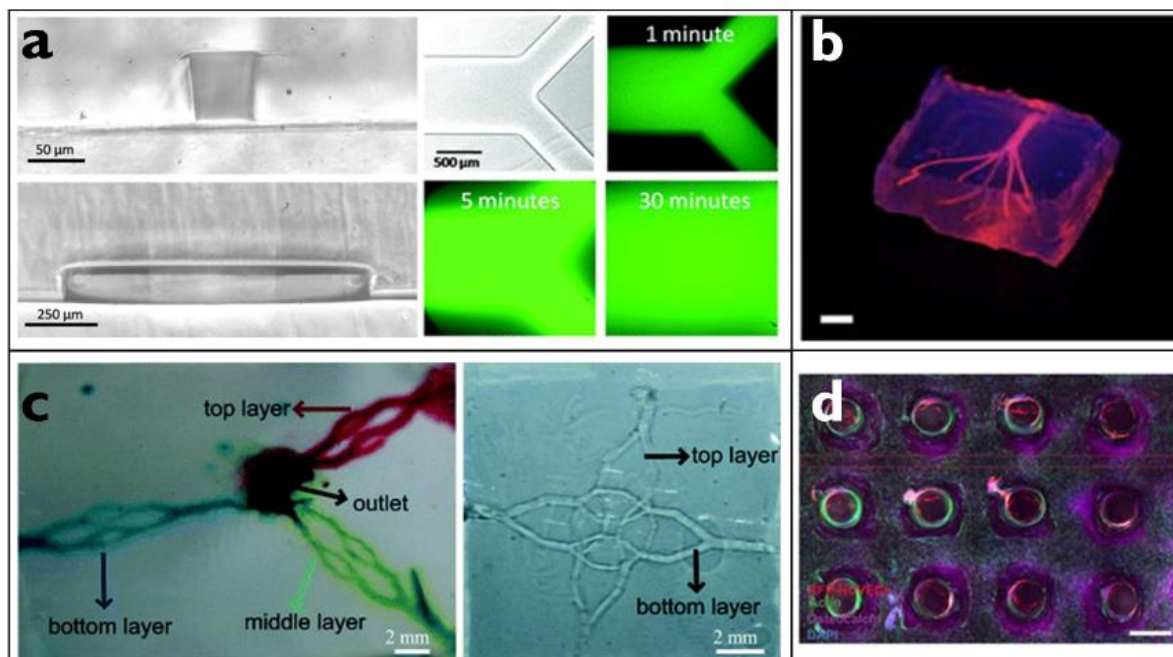


Figure 3. Selected strategies for structure-induced vascularization. **a)** Light micrograph cross sectional images showing channel fidelity and the layer-by-layer interface between hydrogel films of agarose. (top left) A channel 50 μm in width 70 μm in height and (bottom left) 1 mm in width 150 μm in depth are depicted. Diffusion over time of FITC-BSA into the surrounding agarose gel (right)⁷³. **b)** Extruded agarose 'wires' are used to form microchannel within gelatin (top), shown here with a perfusion of red microbeads in solution⁷⁹. **c)** An alginate hydrogel formed in a PDMS mold is embedded within gelatin and dissolved using EDTA, resulting in perfusable microchannels (right). A triple layer 3D microfluidic network in gelatin, perfused with different colours (left)⁸⁶. **d)** A 3D printed sacrificial template of Pluronic F-127 is intercalated between bioprinted hMSCs and the whole structure is embedded in a fibroblast-laden matrix. The sacrificial ink is then removed and the structure perfused with endothelial cells to produce vasculature surrounding the parenchymal and stromal tissue¹³¹. Scale bars: **b)** 3 mm; **d)** 1.5 mm.

Direct Cell Patterning

Techniques that can control cell localization, from multicellular clusters to single cells, have also been utilized in the construction of vascular networks (Figure 4). These techniques make use of the potential for cell self-assembly and autonomous organization into blood vessels to generate vascular patterns. Controlled cell deposition, such that cells are in close proximity to one another, can decrease the time required for cellular self-assembly while simultaneously guiding the direction of lumen formation⁹⁰. Direct cell patterning technologies encompass cell molding, 3D bioprinting, inkjet printing, laser-assisted bioprinting (LAB) and optical guide/tweezers.

Cell-laden hydrogels are used in tissue micromolding techniques to create geometrically defined and multiscale vessels. Baranski et al. showed this by seeding a mixture

of HUVECs and fibroblasts in liquid collagen into 150- μm -wide microchannels of a PDMS mold, where the cells would self-assemble into vascular cords⁵³ (Figure 4a). These were subsequently peeled off and embedded in a fibrin hydrogel, prior to implantation in mice. Patterning vasculature within the construct proved to be beneficial, given that compared to the randomly seeded construct, the former yielded a faster anastomosis with the host, improved vascular network formation, and required a fewer number of cells. Another example was shown by Nikkhah et al., where photomasked channel patterns were formed from cell-laden GelMA, resulting in the formation of vascular cords with a diameter proportional to the channel width⁹¹. Micropatterning techniques, although capable of providing precisely tuned vascular channels, require a plastic support for their formation, which impedes the blend of other tissues within the vasculature and does not provide the ability to recapitulate multi-layered tissue organization.

A classical approach relies on the formation of spheroids, multicellular aggregates that can be used as building blocks to construct tissues⁹². A simple demonstration for vessel assembly consisted on casting vascular spheroids in collagen hydrogels to induce vascular fusion⁹³. The VEGF-treated E8.5 mouse allantois-derived spheroids fused together as coalescent droplets, resulting in the formation of a single lumen and SMCs layer. Control over spheroid location is crucial for efficient vessel assembly, design, and integration with other tissues. This can be provided by 3D bioprinting, which allows for controlled extrusion of material to generate custom-made patterns (Figure 1d). Jakab et al. reported the 3D bioprinting of spheroids into collagen gels which served as support (biopaper) for their assembly⁹⁴. However, uneven gelation and collagen incorporation into the cellular construct led the researchers to replace collagen with agarose⁹⁵ (Figure 4b). Although using spheroids for tissue formation is a simple approach, several drawbacks exist, including the need for several spheroid units, their large size ($\sim 300\ \mu\text{m}$), long fusion times, and resulting inhomogeneous structures⁹⁵. The slow kinetics of spheroid fusion was probably due to the agarose substrate, since this parameter has been described to depend on matrix chemical and physical properties⁵. To circumvent this, the same authors used concentric multicellular cylinders composed of SMCs (inner layer) and fibroblasts (outer layer) to fabricate a vascular tube, representing a macrovessel with tunica media and adventitia, which could be later perfused.

The assembly of vascular channels has been achieved by 3D bioprinting approaches using both natural and synthetic hydrogels as cell carriers. Cell extrusion within ECM-mimicking biomaterials has also been achieved where fibroblasts were encapsulated in gelatin or multi-arm PEG, both premodified with HA^{96,97}. Tubes were built either by vertically printing around acellular layers of HA⁹⁶ or by horizontal deposition on agarose rods⁹⁷. 3D bioprinting technologies may provide the tools to assemble functional large- to medium-sized blood vessels *in vitro*. However, generation of a dense microvascular network resembling the native

situation is yet to be accomplished, as a consequence of the low resolution that current systems offer.

In contrast to 3D bioprinters, inkjet printers have the advantage of high resolution, delivering picoliter droplets with an accuracy of a few micrometres⁹⁸. Both the thermal and piezo modality have been used with some success to fabricate vessel-like shapes^{99,100}. Fibrin strands containing HUVECs with a width smaller than 100 μm could be formed by thermal inkjet printing of a cell-thrombin solution within a fibrinogen substrate⁹⁹. The cells proliferated, aligned in the channels, and showed some integrity when patterned in ring structures. Christensen et al. developed a more complex design that featured a support-free construction of tube with bifurcations as well as horizontal and vertical components¹⁰⁰ (Figure 4c). One drawback of inkjet printing systems is it requires low viscosity solutions to prevent nozzle clogging, thus limiting the choice of materials and range of cell densities⁹⁸.

These material restrictions are not an existing issue for LAB, since it is a nozzle-free system and therefore allows the printing of droplets with various viscosities (1–300 mPa/s) and cell densities⁸. LAB has been used to pattern a microvascular network with a stem and branches composed of HUVECs¹⁰¹. After one day of culture, the cells were seen to stretch out and establish connections with each other that resulted in lumen formation. Lumen size could be controlled by varying the distance between cell deposition and, thus, the cell density per unit area. However, these HUVEC networks were unstable and dissociated after a few days in culture, which could be prevented by depositing juxtaposed SMCs one day after HUVEC printing. Despite the accuracy attained with a LAB setup, the resulting construct was still too thin for use in a clinical setting. In another report, these authors showed that thicker scaffolds (300 μm) could be built by printing HUVECs on top of porous poly(DL-lactide-co-glycolide) biopaper coated with Matrigel¹⁰². Stacking these layers into a thick and functional construct that can be perfused remains to be demonstrated. Despite these successes, LAB suffers from several issues, such as the generation of metallic residues during printing, inhomogeneous cell deposition, and long process duration.

Lastly, optical trapping systems can be used as vessel assembly tools by allowing the contactless manipulation of individual vascular-specific cells into defined positions. Compared to the above mentioned techniques, optical systems offer unmatched precision to control cell location, a great benefit when recreating the multicellular context of vasculature and surrounding tissues. Hocheng et al. provided the proof-of-concept for optical trapping: endothelial cells were guided by laser through microchannels towards a construction area, where cells could be entrapped by laser tweezers and moved in the horizontal or vertical axis¹⁰³. Some efforts have been made to further develop this technology, such as inclusion of biomaterials and perfusion systems, to make it a viable technique.

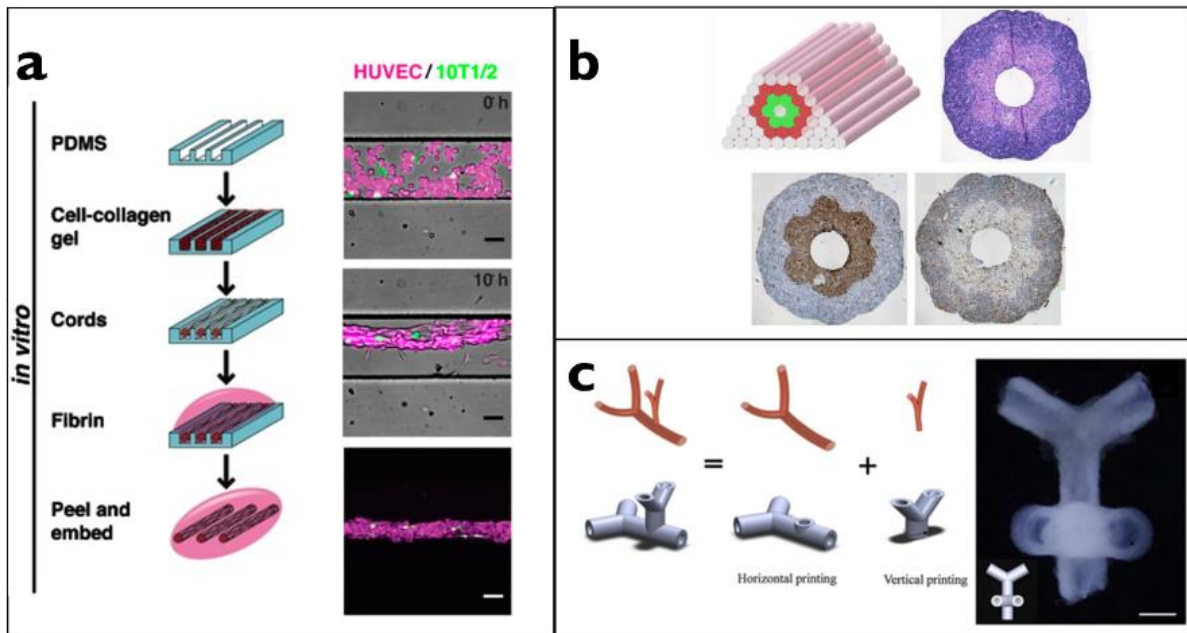


Figure 4. Selected strategies for the fabrication of vascularization utilizing cell patterning. **a)** Left: Schematic representation of the vascular cords assembly through a micromolding technique. Right: Self-assembly of HUVECS and 10T1/2 fibroblasts into vascular cords happens within 10 h⁵³. **b)** 3D printing of concentric multicellular cylinders (top left) enables the formation of a double-layered vascular tube (green represent SMCs and red represents fibroblasts). Histological examination of the tubes after 3 days of fusion show H&E (top right), smooth muscle α -actin (brown, bottom left), and Caspase-3 (brown, bottom right)⁹⁵. **c)** Free-from inkjet printing of sodium alginate and fibroblasts into a bath of calcium chloride enables the fabrication of cell-laden tubular structures with bifurcations, creating well-defined tubular structures with vascular cell type. Scale bars: **a)** 50 μ m **c)** 3 mm.

Addressing Limitations

Despite substantial progress over the past ten years in the vascularization of biomaterials and artificial tissues, obstacles still remain to produce viable, complex and large implants. We have a working understanding of the major signaling molecules, necessary cell types, and ECM properties that both inhibit and promote vascularization. However, the majority of these studies address only the beginning of a complex problem. How do we control the vascularization of multicellular engineered tissue? Within this framework, we propose that three major limitations remain:

- 1) Scalability of prevascularized multicellular engineered tissues;
- 2) Directing and connecting vascular networks of multiple length scale;
- 3) Directing vascularization in the presence of other cell types;

As researchers continue to strive to find the best engineering solution for organ assembly and vascularization, a synergy of technologies will be likely required to overcome existing limitations (Figure 1e). The combined development materials and fabrication

strategies will be essential in addressing these issues, with a number of existing examples shown in Figure 5. This is clearly evident in microfluidic approaches, which have provided powerful tools to simplistically decode physiological processes and assemble tissue functional units (e.g. lung-on-a-chip¹⁰⁴¹⁰⁴, liver sinusoid-on-a-chip¹⁰⁵¹⁰⁵) but have failed to reproduce the native microarchitecture, spatial heterogeneity and cell-matrix interactions¹⁰⁶.

To recreate multicellular structures with high fidelity, Sarveswaran et al. recently showcased a combined approach to build a human capillary¹⁰⁶. Using live cell lithography, vascular cells were entrapped in photopolymerizable hydrogels to create living voxels, which could be stitched together into a single structure. The cell positioning, ratio between different cell types, and embedding material could be finely tuned in order to recreate the cellular architecture and mechanistic environment present in a human blood vessel. This method provided an unprecedented control for the generation of TE constructs, albeit at a much lower scale than the required to create whole organs (Figure 5b). Zhang et al. have also showcased an elegant microfluidic platform to assemble miniature vascularized and functional tissues¹⁰⁷. Referred to as the AngioChip, this engineered platform combines a 3D biodegradable and porous scaffold with a classic microfluidic chip. A 3D stamped poly(octamethylene maleate (anhydride) citrate) (POMaC) microchannel network is assembled within the chip and perfused with endothelial cells in order to form built-in patterned vasculature. Surrounding this rigid structure, a cell-loaded ECM gel (collagen/Matrigel mixture or fibrin) forms the parenchymal space. Several combinations of the vascular phase and involving medium can be achieved, making this a highly versatile platform for organ-on-a-chip engineering. This concept was applied to build a liver construct with drug metabolizing capability and a contractile cardiac tissue responsive to chronotropic stimuli (epinephrine injection). Surgical anastomosis of the chip showcased the ability to sustain native blood circulation and the scalability of this platform to create a human-sized constructs, unique for a microfluidic approach.

With respect to scalability, 3D bioprinting techniques are more advantageous and still allow for an easier custom-design fabrication. An example of this is demonstrated by Kang et al., who devised a 3D printing system incorporating cell-laden hydrogels, sacrificial hydrogels, and biodegradable solid polymers to yield human-scaled tissue constructs with anatomical shape and mechanical integrity. Bone and skeletal muscle tissue replacements were fabricated and implanted, but vascularization within the constructs still relied on capillary invasion from the host, which limits the applicability of this system¹. As previously discussed, other works have already demonstrated the potential of 3D printing techniques to pattern vasculature, either through fabrication of vessel templates and subsequent endothelialization^{10,108} or direct deposition of cells⁹⁵. In a mixed approach, Lee et al. bioprinted a layer of HUVECs/gelatin mixture between a collagen support, which was thereafter liquefied and perfused, leaving behind a cell lining at the materials interface¹⁰⁹ (Figure 5a). Addressing

the need for multi-scale vessels within TE constructs, the same authors reported a variation of this method, by printing and perfusing two large parallel vessels separated by a HUVEC/fibrin mixture, where microvessels spontaneously assembled and integrated with the parent vessels¹¹⁰.

Despite these advances, 3D bioprinting techniques can also benefit from improvements during the printing process. While typically a single hydrogel material is used as a cell carrier, Colosi et al. devised an ingenious system that connects a coaxial nozzle to a microfluidic printhead where two different materials can flow, thus allowing for heterogenic fiber deposition¹¹¹. A HUVEC-loaded GelMA/alginate bioink was extruded through the inner nozzle and crosslinked via calcium chloride flow from the outer nozzle and post-printing UV irradiation. Over culture time, endothelial tubular structures formed as alginate dissolves within the bulk of crosslinked GelMA and cells migrate towards the periphery.

While the existing palette of bioinks offers several possibilities, the development of new extrudable materials, such as polymers that form dynamic molecular networks, will significantly contribute to progress. An example are supramolecular hydrogels, which have been recently investigated in 3D printing applications, mainly due to their interesting characteristics such as shear-thinning and self-healing ability. The spider silk hydrogels reported by Schacht et al.¹¹² or the guest-host HA hydrogels developed by Burdick's group¹¹³ provide good illustrations of this new materials with reversible supramolecular interactions. Using the latter hydrogels, the ability to print cell-laden layers into a cell-containing self-healing construct was demonstrated¹¹⁴ (Figure 5c). Within this approach, the authors showed the possibility to print connecting networks and to perfuse these printed networks, if desired. Through direct printing within hydrogels, intricate structures such as overhangs can be designed and held in place, in contrast to classical bioprinting where the fluid-air interface would lead to material collapse. Systems of supporting hydrogels to accommodate printed inks are not restricted to supramolecular materials, and others examples include alginate, fibrin or collagen in a gelatin support¹¹⁵ or collagen in a Carbopol granular medium¹¹⁶.

One of the most significant hurdles in recapitulating and mimicking the vascularization of natural tissues is the control needed to create an open vascular network over multiple length scales. Small scale of microvessels lie beyond the resolution of physical patterning techniques, leading researchers to harness the highly complex process of neovascularization as it occurs *in vivo*. While we are only beginning to unravel mechanisms to direct it within an engineered tissue, a promising strategy is to rely on gradients within materials or materials patterning for the direction of capillary formation. Currently, a limited number of materials can be tailored for vascularization control in 3D. PEG-based systems dominate the studies due mainly to their ease of synthesis and synthetic addressability. Unfortunately, PEG acrylate systems are not always ideal, especially when attempting to combine multiple fabrication methods. Novel

approaches to create hydrogels based on more biomimetic networks including non-covalent interactions, self-assembled structures, and reversible covalent bonds can all overcome the limitations of a static covalent network.

While these strategies can create small-scale vascular networks that are perfusable and highly distributed for ideal delivery of nutrients and oxygen¹¹⁷, connecting such networks to an organism's vasculature remains a challenge; recent studies have shown that natural anastomosis of prevascularized implants results in a 7-day delay in functional blood flow^{52,118}. This is attributed to the time-consuming 'wrapping and tapping' process of anastomosis¹¹⁹ and subsequent delays associated with the clearance of blood clots that result from initial contact between the host blood and prevascularized vessels⁵². A more rapid approach is to surgically anastomose engineered vasculature, which has been reported as a viable option to rapidly promote integration with host vasculature^{120,121}. While immediate blood flow can be established, this requires a suitably sized vessel in order to be compatible with the surgical procedure. Therefore, in order to ensure viability and function of an implanted tissue construct, a designed interconnected vasculature that spans many orders of magnitude will be required.

The ability to control the vascularization of a tissue or material in the presence of multiple cell types remains to be demonstrated and little is known about the effects of controlling vascularization in a co-culture with other cell types. This is a promising new area of research that can give great insight into the regeneration of complex tissue. Future research will certainly elucidate how to efficiently blend technologies and material resources in this quest for tissue and organ replacements.

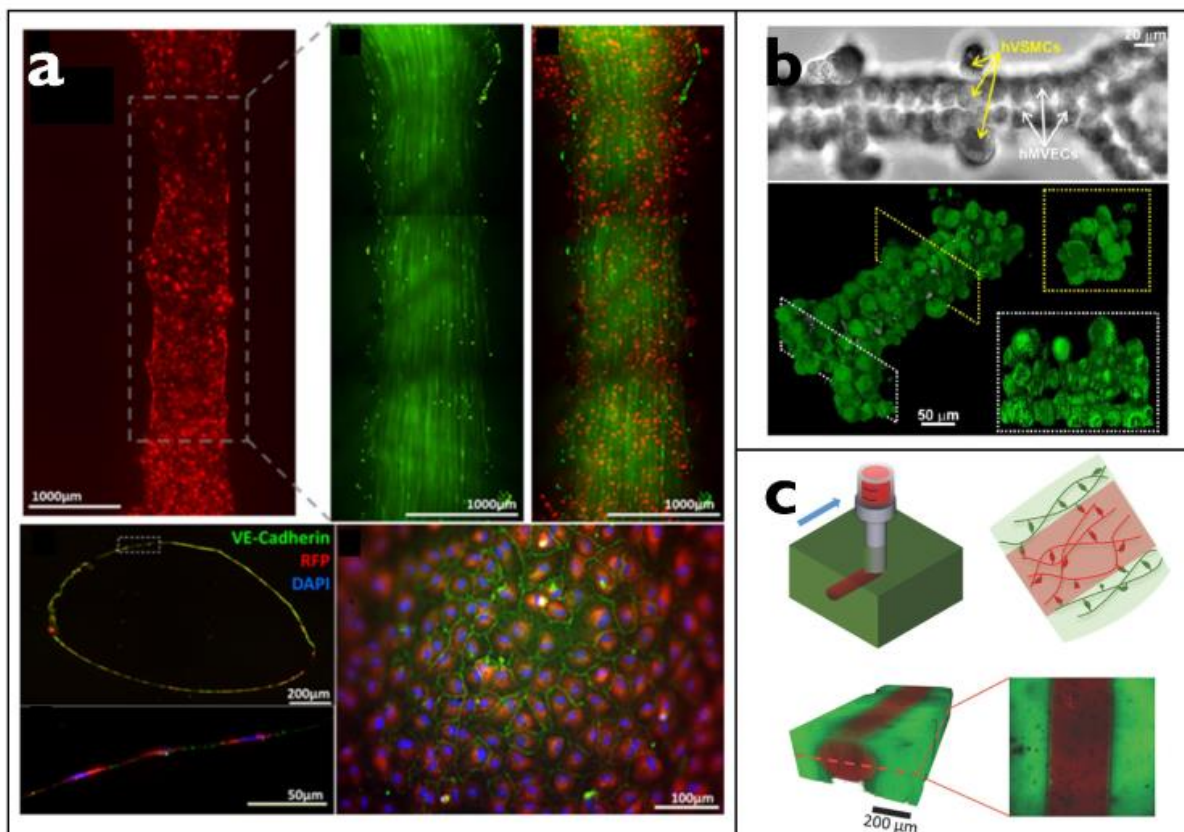


Figure 5. Current approaches utilizing a combination of techniques for vascularization. **a)** Fluorescence imaging of a printed vascular channel fabricated in layer by layer deposition after 1 day of culture on dynamic flow conditions (top, HUVECs are shown in red, flow beads are shown in green). Good monolayer formation is exhibited by fluorescence imaging of both cross-sections of this channel (middle left and bottom left) and the surface of the channel (bottom right, DAPI staining is blue, RFP-transfected HUVECs are red, VE-cadherin staining is green)¹⁰⁹. **b)** Fabrication of a synthetic capillary via live cell lithography¹⁰⁶. Using optical tweezers and photopolymerizable hydrogels, clusters of different cell types can be positioned with great precision and accuracy. **c)** Supramolecular interactions allow self-healing and shear-thinning cell-laden materials¹¹⁴. Here, one cell-laden material (guest, red) can be printed into another cell-laden material (host, green) that deforms to accommodate the ink and self-heals to maintain its position

Future Outlook

While some of the fabrication methods reviewed here require specialized technological expertise and equipment, many of the strategies are robust with low technical overhead. This includes the facile method for microvessel patterning using a sacrificial template of micromolded gelatin⁸⁷ as well as the production of microvascular spheroids and their assembly into larger vascular structures. Prompted by the scientific opportunities of ‘designer’ vascular architecture, we foresee the widespread adoption of these platforms through a combination of further simplification of the fabrication processes and commercial availability, mirroring the proliferation of microfluidic technology. Similar to the introduction of 3D assays over 30 years

ago¹²², these tools will allow us to further elucidate the vascularization process under more controlled conditions to provide both scientific insight as well as strategies to address diseased or damaged tissues. In particular, methods able to design endothelialized channel structures within a 3D multicellular context provide a new way to study the interactions between the vascular system and other cell types or tissues. This includes investigating pathologies: designed vascular models have facilitated the study of extravasation and intravasation processes that enable cancer cells to penetrate the vascular wall and metastasize^{123,124}. Impaired interactions between vasculature and the nervous system have also been implicated in certain pathological disorders¹²⁵, including the role of disrupted cerebral neurovascular coupling in the progression of Alzheimer's disease¹²⁶. Current methods to study this neurovascular coupling rely on *in vivo* models, explanted cortical tissues, or dissociated *in vitro* cultures, providing fertile ground for the development of multicellular vascularized platforms as described in this review.

As these techniques evolve, the most immediate clinical impact will come from a combination of methods to create a meaningful, multiscale vascularization strategy for tissue engineering and regenerative medicine. An ideal combination of micron-sized capillaries (achieved with 'smart' materials) with highly arborized 3D distribution of slight larger microvessels (via 3D cell printing) will ensure sufficient delivery of nutrients; larger connected structures on the millimeter scale (formed by molding techniques) would provide an ideal means of surgically connecting this vascular tree to the blood supply of a patient. The ability to control the size and placement of these vascular structures will also ensure proportioned blood flow throughout. Initial steps toward such combinatorial approaches have been showcased¹²⁷.

The advent of more advanced 3D printing technology will usher in immense potential within the biological and biomedical sciences. As technology and materials continue to evolve, we come closer to emulating the biological complexities we observe *in vivo*. A major limitation in realizing these more advanced printing technologies is the lack of suitable printable materials to control and mimic the natural ECM. Only a few well-characterized synthetic hydrogel systems exist, while many are in their infancy of development. In particular, the dynamic environment of the ECM is often lost in static, covalent polymer hydrogels. Current advances in supramolecular hydrogels and those formed by dynamic covalent chemistry will provide new opportunities for self-healing materials that will allow temporal control of hydrogel properties. With new dynamic gel systems, 'smart' materials will introduce dynamic 3D printing, whereby complex multicellular organization can be realized in both a spatial and temporal manner. This advance will enable maturation of vasculature, which is more effective when the inclusion of mural cells is delayed¹²⁸, followed by the introduction of functional cellular assemblies once the vascular nutrient supply has been established. This also sets the stage for actively recreating

time-dependent developmental and self-organizing processes, such as those observed for bone¹²⁹ and cartilage¹³⁰.

The creation of appropriate vascular networks has long been identified as the challenge that underpins the success of any potential TE strategy. As described above and summarized in Table 1, numerous approaches have been developed towards meeting this challenge. The vascular network is one but of many within the body. While it has become the most popular, neural network regeneration, hepatic portal regeneration, and kidney network regeneration can all benefit from the strategies developed around neovascularization. Without the successful control and engineering of the underlying networks that enable viable tissue, TE and RM cannot progress. Furthermore, the development of increasingly powerful and flexible technological solutions extend far beyond simple vascularization, paving the way to the formation of functional tissues and, eventually, whole organs.

Patterning Approach	Technologies	Resolution (µm)	Type of materials	Pros	Cons
Material-based	<ul style="list-style-type: none"> • 2 Photon-Polymerization • UV polymerization • Gradient polymerization 	10-20	<p>Modifiable materials: PEGDA^{44,57}, acrylated HA⁵³</p> <p>Functional modifications:</p> <ul style="list-style-type: none"> • Crosslinking density • Adhesion peptides (RGD^{58,59}) • MMP-sensible sequences⁵³ • VEGF⁵¹ 	<ul style="list-style-type: none"> • Fine control and rapid creation of constructs • Control at a molecular level • Easily scalable • Post-scaffold functionalization (spatio-temporal possibility) 	<ul style="list-style-type: none"> • Phototoxicity • Limited materials platforms • Expensive to produce custom materials
		5 to 1000	<p>Alginate⁷², agarose⁷³, fibrin, collagen⁷⁴, etc.</p>	<ul style="list-style-type: none"> • Small/patterned/ • Simple/Established • (Some cell encapsulation) 	<ul style="list-style-type: none"> • Layer adhesion • Planar • (Some cell encapsulation)
		76 ⁷⁵ to 1000 ⁷⁷	<p>Templates: Agarose</p>	<ul style="list-style-type: none"> • Monolithic, simple • Cell encapsulation 	<ul style="list-style-type: none"> • Planar/no real patterns/size restriction
Structural-based	Sacrificial	6 ⁸⁷ to 1500 ¹²¹	<p>Sacrificial structures: Pluronic F-127¹³², PLGA-coated carbohydrate glass⁸⁴, Alginate⁸⁵, Gelatin⁸⁷</p>	<ul style="list-style-type: none"> • Monolithic, simple • (Some cell encapsulation) 	<ul style="list-style-type: none"> • Material considerations • (some cell encapsulation)
		2-500	<p>Cell carriers: Collagen⁸³, GelMA¹³³, etc.</p>	<ul style="list-style-type: none"> • High resolution • Simple and cheap procedure 	<ul style="list-style-type: none"> • Requires plastic support • Difficult to integrate with tissues
		>100	<p>Extruded materials: Gelatin¹⁰⁹, Fibrin, PEG-derivatives⁸⁷, etc.</p>	<ul style="list-style-type: none"> • Fast assembly of large structures • Easily scalable • Printing with various type of materials and cell densities 	<ul style="list-style-type: none"> • Low resolution • Requires high number of cells
Cell-based	<p>Inkjet Printing</p> <p>Laser-assisted Bioprinting</p> <p>Optical guide/trapping</p>	20-50 ¹³⁴	<p>Extruded materials: Alginate¹⁰⁰, Fibrin⁹⁹, etc.</p>	<ul style="list-style-type: none"> • High printing resolution 	<ul style="list-style-type: none"> • Requires low viscosity solutions and low cell density
		30-50 ^{101,102}	<p>Biopaper: Matrigel¹⁰¹, PLGA¹⁰²</p>	<ul style="list-style-type: none"> • High printing resolution • Printing of droplets with various viscosities and cell densities 	<ul style="list-style-type: none"> • Generation of metallic residues • Inhomogeneous cell deposition • Time-consuming
		Single cell	<p>Polymeric microbeads¹⁰³; Cells</p>	<ul style="list-style-type: none"> • No direct contact • Control over cell type and position • Control of diameter and length 	<ul style="list-style-type: none"> • Possibility of photodamage • Low scale (only small structures) • Time-consuming
Combination of basic approaches	Live Cell Lithography	10-20 ^{106,135}	<p>Photopolymerizable hydrogels (e.g. PEDGA, GelMA^{106,135}) and cell aggregates</p>	<ul style="list-style-type: none"> • Control over cell type and position • Control of diameter and length • Control over vessel mechanical properties (stiffness, adhesion, degradability) 	<ul style="list-style-type: none"> • Low scale • Time-consuming

Table 1. An overview of vascular patterning techniques and technologies

References

- (1) Kang, H.-W.; Lee, S. J.; Ko, I. K.; Kengla, C.; Yoo, J. J.; Atala, A. A 3D bioprinting system to produce human-scale tissue constructs with structural integrity. *Nat. Biotechnol.* **2016**, *34* (3), 312–322.
- (2) MacNeil, S. Biomaterials for tissue engineering of skin. *Mater. Today* **2008**, *11* (5), 26–35 DOI: 10.1016/S1369-7021(08)70087-7.
- (3) Atala, A.; Bauer, S. B.; Soker, S.; Yoo, J. J.; Retik, A. B. Tissue-engineered autologous bladders for patients needing cystoplasty. *Lancet* **2006**, *367* (9518), 1241–1246 DOI: 10.1016/S0140-6736(06)68438-9.
- (4) Chen, X.; Aledia, A. S.; Ghajar, C. M.; Griffith, C. K.; Putnam, A. J.; Hughes, C. C. W.; George, S. C. Prevascularization of a fibrin-based tissue construct accelerates the formation of functional anastomosis with host vasculature. *Tissue Eng. Part A* **2009**, *15* (6), 1363–1371 DOI: 10.1089/ten.tea.2008.0314.
- (5) Visconti, R. P.; Kasyanov, V.; Gentile, C.; Zhang, J.; Markwald, R. R.; Mironov, V. Towards organ printing: engineering an intra-organ branched vascular tree. *Expert Opin. Biol. Ther.* **2010**, *10* (3), 409–420 DOI: 10.1517/14712590903563352.
- (6) Rouwkema, J.; Rivron, N. C.; van Blitterswijk, C. A. Vascularization in tissue engineering. *Trends Biotechnol.* **2008**, *26* (8), 434–441 DOI: 10.1016/j.tibtech.2008.04.009.
- (7) Nichol, J. W.; Khademhosseini, A. Modular tissue engineering: Engineering biological tissues from the bottom up. *Soft Matters* **2010**, *5* (7), 1312–1319 DOI: 10.1039/b814285h.Modular.
- (8) Guillotin, B.; Guillemot, F. Cell patterning technologies for organotypic tissue fabrication. *Trends Biotechnol.* **2011**, *29* (4), 183–190 DOI: 10.1016/j.tibtech.2010.12.008.
- (9) Levenberg, S.; Rouwkema, J.; Macdonald, M.; Garfein, E. S.; Kohane, D. S.; Darland, D. C.; Marini, R.; Blitterswijk, C. A. van; Mulligan, R. C.; D'Amore, P. A.; et al. Engineering vascularized skeletal muscle tissue. *Nat Biotechnol* **2005**, *23* (7), 879–884 DOI: 10.1038/nbt1109.
- (10) Kolesky, D. B.; Homan, K. A.; Skylar-Scott, M. A.; Lewis, J. A. Three-dimensional bioprinting of thick vascularized tissues. *Proc. Natl. Acad. Sci.* **2016**, *113* (12), 3179–3184 DOI: 10.1073/pnas.1521342113.
- (11) Suuronen, E. J.; McLaughlin, C. R.; Stys, P. K.; Nakamura, M.; Munger, R.; Griffith, M. Functional innervation in tissue engineered models for in vitro study and testing purposes. *Toxicol. Sci.* **2004**, *82* (2), 525–533 DOI: 10.1093/toxsci/kfh270.
- (12) Marx, V. Tissue engineering: Organs from the lab. *Nature* **2015**, *522* (7556), 373–377

DOI: 10.1038/522373a.

- (13) Hariharan, K.; Kurtz, A.; Schmidt-Ott, K. M. Assembling Kidney Tissues from Cells: The Long Road from Organoids to Organs. *Front. Cell Dev. Biol.* **2015**, 3 (November), 1–9 DOI: 10.3389/fcell.2015.00070.
- (14) Xinaris, C.; Brizi, V.; Remuzzi, G. Organoid Models and Applications in Biomedical Research. *Nephron* **2015**, 130 (3), 191–199 DOI: 10.1159/000433566.
- (15) Novosel, E. C.; Kleinhans, C.; Kluger, P. J. Vascularization is the key challenge in tissue engineering. *Adv. Drug Deliv. Rev.* **2011**, 63 (4), 300–311 DOI: 10.1016/j.addr.2011.03.004.
- (16) McGuigan, A. P.; Sefton, M. V. Vascularized organoid engineered by modular assembly enables blood perfusion. *Proc. Natl. Acad. Sci. U. S. A.* **2006**, 103 (31), 11461–11466 DOI: 10.1073/pnas.0602740103.
- (17) Baptista, P. M.; Siddiqui, M. M.; Lozier, G.; Rodriguez, S. R.; Atala, A.; Soker, S. The use of whole organ decellularization for the generation of a vascularized liver organoid. *Hepatology* **2011**, 53 (2), 604–617 DOI: 10.1002/hep.24067.
- (18) van Blitterswijk, C.; Jan de Boer. Tissue Engineering. In *Tissue Engineering*; Elsevier, 2015.
- (19) Potente, M.; Gerhardt, H.; Carmeliet, P. Basic and therapeutic aspects of angiogenesis. *Cell* **2011**, 146 (6), 873–887 DOI: 10.1016/j.cell.2011.08.039.
- (20) Risau, W. Mechanisms of angiogenesis. *Nature* **1997**, 386 (6626), 671–674 DOI: 10.1146/annurev.physiol.49.1.453.
- (21) Carmeliet, P. Mechanisms of angiogenesis and arteriogenesis. *Nat. Med.* **2000**, 6 (4), 389–395 DOI: 10.1038/74651.
- (22) Bussolino, F.; Mantovani, A.; Persico, G. Molecular mechanisms of blood vessel formation. *Trends Biochem. Sci.* **1997**, 22 (7), 251–256 DOI: 10.1016/S0968-0004(97)01074-8.
- (23) Patan, S. Vasculogenesis and angiogenesis as mechanisms of vascular network formation, growth and remodeling. *J. Neurooncol.* **2000**, 50 (1-2), 1–15 DOI: 10.1023/A:1006493130855.
- (24) Rouwkema, J.; Khademhosseini, A. Vascularization and Angiogenesis in Tissue Engineering: Beyond Creating Static Networks. *Trends Biotechnol.* **2016**, *In Press*, 1–13 DOI: 10.1016/j.tibtech.2016.03.002.
- (25) Blinder, Y. J.; Freiman, A.; Raindel, N.; Mooney, D. J.; Levenberg, S. Vasculogenic dynamics in 3D engineered tissue constructs. *Sci. Rep.* **2015**, 5 (DECEMBER), 17840 DOI: 10.1038/srep17840.
- (26) Carmeliet, P. Blood vessels and nerves: common signals, pathways and diseases. *Nat. Rev. Genet.* **2003**, 4 (9), 710–720 DOI: 10.1038/nrg1158.

- (27) Pardali, E.; Goumans, M. J.; ten Dijke, P. Signaling by members of the TGF- β family in vascular morphogenesis and disease. *Trends Cell Biol.* **2010**, *20* (9), 556–567 DOI: 10.1016/j.tcb.2010.06.006.
- (28) Chan, J. M.; Zervantonakis, I. K.; Rimchala, T.; Polacheck, W. J.; Whisler, J.; Kamm, R. D. Engineering of In Vitro 3D Capillary Beds by Self-Directed Angiogenic Sprouting. *PLoS One* **2012**, *7* (12), 1–11 DOI: 10.1371/journal.pone.0050582.
- (29) Eckermann, C. W.; Lehle, K.; Schmid, S. a.; Wheatley, D. N.; Kunz-Schughart, L. a. Characterization and modulation of fibroblast/endothelial cell co-cultures for the *in vitro* preformation of three-dimensional tubular networks. *Cell Biol. Int.* **2011**, *35* (11), 1097–1110 DOI: 10.1042/CBI20100718.
- (30) Baldwin, J.; Antille, M.; Bonda, U.; De-juan-pardo, E. M.; Khosrotehrani, K.; Ivanovski, S.; Petcu, E. B.; Hutmacher, D. W. In vitro pre-vascularisation of tissue-engineered constructs A co-culture perspective. *Vasc. Cell* **2014**, *6* (13), 1–16.
- (31) Cheng, C.-C.; Chang, S.-J.; Chueh, Y.-N.; Huang, T.-S.; Huang, P.-H.; Cheng, S.-M.; Tsai, T.-N.; Chen, J.-W.; Wang, H.-W. Distinct angiogenesis roles and surface markers of early and late endothelial progenitor cells revealed by functional group analyses. *BMC Genomics* **2013**, *14* (1), 182 DOI: 10.1186/1471-2164-14-182.
- (32) Chen, X.; Aledia, A. S.; Popson, S. a; Him, L.; Hughes, C. C. W.; George, S. C. Rapid anastomosis of endothelial progenitor cell-derived vessels with host vasculature is promoted by a high density of cotransplanted fibroblasts. *Tissue Eng. Part A* **2010**, *16* (2), 585–594 DOI: 10.1089/ten.tea.2009.0491.
- (33) Armulik, A.; Genove, G.; Betsholtz, C. Pericytes: Developmental, Physiological, and Pathological Perspectives, Problems, and Promises. *Dev. Cell* **2011**, *21*, 193–215 DOI: 10.1016/j.devcel.2011.07.001.
- (34) Blinder, Y.; Mooney, D.; Levenberg, S. Engineering approaches for inducing blood vessel formation. *Curr. Opin. Chem. Eng.* **2014**, *3*, 56–61 DOI: 10.1016/j.coche.2013.11.003.
- (35) Chwalek, K.; Tsurkan, M. V; Freudenberg, U.; Werner, C. Glycosaminoglycan-based hydrogels to modulate heterocellular communication in in vitro angiogenesis models. *Sci. Rep.* **2014**, *4*, 4414 DOI: 10.1038/srep04414.
- (36) Goodwin, A. M. In vitro assays of angiogenesis for assessment of angiogenic and anti-angiogenic agents. *Microvasc. Res.* **2007**, *74* (2-3), 172–183 DOI: 10.1016/j.mvr.2007.05.006.In.
- (37) Donovan, D.; Brown, N. J.; Bishop, E. T.; Lewis, C. E. Comparison of three in vitro human “angiogenesis” assays with capillaries formed in vivo. *Angiogenesis* **2001**, *4* (2), 113–121 DOI: 10.1023/A:1012218401036.
- (38) Moon, J. J.; Saik, J. E.; Poche, R. A.; Leslie-Barbick, J. E.; Lee, S. H.; Smith, A. A.;

- Dickinson, M. E.; West, J. L. Biomimetic hydrogels with pro-angiogenic properties. *Biomaterials* **2010**, *31* (14), 3840–3847 DOI: 10.1016/j.biomaterials.2010.01.104.
- (39) Sacharidou, A.; Koh, W.; Stratman, A. N.; Mayo, A. M.; Fisher, K. E.; Davis, G. E. Endothelial lumen signaling complexes control 3D matrix – specific tubulogenesis through interdependent Cdc42- and MT1-MMP – mediated events. *Blood* **2010**, *115* (25), 5259–5269 DOI: 10.1182/blood-2009-11-252692.
- (40) Ghajar, C. M.; Blevins, K. S.; Hughes, C. C. W.; George, S. C.; Putnam, A. J. Mesenchymal stem cells enhance angiogenesis in mechanically viable prevascularized tissues via early matrix metalloproteinase upregulation. *Tissue Eng.* **2006**, *12* (10), 2875–2888 DOI: 10.1089/ten.2006.12.ft-237.
- (41) Darland, D. C.; D'Amore, P. A. TGF β is required for the formation of capillary-like structures in three-dimensional cocultures of 10T1 / 2 and endothelial cells. *Angiogenesis* **2001**, *4*, 11–20.
- (42) Phelps, E. A.; Headen, D. M.; Taylor, W. R.; Thulé, P. M.; García, A. J. Vasculogenic bio-synthetic hydrogel for enhancement of pancreatic islet engraftment and function in type 1 diabetes. *Biomaterials* **2013**, *34* (19), 4602–4611 DOI: 10.1016/j.biomaterials.2013.03.012.
- (43) Leslie-Barbick, J. E.; Moon, J. J.; West, J. L. Covalently-immobilized vascular endothelial growth factor promotes endothelial cell tubulogenesis in poly(ethylene glycol) diacrylate hydrogels. *J. Biomater. Sci. Polym. Ed.* **2009**, *20* (12), 1763–1779 DOI: 10.1163/156856208X386381.
- (44) Leslie-Barbick, J. E.; Saik, J. E.; Gould, D. J.; Dickinson, M. E.; West, J. L. The promotion of microvasculature formation in poly(ethylene glycol) diacrylate hydrogels by an immobilized VEGF-mimetic peptide. *Biomaterials* **2011**, *32* (25), 5782–5789 DOI: 10.1016/j.biomaterials.2011.04.060.
- (45) Briquez, P. S.; Clegg, L. E.; Martino, M. M.; Gabhann, F. Mac; Hubbell, J. A. Design principles for therapeutic angiogenic materials. *Nat. Rev. Mater.* **2016**, *1* (1), 1–15 DOI: 10.1038/natrevmats.2015.6.
- (46) Birbrair, A.; Zhang, T.; Wang, Z.-M.; Messi, M. L.; Mintz, A.; Delbono, O. Pericytes at the intersection between tissue regeneration and pathology. *Clin. Sci.* **2015**, *128* (2), 81–93 DOI: 10.1016/j.surg.2006.10.010.Use.
- (47) Blacher, S.; Erpicum, C.; Lenoir, B.; Paupert, J.; Moraes, G.; Ormenese, S.; Bullinger, E.; Noel, A. Cell invasion in the spheroid sprouting assay: A spatial organisation analysis adaptable to cell behaviour. *PLoS One* **2014**, *9* (5), 1–10 DOI: 10.1371/journal.pone.0097019.
- (48) Lovett, M.; Lee, K.; Edwards, A.; Kaplan, D. L. Vascularization strategies for tissue engineering. *Tissue Eng. Part B. Rev.* **2009**, *15* (3), 353–370 DOI:

- 10.1089/ten.teb.2009.0085.
- (49) Laschke, M. W.; Menger, M. D. Prevascularization in tissue engineering: Current concepts and future directions. *Biotechnol. Adv.* **2015**, *34* (2), 112–121 DOI: 10.1016/j.biotechadv.2015.12.004.
- (50) Atluri, P.; Miller, J. S.; Emery, R. J.; Hung, G.; Trubelja, A.; Cohen, J. E.; Lloyd, K.; Han, J.; Gaffey, A. C.; Macarthur, J. W.; et al. Tissue-engineered, hydrogel-based endothelial progenitor cell therapy robustly revascularizes ischemic myocardium and preserves ventricular function. *J. Thorac. Cardiovasc. Surg.* **2014**, *148* (3), 1090–1098 DOI: 10.1016/j.jtcvs.2014.06.038.
- (51) Buitinga, M.; Janeczek Portalska, K.; Cornelissen, D.-J.; Plass, J.; Hanegraaf, M.; Carlotti, F.; de Koning, E.; Engelse, M. A.; van Blitterswijk, C.; Karperien, M.; et al. Co-culturing human islets with proangiogenic support cells to improve islet revascularization at the subcutaneous transplantation site. *Tissue Eng. Part A* **2016**, *22*, 375–385 DOI: 10.1089/ten.TEA.2015.0317.
- (52) White, S. M.; Pittman, C. R.; Hingorani, R.; Arora, R.; Esipova, T. V.; Vinogradov, S. A.; Hughes, C. C. W.; Choi, B.; George, S. C. Implanted Cell-Dense Prevascularized Tissues Develop Functional Vasculature that Supports Reoxygenation Following Thrombosis. *Tissue Eng. Part A* **2014**, *20*, 2316–2328 DOI: 10.1089/ten.tea.2013.0311.
- (53) Baranski, J. D.; Chaturvedi, R. R.; Stevens, K. R.; Eyckmans, J.; Carvalho, B.; Solorzano, R. D.; Yang, M. T.; Miller, J. S.; Bhatia, S. N.; Chen, C. S. Geometric control of vascular networks to enhance engineered tissue integration and function. *Proc. Natl. Acad. Sci.* **2013**, *110* (19), 7586–7591 DOI: 10.1073/pnas.1217796110.
- (54) White, S. M.; Hingorani, R.; Arora, R. P. S.; Hughes, C. C. W.; George, S. C.; Choi, B. Imaging to Assess Blood Flow and Oxygenation in Implantable Engineered Tissues. *Tissue Eng. Part C Methods* **2012**, *18* (9), 697–709 DOI: 10.1089/ten.tec.2011.0744.
- (55) Kucukgul, C.; Ozler, B.; Karakas, H. E.; Gozuacik, D.; Koc, B. 3D hybrid bioprinting of macrovascular structures. *Procedia Eng.* **2013**, *59*, 183–192 DOI: 10.1016/j.proeng.2013.05.109.
- (56) Leslie-Barbick, J. E.; Shen, C.; Chen, C.; West, J. L. Micron-scale spatially patterned, covalently immobilized vascular endothelial growth factor on hydrogels accelerates endothelial tubulogenesis and increases cellular angiogenic responses. *Tissue Eng. Part A* **2011**, *17* (1-2), 221–229 DOI: 10.1089/ten.tea.2010.0202.
- (57) Culver, J. C.; Hoffmann, J. C.; Poche, R. A.; Slater, J. H.; West, J. L.; Dickinson, M. E.; Poch??, R. A.; Slater, J. H.; West, J. L.; Dickinson, M. E. Three-dimensional biomimetic patterning in hydrogels to guide cellular organization. *Adv. Mater.* **2012**, *24* (17), 2344–2348 DOI: 10.1002/adma.201200395.

- (58) Lee, T. T.; García, J. R.; Paez, J. I.; Singh, A.; Phelps, E. A.; Weis, S.; Shafiq, Z.; Shekaran, A.; Del Campo, A.; García, A. J. Light-triggered in vivo activation of adhesive peptides regulates cell adhesion, inflammation and vascularization of biomaterials. *Nat. Mater.* **2015**, *14* (3), 352–360 DOI: 10.1038/nmat4157.
- (59) Hanjaya-Putra, D.; Wong, K. T.; Hirotsu, K.; Khetan, S.; Burdick, J. A.; Gerecht, S. Spatial control of cell-mediated degradation to regulate vasculogenesis and angiogenesis in hyaluronan hydrogels. *Biomaterials* **2012**, *33* (26), 6123–6131 DOI: 10.1016/j.biomaterials.2012.05.027.
- (60) Sokic, S.; Christenson, M. C.; Larson, J. C.; Appel, A. A.; Brey, E. M.; Papavasiliou, G. Evaluation of MMP substrate concentration and specificity for neovascularization of hydrogel scaffolds. *Biomater. Sci.* **2014**, *2* (10), 1343 DOI: 10.1039/C4BM00088A.
- (61) Turturro, M. V.; Christenson, M. C.; Larson, J. C.; Young, D. A.; Brey, E. M.; Papavasiliou, G. MMP-Sensitive PEG Diacrylate Hydrogels with Spatial Variations in Matrix Properties Stimulate Directional Vascular Sprout Formation. *PLoS One* **2013**, *8* (3), e58897 DOI: 10.1371/journal.pone.0058897.
- (62) Akar, B.; Jiang, B.; Somo, S. I.; Appel, A. A.; Larson, J. C.; Tichauer, K. M.; Brey, E. M. Biomaterials with persistent growth factor gradients in vivo accelerate vascularized tissue formation. *Biomaterials* **2015**, *72*, 61–73 DOI: 10.1016/j.biomaterials.2015.08.049.
- (63) Aizawa, Y.; Wylie, R.; Shoichet, M. Endothelial cell guidance in 3D patterned scaffolds. *Adv. Mater.* **2010**, *22* (43), 4831–4835 DOI: 10.1002/adma.201001855.
- (64) Park, K. M.; Gerecht, S. Hypoxia-inducible hydrogels. *Nat. Commun.* **2014**, *5* (May), 1–12 DOI: 10.1038/ncomms5075.
- (65) Kim, P.; Kwon, K. W.; Park, M. C.; Lee, S. H.; Kim, S. M. Soft Lithography for Microfluidics : a Review. *Biochip J.* **2008**, *2* (1), 1–11.
- (66) Smith, Q.; Gerecht, S. Going with the flow: Microfluidic platforms in vascular tissue engineering. *Curr. Opin. Chem. Eng.* **2014**, *3*, 42–50 DOI: 10.1016/j.coche.2013.11.001.
- (67) Vickerman, V.; Chung, S.; Kamm, R. D. Design, Fabrication and Implementation of a Novel Multi Parameter Control Microfluidic Platform for Three-Dimensional Cell Culture and Real-Time Imaging. *Lab Chip* **2008**, *8* (9), 1468–1477 DOI: 10.1039/b802395f.Design.
- (68) Jeon, J. S.; Bersini, S.; Whisler, J. a; Chen, M. B.; Dubini, G.; Charest, J. L.; Moretti, M.; Kamm, R. D. Generation of 3D functional microvascular networks with human mesenchymal stem cells in microfluidic systems. *Integr. Biol. (Camb)*. **2014**, *6* (5), 555–563 DOI: 10.1039/c3ib40267c.
- (69) van der Meer, A. D.; Orlova, V. V; ten Dijke, P.; van den Berg, A.; Mummery, C. L.

- Three-dimensional co-cultures of human endothelial cells and embryonic stem cell-derived pericytes inside a microfluidic device. *Lab Chip* **2013**, *13*, 3562–3568 DOI: 10.1039/c3lc50435b.
- (70) Cuchiara, M. P.; Gould, D. J.; McHale, M. K.; Dickinson, M. E.; West, J. L. Integration of self-assembled microvascular networks with microfabricated PEG-based hydrogels. *Adv. Funct. Mater.* **2012**, *22* (21), 4511–4518 DOI: 10.1002/adfm.201200976.
- (71) Hsu, Y.-H.; Moya, M. L.; Hughes, C. C. W.; George, S. C.; Lee, A. P. A microfluidic platform for generating large-scale nearly identical human microphysiological vascularized tissue arrays. *Lab Chip* **2013**, *13* (15), 2990–2998 DOI: 10.1039/C3LC50424G.
- (72) Cabodi, M.; Choi, N. W.; Gleghorn, J. P.; Lee, C. S. D.; Bonassar, L. J.; Stroock, A. D. A microfluidic biomaterial. *J. Am. Chem. Soc.* **2005**, *127* (40), 13788–13789 DOI: 10.1021/ja054820t.
- (73) Ling, Y.; Rubin, J.; Deng, Y.; Huang, C.; Demirci, U.; Karp, J. M.; Khademhosseini, A. A cell-laden microfluidic hydrogel. *Lab Chip* **2007**, *7* (6), 756–762 DOI: 10.1039/b615486g.
- (74) Price, G. M.; Chu, K. K.; Truslow, J. G.; Tang-Schomer, M. D.; Golden, A. P.; Mertz, J.; Tien, J. Bonding of macromolecular hydrogels using perturbants. *J. Am. Chem. Soc.* **2008**, *130* (21), 6664–6665 DOI: 10.1021/ja7111340d.
- (75) Choi, Nak, W.; Cabodi, M.; Held, B.; Gleghorn, J. P.; Bonassar, L. J.; Stroock, A. D. Microfluidic scaffolds for tissue engineering. *Nat. Mater.* **2007**, *6* (11), 908–915 DOI: 10.1038/nmat2022.
- (76) Sakaguchi, K.; Shimizu, T.; Horaguchi, S.; Sekine, H.; Yamato, M.; Umezu, M.; Okano, T. In vitro engineering of vascularized tissue surrogates. *Sci. Rep.* **2013**, *3*, 1316 DOI: 10.1038/srep01316.
- (77) Nichol, J. W.; Koshy, S. T.; Bae, H.; Hwang, C. M.; Yamanlar, S.; Khademhosseini, A. Cell-laden microengineered gelatin methacrylate hydrogels. *Biomaterials* **2010**, *31* (21), 5536–5544 DOI: 10.1016/j.biomaterials.2010.03.064.
- (78) Vernon, R. B.; Gooden, M. D.; Lara, S. L.; Wight, T. N. Native fibrillar collagen membranes of micron-scale and submicron thicknesses for cell support and perfusion. *Biomaterials* **2005**, *26* (september), 1109–1117 DOI: 10.1016/j.biomaterials.2004.04.019.
- (79) Bertassoni, L. E.; Cecconi, M.; Manoharan, V.; Nikkhah, M.; Hjortnaes, J.; Cristino, A. L.; Barabaschi, G.; Demarchi, D.; Dokmeci, M. R.; Yang, Y.; et al. Hydrogel bioprinted microchannel networks for vascularization of tissue engineering constructs. *Lab Chip* **2014**, *14* (13), 2202–2211 DOI: 10.1039/c4lc00030g.
- (80) Jiménez-Torres, J. A.; Peery, S. L.; Sung, K. E.; Beebe, D. J. LumeNEXT: A Practical

- Method to Pattern Luminal Structures in ECM Gels. *Adv. Healthc. Mater.* **2016**, *5* (2), 198–204 DOI: 10.1002/adhm.201500608.
- (81) Bellan, L. M.; Pearsall, M.; Cropek, D. M.; Langer, R. A 3D interconnected microchannel network formed in gelatin by sacrificial shellac microfibers. *Adv. Mater.* **2012**, *24* (38), 5187–5191 DOI: 10.1002/adma.201200810.
- (82) Tocchio, A.; Tamplenizza, M.; Martello, F.; Gerges, I.; Rossi, E.; Argenti, S.; Rodighiero, S.; Zhao, W.; Milani, P.; Lenardi, C. Versatile fabrication of vascularizable scaffolds for large tissue engineering in bioreactor. *Biomaterials* **2015**, *45*, 124–131 DOI: 10.1016/j.biomaterials.2014.12.031.
- (83) Huling, J.; Ko, I. K.; Atala, A.; Yoo, J. J. Fabrication of biomimetic vascular scaffolds for 3D tissue constructs using vascular corrosion casts. *Acta Biomater.* **2016**, *32*, 1–8 DOI: 10.1016/j.actbio.2016.01.005.
- (84) Miller, J. S.; Stevens, K. R.; Yang, M. T.; Baker, B. M.; Nguyen, D.-H. T.; Cohen, D. M.; Toro, E.; Chen, A. a.; Galie, P. a.; Yu, X.; et al. Rapid casting of patterned vascular networks for perfusable engineered three-dimensional tissues. *Nat. Mater.* **2012**, *11* (9), 768–774 DOI: 10.1038/nmat3357.
- (85) Vollert, I.; Seiffert, M.; Bachmair, J.; Sander, M.; Eder, A.; Conradi, L.; Vogelsang, A.; Schulze, T.; Uebeler, J.; Holthöner, W.; et al. In vitro perfusion of engineered heart tissue through endothelialized channels. *Tissue Eng. Part A* **2014**, *20* (3-4), 854–863 DOI: 10.1089/ten.TEA.2013.0214.
- (86) Wang, X.-Y.; Jin, Z.-H.; Gan, B.-W.; Lv, S.-W.; Xie, M.; Huang, W.-H. Engineering interconnected 3D vascular networks in hydrogels using molded sodium alginate lattice as the sacrificial template. *Lab Chip* **2014**, *14* (15), 2709–2716 DOI: 10.1039/C4LC00069B.
- (87) Golden, A. P.; Tien, J. Fabrication of microfluidic hydrogels using molded gelatin as a sacrificial element. *Lab Chip* **2007**, *7* (6), 720–725 DOI: 10.1039/b618409j.
- (88) Lee, J. B.; Wang, X.; Faley, S.; Baer, B.; Balikov, D. A.; Sung, H.-J.; Bellan, L. M. Development of 3D Microvascular Networks Within Gelatin Hydrogels Using Thermoresponsive Sacrificial Microfibers. *Adv. Healthc. Mater.* **2016**, *5*, 781–785 DOI: 10.1002/adhm.201500792.
- (89) Kolesky, D. B.; Truby, R. L.; Gladman, A. S.; Busbee, T. A.; Homan, K. A.; Lewis, J. A. 3D bioprinting of vascularized, heterogeneous cell-laden tissue constructs. *Adv. Mater.* **2014**, *26* (19), 3124–3130 DOI: 10.1002/adma.201305506.
- (90) Hoch, E.; Tovar, G. E. M.; Borchers, K. Bioprinting of artificial blood vessels: current approaches towards a demanding goal. *Eur. J. Cardiothorac. Surg.* **2014**, *46* (June), 1–12 DOI: 10.1093/ejcts/ezu242.
- (91) Nikkhah, M.; Eshak, N.; Zorlutuna, P.; Annabi, N.; Castello, M.; Kim, K.; Dolatshahi-

- Pirouz, A.; Edalat, F.; Bae, H.; Yang, Y.; et al. Directed endothelial cell morphogenesis in micropatterned gelatin methacrylate hydrogels. *Biomaterials* **2012**, *33* (35), 9009–9018 DOI: 10.1016/j.biomaterials.2012.08.068.
- (92) Mironov, V.; Visconti, R. P.; Kasyanov, V.; Forgacs, G.; Drake, C. J.; Markwald, R. R. Organ printing: Tissue spheroids as building blocks. *Biomaterials* **2009**, *30* (12), 2164–2174 DOI: 10.1016/j.biomaterials.2008.12.084.
- (93) Fleming, P. A.; Argraves, W. S.; Gentile, C.; Neagu, A.; Forgacs, G.; Drake, C. J. Fusion of uniluminal vascular spheroids: A model for assembly of blood vessels. *Dev. Dyn.* **2010**, *239* (2), 398–406 DOI: 10.1002/dvdy.22161.
- (94) Jakab, K.; Norotte, C.; Damon, B.; Marga, F.; Neagu, A.; Besch-Williford, C. L.; Kachurin, A.; Church, K. H.; Park, H.; Mironov, V.; et al. Tissue engineering by self-assembly of cells printed into topologically defined structures. *Tissue Eng. Part A* **2008**, *14* (3), 413–421 DOI: 10.1089/ten.2007.0173.
- (95) Norotte, C.; Marga, F. S.; Niklason, L. E.; Forgacs, G. Scaffold-free vascular tissue engineering using bioprinting. *Biomaterials* **2009**, *30* (30), 5910–5917 DOI: 10.1016/j.biomaterials.2009.06.034.
- (96) Skardal, A.; Zhang, J.; McCoard, L.; Xu, X.; Oottamasathien, S.; Prestwich, G. D. Photocrosslinkable Hyaluronan-Gelatin Hydrogels for Two-Step Bioprinting. *Tissue Eng. Part A* **2010**, *16* (8), 2675–2685 DOI: 10.1089/ten.tea.2009.0798.
- (97) Skardal, A.; Zhang, J.; Prestwich, G. D. Bioprinting vessel-like constructs using hyaluronan hydrogels crosslinked with tetrahedral polyethylene glycol tetracrylates. *Biomaterials* **2010**, *31* (24), 6173–6181 DOI: 10.1016/j.biomaterials.2010.04.045.
1. (98) Derby, B. Bioprinting: inkjet printing proteins and hybrid cell-containing materials and structures. *J. Mater. Chem.* **2008**, *18*, 5717–5721 DOI: 10.1039/b807560c.
- (99) Cui, X.; Boland, T. Human microvasculature fabrication using thermal inkjet printing technology. *Biomaterials* **2009**, *30* (31), 6221–6227 DOI: 10.1016/j.biomaterials.2009.07.056.
- (100) Christensen, K.; Xu, C.; Chai, W.; Zhang, Z.; Fu, J.; Huang, Y. Freeform inkjet printing of cellular structures with bifurcations. *Biotechnol. Bioeng.* **2015**, *112* (5), 1047–1055 DOI: 10.1002/bit.25501.
- (101) Wu, P. K.; Ringeisen, B. R. Development of human umbilical vein endothelial cell (HUVEC) and human umbilical vein smooth muscle cell (HUVSMC) branch/stem structures on hydrogel layers via biological laser printing (BioLP). *Biofabrication* **2010**, *2*, 014111 DOI: 10.1088/1758-5082/2/1/014111.
- (102) Pirlo, R. K.; Wu, P.; Liu, J.; Ringeisen, B. PLGA/hydrogel biopapers as a stackable substrate for printing HUVEC networks via BioLP. *Biotechnol. Bioeng.* **2012**, *109* (1),

262–273 DOI: 10.1002/bit.23295.

- (103) Hocheng, H.; Tseng, C. Mechanical and optical design for assembly of vascular endothelial cells using laser guidance and tweezers. *Opt. Commun.* **2008**, *281* (17), 4435–4441 DOI: 10.1016/j.optcom.2008.05.006.
- (104) Huh, D.; Matthews, B. D.; Mammoto, A.; Hsin, H. Y.; Ingber, D. E. Reconstituting Organ-Level Lung Functions on a Chip. **2009**.
- (105) Kang, Y. B. A.; Sodunke, T. R.; Lamontagne, J.; Cirillo, J.; Rajiv, C.; Bouchard, M. J.; Noh, M. Liver sinusoid on a chip: Long-term layered co-culture of primary rat hepatocytes and endothelial cells in microfluidic platforms. *Biotechnol. Bioeng.* **2015**, *112* (12), 2571–2582 DOI: 10.1002/bit.25659.
- (106) Sarveswaran, K.; Kurz, V.; Dong, Z.; Tanaka, T.; Penny, S.; Timp, G. Synthetic Capillaries to Control Microscopic Blood Flow. *Sci. Rep.* **2016**, *6* (February), 21885 DOI: 10.1038/srep21885.
- (107) Zhang, B.; Montgomery, M.; Chamberlain, M. D.; Ogawa, S.; Korolj, A.; Pahnke, A.; Wells, L. A.; Massé, S.; Kim, J.; Reis, L.; et al. Biodegradable scaffold with built-in vasculature for organ-on-a-chip engineering and direct surgical anastomosis. *Nat. Mater.* **2016**, *1* (March), 1–42 DOI: 10.1038/nmat4570.
- (108) Kolesky, D. B.; Truby, R. L.; Gladman, a. S.; Busbee, T. a.; Homan, K. a.; Lewis, J. a. 3D bioprinting of vascularized, heterogeneous cell-laden tissue constructs. *Adv. Mater.* **2014**, *26* (19), 3124–3130 DOI: 10.1002/adma.201305506.
- (109) Lee, V. K.; Kim, D. Y.; Ngo, H.; Lee, Y.; Seo, L.; Yoo, S. S.; Vincent, P. a.; Dai, G. Creating perfused functional vascular channels using 3D bio-printing technology. *Biomaterials* **2014**, *35*, 8092–8102 DOI: 10.1016/j.biomaterials.2014.05.083.
- (110) Lee, V. K.; Lanzi, A. M.; Ngo, H.; Yoo, S. S.; Vincent, P. A.; Dai, G. Generation of multi-scale vascular network system within 3D hydrogel using 3D bio-printing technology. *Cell. Mol. Bioeng.* **2014**, *7* (3), 460–472 DOI: 10.1007/s12195-014-0340-0.
- (111) Colosi, C.; Shin, S. R.; Manoharan, V.; Massa, S.; Costantini, M.; Barbetta, A.; Dokmeci, M. R.; Dentini, M.; Khademhosseini, A. Microfluidic Bioprinting of Heterogeneous 3D Tissue Constructs Using Low-Viscosity Bioink. *Adv. Mater.* **2016**, *28* (4), 677–684a DOI: 10.1002/adma.201503310.
- (112) Schacht, K.; Jüngst, T.; Schweinlin, M.; Ewald, A.; Groll, J.; Scheibel, T. Biofabrication of Cell-Loaded 3D Spider Silk Constructs. *Angew. Chemie Int. Ed.* **2015**, *54* (9), 2816–2820 DOI: 10.1002/anie.201409846.
- (113) Ouyang, L.; Highley, C. B.; Rodell, C. B.; Sun, W.; Burdick, J. A. 3D Printing of Shear-Thinning Hyaluronic Acid Hydrogels with Secondary Cross-Linking. *ACS Biomater. Sci. Eng.* **2016**, acsbiomaterials.6b00158 DOI: 10.1021/acsbiomaterials.6b00158.
- (114) Highley, C. B.; Rodell, C. B.; Burdick, J. a. Direct 3D Printing of Shear-Thinning

- Hydrogels into Self-Healing Hydrogels. *Adv. Mater.* **2015**, n/a – n/a DOI: 10.1002/adma.201501234.
- (115) Hinton, T. J.; Jallerat, Q.; Palchesko, R. N.; Park, J. H.; Grodzicki, M. S.; Shue, H.-J.; Ramadan, M. H.; Hudson, A. R.; Feinberg, A. W. Three-dimensional printing of complex biological structures by freeform reversible embedding of suspended hydrogels. *Sci. Adv.* **2015**, *1* (9), e1500758–e1500758 DOI: 10.1126/sciadv.1500758.
- (116) Bhattacharjee, T.; Zehnder, S. M.; Rowe, K. G.; Jain, S.; Nixon, R. M.; Sawyer, W. G.; Angelini, T. E. Writing in the granular gel medium. *Sci. Adv.* **2015**, *1* (8), e1500655 DOI: 10.1126/sciadv.1500655.
- (117) Coulombe, K. L. K.; Bajpai, V. K.; Andreadis, S. T.; Murry, C. E. Heart Regeneration with Engineered Myocardial Tissue. *Annu. Rev. Biomed. Eng.* **2014**, *16*, 1–28 DOI: 10.1016/j.surg.2006.10.010.Use.
- (118) Riegler, J.; Gillich, A.; Shen, Q.; Gold, J. D.; Wu, J. C. Cardiac tissue slice transplantation as a model to assess tissue-engineered graft thickness, survival, and function. *Circulation* **2014**, *1* (30), S77–S86 DOI: 10.1161/CIRCULATIONAHA.113.007920.
- (119) Cheng, G.; Liao, S.; Wong, H. K.; Lacorre, D. A.; Di Tomaso, E.; Au, P.; Fukumura, D.; Jain, R. K.; Munn, L. L. Engineered blood vessel networks connect to host vasculature via wrapping-and-tapping anastomosis. *Blood* **2011**, *118* (17), 4740–4749 DOI: 10.1182/blood-2011-02-338426.
- (120) Sooppan, R.; Paulsen, S. J.; Han, J.; Ta, A. H.; Dinh, P.; Gaffey, A. C.; Venkataraman, C.; Trubelja, A.; Hung, G.; Miller, J. S.; et al. In Vivo Anastomosis and Perfusion of a Three-Dimensionally-Printed Construct Containing Microchannel Networks. *Tissue Eng. Part C* **2016**, *22* (1), 1–7 DOI: 10.1089/ten.tec.2015.0239.
- (121) Hooper, R. C.; Hernandez, K. a; Boyko, T.; Harper, A.; Joyce, J.; Golas, A. R.; Spector, J. a. Fabrication and in vivo microanastomosis of vascularized tissue-engineered constructs. *Tissue Eng. Part A* **2014**, *20* (19-20), 2711–2719 DOI: 10.1089/ten.TEA.2013.0583.
- (122) Montesano, R.; Orci, L.; Vassalli, P. In vitro rapid organization of endothelial cells into capillary-like networks is promoted by collagen matrices. *J. Cell Biol.* **1983**, *97* (5 I), 1648–1652 DOI: 10.1083/jcb.97.5.1648.
- (123) Zervantonakis, I. K.; Hughes-Alford, S. K.; Charest, J. L.; Condeelis, J. S.; Gertler, F. B.; Kamm, R. D. Three-dimensional microfluidic model for tumor cell intravasation and endothelial barrier function. *Proc. Natl. Acad. Sci.* **2012**, *109* (34), 13515–13520 DOI: 10.1073/pnas.1210182109.
- (124) Bersini, S.; Jeon, J. S.; Dubini, G.; Arrigoni, C.; Chung, S.; Charest, J. L.; Moretti, M.; Kamm, R. D. A Microfluidic 3D In Vitro Model for Specificity of Breast Cancer

- Metastasis to Bone. *Biomaterials* **2014**, 35 (8), 2454–2461 DOI: 10.1038/nature13314.A.
- (125) Quaegebeur, A.; Lange, C.; Carmeliet, P. The neurovascular link in health and disease: Molecular mechanisms and therapeutic implications. *Neuron* **2011**, 71 (3), 406–424 DOI: 10.1016/j.neuron.2011.07.013.
- (126) Nicolakakis, N.; Hamel, E. Neurovascular function in Alzheimer's disease patients and experimental models. *J. Cereb. Blood Flow Metab.* **2011**, 31 (6), 1354–1370 DOI: 10.1038/jcbfm.2011.43.
- (127) Kang, Y.; Mochizuki, N.; Khademhosseini, A.; Fukuda, J.; Yang, Y. Engineering a vascularized collagen-beta-tricalcium phosphate graft using an electrochemical approach. *Acta Biomater.* **2015**, 11 (1), 449–458 DOI: 10.1016/j.actbio.2014.09.035.
- (128) McFadden, T. M.; Duffy, G. P.; Allen, A. B.; Stevens, H. Y.; Schwarzmaier, S. M.; Plesnila, N.; Murphy, J. M.; Barry, F. P.; Guldborg, R. E.; O'Brien, F. J. The delayed addition of human mesenchymal stem cells to pre-formed endothelial cell networks results in functional vascularization of a collagen-glycosaminoglycan scaffold in vivo. *Acta Biomater.* **2013**, 9 (12), 9303–9316 DOI: 10.1016/j.actbio.2013.08.014.
- (129) Bayer, E. A.; Gottardi, R.; Fedorchak, M. V.; Little, S. R. The scope and sequence of growth factor delivery for vascularized bone tissue regeneration. *J. Control. Release* **2015**, 219, 129–140 DOI: 10.1016/j.jconrel.2015.08.004.
- (130) Gadjanski, I.; Spiller, K.; Vunjak-Novakovic, G. Time-dependent processes in stem cell-based tissue engineering of articular cartilage. *Stem Cell Rev.* **2012**, 8 (3), 863–881 DOI: 10.1016/j.surg.2006.10.010.Use.
- (131) Kolesky, D. B.; Homan, K. A.; Skylar-Scott, M. A.; Lewis, J. A. Three-dimensional bioprinting of thick vascularized tissues. *Proc. Natl. Acad. Sci.* **2016**, 201521342 DOI: 10.1073/pnas.1521342113.
- (132) Wu, W.; Deconinck, A.; Lewis, J. a. Omnidirectional printing of 3D microvascular networks. *Adv. Mater.* **2011**, 23 (24), 178–183 DOI: 10.1002/adma.201004625.
- (133) Highley, C. B.; Rodell, C. B.; Burdick, J. a. Direct 3D Printing of Shear-Thinning Hydrogels into Self-Healing Hydrogels. *Adv. Mater.* **2015**, 27, 5075–5079 DOI: 10.1002/adma.201501234.
- (134) Derby, B. Inkjet Printing of Functional and Structural Materials: Fluid Property Requirements, Feature Stability, and Resolution. *Annu. Rev. Mater. Res.* **2010**, 40 (1), 395–414 DOI: 10.1146/annurev-matsci-070909-104502.
- (135) Linnenberger, A.; Bodine, M. I.; Fiedler, C.; Roberts, J. J.; Skaalure, S. C.; Quinn, J. P.; Bryant, S. J.; Cole, M.; McLeod, R. R.; James, C. D.; et al. Three dimensional live cell lithography. *Biomed. Eng. J. Neurosci. Methods* **2000**, 47 (1602), 17–21 DOI: 10.1364/OE.21.010269.

- (136) Mirsaidov, U.; Scrimgeour, J.; Timp, W.; Beck, K.; Mir, M.; Matsudaira, P.; Timp, G.
Live cell lithography: using optical tweezers to create synthetic tissue. *Lab Chip* **2008**,
8 (12), 2174–2181 DOI: 10.1039/b807987k.

Chapter 3

A three-dimensional biomimetic peripheral nerve model for drug testing and disease modelling

Afonso Malheiro, Francis Morgan, Matthew Baker, Lorenzo Moroni, Paul Wieringa

Department of Complex Tissue Regeneration, MERLN Institute for Technology-Inspired Regenerative Medicine, Maastricht University, 6200 MD Maastricht, The Netherlands

Abstract

In vitro peripheral nerve models provide valuable tools to study neurobiology questions and assess drug performance, in a regenerative or pathology context. To this end, we have developed a representative model of the peripheral nerve that displays three-dimensional (3D) neural anisotropy and myelination, which we showcase here as a simple and low-cost platform for drug screening. The model is composed of three main parts, including rat primary Schwann cells (SCs) seeded onto an electrospun scaffold to create bands of Büngner (BoB), primed PC12 cells as neuronal cell population, and a fibrin hydrogel to provide three-dimensionality. We also validated the use of primed PC12 as a neuron population by comparing it to rat dorsal root ganglions (DRGs) neurons. In both models we could obtain well aligned neurites and mature myelin segments. In short term cultures (7 days), we found that the addition of exogenous SCs enhanced neurite length and neurite growth area, compared to scaffolds with a laminin coating only. Addition of fibrin also lead to increased outgrowth of DRG and primed PC12 neurites, compared to 2D cultures. Moreover, neurite outgrowth in fibrin cultures was simultaneously multiplanar and anisotropic, suggesting that the SC-seeded scaffold can direct not only the growth of adjacent neurites, but also those growing above it. These results highlight the feasibility of the combination of a SC pre-seeded scaffold with a fibrin hydrogel, to direct and improve neurite growth in 3D. To demonstrate the model potential, we tested our platform at an immature (7 days *in vitro*) and mature state (28 days *in vitro*) of development. At the immature stage we could inhibit neurite growth through protein blocking (via antibody binding) and show suramin (200 μ M) neurotoxicity on cells. At the mature stage, when myelin is compact, we exposed cells to hyperglycemic conditions (45 mM glucose) to mimic diabetic conditions and showed that myelin deforms consequently. Moreover, we demonstrated that by supplementing cultures with epalrestat (1 μ M), myelin deformation can be partly prevented.

In sum, we developed a biomimetic nerve platform using an affordable and accessible cell line as neuronal population, which displays similar results to primary neurons, but does not require recurrent animal sacrifice. This platform holds great promise as it can be used to conveniently and inexpensively perform drug screenings on peripheral nerve-like tissue, in a normal or pathological state.

Introduction

Peripheral neuropathies caused by traumatic injuries or other pathologies (e.g. diabetes) are a common worldwide problem^{1,2}. Despite the inherent regenerative potential of the peripheral nervous system, clinical intervention is often needed. For this, clinicians need to use therapeutic products that have been traditionally validated via animal experimentation. However, the economic burden and ethical issues concerning animal use have prompted the development of *in vitro* peripheral nerve (PN) models³. These models aim to replicate the anatomy and function of the native nerve, in order to provide a simple and cost-effective alternative to animal use, while providing a similar and reliable outcome. Using these models, researchers can predict the performance and side effects of certain bio-products such as growth factors (e.g. neurotrophic factors⁴), cells (e.g. stem cell derived glial cells⁵), biomaterials⁶ and drugs⁷. Moreover, pathological conditions can be induced in order to study disease progression and to screen appropriate therapeutic drugs⁸.

Anatomically, the native PN consists of highly anisotropic bundles of axons, supported by extracellular matrix molecules (ECM), such as fibronectin, laminin and collagen type IV. Schwann cells (SCs) surround these axons, ensheathing them and producing myelin sections separated by short gaps (Nodes of Ranvier) for saltatory conduction. Non-myelinating SCs are also present, forming Remak bundles within the PN⁹. In addition, SCs are also of critical importance during nerve regeneration. Upon nerve injury, SCs dedifferentiate and increase production of cell adhesion (e.g. L1CAM) and ECM molecules (e.g. fibronectin), while proliferating over the basal lamina. The result is the formation of aligned cell tracks, termed Bands of Büngner (BoB), which serve to guide axons back to their distal targets^{10,11}. Considering these aspects, an ideal PN model should mimic the three-dimensionality (3D), ECM presence and axon myelination. To specifically model nerve regeneration after injury, SCs should also be stimulated to form BoB-like structures prior to having contact with neurons. Moreover, cell functionality/drug screening tests should be feasible and relatively simple to perform.

To achieve compact myelination, a co-culture of a neurons/SCs must proceed for at least 21 days¹². Several works have reported the achievement of mature myelinated neural

networks¹²⁻¹³, but most strategies use co-cultures grown on flat planar substrates, which do not maintain BoB-like architecture and ultimately leads to a disorganized two-dimensional (2D) neural network. Some approaches are able to create spatial anisotropic arrangements,^{14,15} including aligned electrospun (ESP) scaffolds reported to induced organized neuron/glia anisotropy¹⁶. While the anisotropic growth of dorsal root ganglion (DRG) and NG108-15 neurites was able to achieve a maximal length of 2500 μm and 140 μm , respectively, no myelination was shown and axonal growth was confined to a 2D plane, thus not reflecting the true 3D PN architecture. To create both the anisotropy and three-dimensionality, Pawar et al.⁶ developed an anisotropic alginate-based hydrogel with defined capillaries for cell ingrowth. The authors reported a concomitant axonal and SC invasion from a DRG, which varied according to the capillaries diameter and coating type. However, even in the best conditions, both the maximum neurite length ($< 450 \mu\text{m}$) and density ($< 25\%$) are low compared to typical reports of DRG cultures. Moreover, the neurites and SCs are unevenly distributed, with the latter not showing signs of BoB formation or myelination. To improve upon this, Khoshakhlagh et al.¹⁷ developed a 3D hydrogel platform that produces anisotropic and myelinated neurons from a DRG population, either with or without exogenous SCs in the hydrogel. Addition of exogenous SCs increased the volume of produced myelin within the platform, but because SCs are randomly dispersed through the gel, with no clear organisation, it does not represent the regrowing stages after PN injury, thus limiting the platform application. Moreover, the platform is also reported as a PN model for *in vitro* testing, but despite showing electrophysiology testing, drug or pathology tests have yet to be shown.

To avoid extensive animal sacrifice and develop more translational models, research has been devoted to use stem cell-derived neurons as a neuronal cell population for PN models. Recently, some works have reported physiologically relevant and myelinated tissue using stem cell-derived neurons¹⁸⁻¹⁹. Sharma et al.¹⁹ reported a 3D hydrogel platform with aligned and myelinated iPSCs-derived neurons, but lack the demonstration of applicability in regard to drug testing and disease modelling. On the other hand, the work of Clark et al.¹⁸ shows model applications but their reported model is a 2D disorganised neural network. While a promising approach, stem cell differentiation is an expensive and laborious process. As an alternative, cell lines can provide a cost-effective, simple and quick solution to generate neuronal models for preliminary testing, and at the same time avoid the routine animal sacrificing³. Moreover, protocols for cell lines are currently more standardized than for stem cell differentiation, which allows a faster process implementation. Among these, the rat pheochromocytoma PC12 cell line is a robust cell line that has been used extensively in neurosciences. Derived from adrenal chromaffin cells of neural crest origin, these cells can be terminally differentiated into a neuronal phenotype, similar to sympathetic ganglion neurons, upon nerve growth factor (NGF) stimulation²⁰. Differentiated cells can extend neurites and

secrete neurotransmitters, such as acetylcholine and dopamine, making them a useful tool to investigate drug effects on cell morphology and its secretome²⁰⁻²¹. Contrary to other cell lines, such as 50B11 cells, which only last for 72 h³, differentiated PC12 can be maintained for a period long enough to achieve compact myelination, as shown by Sango et al. in a 2D co-culture model¹³. Furthermore, the robustness of PC12 cells provides an accessible tool to obtain a desired neuronal phenotype via transfection. For instance, several reports have shown the induction of transient receptor potential cation channels (TRPV family) expression in transfected PC12 cells, which can later be targeted and studied²²⁻²³.

Here, we show the development of a biomimetic PN model and illustrate its applications in drug testing and disease modelling. Our proposed model relies on simple, low-cost components to nevertheless produce complex and meaningful tissue architectures, such as 3D anisotropic myelinated neurons. This model consists of three main components as illustrated in Fig. 1: 1) SC-seeded scaffold that mimics the BoB; 2) neuronal cell population sitting on top of the scaffold and 3) a fibrin hydrogel embedding to allow 3D cell growth. As neuronal population we chose pre-differentiated (primed) PC12 cells. Because these cells only represent a physiological subset of neurons, we corroborate our model using the classic DRG explants, to validate the flexibility and versatility of the platform in producing myelinated nerve fibers of different phenotypes.

To better emulate native BoB tissue organization, we combined primary SCs with an aligned microfibrillar scaffold to induce the formation of anisotropic SC bands. Besides the oriented cell organization, we also show for the first time (to the best of our knowledge) that we can mimic the BoB in terms of the SC production of ECM milieu and cell-adhesion molecules. The results we show here represent a significant improvement in terms of biomimicry over other works that attempted BoB formation via similar combinations of aligned scaffolds and SCs^{4,16,24}. Due to this BoB substrate, we could trigger a rapid, vast and anisotropic neurite growth from either DRGs or PC12 cells. The values here reported are around 3000 μm (for DRGs) and 800 μm (for PC12) in length after 7 days of culture, exceeding growth rates reported by similar strategies^{6,16,17}. When maintaining these cells for a longer period of 28 days, we could obtain neurites with around 3200 μm (for DRGs) and 2000 μm (for PC12) in length as well as a compact and thick myelin sheath. Particularly for PC12 cells, the results shown here constitute a major improvement in terms of tissue size and morphology compared to other reports using this cell line¹³.

By combining our BoB substrate with a fibrin hydrogel, we also achieved organized 3D neurite outgrowth to better recapitulate the native PN architecture. Our strategy of pre-forming BoB structures by culturing a SC-seeded scaffold prior to encasing in a hydrogel constitutes a novel approach to generate 3D anisotropic myelinated neurons in a quick and efficient manner. With this approach, we have generated a unique and more representative PN regeneration

model and, further, we are able to form mature 3D neural tissue, from either DRGs or PC12 cells. The level of maturity and overall tissue growth here displayed is comparatively higher to other recent works that also combine aligned fibrous scaffolds with hydrogels to generate 3D aligned neuronal tissue^{25,26}. Moreover, in our model we show that growing axons guided by topographical cues within a 3D environment can influence the direction of neighbouring axons located in a different plane and not in contact with the same cues. While this phenomenon has been demonstrated in other 3D *in vitro* works representing simplistic forms of the central nervous system²⁷, this is the first time that this has been demonstrated in a 3D PN model, and particularly for large distances (~100 µm for DRGs and ~50 µm for PC12 cells).

Using PC12 cells, we show applicability of this platform to perform tests at an early (repair) stage or mature (myelinated) stage of neuronal growth. At an earlier stage, we take advantage of our pre-formed BoB to simulate a regenerative setting and probe how neuron/SC or neuron/ECM interactions can affect neurite growth. Additionally, we also show the ability to perform and assess neurotoxicity of substances, using suramin, a known neurotoxic drug, as an example⁷. Finally, at the mature (myelinated) stage, we show the potential to investigate myelin damage as a result of hyperglycemia and to screen therapeutic drugs that mitigate this damage.

These various applications demonstrate the versatility of our platform, which can be built and used to provide the needed information depending on the subject of study. For instance, the ability to selectively determine the presence or absence of SCs is particularly useful to either build a fully aligned and myelinated model, to investigate myelin damage, or an aligned but unmyelinated model, to investigate axonal signalling. With our method we also aim to provide a simple yet reliable alternative to recurrent animal use, which is of particular interest when evaluating how neural tissue can be affected by potential therapeutics, such as drugs, biomaterials, or biomolecules.

Materials and Methods

Polydimethylsiloxane (PDMS) support fabrication

To produce the scaffold supports (outer diameter of 20 mm; inner diameter of 16 mm and height of 1.5 mm) we used a custom-made mold created through the milling (monoFAB SRM-20, Roland) of a poly(methyl methacrylate) (PMMA) slab (Fig. S1). We then poured a PDMS solution (10:1 monomer:curing agent) (Farnell) on the mold and cured at 80°C for 2 h. Afterwards, individual supports were punched out and post-cured/sterilized at 160°C for 4 h. The supports were kept in sterile conditions until further use.

Scaffold fabrication

To fabricate aligned nanofibrous scaffolds we did a two-step process, using a custom-built electrospinning apparatus with humidity and temperature control. The first step was the production of a release layer by electro spraying a solution of 50% polyethyleneoxide (PEO, Mn = 3350, Sigma-Aldrich) in Milli-Q onto aluminum foil. For this, the solution flowed through a 0.8 mm inner diameter stainless steel needle (Unimed S.A.) at 2 ml/h, while subjected to 20 kV and at a distance of 10 cm from a 60 mm diameter mandrel rotating at 5000 rpm. Afterwards, a nonwoven polyurethane mesh (6691 LL (40 g/m²), a kind gift from Lantor B.V., the Netherlands) was prepared by punching an array of 12 mm circular holes and placed on the mandrel, covering the PEO sprayed-foil. We then produced the scaffolds by electrospinning (ESP) a solution of 300PEOT55PBT45 (PolyVation) in 75:25 Chloroform/1,1,3,3-hexafluoroisopropanol onto the mesh support structure. For this process, the solution flowed through a 0.5 mm inner diameter stainless steel needle (Unimed S.A.) at 0.75 ml/h, while applying a voltage of 12 kV and at a distance of 10 cm from a rotating mandrel (at 5000 rpm). During both processes, the humidity remained at 35-40% and the temperature at 22-24 °C. Finally, we generated individual scaffolds from the polyurethane mesh by punching 15 mm-outer diameter sections concentric to the 12 mm holes, resulting in a thin ESP membrane supported by a polyurethane mesh ring. Scaffolds were dipped in deionized water to detach from the Al foil, then left in phosphate buffered saline (PBS) until further use.

Schwann cell (SCs) isolation and purification

Primary Schwann cells (SCs) were harvested from the sciatic nerves of neonatal (P1-P3) Wistar rat pups, following local and Dutch animal use guidelines. Nerve segments were extracted and digested, followed by cell isolation and purification as described by Kaewkhaw et al.²⁸. Briefly, the collected nerves were chopped and digested in a 0.05% (wt/vol) collagenase solution for 60 min at 37°C, 5% CO₂. The resultant cell suspension was filtered through a 40 µm cell strainer, centrifuged for 6 min at 400 g, followed by supernatant removal and cell pellet washing with DMEM containing 10% fetal bovine serum (FBS) and 100 U/ml penicillin and 100 µg/ml streptomycin. Cells were centrifuged again at 400 g for 6 min and the supernatant discarded. Finally, cells were re-suspended with 2 ml of Schwann cell medium, composed of DMEM, D-valine (Cell Culture Technologies), 2 mM L-glutamine, 10% (v/v) FBS, 1% (v/v) N2 supplement (R&D Systems), 20 µg/ml bovine pituitary extract, 5 µM forskolin, 100 U/ml penicillin and 100 µg/ml streptomycin, and 0.25 µg/ml amphotericin B (all Sigma-Aldrich), then plated on 35 mm petri dish pre-coated with 1 µg/ml laminin (R&D systems) and incubated at 37°C, 5% CO₂. The use of D-valine in place of L-valine serves to inhibit fibroblast growth while permitting SCs survival and proliferation. 1 ml of fresh medium was added at day 7 of

culture and subsequently changed every 2 days until confluency. Cells were used between passage number 3 and 8 (P3-P8).

Scaffold sterilization and laminin coating

The scaffolds were sterilized in 70% ethanol, air dried and left in PBS until further use. For laminin coating, we added 100 µl of a 1 µg/ml laminin-1 (R&D systems) and 2 µg/ml poly-D-lysine (Sigma Aldrich) solution in PBS to each scaffold, followed by overnight incubation at 37 °C. The next day, the scaffolds were washed twice with PBS and left in this buffer until further use.

SCs seeding on scaffolds

To form Bands of Büngner-like structures, we seeded SCs on the aligned ESP scaffolds (either coated or not with laminin) and cultured them for 7 days. 100×10^3 SCs were seeded in 250 µl of SC proliferation medium, composed of high glucose DMEM, 10% (v/v) FBS, 20 µg/ml bovine pituitary extract, 5 µM forskolin (all Sigma-Aldrich), 4 mM L-glutamine, N2 supplement and 100 U/ml penicillin and 100 µg/ml streptomycin (Thermo Fisher Scientific). Extra medium was added the day after and the medium changed every other day until day 7 of culture.

Neuronal co-cultures:

For both neuronal co-cultures, we started by culturing the SCs alone on the scaffold for 7 days. After this period, we added a neuronal cell population, which were either primary cells (dorsal root ganglions, DRGs) or a cell line (PC12 cells) and switched to the appropriate co-culture medium (described below).

a) DRG isolation and co-culture on scaffolds

DRGs were dissected from P7 Brown Norway rats, previously sacrificed by decapitation, following local and Dutch animal use guidelines. After being stripped from the nerve roots, one DRG was carefully placed in the center of each scaffold containing 150 µl of DRG/SC co-culture medium and left to attach overnight. This medium was composed of Neurobasal Medium, 0.5 mM Glutamax, 100 U/ml penicillin and 100 µg/ml streptomycin (all Thermo Fisher Scientific), 100 µg/ml aprotinin, 50 ng/ml human nerve growth factor (NGF), 50 µg/ml ascorbic acid (all Sigma-Aldrich), 25 ng/ml human neuregulin-1 type III (NRG-1 SMDF) and N21 supplement (both from R&D systems). Scaffolds for fibrin embedding were first transferred to the PDMS supports and the culture medium replaced with 150 µl of a filter sterilized bovine fibrinogen (7 mg/ml) and aprotinin (200 µg/ml) solution in PBS. Immediately after this, we added 150 µl of a filter sterilized-thrombin (10 U/ml) and calcium chloride (5 mM) solution in PBS and incubated at 37 °C for about 15 min (all reagents from Sigma-Aldrich).

After gel formation, we added 1 ml of DRG/SCs co-culture medium. For conditions without fibrin hydrogel embedding, we directly added extra medium the day after seeding. In both conditions, the medium was refreshed every other day.

b) PC12 priming and co-culture on scaffolds

PC12 cells (DSMZ, Germany) were expanded in suspension with PC12 proliferation medium composed of RPMI 1640 (Thermo Fisher Scientific), 10% (vol/vol) Horse Serum and 5% (vol/vol) FBS (both Sigma-Aldrich). For the priming process, we first coated a 100 mm petri dish with 1 mg/ml rat collagen (Corning) solution in 0.02 M acetic acid overnight at 37°C. Then we seeded 275×10^3 PC12 cells in high glucose DMEM containing 5% (vol/vol) FBS. The following day, we replaced this medium with PC12 priming medium composed of high glucose DMEM, N2 supplement, 50 µg/ml ascorbic acid and 50 ng/ml NGF. This medium was refreshed every other day and the culture maintained for a total of 7 days. After this period, we seeded either the primed or non-primed PC12 on SC-seeded scaffolds and switched to PC12/SCs co-culture medium, composed of high glucose DMEM, N21 supplement, 1% (v/v) Horse Serum, 100 U/ml penicillin and 100 µg/ml streptomycin, 50 µg/ml ascorbic acid, 100 ng/ml NGF and 25 ng/ml NRG-1 type III. For short term co-cultures (7 days) we seeded 2.5×10^3 cells per scaffold while for long term cultures (21 or 28 days) we reduced the seeding number to 350 cells. Similar to the DRG experiment, for samples without fibrin embedding, we directly added extra medium the day after seeding, while for those with fibrin coverage we followed the same procedure. For all conditions, medium changes were performed every other day.

PC12/SCs co-culture with antibodies

To probe the effect of L1CAM or integrin alpha-6 blocking, we supplemented the co-culture medium with antibodies that target those specific proteins. Briefly, we seeded 2.5×10^3 primed PC12 on SC-seeded scaffolds with normal PC12/SCs co-culture medium and left cells to attach overnight. The next day, we changed the medium to one containing either anti-L1CAM (Abcam, ab123990, 1:200) or anti-integrin alpha-6 (Bosterbio, M01693, 1:100). The medium was changed every other day and the samples analyzed at day 7.

Suramin exposure and cell viability test

Primed PC12 cells were cultured for 7 days on laminin coated scaffolds or laminin coated coverslips and then incubated for 24 h with 200 µM of suramin (Sigma-Aldrich, S2671) in PC12/SCs co-culture medium. Control samples were cultured with just PC12/SCs co-culture medium. Following the 24 h incubation, samples were fixed for immunostaining or tested for viability according to the manufacturer protocol (PrestoBlue™ Cell Viability Reagent, Thermo

Fischer Scientific, A13261) followed by correspondent DNA quantification on the same samples.

Hyperglycemia test

Co-cultures of primed PC12 and SCs were maintained until day 28. At that point the medium was changed to either normal medium; hyperglycemic medium composed of normal medium supplemented with 45 mM glucose or hyperglycemic medium plus 45 mM glucose and 1 μ M epalrestat (Sigma-Aldrich, SML0527). Cultures were kept at 37 °C, 5% CO₂ for additional 48 h and then fixed with 4% paraformaldehyde for 20 min at room temperature. Following this the samples were prepared for TEM as described below.

DNA extraction and quantification

Samples were freeze-thawed 3x, then incubated with 1 mg/ml proteinase K in Tris/EDTA buffer at 56 °C for 16 h and freeze-thawed 3x once more. For cell lysis and DNA quantification, we used the CyQUANT™ Cell Proliferation Assay (Thermo Fisher Scientific, C7026) and detected the emitted fluorescence signal using a microplate reader (CLARIOstar Plus) set for excitation at 480 nm and emission at 520 nm.

LIVE/DEAD assay

To quickly and visually assess cell viability, we used the LIVE/DEAD staining kit according to the manufacturer's manual (Thermo Fisher Scientific, L3224). Briefly, the samples were washed twice with PBS, then incubated with staining solution containing 1 μ M calcein AM and 2.5 μ M ethidium homodimer-1 in PBS for 30 min at 37 °C, 5% CO₂. Following this, samples were washed with PBS and left at 4°C until imaging (same day). Finally, images were acquired using a confocal laser scanning microscope (Leica TCS SP8).

Immunocytochemistry (ICC)

Samples were fixed with 4% paraformaldehyde (PFA) for 20 min at room temperature (RT), rinsed thoroughly with PBS, and left hydrated before further use. Permeabilization was carried for 20 min at RT with 0.1% Triton X-100 in PBS, followed by rinsing with PBS and blocking with blocking buffer composed of 5% goat serum, 0.05% Tween20, and 1% bovine serum albumin (BSA) in PBS for 2 h at RT. Immediately, samples were incubated overnight at 4°C with primary antibody solutions in blocking buffer. On the next day, the samples were washed with a wash buffer composed of 0.05% Tween20 and 1% BSA in PBS and incubated for 2 h at RT with secondary antibody solutions in wash buffer. Following this, we rinsed the samples with PBS, stained with DAPI (0.2 μ g/ml) for 10 min at RT, and left them in PBS until imaging. For F-actin staining we used Alexa Fluor 568 phalloidin (Thermo Fisher Scientific) at

1:100 dilution in PBS for 1 h at RT. The primary antibodies used were the following: anti-L1CAM (Abcam, ab123990, 1:100), anti-fibronectin (Abcam, ab6328, 1:200), anti-laminin (Bioconnect, aa1420-1500, 1:100), anti-collagen IV (Nordic, MUB0338S, 1:100), anti- β III tubulin (Sigma-Aldrich, T8578, 1:1000), anti-S100 (Sigma-Aldrich, S2644, 1:100), anti-Myelin Basic Protein, MBP (Thermo Fisher Scientific, PA1-46447, 1:50), cleaved caspase-3 (Cell Signaling Technology, 9661, 1:400), anti-Pan Nav (Alomone Labs, ASC-003, 1:150). Finally, the used secondary antibodies were the following: goat anti-mouse conjugated with Alexa Fluor 488; goat anti-mouse conjugated with Alexa Fluor 568, goat anti-rabbit conjugated with Alexa Fluor 488 and goat anti-rabbit conjugated with Alexa Fluor 568 (all Thermo Fisher Scientific). Finally, images were acquired using either a confocal laser scanning microscope (Leica TCS SP8) or a 2-photon microscope (Leica STP6000).

Scanning Electron Microscopy (SEM)

The SC-seeded scaffolds were washed 3x with PBS, fixed with 4% paraformaldehyde (PFA) for 20 min at room temperature (RT), washed again 3x with PBS, dehydrated in a series of ethanol dilutions (1x 50, 60, 70, 80, 90, and 96% and 2x 100%) for 30 min and then critical point dried with liquid carbon dioxide (Leica EM CPD 300). Following this, samples were gold-sputtered (Cressington Sputter Coater 108 auto) for 40 s at 30 mA and then imaged using a SEM (FEI/Philips XL-30 ESEM) at $V= 10$ kV. Samples not containing cells were only gold-sputtered prior to imaging.

Transmission Electron Microscopy (TEM)

Samples were prepared by fixation in 4% PFA in PBS, followed by washing with 0.1 M Cacodylate (3x for 15 min). Cells were fixed again with 2.5% glutaraldehyde in Cacodylate 0.1 M overnight (minimum of 1 h), followed by washing with 0.1 M Cacodylate (3x for 15 min), postfixed with 1% Osmiumteroxide + 1.5% potassium hexacyanoferrate (II) trihydrate in Cacodylate 0.1 M, then washed again with 0.1 M Cacodylate 3x 15 min. Then we proceeded to a dehydration series (70% for 30 min, 90% for 30 min and 2x 100% for 30 min), followed by propylenoxide 2x for 30 min and Propylenoxide:Epon LX112 (1:1) overnight with stirring. Samples were covered with fresh epon LX112 for 7 h with stirring and embedded in beam capsules with fresh epon 3 days at 60°C. 60 nm sections were then cut with a diamond knife, stained with uranyl acetate and lead citrate and imaged with a TEM (FEI Tecnai G2 Spirit BioTWIN iCorr).

Image Analysis

3D cell reconstructions were created from z-stacks (showing immunostaining to β III-tubulin) with the Leica Application Suite X (LAS X) software. All the other images were

prepared and analyzed using Fiji software (<https://fiji.sc/>). To quantify degree of fiber or cell orientation, we used the OrientationJ plugin²⁹ and applied the Measure function over identical circular ROIs to obtain the coherence value, (where 0 is full isotropy and 1 is full anisotropy). To measure neurite length, we used the Simple Neurite Tracer plugin³⁰, and measured the distance between the cell body and the edge of the respective axon. Cell counts were performed using the standard Analyze Particles function to DAPI⁺ objects. To measure axonal area, we first converted images of β III tubulin⁺ cells to binary images and measured the pixel area occupied by the neurites, excluding cell bodies. Then, we divided this value by the total image area to obtain the axonal area, which is shown as % of total area. The normalized axonal area values were obtained by dividing the axonal area by the total volume of the construct (300 μm^3). This operation was performed to better compare the differences between scaffold only and fibrin conditions, rather than just comparing the total axonal area. For the myelination area, we measured the pixel area of MBP⁺ segments and divided this value by the axonal area of the corresponding image. To analyze the myelin thickness, g-ratio and myelin decompaction we used the TEM micrographs of myelin cross sections. For the myelin thickness measurements, we simply drawn a straight line from the most inner to the most outer myelin ring and determined its length. G-ratio measurements were done using the G ratio plugin (<http://gratio.efil.de/>)³¹. Myelin decompaction analysis were carried by first measuring the area below the most outer ring and the most inner ring (expected myelin area). Then, the image was converted to binary image and the same areas were determined (actual myelin area). To determine the decompaction area we used the following formula: $(1 - (\text{expected myelin area} / \text{actual myelin area})) \times 100$. In figure S17 we depicted this process. In every analysis (except for the hyperglycemia measurements where we used $n = 4$ and 5 measurements per sample) we used a minimum of $n = 6$ per condition and took at least 20 measurements per sample (for the neurite length quantification) or 10 measurements per sample (axonal area and normalized axonal area quantification).

Statistical Analysis

Using the software GraphPad Prism, statistical significances were determined employing an unpaired t-test, one-way or two-way analysis of variance (ANOVA) followed by a Tukey's honestly significant difference (HSD) post-hoc test ($*p < 0.05$, $** p < 0.01$, $***p < 0.005$, $****p < 0.0001$ and ns is $p > 0.05$). Comparisons are done relatively to the laminin samples, except when otherwise indicated by connecting bars. All data is expressed as mean \pm standard deviation (SD) or as boxplots showing data between the 1-99 percentile.

Results

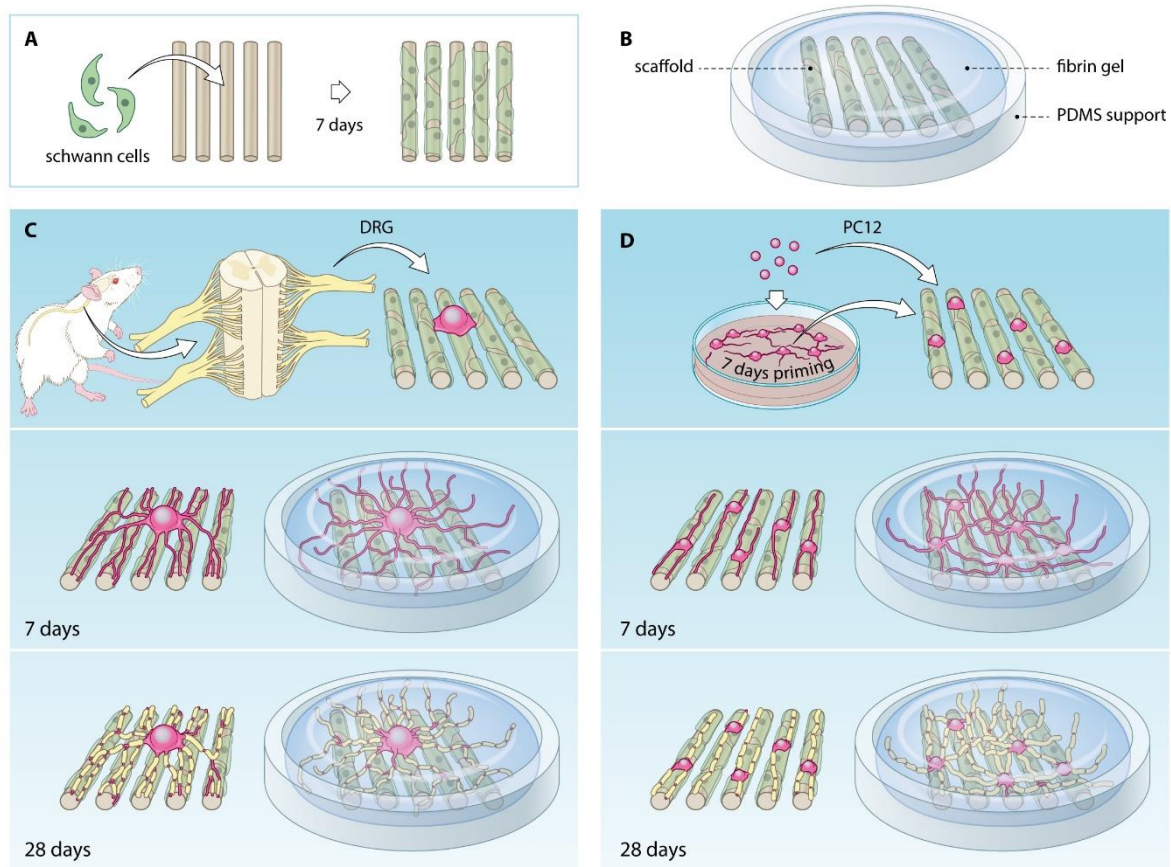


Figure 1. Illustration of PN model fabrication process. A) Formation of Bands of Büngner (BoB); B) Overview of the model components; C) DRG/SC co-culture procedure; D) PC12/SCs co-culture procedure.

Formation of Bands of Büngner (BoB)

To engineer tissue structures resembling BoB, we harvested and purified SCs from the sciatic nerve of neonatal rat pups (Fig. S2) and seeded them onto aligned ultrathin scaffolds (Fig. 1A, Fig. 2). These scaffolds, formed by electrospinning of a PEOT/PBT solution on a rotating mandrel, consisted of aligned fibers with a $1.37 \pm 0.20 \mu\text{m}$ diameter (Fig. 2A, Fig. S3A) and an overall coherence value of 0.74 ± 0.04 (Fig. S3B). Previous research has shown that aligned scaffolds with $1 \mu\text{m}$ fiber diameter lead to higher neurite growth than other microfiber sizes ($5 \mu\text{m}$ and $8 \mu\text{m}$)¹⁶. For comparison, scaffolds were produced with a similar fiber diameter ($1.53 \pm 0.19 \mu\text{m}$) and random fiber orientation with a coherence value of 0.19 ± 0.80 (Fig. S3B).

7 days after SC seeding, both scaffold architectures allowed cell attachment and complete surface covering. However, while the scaffold with randomly oriented fibers led to an isotropic cell distribution (coherence value of 0.14 ± 0.03), the scaffold with an aligned

substrate directed the SCs into anisotropic bands (coherence value of 0.46 ± 0.08) (Fig. S3B, Fig. S3C; Fig. 2B). In this latter scenario, SCs enwrapped around the fibers, forming highly aligned 3D bands, as evidenced by F-actin staining in Fig. 2C.

We also investigated how coating aligned scaffolds with laminin would affect the formation of a BoB scaffold. Laminin is abundantly present in the basal lamina of the native PN, where SCs migrate and proliferate to form BoB during PN regeneration¹⁰. As evidenced in Fig. S3D, initial SC attachment is similar on both coated and uncoated constructs, but after a period of 7 days, proliferation is favored by the presence of laminin, leading to a cell number almost 2-fold higher. In addition to cell morphology, we also performed immunostaining for proteins expressed when SCs are in a regenerative state, including the neural cell adhesion marker L1CAM and ECM proteins, such as fibronectin, laminin and collagen type IV (Fig. 2D). After 7 days *in vitro* (DIV), the surface marker L1CAM was robustly expressed and expectedly followed the same anisotropic pattern of F-actin. Finally, the characteristic nerve ECM proteins — fibronectin, laminin and collagen type IV — were all deposited and scattered through the scaffold as shown in Fig. 2D (particularly for the laminin, we also show its extracellular deposition in Fig. S4).

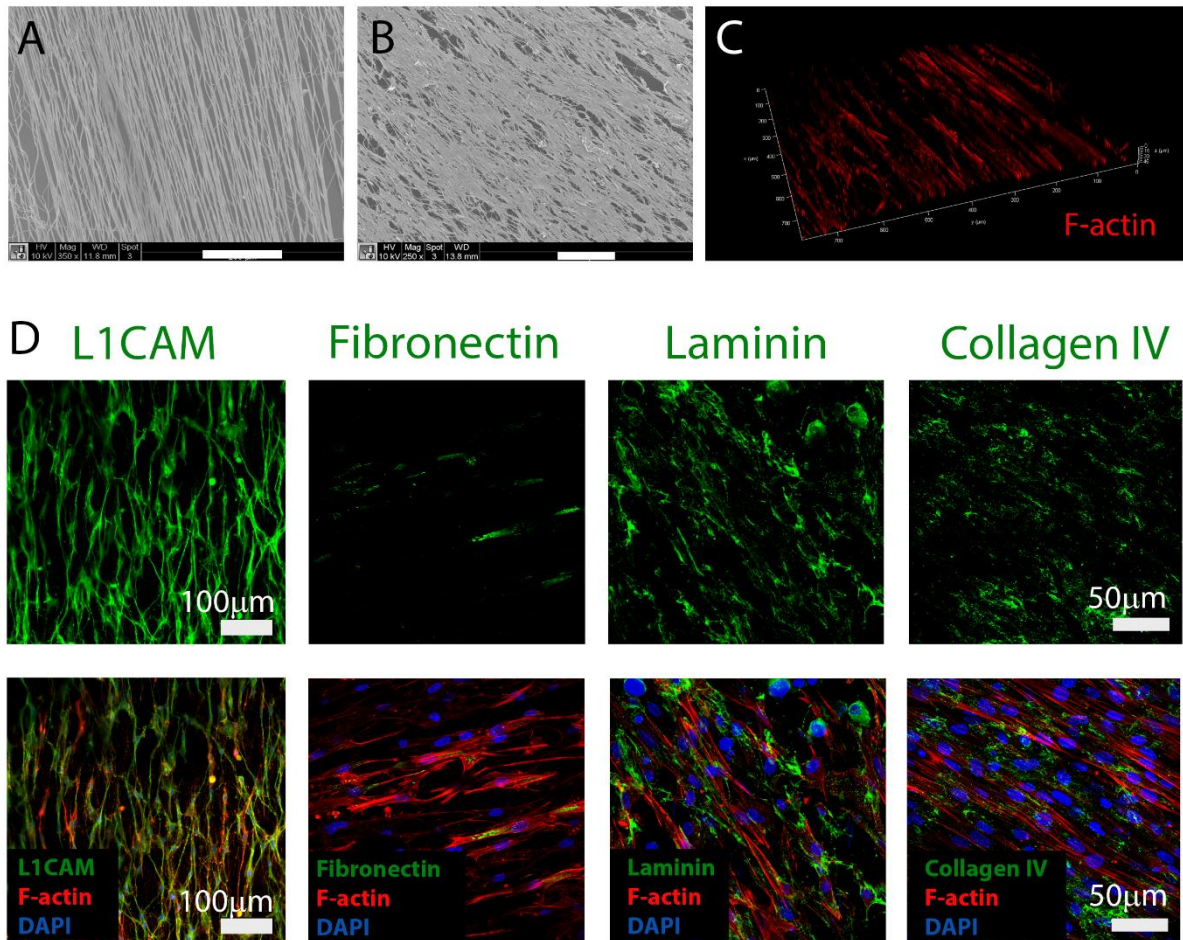


Figure 2. Formation of BoB-like structures. A) SEM micrograph of the electrospun scaffold. B) SEM micrograph of a SC-seeded scaffold cultured for 7 days. Scale bar is 200 μm for both. C) 3D reconstruction of F-actin from SCs seeded on an electrospun scaffold and cultured for 7 days. D) Immunostaining of the cell surface marker L1CAM (in green) and the ECM proteins: fibronectin, laminin and collagen IV (in green); F-actin (red) and DAPI (blue).

Short term neural co-cultures

To establish a PN model composed of neurons and SCs, we added either a DRG or PC12 cells to the BoB substrate as illustrated in Fig. 1C and Fig. 1D. These cells were co-cultured for 7 days to investigate the initial neurite network development and contributing effects of SCs. We further investigated the impact of a laminin coating by comparing neurite growth on scaffolds with a laminin coating, a SC-only BoB scaffold, or a BoB scaffolds with both laminin and SCs together. Moreover, we also investigated short-term (7 day) neurite growth emanating from scaffolds embedded within a fibrin gel (mechanical properties described in Fig. S5). With the addition of this hydrogel, we aimed to recreate the 3D microenvironment of a PN and compare tissue formation with a bare scaffold.

DRG/SCs co-culture

The DRG/SCs platform was produced by explanting a DRG and placing it in the center of the SC-seeded scaffold (Fig. 1C). With this, we aimed to direct neurites extension longitudinally to mimic the PN organization, making it also easier to assess growth. As shown in Fig. 3A, we detected a vast neurite outgrowth from the DRG towards the periphery of the scaffolds in all conditions, with no statistically significant differences in neurite length (average length ~2 mm; Fig. 4A) or neurite alignment (average coherence value ~0.6; Fig. S7A). Neurite density, however, was significantly enhanced ($p < 0.0001$) when the BoB substrate was used, i.e. SCs were exogenously added to the scaffolds, compared to laminin-coated scaffolds. In particular, we also noticed that BoB substrates with no pre-coating of laminin led to a significantly higher ($p < 0.01$) axonal area (Fig. 3A and Fig. 4B).

In all conditions, we could already observe an intimate association between SCs (S100⁺) and neurites (β III-tubulin⁺) (Fig. 3B), although it was unclear if these SCs originated from the explanted DRG or from the pre-seeded population.

To better emulate the 3D *in vivo* environment, we encased DRG/SC constructs in fibrin hydrogel (Fig. 1C). While neurite growth in the absence of the hydrogel was constrained to the plane of the scaffold, the fibrin embedding allowed neurites to extend along and above the scaffold in multiple layers (Fig. 3C). Similar to scaffolds without hydrogel, we noted that fibrin-embedded scaffolds exhibited similar neurite growth for all scaffold conditions (laminin, SC-only BoB, and laminin plus SC BoB) and that neurite length was slightly less comparatively to gel-free scaffolds (Fig. S8C). Similarly, neurite alignment in scaffolds supplemented with fibrin was constant across conditions but reduced compared to scaffolds only (Fig. S8A and S8B); despite axons not being in direct contact with the oriented fiber scaffold, we still observed a substantial degree of anisotropy of neurites as visible in Fig. 3C. To understand the role of our scaffold in directing neurite growth, we cultured DRGs on laminin-coated coverslips or laminin-coated scaffolds and embedded these in fibrin to provide a 3D environment (Fig. S6). Analyzing the neurite growth, it is clear from these images that without a scaffold of aligned fibres axons protrude radially from the DRG and assume a meandering pattern with multiple crossovers (Fig. S6A and S6C). In contrast, our scaffolds are able to direct axonal sprouting into an aligned pattern, and the growth both on the scaffold and in the gel is mostly parallel. This suggests a 'guidance at a distance' mechanism through which the scaffold induces neurite alignment while not being in immediate contact. Most interestingly, we noted that scaffolds with or without added SCs contained upper axons (not in physical contact with the scaffold), following the same direction of bottom axons (in physical contact with the scaffold) (Fig. 3C, S6B and S6D).

Finally, we measured the ratio between axonal area and construct volume to quantify and compare axonal growth between our 2D and 3D conditions. Shown in Fig. 4C, we observe

that the addition of fibrin leads to a small increase in axonal area, although not significantly different than scaffolds with no hydrogel added.

PC12/SCs co-culture

To generate the PC12/SCs co-culture system we adopted two different strategies, as visible in the scheme of Fig. 1D. Specifically, PC12 cells were either added directly to the scaffold in an undifferentiated form (non-primed) or instead differentiated for 7 days (primed) in collagen coated-plates, prior to scaffold seeding (see Materials and Methods). Cells that were primed displayed longer neurites for all scaffold conditions (Fig. S9A). Interestingly, primed and non-primed cells showed similar axonal area as well as neurite alignment across the different conditions (Fig. S9B and S9D). Counting the number of cells (DAPI⁺ objects) for scaffolds with laminin coating only showed substantially more cells on scaffolds seeded with non-primed cells compared to those with primed ones, despite the same initial seeding density (Fig. S9C). This indicates a continued proliferation of non-primed PC12, while primed cultures remained committed to a differentiated phenotype. Initial observations of PC12 cells grown in fibrin showed that non-primed cells also rapidly degraded the fibrin gel, likely due to continued proliferation and subsequent extensive tissue plasminogen activator secretion (necessary for conversion of plasminogen to plasmin and subsequent fibrin degradation³²). For these reasons, primed cultures were selected for all remaining experiments.

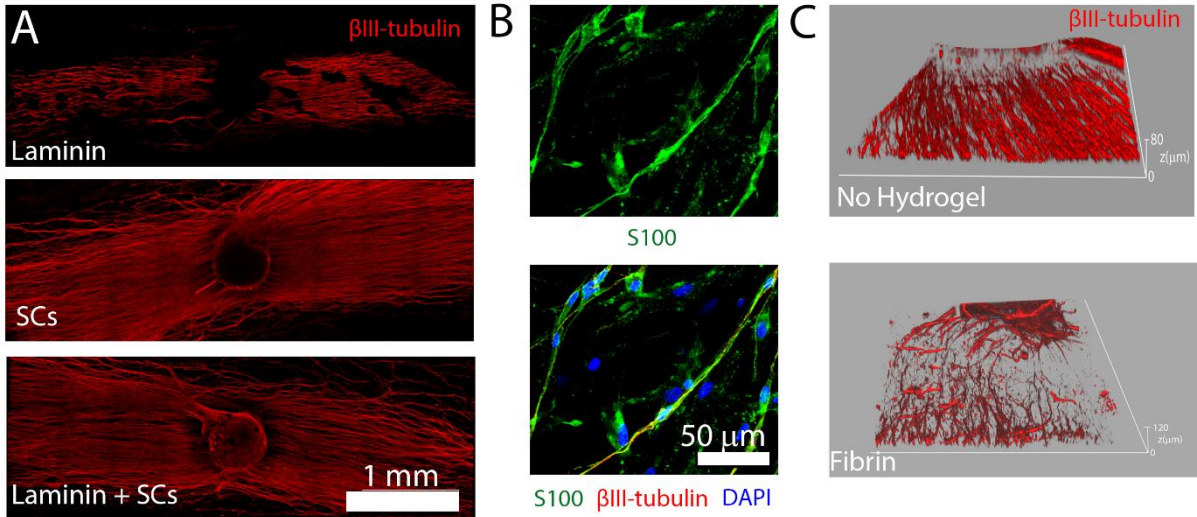
Among the conditions shown in Fig. 4, we noted that the BoB substrate with just SCs led to a significant increase in neurite length ($p < 0.01$) compared to laminin only scaffolds (Fig. 4D). Interestingly, we did not observe any significant difference in length between Bob substrates pre-coated with laminin and scaffolds with only laminin coating. In terms of axonal area (Fig. 4E), we observed that both BoB substrates, either with just SCs ($p < 0.001$) or laminin plus SCs ($p < 0.01$), showed increased values compared to scaffolds with just laminin.

Comparing with the DRG platform, PC12 neurites were in average 10 times shorter and density 20 times lower. Analogously to the DRG/SCs co-cultures, we could detect already a co-localization between PC12 axons and SCs (Fig. 3E) but, in contrast to the primary neuron platform, these SCs were undoubtedly originating from the BoB substrate.

Lastly, Fig. 3F shows the difference between PC12 neurons grown on a construct with and without fibrin embedding. It was clear that fibrin coverage allowed cells to grow along and beyond the scaffold plane, as seen with the DRG/SCs co-cultures. We registered a decrease in neurite length, in some conditions to almost 50% less compared to scaffolds with no hydrogel (Fig. 4D and Fig. S9E). However, regarding axonal density, the presence of fibrin resulted in a substantial increase (almost 3-fold) compared to scaffolds with no hydrogel (Fig. 4F). In terms of neurite alignment, we did not see any differences between scaffolds with fibrin compared to scaffolds with no hydrogel (Fig. S9D and Fig. S9F). In scaffolds with added fibrin, neurite

alignment was fairly constant among conditions, registering the highest value for the laminin condition, as seen in the DRG cultures. Again, we noticed that upper axons tended to follow the direction of those in contact with the scaffold, as shown in Fig. 3F. Since this effect was also visible in laminin coated-scaffolds, which are devoid of SCs, we can hypothesize that this parallel growth is being orchestrated via neuron-neuron communication, rather than neuron-SCs.

DRG/SCs co-culture 7 DIV



PC12/SCs co-culture 7 DIV

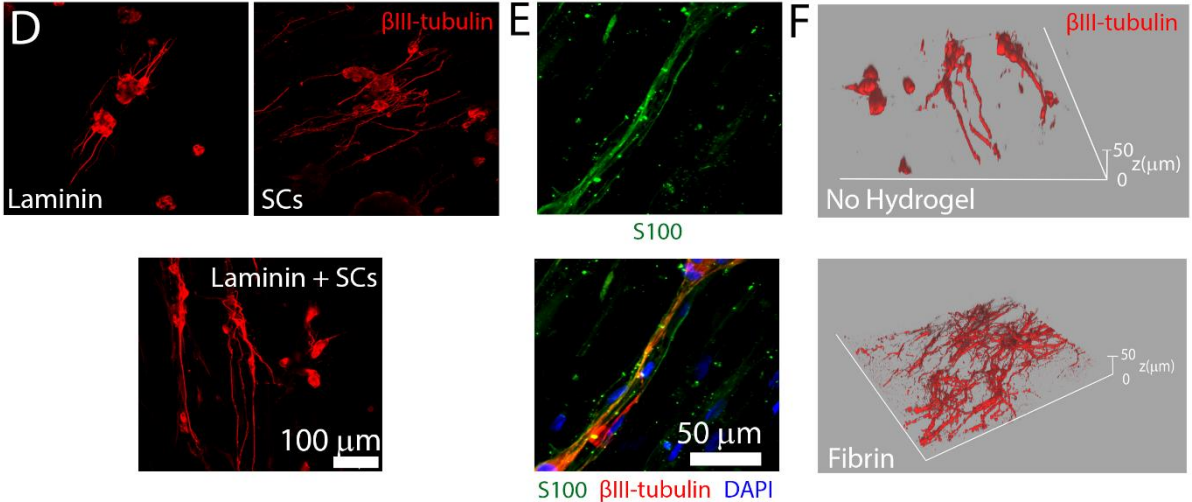
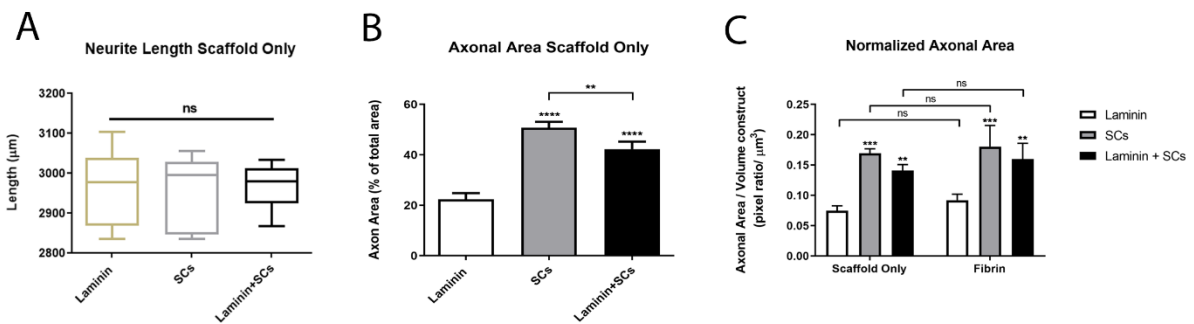


Figure 3. Short term co-culture of SCs with DRGs or PC12 cells. Top panel - DRG/SCs co-culture: A) Neurite growth overview across the scaffold with different coatings (βIII-tubulin – red); B) SC co-localization with neurites (S100 – green; βIII-tubulin – red; DAPI – blue); C) 3D profile of DRG neurites growth (red is βIII-tubulin) on scaffolds with (bottom image; z-scale spans from 0 to 120 μm) and without fibrin embedding (top image; z-scale spans from 0 to 80 μm). Bottom panel – PC12/SCs co-culture: D) Neurite growth on scaffolds with different

coatings (β III-tubulin – red); E) SC co-localization with neurites (S100 – green; β III-tubulin – red; DAPI – blue); F) 3D profile of PC12 neurites growth on scaffolds without fibrin embedding (top image; z-scale spans from 0 to 50 μm) and with fibrin embedding (bottom image; z-scale spans from 0 to 50 μm).

DRG/SCs co-culture 7 DIV



PC12/SCs co-culture 7 DIV

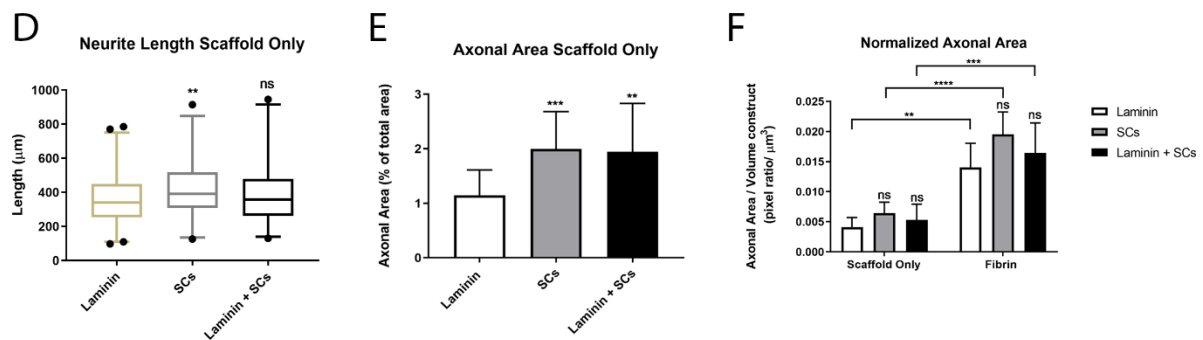


Figure 4. Analysis of short term co-cultures. Top panel – DRG/SCs co-culture: Neurite Length (A) and Axonal Area (B) on scaffolds with no fibrin. C) Axonal area normalized to the total construct volume on scaffolds with and without fibrin embedding. Bottom panel – Primed PC12/SCs co-culture: Neurite Length (D) and Axonal Area (E) on scaffolds with no fibrin. F) Axonal area normalized to the total construct volume on scaffolds with and without fibrin embedding. The neurite length represented in A) and D) is shown as the length (in μm) between the cell body and the edge of the respective axon. The boxplots represent data points in the 1-99 percentile. The axonal area in B) and E) is shown as the ratio (in %) between the area occupied by the neurites (excluding the cell bodies) and the total scaffold area. The normalized axonal area values in C) and F) were obtained by dividing the axonal area by the total volume of the construct ($300 \mu\text{m}^3$). Bar graphs represent the mean value \pm SD. In all experiments, a minimum of 6 replicates were used per condition and we took at least 20 measurements per sample (for the neurite length quantification) or 10 measurements per sample (axonal area and normalized axonal area quantification). These experiments were

performed twice and the statistics were executed with one-way ANOVA (in A, B, D and E) or with two-way ANOVA (in C and F), followed by a Tukey's HSD post-hoc test where ****p < 0.0001, ***p < 0.001, **p < 0.01, ns denotes p > 0.05.

Long term neural co-cultures

To generate a myelinated neural model, we continued both DRG and PC12 co-cultures for up to 28 DIV, as illustrated in Fig. 1C and Fig. 1D. We investigated the neurite network development and myelination for both co-culture systems, again comparing scaffolds (laminin coating, seeded SC or both) and the influence of a 3D environment provided by the addition of fibrin.

DRG/SCs co-culture

When extending the culture period to 28 days, DRG neurites continue to grow and populate the construct in an anisotropic manner (Fig. 5A). However, in scaffolds without fibrin embedding (Fig. 5B), neurites only slightly increased compared to scaffolds at 7 DIV (Fig. 4B), with the DRGs neurites reaching the boundary of the scaffold for a maximum length of approximately 3200 μm . Again, we saw that BoB scaffolds with SCs generated a significantly higher axonal area ($p < 0.01$) than laminin controls (Fig. 5B). When the construct is embedded within fibrin, we could detect a larger increase in neurite density from 7 to 28 DIV (fibrin group from Fig. 4C and Fig. 5C). In Fig. 5C, we also compare the normalized axonal area of bare and fibrin-embedded scaffolds. As already seen for 7 DIV, there were no significant differences between these groups.

At this time point, myelination was achieved, indicating maturation of these neural networks. As depicted in Fig. 6A, many aligned myelin segments (MBP⁺/ β III⁺ segments) can be found throughout the scaffold. These segments could be found in every scaffold condition, including those with only laminin coating. In this case, myelination is a result of endogenous SCs that have migrated from the DRG cluster to populate the scaffold. However, when the scaffold is supplemented with additional SCs, myelination is observed to be enhanced, as depicted in Fig. 6B. In the presence of fibrin, these myelin segments are present across the volume of the gel, forming a truly 3D myelinated nerve model (Fig. 6C).

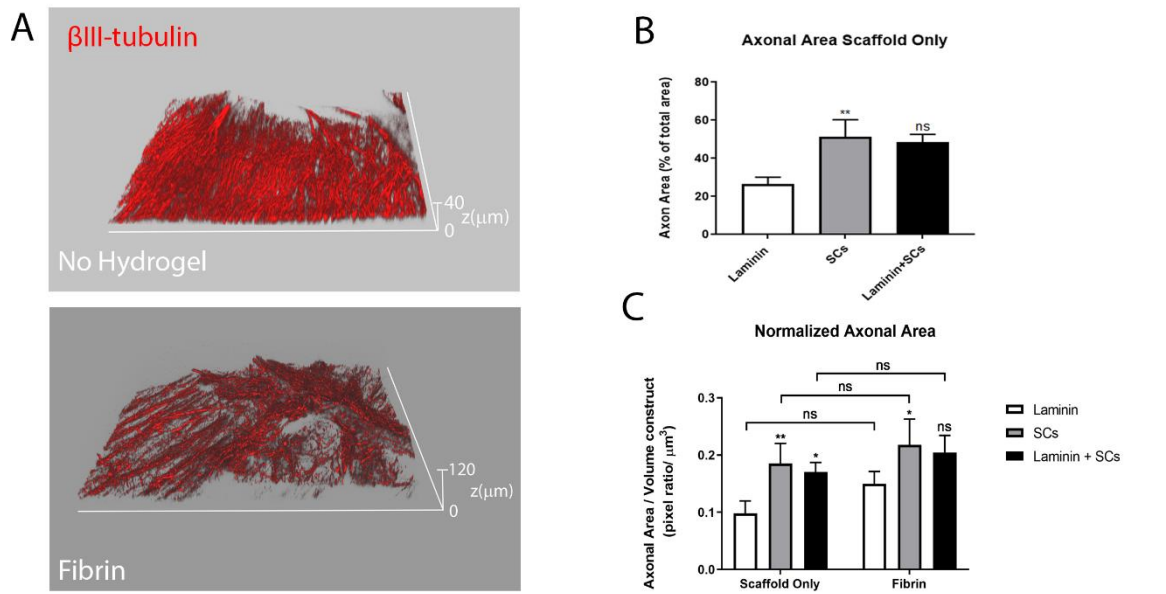
Using TEM analysis to exam scaffold cross sections, thick and compact myelin surrounding the axons can be found for scaffold both in the presence or absence of fibrin (Fig. 6D). No significant differences were found in myelin thickness among different coatings and regardless of fibrin presence, averaging between 384 to 561 nm (Fig. S10A).

PC12/SCs co-culture

Primed PC12 neurites continued to grow on scaffolds overtime, achieving a marked increase in density at 21 DIV, as demonstrated in Fig. 5D. The highest axonal area was attained in the laminin-only condition, while both BoB scaffolds revealed similar axonal coverage (Fig. 5G). From 21 to 28 DIV, we registered a decrease in axonal area across all conditions, with a particularly marked reduction for laminin-only scaffolds (Fig. 5D and 5G); this led to similar axonal area across all scaffolds types. Despite this decrease, at 28 DIV the scaffolds were vastly covered by an aligned network of long neurites (Fig. 5E), with a maximal size around 2000 μm , reminiscent (albeit at lower degree) of the DRG platform (see Fig. 3A). In the presence of fibrin, neurite networks showed high degree of alignment, but displayed multiple layers of axons, spanning through the volume of the constructs (Fig. 5F), which resulted in a larger normalized axonal area compared to bare scaffolds ($p < 0.05$; Fig. 5H).

In long term cultures, laminin-only scaffolds (devoid of SCs) showed no signs of myelination. In contrast, at both 21 and 28 DIV, BoB scaffolds showed the presence of longitudinal myelin segments, evidenced by the co-localization of MBP⁺ and β ⁺ markers (Fig. 6E). Moreover, myelin maturation was confirmed by the presence of nodes of Ranvier, as indicated by segregated clusters of sodium channels at regular interval along the axonal length (Fig. 6F). Measurements of myelin area showed a constant value between both time points and no significant differences between BoB composed of SCs or laminin plus SCs (Fig. 6G). Despite this invariance of myelin area overtime, we detected a clear increase in myelin thickness from 21 to 28 DIV (from 24.5 ± 2.4 nm to 98.9 ± 5.0 nm) as shown by TEM micrographs (Fig. 6H and quantification in Fig. S10). Finally, with the addition of fibrin, we could obtain multi-planar myelin segments, highlighted by the 3D reconstruction of MBP⁺ structures shown in Fig. 6I. Additionally, we showed by TEM analysis (Fig. S11) that compact myelination of axons can be found throughout the construct. Again, similarly to the DRG cultures, fibrin embedding did not induce statistically significant differences in myelin thickness, with the respective values averaging between 75 and 100 nm for samples at 28 DIV (Fig. S12).

DRG/SCs co-culture - 28 DIV



PC12/SCs co-culture - 21 & 28 DIV

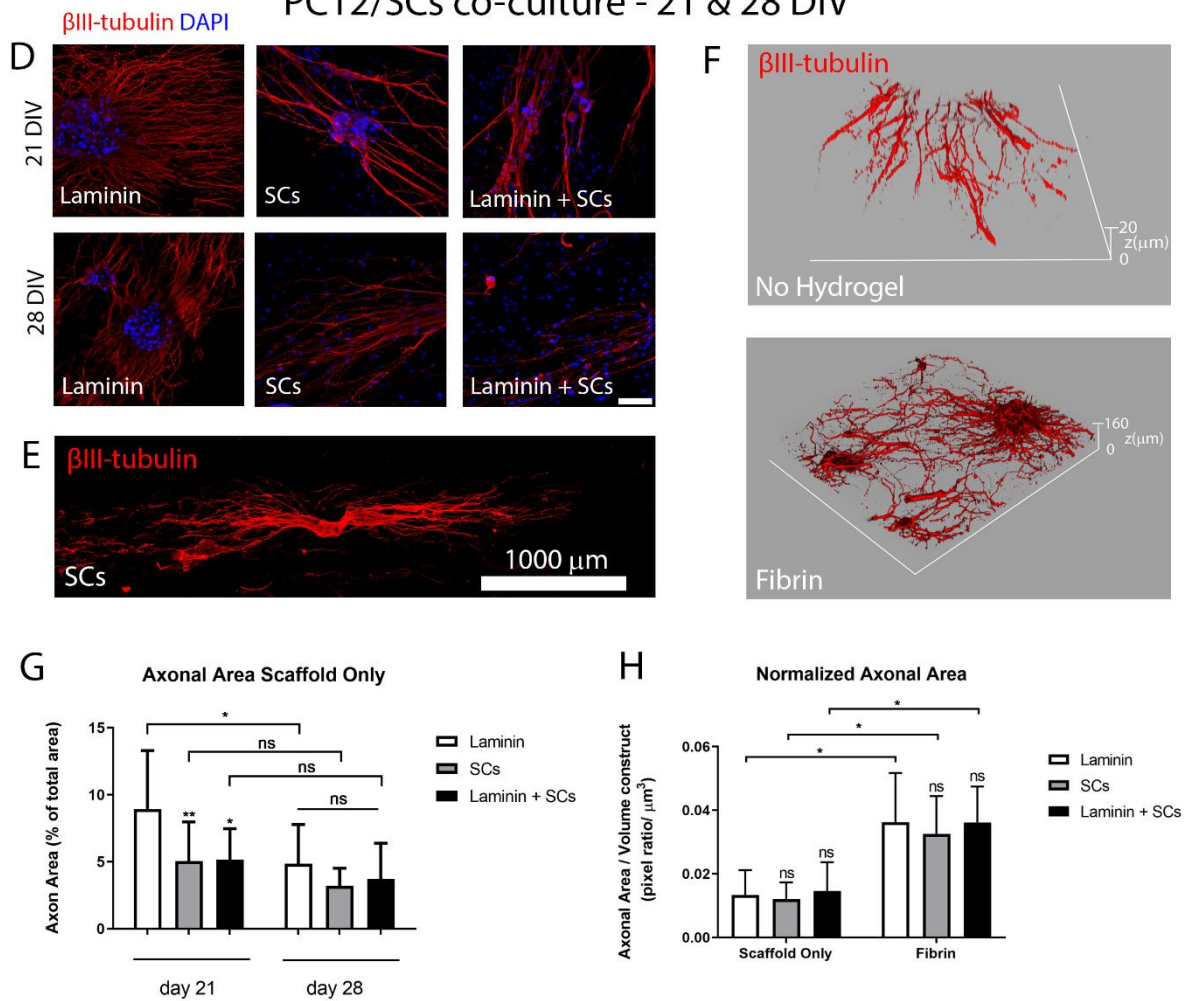
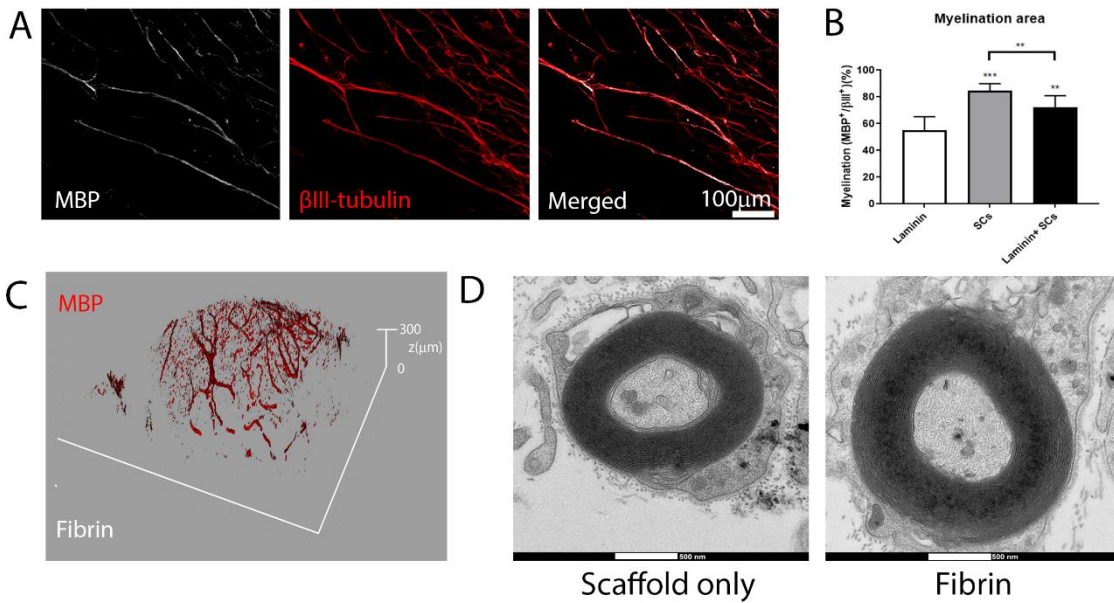


Figure 5. Evaluation of axonal networks on long term co-cultures of SCs with DRGs or PC12 cells. Top panel - DRG/SCs co-culture at 28 DIV: A) 3D profile of DRG neurites (red is β III-tubulin)

tubulin) grown on scaffolds with (bottom image; z-scale spans from 0 to 120 μm) and without fibrin embedding (top image; z-scale spans from 0 to 40 μm). B) Axonal area of DRGs cultured in bare scaffolds. C) Axonal area normalized to the total construct volume on scaffolds with and without fibrin embedding. Bottom panel – PC12/SCs co-culture at 21 and 28 DIV. D) Neurite development on scaffolds with different coatings at 21 and 28 DIV (β III-tubulin – red; DAPI – blue). E) Neurite growth overview across the scaffolds at 28 DIV on a scaffold with SCs (β III-tubulin – red; scale bar is 1000 μm). F) 3D profile of PC12 neurites (red is β III-tubulin) grown on scaffolds with (bottom image; z-scale spans from 0 to 160 μm) and without fibrin embedding (top image; z-scale spans from 0 to 20 μm). G) Axonal area occupied by primed PC12 cells at 21 and 28 DIV. H) Axonal area normalized to the total construct volume of primed PC12 cells at 28 DIV when cultured with or without fibrin embedding. The axonal area in B) and G) is shown as the ratio (in %) between the area occupied by the neurites (excluding the cell bodies) and the total scaffold area. The normalized axonal area values in C) and H) were obtained by dividing the axonal area by the total volume of the construct ($300 \mu\text{m}^3$). Bar graphs represent the mean value \pm SD. In all experiments, a minimum of 6 replicates were used per condition and we took at least 10 measurements per sample. These experiments were performed twice and the statistics were executed with one-way ANOVA (in B) or with two-way ANOVA (in C, G and H), followed by a Tukey's HSD post-hoc test where ** $p < 0.01$, * $p < 0.05$ and ns denotes $p > 0.05$.

DRG/SCs co-culture 28 DIV



PC12/SCs co-culture 28 DIV

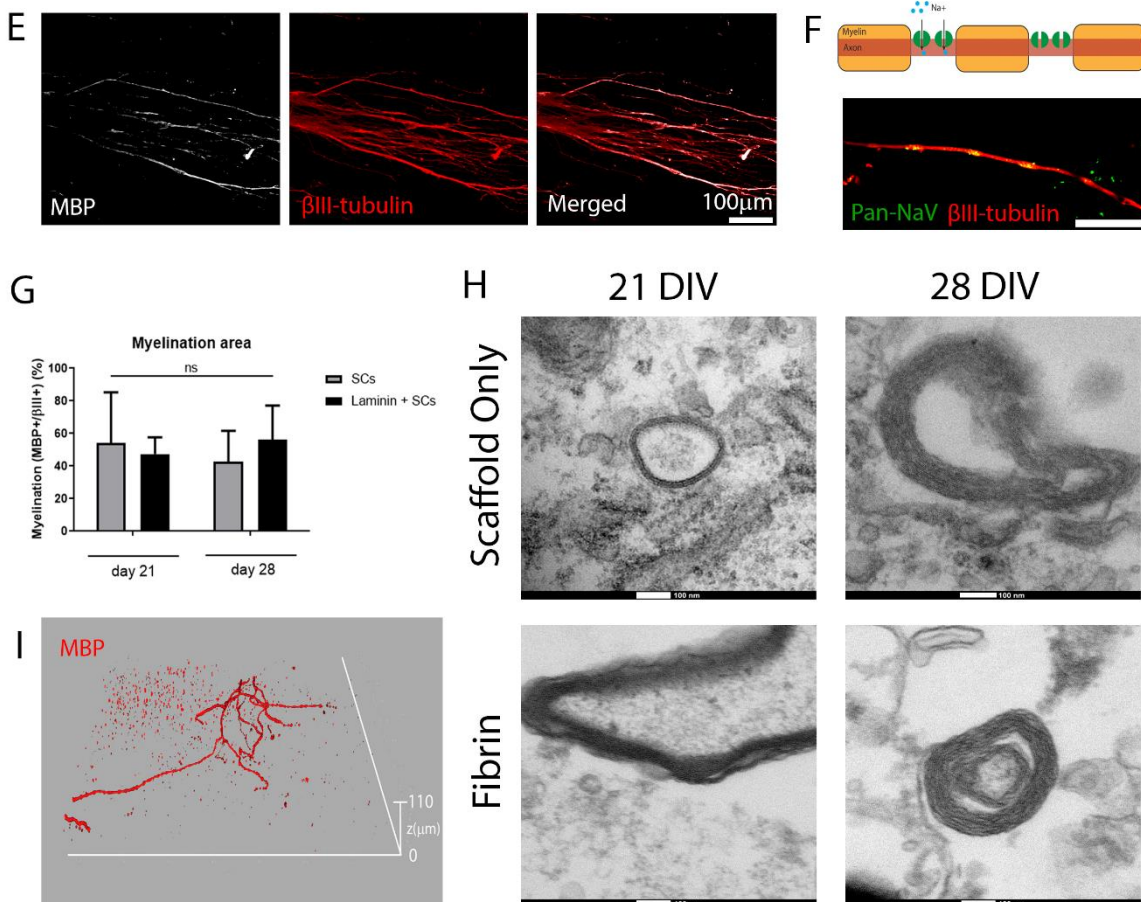


Figure 6. Myelination on long term co-cultures. Top panel – DRG/SCs co-culture: A) Immunostaining images of MBP⁺ (in gray) and β⁺ (in red) segments. B) Myelination area on

bare scaffolds with different coatings. C) 3D reconstruction of MBP⁺ segments from a scaffold with fibrin embedding (MBP is shown in red and the z-scale spans from 0 to 300 μm). D) TEM micrograph of a myelinated axon cross section, highlighting the myelin in scaffolds with and without fibrin (scale bar is 500 nm). Bottom panel – PC12/SCs co-culture. E) Immunostaining images of MBP⁺ (in gray) and β^+ (in red) segments acquired from 28 DIV samples. F) Presence of nodes of Ranvier, evidenced by segregated sodium channels (Pan Na_v – green; β III-tubulin – red; scale bar is 50 μm). G) Myelination area on bare scaffolds with different coatings at 21 and 28 DIV. H) TEM images of myelin in samples with and without fibrin embedding at 21 and 28 DIV (scale bar is 100 nm). I) 3D reconstruction of MBP⁺ segments from a scaffold with fibrin embedding (MBP is in red and the z-scale spans from 0 to 110 μm). Myelination area displayed in B) and G) was calculated from the ratio of the area occupied by MBP⁺ segments with the area occupied by β III-tubulin⁺ segment within the same image. The bars represent mean values \pm SD and the statistics were executed with one-way ANOVA followed by a Tukey's HSD post-hoc test, where ***p < 0.001, ** p < 0.01 and ns denotes p > 0.05.

Applications of the PC12/SCs model

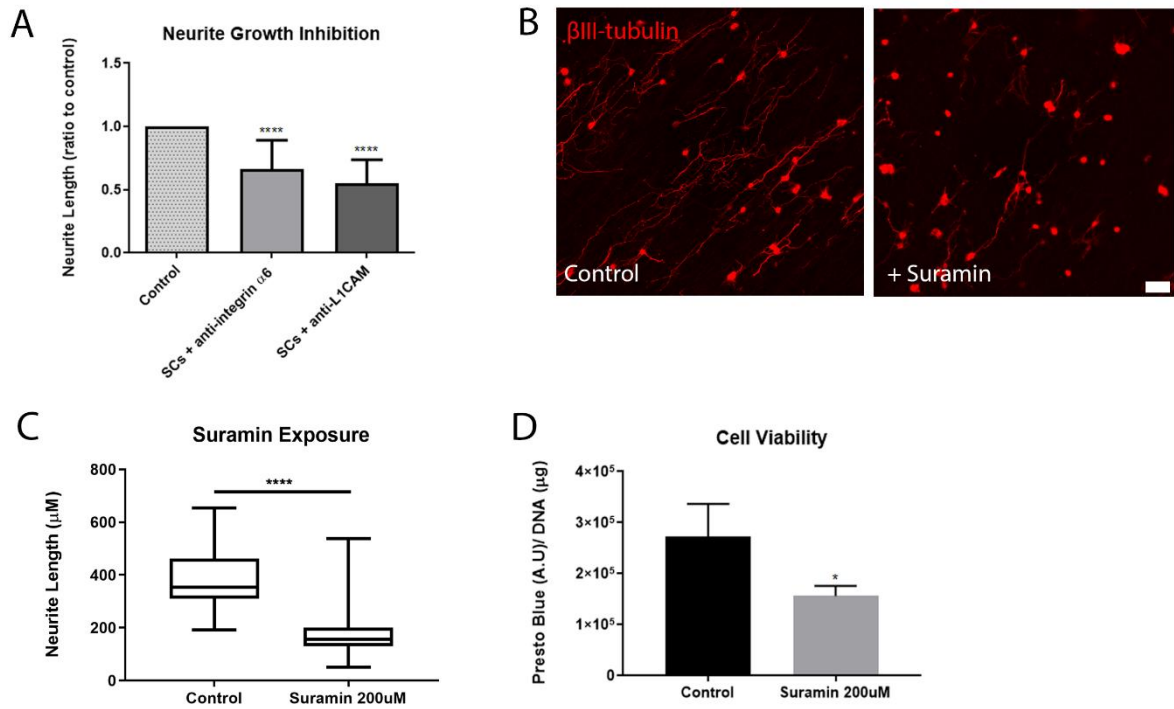
To showcase the utility of our biomimetic PN model constructed with the PC12 cell line, we performed some screenings on regenerating/immature (short term) and mature (long term) cultures. On regenerating/immature cultures we probed neuron/ECM and neuron/SC interactions during axonal growth, looking respectively at the contribution of integrin alpha-6, a laminin-specific integrin, and L1CAM, a homophilic cell adhesion transmembrane protein expressed by both neurons and SCs. Applying an antibody-blocking assay to primed PC12 on fibrin-free scaffolds, blocking alpha-6 caused almost a 40% decrease in neurite length compared to the control while blocking L1CAM resulted in an even steeper decrease of 45% (Fig. 7A). Cultures containing antibodies within the medium did not show a visible reduction in cell viability (Fig. S14A), thus suggesting that growth reduction is a direct influence of protein blocking and not cell death.

We also utilized regenerating/immature cultures to evaluate how developing axonal networks are affected by suramin, a drug used to treat African trypanosomiasis with known neurotoxic effects. We incubated primed PC12 cells (no SCs) for 24 h with 200 μM of suramin (in medium) and evaluated cell morphology and viability. As visible in Fig. 7B, the addition of suramin resulted in a substantial neurite retraction, which is quantified in Fig. 7C. Additionally, cell viability was significantly diminished in drug-containing cultures (Fig. 7D), which also showed signs of apoptosis as illustrated in Fig. S14B by cleaved caspase-3 immunostaining. To show the utility of our scaffold, we compared our approach to traditional glass coverslip substrates. As visible in Figure S13A, PC12 could grow extensive neurites on both substrates,

but scaffold-supported growth appears substantially more aligned as quantified in Figure S13B. In contrast, PC12 neurites on coverslips are disorganised and overlapping at various points. While the application of suramin triggered neurite retraction for both substrates, the fiber scaffolds proved to be more sensitive to morphological changes, exhibiting 46 % decrease in neurite length, compared to coverslip cultures which experienced only a 28 % decrease.

Finally, we demonstrated the ability of our mature culture platform to simulate pathological conditions and screen appropriate therapeutic drugs. We induced diabetic conditions by exposing mature cultures (28 DIV) to a hyperglycemic state (45 mM glucose in medium) and compared the resulting myelin morphology with normal glycemia or hyperglycemia containing 1 μ M epalrestat, an aldose reductase inhibitor that reduces sorbitol accumulation and thus can prevent diabetic neuropathy^{2,33}. As visible in the TEM micrographs of Fig. 7E, hyperglycemia led to the appearance of myelin aberrations, characterized by decompaction and large separation of myelin layers, as well as irregular shapes (indicated by red arrows). In contrast, myelin under normal glycemic conditions appeared well compact and regular. When 1 μ M epalrestat was supplemented to cultures under hyperglycemic conditions, the high glucose effect was mitigated, and myelin morphology resembled normal glycemic conditions, although with some decompaction still evident. As a result of this myelin layer decompaction, the traditional g-ratio measurement for myelin quality resulted in both the hyperglycemic condition and hyperglycemic + epalrestat condition having a reduced g-ratio (~ 0.48) compared to the control (~ 0.54; $p < 0.05$) and no differences between these two conditions (Fig. 7F). However, when measuring myelin decompaction, we registered a significant increase ($p < 0.001$) in hyperglycemic cultures (~ 26% decompaction) which was reduced in hyperglycemic plus epalrestat cultures (~16% decompaction) and approached levels observed in the normal glycemia cultures (~8% decompaction).

PC12/SCs co-culture - 7 DIV tests



PC12/SCs co-culture - 28 DIV tests

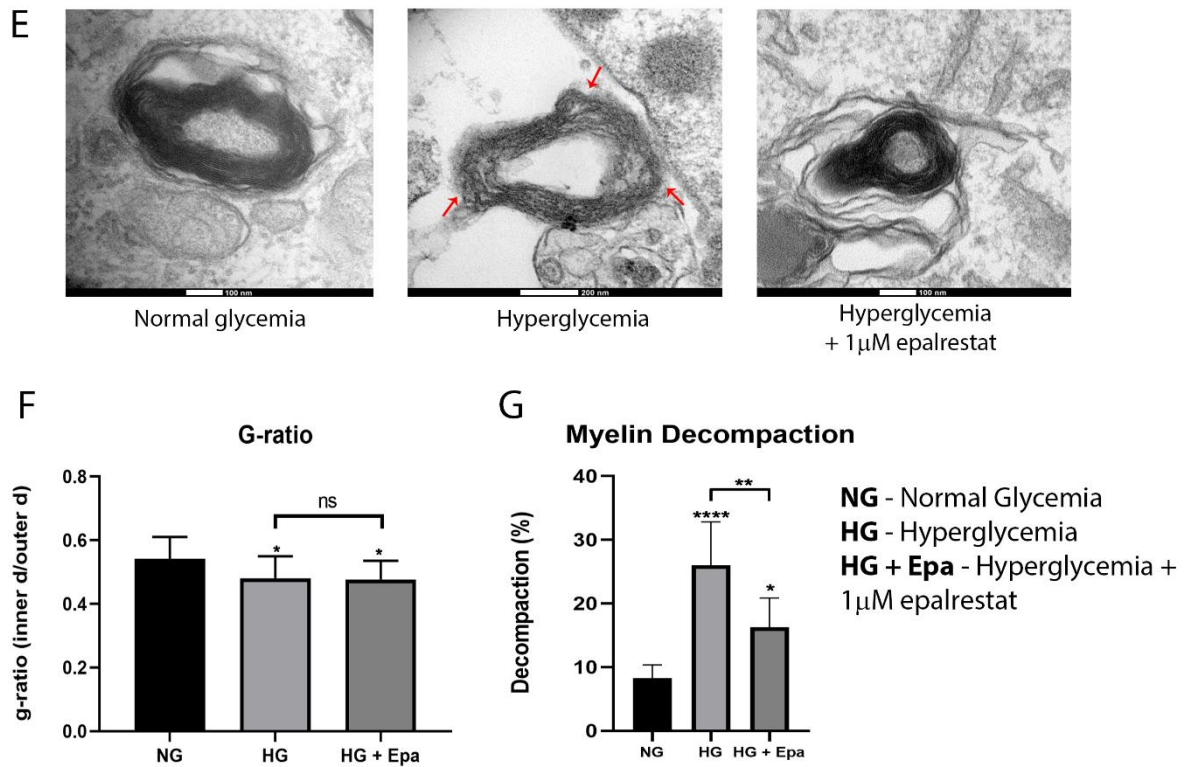


Figure 7. Applications of the PC12/SCs model with short or long term co-culture periods. A) Neurite outgrowth in PC12/SCs cultures with medium containing antibodies against integrin α6 or L1CAM compared to normal culture medium. B), C) and D): Neurotoxicity test on PC12 only

cultures using medium containing suramin at the concentration of 200 μM versus control medium (normal culture medium). B) Immunostaining to $\beta\text{III-tubulin}$ ($\beta\text{III-tubulin}$ – red; scale bar is 100 μm). C) Neurite length and D) Cell viability shown via the ratio of cell metabolic activity (presto blue fluorescent units) and cell number (amount of DNA). E), F) and G) Hyperglycemia test on 28 DIV PC12/SCs co-cultures in normal glycemia (normal medium), hyperglycemia (normal medium plus 45 mM glucose) or hyperglycemia + 1 μM epalrestat (normal medium plus 45 mM glucose and 1 μM epalrestat). E) TEM micrographs of myelin cross-sections showing the myelin morphology for the different conditions, where it is noticeable the increase layer decompaction on hyperglycemic conditions and the rescue effect of epalrestat (scale bar is 100 nm for left and right image and 200 nm for the image in the centre). F) G-ratio and G) decompaction measurements obtained from the analysis of TEM micrographs. This experiment was repeated once, with at least 5 measurements taken by each sample ($n = 4$). Statistics were determined with one-way ANOVA (A, F and G) followed by a Tukey's HSD post-hoc test or unpaired t-test (C and D). **** $p < 0.0001$, *** $p < 0.001$, * $p < 0.05$ and ns denotes $p > 0.05$. Bars represent mean \pm SD and boxplots represent data points in the 1-99 percentile.

Discussion

In vitro PN models can serve as powerful tools to quickly assess product performance with minimal to no use of animals. Currently, the development of PN models is still at its infancy, with only few strategies revealing the successful development of 3D biomimetic structures. In this pursuit, researchers started by establishing 2D co-cultures that yielded the formation of mature myelin. Several reports using primary cells^{34,35}, cell lines¹³ or differentiated stem cells¹⁸ have already successfully shown this. However, most strategies lack proper tissue arrangement, most notably anisotropic BoB structures and subsequent aligned and myelinated neurons. To improve this, strategies that employ axon guides such as microfibrillar scaffolds^{4,16}, anisotropic hydrogels^{6,36} or compartmentalized platforms^{37,19} have shown the ability to direct axonal growth longitudinally. Capitalizing on some of these concepts, we aimed to build to a mature PN model that would also recapitulate the nerve architecture. At the same time, our goal was to achieve this using a neural cell line and to build the platform with relatively simple and inexpensive materials and biofabrication techniques. In this way, we can provide an affordable tool for researchers to quickly investigate biological mechanisms and screen therapeutic compounds. Furthermore, the use of a defined and well-established cell line facilitates experimental reproduction. Particularly for models using iPSCs-derived cells this is a concern since the potential for cell population heterogeneity is substantially higher³⁸. To produce this model we used three main components: 1) BoB substrate; 2) Fibrin gel embedding (3D environment); and 3) a neuronal cell population. The BoB substrate aims to

mimic/induce a key early event during PN regeneration. Following nerve damage, the formation of these SC bands provide haptotactic guidance and trophic support for regrowing axons^{10,11}. In order to produce a structure resembling these bands, we fabricated aligned ultrathin scaffolds via electrospinning with a rotating mandrel. This allowed the rapid and reproducible production of scaffolds composed of PEOT/PBT, a material already used for nerve conduit fabrication³⁹. Primary SCs can be harvested in high yield from rat sciatic nerves, and easily purified as illustrated in Fig. S2. Although this process requires animal use, only a small number of animals are necessary to extract and store large amounts of cells for later usage. Alternatively, researchers may simply purchase primary SCs from commercial sources. The choice of primary SCs over SC lines, such as RT4-D6P2T, is largely superior for the formation of myelination models, as the latter are difficult to maintain in long term cultures or do not express an appropriate phenotype for myelination³.

After seeding the aligned scaffolds with purified SCs, we cultured it for 7 days, after which we obtained highly anisotropic 3D SC bands that robustly expressed nerve ECM molecules and L1CAM, a facilitator of axon-SC adhesion⁴⁰ (Fig. 2). At this stage, our SC-seeded scaffold resembled native BoB, with abundant aligned SCs and a rich ECM milieu creating a favorable environment for axons to grow. Additionally, we also coated the scaffolds with laminin-1 prior to SC seeding, to better reproduce the basal lamina that supports SCs natively. Laminins are known to enhance SC proliferation and to initiate bipolar shape formation⁴¹. Indeed, it resulted in higher SC coverage of the scaffold (Fig. S3) but not in better neural tissue growth, as we will discuss further.

Our chosen material to emulate a 3D environment was a fibrin hydrogel. Fibrin is a natural material, which appears and forms aligned fibers during the initial stages of peripheral nerve regeneration. In addition, its low cost, handling simplicity, and success in promoting neuron outgrowth has led to wide use for PN tissue engineering and PN models^{1,42-43}. Potential drawbacks of its use in tissue engineering stem from the material's mechanical properties, such as its low stiffness, shrinkage and degradation rate, which may be too quick, particularly for long-term *in vitro* cultures⁴⁴. For *in vivo* applications, there is a risk that fibrin proteins may trigger a host's immune response. However, these concerns are not applicable in our model, since we developed a platform that emulates the PN, a soft tissue, and is intended for *in vitro* work only. To ensure gel stability, we supply aprotinin to the medium to prevent the degradation activity of tissue plasminogen activator (tPA). When added on top of the scaffold, the fibrin hydrogel intertwines with the scaffold's fibers and remains stable throughout the entire culture period.

The hydrogel addition allows both neurons and SCs to grow beyond the 2D scaffold plane to a 3D space, in order to create a truly 3D PN model. Placing a DRG on top of the BoB substrate resulted in a rapid and vast neurite outgrowth, which could be augmented by fibrin

hydrogel addition. However, the difference between bare constructs and those with fibrin coverage was not significant, since the number of upper axons was dwarfed by the vast number of axons in the plane of the scaffold (Fig. 3 and Fig. 4). Long-term DRG cultures generated matured myelination, as evidenced by thick and compact myelin layers (Fig. 6). For both timepoints, the inclusion of exogenous SCs resulted in denser axonal and myelin area compared to laminin samples and this improvement happened to a lesser extent for BoB substrates that were pre-coated with laminin (before SC seeding). In neural development, the radial sorting of axons by SCs is critical for maturation and can only proceed after SCs and axons reach a 1:1 relationship⁴⁵. Since laminin promoted SC proliferation and thus higher scaffold coverage, we hypothesize that this increase in SC number may be detrimental for axonal growth and myelin formation because of delayed radial sorting and overcrowding. In our observations of mature (28 DIV) samples we noted that most myelin segments were in the periphery of the scaffold where SC density is lower rather than in the vicinity of the cluster where SC density is higher (data not shown), which supports the hypothesis that empty space surrounding cells is needed for myelination to proceed. This initial observation indicates an additional requirement for optimal scaffold design in order to maximize proper myelination and mature peripheral nerve tissue formation.

We wanted to demonstrate the ability to use PC12 cells as a neuronal cell population, which can be easily and cheaply expanded, thus simplifying the fabrication of the model and alleviating the need of animals. While DRGs are the gold standard in PN models, a side-by-side comparison is not possible because of intrinsic differences. DRGs are explanted cell aggregates containing a high number of neurons mixed with SCs and other cell types, which cannot be removed, without further dissociation and processing, meaning DRG cultures will always contain endogenous SCs compared to PC12 monocultures. It is noteworthy that we deliberately chose to use single cells instead of PC12 clusters. In a bid to better mimic DRG explants, we formed PC12 clusters using agarose microwells and evaluated their use (Fig. S7). However, clusters were irregular in size/shape, differentiated more slowly and with less neurite growth compared to single cells, which also naturally self-aggregate over time, particularly when SCs are absent (as shown in Fig. 5D). Keeping in mind these differences, we used the obtained results with DRG cultures as a yardstick to evaluate PC12 cells as a viable alternative.

For the PC12 cell model, we adopted a different strategy and simply seeded the PC12 on the BoB scaffolds. Because priming PC12 cells has been shown to accelerate axonal development in response to NGF^{46,47}, we were interested in testing if priming would result in longer and more numerous axons. Our data indicates that after 7 DIV, primed PC12 produced longer neurites than non-primed cells for all scaffold conditions (Fig. S9A). This can be explained by the synthesis of precursor molecules during the priming process, in turn leading

to earlier and faster neurite extension⁴⁷. However, in terms of total axonal area, at 7 DIV there were no significant differences between conditions with primed or non-primed cells (Fig. S9B). To explain this, we propose that primed cells remain differentiated and non-proliferative throughout time, while non-primed cells still partly proliferate. This could be verified by the PC12 cell count 7 days after scaffold seeding, in which we saw a 4-fold increase in cell number for non-primed cells despite the same initial seeding density as the primed condition (Fig. S9C). Therefore, while having shorter axons, non-primed cells are present in larger number, thus achieving the same axonal area as primed cells. The high proliferative capacity of non-primed PC12 also prevented long-term experiments with fibrin because of rapid gel degradation and scaffold overcrowding. For this reason, we selected primed PC12 for the assembly of the cell line PN model.

In short term cultures, we noticed that the inclusion of SCs to the scaffold resulted in larger axonal length and area compared to scaffolds with laminin coating alone (Fig. 4D and 4E) owing to the trophic support, contact guidance and ECM production by SCs¹⁰. On the other hand, long term cultures exhibited the opposite trend (Fig. 5G). We hypothesize that SC-axon association halts further neurite growth while the absence of SCs allows PC12 cells to freely extend neurites. In addition to this, we noted a decrease in axonal area from 21 to 28 DIV, indicating some axonal pruning overtime, which was mitigated in the presence of SCs, perhaps due to stabilization and maturation afforded by SC-axon association (Fig. 5G). This maturation is evidenced by the presence of compact and thick myelin layers, intercalated by nodes of Ranvier (Fig. 6F). Coating the scaffolds with laminin prior to SC addition did not seem to produce a difference in axonal or myelin area. Despite the known benefits of laminin presence to SC phenotype⁴¹ and our observed enhancement of SC proliferation (Fig. S3), this did not translate in a better PN model. As shown in Fig. 2 and Fig. S4, SCs are also able to produce and secrete laminin, and perhaps this exogenous supply sufficiently or more optimally maintained overall SC function.

To mimic the PN 3D environment and to permit multiplanar cell growth, we covered the cell-seeded scaffolds with a fibrin hydrogel. However, we were initially concerned that axons within the fibrin matrix would lose their anisotropy without direct topographical guidance. To investigate this, we cultured a DRG in a scaffold embedded with fibrin and assessed the resulting neurite growth pattern throughout the whole construct. As exemplified in Fig. S6B and S6D, in the plane of the scaffold neurites follow an aligned pattern, which is expected from the contact guidance provided by the aligned microfibers. Interestingly, axons in the vicinity, but not in direct contact with the scaffold, also follow the substrate direction, even at a distance of 100 μm from the substrate (Fig. 3C and Fig. S6D). Conversely, if an isotropic substrate such as a glass coverslip is used, neurite growth is isotropic in all planes of the construct (Fig. S6A and S6C). Since SCs are known to generate neurotropic factors that influence neurite growth,

our initial hypothesis was that endogenous SCs migrating from the DRG explant along the aligned scaffold might be generating a local gradient to direct neurite growth throughout the 3D construct.

To investigate this possibility, we took advantage of the homogeneity of the PC12 system and the specific lack of endogenous glial cells. Even compared to iPSC-derived neural cultures, which also exhibit uncontrolled generation of endogenous glial cells⁴⁸, our PC12 cultures offer a clear model to study such interactions, where one can more assertively determine the mechanisms behind this behaviour. Using this model, we could clearly detect an overall anisotropic neurite pattern throughout the construct (Fig. 3C and Fig. 3F) with similar coherence values to bare scaffolds (Fig. S9D and S9F) regardless of whether SCs were added to the system. Particularly for fibrin-embedded scaffolds, neurite orientation was fairly constant among different conditions (Fig. S9F) and the highest for the laminin-coated scaffolds, such as in the DRG system. This suggests that the bottom axons, in contact with the directional substrate, are guiding top axons via paracrine signalling (up to a distance of 50 μm) and the similarity between DRG and PC12 cultures indicates that this mechanism is conserved between systems. While it is well known that many attractive and repulsive signals are active during axonal development for appropriate patterning, the identification of axon-axon paracrine signalling to guide growth is relatively recent^{49,50,51}. Thus, we show a combination of contact guidance and cell-to-cell communication can synergistically generate anisotropic 3D neural growth. Further investigation would be required to determine the exact molecular players involved, but these preliminary results highlight the benefits of using this platform to explore this phenomenon compared simple 2D systems⁵² or animal models⁵¹.

Finally, to further emphasize the application potential of the PC12/SCs model we performed some tests at both an immature and mature stage of neural development. In the first days of the co-culture, axons are growing and still establishing an intimate association with SCs. This offers a window of opportunity to study specific proteins involved in axonal development and regeneration. To showcase this, we used antibodies to selectively block either axon-laminin (via integrin alpha-6) or axon-SC (via L1CAM) binding. Both antibodies resulted in partial neurite length reduction compared to control, evidencing the influence of either ECM or SCs during axonal growth (Fig. 7A). At this timepoint, we also used our system as a drug testing platform. For this, we tested the effects of suramin, a compound used to treat African trypanosomiasis (or sleeping sickness), on neuron morphology and viability. Suramin is known to produce adverse side effects that may result in peripheral neuropathies, resultant from large calcium influxes into the cytosol⁷. As suggested by Franze et al.⁵³, calcium influxes and intracellular level rise are also the first step in neurite retraction. Therefore, we hypothesized that suramin-induced calcium influxes would result in a reduced cell viability and neurite length. The report of Von der Ahe et al. show a marked toxicity on DRG cultures above

300 μM exposure for 24 h⁷. From our data, we concluded that 24 h exposure to suramin (at 200 μM) results in decreased PC12 neurite length and cell viability (Fig. 7B, C and D). Additionally, we also compared the performance of our scaffold with a traditional glass coverslip, which is the most common cell substrate to evaluate drug effects on neuronal cells. As seen in Figure S13, PC12 grown in scaffolds have neurites substantially more aligned compared to the isotropic and overlapping neurite growth observed on coverslips. This overlapping in particular makes evaluating neurite length a considerable challenge compared to the oriented growth on scaffolds. But more significantly, cells cultured on scaffolds exhibited a larger neurite retraction than cells cultured in coverslips (46% versus a 28% decrease compared to control, as seen in Figure S13C,). This denotes a higher sensitivity of our scaffold platform to evaluate neurotoxicity. We attribute this to the aligned neurites being able to undergo an easier, more natural neurite retraction compared to the randomly oriented neurites. Additionally, we believe that the scaffold stiffness, which is considerably softer than glass, can play a major role in enhancing neurite retraction. It is well reported that neurons prefer softer substrates to grown onto and that neurite retraction is facilitated by softer, more compliant environments⁵³. Therefore, we conclude that our scaffold system, because it is softer and directs neurites into an aligned pattern is a superior alternative to traditional glass coverslips.

Suramin was here selected as a proof of concept for drug testing. However, since this platform is affordable to produce and neurite morphology simple to quantify, high throughput screenings may also be conducted with several drug candidates at diverse concentrations. Besides neurotoxic substances, drugs with neurotrophic properties can be tested for their performance in an environment that recreates the initial stages of PN regeneration as provided by this platform.

Long term cultures result in mature tissue formation and this allows the study of certain pathologies and drugs that affect the PN microenvironment. In diabetes, high blood glucose levels cause sorbitol accumulation, leading to tissue damage, such as myelin deformations, that ultimately can result in decreased nerve conduction velocity^{2,54,55}. To prevent the detrimental consequences of sorbitol accumulation, some strategies aim at blocking the conversion of glucose to sorbitol by inhibiting aldose reductase, the reaction catalyzer^{2,55,56}. Aldose reductase inhibitors, such as epalrestat, have shown some promising results in *in vivo* and clinical studies^{2,33,57}. To determine the efficiency of diabetes treatments, tools such as TEM are indispensable to evaluate and quantify myelin quality and deformations. These deformations are characterized by myelin layer decompaction, infoldings, outfoldings and other aberrant shapes, and can be qualitatively assessed via morphometric analysis⁵⁴ or quantitatively measured via formulas such as the g-ratio or myelin decompaction percentage^{2,58}. When looking at myelin cross sections representing the different culture settings (Fig. 7E), it is evident from the TEM micrographs that in hyperglycemic conditions,

myelin layers assume aberrant forms and become decompacted, as opposed to well defined concentric rings seen in a normal glycemia setting. These results are strikingly similar to those seen in the sciatic nerve cross sections of diabetic mice, reported by Hao et al.², which highlight the applicability of this platform as a substitute for *in vivo* models. The addition of epalrestat (at 1 μ M) in hyperglycemia cultures lead to a visible reduction in the appearance of aberrations and layer decompaction, although still exhibiting less compacted layers than the control cultures (Fig. 7E and Fig. S16). To analyse these results, we used the well established metrics of g-ratio and myelin decompaction percentage to determine the efficiency of the treatment. When measuring the g-ratio, we noted a significant decrease in hyperglycemic conditions, related with the presence of myelin abnormalities and decompacted layers. This is actually contrary to what was observed in other studies of diabetic rodents^{2,54}, in which a higher g-ratio was observed, although marginally. We hypothesize that this is because these studies happened over a much longer period (> 1 month), during which demyelination (causes thinner myelin, thus higher g-ratio value) also takes place. Instead, our studies focuses on hyperglycemic exposure over a relatively short 48 h period, revealing that decompaction is dominant for acute hyperglycemia and not demyelination. When quantifying this decompaction, we indeed registered a marked increase in hyperglycemia cultures (Fig. 7G). On the other hand, when adding epalrestat in hyperglycemia cultures, myelin decompaction could be significantly mitigated to values close to normal glycemia cultures. However, the presence of still residual decompaction can explain why the g-ratio values were still lower compared to normal glycemia cultures (Fig. 7F). These results show that our model provides a simple and fast route to assess pathophysiological conditions and screen pharmacological candidates.

In summary, we built a platform that mimics the PN architecture, using a unique combination of primary SCs and neuronal cell line. In this way, we showed here the efficient and low-cost fabrication of large mature tissue comparable to all-animal based models. With this platform we illustrate here its potential to investigate mechanisms of neurite growth test and pathological axon and myelin damage, thus highlighting its usefulness in fundamental studies and preliminary testing.

Acknowledgements

We thank the Microscopy CORE Lab (M41 Maastricht University), especially Hans Duimel and Kevin Knoop for their help in TEM and confocal imaging. We also thank the province of Limburg for the project funding. This work is part of the research programme Veni 2017 STW-project 15900, which is (partly) financed by the Dutch Research Council (NWO).

References

1. Gu, X., Ding, F. & Williams, D. F. Neural tissue engineering options for peripheral nerve regeneration. *Biomaterials* **35**, 6143–6156 (2014).
2. Hao, W. *et al.* Hyperglycemia promotes Schwann cell de-differentiation and demyelination via sorbitol accumulation and Igf1 protein down-regulation. *J. Biol. Chem.* **290**, 17106–17115 (2015).
3. Geuna, S., Raimondo, S., Fregnan, F., Haastert-Talini, K. & Grothe, C. In vitro models for peripheral nerve regeneration. *Eur. J. Neurosci.* **43**, 287–296 (2016).
4. Ribeiro-resende, V. T., Koenig, B., Nichterwitz, S., Oberhoffner, S. & Schlosshauer, B. Strategies for inducing the formation of bands of Büngner in peripheral nerve regeneration. *Biomaterials* **30**, 5251–5259 (2009).
5. Xu, Y. *et al.* Myelin-forming ability of Schwann cell-like cells induced from rat adipose-derived stem cells in vitro. *Brain Res.* **1239**, 49–55 (2008).
6. Pawar, K. *et al.* Increasing capillary diameter and the incorporation of gelatin enhance axon outgrowth in alginate-based anisotropic hydrogels. *Acta Biomater.* **7**, 2826–2834 (2011).
7. Von Der Ahe, D. *et al.* Suramin-induced neurotoxicity: Preclinical models and neuroprotective strategies. *Molecules* **23**, 1–15 (2018).
8. Osaki, T., Uzel, S. G. M. & Kamm, R. D. Microphysiological 3D model of amyotrophic lateral sclerosis (ALS) from human iPSC-derived muscle cells and optogenetic motor neurons. *Sci. Adv.* **4** 1–16 (2018).
9. Wieringa, P. A., Gonçalves de Pinho, A. R., Micera, S., van Wezel, R. J. A. & Moroni, L. Biomimetic Architectures for Peripheral Nerve Repair: A Review of Biofabrication Strategies. *Adv. Healthc. Mater.* **1701164**, 1–19 (2018).
10. Cattin, A. L. & Lloyd, A. C. The multicellular complexity of peripheral nerve regeneration. *Curr. Opin. Neurobiol.* **39**, 38–46 (2016).
11. Jessen, K. R. & Mirsky, R. The repair Schwann cell and its function in regenerating. *J. Physiol.* **13**, 3521–3531 (2016).
12. Callizot, N., Combes, M., Steinschneider, R. & Poindron, P. A new long term in vitro model of myelination. *Exp. Cell Res.* **317**, 2374–2383 (2011).
13. Sango, K., Kawakami, E. & Yanagisawa, H. Myelination in coculture of established neuronal and Schwann cell lines. *Histochem Cell Biol* 829–839 (2012).
14. Johnson, B. N. *et al.* 3D printed nervous system on a chip. *Lab Chip* 1393–1400 (2016)
15. Sakai, K., Shimba, K., Kotani, K. & Jimbo, Y. A co-culture microtunnel technique demonstrating a significant contribution of unmyelinated Schwann cells to the acceleration of axonal conduction in Schwann cell-regulated peripheral nerve development. *Integr. Biol.* **9** 678–686 (2017)

16. Daud, M. F. B., Pawar, K. C., Claeysens, F., Ryan, A. J. & Haycock, J. W. An aligned 3D neuronal-glia co-culture model for peripheral nerve studies. *Biomaterials*. **33**, (2012).
17. Khoshakhlagh, P., Sivakumar, A., Pace, L., Sazer, D. & Moore, M. J. Methods for fabrication and evaluation of a 3D microengineered model of myelinated peripheral nerve. *J. Neural Eng.* (2018).
18. Clark, A. J. *et al.* Co-cultures with stem cell-derived human sensory neurons reveal regulators of peripheral myelination. *Brain* **140**, 898–913 (2017).
19. Sharma, A. D. *et al.* Engineering a 3D functional human peripheral nerve in vitro using the Nerve-on-a-Chip platform. *Sci. Rep.* **9**, 1–12 (2019).
20. Ewing, R. H. S. W. and A. G. The PC12 cell as model for neurosecretion. *Acta Physiol* **192**, 273–285 (2009).
21. Id, K. T. *et al.* Cholinesterase inhibitor rivastigmine enhances nerve growth factor-induced neurite outgrowth in PC12 cells via sigma-1 and sigma-2 receptors. *PLoS ONE* 1–16 (2018).
22. Xue, Q., Jong, B., Chen, T. & Schumacher, M. A. Transcription of rat TRPV1 utilizes a dual promoter system that is positively regulated by nerve growth factor. *J. Neurochem.* **101**, 212–222 (2007).
23. Cohen, M. R. *et al.* Nerve Growth Factor Regulates Transient Receptor Potential Vanilloid 2 via Extracellular Signal-Regulated Kinase Signaling To Enhance Neurite Outgrowth in Developing Neurons Matthew. *Mol Cell Biol.* **35**, 4238–4252 (2015).
24. Yian, S., Mi, R., Hoke, A. & Leong, K. W. The effect of the alignment of electrospun fibrous scaffolds on Schwann cell maturation. *Biomaterials*. **29**, 653–661 (2008).
25. Wang, L., Wu, Y., Hu, T., Ma, P. X. & Guo, B. Aligned conductive core-shell biomimetic scaffolds based on nanofiber yarns / hydrogel for enhanced 3D neurite outgrowth alignment and elongation. *Acta Biomater.* **96**, 175–187 (2019).
26. Omidinia-anarkoli, A. *et al.* An Injectable Hybrid Hydrogel with Oriented Short Fibers Induces Unidirectional Growth of Functional Nerve Cells. *Small*. 1–8 (2019)
27. Luttge, R. Nanogroove-Enhanced Hydrogel Scaffolds for 3D Neuronal Cell Culture: An Easy Access Brain-on-Chip Model. *Micromachines*. **10** (2019)
28. Kaewkhaw, R., Scutt, A. M. & Haycock, J. W. Integrated culture and purification of rat Schwann cells from freshly isolated adult tissue. *Nat Protoc* **7**, 1996–2004 (2012).
29. Püspöki, Z., Storath, M., Sage, D. & Unser, M. Transforms and Operators for Directional Bioimage Analysis: A Survey. *Focus Bio-Image Informatics* 69–93 (2016)
30. Longair, M. H., Baker, D. A. & Armstrong, J. D. Simple neurite tracer: Open source software for reconstruction, visualization and analysis of neuronal processes. *Bioinformatics* **27**, 2453–2454 (2011).
31. Goebbels, S. *et al.* Elevated phosphatidylinositol 3,4,5-trisphosphate in glia triggers cell-autonomous membrane wrapping and myelination. *J. Neurosci.* **30**, 8953–8964

- (2010).
32. Pittman, R. N. & DiBenedetto, A. J. PC12 Cells Overexpressing Tissue Plasminogen Activator Regenerate Neurites to a Greater Extent and Migrate Faster than Control Cells in Complex Extracellular Matrix. *J. Neurochem.* **64**, 566–575 (1995).
 33. Ramirez, M. A. & Borja, N. L. Epalrestat: An aldose reductase inhibitor for the treatment of diabetic neuropathy. *Pharmacotherapy* **28**, 646–655 (2008).
 34. Päiväläinen, S. *et al.* Myelination in mouse dorsal root ganglion / Schwann cell cocultures. *Mol. Cell. Neurosci.* **37**, 568–578 (2008).
 35. Hyung, S. *et al.* Coculture of Primary Motor Neurons and Schwann Cells as a Model for In Vitro Myelination. *Sci Rep.* 1–11 (2015)
 36. Prang, P. *et al.* The promotion of oriented axonal regrowth in the injured spinal cord by alginate-based anisotropic capillary hydrogels. *Biomaterials* **27**, 3560–3569 (2006).
 37. Uzel, S. G. M. *et al.* Microfluidic device for the formation of optically excitable, three-dimensional, compartmentalized motor units. *Sci. Adv.* (2016).
 38. Volpato, V. & Webber, C. Addressing variability in iPSC-derived models of human disease : guidelines to promote reproducibility. *Disease Models & Mechanisms* (2020)
 39. Santos, D., Wieringa, P., Moroni, L., Navarro, X. & Valle, J. Del. PEOT/PBT Guides Enhance Nerve Regeneration in Long Gap Defects. *Adv. Healthc. Mater.* **6**, (2017).
 40. Romano, N. H., Madl, C. M. & Heilshorn, S. C. Matrix RGD ligand density and L1CAM-mediated Schwann cell interactions synergistically enhance neurite outgrowth. *Acta Biomater.* **11**, 48–57 (2015).
 41. Yu, W., Chen, Z., North, A. J. & Strickland, S. Laminin is required for Schwann cell morphogenesis. *Journal of Cell Science.* **122**, 929–936 (2009)
 42. Osaki, T., Shin, Y., Sivathanu, V., Campisi, M. & Kamm, R. D. In Vitro Microfluidic Models for Neurodegenerative Disorders. *Adv. Healthcare Mater.* **7**, 1700489, 1–29 (2018).
 43. Daly, W., Yao, L., Zeugolis, D., Windebank, A. & Pandit, A. A biomaterials approach to peripheral nerve regeneration : bridging the peripheral nerve gap and enhancing functional recovery. *J. R. Soc. Interface.* 202–221 (2012).
 44. Ahmed, T., Dare, E. & Hincke, M. T. Fibrin: A Versatile Scaffold for Tissue Engineering Applications. *Tissue Engineering: Part B.* **14** (2008).
 45. Monk, K. R., Feltri, M. L. & Taveggia, C. New insights on Schwann cell development. *Glia* **63**, 1376–93 (2015).
 46. Rukenstein, A. & Greene, L. A. The quantitative bioassay of nerve growth factor: use of frozen 'primed' PC12 pheochromocytoma cells. *Brain Res.* **263**, 177–180 (1983).
 47. Schmidt, G. & Wittinghofer, A. Priming of PC12 cells for semiquantitative microinjection studies involving Ras. *FEBS Lett.* **474**, 184–188 (2000).
 48. Paavilainen, T. *et al.* Effect of prolonged differentiation on functional maturation of

- human pluripotent stem cell-derived neuronal cultures. *Stem Cell Res.* **27**, 151–161 (2018).
49. Plachez, C. & Richards, L. J. Mechanisms of Axon Guidance in the Developing Nervous System. *Curr. Top. Dev. Biol.* **69**, 267–346 (2005).
 50. Winberg, M. L. *et al.* Plexin A is a neuronal semaphorin receptor that controls axon guidance. *Cell* **95**, 903–916 (1998).
 51. Kitsukawa, T. *et al.* Neuropilin-semaphorin III/D-mediated chemorepulsive signals play a crucial role in peripheral nerve projection in mice. *Neuron* **19**, 995–1005 (1997).
 52. Mccurdy, E. P. *et al.* Article Promotion of Axon Growth by the Secreted End of a Transcription Factor. *CellReports* **29**, 363-377.e5 (2019).
 53. Franze, K. *et al.* Neurite Branch Retraction Is Caused by a Threshold-Dependent Mechanical Impact. *Biophysical Journal* **97**, 1883–1890 (2009).
 54. Cermenati, G. *et al.* Diabetes-induced myelin abnormalities are associated with an altered lipid pattern: Protective effects of LXR activation. *J. Lipid Res.* **53**, 300–310 (2012).
 55. Obrosova, I. G. Diabetes and the peripheral nerve. *BBA - Mol. Basis Dis.* **1792**, 931–940 (2009).
 56. Mizisin, A. P., Shelton, G. D., Wagner, S., Rusbridge, C. & Powell, H. C. Myelin splitting, Schwann cell injury and demyelination in feline diabetic neuropathy. *Acta Neuropathol.* 171–174 (1998).
 57. Hotta, N *et al.* Long-Term Clinical Effects of Epalrestat, an Aldose Reductase Inhibitor, on Diabetic Peripheral Neuropathy. *Diabetes Care.* **29**, 1538-1544 (2006)
 58. Payne, S. C., Bartlett, C. A., Harvey, A. R., Dunlop, S. A. & Fitzgerald, M. Functional Loss during Chronic Secondary Degeneration in Rat Optic Nerve. *IOVS*, **53**, (2012).

Supplementary Information

A three-dimensional biomimetic peripheral nerve model for drug testing and disease modelling

Afonso Malheiro, Francis Morgan, Matthew Baker, Lorenzo Moroni, Paul Wieringa

Department of Complex Tissue Regeneration, MERLN Institute for Technology-Inspired Regenerative Medicine, Maastricht University, 6200 MD Maastricht, The Netherlands

Supplementary Figures

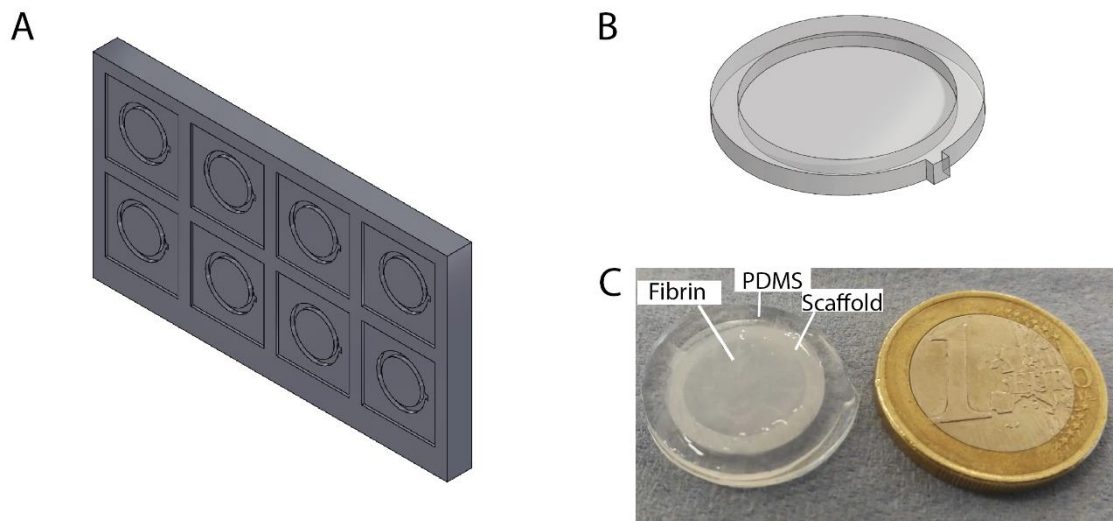


Figure S1. PDMS support fabrication. A) Milled PMMA slab as a negative mold for the support. B) PDMS support with 16 mm inner diameter, 20 mm outer diameter and 1.5 mm height. C) PDMS support with a scaffold and fibrin hydrogel inside.

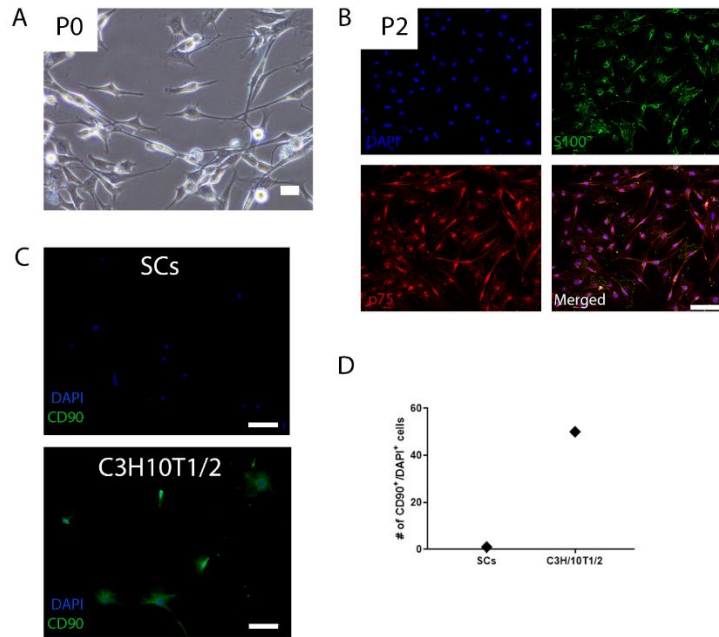


Figure S2. Characterization of Schwann cells (SCs) after isolation and purification. A) Brightfield microscopy image of SCs at P0. B) Immunoreactivity to S100 and P75 of SCs at P2. C) Immunoreactivity to CD90 of SCs or C3H/10T1/2 cells and respective positive event counting in D) (50 measurements in total). Scale bar is 100 μm in A) and C) and 50 μm in B).

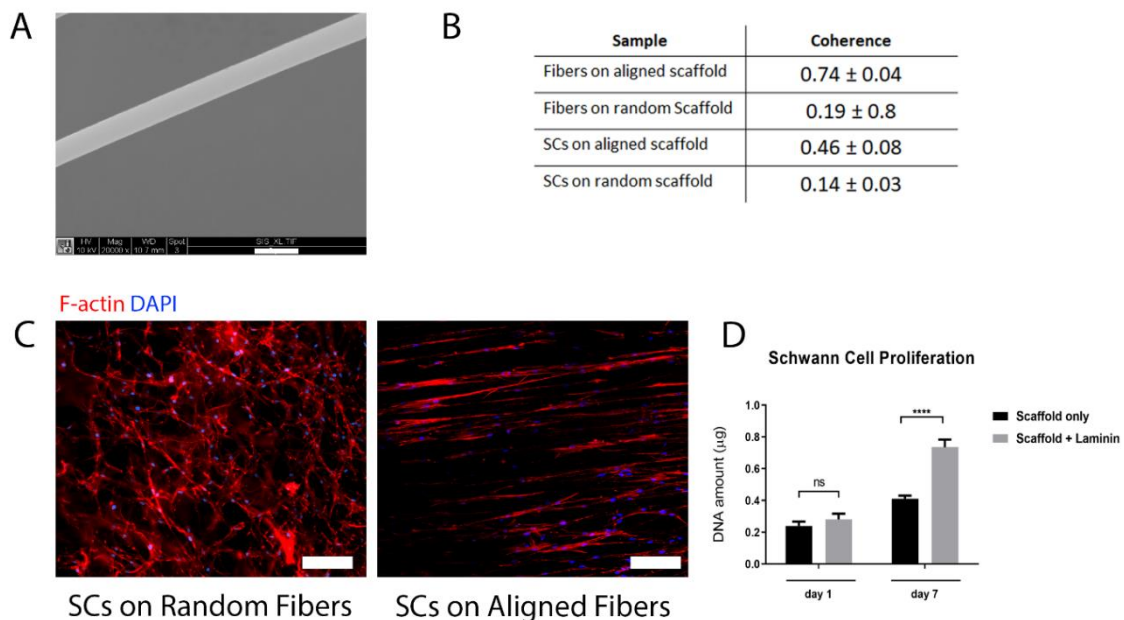


Figure S3. Effect of fiber orientation and laminin coating on SCs. A) SEM micrograph of a scaffold's individual fiber (average diameter of $1.36 \pm 0.2 \mu\text{m}$). B) Measurement of SC orientation on scaffolds with a random fiber morphology or with aligned fibers. C) Morphology

of SCs on random fiber or aligned fiber scaffolds (red: F-actin; blue: DAPI; scale bar is 100 μm). D) SC proliferation over 7 days on aligned scaffolds with and without laminin coating. For this experiment we used $n = 4$ and repeated it once. The statistics were performed with two-way ANOVA, followed by a Tukey's HSD post-hoc test where $**p < 0.0001$ and ns means no significant difference, with $p > 0.05$.

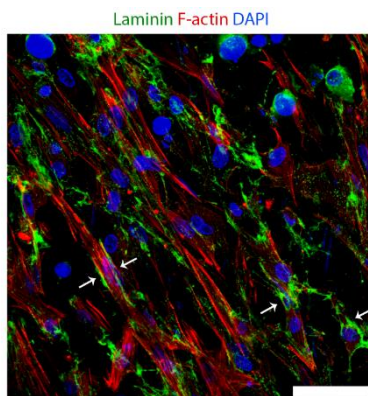


Figure S4. Extracellular deposition of laminin by SCs on the scaffold milieu. Immunostaining to a non-permeabilized sample showing only secreted laminin as visible by the white arrows (green: laminin; red: F-actin; blue: DAPI; scale bar is 50 μm).

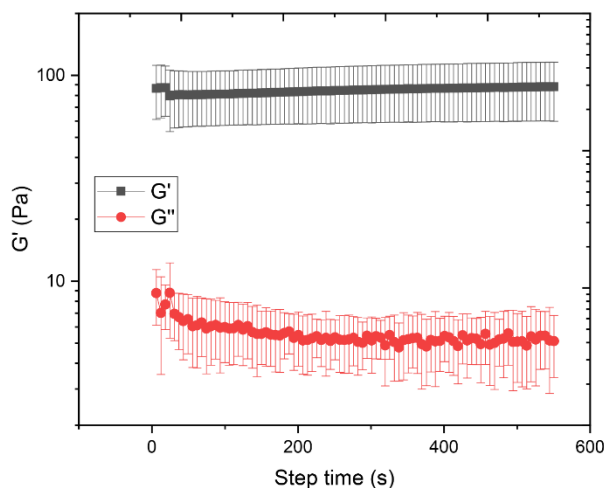


Figure S5. Fibrin gel rheological measurements. The measured storage modulus (G') was around 100 Pa and the loss modulus (G'') around 7 Pa. These values correlate with those reported by Sun et al.¹ for fibrin gels of similar formulation.

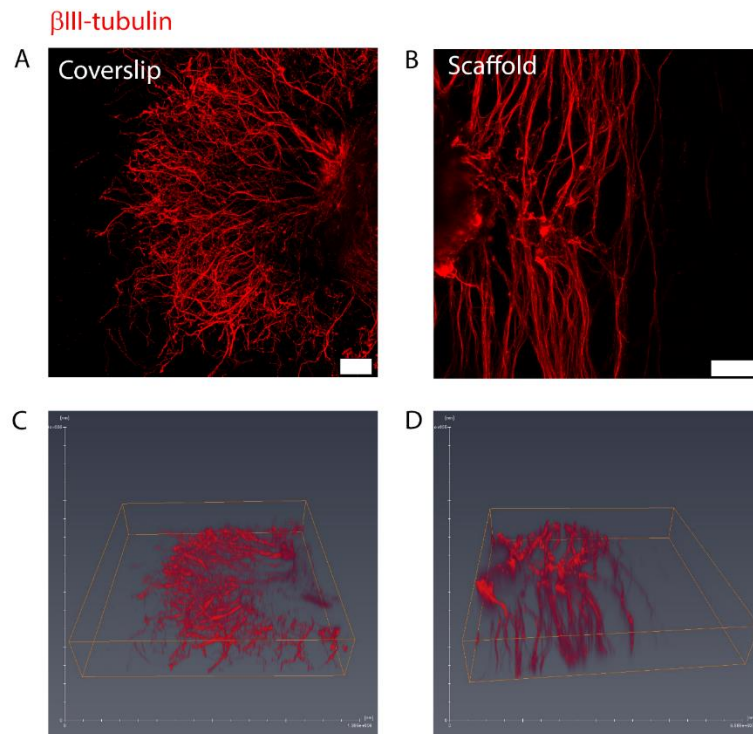


Figure S6. DRG neurite outgrowth after 7 days when cultured on a coverslip or scaffold with fibrin embedding. A) and C) When on top of a coverslip, neurites extend radially; B) and D) When cultured on top of the scaffold, DRG neurites extend anisotropically on the scaffold plane and on upper layers. A) and B) Immunostaining to β III-tubulin (red; scale bar is 100 μ m). C) and D) respective 3D reconstructions.

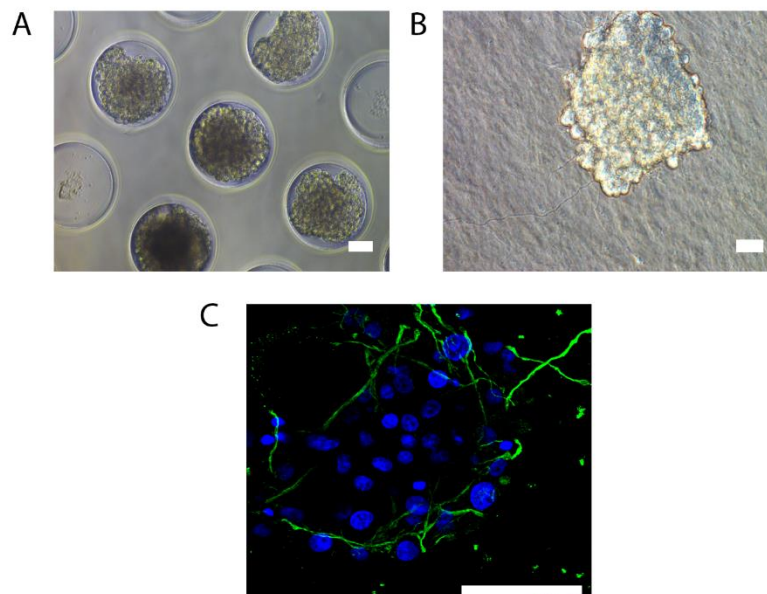


Figure S7. PC12 spheroid formation and culture in fibrin gel. A) Spheroid formation on 200 μ m agarose microwells (~50 cells per well; image taken at day 7, scale bar is 100 μ m). B) and C)

Spheroid culture in fibrin gel at day 7. B) Brightfield image; scale bar is 100 μm ; C) Immunostaining image of the differentiated spheroid (β III-tubulin in green and DAPI in blue; scale bar is 50 μm).

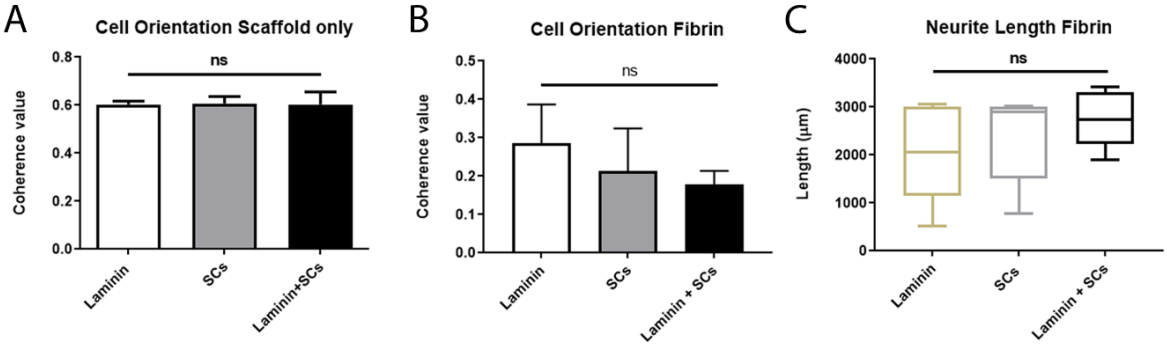


Figure S8. Appendix of DRG/SCs short term co-culture analysis. Measurement of neurite alignment on scaffolds without (A) and with fibrin embedding (B). C) Neurite length on samples with fibrin embedding. Cell orientation in A) and B) is displayed as the coherence value, where 0 is full isotropy and 1 is full anisotropy. Bars represent mean value \pm SD. Neurite length in C), was calculated as the distance (in μm) between the cell body and the edge of the respective axon. The boxplots represent data points in the 1-99 percentile. In these experiments we used $n = 6$ and took either 10 (A and B) or 20 measurements (C) per sample. Statistics were done using one-way ANOVA, followed by a Tukey's HSD post-hoc test where ns means no significant difference, with $p > 0.05$.

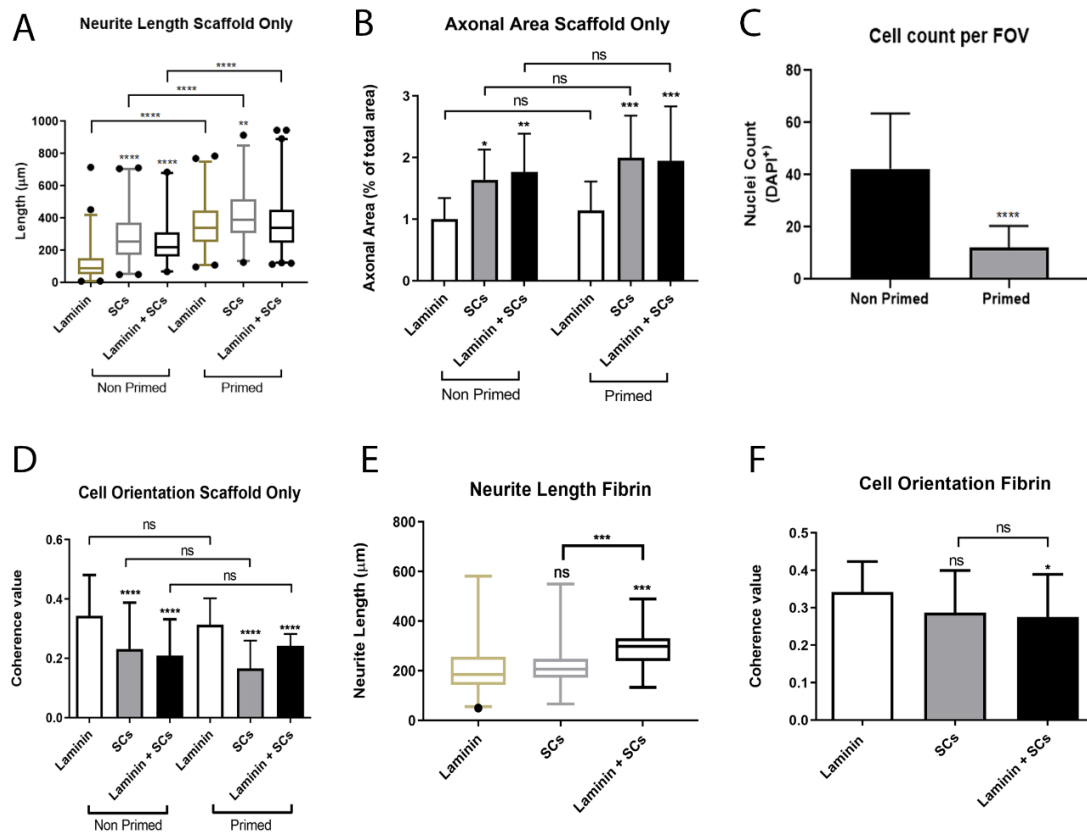


Figure S9. Appendix of PC12/SCs short term co-culture analysis. Measurements of (A) neurite length, (B) axonal area and (D) cell orientation of primed and non primed PC12 cells cultured on scaffold only. (C) Nuclei count per field of view (FOV) of primed and non primed PC12 cells cultured on laminin only scaffolds. (E) Neurite length and (F) cell orientation of primed PC12 cultured in scaffolds with fibrin embedding. Neurite length, axonal area and cell orientation were measured as stated in other figures. For these experiments we used $n = 6$ and repeated the experiment once. To determine neurite length, we acquired at least 20 measurements per sample. For axonal area and cell orientation calculation, we acquired 10 measurements per sample. **** $p < 0.0001$, *** $p < 0.01$, ** $p < 0.01$, * $p < 0.05$, ns is not significant ($p > 0.05$); one-way ANOVA followed by a Tukey's HSD post-hoc test (A, B, D, E and F) or unpaired t-test (C). Bars represent mean \pm SD and boxplots represent data points in the 1-99 percentile.

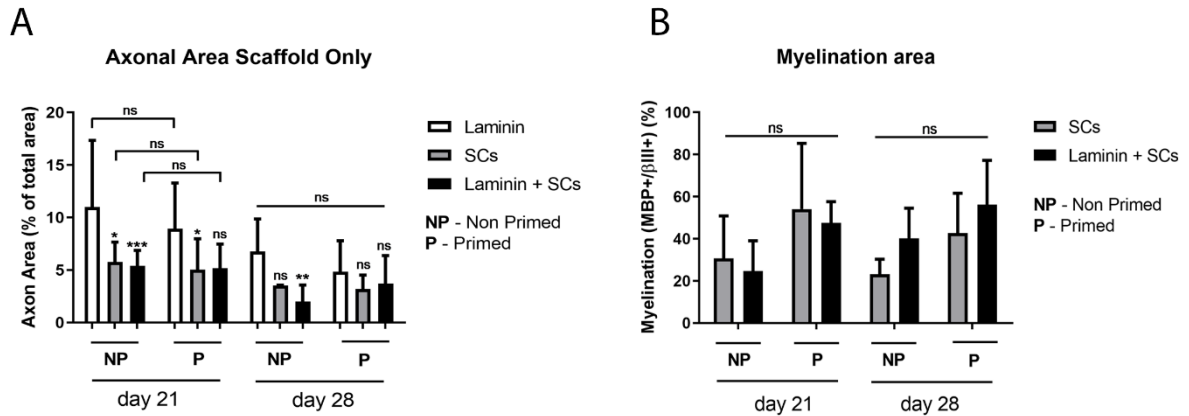


Figure S10. Axonal and myelination area of primed and non primed PC12/SCs co-cultures. Axonal area was determined as the ratio of β III-tubulin⁺ segments area and total image area. Myelination area is the ratio between MBP⁺ segments area and correspondent axonal area. 6 replicates were used per experiment and the experiment repeated once. Statistics were determined with a two-way ANOVA test followed by a Tukey's HSD post-hoc test. *** $p < 0.01$, ** $p < 0.01$, * $p < 0.05$, ns is not significant ($p > 0.05$);

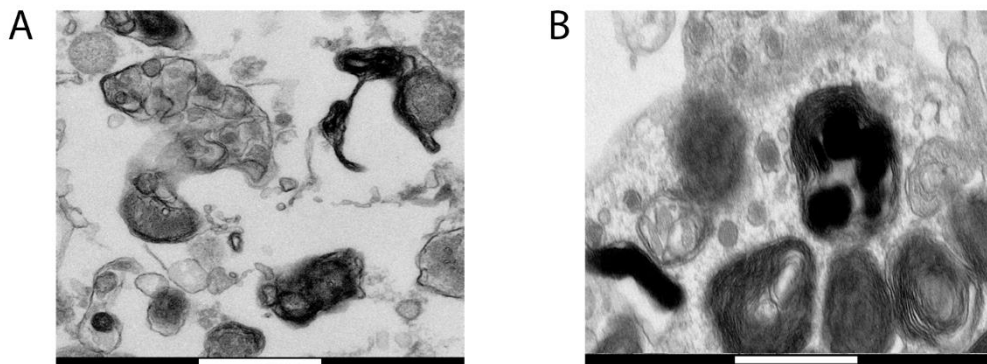


Figure S11. TEM micrographs of primed PC12/SCs scaffolds embedded in fibrin and cultured for 28 days. Overview of several myelin segments cross-section, evidencing that the formation of compact myelin rings is repeated and in abundance throughout the construct. Scale bar is 200 nm for A) and 500 nm for B).

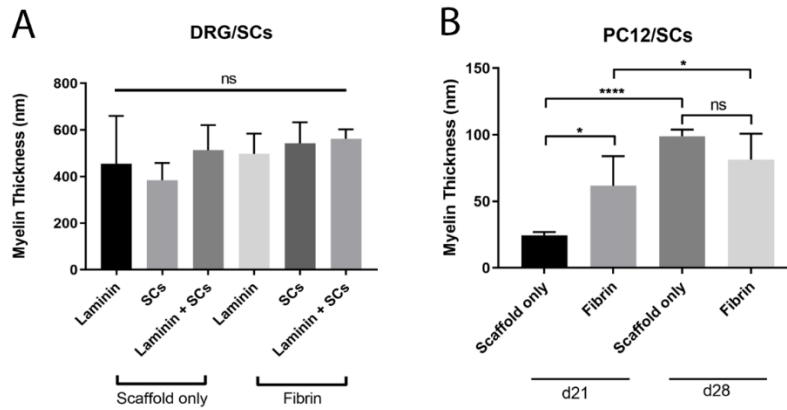


Figure S12. Myelin thickness on A) DRG/SCs co-culture samples and B) PC12/SCs co-culture samples cultured for 28 days with or without fibrin embedding. In both experiments we used $n = 6$ and repeated these experiments once. Statistics were done with one-way ANOVA followed by a Tukey's HSD post-hoc test, where * $p < 0.0001$, * $p < 0.05$ and ns denotes not significant with $p > 0.05$. Bars represent mean value \pm SD.

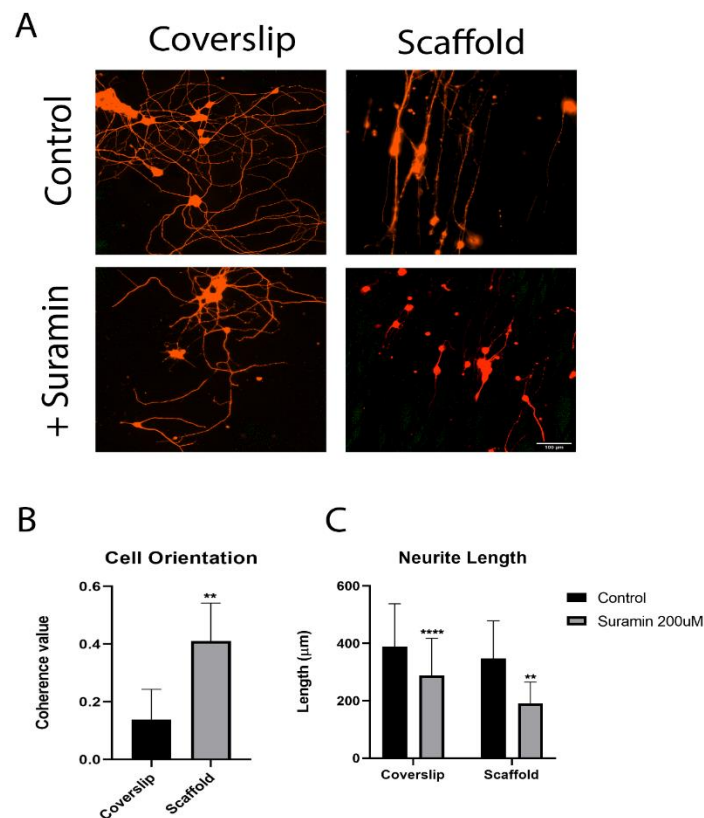


Figure S13. Suramin test in primed PC12 cultured in coverslips or scaffolds for 7 days. Suramin was applied at $200 \mu\text{M}$ for 24h. As control, cells were cultured in normal medium. Cells are immunostained by β III-tubulin, shown in red. B) Quantification of cell orientation for control cells in coverslips or scaffolds. C) Neurite length of control and suramin exposed cells cultured in coverslips or scaffolds. Cell orientation and neurite length were measured as

described above. For this experiment, we used 5 replicates and took around 20 measurements per sample. Statistics were performed using an unpaired t-test (B) or one-way ANOVA followed by a Tukey's HSD post-hoc test (C). **** $p < 0.0001$, ** $p < 0.01$.

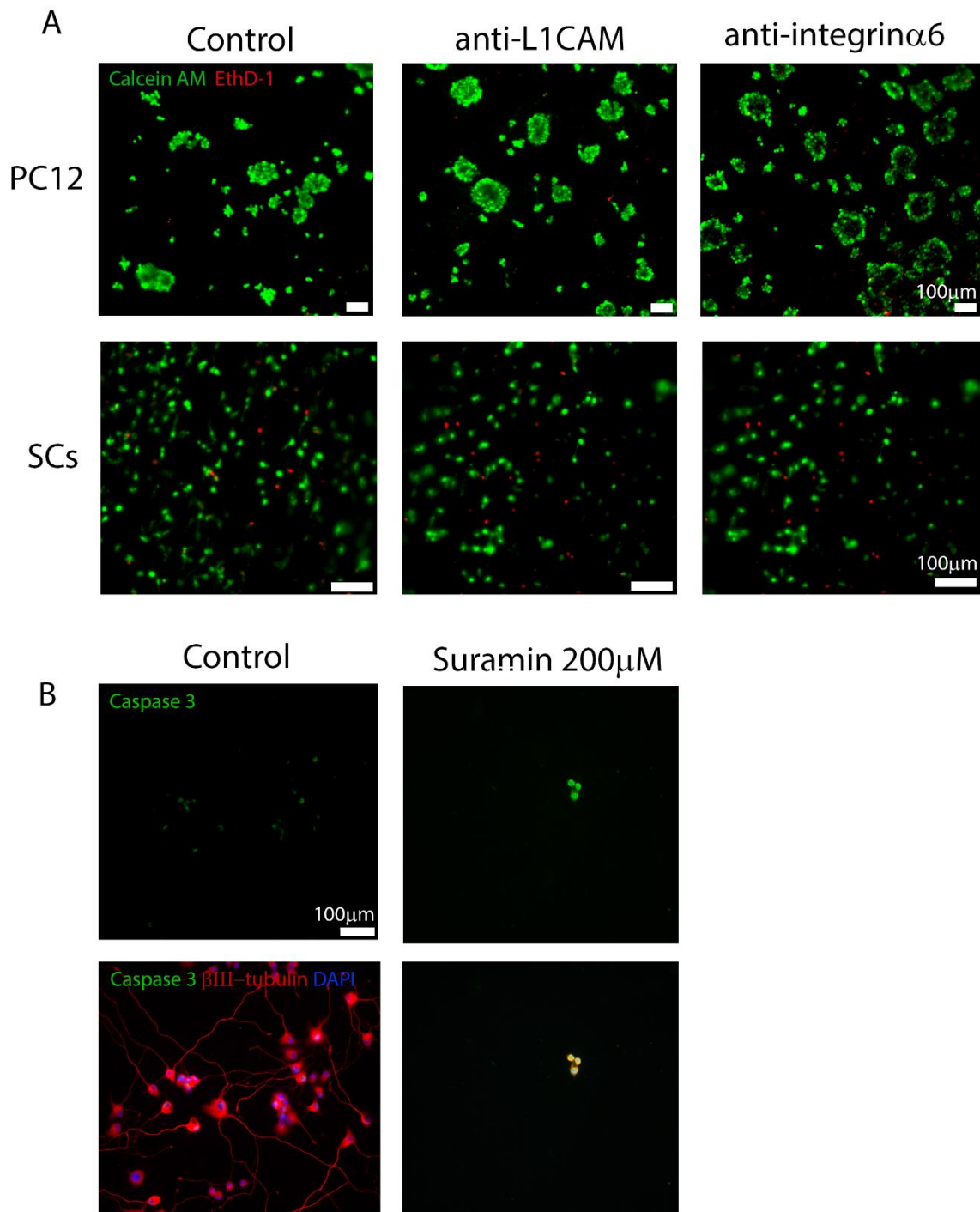


Figure S14. A) Live/Dead assay on PC12 cells (top row) and SCs (bottom row) in the presence of antibodies anti-L1CAM and anti-integrin α 6 (control: medium with no antibodies; green: live cells stained by calcein-AM; red: dead cells stained by ethidium homodimer-1). B) Neurite retraction and apoptosis on PC12 cells cultured in coverslips and incubated for 24 h with 200

μM suramin. Control cultures were done with normal culture medium; Top panel shows cleaved caspase-3 staining (in green) and the bottom panel shows cleaved caspase-3 staining (in green), β III-tubulin (in red) and DAPI (in blue). Scale bar is 100 μm .

Figure S15. Brightfield micrograph of a PC12/SCs co-culture in coverslips for 28 days. It is well visible the formation of myelin bands that appear as thicker and more light reflecting than



unmyelinated neurites seen as thin dark filaments. It is also visible that myelin bands form in multiple directions and that many SCs do not associate with neurites.

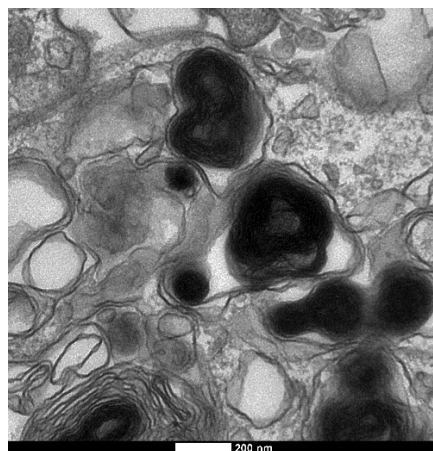


Figure S16. TEM micrograph showing an overview of several myelin cross sections from PC12/SCs cultured for 28 days and exposed to hyperglycemia (medium + 45mM glucose) with epalrestat (1 μM) supplemented. It is visible the widespread protective effect of epalrestat addition in mitigating myelin abnormalities and decompaction, although some are still visible. Scale bar is 200 nm.

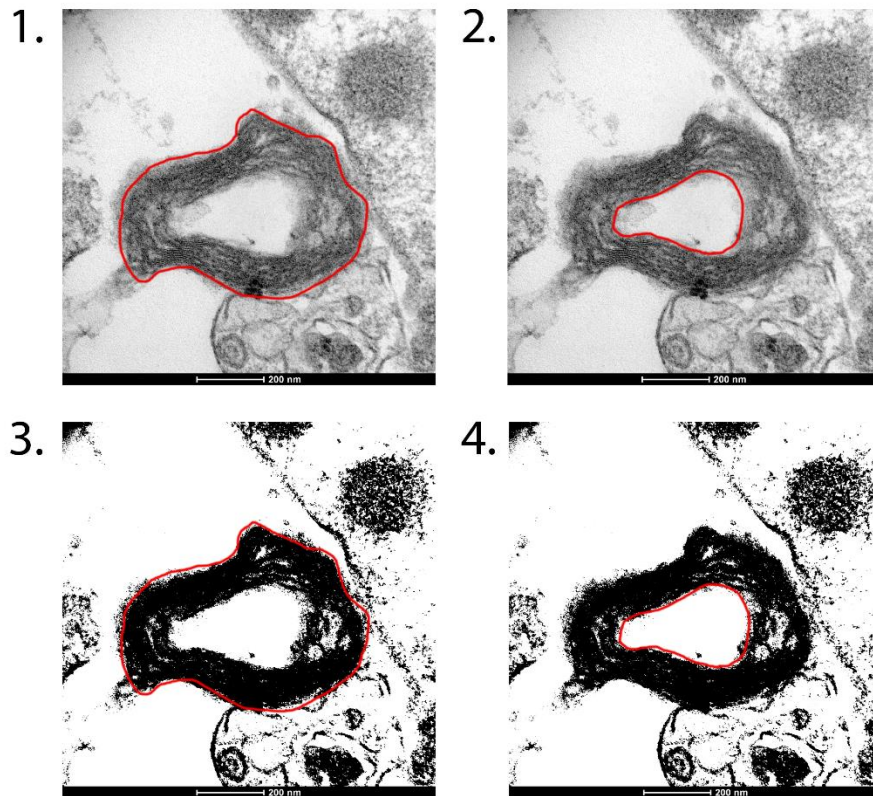


Figure S17. Myelin decompaction analysis protocol. 1) A region of interest (ROI) is defined by surrounding the most outer myelin ring. This ROI is saved and the area calculated. 2) A second ROI is traced surrounding the most inner myelin ring. Again, the ROI is saved and the area calculated. 3) The original image is converted to binary and the threshold adjusted to show myelin in black and decompacted/non-myelin existing areas in white. After, the area is calculated. 4) The same is done using the second ROI. The value of expected myelin area corresponds to area (1) – area (2). The value of actual myelin corresponds to area (3) – area (4). The final decompaction value is calculated by the formula: $(1 - (\text{expected myelin area} / \text{actual myelin area})) \times 100$.

Supplementary Methods

Agarose microwell fabrication and PC12 seeding

A 3% (w/v) sterile agarose solution was prepared and boiled until well dissolved. Then, 8 ml were poured into a 6 well-plate containing an in-house fabricated PDMS stamp containing the pattern of the microwells. After centrifugation at 3500 rpm, the plate was chilled for 45 min at 4°C for agarose solidification. When solid, the agarose blocks were removed, cut and placed on a 12 well-plate and left in medium until further use.

For cell seeding, PC12 cell suspensions were seeded at 350 cells per microwell and left to aggregate for 3 days before further use. To remove, cells were flushed and transferred to laminin coated coverslips or fibrin gels.

Bibliography

1. Sun, Y. & Giraudier, O. Rheological Characterization and Dissolution Kinetics of Fibrin Gels Crosslinked by a Microbial Transglutaminase. 257–263 (2005).
doi:10.1002/bip.20177

Chapter 4

3D culture platform of human iPSCs-derived nociceptors for peripheral nerve modelling and tissue innervation

Afonso Malheiro^{1}, Abhishek Harichandan^{1*}, Joyce Bernard², Adrián Seijas-Gamardo¹, Gonda F. Konings³, Paul G.A Volders², Andrea Romano³, Carlos Mota¹, Paul Wieringa¹, Lorenzo Moroni¹*

1. MERLN Institute for Technology-Inspired Regenerative Medicine, Complex Tissue Regeneration department, Maastricht University, The Netherlands
2. CARIM School for Cardiovascular Diseases, Department of Cardiology, Maastricht University, The Netherlands
3. GROW School for Oncology and Developmental Biology, Department of Gynaecology, Maastricht University, The Netherlands

**these authors have contributed equally to this work*

Abstract

Functional humanized *in vitro* nerve models are coveted as an alternative to animal models due to their ease of access, lower cost, clinical relevance and no need for recurrent animal sacrifice. To this end, we developed a sensory nerve model using induced pluripotent stem cells (iPSCs)-derived nociceptors that are electrically active and exhibit a functional response to noxious stimuli. The differentiated neurons were co-cultured with primary Schwann cells on an aligned microfibrinous scaffold to produce biomimetic peripheral nerve tissue. Compared to glass coverslips, our scaffold enhances tissue development and stabilization. Using this model, we demonstrate that myelin damage can be induced from hyperglycemia exposure (glucose at 45 mM) and mitigated by epalrestat (1 μ M) supplementation. Through fibrin embedding of the platform, we were able to create 3D anisotropic myelinated tissue, reaching over 6.5 mm in length. Finally, as a proof-of-concept, we incorporated pancreatic pseudoislets and endometrial organoids into our nerve platform, to build nociceptor innervation models. In

summary, we propose here an improved tool for neurobiology research that permits pathology modelling, drug screening and target tissue innervation.

Introduction

The ability to detect external noxious stimuli and internal organ dysfunction signals is essential to maintain physical integrity and homeostasis¹. This process is mediated by nociceptors, which recognize this input via specialized receptors, such as the transient receptor potential vanilloid 1 (TRPV-1), and conduct the information to the central nervous system (CNS), whilst also locally releasing neuropeptides, e.g. substance P, at the site of stimulus^{2,3}. The perception of nociceptive pain is contingent on the continuity of sensory peripheral nerve (PN) fibers between target organs and the CNS⁴. However, the PN is a fragile and exposed tissue, prone to damage by trauma or disease⁵. Most cases of PN damage arise from diabetes type II pathophysiological imbalances⁶, which has prompted significant research into prevention and mitigation of diabetes-related disorders as well as strategies for neural tissue repair^{7,8}. In other pathological situations, the aberrant presence of nociceptors within organs can lead to abnormal and excessive pain. That is the case of chronic pancreatitis (CP), in which the main symptom is severe abdominal pain, caused in part by peripheral sensitization^{9,10,11}. Similarly, women with endometriosis, a benign condition affecting up to 10% of reproductive-aged women, experience nociceptive pain because of infiltrating nociceptors within endometriotic implants and inflammatory sensitization of peripheral nociceptors¹².

To better understand PNs growth, repair methods and involvement in associated pathologies, it is necessary to develop improved neurobiology research platforms. Furthermore, such platforms are instrumental in discovering compounds for neuropathy prevention, pain alleviation and nerve repair. To this end, biomimetic and functional three-dimensional (3D) *in vitro* models of PNs and tissue innervation can provide a simple, cost-effective and clinically relevant research tool to substitute the expensive and ethically loaded animal models. In this pursuit, few *in vitro* models using human sensory neurons and nociceptors in particular, have been reported. Wainger et al. proposed a model using nociceptors from reprogrammed fibroblasts that were electrically active and sensitive to noxious stimuli¹³. Similarly, Jones et al.¹⁴ reported a sensory neuron model, with electrically excitable cells, obtained from human embryonic stem cell differentiation. Both models consist, however, of 2D disorganised and non-myelinated cultures, which do not reflect the biological architecture of mature nerves. To achieve myelination, Clark et al.¹⁵ generated co-cultures of induced pluripotent stem cells (iPSCs) derived sensory neurons with primary rat Schwann cells (SCs) on Matrigel-coated coverslips. However, the use of Matrigel limits clinical applicability (potential batch-to-batch variability) and the resultant tissue morphology is still flat and random.

While 3D cultures exhibiting anisotropic neurites from iPSCs-derived motor neurons have already been reported for the creation of motor nerve¹⁶ or innervated muscle platforms^{17,18}, 3D biomimetic models with functional sensory neurons remain to be established.

We show here the development of a 3D sensory nerve model with biomimetic architecture and applicability for pathology modelling, drug testing and target tissue innervation. First, we developed a method to produce, in large-scale, uniform iPSCs-derived trunk neural crest (NC) spheroids (neurospheres) within an agarose mold. The neurospheres can be harvested from the mold and further differentiated into functional nociceptors that exhibit electrical activity and sensitivity to noxious stimuli (resiniferatoxin, RTX). To develop a biomimetic nerve model, we co-cultured the neurospheres with primary rat SCs on an aligned microfibrinous scaffold, which enhances neural tissue formation in terms of length, alignment and area, and improves tissue stabilization, compared to traditional glass coverslips. Using our 3D co-culture platform, we modelled diabetes-related myelin damage, through acute hyperglycemia exposure, and show that epalrestat is able to mitigate the damage. To upscale tissue formation, we combined the scaffold platform with a fibrin hydrogel, to create anisotropic myelinated axons, with over 6.5 mm in length, densely packed within a 3D matrix. Finally, using the fibrin/scaffold nerve platform, we demonstrate that pancreatic pseudoislets and endometrial organoids can be incorporated to produce nociceptor-innervated tissue models.

Materials and Methods

Agarose microwell platform fabrication

A 3% (w/v) sterile agarose (Thermo Fisher Scientific) solution was prepared in PBS. 8 ml of agarose solution were poured onto an in-house fabricated PDMS stamp with the negative template of 1580 microwells with 400 μm diameter. Centrifugation at 845 g was performed to remove air bubbles, followed by chilling for 45 min at 4°C for agarose solidification. When solid, the agarose blocks were removed, cut to fit in a 12 well-plate, washed with 70% ethanol, then washed twice in phosphate buffered saline (PBS) solution and left at 4°C until further use. The day before cell seeding, PBS was replaced with DMEM/F-12 medium (Thermo Fisher Scientific) and kept in the incubator at 37°C, 5% CO₂ overnight.

iPSCs culture

The human iPSC line LUMC0031iCTRL08 (Provided by the Leids Universitair Medisch Centrum iPSC core facility) was cultured on Geltrex coated dishes at a density of $10 \times 10^3/\text{cm}^2$ in mTESR1 medium (Stem Cell Technology). Cells were fed every day with completely fresh medium and passaged weekly using Gentle Cell Dissociation Reagent (Stemcell Technologies).

iPSCs differentiation into nociceptors and neurosphere formation

In order to induce iPSCs differentiation into nociceptors, we adapted and modified the protocol published by Chambers et al¹⁹. Nociceptor induction was initiated using single cell suspension of undifferentiated iPSCs detached with accutase, followed by seeding of 200 cells/microwell in mTESR1 medium supplemented with 10 μM of Y-27632 and 0.5 % Geltrex (in solution) onto 400 μm agarose microwells. Cell suspension was forced to settle by centrifugation at 290 g for 2 min. Afterwards, cells were incubated for 24 h and were given a complete media change with mTESR1 medium. At this time, the cellular spheroid is formed and cell synchronization is initiated by the addition of mTESR1 medium supplemented with 1% dimethyl sulfoxide (DMSO). The cells were maintained for 72 h in the synchronization medium. Post synchronization cells were given a PBS wash and nociceptor induction was initiated by addition of dual SMAD inhibition media containing Advanced RPMI 1640 supplemented with Glutamax (both Thermo Fisher Scientific), 100 nM LDN-193189 (Tocris) and 10 μM SB431542 (Tocris). The spheres were maintained for 48 h in the dual SMAD inhibition media. Following this, neural crest commitment was induced via media containing Advanced RPMI 1640 supplemented with Glutamax, 3 μM CHIR99021 (Tocris) and 1 μM retinoic acid (Tocris). The spheres were maintained in the neural crest induction media for 5 days with media change every alternate day. Following this stage, the spheres were incubated in notch inhibition media, consisting of Advanced RPMI supplemented with Glutamax, 10 μM SU5402 (Tocris) and 10 μM DAPT (Tocris), for 48 h.

Finally, the neurospheres, composed of trunk neural crest cells, were collected and seeded on coverslips or scaffolds. In these substrates, cells were cultured in neural maturation medium for at least 5 days to reach the nociceptor phenotype. The neural medium is composed of Neurobasal Medium, 0.5 mM Glutamax, 100 U/ml penicillin and 100 $\mu\text{g}/\text{ml}$ streptomycin (all Thermo Fisher Scientific), 100 ng/ml human nerve growth factor (NGF), 50 $\mu\text{g}/\text{ml}$ ascorbic acid (all Sigma-Aldrich), 25 ng/ml human neuregulin-1 type III (NRG-1 SMDF) and N21 supplement (both from R&D systems).

Dissociated sensory neuron culture

iPSCs neurospheres were collected on day 9 of differentiation in an Eppendorf containing Advanced RPMI supplemented with Glutamax, and dissociated enzymatically with 1ml of Trypsin EDTA for 10 min at 37°C and 5% CO₂. Cells were pelleted at 290 g for 7 min and resuspended in neural maturation medium, followed by mechanical dissociation through gentle repeated pipetting. 5×10^3 cells/cm² were seeded on Matrigel coated (1:200 in DMEM) 35 mm petri dishes (for the patch clamp experiment) or 5×10^4 cells/cm² on a 6 well plate (EIA experiment) and extra medium was added. The cultures were maintained in the same medium for up to 45 days, at 37°C, 5% CO₂, with medium refreshments every 3 days.

Primary Schwann Cells harvesting, purification and culture

Primary Schwann cells (SCs) were harvested from the sciatic nerves of neonatal Wistar rat pups, following local and Dutch animal use guidelines. Nerve segments were extracted and digested, followed by cell isolation and purification as described by Kaewkhaw et al.²⁰. Briefly, the collected nerves were sliced and digested in a 0.05% (w/v) collagenase solution for 60 min at 37°C, 5% CO₂. The cell suspension was filtered through a 40 µm cell strainer, centrifuged for 6 min at 400 g, followed by supernatant removal and cell pellet washing with DMEM containing 10% foetal bovine serum (FBS) and 100 U/ml penicillin and 100 µg/ml streptomycin. Cells were centrifuged again at 400 g for 6 min and the supernatant discarded. Finally, cell pellets were re-suspended with 2 ml of Schwann cell proliferation and purification medium, composed of DMEM D-valine (Cell Culture Technologies), 2 mM L-glutamine, 10% (v/v) FBS, 1% (v/v) N2 supplement (R&D Systems), 20 µg/ml bovine pituitary extract, 5 µM forskolin, 100 U/ml penicillin and 100 µg/ml streptomycin, and 0.25 µg/ml amphotericin B (all Sigma-Aldrich). Cells were then plated on 35 mm petri dish pre-coated with 0.01% (v/v) poly-L-lysine (Sigma –Aldrich) and 1 µg/ml Laminin (R&D systems) and incubated at 37°C, 5% CO₂ for 7 days. The use of D-valine in place of L-valine was to inhibit fibroblast growth while permitting SCs survival and proliferation. On day 7, 1 ml of fresh medium was added and the medium changed every 2 days until 70 % confluency. Cells were used between passage 3 and 6 (P3-P6).

Scaffold fabrication and sterilization

The scaffolds were fabricated via a two-step electrospinning (ESP) process with a custom-built apparatus. The first step was the production of a release layer by electrospaying a solution of 50% polyethyleneoxide (PEO, Mn = 3350, Sigma-Aldrich) in Milli-Q onto aluminum foil. For this, the solution flowed through a 0.8 mm inner diameter stainless steel needle (Unimed S.A.) at 2 ml/h, while subjected to 20 kV onto a 60 mm diameter mandrel, placed at 10 cm of distance and rotating at 5000 rpm. Afterwards, a nonwoven polyurethane mesh (6691

LL (40 g/m²), provided by Lantor B.V., The Netherlands) was prepared by punching an array of 12 mm circular holes and placed on the mandrel, over the PEO sprayed-foil. We then produced the scaffolds by ESP of 300PEOT55PBT45 (PolyVation) in 75:25 Chloroform/1,1,3,3-hexafluoroisopropanol solution onto the mesh support on the mandrel. For this process, the solution flowed through a 0.5 mm inner diameter stainless steel needle (Unimed S.A.) at 0.75 ml/h, while applying a voltage of 12 kV and at a distance of 10 cm from a rotating mandrel (at 5000 rpm). During both processes, the humidity was maintained at 35-40% and the temperature at 22-24°C. Finally, we generated individual scaffolds from the polyurethane mesh by punching 15 mm-outer diameter sections concentric to the 12 mm holes, resulting in a thin ESP membrane supported by a polyurethane mesh ring. To detach the individual scaffolds, these were dipped in deionized water and left in PBS until further use. When required for cell seeding, the scaffolds were transferred to a 24 well plate and immersed in 70% ethanol for 1 h for sterilization, followed by several PBS washes and air-drying. These were then maintained in sterile PBS until needed.

Peripheral nerve platform generation

To fabricate our PN platform we followed the process graphically illustrated in Fig. 1. While the iPSCs differentiate and form neurospheres as described above (Fig. 1 b1), we simultaneously seeded the scaffolds with 100 x 10³ primary SCs and cultured these for 7 days with SC medium. During this time, cells proliferate and aligned with the scaffold fibers to form highly anisotropic SCs bands (Fig. 1 b2). After 7 days, when SCs bands are fully formed, we manually seeded one neurosphere per scaffold (Fig. 1 b3). After this, we let the neurospheres adhere to the substrate for at least 6 hours, before adding neural medium.

For comparison, we also cultured neurospheres on scaffolds devoid of SCs, but with laminin coating, Matrigel coating or no coating at all. For this, we incubated the scaffolds overnight with laminin solution: 100 µl of 1 µg/ml laminin-1 (R&D systems) and 2 µg/ml poly-D-lysine (Sigma Aldrich) in PBS; or Matrigel solution: 100 ul of 1:200 dilution of Matrigel stock (Fisher Scientific) in DMEM. The following day, we washed off the coating twice with sterile PBS and followed the same procedure for neurosphere seeding. All culture conditions were maintained for 7 or 21 days at 37°C, 5% CO₂, with medium refreshment every other day.

Coverslip cultures

For sensory neuron marker characterization, we coated a 12 mm glass coverslip with laminin (same procedure as scaffold coating) and seeded one neurosphere as described above. The neurons were further cultured for 7 days with neural medium to induce maturation.

As a control for the scaffolds, we cultured neurospheres on bare (no coating), laminin, Matrigel-coated or SCs-seeded 12 mm glass coverslips (same culture area as scaffolds). The

laminin or Matrigel coating procedure was identical to the scaffolds. SCs were seeded 7 days prior to neurosphere addition with the same cell density used for scaffold seeding (100×10^3 cells in total; $\sim 8.3 \times 10^3$ cells/cm²). The cultures were maintained in neural medium for 7 or 21 days at 37°C, 5% CO₂, with medium refreshments every other day.

Fibrin embedded peripheral nerve platform

To produce a 3D biomimetic PN platform we combined a SCs-seeded scaffold with a neurosphere in a fibrin hydrogel. To achieve this, we followed a similar process as described above and illustrated in Fig.1. First, 100×10^3 SCs were seeded on the scaffolds and induced to proliferate for 7 days. Thereafter, one neurosphere was seeded and the medium change to neural medium. After 1 day, we removed the medium and embedded the constructs into a fibrin hydrogel, composed of 3.5 mg/ml human fibrinogen (Enzyme Research Laboratories), 5 U/ml thrombin (Sigma-Aldrich) and 2.5 mM CaCl₂. After gelation (~15 min), neural medium containing 100 µg/ml aprotinin was added. The cultures were maintained for 7 or 21 days at 37°C, 5% CO₂ with medium refreshments every other day.

Pancreatic pseudoislets generation and innervation

To innervate pancreatic pseudoislets, we first generated spheroids composed of a mixture of alpha TC1 clone 6 cells (ATCC, CRL-2934) and INS1E cells (AddexBio), then added these onto a neurosphere seeded scaffold. To do this, we started by expanding alpha TC cells in medium composed of DMEM, 15 mM HEPES, 0.1 mM non-essential aminoacids, 2 g/L glucose (all Thermo Fisher Scientific), 10% FBS, 1.5 g/L sodium bicarbonate (both Sigma-Aldrich), 0.02% BSA (VWR) and INS1E cells in medium composed of RPMI, 2-mercaptoethanol, glutamax, HEPES, 100 U/ml penicillin and 100 µg/ml streptomycin (all Thermo Fisher Scientific) and 10% heat inactivated FBS (Sigma-Aldrich). When ready, the cells were seeded on a 200 µm agarose microwell platform at a ratio of 3:7 alpha TC / INS1E cells to yield approximately 250 cells per spheroid. The spheroids were cultured for 3 days in medium composed of 1:1 alpha TC / INS1E medium, then flushed from the platform and carefully pipetted onto a laminin-coated scaffold already containing one 7-day grown neurosphere. The spheroids were left to adhere overnight, after which we added 300 µl of fibrin hydrogel composed of 3.5 mg/ml human fibrinogen (Enzyme Research Laboratories), 5 U/ml thrombin (Sigma-Aldrich) and 2.5 mM CaCl₂. Cultures were maintained for 10 days with medium composed of 2:1:1 neural medium / alpha TC medium / INS1E medium at 37°C, 5% CO₂.

Endometrium spheroids generation and innervation

The human endometrial adenocarcinoma cell line Ishi-M3-HSD-A is derived from Ishikawa cell line after genetic modification to introduce the luciferase fused with the green

fluorescent reporters genes²¹. Cell line Ishi-M3-HSD-A used in the present experiment was authenticated by Short Tandem Repeat (AmpFISTR Identifier™ PCR Amplification Kit; Thermo Fisher Scientific) profiling and tested negative for mycoplasma (MycoAlert, Promega).

Cells were maintained in standard monolayer culture as described earlier²¹, using RPMI 1640 medium (Thermo Fisher Scientific) supplemented with sodium-pyruvate, L-glutamine, penicillin-streptomycin and 5% FBS at 37°C with 5% CO₂ in humidified air. For organoid formation, cells were detached using with Accutase (Thermo Fisher Scientific), pelleted and resuspended in ice-cold Matrigel (Becton Dickinson). Droplets of 25 µl Matrigel suspension were pipetted into a 6-wells plate to form domes containing 2000 cells each. Matrigel domes were allowed to polymerize for 15 min at 37°C, 5% CO₂ and were subsequently covered with pre-warmed endometrium organoid culture medium (RPMI 1640, sodium-pyruvate, L-glutamine, penicillin-streptomycin and 5% fetal bovine serum). Medium was refreshed twice a week, while monitoring the organoids condition.

For the innervation experiments, we carefully picked up the Matrigel domes with a sterile spatula and transferred to a laminin-coated scaffold containing one 7-day grown neurosphere. The spheroids were left to adhere overnight, after which we added 300 µl of fibrin hydrogel composed of 3.5 mg/ml human fibrinogen (Enzyme Research Laboratories), 5 U/ml thrombin (Sigma-Aldrich) and 2.5 mM CaCl₂. Cultures were maintained for 10 days with medium of neural/endometrium at 1:1 ratio, containing 100 ng/ml NGF, at 37°C, 5% CO₂.

Flow cytometry

iPSCs (100 x 10³) were blocked for non-specific binding with 0.2 µg of polyglobin (Grifols) for 15 min at 4°C, then incubated with the antibodies against human SSEA-3-AF647, SSEA-4-AF647, TRA 1-60-PE, TRA 1-81-PE (all from BD Biosciences) for 15 min at 4°C. The cells were then washed twice in FACS buffer containing PBS supplemented with 0.1% bovine serum albumin (Sigma-Aldrich) and 0.0005% sodium azide (Sigma-Aldrich). The cells were further were incubated for 10 min at 4°C with 1:1000 dilution of 1mg/ml propidium iodide (PI) for the detection of dead cells. The cells were analyzed on a FACS Accuri flow cytometer analyzer (Becton Dickinson). The primary gating for selection of cells for analysis was done by selecting PI negative cells, which were further analyzed for the expression of the individual respective markers. The data acquired were analyzed using FlowJo software (FlowJo).

RNA extraction, reverse transcription, and quantitative RT-PCR

Harvested neural spheroids or cells were lysed in Trizol (ThermoFisher Scientific) and total RNA was isolated using an RNeasy Mini Kit (Qiagen). The RNA was reverse-transcribed with random primers and iScript™ cDNA Synthesis Kit (Invitrogen). Quantitative PCR was carried out using a Real-Time PCR System (Biorad) and iQ SYBR Green Supermix for qPCR

(Biorad). Relative mRNA expression levels were analyzed by the $\Delta\Delta\text{CT}$ method and normalized to GAPDH gene expression. Three replicates were used per condition. Detailed primer information is provided in table S1.

Electrophysiology

Membrane potential of iPSC neurons of ~40 days post-differentiation was recorded in current-clamp mode. Action potentials (AP) were elicited by application of 200 pA current for 5 ms at a cycle length of 1 s. All measurements were performed in the whole-cell configuration at physiological temperature (37°C). Cells were superfused with an extracellular solution containing: 145 mM NaCl, 5.4 mM KCl, 1 mM MgCl₂, 10 mM HEPES, 1.8 mM CaCl₂, 10 mM glucose, adjusted at pH 7.4 with NaOH. Borosilicate glass pipettes were pulled (DMZ Universal Puller) at a resistance of 1.5-2.5 MΩ when filled with an internal solution containing: 110 mM KCl, 15 mM NaCl, 0.2 mM EGTA-KOH, 0.1 mM CaCl₂, 10 mM HEPES-KOH, 5 mM ATPMg²⁺-salt, 10 mM glucose, adjusted at pH 7.2 with KOH. Membrane capacitance and series resistance were measured and compensated in every cell. Signals were acquired with an AxoPatch-1D amplifier (Axon Instrument), connected to a Digidata 1322A (Axon Instrument) and sampled at 1 KHz after low-pass filtering at 10 KHz. The final results were taken from an average of 11 measurements, display in table S2.

Quantification of substance P released from iPSCs-derived nociceptors after resiniferatoxin stimulation

Dissociated neurosphere cultures were prepared as described before and cultured for 10 days. Before changing the medium for the experiment, the cells were washed thoroughly with PBS. Then, 250 μl of control medium (normal neural medium), neural medium containing 100 nM resiniferatoxin (RTX) (Alomone Labs) or neural medium containing 100 mM potassium chloride (KCl) were added to the cultures. These were conditions incubated at 37°C, 5% CO₂ for 5 min with gentle agitation. The supernatant was collected from each condition and immediately stored at -80°C. To quantify the amount of substance P, we used the human substance P EIA kit (Phoenix PharmaceuticalsT, EK-061-05), and followed the manufacturer protocol. This experiment was performed once and five replicates per condition were used.

iPSCs-derived nociceptors morphology after resiniferatoxin and capsaizepine stimulation

Neurospheres were seeded on laminin-coated coverslips as described above and cultured for 7 days. After this period, the culture medium was changed to control medium (normal neural medium), neural medium containing 1% ethanol (EtOH, vehicle control), neural medium containing 10 μM RTX or neural medium containing 10 μM RTX and 100 μM capsaizepine (CPZ) (Sigma-Aldrich) (both with 1% EtOH). To evaluate the neurite morphology,

the initial 24 h of culture was tracked with brightfield microscopy and after this period the cells were fixed for subsequent immunostaining to β III-tubulin. At $t = 24$ h cell viability was also quantified with the PrestoBlue™ Cell Viability Reagent (Thermo Fisher Scientific). Minimum of five replicates were used per condition.

Brightfield microscopy for live cells

To capture micrographs of live cells, we used the Nikon Eclipse TI-E microscope with an Okolabs environmental control. For the tracking of neurite morphology during the RTX/CPZ experiment, we transferred the coverslips containing the cell cultures to a 35 mm petri dish (Ibidi) and added control medium or medium supplemented with the drugs. The images were acquired immediately, taking frames every 5 min for 24 h.

Hyperglycemia test

The PN platform (without fibrin embedding) composed of SCs and one neurosphere was fabricated as described above and cultured for 21 days to allow mature myelin formation. At that point the medium was changed to either control medium (normal neural medium), hyperglycemic medium composed of normal medium supplemented with 45 mM glucose (Sigma-Aldrich, G7021) or hyperglycemic medium plus 1 μ M epalrestat (Sigma-Aldrich, SML0527). Cultures were kept at 37°C, 5% CO₂ for additional 48 h and then fixed with 4% paraformaldehyde for 20 min at room temperature. Following this, the samples were prepared for immunostaining and TEM as described below. Five replicates were used per condition.

Immunocytochemistry and fluorescence microscopy

Samples were fixed with 4% paraformaldehyde (PFA) for 20 min at room temperature (RT), rinsed thoroughly with PBS, and left in PBS until further use. Samples were permeabilized for 30 min at RT with 0.1% Triton X-100 in PBS, followed by rinsing with PBS and blocking with blocking buffer composed of 5% goat serum, 0.05% Tween-20, and 1% bovine serum albumin (BSA) in PBS, overnight at 4°C, under mild agitation. Afterwards, samples were incubated overnight at 4°C with primary antibody solutions in blocking buffer. The next day, the samples were washed with a wash buffer composed of 0.05% Tween20 and 1% BSA in PBS and incubated for 2 h at RT with secondary antibody solutions in wash buffer. Following this, we rinsed the samples with PBS, stained with DAPI (0.2 μ g/ml) for 10 min at RT, and left them in PBS until imaging. The detailed list of used primary and secondary antibodies can be found in table S3 and S4 respectively. Images were acquired using either an inverted epifluorescence microscope (Nikon Eclipse Ti-e) or a confocal laser scanning microscope (Leica TCS SP8).

Transmission electron microscopy

Samples were prepared by fixation with 4% PFA in PBS, followed by washing with 0.1 M Cacodylate (3x for 15 min). Cells were fixed again with 2.5% glutaraldehyde in Cacodylate 0.1 M overnight (minimum of 1 h), followed by washing with 0.1 M Cacodylate (3x 15min), post-fixed with 1% Osmium tetroxide + 1.5% potassium hexacyanoferrate (II) trihydrate in Cacodylate 0.1 M, then washed again with 0.1 M Cacodylate 3x for 15 min. Then we proceeded to a dehydration series (70% for 30 min, 90% for 30 min and 2x 100% for 30 min), followed by propylenoxide 2x 30 min and Propylenoxide:Epon LX112 (1:1) overnight with stirring. Samples were covered with fresh epon LX112 7 h with stirring and embedded in beemcapsules with fresh epon 3 days at 60 °C. 60 nm sections were then cut with a diamond knife, stained with uranyl acetate and lead citrate and imaged with a TEM (FEI Tecnai G2 Spirit BioTWIN iCorr).

Image Analysis

3D image reconstructions and neurite/myelin volume measurements were processed with Amira (Thermo Fisher Scientific). All other images were prepared and analyzed using Fiji software (<https://fiji.sc/>). To quantify the different parameters of tissue morphology, we obtained and analyzed images of the whole sample. To measure the orientation degree of fibers, neurites and myelin, we used the OrientationJ plugin²² and applied the *Measure* function over circular ROIs that capture the whole tissue to obtain the coherence values (where 0 is full isotropy and 1 is full anisotropy). To measure the neurite length, we used the Simple Neurite Tracer plugin²³, and measured the distance between the cell bodies and the edge of the respective axons. Cell counts were performed using the standard *Analyze Particles* function to DAPI⁺ objects. To measure the axonal area, we first converted images of β III tubulin⁺ cells to binary images and measured the pixel area occupied by the neurites, excluding cell bodies. Then, we divided this value by the total area of the scaffold. For the myelination area, we measured the pixel area of MBP⁺ segments and divided this value by the area of the scaffold. G-ratio measurements were done using the G-ratio plugin (<http://gratio.efil.de/>)²⁴. Myelin decompaction analysis was carried by first measuring the area below the most outer ring and the most inner ring (expected myelin area). Then, the image was converted to binary image and the same areas were determined (actual myelin area). To determine the decompaction area we used the following formula: $(1 - (\text{expected myelin area} / \text{actual myelin area})) \times 100$. For all experiments we used at least 5 biological replicates per condition. For the tissue morphological analysis (neurite alignment, axonal area and myelin area) we imaged and analyzed the whole sample. For neurite length quantification we took at least 15 measurements per sample. For myelin morphometric analysis (g-ratio and myelin decompaction) we took at least 5 measurements per sample.

Statistical Analysis

The graphs were built and the data was analyzed using the software GraphPad Prism. Bar graphs are shown as mean \pm SD and boxplots represent data point between the minimal and maximal value. Statistical significances were determined employing an unpaired t-test, one-way or two-way analysis of variance (ANOVA) followed by a Tukey's honestly significant difference (HSD) post-hoc test (* $p < 0.05$, ** $p < 0.01$, *** $p < 0.005$, **** $p < 0.0001$ and ns is $p > 0.05$).

Illustrations

Illustrations were designed with either Adobe Illustrator CC 2018 (Adobe), SolidWorks (Dassault Systèmes) or with biorender (<https://biorender.com/>).

Results

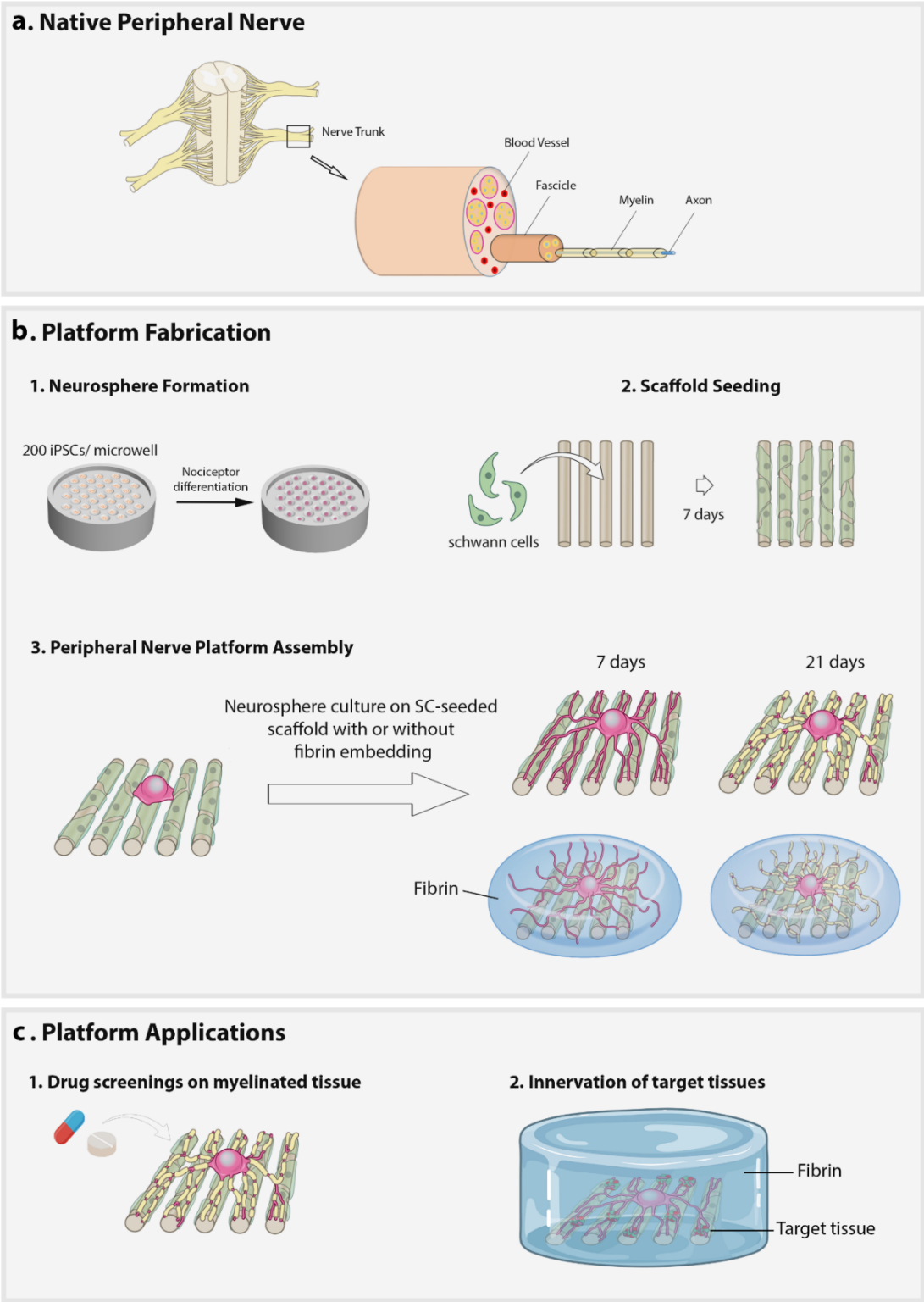


Figure 1. Illustration of the fabrication steps for our PN *in vitro* platform and its applications. A) Illustration of a native PN depicting its hierarchical organisation and the presence of organised bundles with myelinated axons. B) Platform fabrication steps: 1) iPSCs differentiation into trunk neural crest cells and neurosphere formation (~ 200 cells per sphere); 2) Scaffold seeding with

primary rat SCs (100×10^3 cells) and formation of aligned SC bands after 7 days of culture; 3) 3D PN platform assembly by neurosphere placement into the SC-seeded scaffold and co-culture for 7 or 21 days. Fibrin hydrogel embedding permits 3D neural growth. C) Nerve platform applications: 1) Drug screening on mature myelinated tissue, under normal or pathological conditions; 2) Incorporation of target tissues to investigate nerve/target interactions.

Generation of human nociceptor neurospheres from iPSCs

To generate human nociceptor neurospheres we followed a two-step process detailed in Fig. 2a. First, human iPSCs displaying a pluripotency phenotype (Fig. S1) were seeded on a 400 μm agarose microwell mold (200 cells/microwell; 1580 microwells) and the cells synchronized via DMSO treatment for 3 days. We then followed a differentiation protocol adapted from Chambers et al.¹⁹, in which human iPSCs were driven towards nociceptors, via a neural crest intermediate, in a quick and efficient manner. At day 2, and for 5 days, retinoic acid was supplemented together with CHIR99021 to promote cell aggregation. Retinoic acid supplementation is essential for the integrity of the spheroids, as its absence leads to poorly formed and loose clusters (Fig. S2b). At day 7, cells reached the neural crest stage denoted by the presence of SOX10⁺ cells (Fig. S2a). To distinguish between cranial and trunk neural crest cells, we immunostained cells for ETS1, a cranial marker, and Phox2B, a trunk marker²⁵. As shown in Fig. 2b, most cells were Phox2B⁺ rather than ETS1⁺, evidencing commitment to the trunk phenotype. To confirm this, we also analysed gene expression at different time points (Fig. 2c). At day 2, the expression of both markers was null. After 3 days, cells displayed a robust expression of ETS1, while Phox2B expression was still null. However, after 4 days of differentiation, we observed an inversion in marker expression, as cells exhibited an upregulation of Phox2B and downregulation of ETS1. Finally, at day 7 cells expressed only Phox2B, while ETS1 expression was null. At day 7 and for 2 days, we inhibited the notch signalling pathway through DAPT and SU5402 supplementation. At this stage, multiple uniform and cohesive spheroids (Fig. 2d and Fig. S2c) with an average diameter of $308.7 \pm 38.6 \mu\text{m}$ were achieved. For the second part of the process (at day 9 of differentiation), the neurospheres were harvested from the mold, seeded in a substrate of choice, and cultured with NGF-containing medium for at least 7 days, to finalize the nociceptor differentiation protocol, whilst growing neurites *in situ*. To validate the acquisition of a nociceptor phenotype, we cultured the neurospheres on laminin-coated coverslips for 7 days and immunostained for the nociceptor-specific markers —substance P, CGRP and TRPV-1— and for the sensory neuron transcription factor —BRN3A. As shown in Fig. 2e, all markers were expressed within grown neurons and located either along the length of the axons (substance P, CGRP and TRPV-1 correlated with β III-tubulin) or in the nucleus (BRN3A correlated with DAPI). In sum,

we were able to generate a large number of even-sized nociceptor neurospheres in simple and quick manner.

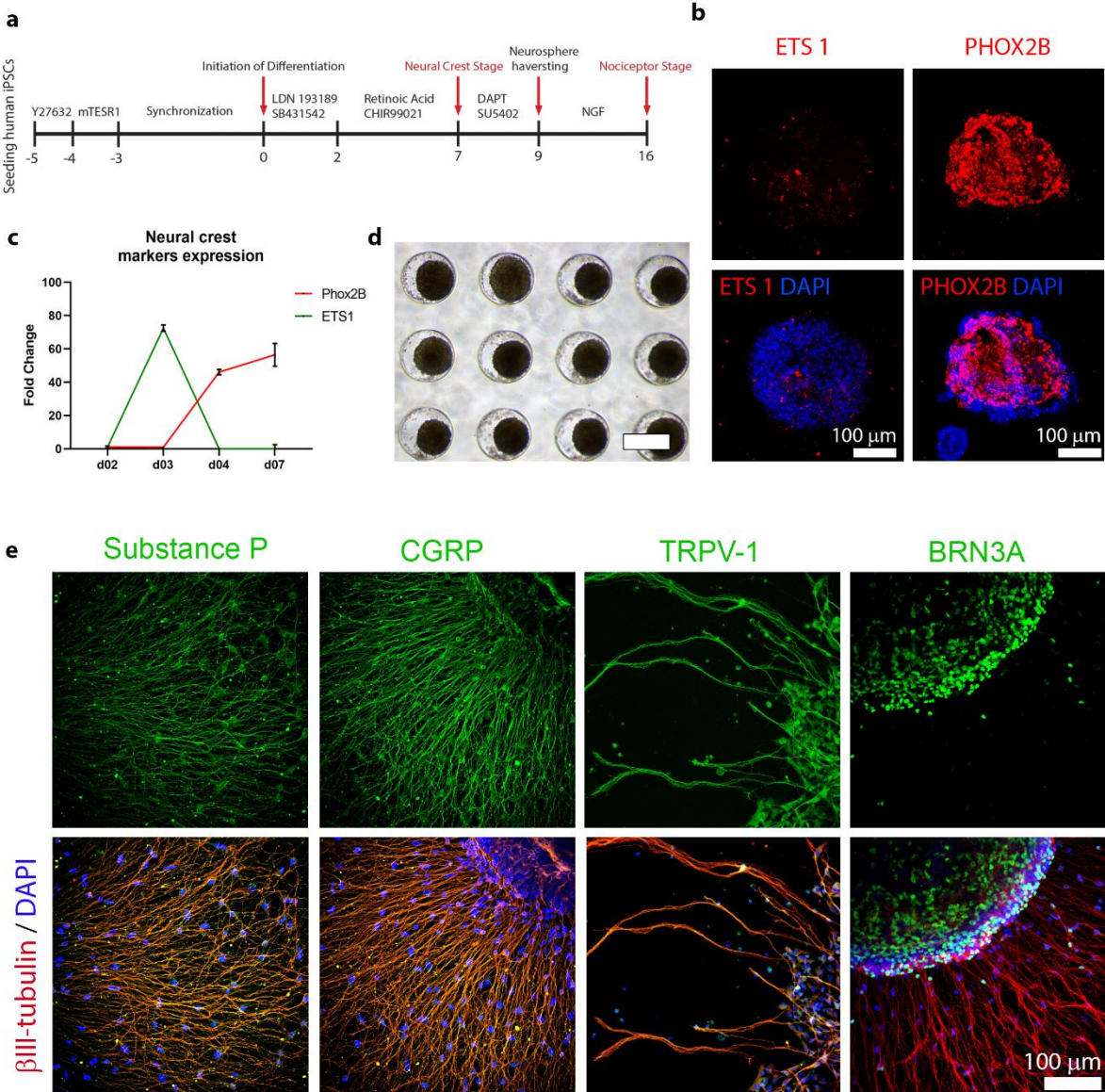


Figure 2. Differentiation process of iPSCs into nociceptor neurons. A) Timeline of the protocol used to generate nociceptor spheroids from iPSCs cells. B) Immunostaining of ETS1 (cranial marker; in red) or Phox2B (trunk marker; in red) on neural crest clusters (DAPI is shown in blue). C) Gene expression kinetics determined by quantitative RT-PCR analysis. Relative gene expression levels of transcripts to GAPDH expression at the indicated day point of differentiation of neural crest markers ETS1 (cranial) and Phox2B (trunk) (n = 3). D) Brightfield micrograph of agarose microwells containing round and uniformly sized clusters with $308.7 \pm 38.6 \mu\text{m}$ of diameter (scale bar is 400 μm). E) Immunostaining to sensory neuron markers (in green) — substance P, CGRP, TRPV-1 and BRN3A — shows the successful differentiation of

iPSCs into nociceptor neurons. Images are from neurospheres cultured for 7 days on laminin-coated coverslips. β III-tubulin is shown in red and DAPI in blue.

Neuron function testing on nociceptor neurospheres

Nociceptor neurospheres were either dissociated to single cells (Fig. 3a-c) or kept intact (Fig. 3d-g) in order to validate neuron function, i.e., electrical excitability, and nociceptor function in particular, i.e., responsiveness to noxious stimuli. Whole-cell patch clamp measurements from dissociated neurospheres showed a mean membrane capacitance of 16.2 ± 4.2 pF, a mean resting membrane potential (RMP) of -44.1 ± 7.1 mV. All probed neurons ($n = 11$) were excitable and able to fire APs with a mean AP amplitude of 67.4 ± 26.2 mV and an overshoot peak of 23.3 ± 28.5 mV ($n = 8$) (Fig. 3b). To probe sensitivity to noxious stimuli, we measured the secretion of substance P after stimulation with RTX, a TRPV-1 agonist and analog of capsaicin²⁶. As exhibited in Fig. 3c, RTX exposure led to an immediate release of substance P from the nociceptor population. Specifically, RTX-stimulated neurons displayed a 2.12-fold increase of released substance P per DNA ($p < 0.05$) compared to unstimulated neurons. KCl-depolarized neurons showed an increment of 1.6 times compared to RTX-stimulated neurons ($p < 0.01$) and 3.8 times compared to unstimulated cells ($p < 0.0001$). Literature reports have shown that capsaicin exposure can lead to nerve fiber retraction and local denervation, after topical application of capsaicin on the skin²⁷. Because of this, we explored if RTX exposure would lead to neurite retraction and if that effect could be mitigated by blocking the TRPV-1 channel with the antagonist capsazepine (CPZ)²⁶. To this end, the neurite morphology of nociceptor neurospheres was monitored for 24 h after the application of RTX alone or with RTX together with CPZ and compared with unstimulated cells or cells stimulated with vehicle medium (neural medium with 1% EtOH). As visible in Fig. 3d, the neurites of neurospheres stimulated with vehicle (Fig. 3d left column and movie S1) or RTX plus CPZ (Fig. 3d right column and movie S3) remained unaffected and showed little movement, except for the natural movement of live neurons. Contrarily, when stimulated with RTX only (Fig. 3d middle column and movie S2), we could observe an immediate neurite retraction (first 15 m), followed by a lag period and neurite regrowth. As a consequence, after 24 h of culture in these conditions, neurites of RTX-stimulated neurospheres were significantly shorter than untreated cultures ($p < 0.001$), vehicle control ($p < 0.01$) and RTX/CPZ-stimulated neurospheres ($p < 0.05$) (Fig. 3d and 3f). Notably, neurite length in vehicle control samples and RTX/CPZ-stimulated neurospheres was not significantly different ($p > 0.05$) than untreated cultures. Finally, we also measured cell metabolic activity after 24 h of culture under these conditions and observed that there was no significant difference ($p > 0.05$) among them, evidencing that despite neurite retraction, the neurons remain viable after RTX exposure (Fig. 3g). In sum, the differentiated nociceptors were electrically active and could sense and react

to noxious stimuli.

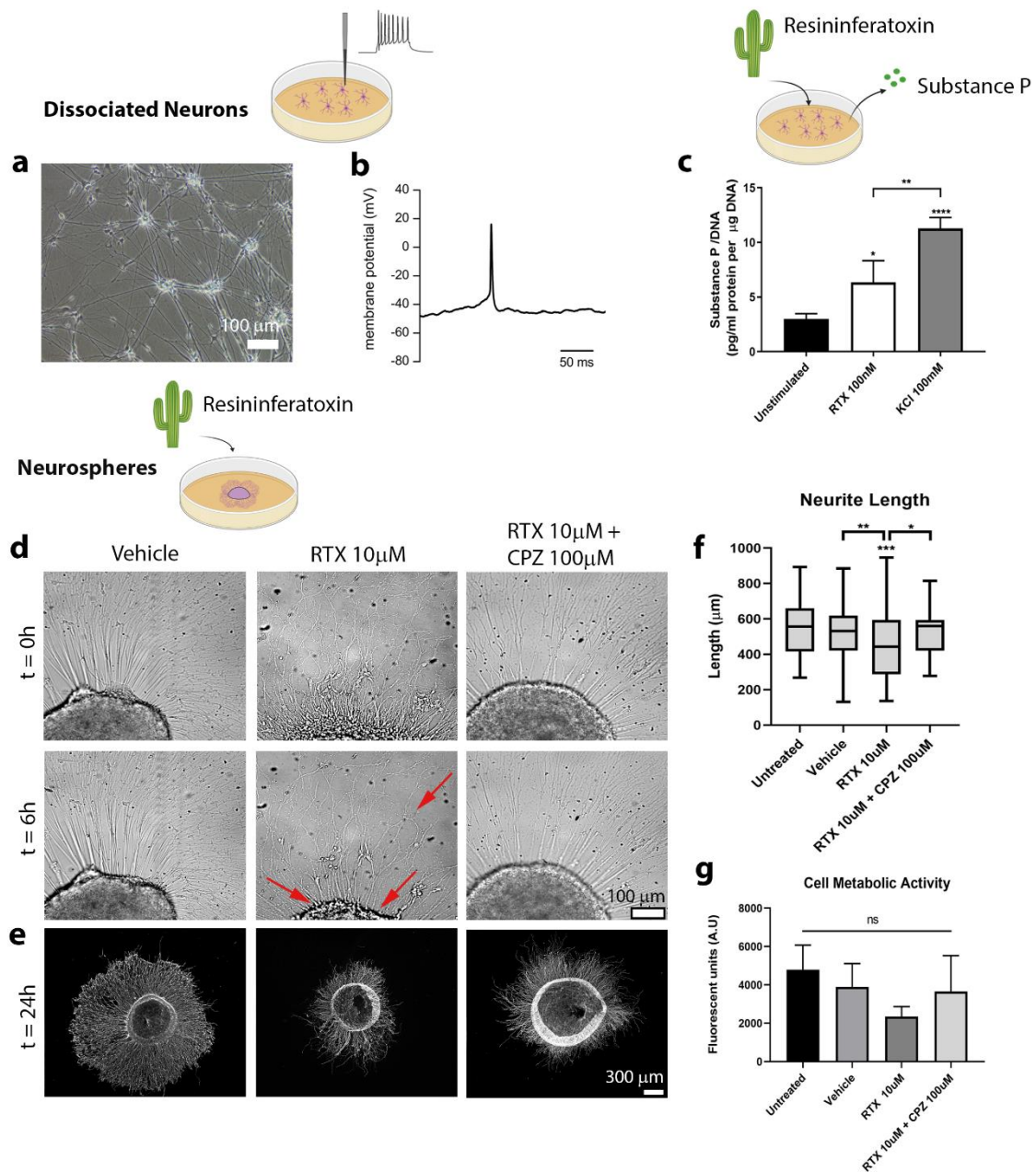


Figure 3. Neuron function tests on iPSCs-derived nociceptors. Top panel (A-C): tests on dissociated neurons. Bottom panel (D-G): tests on neurospheres. A) Brightfield micrograph of ~40 days old dissociated neurons. B) Representative action potential recorded from the neurons in response to 200 pA current injection for 5 ms. The mean RMP was -44.1 mV and the mean overshoot was 23.3 mV. C) Release of substance P in response to a noxious stimulus (resiniferatoxin, RTX; white bars) from 10-day old nociceptors. Untreated cells (black bars) and KCl-stimulated cells (gray bars) were used as controls. Graphical representation of the released substance P (in pg) relative to DNA amount (in µg). D-E: stimulation of nociceptor neurospheres with RTX 10 µM or RTX 10 µM plus CPZ 100 µM. Untreated (normal neural

medium) or vehicle (neural medium with 1% EtOH) were used as controls. D) Live cell brightfield frames at $t = 0$ h or $t = 6$ h. The red arrows point to areas where neurite retraction overtime is visible (scale bar is $100\ \mu\text{m}$). E) Immunostaining to β III-tubulin of samples fixed 24 h after drug exposure. F) Corresponding neurite length measurements (15 measurements per sample) and G) Cell metabolic activity (in arbitrary units) of samples 24 h after drug exposure. For D) and E) note that untreated cultures are not shown. All experiments were performed once and a minimum of 5 replicates were used per condition. The boxplots in F) represent data points from the minimum to maximum value. All graph bars are represented as mean value \pm SD and the statistics were performed with one-way ANOVA followed by a Tukey's HSD post-hoc test, where **** $p < 0.0001$, *** $p < 0.001$, ** $p < 0.01$, * $p < 0.05$ and ns denotes $p > 0.05$.

Fabrication of 2D PN platform:

7 days culture

After characterization of nociceptor functionality, we developed a 3D biomimetic PN platform composed of a neurosphere/SCs co-culture on an aligned microfibrinous scaffold (Fig. S3a). The scaffold is composed of aligned microfibers with an average diameter of $1.37 \pm 0.20\ \mu\text{m}$ and coherence (alignment degree) of 0.74 ± 0.04 . To investigate the impact of the scaffold, we also cultured cells on glass coverslips and evaluated the performance of both substrates after 7 days of culture (Fig. 1b2). The scaffold fibers generated aligned and elongated bands of SCs, in stark contrast to the flattened and isotropic morphology of SCs cultured on glass coverslips (Fig. S3b).

Neurospheres at day 9 of differentiation were placed on SC pre-cultured scaffolds/coverslips (one neurosphere per substrate) to establish the co-culture system. The effect of exogenous SCs on neurite growth and morphology was compared to coverslips/scaffolds that were uncoated, laminin-coated or matrigel-coated (Fig. 4). Uncoated coverslips did not even permit neurosphere attachment, while uncoated scaffolds allowed both neuron attachment and neurite outgrowth. This growth was however significantly shorter than all scaffolds with any form of coating ($p < 0.0001$) (Fig. S4a). When coverslips were pre-coated with laminin, matrigel or SCs, the neurospheres could attach and grow neurites (Fig. 4a, left column). The neurosphere morphology depended on the coverslips coating, as the cluster remained intact when coated with laminin (Fig. 4a top left image) or seeded with SCs (Fig. 4a bottom left image), but not when coated with Matrigel (Fig. 4a middle left image). In the latter, neurons dissociated from the cluster, proliferated and migrated outwards. As a result, we could not measure the axonal area, due to an unclear contrast between cell bodies and neurites. For the other two conditions, neurites were clearly emanating from the neurosphere and covered a total area of $3.6 \pm 2.4\%$ (laminin coating) or $3.4 \pm 1.4\%$ (SC seeding), not significantly different

($p > 0.05$) compared to uncoated scaffolds ($2.4 \pm 1.0\%$). When comparing neurite length, only coverslips with SCs were significantly higher compared to all other conditions ($p < 0.0001$) showing a mean length of $644.7 \pm 258.2 \mu\text{m}$ (Fig. 4B). Regarding neurite alignment (Fig. 4c), coherence measurements indicated isotropic growth for all conditions with no significant differences between substrates.

By comparison, neurospheres cultured on scaffolds showed significantly increased ($p < 0.0001$) neurite length and overall neurite alignment compared to coverslips with equivalent coatings (Fig. 4b and 4c). Scaffolds coated with Matrigel exhibited the longest neurite length ($3071.0 \pm 1568.0 \mu\text{m}$) and highest coherence value (0.58 ± 0.09). SC-seeded scaffolds performed better than no coating or Laminin-coated scaffolds, showing a mean neurite length of $1612.0 \pm 491.0 \mu\text{m}$ compared to $544.3 \pm 189.3 \mu\text{m}$ for no coating and $966.1 \pm 378.2 \mu\text{m}$ for laminin and an alignment of 0.38 ± 0.06 in contrast with 0.20 ± 0.05 for no coating and 0.38 ± 0.12 for laminin; interestingly, scaffolds with no coating showed a statistically similar neurite length compared to growth on a SC-coated coverslip ($p > 0.05$), indicating that the lowest performing scaffold is equivalent to the optimal coverslip condition after 7 days of culture. Regarding axonal area, a Matrigel coating led to a significantly larger scaffold coverage ($13.3 \pm 6.4\%$; $p < 0.001$) compared to laminin or SCs ($3.4 \pm 1.9\%$ and $3.9 \pm 2.4\%$, respectively), which was similar to coverslips. Scaffolds with no coating, resulted in a neurite area of 2.4% , the lowest value from all scaffold conditions.

SCs that were pre-seeded on either scaffolds or coverslips achieved an intimate association with neurites, although with clear differences regarding overall tissue organization (Fig. S3c). In coverslips (Fig. S3c top images), neurite projection was radial, isotropic and disorganised. Moreover, SCs tended to migrate towards the neurosphere, grouping around it in high density. In contrast, SCs seeded on scaffolds maintained their aligned morphology (Fig. S3c bottom images) and neurites appeared to follow the directional cues provided by the fiber topography and aligned SCs, leading to an organised and anisotropic pattern. In sum, scaffolds preserved the neuron clustering and promoted longer and more aligned neurite outgrowth compared to coverslips.

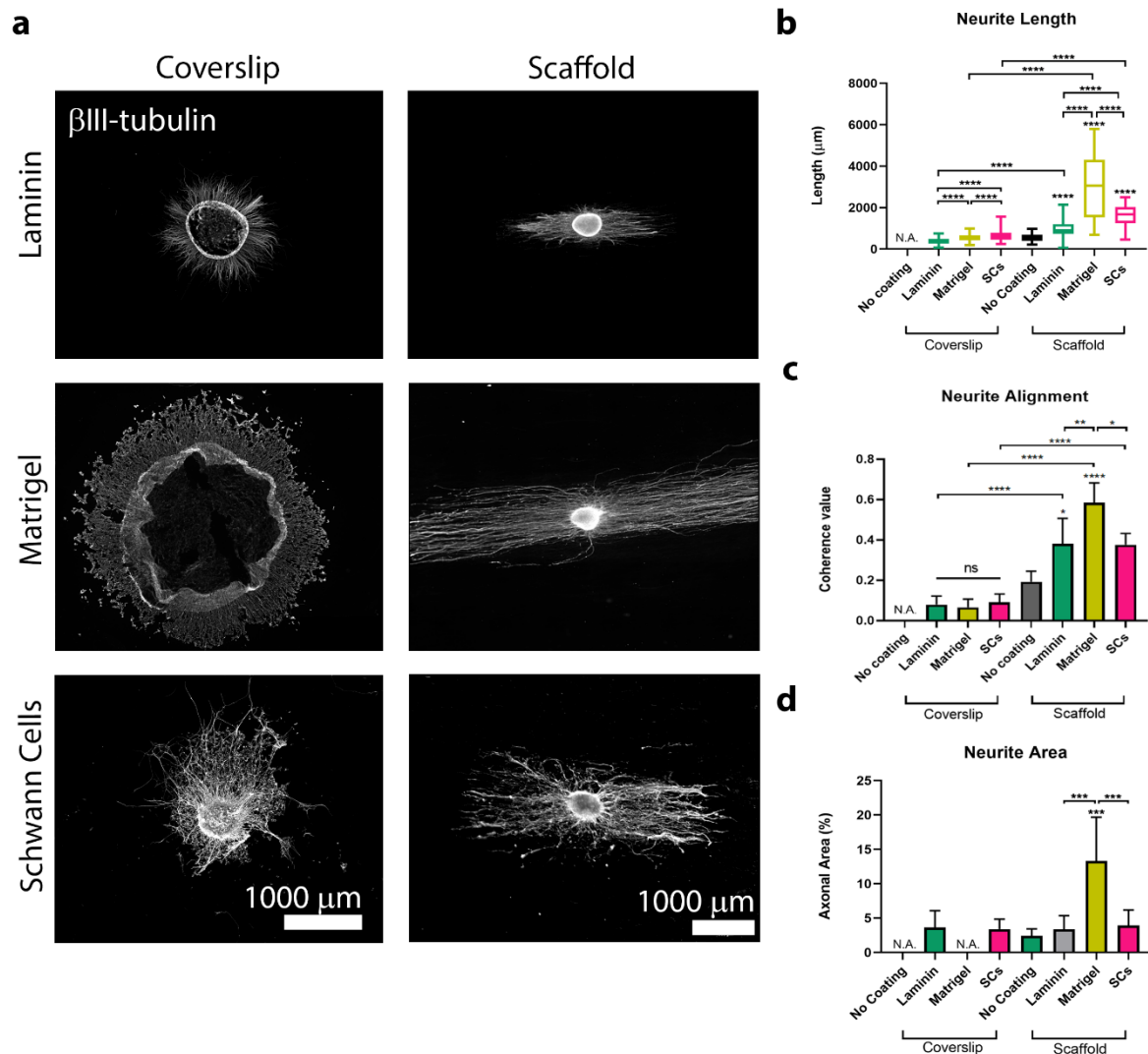


Figure 4. Characterization of neurosphere morphology in coverslips or scaffolds, with different coatings, after 7 days culture. A) Immunostaining to β III-tubulin showing the overall axonal growth on coverslips (left column) or scaffolds (right column) coated with laminin (top row), matrigel (1:100 in DMEM; middle row) or SCs (bottom row). Quantification of B) neurite length (in μm) (at least 15 measurements per sample), C) neurite alignment (0 is full isotropy and 1 is full anisotropy) and D) neurite area (% of total area). The boxplots represent data points between the minimum and maximum values. The graphs bars represent mean value \pm SD. In all experiments, a minimum of 5 replicates were used per condition, and the experiments were performed twice. Statistics were performed with two-way ANOVA followed by a Tukey's HSD post-hoc test, where **** $p < 0.0001$, *** $p < 0.001$, ** $p < 0.01$, ns denotes $p > 0.05$. N.A. means not applicable. On the scaffold group, the stars with no associated bar represent comparisons with the no coating condition.

21 days culture

After 21 days of culture, both neurite length and area increased compared to day 7. In coverslips cultures, SCs gradually led to neurosphere dissociation, similarly to the Matrigel-coated coverslips, resulting in a neural network of multiple interconnected clusters; this hampered further axonal area quantification for both conditions. Only the laminin-coated coverslip preserved neurosphere integrity (Fig. 5a left column), with a neurite area of $12.4 \pm 7.1\%$ (Fig. 5d) and the longest neurite growth (mean length of $1335.8 \pm 772.8 \mu\text{m}$) of all coverslip conditions (Fig. 5b). From day 7 to day 21 (Fig. S5), we detected a 3.5-fold increase in growth for the laminin condition, whereas Matrigel condition only imparted a 1.15-fold increase and the SCs condition registered a 0.69-fold decrease. This suggests that the maintenance of the neurosphere integrity is beneficial for enhanced neurite outgrowth, as cluster dissociation leads to the formation of a network with reduced outgrowth. Despite differences in growth, there was a generalized lack of preferred orientation with no differences in neurite alignment among conditions (Fig. 5c).

All scaffold cultures, including uncoated scaffolds, exhibited an increase in length and axonal area compared to the earlier time point (Fig. 5a right column, Fig. S4b and Fig. S5). In terms of neurite length this temporal increment corresponded to 1.61 times for uncoated, 2.2 times for laminin, 1.25 times for Matrigel and 1.9 times for SCs samples (Fig. S5). Compared to coverslips cultures, the neurite length (Fig. 5b) was significantly enhanced ($p < 0.0001$) in all scaffold conditions. Matrigel-coated scaffolds promoted again the largest neurite extension, with a mean length of $3858.4 \pm 1083.0 \mu\text{m}$ and area of $38.9 \pm 14.6\%$, followed by SC-seeded scaffolds with a mean length of $3076.5 \pm 995.8 \mu\text{m}$ and area of $18.95 \pm 5.2\%$, then laminin-coated scaffolds with a mean length of $2130.1 \pm 619.4 \mu\text{m}$ and area of $16.21 \pm 5.3\%$ and finally uncoated scaffolds with a mean length of $878.1 \pm 292.3 \mu\text{m}$ and area of $4.16 \pm 1.16\%$ (Fig. 4b and 4c).

In the early stages (up to 7 days), SCs promote a more accelerated neurite outgrowth compared to laminin coatings, but this growth tends to slow down as SCs begin to myelinate axons. Since myelination results in thicker and straighter segments²⁸ (Fig. 6a and Fig. S6), this hypothetically explains why we detected the highest neurite alignment for SC-seeded scaffolds (0.44 ± 0.16) (Fig 5a). All scaffold conditions at 21 days *in vitro* (DIV) led to increased ($p < 0.05$) alignment compared to similarly coated coverslips.

For both coverslips and scaffolds, myelination was observed by day 21 as an abundance of MBP⁺ segments that spatially correlated with β III-tubulin⁺ structures (Fig 6). In coverslips, the myelin was disorganised, randomly oriented and partially overlapping (Fig. 6a, Fig. S6a and Fig. S6b). These myelinated cultures were mechanical unstable, attributed to the high lipid content that results in poor surface attachment (data not shown). On the other hand, co-cultures in scaffolds resulted in long, straight and anisotropic myelin bundles (Fig. 6a bottom

image), with overall great mechanical stability. The presence of other mature myelin proteins, such as myelin protein zero (P0) was also detected (Fig. S6c).

Quantification of myelin formation and morphology revealed that scaffolds had a larger myelin area ($62.2 \pm 19.73\%$ versus $28.78 \pm 21.34\%$ in coverslips; Fig. 6c) and improved myelin alignment (0.25 ± 0.09 versus 0.07 ± 0.05 in coverslips; Fig. 6d). Further in-depth TEM analysis of a scaffold cross-section (Fig. 6e) detected the presence of several compacted myelin layers, with an average thickness of 89.1 ± 17.6 nm.

In brief, scaffolds promoted a continuous neural growth and long-term stability of the cluster, as well as longer and more aligned neurites than coverslips. Myelination was also enhanced and more anisotropic in scaffold co-cultures.

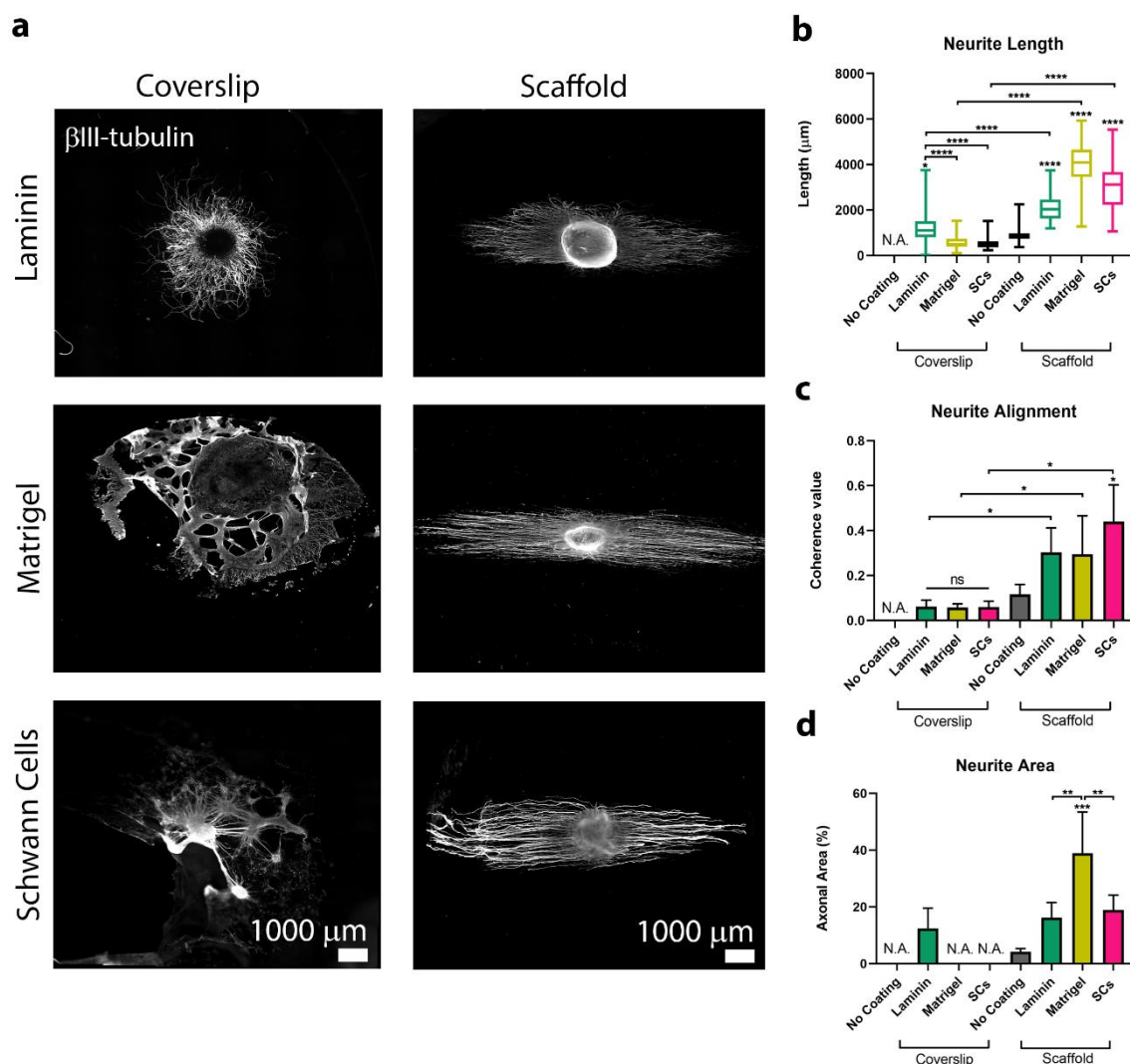


Figure 5. Characterization of neurosphere morphology in coverslips or scaffolds, with different coatings, after 21 days culture. A) Immunostaining to β III-tubulin showing the overall axonal growth on coverslips (left column) or scaffolds (right column) coated with laminin (top row), Matrigel (1:100 in DMEM; middle row) or SCs (bottom row). Quantification of B) neurite length (in μ m) (at least 15 measurements per sample), C) neurite alignment (0 is full isotropy and 1

is full anisotropy) and D) neurite area (% of total area). The boxplots represent data points between the minimum and maximum values. The graphs bars represent mean value \pm SD. In all experiments, a minimum of 5 replicates were used per condition, and the experiments were performed twice. Statistics were performed with two-way ANOVA followed by a Tukey's HSD post-hoc test, where **** $p < 0.0001$, *** $p < 0.001$, ** $p < 0.01$, ns denotes $p > 0.05$. N.A. means not applicable. On the scaffold group, the stars with no associated bar represent comparisons with the no coating condition.

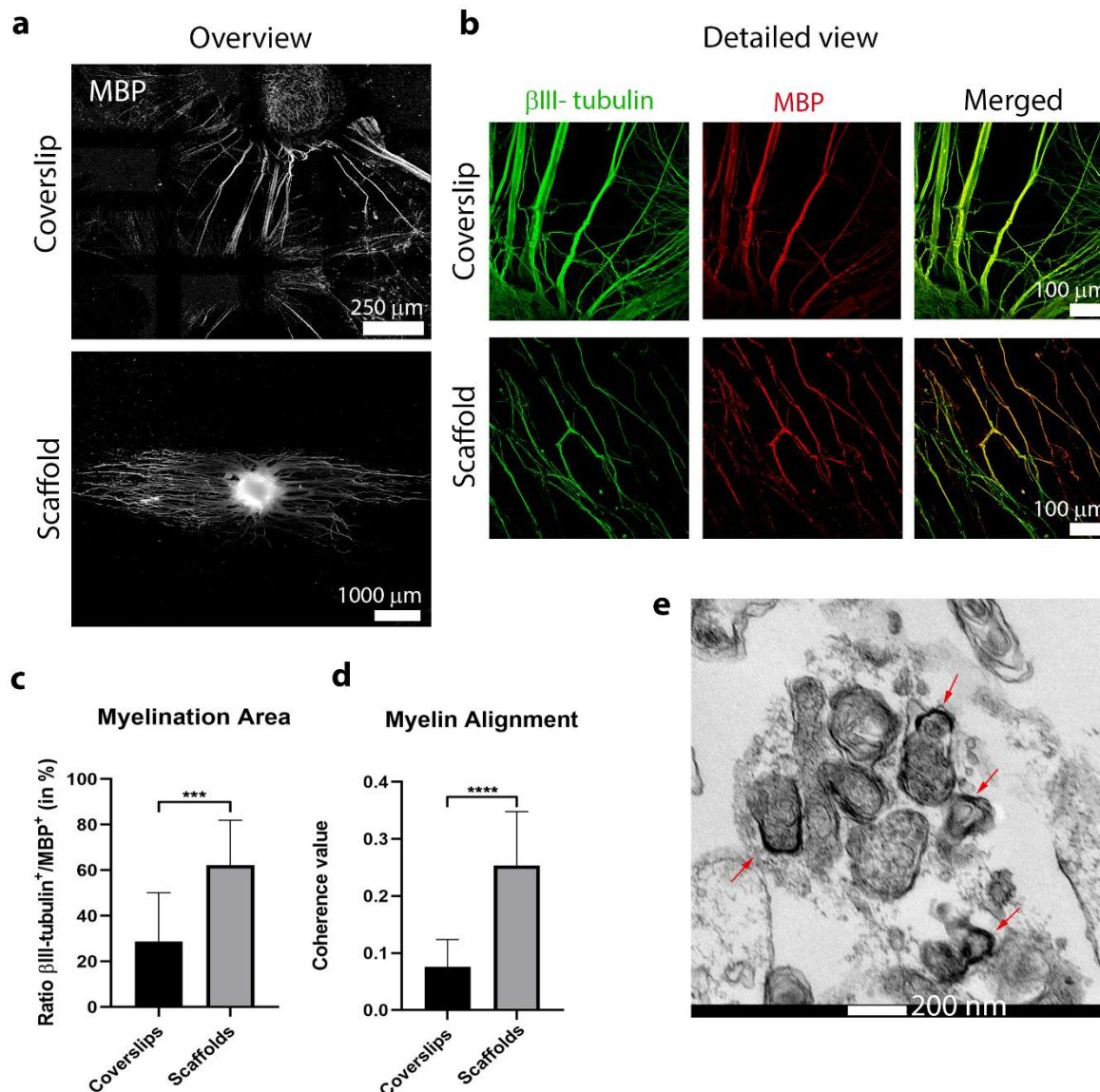


Figure 6. Myelin visualization and quantification of neurosphere/SCs co-cultures on coverslips or scaffolds for 21 days. A) Overview of myelin segments (marked by MBP in gray) on coverslips (top) and scaffolds (bottom). B) Detailed view of myelin segments from coverslips (top row) or scaffold cultures (bottom row), showing the co-localization of neurites (left column; β III-tubulin staining in green) and myelin (middle column; MBP in red). C) Myelination area (% of total area). D) Myelin alignment (coherence value). E) Transmission electron micrograph showing myelin segments (red arrows).

of β III-tubulin⁺ area /MBP⁺ area). D) Myelin alignment (0 is full isotropy and 1 is full anisotropy). Both graph bars show the mean value \pm SD. E) TEM micrograph of a myelin cross section, from a 21-day old scaffold co-culture, depicting compact and thick myelin layers (average thickness is 89.1 ± 17.6 nm). The red arrows point to spots where the presence of compact myelin is visible. Scale bar is 200 nm. These experiments were performed twice (n = 5). For imaging analysis, we took at least 5 images per sample. Statistics were performed with an unpaired t-test, where ****p < 0.0001 and ***p < 0.001.

Hyperglycemia model and drug testing

After establishing the myelinated co-culture scaffold platform, we investigated hyperglycemia-induced damage on myelin and evaluated the mitigating effect of epalrestat, an aldose reductase inhibitor²⁹ (Fig. 7a). After 21 days of co-culture, the cells were cultured for 48 h in just hyperglycemia (45 mM glucose) or hyperglycemia plus epalrestat (glucose at 45 mM plus epalrestat at 1 μ M); normal neural medium was used as control. As shown in Fig. 7b, control cultures (left column) and those supplemented with epalrestat (right column) appeared normal, with no significant damage. Contrarily, hyperglycemia cultures (middle column) showed signs of myelin disruption, particularly visible by MBP immunostaining (in red). TEM micrographs of control cultures (Fig. 7c left image) revealed compact myelin layers with no particular irregularities. In hyperglycemia cultures (Fig. 7c middle image), it was particularly evident that myelin layers separated from each other, exhibiting a decompacted structure. Finally, myelin morphology in hyperglycemia with added epalrestat condition (Fig. 7c right image) resembled control cultures, with most layers well compacted and with no signs of abnormalities. TEM images were quantified according to g-ratio, a standard parameter, and myelin decompaction percentage, based on an established algorithm³⁰. G-ratio measurements showed that both control and glucose plus epalrestat groups produced similar results, with a g-ratio value of 0.66 and 0.63, respectively (Fig. 7d). The glucose-only group produced a lower value of 0.46 ($p < 0.0001$), due to myelin layer decompaction. This was reflected in the myelin decompaction measurements, where the control group had the lowest decompaction (8.4%), the hyperglycemic condition had the highest decompaction (22.2%), and the condition of hyperglycemia with epalrestat registered decompaction value (13.8%) that was equivalent to control and significantly lower than hyperglycemia alone ($p < 0.05$).

In sum, hyperglycemia induce myelin damage, evidenced by layer decompaction, which could be mitigated with epalrestat supplementation.

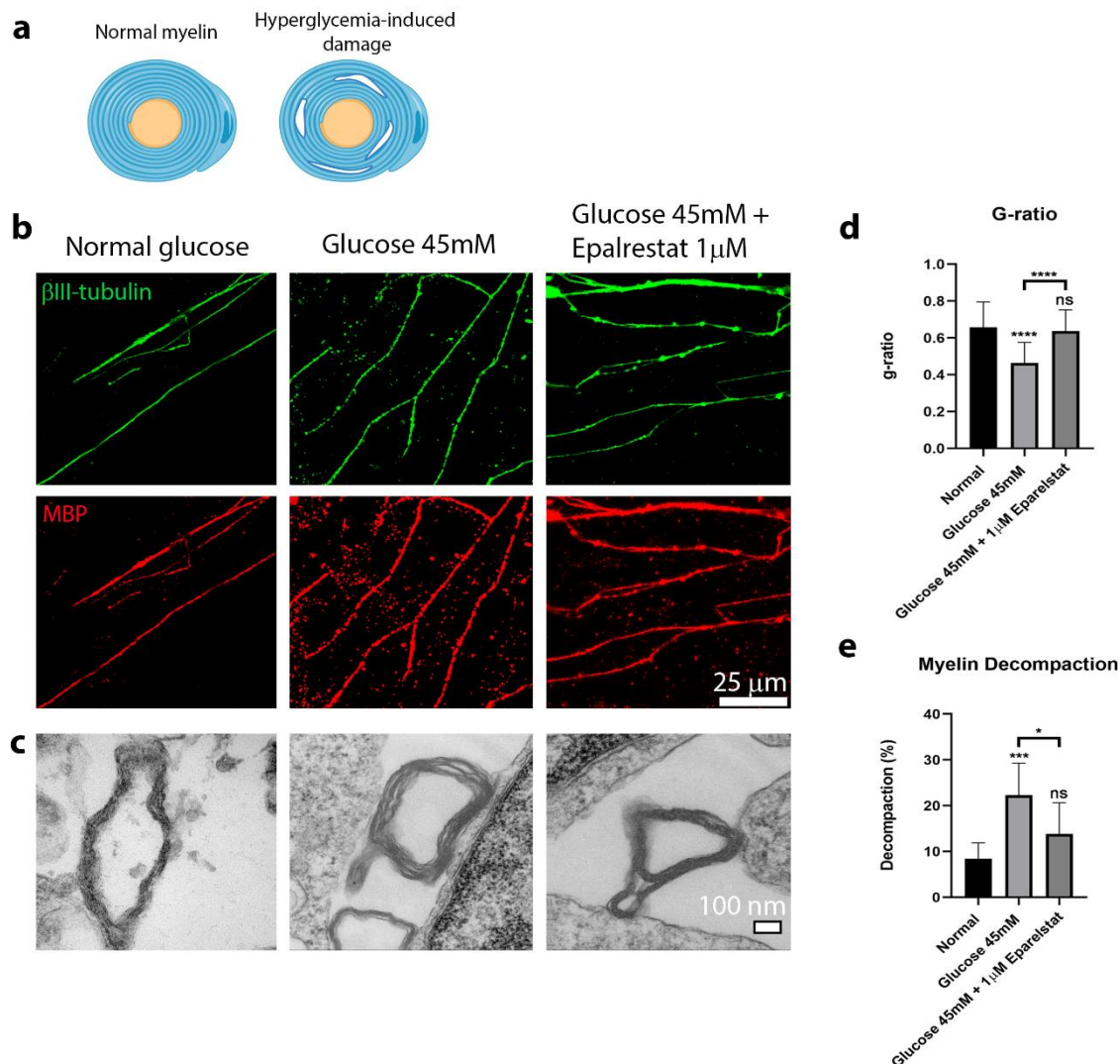


Figure 7. Hyperglycemia-induced damage and epalrestat prevention, on 21-day scaffold co-cultures. A) Illustration of the myelin morphology in normal (left image) or hyperglycemic (right image) state, where aberrations such as layer decompaction are present. At day 21, co-cultures were treated for 48 h with glucose (45 mM) (middle column) or glucose (45 mM) + epalrestat (1 μ M) (right column) within neural medium. Untreated cells (normal medium) were used as control. B) Immunostaining for β III-tubulin (green, top row) and MBP (red, bottom row) shows that exposure of myelinated cultures to high glucose concentrations leads to myelin damage. However, when epalrestat is supplemented, myelin disruption can be mitigated. C) TEM micrographs of myelin cross sections, evidencing myelin layers decompaction and abnormalities in hyperglycemic conditions. In normal conditions or hyperglycemic conditions containing epalrestat, myelin appears normal. D) G-ratio and E) myelin decompaction measurements from TEM micrographs, shown as mean value \pm SD. Experiments were performed twice ($n = 4$). Statistics were obtained with one-way ANOVA followed by a Tukey's HSD post-hoc test, where **** $p < 0.0001$, *** $p < 0.001$, * $p < 0.05$ and ns means $p > 0.05$.

Development of a large PN biomimetic platform

To develop a more representative model that better emulates the 3D hierarchical microarchitecture of a PN, scaffolds containing neural and glial tissue were embedded in a fibrin hydrogel. In the 3D image reconstructions shown in Fig. 8a, scaffolds with no hydrogel generated an anisotropic and planar neurite growth (Fig. 8a left column) with only a small volume increase from day 7 to day 21, from $0.0025 \mu\text{m}^3$ to $0.0039 \mu\text{m}^3$, respectively (Fig. 8b). When co-cultures were supplemented with fibrin, neurite growth maintained directional alignment (similar to all conditions and time points, Fig. S7) but was notably multiplanar (Fig. 8a right column), with still a small increase overtime but comparatively larger than bare scaffolds at both 7 DIV (~3 fold; $0.0078 \mu\text{m}^3$) and 21 DIV (~2 fold; $0.0094 \mu\text{m}^3$) (Fig. 8b and movie S4). Fibrin embedding also promoted a significant increase ($p < 0.001$) of myelin volume at day 21 compared to scaffold-only co-cultures (Fig. 8c), with a mean myelin volume of $0.0012 \mu\text{m}^3$ versus $0.00046 \mu\text{m}^3$, respectively. This was also reflected in histological cross-sections (Fig. 8d), which showed a larger number of myelin rings in fibrin-scaffolds than in bare scaffolds.

To showcase the long-term development and stability of this fibrin-embedded platform, we maintained the co-cultures for 35 days and evaluated the resulting tissue morphology. The engineered neural tissue retained its 3D organisation and exhibited highly aligned myelinated axons that achieved over 6.5 mm in length in all growth planes (Fig. 8e, 8f), which is the largest reported value in literature, to the best of our knowledge.

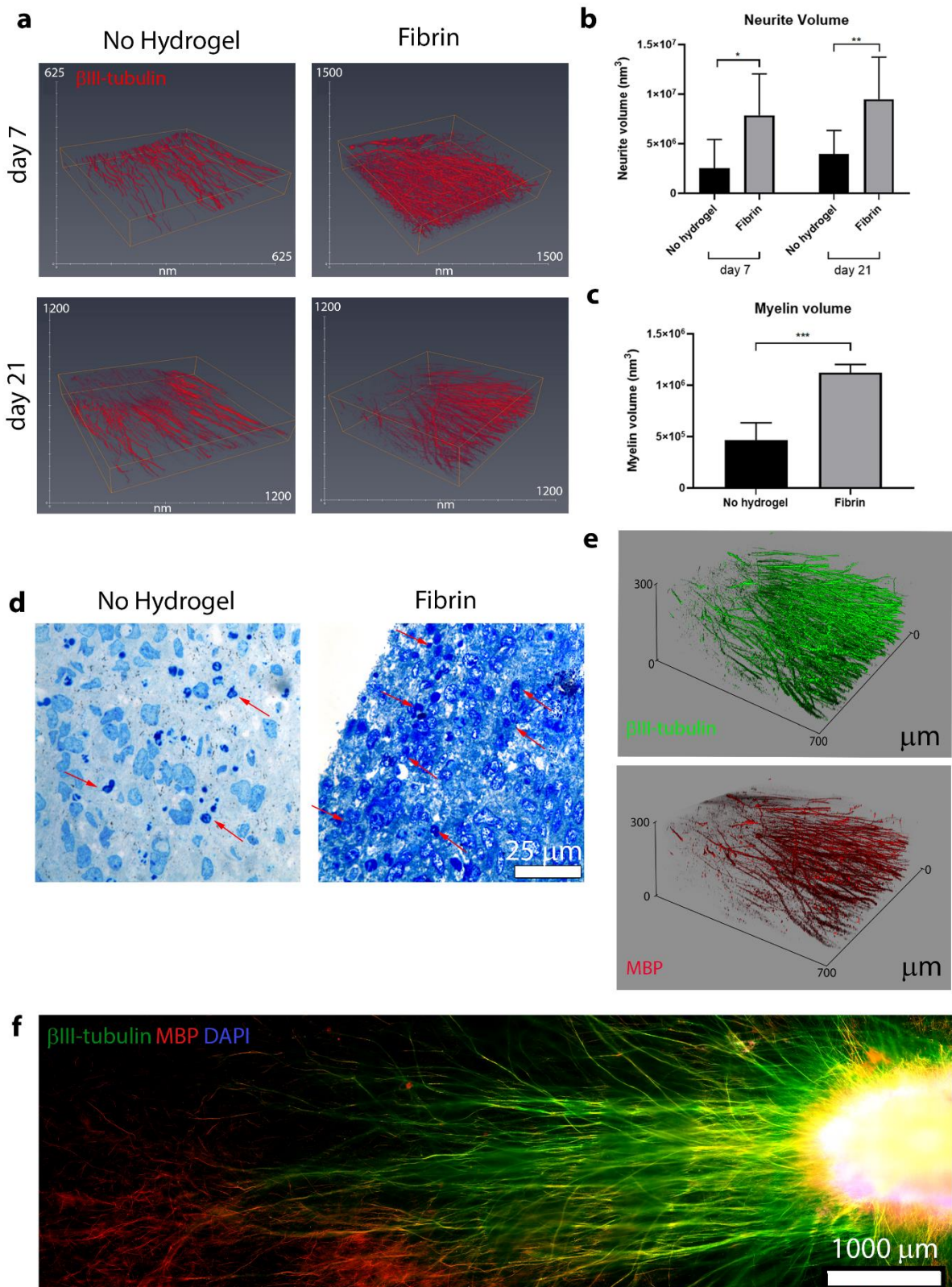


Figure 8. Enhancement of the PN platform via fibrin hydrogel addition on the neurosphere/SC scaffold co-culture. A) 3D reconstruction of the neurite volume of neurospheres embedded with (right column) or without (left column) fibrin at 7 days (top row) and 21 days (bottom row)

of culture. B) Quantification of the neurite volume in cultures with (grey bars) and without (black bars) fibrin embedding at 7 (left side) and 21 (right side) days of culture, indicating that fibrin addition significantly increased neurite volume. C) Quantification of the myelin volume in cultures with (grey bars) and without (black bars) fibrin embedding at 21 days of culture, showing an increase in myelin volume in cultures embedded with fibrin hydrogel. In both B) and C), the graph bars are represented as mean value \pm SD. Experiments were performed twice (n = 5). Statistics were performed with two-way ANOVA followed by a Tukey's HSD post-hoc test (B) or an unpaired t-test (C), where ***p < 0.001, **p < 0.01 and *p < 0.05. D) Toluidine blue-stained tissue sections showing myelin cross-sections in dark blue (pointed by red arrows), evidencing a higher density of dark blue spots in the fibrin condition. Scale bar is 25 μ m. E) 3D reconstruction of a neurosphere/SCs platform cultured with fibrin for 35 days, showing the formation of layered and highly aligned myelinated neurites. F) Overview of the growth of a 35 DIV co-culture, showing the formation of highly aligned and long (over 6.5 mm) neurites throughout the platform. For E) and F) β III-tubulin is shown in green, MBP in red and DAPI in blue.

Target tissue innervation

To demonstrate the potential of the fibrin PN platform to create innervated tissue models, we show a proof-of-concept using pancreatic pseudoislets (Fig.9 a-d) and endometrial organoids (Fig.9 e-h). Pancreatic pseudoislets were generated with a mean diameter of $41.9 \pm 2.98 \mu$ m (Fig. S8a and S8b), composed of alpha (alpha TC1) and beta cells (INS1E) at a ratio of 3:7³¹. Neurospheres were cultured on laminin-coated scaffolds for 7 days to initiate neural growth, after which several pancreatic pseudoislets were added and the entire construct embedded in fibrin. The co-cultures were maintained for an additional 10 days, during which time the pseudoislets survived and nociceptors from the neurospheres extended to surround and innervate them (Fig. 9c, 9d). Further reflecting native rodent pancreatic tissue, alpha (glucagon⁺; in green) and beta cells (insulin⁺; in red) reorganised and formed segregated clusters according to cell type³². Immunostaining for substance P (white) revealed that nociceptor axons were able to penetrate the cluster and establish an intimate association with the pancreatic cells, particularly insulin⁺ cells.

To create an endometrium model, a GFP⁺ human endometrial adenocarcinoma cell line (Ishi-M3-HSD-A)²¹ was seeded within Matrigel domes to form organoids of regular size, with a mean diameter of $59.9 \pm 12.1 \mu$ m (Fig. 9e-f; S8c-d). Matrigel domes containing several organoids were picked and positioned on a laminin-coated scaffold close to a 7 DIV neurosphere. After an additional 10 days, we confirmed that the endometrial organoids attached, survived, and retained their spherical shape throughout the co-culture period (Fig. S9). Nociceptors innervated the surrounding endometrial organoids, with neurites able to

penetrate through the Matrigel domes and establish an intimate association with endometrial cells (Fig. 9g, 9h, and S9).

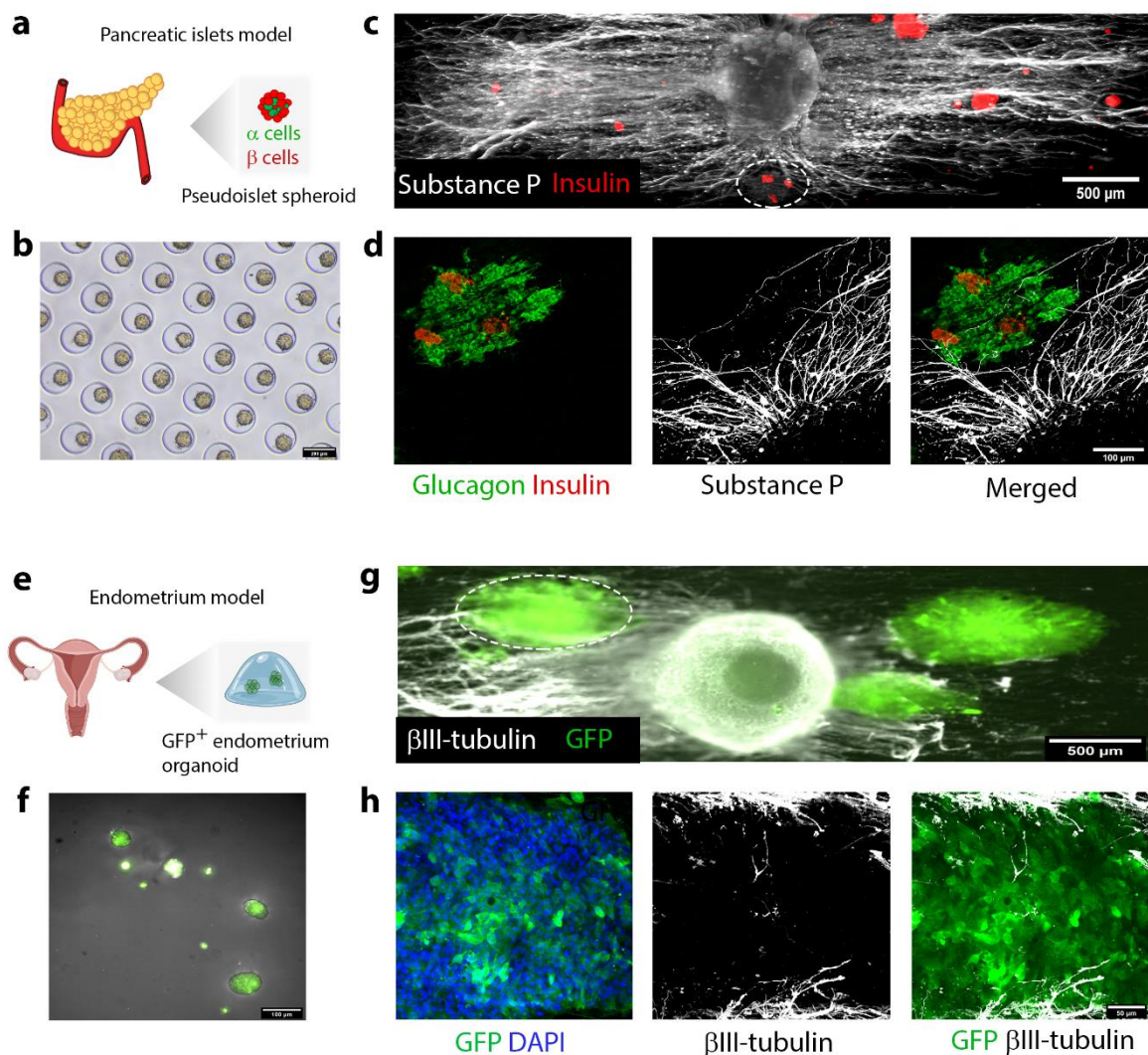


Figure 9. Nociceptor innervation of target tissues within the fibrin-embedded PN platform. (A-D) Pancreatic pseudoislets innervation. A) Illustration of the used pancreatic islet model composed of α cells (alpha TC cells) and β cells (INS1E cells) at 3:7 ratio respectively. B) Agarose microwell mold containing several spheroids with $41.9 \pm 2.98 \mu\text{m}$. Scale bar is $200 \mu\text{m}$. C) Overview of the platform showing the presence of several pancreatic pseudoislets (insulin, red) surrounding the neurosphere (substance P, white). D) Detailed view of the white dashed ellipse shown in C) showing infiltrating nociceptor fibers within the pseudoislets. Glucagon is shown in red and DAPI in blue. Scale bar is $500 \mu\text{m}$ for C) and $100 \mu\text{m}$ for D). (E-H) Endometrial organoid innervation. E) Illustration of the endometrial model composed of GFP⁺ Ishikawa organoids formed within Matrigel domes. F) Brightfield image superimposed with the green fluorescent channel showing the cultured endometrium organoids, with a diameter of $59.9 \pm 12.1 \mu\text{m}$. Scale bar is $100 \mu\text{m}$. G) Overview of the co-culture platform

showing several organoids (GFP, green) around the neurosphere (β III-tubulin). H) Detailed view of the white dashed ellipse shown in G), depicting neurite invasion on the endometrial organoid. DAPI is shown in blue. Scale bar is 500 μ m in G) and 50 μ m in H).

Discussion

Nociceptive pain perception is essential for normal organ function and physical integrity maintenance. However, sensory nerves can be affected by a multitude of insults, ranging from trauma to disease-induced neuropathies, which hinder this sensorial ability. At the same time, nociceptive pain is a common symptom of a large range of pathologies, bringing discomfort and reduced life quality to diseased individuals. Current understanding of neuropathies and pain mechanisms in a pathological context is limited by current research tools, which consist of animal models or oversimplified 2D *in vitro* models. Animal models are expensive, difficult to assess and are not always clinically translatable to humans³³. *In vitro* models, on the other hand, can provide an inexpensive, simple and direct translational research platform³⁴. To date, some *in vitro* human nociceptor models, containing neurons that are able to elicit APs and are sensitive to noxious stimuli, have already been reported^{13,14}. However, the tissue in these models does not replicate the 3D anisotropic axonal morphology that characterizes the PN (Fig. 1a). Moreover, the reported neurons are unmyelinated, which represents only the slow transmission nociceptors (C-fibers) and not the myelinated fast transmission fibers (A δ)^{1,2}. This lack of proper architectural and cellular representation limits the translational potential of the models and demands for improved biomimetic PN platforms.

In this work, we demonstrate the fabrication of a 3D culture platform containing functional iPSCs-derived nociceptors neurospheres with myelinated or unmyelinated anisotropic neurites. To produce these neurospheres we modified the protocol described by Chambers et al. for accelerated conversion of iPSCs into nociceptors¹⁹. In our two-step method, we started by seeding iPSCs on an agarose microwell device that induces the formation of spheroids via cell self-aggregation. Because of this, we were able to generate a large number of uniformly sized cell clusters (over 1500) that mimic the dorsal root ganglion (DRG) morphology and can be easily picked and handled manually (Fig. 1b and 2D). Contrarily, other nociceptor differentiation protocols culture cells on flat surfaces, producing disorganised and non-homogeneous cultures^{19,35}. Before commencing differentiation, we adopted a strategy for cell synchronization via DMSO treatment, which has been reported as an effective method to arrest the cell cycle³⁶. Following this, the differentiation protocol was initiated and after 7 days, cells exhibited a trunk neural crest phenotype (Fig. 2b and 2c). Contrary to Chambers et al. protocol, we supplied retinoic acid after day 2, which has been reported as a promoter of trunk neural crest specification²⁵ and enhanced the spheroids

cohesion (Fig. S2b). At day 9 of differentiation, the neurospheres were harvested for the second part of the process, where these were placed on the desired culture substrate and cultured for at least 7 days, to simultaneously promote maturation to a nociceptor phenotype and neurite outgrowth on the substrate. The use of neurotrophic factors in this last stage was reduced to just NGF, which proved enough to promote growth and phenotype acquisition. In just a three-week period, we were able to obtain several neurospheres (over 1500) exhibiting characteristic nociceptor markers such as substance P, CGRP and TRPV-1 expression (Fig. 2e). The obtained neurons were electrically active, presenting a RMP value slightly higher than other reported iPSCs neurons^{37,38}, but all able to elicit APs when stimulated (40 DIV cultures; Fig. 3a; table S2). These differentiated nociceptors also released substance P in response to a noxious stimulus (RTX) (10 DIV cultures; Fig. 3B), denoting the presence of a functional TRPV-1 channel^{26,35}. For these experiments, we used dissociated neuron cultures in order to improve the access of the electrical probe to single cells and ensure that substance P release was unhindered by the cell cluster. Clustered nociceptors, representing a more biomimetic form, also revealed functionality, as shown by the reversible RTX-induced neurite retraction from 7 DIV neurospheres (movie S2). RTX (or capsaicin) activation of TRPV-1 promotes calcium influx, which in turn can lead to mitochondrial dysfunction and inhibition of metabolism, resulting in the collapse of nerve endings³⁹. This effect is observed on the skin, where after topical capsaicin treatment, epidermal nociceptor fibers are reversibly lost²⁷. We could replicate this process using RTX, and additionally, neurite retraction could be significantly reduced by co-addition of a TRPV-1 antagonist (CPZ) (Fig. 3d, 3e, 3f; movie S3). After 24 h, all conditions showed similar metabolic activity (Fig. 3g), evidencing that nociceptors neurites can be targeted, without loss of viability, using a RTX sub-toxic application (10 μ M).

After establishing nociceptor functionality, we developed a PN model that replicates the native morphology using an aligned microfibrillar scaffold (Fig. 1b), which we previously reported as suitable to induce anisotropic neurite and myelin formation from rat DRGs and PC12 cells³⁰. Unlike other strategies that rely on platform wall constraining to induce axonal alignment^{16,17}, we simply used a substrate whose fibers are highly efficient in directing parallel axonal growth. Moreover, the fibers coating can be easily customized, which endows the platform with high versatility regarding the chemical and cellular composition. To recreate a PN tissue, we pre-seeded the scaffold with SCs, which proliferated and organised in highly aligned cell bands within 7 days (Fig. S3b). These SC bands replicate the native bands of Büngner, which form in the regenerating PN, to stimulate and guide regrowing axons to their targets⁴⁰. As a cell source, we used the rat sciatic nerves, from which SCs can be extracted in high yield, are easily purified²⁰, and have been shown to efficiently myelinate human iPSC-derived sensory neurons¹⁵. To better evaluate the influence of SCs in promoting neural growth, we compared them with scaffolds coated with laminin (major nerve ECM protein)⁴¹ and matrigel

(assortment of ECM proteins)⁴², which are standard coatings in *in vitro* PN models⁵. Matrigel-coated scaffolds promoted the highest neural growth followed by SCs-containing scaffolds, which additionally were composed of vast and anisotropic myelinated neurites. Compared to glass coverslips, our scaffold promoted higher neurite length, alignment and area after 7 and 21 days of culture. (Fig. 4 and Fig. 5). Scaffolds also displayed larger amounts of myelin and more aligned segments than coverslips cultures (Fig. 6) and, unlike coverslip coatings, all scaffold coatings maintained an intact neuron cluster that permitted neurite outgrowth comparable to a DRG explant. Uncoated substrates, i.e. not containing any adhesive units, such as laminin, are traditionally not supportive of neuron attachment, survival and growth⁴³. However, uncoated scaffolds supported neural growth (Fig. S4) while uncoated coverslips could not even allow cell attachment. This can be explained by the scaffold favourable chemical and topographical properties. On one hand, PEOT/PBT does not require functionalization to allow nerve growth⁴⁴, contrary to glass⁴³. On the other hand, the aligned microfibers promote cell entrapment and induce anisotropic neural growth^{45,46,47}, contrary to flat isotropic substrates. In sum, our scaffold provided a superior substrate than glass coverslips, by promoting PN tissue development with higher efficiency, robustness and biomimicry level.

Using the scaffold co-culture system, we produced myelinated tissue to investigate the resulting damage from acute hyperglycemia exposure. Hyperglycemia is a common pathophysiological imbalance resulting from diabetes mellitus type II and a cause of peripheral neuropathy^{7,48}. In this situation, excess intracellular glucose is converted to sorbitol by aldose reductase, resulting in sorbitol accumulation, and consequently in increased cellular osmolarity, oxidative stress and mitochondrial dysfunction that lead to cellular damage^{8,48,49}. Hyperglycemia damage is characterized by axonal degeneration and myelin abnormalities, such as layer decompaction^{50,49} (Fig. 7a). Thus, morphological evaluation can be used to determine the presence of damage, and if so, if it can be prevented by drug supplementation. Among the existing drugs, aldose reductase inhibitors such as epalrestat, have been explored as a method to reduce sorbitol levels, with a positive influence in mitigating hyperglycemic damage^{8,29}. To achieve an acute hyperglycemic state, supraphysiological glucose concentrations (45 mM) can be supplied in the culture medium, allowing a rapid modelling of blood glucose spikes³⁰. In our experiment, acute hyperglycemic exposure caused axonal and myelin damage, morphologically similar to diabetic type II mice⁸, which was quantitatively manifested in increased layer decompaction and decreased g-ratio (due to layer separation), compared to control cultures. Supplementation of epalrestat to hyperglycemic cultures effectively mitigated the cellular damage, denoting a benefit of sorbitol reduction in damage prevention (Fig. 7). These results highlight the advantages that *in vitro* platforms provide in comparison to animal models, by permitting a rapid, simple and inexpensive but still accurate

modelling of pathologies, as well as testing of therapeutic compounds. Additionally, in diabetic animal models there are several physiological processes altered at once, causing a systemic damage that reduces the level of experimental control and undermines data reliability^{50,51}.

To develop a more biomimetic PN model, we embedded the cell-seeded scaffold in a fibrin hydrogel. Fibrin is a natural material present during nerve regeneration and widely used within PN conduits and models^{52,53}. Its addition permitted neurites to grow beyond the scaffold, resulting in a neurite and myelin volume enhancement compared to bare scaffolds, while maintaining anisotropy (Fig. 8 and movie S4). This suggests that the topographical guidance provided by the scaffold, at the bottom of the construct, is sufficient to induce an overall neurite alignment, in a process potentially governed by axonal paracrine signalling^{30,54,55}. Using the fibrin/scaffold PN platform, we demonstrated the ability to create myelinated tissue with long-term stability and exhibiting neurite dimensions (over 6.5 mm) that, for *in vitro* platforms, are the highest reported to date, to the best of our knowledge^{16,56}.

Finally, as a proof-of-concept, we build different nociceptor innervation models by incorporating target tissues within the fibrin/scaffold PN platform. As targets, we selected the pancreas, represented by pancreatic pseudoislets, and the endometrium, represented by endometrial organoids. Both the pancreas, during CP^{9,10}, and the endometrium, during endometriosis^{57,58}, are innervated by unmyelinated nociceptors, which can become sensitized and trigger nociceptive pain. However, the exact pain pathophysiological mechanisms remain to be elucidated and current research is exclusively conducted in animal models, due to a lack of representative *in vitro* models. In this work, we established culture conditions that permitted simultaneous survival of all tissues and nociceptor ingrowth towards the target tissue, within 10 days of co-culture (Fig. 9). We did not further explore the mechanisms of nociceptor innervation or sensitization, as we intended to show the versatility of this platform in generating various nociceptor innervation models. With further development, this platform can provide a simple and inexpensive research tool to understand tissue-specific pathophysiology of pain as well as safely and quickly screen analgesic compounds.

In summary, we demonstrate here the formation of a 3D biomimetic nociceptor platform that can be used to assess neural growth in fine-tuned microenvironments, to model diabetes-related pathologies and to produce innervation models. We believe that the platform here proposed could be a new highly relevant tool for neuroscience, and in general for biomedical sciences.

Acknowledgements

We thank the Microscopy CORE Lab (M4I Maastricht University), especially Hans Duimel and Kevin Knoop for their help in TEM and confocal imaging. We also thank the province of

Limburg for the project funding. This work was partly supported by the research programme VENI 2017 STW- project 15900 financed by the Dutch Research Council (NWO).

References

1. Inquimbert, P. & Scholz, J. *Pain. Basic Neurochemistry* **8**, (2012).
2. Dubin, A. E. & Patapoutian, A. Nociceptors: the sensors of the pain pathway. *J. Clin. Invest.* **120**, 3760–3772 (2010).
3. Zieglgänsberger, W. Substance P and pain chronicity. *Cell Tissue Res.* **375**, 227–241 (2019).
4. Barbara Frias, Merighi, A. Capsaicin, Nociception and Pain. *Molecules* **21**, (2016).
5. Wieringa, P. A., Gonçalves de Pinho, A. R., Micera, S., van Wezel, R. J. A. & Moroni, L. Biomimetic Architectures for Peripheral Nerve Repair: A Review of Biofabrication Strategies. *Adv. Healthc. Mater.* **1701164**, 1–19 (2018).
6. Rajchgot, T. *et al.* Neurons and microglia; a sickly-sweet duo in diabetic pain neuropathy. *Front. Neurosci.* **13**, 1–17 (2019).
7. Yagihashi, S., Mizukami, H. & Sugimoto, K. Mechanism of diabetic neuropathy: Where are we now and where to go? *J. Diabetes Investig.* **2**, 18–32 (2011).
8. Hao, W. *et al.* Hyperglycemia promotes Schwann cell de-differentiation and demyelination via sorbitol accumulation and Igf1 protein down-regulation. *J. Biol. Chem.* **290**, 17106–17115 (2015).
9. Li, Q. & Peng, J. Sensory nerves and pancreatitis. *Gland Surg.* **3**, 284–92 (2014).
10. Atsawarungrangkit, A. Current understanding of the neuropathophysiology of pain in chronic pancreatitis. *World J. Gastrointest. Pathophysiol.* **6**, 193 (2015).
11. Demir, I. E., Tieftrunk, E., Maak, M., Friess, H. & Ceyhan, G. O. Pain mechanisms in chronic pancreatitis: Of a master and his fire. *Langenbeck's Arch. Surg.* **396**, 151–160 (2011).
12. Zondervan, K. T. *et al.* Endometriosis. *Nat. Rev. Dis. Prim.* **4**, 9 (2018).
13. Wainger, B. J. *et al.* Modeling pain in vitro using nociceptor neurons reprogrammed from fibroblasts. *Nat Neurosci* **18**, 17–24 (2015).
14. Jones, I. *et al.* Development and validation of an in vitro model system to study peripheral sensory neuron development and injury. *Sci. Rep.* **8**, 1–15 (2018).

15. Clark, A. J. *et al.* Co-cultures with stem cell-derived human sensory neurons reveal regulators of peripheral myelination. *Brain* **140**, 898–913 (2017).
16. Sharma, A. D. *et al.* Engineering a 3D functional human peripheral nerve in vitro using the Nerve-on-a-Chip platform. *Sci. Rep.* **9**, 1–12 (2019).
17. Uzel, S. G. M. *et al.* Microfluidic device for the formation of optically excitable, three-dimensional, compartmentalized motor units. *Sci. Adv.* **2**, (2016).
18. Osaki, T., Uzel, S. G. M. & Kamm, R. D. Microphysiological 3D model of amyotrophic lateral sclerosis (ALS) from human iPS-derived muscle cells and optogenetic motor neurons. *Sci. Adv.* **4**, 1–16 (2018).
19. Chambers, S. M. *et al.* Combined small-molecule inhibition accelerates developmental timing and converts human pluripotent stem cells into nociceptors. *Nat. Biotechnol.* **30**, 715–720 (2012).
20. Kaewkhaw, R., Scutt, A. M. & Haycock, J. W. Integrated culture and purification of rat Schwann cells from freshly isolated adult tissue. *Nat Protoc* **7**, 1996–2004 (2012).
21. Konings, G. F. J., Cornel, K. M. C., Xanthoulea, S., Delvoux, B. & Skowron, M. A. Blocking 17 beta-hydroxysteroid dehydrogenase type 1 in endometrial cancer: a potential novel endocrine therapeutic approach. *J Pathol* **244**, 203–214 (2018).
22. Püspöki, Z., Storath, M., Sage, D. & Unser, M. Transforms and Operators for Directional Bioimage Analysis: A Survey. *Focus Bio-Image Informatics* 69–93 (2016)
23. Longair, M. H., Baker, D. A. & Armstrong, J. D. Simple neurite tracer: Open-source software for reconstruction, visualization and analysis of neuronal processes. *Bioinformatics* **27**, 2453–2454 (2011).
24. Goebbels, S. *et al.* Elevated phosphatidylinositol 3,4,5-trisphosphate in glia triggers cell-autonomous membrane wrapping and myelination. *J. Neurosci.* **30**, 8953–8964 (2010).
25. Huang, M. *et al.* Generating trunk neural crest from human pluripotent stem cells. *Sci. Rep.* **6**, 1–9 (2016).
26. Seabrook, G. U. Y. R. *et al.* Functional Properties of the High-Affinity TRPV1 (VR1) Vanilloid Receptor Antagonist (4-Hydroxy-5-iodo-3- methoxyphenylacetate ester) Iodo-Resiniferatoxin. *J. Pharmacol. Exp. Ther.* **303**, 1052–1060 (2002).
27. Anand, P. & Bley, K. Topical capsaicin for pain management: Therapeutic potential and mechanisms of action of the new high-concentration capsaicin 8 patch. *Br. J.*

- Anaesth.* **107**, 490–502 (2011).
28. Willingham, K. D. L. *et al.* Development of a central nervous system axonal myelination assay for high throughput screening. *BMC Neurosci.* **17**, 1–13 (2016).
 29. Ramirez, M. A. & Borja, N. L. Epalrestat: An aldose reductase inhibitor for the treatment of diabetic neuropathy. *Pharmacotherapy* **28**, 646–655 (2008).
 30. Malheiro, A., Morgan, F., Baker, M., Moroni, L. & Wieringa, P. A three-dimensional biomimetic peripheral nerve model for drug testing and disease modelling. *Biomaterials* **257**, 120230 (2020).
 31. Malenczyk, K. *et al.* Fetal endocannabinoids orchestrate the organization of pancreatic islet microarchitecture. *Proc. Natl. Acad. Sci. U. S. A.* **112**, E6185–E6194 (2015).
 32. Hoang, D. T. *et al.* A conserved rule for pancreatic islet organization. *PLoS One* **9**, 1–9 (2014).
 33. Barré-Sinoussi, F. & Montagutelli, X. Animal models are essential to biological research: Issues and perspectives. *Futur. Sci. OA* **1**, 4–6 (2015).
 34. Zhang, B. & Radisic, M. Organ-on-a-chip devices advance to market. *Lab Chip*, **17** 2395–2420 (2017)
 35. Guimarães, M. Z. P. *et al.* Generation of iPSC-Derived Human Peripheral Sensory Neurons Releasing Substance P Elicited by TRPV1 Agonists. *Front. Mol. Neurosci.* **11**, 1–17 (2018).
 36. Yiangou, L. *et al.* Method to Synchronize Cell Cycle of Human Pluripotent Stem Cells without Affecting Their Fundamental Characteristics. *Stem Cell Reports* **12**, 165–179 (2019).
 37. Nestor, M. W. *et al.* A Time Course Analysis of the Electrophysiological Properties of Neurons Differentiated from Human Induced Pluripotent Stem Cells (iPSCs). *PLoS One* **9**, (2014).
 38. Meents, J. E. *et al.* The role of Nav1.7 in human nociceptors: Insights from human induced pluripotent stem cell-derived sensory neurons of erythromelalgia patients. *Pain* **160**, 1327–1341 (2019).
 39. Olah, Z. *et al.* Ligand-induced Dynamic Membrane Changes and Cell Deletion Conferred by Vanilloid Receptor 1. *J. Biol. Chem.* **276**, 11021–11030 (2001).
 40. Gomez-Sanchez, J. A. *et al.* After nerve injury, lineage tracing shows that myelin and Remak Schwann cells elongate extensively and branch to form repair Schwann cells,

- which shorten radically on remyelination. *J. Neurosci.* **37**, 9086–9099 (2017).
41. Gonzalez-Perez, F., Udina, E. & Navarro, X. *Extracellular matrix components in peripheral nerve regeneration. International Review of Neurobiology* vol. 108 (Elsevier Inc., 2013).
 42. Hughes, C. S., Postovit, L. M. & Lajoie, G. A. Matrigel: A complex protein mixture required for optimal growth of cell culture. *Proteomics* **10**, 1886–1890 (2010).
 43. Farrukh, A., Zhao, S. & Campo, A. Microenvironments Designed to Support Growth and Function of Neuronal Cells. **5**, 1–22 (2018).
 44. Santos, D., Wieringa, P., Moroni, L., Navarro, X. & Valle, J. Del. PEOT/PBT Guides Enhance Nerve Regeneration in Long Gap Defects. *Adv. Healthc. Mater.* **6**, (2017).
 45. Du, J. *et al.* Prompt peripheral nerve regeneration induced by a hierarchically aligned fibrin nanofiber hydrogel. *Acta Biomater.* **55**, 296–309 (2017).
 46. Gnani, S., Fornasari, B. E., Tonda-turo, C. & Laurano, R. The Effect of Electrospun Gelatin Fibers Alignment on Schwann Cell and Axon Behavior and Organization in the Perspective of Artificial Nerve Design. *Int. J. Mol. Sci.* **16**, 12925–12942 (2015).
 47. Daud, M. F. B., Pawar, K. C., Claeysens, F., Ryan, A. J. & Haycock, J. W. An aligned 3D neuronal-glia co-culture model for peripheral nerve studies. **33**, (2012).
 48. Gonçalves, N. P. *et al.* Schwann cell interactions with axons and microvessels in diabetic neuropathy. *Nat. Rev. Neurol.* **13**, 135–147 (2017).
 49. Vægter, C. B. Peripheral Glial Cells in the Development of Diabetic neuropathy. **9**, 1–9 (2018).
 50. Cermenati, G. *et al.* Diabetes-induced myelin abnormalities are associated with an altered lipid pattern: Protective effects of LXR activation. *J. Lipid Res.* **53**, 300–310 (2012).
 51. Wang-Fischer, Y. & Garyantes, T. Improving the reliability and utility of streptozotocin-induced rat diabetic model. *J. Diabetes Res.* (2018).
 52. Wood, M. D. *et al.* Fibrin Matrices With Affinity-Based Delivery Systems and Neurotrophic Factors Promote Functional Nerve Regeneration. *Biotechnol. Bioeng.* **106**, 970–979 (2010).
 53. Belkas, J. S., Shoichet, M. S., Midha, R. & Fracs, C. Axonal Guidance Channels in Peripheral Nerve Regeneration. *Oper. Tech. Orthopaedics* 190–198 (2004)
 54. Kitsukawa, T. *et al.* Neuropilin-semaphorin III/D-mediated chemorepulsive signals play

- a crucial role in peripheral nerve projection in mice. *Neuron* **19**, 995–1005 (1997).
55. Plachez, C. & Richards, L. J. Mechanisms of Axon Guidance in the Developing Nervous System. *Curr. Top. Dev. Biol.* **69**, 267–346 (2005).
 56. Pagan-diaz, G. J. *et al.* Engineering geometrical 3-dimensional untethered in vitro neural tissue mimic. *PNAS*, **116**, 25932–25940 (2019).
 57. Morotti, M., Vincent, K., Brawn, J., Zondervan, K. T. & Becker, C. M. Peripheral changes in endometriosis- associated pain. *Hum. Reprod. Update* **20**, 717–736 (2014).
 58. Morotti, M., Vincent, K. & Becker, C. M. Mechanisms of pain in endometriosis. *Eur. J. Obstet. Gynecol.* **209**, 8–13 (2017).

Supplementary Information

3D culture platform of human iPSCs-derived nociceptors for peripheral nerve modelling and tissue innervation

Afonso Malheiro^{1}, Abhishek Harichandan^{1*}, Joyce Bernard², Adrián Seijas-Gamardo¹, Gonda F. Konings³, Paul G.A Volders², Andrea Romano³, Carlos Mota¹, Paul Wieringa¹, Lorenzo Moroni¹*

1. MERLN Institute for Technology-Inspired Regenerative Medicine, Complex Tissue Regeneration department, Maastricht University, The Netherlands
2. CARIM School for Cardiovascular Diseases, Department of Cardiology, Maastricht University, The Netherlands
3. GROW School for Oncology and Developmental Biology, Department of Gynaecology, Maastricht University, The Netherlands

**these authors have contributed equally to this work*

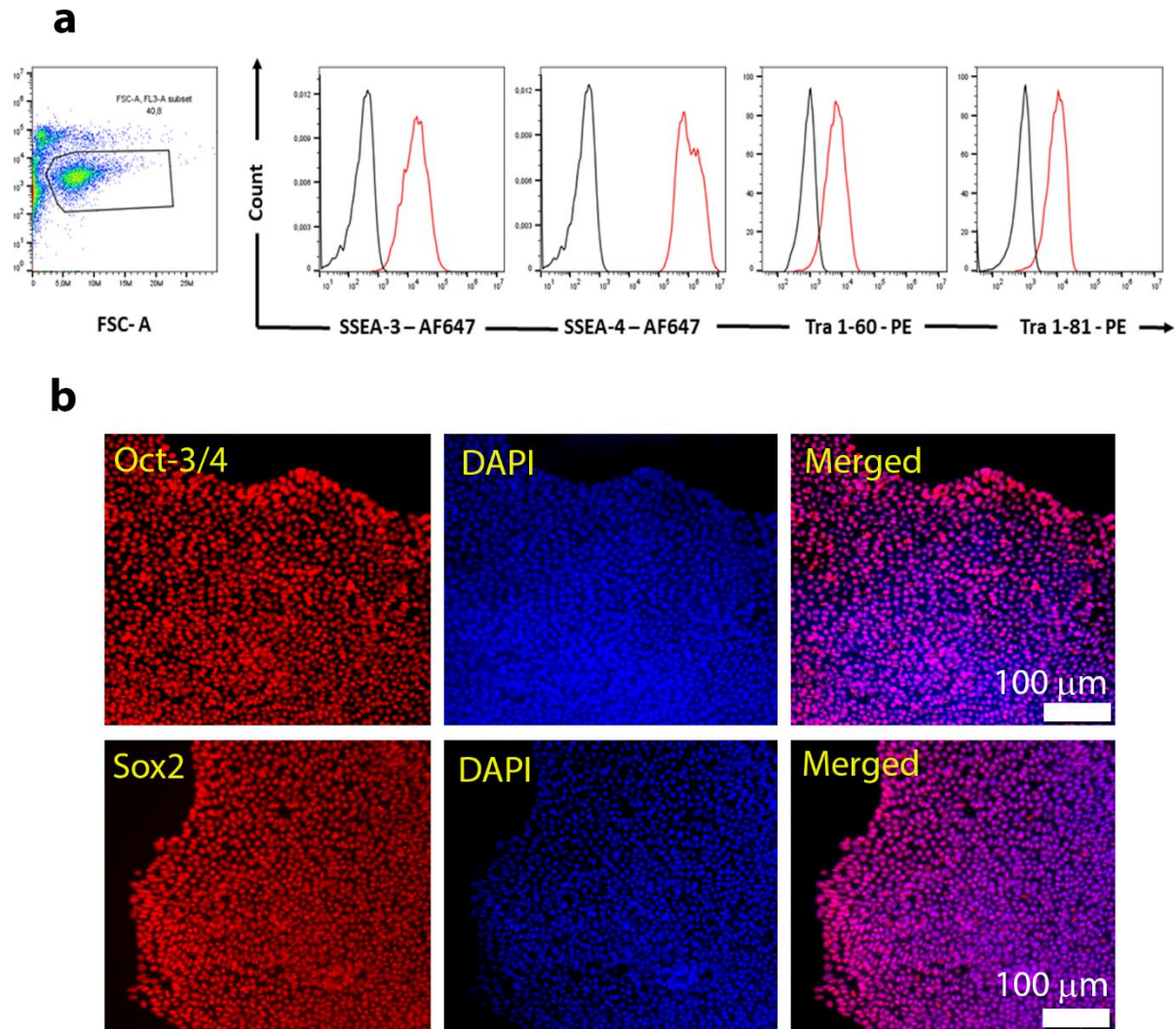


Figure S1. Characterization of human iPSCs pluripotency. A) Flow cytometry analysis to the iPSCs surface markers: stage specific embryonic antigen 3 (SSEA-3) and antigen 4 (SSEA-4) (both conjugated with Alexa Fluor 647, AF647) and podocalyxin (Tra 1-60 and Tra 1-81) (both conjugated with phycoerythrin, PE). B) Immunostaining on iPSCs clusters to the pluripotency markers Oct-3/4 (top panel, red) and Sox2 (bottom panel, red), showing the robust expression of these markers on all cells. DAPI is shown in blue and the scale bar is 100 μm .

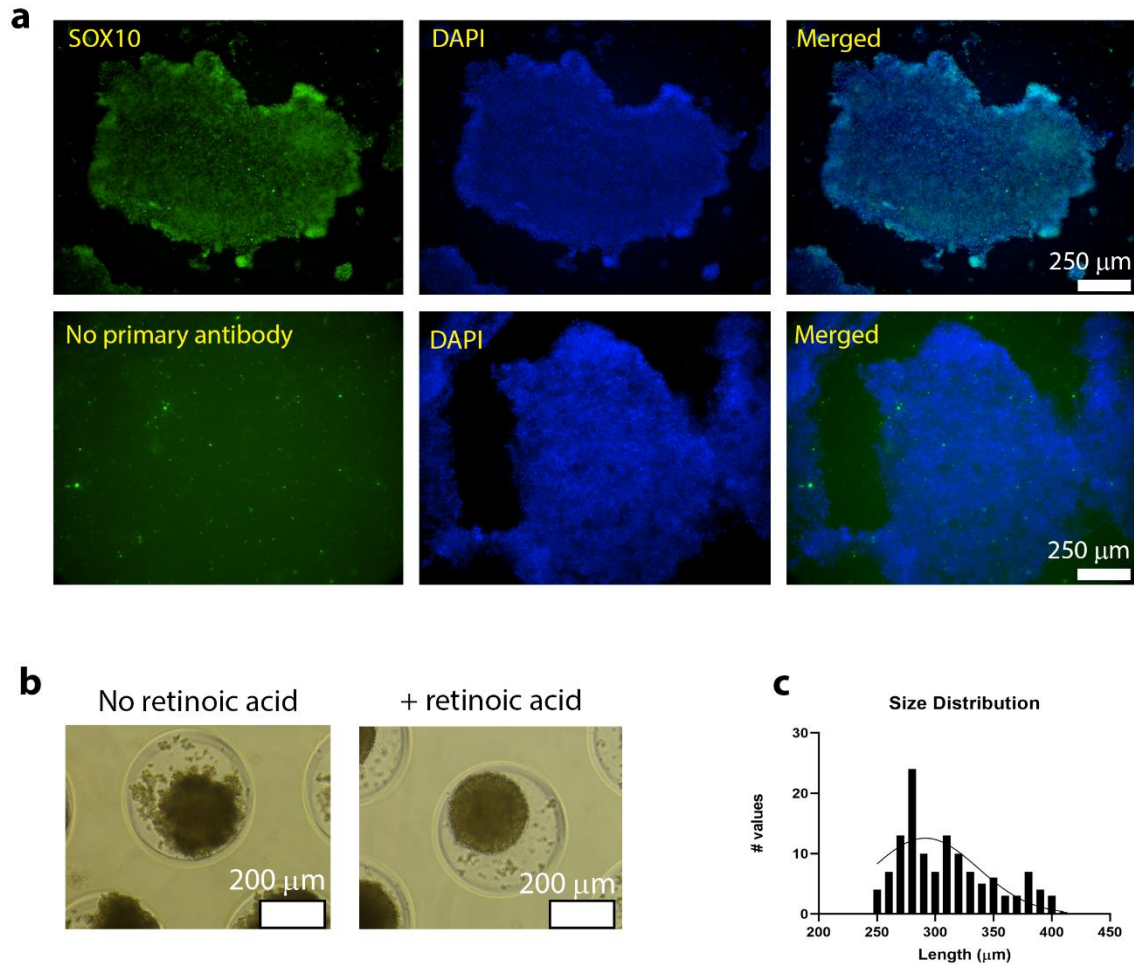


Figure S2. Characterization of neural crest cells obtained from iPSCs neural differentiation. A) SOX10 marker (green, top panel) indicates the acquisition of a neural crest phenotype. On bottom panel, the secondary antibody control (no primary antibody added), indicates the specific binding of the used SOX10 antibody. DAPI is shown in blue and the scale bar is 250 μm . B) Cell clusters at the neural crest stage require retinoic acid for cluster aggregation. The image of the left shows cultures with no retinoic acid added showing their poor integrity. On the right side, cultures with added retinoic acid, evidence good cell aggregation and cluster integrity. The scale bar is 100 μm . C) Size distribution of clusters at the end point of the differentiation process (with retinoic acid).

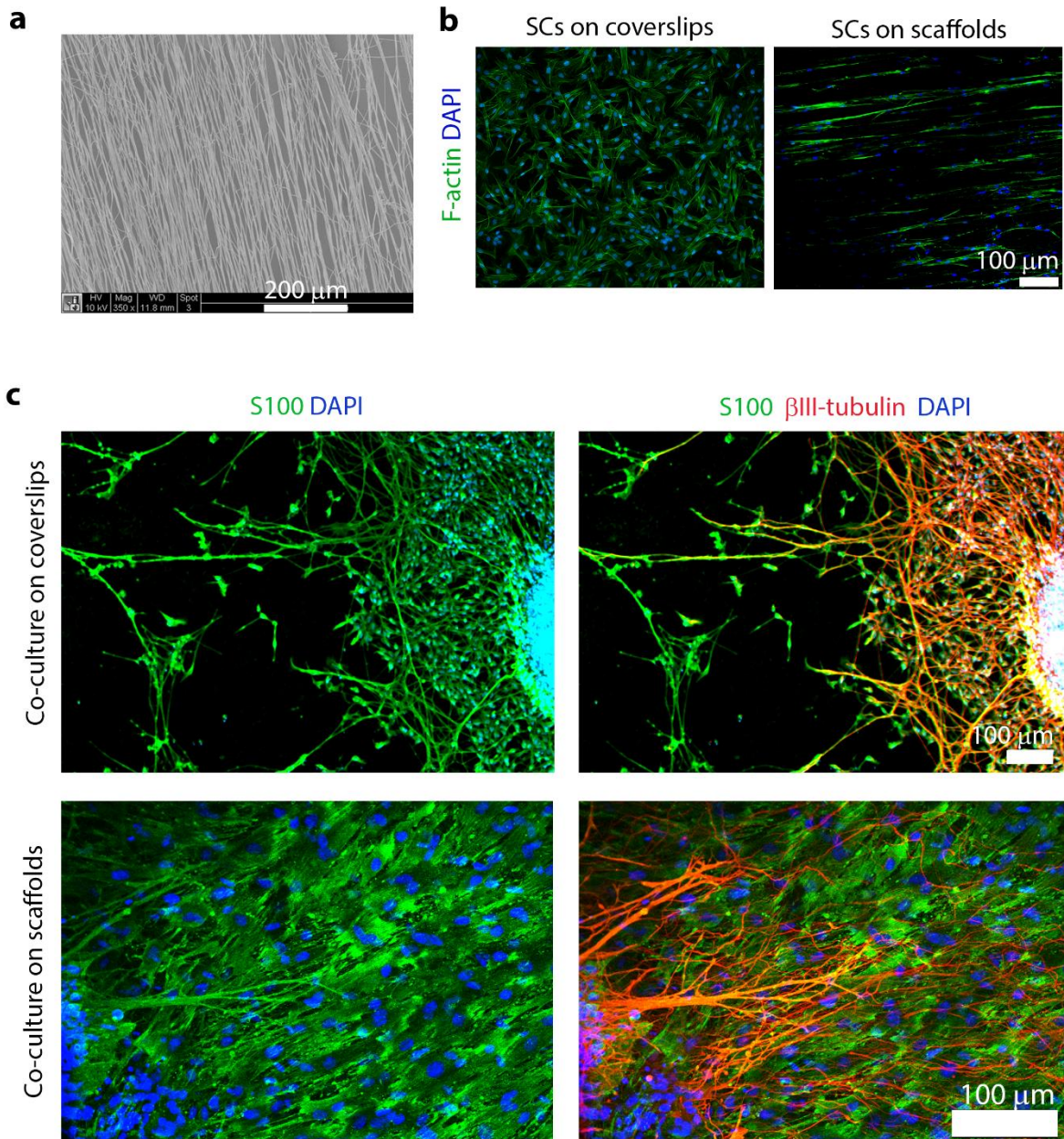


Figure S3. SCs morphology after culture on coverslips or scaffolds. A) SEM micrograph of the scaffold fibers. Scale bar is 200 μm. B) SCs morphology after 7 days of culture on coverslips (left side) and scaffolds (right side). On coverslips, SCs are located randomly and are isotropic, while on scaffolds, SCs are well aligned. F-actin is shown in green and DAPI in blue. Scale bar is 100 μm. C) Co-culture of iPSCs neurospheres with SCs on coverslips (top panel) or scaffolds (bottom panel). SCs (marked by S100 in green) on coverslips cultures tend to group around the neurosphere in large numbers, while few cells remain randomly spread throughout the coverslip. On the scaffold cultures, SCs are tightly packed and remain well aligned over the whole scaffold. In both culture systems, axons (marked by βIII-tubulin in red) tend to follow and intimately associated with SCs. In coverslips, neurite projection is short and radial, while in

scaffolds the neurites are long and aligned with the SCs direction. In both panels, DAPI is shown in blue and the scale bar is 100 μm .

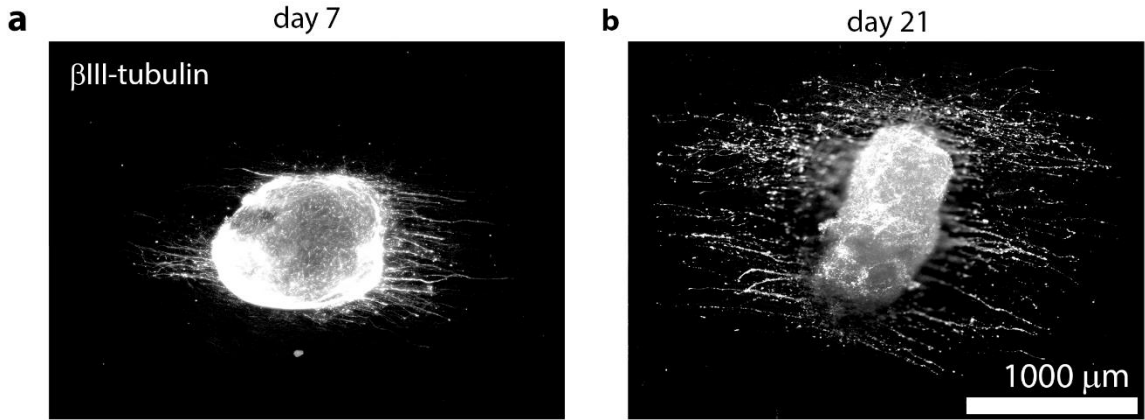


Figure S4. iPSCs neurosphere morphology on scaffolds without coating or seeded SCs. A) iPSCs neurosphere after 7 days of culture and B) 21 days of culture. β III-tubulin is shown in white and the scale bar is 1000 μm .

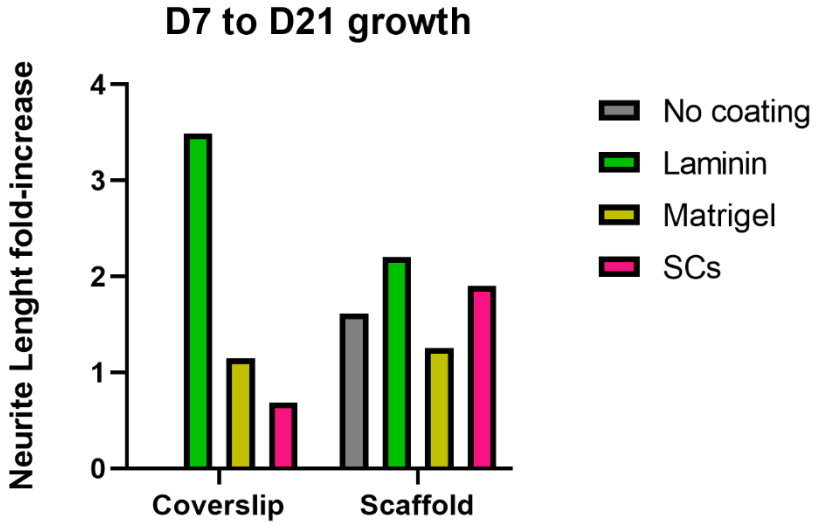


Figure S5. Neurosphere neurite growth increment from day 7 to day 21 in coverslips and scaffolds. The bars represent the ratio between the mean length at day 21 and the mean length at day 7. As visible, the laminin condition was the one that promoted the largest growth increment between these time points.

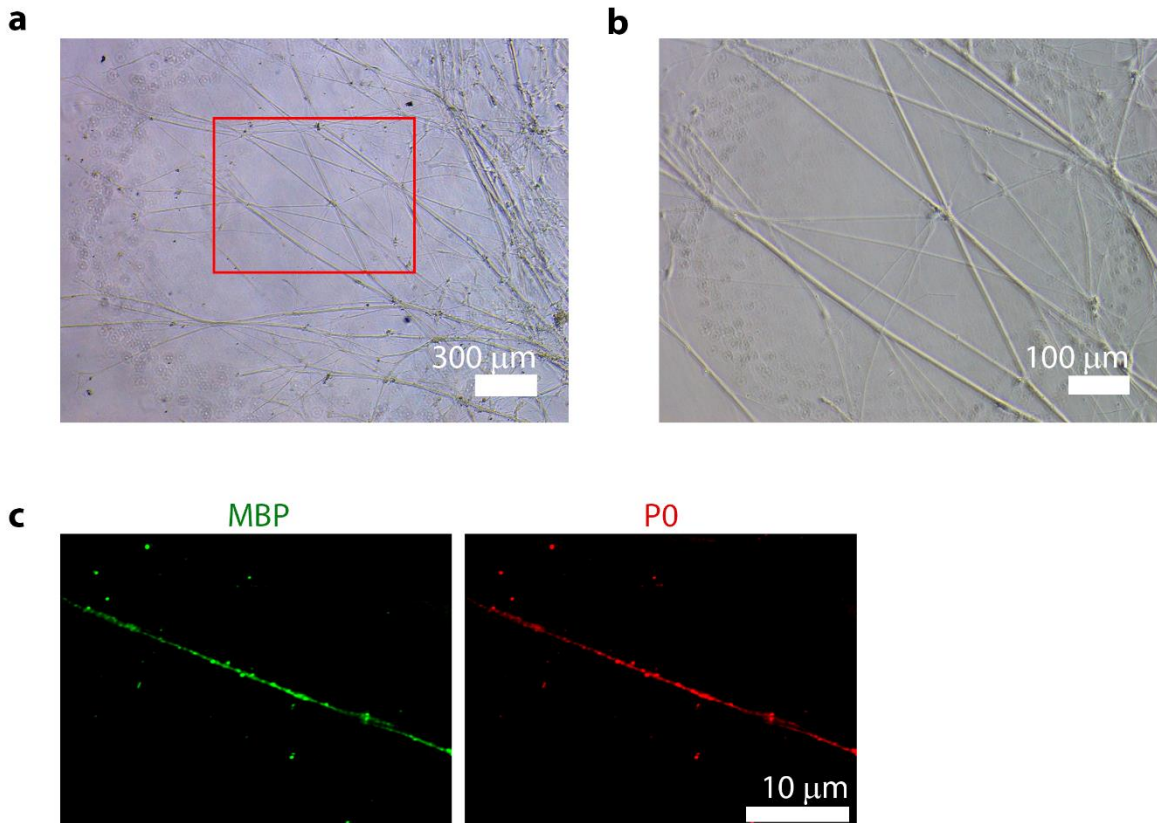


Figure S6. Myelin morphology and characterization on 21 DIV iPSCs/SCs cultures. A) Brightfield image of iPSCs/SCs co-culture on coverslips, depicting the existence of several myelin segments. Scale bar is 300 μm . B) Detailed view of the area highlighted by the red box in A). Scale bar is 100 μm . Myelin segments, which appear thick, straight and gleamy, can be easily distinguished from unmyelinated axons that look thin, irregular and less reflecting. C) High magnification view of a myelin segment, immunostained for MBP (green) and protein P0 (red).

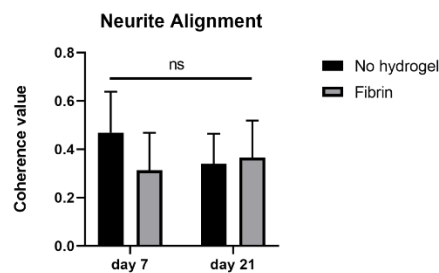


Figure S7. Neurite alignment measurement on neurosphere/SCs scaffold co-cultures with (black bars) and without (gray bars) fibrin embedding over 7 (left side) and 21 days (right side). The values represent the coherence of identical ROIs containing the neurites, where 0 is full isotropy and 1 is full anisotropy. The bar graphs are shown as mean \pm SD. We performed this experiment once, and took over 5 images per sample ($n = 4$). Statistics were performed with two-way ANOVA followed by a Tukey's HSD post-hoc test, where ns is $p > 0.05$.

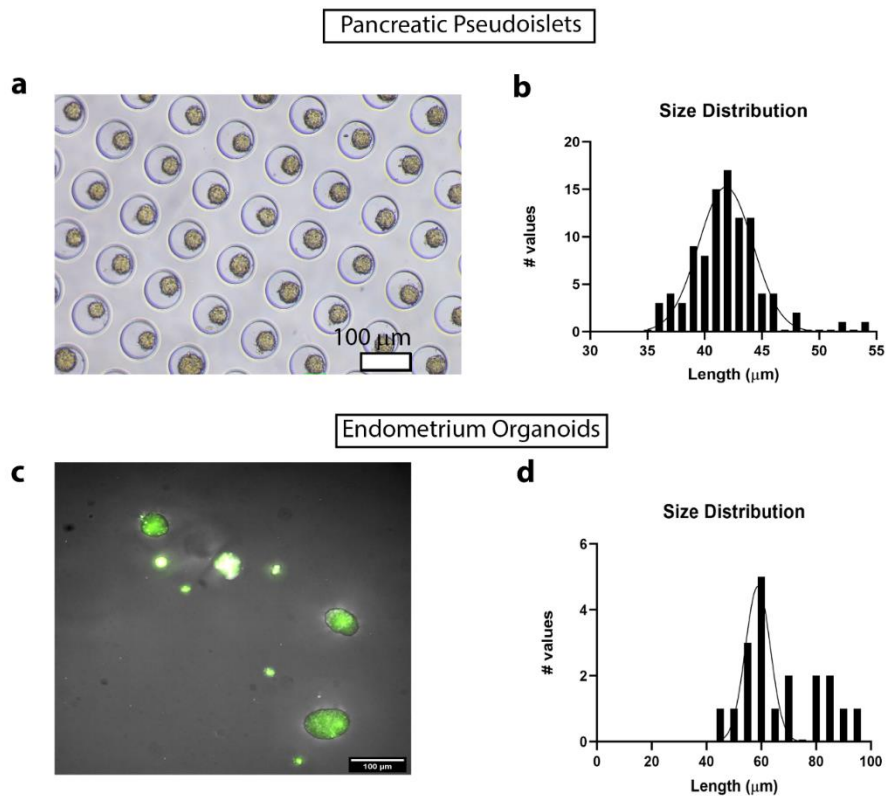


Figure S8. Generation and characterization of tissue spheroids for innervation within the peripheral nerve platform. A) Pancreatic pseudoislets made from alpha TC and INS1E cells and B) correspondent size distribution. C) Endometrium organoids formed from GFP⁺ Ishikawa cells within matrigel domes and D) respective size distribution. All scale bar are 100 μm.



Figure S9. Endometrium organoid innervation in a 10-day co-culture platform. The organoids retain their shape as seen in the image, showing spatial correlation of GFP (in green) and DAPI (in blue). Nociceptor neurites are seen in the image on the middle by βIII-tubulin immunostaining (in red), and as demonstrated in the merged image (right hand side) these

neurites interact and surround the endometrium spheroid, to establish innervation. Scale bar is 100 μm .

Human	PHOX2B	Forward	TACGCCGCAGTTCCTTACAA
Human	PHOX2B	Reverse	GAAGACCCTTTCCAGCTCTTT
Human	ETS1	Forward	GCAGAATGAGCTACTTTGTGGA
Human	ETS1	Reverse	TTGCTAGGTCCTTGCCTCA

Table S1. Used primers for qPCR of PHOX2B and ETS1 genes.

Cell #	Cm (pF)	RMP (mV)	Overshoot (mV)	AP amplitude (mV)	I step (pA)
#1	24,0	-44,2	55,4	99,6	200
#2	11,9	-40,6	67,2	107,8	200
#3	14,0	-60,3	-9,1	51,2	200
#4	13,0	-38,5	24,1	62,6	200
#5	20,0	-44,7	-8,7	36,0	200
#6	16,0	-37,5	13,1	50,6	200
#7	13,0	-42,8	6,1	48,9	200
#8	18,0	-44,1	38,6	82,7	200

Table S2. Patch clamp results from 40 DIV dissociated iPSCs-derived nociceptors.

Target protein	Source	Used dilution
β III tubulin	Sigma-Aldrich, T8578	1:500
S100	Sigma-Aldrich, S2644	1:100
MBP	Thermo Fisher Scientific, PA1-46447	1:50
Phox2B	Santa Cruz Biotechnology, sc-376997	1:50
ETS1	Santa Cruz Biotechnology, sc-55581	1:50
Substance P	Abcam, ab14184	1:100
CGRP	Abcam, ab22560	1:500
TRPV-1	Alomone Labs, ACC-030	1:100
BRN3A	Merck Millipore, MAB1585	1:100
Myelin Protein Zero (P0)	Novus Biologicals, NB100-1607	1:50
Insulin	Abcam, ab7842	1:50
Glucagon	Bio-Techne, NBP1-67575	1:750

Table S3. List of used primary antibodies.

Host	Target	Conjugated fluorophore	Source	Dilution
Goat	Mouse IgG	488	Thermo Fischer Scientific	1:500
Goat	Mouse IgG	568	Thermo Fischer Scientific	1:500

Goat	Mouse IgG	647	Thermo Fischer Scientific	1:500
Goat	Rabbit IgG	488	Thermo Fischer Scientific	1:500
Goat	Rabbit IgG	568	Thermo Fischer Scientific	1:500
Goat	Guinea Pig IgG	647	Thermo Fischer Scientific	1:500
Donkey	Sheep IgG	488	Thermo Fischer Scientific	1:500

Table S4. List of used secondary antibodies.

Chapter 5

Investigating the effect of phosphodiesterase-4 (PDE4) inhibitors on Schwann cells myelination in a 3D regeneration model and in a hyperglycemia model

Afonso Malheiro^{1*}, Melissa Scheppers^{2,3*}, Adrián Seijas Gamardo¹, Jos Prickaerts³, Lorenzo Moroni¹, Tim Vanmierlo^{2,3+}, Paul Wieringa¹⁺

1. MERLN Institute for Technology-Inspired Regenerative Medicine, Maastricht University
2. Department of Neuro-immunology, Biomedical Research Institute, Hasselt University, Hasselt 3500, Belgium.
3. Department Psychiatry and Neuropsychology, European Graduate School of Neuroscience, School for Mental Health and Neuroscience, Maastricht University, Maastricht 6200 MD, The Netherlands.

**these authors have contributed equally in this work*

+corresponding author

Abstract

Phosphodiesterases type 4 (PDE4s) inhibitors have been extensively researched for diverse applications due to their anti-inflammatory and neuroregenerative properties. Recent formulations, with low emetic responses, such as roflumilast (ROFLU) and BPN17440 (BPN), have demonstrated cognitive enhancement benefits, but have not been tested yet in the context of peripheral nerve (PN) tissue regeneration and neuropathy. In this work, we demonstrate the impact of ROFLU and BPN treatment on Schwann cells (SCs) *in vitro* acquisition and maintenance of a myelinating phenotype, in a regeneration and diabetes model. Using a PN regeneration model, we showed that ROFLU significantly enhanced the expression of myelin genes (MAG, MBP and PLP) compared to the control vehicle (DMSO), while BPN dosing led to an increased production of MAG and MBP. SC treatment with PDE4 inhibitors did not impede axonal outgrowth and myelination of iPSCs-derived nociceptors. In a

diabetes model representing a hyperglycemia scenario, SCs were induced to a myelination phenotype and then exposed to different hyperglycemia levels. ROFLU was tested for the prevention of de-differentiation and as a promoter of re-differentiation upon returning to normoglycemia. Under both regimes, the addition of ROFLU promoted increased expression and production of MBP. After returning to normoglycemia, ROFLU-treated SCs also expressed increased levels of PLP. In sum, we demonstrate here that *in vitro* applications of PDE4 inhibitors result in the enhancement and maintenance of SCs myelination phenotype, in a repair and pathophysiological scenario. Despite containing preliminary findings, this work suggests a potential benefit of PDE4 inhibitors for PN regeneration enhancement and as therapeutics for PN-related disorders such as diabetic neuropathy.

Introduction

Phosphodiesterases (PDEs) are a super family of enzymes responsible for the degradation of cyclic nucleotides, such as cyclic adenosine monophosphate (cAMP) and cyclic guanosine monophosphate (cGMP). PDE4 enzymes, a sub-family of PDEs with over 25 isoforms, regulate cAMP dynamics in neuron and glial cells, accounting for 70 to 80% of PDEs in neural tissue^{1,2}. Both cAMPs and cGMPs are well-established cognitive enhancers, contributing to long-term potentiation and memory formation/consolidation³. Abnormal cAMP signalling, resultant from anomalous PDE4 function, is associated with cognitive defects in neurodegenerative diseases, such as Alzheimer's disease (AD)¹. To combat these pathologies, the use of inhibitors of PDE4 isoforms has been investigated. Among these, rolipram has shown extensive evidence in preventing AD progression and enhancing cognitive abilities in AD mice models^{1,4,5}. cAMP elevation is also required for glial cell differentiation and neural regeneration, in both the central and peripheral nervous system (CNS and PNS). In the CNS, multiple sclerosis (MS) is caused by demyelination which leads to nerve conduction block and axonal loss. To promote remyelination, cAMP elevation strategies using rolipram or via exogenous cAMP dosing, have shown improvement of oligodendrocyte precursor cells (OPCs) differentiation into oligodendrocytes, which are capable of *de novo* myelin formation after injury⁶. Rolipram treatment for spinal cord injury was also effective in promoting axonal regrowth and motor function recovery².

In the PNS, cAMP level regulation via PDE4 activity plays a crucial role, particularly in the events following a nerve injury⁷. In the initial stages of repair, Schwann cells (SCs) de-differentiate to a regeneration phenotype and proliferate in high numbers to form cell bands termed bands of Büngner⁸. During this process, cAMP combination with other growth factors (GFs) is essential to stimulate SC proliferation⁹. Besides acting as a mitogen, cAMP also signals differentiation, by promoting the exit of cell cycle and adoption of a pre-myelinating phenotype⁹. This phenotype switch is characterized by upregulation of the transcription factor

Krox20 and concomitant downregulation of cJUN¹⁰, as well as upregulation of myelin-related genes such as myelin associated glycoprotein (MAG), myelin basic protein (MBP) and oligodendrocyte marker O1 (O1)^{9,10,11}. The therapeutic efficacy of PDE4 inhibitors in peripheral nerve (PN) repair was clearly shown in mice via rolipram application within a nerve guide, resulting in faster regeneration of both motor and sensory nerve fibers compared to the saline-treated group¹². However, it remains to be investigated if PDE4 inhibitors are therapeutic candidates to stimulate remyelination and to treat peripheral demyelinating neuropathies, similar to their application in the CNS. In particular, diabetes-induced neuropathies represent a highly prevalent and challenging pathology in which recurring transient hyperglycemia is responsible for SC de-differentiation, demyelination and ultimately axonopathy^{13,14,15}. In this regard, PDE4 inhibitors could be explored as prophylactic measures to prevent SC de-differentiation or as compounds that both promote PN regeneration and successful remyelination after a neuropathic episode. Despite its success in promoting neuroregeneration, rolipram has been associated with adverse side effects such as nausea and emesis, which further motivated the development of new formulations^{4,16}. Second generation PDE4 inhibitors such as roflumilast (ROFLU) and BPN14770 (BPN) have both shown cognition enhancing properties, whilst triggering a milder emetic response⁴. However there is yet no evidence on the use of these drugs and other similar formulations for PN applications.

In this work, we have developed three-dimensional (3D) *in vitro* models to test the influence of PDE4 inhibitors on SCs myelination phenotype, in a regenerative and hyperglycemia setting. Building on a PN regeneration *in vitro* model previously described in chapters 3¹⁷ and 4, we used the 3D SC-seeded scaffold to build an analogue of bands of Büngner, and tested the effect of the PDE4 inhibitors, ROFLU (5 and 10 μ M) and BPN (1 and 5 μ M), on the SC myelination phenotype. We discovered that ROFLU treatment promoted a significant upregulation of the myelin genes (MBP, MAG and PLP) and the transcription factor SOX10, whilst BPN administration had a low impact on SC gene expression. However, at the protein level, we detected the opposite, with the BPN-treatment leading to the highest MBP production. Co-cultures with iPSCs-derived neurons resulted in myelinated cultures after 14 and 21 days, with no statistical significant differences between conditions (using the current metrics). To build a hyperglycemia *in vitro* model, we differentiated SCs on 2D laminin-coated surfaces and exposed them to high glucose culture conditions (30 and 45 mM glucose). ROFLU (10 μ M) was supplemented to the cultures to investigate potential cell protective properties. Even in a hyperglycemic environment, ROFLU was able to enhance the SCs myelination phenotype. After return to normoglycemic levels, ROFLU-treated SCs exhibited repair characteristics such as high cJUN expression, but also high expression of MBP and PLP.

The PDE4 inhibitors here tested showed promising results in the context of PN regeneration, after injury or disease. The use of 3D *in vitro* models for such investigations provides a useful research tool to screen different formulations/doses and assess their biological effects with great ease. Further in-depth analysis of PDE4 inhibitors action may result in the discovery of new therapies for current untreatable maladies.

Materials and Methods

Scaffold fabrication and sterilization

The scaffolds were made via an electrospinning (ESP) process with a house-built system. The first step was the production of a release layer by electro spraying a solution of 50% polyethyleneoxide (PEO, Mn = 3350, Sigma-Aldrich) in Milli-Q onto aluminum foil. For this, the solution flowed through a 0.8 mm inner diameter stainless steel needle (Unimed S.A.) at 2 ml/h, while at 20 kV and at a distance of 10 cm from a 60 mm diameter mandrel rotating at 5000 rpm. Afterwards, a nonwoven polyurethane mesh (6691 LL (40 g/m²), a kind gift from Lantor B.V., The Netherlands) was prepared by punching an array of 12 mm circular holes and placed on the mandrel, covering the PEO sprayed-foil. We then produced the scaffolds by ESP of 300PEOT55PBT45 (PolyVation) in 75:25 Chloroform/1,1,3,3-hexafluoroisopropanol solution onto the mesh support structure. For this, the solution flowed through a 0.5 mm inner diameter stainless steel needle (Unimed S.A.) at 0.75 ml/h, while applying a voltage of 12 kV and at a distance of 10 cm from a rotating mandrel (at 5000 rpm). During both processes, the humidity remained at 35-40% and the temperature at 22-24°C. Finally, we generated individual scaffolds from the polyurethane mesh by punching 15 mm-outer diameter sections concentric to the 12 mm holes, resulting in a thin ESP membrane supported by a polyurethane mesh ring. To detach the scaffolds, these were immersed in deionized water and left in phosphate buffered saline (PBS) until further use. When required for cell seeding, the scaffolds were transferred to a 24 well plate and immersed in 70% ethanol for sterilization during 1-2 h, followed by repeated PBS washes and air-drying. These were then maintained in sterile PBS until requested.

Agarose microwell platform fabrication

A 3% (w/v) sterile agarose (Thermo Fisher Scientific) solution was prepared in PBS. 8 ml of agarose solution were poured onto an in-house fabricated PDMS stamp with the negative template of 1580 microwells with 400 µm diameter. Centrifugation at 845 g was performed to remove air bubbles, followed by chilling for 45 min at 4°C for agarose solidification. When solid, the agarose blocks were removed, cut to fit in a 12 well-plate, washed with 70% ethanol, then washed twice in phosphate buffered saline (PBS) solution and left at 4°C until further use. The

day before cell seeding, PBS was replaced with culture media containing Advanced RPMI 1640 supplemented with 1X glutamax (Thermo Fisher Scientific) and kept in the incubator at 37°C, 5% CO₂ overnight.

Primary Schwann Cells harvesting, purification and culture

Primary Schwann cells (SCs) were harvested from the sciatic nerves of neonatal Wistar rat pups, following local and Dutch animal use guidelines. Nerve segments were extracted and digested, followed by cell isolation and purification as described by Kaewkhaw et al.¹⁸ Briefly, the collected nerves were sliced and digested in a 0.05% (wt/vol) collagenase solution for 60 min at 37°C, 5% CO₂. The cell suspension was filtered through a 40 µm cell strainer, centrifuged for 6 min at 400 g, followed by supernatant removal and cell pellet washing with DMEM containing 10% fetal bovine serum (FBS) and 100 U/ml penicillin and 100 µg/ml streptomycin. Cells were centrifuged again at 400 g for 6 min and the supernatant discarded. Finally, cells were re-suspended with 2 ml of Schwann cell proliferation and purification medium, composed of DMEM D-valine (Cell Culture Technologies), 2 mM L-glutamine, 10% (v/v) foetal bovine serum (FBS), 1x N2 supplement (R&D Systems), 20 µg/ml bovine pituitary extract, 5 µM forskolin, 100 U/ml penicillin and 100 µg/ml streptomycin, and 0.25 µg/ml amphotericin B (all Sigma-Aldrich), then plated on 35 mm petri dish pre-coated with 0.01% (v/v) poly-L-lysine (Sigma –Aldrich) and 1 µg/ml laminin (R&D systems) and incubated at 37°C, 5% CO₂. The use of D-valine in place of L-valine serves to inhibit fibroblast growth while permitting SCs survival and proliferation. 1 ml of fresh medium was added at day 7 of culture and subsequently changed every 2 days until confluency. Cells were used between passage number 3 and 6 (P3-P6).

iPSCs culture

Human iPSC line LUMC0031iCTRL08 (Provided by the LUMC iPSC core facility) was cultured on Geltrex coated dishes at a density of 10 x 10³/cm² in mTESR1 medium (Stem Cell Technology). Cells were fed every alternate day with completely fresh medium and passaged weekly using Accutase (Stem Cell Technology). Upon splitting, cells were cultured in mTESR1 medium supplement with 10 µM of Y-27632 (Tocris) for 24 h and replaced with mTESR1 medium for further maintenance.

iPSCs differentiation into nociceptive neurons and neurosphere formation

In order to induce iPSCs differentiation into nociceptors, we adapted and modified the protocol published by Chambers et al. Nociceptor induction was initiated using single cell suspension of undifferentiated iPSCs detached with accutase, followed by seeding of 200 cells/microwell in mTESR1 medium supplemented with 10 µM of Y-27632 and 0.5% Geltrex

(in solution) onto 400 µm agarose microwells. Cell suspension was forced to settle by centrifugation at 290 g for 2 min. Afterwards, cells were incubated for 24 h and were given a complete media change with mTESR1 medium. At this time, the cellular spheroid is formed and cell synchronization is initiated by the addition of mTESR1 medium supplemented with 1% dimethyl sulfoxide (DMSO). The cells were maintained for 72 h in the synchronization medium. Post synchronization cells were given a PBS wash and nociceptor induction was initiated by addition of dual SMAD inhibition media containing Advanced RPMI 1640 supplemented with Glutamax (both Thermo Fisher Scientific), 100 nM LDN-193189 (Tocris) and 10 µM SB431542 (Tocris). The spheres were maintained for 48 h in the dual SMAD inhibition media. Following this, neural crest commitment was induced via media containing Advanced RPMI 1640 supplemented with Glutamax, 3 µM CHIR99021 (Tocris) and 1 µM retinoic acid (Tocris). The spheres were maintained in the neural crest induction media for 5 days with media change every alternate day. Following this stage, the spheres were incubated in notch inhibition media, consisting of Advanced RPMI supplemented with Glutamax, 10 µM SU5402 (Tocris) and 10 µM DAPT (Tocris), for 48 h.

Finally, the neurospheres, composed of trunk neural crest cells, were collected and seeded on coverslips or scaffolds. In these substrates, cells were cultured in neural maturation medium for at least 5 days to reach the nociceptor phenotype. The neural medium was composed of Neurobasal Medium, 0.5 mM Glutamax, 100 U/ml penicillin and 100 µg/ml streptomycin (all Thermo Fisher Scientific), 100 ng/ml human nerve growth factor (NGF), 50 µg/ml ascorbic acid (all Sigma-Aldrich), 25 ng/ml human neuregulin-1 type III (NRG-1 SMDF) and N21 supplement (both from R&D systems).

SCs culture on scaffolds

SCs were seeded on scaffolds at a density of 100×10^3 cells per scaffold and cultured for 7 days in SC proliferation medium, at 37°C, 5% CO₂. This medium was composed of high glucose DMEM, 4 mM L-glutamine, 100 U/ml penicillin and 100 µg/ml streptomycin (all Thermo Fisher Scientific), 10% (v/v) FBS, 20 µg/ml bovine pituitary extract, 5 µM forskolin (all Sigma-Aldrich) and 1x N2 supplement (R&D Systems). At day 7 of culture, the medium was changed to SC proliferation medium containing either DMSO (0.1% v/v), ROFLU (at 5 or 10 µM in DMSO) or BPN14770 (BPN, at 1 or 5 µM in DMSO). The cells were cultured for 7 more days, at 37°C, 5% CO₂, with medium refreshments every other day.

iPSCs / SCs co-culture on scaffolds

SCs were seeded on the scaffolds and cultured with the PDE4 inhibitors as described above. For this experiment we used only SCs exposed to DMSO (control; 0.1% v/v); ROFLU (at 10 µM) and BPN (at 5 µM). At day 14 of culture in the scaffolds, the PDE4 inhibitors were removed and replaced with neural medium, composed of Neurobasal Medium, 0.5 mM

Glutamax, 100 U/ml penicillin and 100 µg/ml streptomycin (all Thermo Fisher Scientific), 100 ng/ml human nerve growth factor (NGF), 50 µg/ml ascorbic acid (all Sigma-Aldrich), 25 ng/ml human neuregulin-1 type III (NRG-1 SMDF) and N21 supplement (both from R&D systems). At this stage, iPSCs-derived neurospheres were collected from agarose molds and seeded on the scaffolds (one neurosphere per scaffold) and culture continued until day 21.

2D SCs culture and hyperglycemia model

SCs were seeded at 25×10^3 cells/cm² on glass coverslips (12 mm) or tissue culture treated 24-well plates, both pre-coated with 1 µg/ml laminin-1 (R&D systems) and 2 µg/ml poly-D-lysine (Sigma Aldrich) the day before and incubated overnight at 37°C, 5% CO₂. The seeding medium was composed by DMEM low glucose with 10% FBS (v/v). After 24 h of culture, the medium was changed to serum deprivation medium composed by DMEM low glucose with 1% FBS (v/v). After 24 h, the medium was changed to differentiation medium that contained DMEM low glucose with 1 % FBS (v/v) and 250 µM of 8-(4-Chlorophenylthio)adenosine 3',5'-cyclic monophosphate sodium salt (cAMP, Sigma-Aldrich, C3912) diluted in H₂O. Cells were cultured in these conditions for 3 days, then evaluated for the first time point (identical medium but lacking cAMP was used as control). For the de-differentiation experiments, the cells were cultured in the referred conditions until the first time point, then the medium was changed to hyperglycemia medium composed of DMEM low-glucose supplemented with either 30 or 45 mM D-glucose (Sigma-Aldrich, G8270), 1% FBS (v/v), 250 µM cAMP and PDE4 inhibitors (ROFLU at 10 µM; BPN at 5 µM) or DMSO (0.1% v/v). Control medium was composed of DMEM low-glucose, 1% FBS (v/v), 250 µM cAMP and DMSO (0.1% v/v). The cells were cultured for 7 days, with medium changes every other day. After this period, the cells were analysed or maintained in culture with re-differentiation medium. This medium was composed by DMEM low-glucose, 1% FBS (v/v), 250 µM cAMP and supplemented with either ROFLU (at 10 µM), BPN (at 5 µM) or DMSO. The cells were cultured for additional 7 days, until the final timepoint, with medium changes every other day. Control medium was composed of DMEM low-glucose, 1% FBS (v/v), 250 µM cAMP and DMSO (0.1% v/v).

Quantitative polymerase chain reaction (qPCR)

Total RNA was isolated from primary rat SCs (n = 5) using Qiazol reagent (Qiagen), before cDNA synthesis using the qScript cDNA synthesis kit (Quanta) according to the manufacturer's instructions. Gene expression analysis was performed using a StepOnePlus detection system (Applied Biosystems). The reaction mixture consisted of SYBR Green master mix (Applied Biosystems), 10 µM forward and reverse primers, nuclease free water and cDNA template (5 ng/µl), up to a total reaction volume of 10 µl. The primer pairs used for amplification are listed below (table 1). Results were analyzed by the comparative Ct method and were normalized to the most stable housekeeping genes, determined by Genorm.

	FORWARD SEQUENCE (5'-3')	REVERSE SEQUENCE (5'-3')
Sox10	GCACGCAGAAAGTTAGCC	TGTCACTCTCGTTCAGCAAC
PLP	TCTGCAAAACAGCCGAGTTC	TGGCAGCAATCATGAAGGTG
cJUN	TCCACGGCCACGGCCAACATGCT	CCACTGTTAACGTGGTTCATGAC
MAG	GCTACAACCAGTACACCTTCTC	TGACCTCTACTTCCGTTCTG
MBP	ACGCGCATCTTGTTAATCCG	AAGTTTCGTCCCTGCGTTTC
Krox20	GCCCCTTTGACCAGATGAAC	GGAGAATTTGCCCATGTAAGTG
BCL2	ATCGTCTGTGGATGACTGAGTAC	AGAGACAGCCAGGAGAAATCAAAC
Bax	CCAGGACGCATCCACCAAGAAGC	TGCCACACGGAAGAAGACCTCTCG
YWHAZ	GATGAAGCCATTGCTGAACTTG	GTCTCCTTGGGTATCCGATGTC
ACTB	TGTCACCAACTGGGACGATA	GGGGTGTGAAGGTCTCAA

Table 1 –Rat primers for qPCR.

Western blot

Cells were lysed with RIPA buffer (150 mM sodium chloride, 1% Triton X-100, 5% sodium deoxycholate, 0.1% SDS, 50 mM Tris, pH 8.0, containing 10 µl/ml protease and phosphatase inhibitor) and pooled (n = 8) onto a 15 ml falcon tube that was immediately placed at -80°C. After that, the samples were separated with SDS-PAGE and the proteins transferred onto a PVDF membrane, which was subsequently blocked (5% non-fat dry milk, Tris-buffered saline with 0.1% Tween-20) for 1 h at room temperature. The membranes were incubated with primary antibody overnight at 4°C. The used antibody was 1:500 rat anti-MBP (MAB386 Millipore, USA). For normalization, 1:1000 mouse anti-β-actin was (Santa Cruz Biotechnology, USA) used. The membranes were washed with TBS and TBS-Tween, and subsequently incubated with secondary antibody for 1 h at room temperature: 1:2000 Rabbit anti-rat (DAKO, Belgium), and 1:2000 Rabbit anti-mouse (DAKO, Belgium). Membranes were washed in TBS and TBS-Tween and bands were visualized using the ECL Plus detection kit (Thermo Fisher Scientific, Belgium) and the generated chemiluminescent signal was detected by a luminescent image analyzer (ImageQuant LAS 4000 mini; GE Healthcare, Belgium). ImageJ (<http://imagej.nih.gov/ij/>) was used to quantify the protein bands intensity. The measured intensity was corrected for background signals.

Immunostaining

Samples were fixed with 4% paraformaldehyde (PFA) for 20 min at room temperature (RT), rinsed thoroughly with PBS, and left in PBS until further use. Permeabilization was

carried for 30 min at RT with 0.1% Triton X-100 in PBS, followed by rinsing with PBS and blocking with blocking buffer composed of 5% goat serum, 0.05% Tween-20, and 1% bovine serum albumin (BSA) in PBS for overnight at 4°C, under mild agitation. Afterwards, samples were incubated overnight at 4°C with primary antibody solutions in blocking buffer. The next day, the samples were washed with a wash buffer composed of 0.05% Tween20 and 1% BSA in PBS and incubated for 2 hr at RT with secondary antibody solutions in wash buffer. Following this, we rinsed the samples with PBS, stained with DAPI (0.2 µg/ml) for 10 min at RT, and left them in PBS until imaging.

The primary antibodies used were the following: anti-βIII tubulin (Sigma-Aldrich, T8578, 1:500), anti-myelin basic protein, MBP (Thermo Fisher Scientific, PA1-46447, 1:50) and anti-myelin associated glycoprotein, MAG (Abcam, ab89780, 1:100), anti-oligodendrocyte marker 1, O1 (Novus Biologicals, MAB1327, 1:100), anti-Krox20 (Sigma-Aldrich, ABE1374, 1:100), anti-cJun (Cell Signaling Technologies, 9165S, 1:300), anti-p75 (Alomone Labs, ANT-007, 1:50). The used secondary antibodies were the following: goat anti-mouse conjugated with Alexa Fluor 488; goat anti-mouse conjugated with Alexa Fluor 568 and goat anti-rabbit conjugated with Alexa Fluor 568 (all used at 1:1000).

Microscopy and image analysis

Images were acquired using either an inverted epifluorescence microscope (Nikon Eclipse Ti-e) or a confocal laser scanning microscope (Leica TCS SP8) and prepared and analysed using Fiji software (<https://fiji.sc/>). To quantify marker expression in 2D samples (coverslips and well-plates) and 3D scaffolds, we measured the mean signal intensity of each marker and divided this value by the total number of cells in the image. Cell count was performed using the standard Analyze Particles function to DAPI⁺ objects. For this experiment, we took at least 10 images per sample, and 5 replicates per conditions. To quantify protein presence in the western blot experiment, we first measured the intensity of the background (average of multiple spots). Then, histograms were acquired to quantify the pixels, their intensity and crossproduct of both. Only crossproducts that exceeded the background were registered and the sum of crossproducts is taken. The same was done for β-actin. Finally, MBP crossproduct was divided by β-actin crossproduct and the results expressed relative to control. To measure the axonal area, we first converted images of βIII tubulin⁺ cells to binary images and measured the pixel area occupied by the neurites, excluding cell bodies. Then, we divided this value by the total area of the scaffold. For the myelination area, we measured the pixel area of MBP⁺ segments and divided this value by the area of the scaffold. The myelination ratio was obtained by dividing the total myelin area by the corresponding total axonal area. To measure the neurite length, we used the Simple Neurite Tracer plugin (<https://imagej.net/SNT>) and measured the distance between the cell bodies and the edge of the respective axons.

Statistics

We have generated the graphs and analyzed the data using the software GraphPad Prism. Bar graphs are shown as mean \pm standard error mean (SEM). Statistical significances were determined employing an one-way analysis of variance (ANOVA) followed by a Tukey's honestly significant difference (HSD) post-hoc test or a two-way ANOVA followed by Sidak's multiple comparison test (* $p < 0.05$, ** $p < 0.01$, *** $p < 0.005$, **** $p < 0.0001$ and ns is $p > 0.05$). In the first part (3D remyelination model) the comparisons are done relative to the DMSO control. In the second part (2D hyperglycemia model) the comparisons are done relatively to low-glucose controls (shown as control in the graphs).

Results

Fabrication of a 3D regeneration model and influence of PDE4 inhibitors on SCs myelination phenotype

To build a model that replicates the initial stages of PN regeneration, we applied the same strategy followed in chapter 3. Briefly, primary rat SCs were seeded onto an electrospun scaffold (100×10^3 cells/scaffold), composed of aligned and ultrathin PEOT/PBT fibers (fig. S1A). The cells were left to proliferate and align with the scaffold, over the course of 7 days, while in SC proliferation medium. After this period, the scaffold was fully covered with highly anisotropic SC bands (fig. S1B). To evaluate the influence of PDE4 inhibitors on SC myelination phenotype, we cultured the cells for additional 7 days in SC proliferation medium supplemented with either ROFLU (5 or 10 μM), BPN (1 or 5 μM), or DMSO (vehicle control) (fig. 1A). At this time point, we could detect a contribution of PDE4 inhibitors supplementation to the acquisition of a myelinated phenotype, at both gene (fig. 1B) and protein level (fig. 2). The chosen set of genes for analysis comprised myelin basic protein (MBP), which encodes for a major constituent of the central and peripheral myelin sheath¹⁹; myelin-associated glycoprotein (MAG), encoding for a transmembrane protein that mediates axonal adhesion⁸; myelin proteolipid protein (PLP), a gene expressed by SCs but whose protein is not incorporated in the myelin sheath²⁰; and SOX10, a gene encoding for the transcription factor that directs differentiation from neural crest cells towards SCs²¹. ROFLU addition promoted a significant upregulation of all these genes compared to control samples. Particularly for MBP expression, this increase was of 6.4-fold ($p < 0.01$) and 9.17-fold ($p < 0.0001$), for ROFLU at 5 and 10 μM , respectively. For MAG expression, ROFLU addition led to an increase of 2.6-fold ($p < 0.001$) when at 5 μM , and 2.1-fold ($p < 0.05$) when at 10 μM . PLP expression was similar in both ROFLU concentrations, showing 3.5-fold increase ($p < 0.0001$) compared to control samples. Finally, for SOX10, ROFLU supplementation at 5 μM led to 3.0-fold expression increase, while at 10 μM the increase was of 2.2-fold. In general, BPN also promoted an

increase in the expression of these genes. However, only PLP was significantly ($p < 0.05$) upregulated compared to control, and for 5 μM in particular.

Because the SC proliferation medium contains forskolin, a chemical that enhances intracellular levels of cAMP, we evaluated the influence of its addition on the SCs phenotype, as well as eventual synergies with the PDE4 inhibitors. For this experiment, we selected only one concentration for each PDE4 inhibitor (for simplicity reasons), using ROFLU at 10 μM and BPN at 5 μM , again with DMSO only as control (fig. S2). Besides the previously tested genes (MBP, MAG, PLP and SOX10), we also evaluated the expression of c-Jun, a transcription factor controlling the activation of SCs repair phenotype²²; BCL2, an apoptosis inhibitor²³; and Krox20, a transcription factor controlling SCs myelinating phenotype²⁴. The myelin-related genes — MBP, MAG and PLP — all showed a significant higher expression in samples cultured with forskolin compared to those without. The only exception was for MBP, which presented equal transcript expression when supplemented with BPN, regardless of forskolin presence. In DMSO only samples, the individual contribution of forskolin could be better appreciated and it was clear that its presence alone had a large influence, by dramatically enhancing MBP ($p < 0.001$), MAG ($p < 0.0001$) and PLP ($p < 0.0001$) expression. Still, gene expression was further increased when forskolin+ cultures were co-added with PDE4 inhibitors instead, particularly with ROFLU. In cultures without forskolin, the influence of PDE4 inhibitors was less noticeable, and only BPN could significantly ($p < 0.05$) enhance MBP expression compared to DMSO control. The transcription factor genes, c-Jun and Krox20, and the apoptosis regulator gene BCL2, showed a similar pattern of expression regardless of forskolin presence, with ROFLU promoting a small but not significant increment. Finally, SOX10 expression was greatly improved by forskolin presence, but only when co-added with ROFLU ($p < 0.0001$) and BPN ($p < 0.05$).

In regard to myelin proteins production, namely MAG and MBP, there was also a generalized increment due to PDE4 inhibitors. ROFLU and BPN, at both tested concentrations, induced a stronger MAG and MBP expression on the 3D SCs bands, compared to DMSO control (fig. 2A). This expression was quantified and normalized to the total cell number (fig. 2B), which showed that BPN at 5 μM led to an expression of MAG ($p < 0.0001$) and MBP ($p < 0.01$) twice as large as control samples. To further validate these results, we collected and quantified the amount of produced MBP via western blot and verified that all PDE4 inhibitors led to a higher production of this protein compared to DMSO cultures (fig. 2C and 2D).

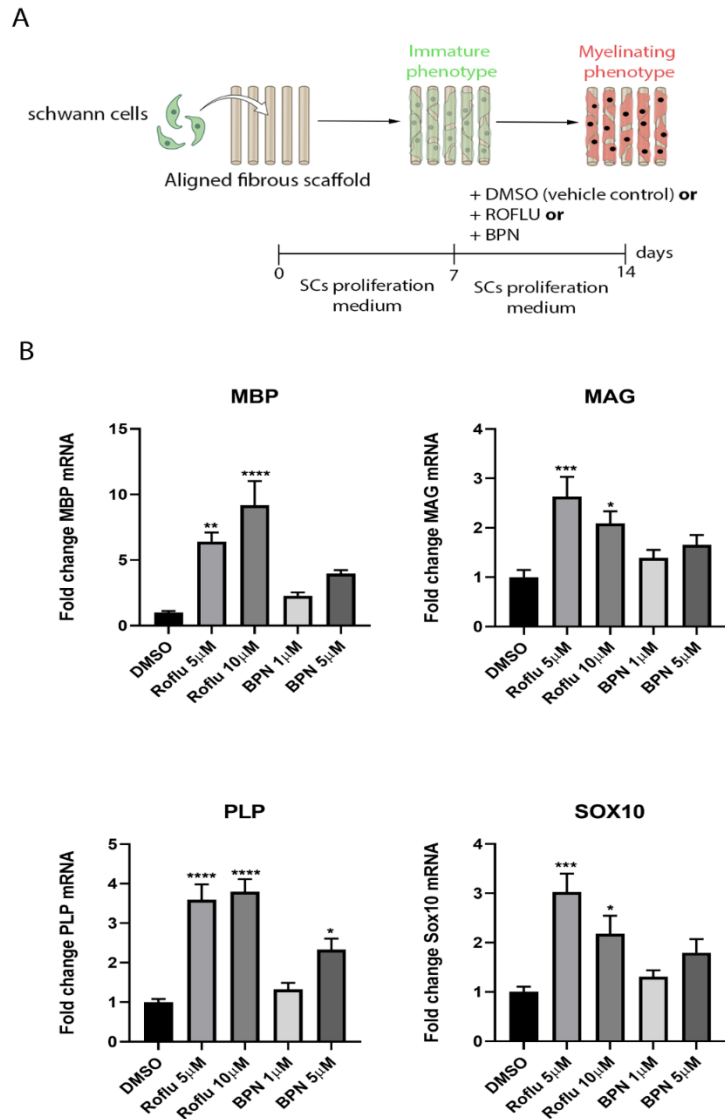


Figure 1. A) Illustration of the strategy followed to generate the SCs regeneration bands. SCs are seeded on aligned fibrous scaffold (100×10^3 cells per scaffold) and cultured for 7 days in proliferation medium. After this, the medium is changed to proliferation medium containing ROFLU (at 5 or 10 μM), BPN (at 1 or 5 μM) or DMSO (vehicle control at 0.1% v/v) and cultured for additional 7 days. B) SC gene expression after culture with ROFLU, BPN or DMSO. Supplementation with ROFLU, at 5 or 10 μM , significantly upregulates the expression of MBP, MAG, PLP and SOX10 compared to DMSO control. BPN supplementation promotes a small but not significant gene upregulation, except for PLP, when at 5 μM . Transcript expression level is normalized to DMSO values. This experiment was performed twice, using five replicates per condition. Bar graphs represent mean \pm SEM. Statistics were performed using one-way ANOVA followed by Tukey's HSD post-hoc test where **** $p < 0.0001$, *** $p < 0.001$, ** $p < 0.01$ and * $p < 0.05$. Illustration was designed with biorender (<https://biorender.com/>).

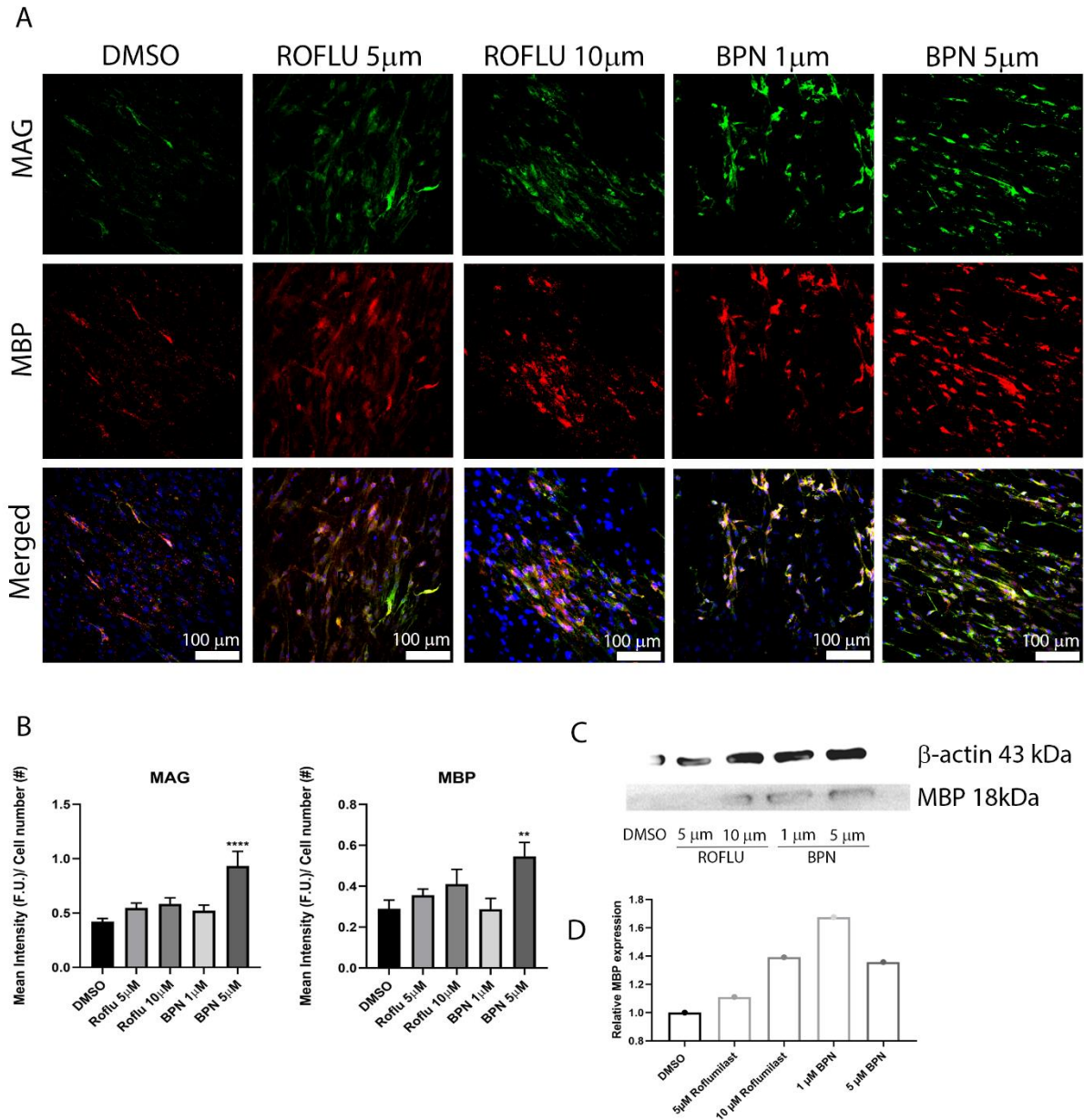


Figure 2. Expression of myelin proteins on SCs regeneration bands after culture with DMSO, ROFLU or BPN. A) Immunostaining of MAG (top row, green) and MBP (middle row, red) on the SCs bands after culture with the PDE4 inhibitors. The bottom row shows the merged channels, where DAPI is shown in blue and scale bars are 100 μ m. The expression of MAG and MBP was higher in the conditions supplemented with the PDE4 inhibitors compared to control, particularly for BPN at 5 μ M. B) Quantification of the immunostaining images, confirming a significantly higher expression of MAG and MBP in cultures with added BPN (at 5 μ M), compared to control. This quantification was performed by dividing the mean signal intensity of MAG⁺ or MBP⁺ cells by the total number of cells in the image (DAPI count). This experiment was performed twice, using at least five replicates per condition. For imaging analysis, at least five images were taken per sample. Bar graphs represent mean \pm SEM.

Statistics were performed using one-way ANOVA followed by Tukey's HSD post-hoc test where **** $p < 0.0001$, *** $p < 0.001$, ** $p < 0.01$ and * $p < 0.05$. C) Western blot analysis of MBP and β -actin. D) Quantification of band signal intensity, showing higher MBP production in cultures supplemented with ROFLU and BPN compared to control. This experiment was performed twice using 8 pooled replicates per condition.

Co-culture of iPSCs-derived neurospheres with SCs in a 3D myelination model

After discovering a positive influence of PDE4 inhibitors on SC myelination phenotype, at both gene and protein level, we proceeded to investigate if that would translate to higher myelination capacity of co-cultured iPSCs-derived neurons. To test this, we followed the same protocol described in fig. 1A to generate 3D SCs bands cultured with PDE4 inhibitors, in particular ROFLU at 10 μ M, BPN at 5 μ M or DMSO only. At day 14, we added the iPSCs-derived neuron spheroid, generated via the method described in chapter 4, and maintained the co-cultures for additional 14 or 21 days in neural medium (same for all conditions and absent of PDE4 inhibitors). All conditions promoted a dense and long neurite outgrowth from the cluster region, in a highly aligned fashion that resembled the native peripheral nerve tissue architecture (fig. 3A). At the end of the culture period, a high number of neurites were fully covered with a myelin sheath, evidencing proper nerve tissue maturation (better visible in fig. S4) and displayed an average length of $4165.9 \pm 700.9 \mu\text{m}$ for DMSO, $4381.1 \pm 385.0 \mu\text{m}$ for ROFLU and $4532.4 \pm 938.6 \mu\text{m}$ for BPN. To further quantify nerve tissue formation, we analysed the axonal area, myelin area and myelination ratio (obtained from the ratio of the first two). After 14 days of culture, ROFLU scaffolds contained the highest axonal area ($0.68 \pm 0.24\%$) and consequently myelination area ($0.30 \pm 0.14\%$) compared to DMSO ($0.23 \pm 0.02\%$ axonal area and $0.07 \pm 0.01\%$ myelination area) and BPN ($0.17 \pm 0.03\%$ axonal area and $0.08 \pm 0.02\%$ myelination area) scaffolds (fig. S3A and S3B). In terms of myelination ratio, all conditions presented similar results with actually BPN scaffolds containing the highest ratios ($48.47 \pm 6.83\%$), followed by ROFLU ($38.43 \pm 7.47\%$) and DMSO ($31.3 \pm 3.648\%$) scaffolds (fig. S3C). After 21 days of culture, the same trend continued with ROFLU supplemented cultures presenting the highest axonal area ($4.12 \pm 0.94\%$) and myelination area ($2.84 \pm 0.58\%$). BPN added samples led to the second highest values, with $3.15 \pm 0.33\%$ of axonal area and $1.17 \pm 0.31\%$ of myelination area and finally DMSO only scaffolds produced an axonal area of $2.47 \pm 0.69\%$ and a myelination area of $1.16 \pm 0.52\%$ (fig. 3B and 3C). Myelination ratio analysis showed that ROFLU samples led to highest values ($72.47 \pm 5.03\%$), however not significantly different than BPN ($53.24 \pm 5.07\%$) and DMSO ($70.04 \pm 8.98\%$) cultures (fig. 3D).

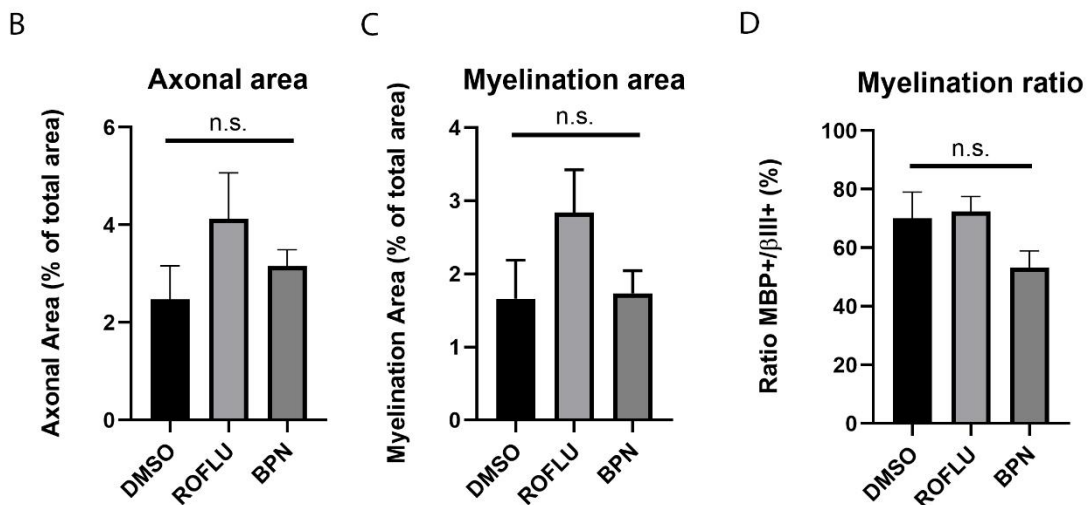
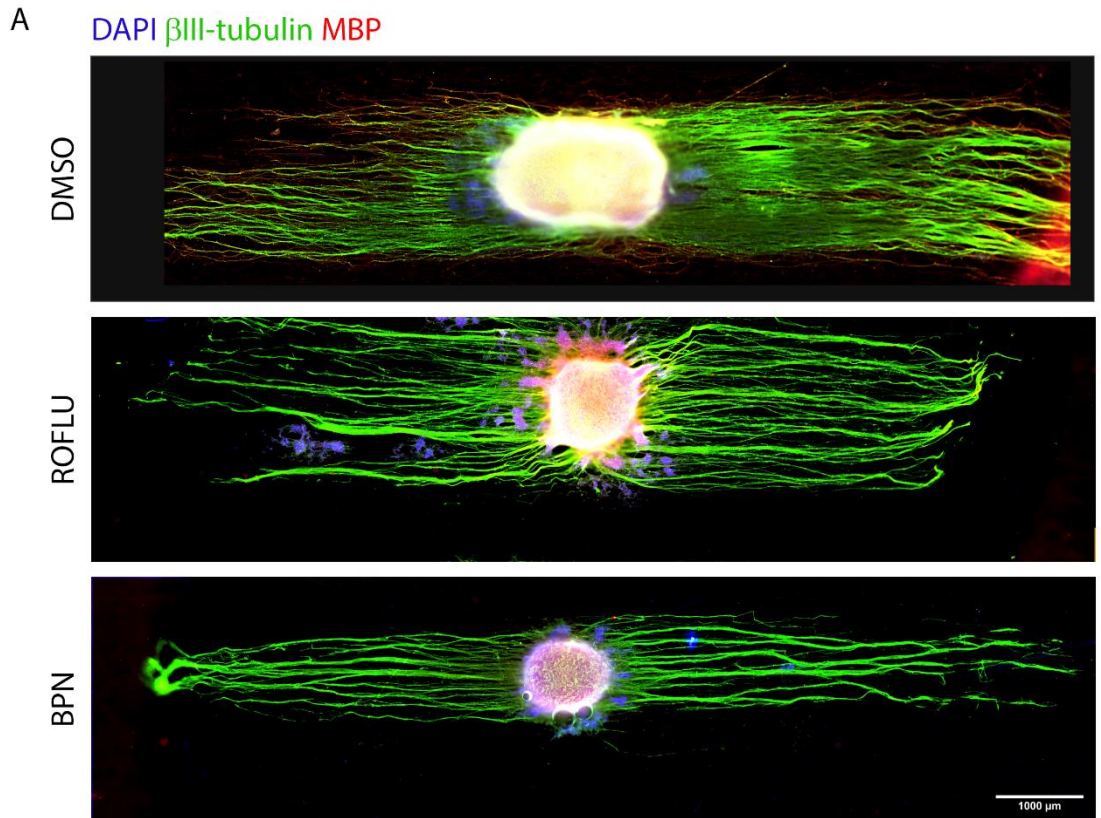


Figure 3. 3D scaffold co-culture of SCs and iPSCs-derived neurons for 21 days. Prior to neuron seeding, SCs (100×10^3 cells/ scaffold) were cultured initially in SC proliferation medium (for 7 days) and then on SC proliferation medium with either ROFLU ($10 \mu\text{M}$, middle image), BPN ($5 \mu\text{M}$, bottom image) or DMSO (control, 0.1% v/v, top image) for extra 7 days. A) Immunostaining micrographs of β III-tubulin (green), MBP (red) and DAPI (blue), showing the neurite outgrowth and myelination of iPSCs-derived neurons. Scale bar is $1000 \mu\text{m}$. B), C) and D): Quantification of the axonal area (B), myelination area (C) and myelination ratio (D) from the 3D co-cultures. Axonal area was determined by the ratio of β III-tubulin⁺ segment area (excluding cell body area) with the total scaffold area. Myelination area was determined by the

ratio of MBP⁺ segment area (excluding cell body area) with the total scaffold area. Myelination ratio was calculated from the ratio of MBP⁺ with β III-tubulin⁺ segments on the same image. This experiment was performed twice with 5 replicates per condition. For the image analysis we took one image per sample, capturing the whole tissue. Statistics were done using one-way ANOVA followed by Tukey's post-hoc test. The note n.s. means not significant.

SCs differentiation into a myelinating phenotype

To test a potential protecting role of PDE4 inhibitors on SCs cultured under hyperglycemic conditions, we devised a 2D hyperglycemia model that allows to easily screen the SCs phenotype under different circumstances (fig. 4A). To build this model, we seeded the SCs (25×10^3 cells/cm²) on laminin-coated surfaces (glass coverslips or tissue treated well-plates) and after 24 h we deprived the cells of serum (reduced from 10% to 1 %) in order to arrest the cell cycle and induce cell synchronization²⁵. After that, we induced SCs differentiation into a myelinating phenotype by exposing cells to a culture medium containing a cell membrane permeable cAMP analog. cAMP elevation correlates with a SCs shift to a myelination phenotype and *in vitro* reports show that exogenous cAMP supplementation is a robust promoter of this phenotype switch^{10,26}. After 3 days of culture with cAMP (at 250 μ M), we noticed a dramatic shift in SCs morphology and phenotype. Regarding cell morphology, SCs exposed to cAMP adopted a flattened shape with a large cytoplasmic-to-nuclei ratio, while SCs in control conditions remained elongated with a low cytoplasmic-to-nuclei ratio (fig. 4B).

Quantification of cell area showed that cAMP-treated SCs enlarged to over 5 times the area of control SCs ($p < 0.05$, fig. 4C). Gene expression analysis (fig. 4D) revealed that the cAMP treatment induced a dramatic upregulation of Krox20 to 16-fold ($p < 0.001$) compared control, whereas cJUN expression was 3-fold lower ($p < 0.0001$). The myelin gene PLP remained at similar expression levels, but MBP expression was nearly 4-fold higher ($p < 0.01$) in cAMP-treated SCs. Both SOX10 and BCL2 gene analysis showed a 5-fold ($p < 0.0001$) downregulation in differentiated cells. Protein expression was also visualized and quantified via immunostaining analysis (fig. 4E and 4F). Again, Krox20 expression is significantly increased ($p < 0.05$) in differentiated SCs, while cJUN is significantly reduced ($p < 0.05$). Despite some visual differences (fig. 4E), the overall quantification analysis of MAG, MBP, O1 (oligodendrocyte marker O1, which is associated with SCs myelinating phenotype switch¹⁰) and p75 (modulator for SC myelination and promoter of nerve regeneration²⁷) expression did not show any major discrepancies between both conditions (fig. 4F).

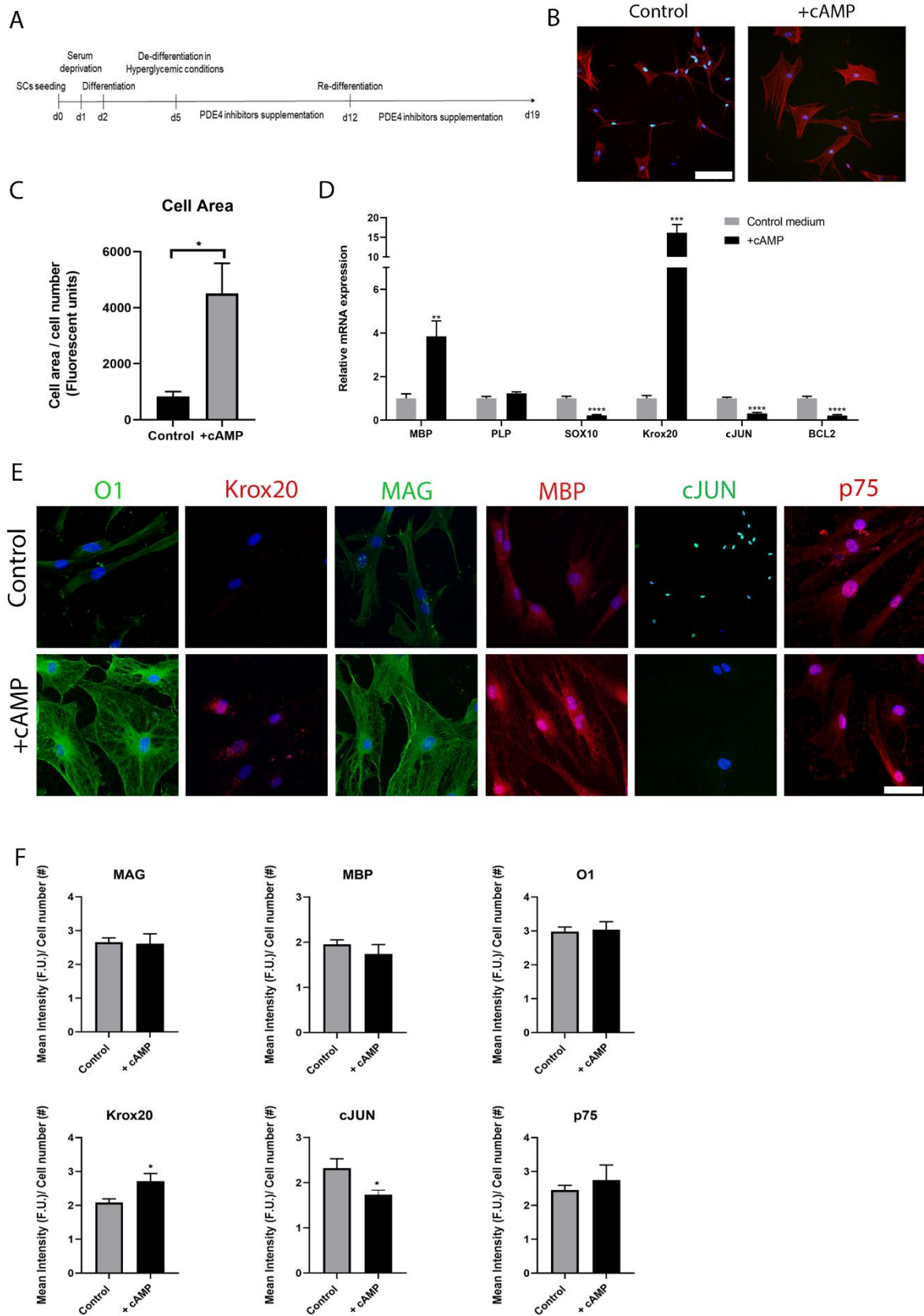


Figure 4. 2D differentiation of SCs into a myelinating phenotype. A) The designed culture protocol to create a 2D model of hyperglycemia on differentiated SCs, while testing PDE4 inhibitors action. B) SCs morphology at day 5 after culture in medium containing cAMP (right

image) or not (left image). Red is F-actin and blue is DAPI. Scale bar is 100 μm . C) Cell area measurements of day 5 differentiated SCs, showing that the cAMP treatment induces cell enlargement. The values are shown as cell area (pixel area of F-actin) divided by cell number (DAPI count). D) SC gene expression at day 5 after culture with cAMP. Control medium was absent of cAMP. Transcript expression level is normalized to control values. E) Immunostaining micrographs taken from day 5 SCs after differentiation with cAMP (top row). Control medium (bottom row) was absent of cAMP. O1, MAG and c-Jun are shown in green. Krox20, MBP and p75 are shown in red. DAPI is shown in blue. Scale bar is 50 μm . F) Respective quantification of the marker expression intensity normalized to the cell number (DAPI count). This set of experiments was performed once, using five replicates per condition. Bar graphs represent mean \pm SEM. Statistics were performed using an unpaired t-test where **** $p < 0.0001$, *** $p < 0.001$, ** $p < 0.01$ and * $p < 0.05$.

2D hyperglycemia model and PDE4 inhibitors influence on SC de-differentiation

After differentiating SCs to a myelination phenotype via cAMP exposure, we probed cell de-differentiation as a result of hyperglycemia and tested if the PDE4 inhibitor ROFLU is able to mitigate it. For this, we cultured the differentiated cells for 7 days under 30 mM or 45 mM, with ROFLU (added at 10 μM) or DMSO (at 0.1% v/v). Low glucose (5.5 mM) medium containing DMSO (0.1% v/v) was used as control (fig. 4A). Gene analysis (fig. 5A) showed that despite cJUN expression levels remaining unchanged throughout the different conditions, a reduced Krox20 expression in high glucose conditions suggests a hyperglycemia-induced SC de-differentiation. Regarding MBP, we observed an increased expression in both 45 mM glucose samples, but with a substantial upregulation to 4-fold ($p < 0.001$) in ROFLU-supplemented cultures. The other myelin gene, PLP, also showed a moderate increase ($p < 0.05$) for both 45 mM glucose conditions. Finally, SOX10 expression was dramatically enhanced due to ROFLU addition, exhibiting a 6-fold increase ($p < 0.05$) at 30 mM and a 4-fold increase at 45 mM. Contrarily, DMSO conditions showed SOX10 expression levels similar to control samples.

Phenotype analysis, via immunostaining micrograph quantification (fig. 5B), revealed that MAG and p75 expression remained unaffected in high glucose environment cultures. Similarly to gene expression, MBP presence was also significantly enhanced ($p < 0.0001$) in ROFLU-containing cultures exposed to 45 mM glucose. In contrast with Krox20 gene expression, the presence of this marker was increased in the 45 mM glucose condition, particularly in samples supplemented with ROFLU ($p < 0.001$). Finally, O1 marker presence was significantly enhanced in both ROFLU concentrations, with the highest values corresponding to the 45 mM condition.

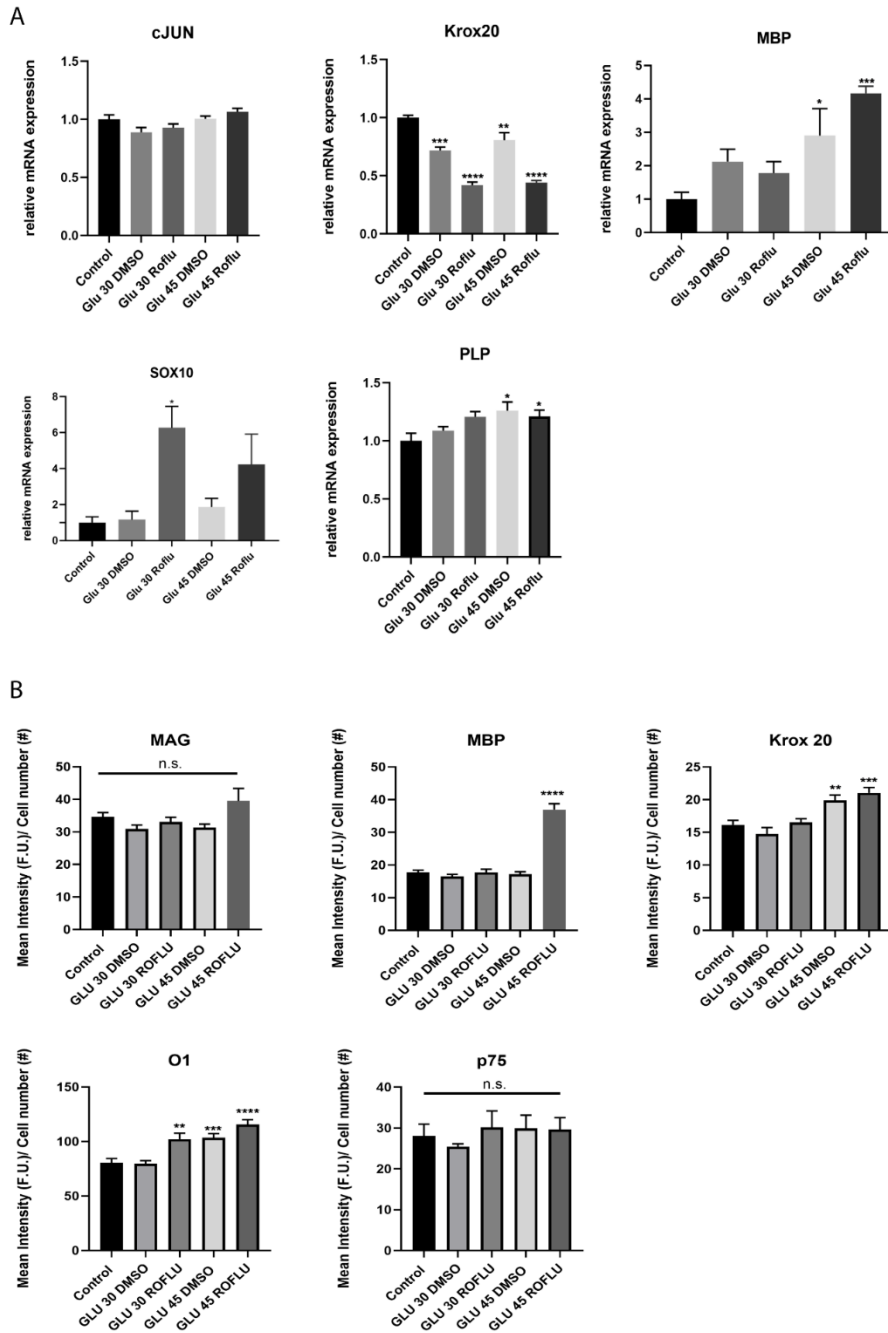


Figure 5. 2D culture of differentiated SCs in hyperglycemic conditions for 7 days, in the presence of ROFLU (at 10 μ M) or DMSO (vehicle control). Glu 30 means glucose at 30 mM and Glu 45 means glucose at 45 mM. Control medium contained 5.5 mM glucose. A) Immunostaining micrograph quantification calculated from the mean marker intensity divided by the cell number (DAPI count). B) SC gene expression level normalized to control values as determined by qPCR. This set of experiments was performed once with 5 replicates per condition. For the image analysis we took at least 8 images per sample. Statistics were done using two-way ANOVA followed by Dunnett's multiple comparisons test, where **** $p < 0.0001$, *** $p < 0.001$, ** $p < 0.01$, * $p < 0.05$ and n.s. means not significant.

SCs re-differentiation in normoglycemia

After culturing the cells in hyperglycemic medium for 7 days to induce de-differentiation, we exposed the SCs to medium containing low-glucose and ROFLU (10 μ M), for another 7 days, to investigate its influence in promoting re-differentiation (fig. 4A). Analysis to the gene profile (fig. 6A) demonstrated that the transcription factor cJUN was significantly upregulated ($p < 0.05$) in conditions pre-exposed to 45 mM glucose and treated with ROFLU, while the other conditions presented similar values to control. Krox20 gene expression showed that all hyperglycemic conditions were downregulated compared to control and that ROFLU-treated samples exhibited the lowest Krox20 expression levels. These results suggest lack of differentiation, however when analysing MBP and PLP expression we found contrary evidence. Both ROFLU treated groups presented higher (although not significant) levels of MBP expression. PLP expression was also higher in the ROFLU-treated condition, when at 30 mM, but not at 45 mM glucose. The high glucose conditions with DMSO showed lower PLP expression levels compared to control.

Regarding protein expression, the p75 marker was present in higher quantities in most hyperglycemic conditions (except for the 45 mM DMSO group), while Krox20 expression was found slightly lower, but not significantly, in these conditions. Regarding O1 expression, all groups exhibited almost equal values. The myelin marker MBP showed equal values compared to control for the 30 mM DMSO and 45 mM ROFLU group, while the other conditions showed slightly lower values. Finally, MAG expression was even increased (not significantly) in the 30 mM DMSO and 45 mM ROFLU groups, while the remaining conditions showed again expression values at a lower level than control samples.

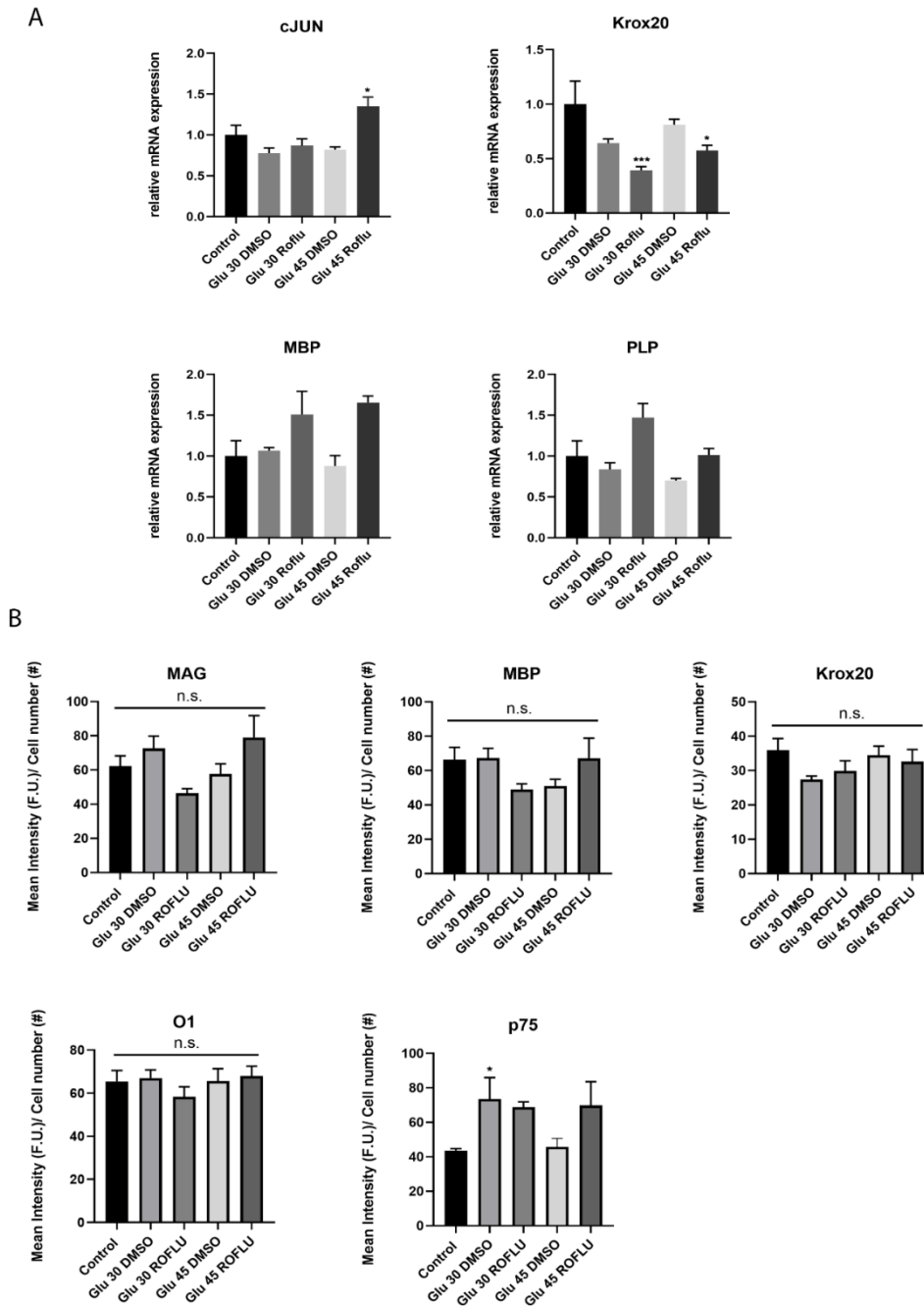


Figure 6. 2D culture of de-differentiated SCs in differentiation medium for 7 days, in the presence of ROFLU (at 10 μ M) or DMSO (vehicle control). Cells were previously cultured in hyperglycemic conditions for 7 days, where Glu 30 means glucose at 30 mM, Glu 45 means glucose at 45 mM and control refers to cells cultured in low glucose (5.5 mM) A) Immunostaining micrograph quantification calculated from the mean marker intensity divided by the cell number (DAPI count). B) SC gene expression level normalized to control values as determined by qPCR. This set of experiments was performed once with 5 replicates per condition. For the image analysis we at least 8 images per sample. Statistics were done using two-way ANOVA followed by Dunnett's multiple comparisons test, where ****p < 0.0001, ***p < 0.001, **p < 0.01, *p < 0.05 and n.s. means not significant.

Discussion

PDE4 inhibitors hold great promise as therapeutics for the treatment of several disorders. By preventing the degradative action of PDE4 enzymes, the intracellular levels of cAMP can be raised, leading to increased activation of protein kinase A (pKA), cyclic nucleotide-gated ion channels and exchange proteins directly activated by cAMP (EPAC)^{5,28}. These downstream effectors are involved in the regulation of several physiological processes, including immunomodulation, glial cell differentiation and neural regeneration^{1,12,28}. For this reason, PDE4 inhibitors have been investigated in the combat of inflammatory diseases, such as atopic dermatitis²⁹ or chronic obstructive pulmonary disease³⁰, neurodegenerative diseases, such as AD⁴ or MS⁷, and also as drugs that can enhance neural regrowth after injury (in animal models)^{2,12}. With respect to the neural tissue, most reports to date have solely focused on CNS disorders, neglecting a possible therapeutic impact of PDE4 inhibitors on PN repair. At the same time, PN physical injuries and neuropathies are common and worldwide debilitating circumstances, in need of new and improved therapies.

The goal of this project was to test the efficacy of PDE4 inhibitors in driving or maintaining the myelinating phenotype of SCs, during a repair or demyelinating pathological state (hyperglycemia), using *in vitro* models that we established in-house. In the initial stages of PN repair, SCs proliferate in high number to form the bands of Büngner, which will conduce axonal regrowth. This process is driven by cAMP, which despite a reduction from normal levels (of 8 to 10 %), is necessary for combination with the GFs in the milieu (e.g. basic fibroblast growth factor, insulin-like growth factor, neuregulin 1 etc.), to activate pKA and promote SC proliferation^{7,9,10,31}. Increased SC proliferation is associated with a phenotype switch from a mature to a repair state, promoted by c-Jun, which is expressed as the neuregulin 1/ErbB2 receptor becomes activated³². This repair programme also entails upregulation of neurotrophic factors and cell-adhesion molecules and simultaneous downregulation of myelin-related proteins^{33,34}. To simulate the formation of bands of Büngner, we cultured SCs on a microfibrillar aligned scaffold (as described on chapter 3)¹⁷, which directs SC morphology into highly aligned 3D bands, analogous to the native structures (fig. S1). To further replicate the *in vivo* process, SCs were cultured in the presence of forskolin, a cAMP elevation agent^{7,35}, whose combination with GFs contained in the serum-rich medium, promotes pKA activity and SC proliferation^{10,26}.

During PN repair, as axons regrow and regain glial contact, SCs are signalled to re-differentiate, exiting the cell cycle and assuming a premyelinating phenotype, characterized by myelin proteins upregulation and new myelin synthesis⁹. Again, this process is highly dependent on cAMP, which acts on a different downstream effector, EPAC, and in Krox-20 to drive remyelination^{9,31,36}. cAMP level regulation, necessary to trigger SCs phenotype switch, is tightly controlled by PDE4 enzymes. This can be further evidenced by the ability of rolipram to elevate cAMP levels within damaged PN tissue from a rat model⁷.

Our aim was to test the potential of the second generation PDE4 inhibitors, ROFLU and BPN, in enhancing SCs transition, after band formation, into a premyelinating phenotype (fig. 1A). We detected that ROFLU, at both tested concentrations (5 and 10 μ M), produced a significant enhancement of myelin-related genes (MAG, MBP and PLP) and SOX10 expression, causing a stronger impact than BPN supplementation (fig. 1B). However, this gene upregulation was strongly dependent on forskolin presence, as its removal led to significantly lower levels of transcript expression, especially of MAG and PLP (fig. S2). This finding suggests that PDE4 inhibition alone is not sufficient to elevate the endogenous cAMP to levels required for a fast transition to a premyelination phenotype. In the native PN, injured neurons produce cAMP as a response to the large influx of calcium and sodium ions³⁷. However, in our *in vitro* model of SCs, a cAMP promoter agent, such as forskolin, is needed to quickly raise the cAMP levels, which can then be maintained by inhibiting their degradation. Because Krox20 expression showed a similar pattern regardless of forskolin presence, with slightly higher values for the group with no forskolin, PDE4 inhibition alone may be sufficient to drive this phenotype switch, although at a slower rate than when a cAMP promoter is present.

At the protein level, we observed that BPN rather than ROFLU, led to a higher myelin protein synthesis (MAG and MBP), which demonstrates a disparity between gene expression and protein production at the observed timepoint (fig. 2). These results suggest that the tested PDE4 inhibitors trigger a different temporal response on SCs, with BPN probably leading to a quicker myelin gene upregulation, followed by protein synthesis and gene downregulation. During the same period, ROFLU treatment likely triggered a slower influence on SCs, which at chosen timepoint, were still in the first stage of response, denoted by myelin gene upregulation. Regardless of these temporal differences, it was clear that PDE4 inhibitor supplementation, and particularly in combination with forskolin, produced a visible phenotype change to a premyelinating state. To investigate if this treatment would affect myelination capacity, we co-cultured iPSCs-derived neurons with the pre-differentiated SC bands. All culture conditions resulted in the formation of long, highly aligned and myelinated neural tissue (fig. 3A and fig. S4). After 14 and 21 days, we observed that ROFLU-treated conditions promoted the highest axonal and myelin density (fig. S3 and fig. 3B). Because ROFLU-treated cells presented a high c-Jun expression (fig. S2) regardless of forskolin presence, we hypothesize that the production of neurotrophic factors by these SCs might have been increased, thus stimulating a faster axonal outgrowth. We also observed no significant difference in myelination ratio measurements between conditions, indicating that the PDE4 inhibitors did not interfere in the remyelination process, and that faster grown neural tissue as in the ROFLU group, could be equally myelinated. This can be explained by the fact that the establishment of axonal contact signals SC redifferentiation³⁸. Furthermore, the attained myelination ratio when compared to other works using primary neurons from a rat dorsal root

ganglion³⁹, exhibited similar values. Though outside of the scope of the current study, further examination at an earlier time point (e.g. day 7) may also indicate if SC pre-differentiation would improve the rate of remyelination. Furthermore, a transmission electron microscope (TEM) analysis would permit to visualize the myelin sheath diameter and compaction state to determine more accurately the maturation level of the engineered PN tissue, and verify if SC pre-differentiation results in more mature myelin. Finally, since PDE4 inhibitors were removed once the co-culture was initiated, the overall cAMP levels might have dropped, leading SCs to reduce (or partly reduce) the expression of its myelination transcript program. A continuous PDE4 inhibitor supplementation throughout all culture period would shed light on this matter.

In the second part of this work, we analysed the influence of ROFLU on SCs phenotype, when cells are cultured under hyperglycemic conditions. Hyperglycemia is one of the major physiological imbalances caused by diabetes type II that commonly leads to diabetic neuropathy^{40,41}. In a hyperglycemic situation, excess glucose is converted to sorbitol by aldose reductase, resulting in sorbitol accumulation. Due to this, increased cellular osmolarity, oxidative stress and mitochondrial dysfunction ensues, perturbing the SCs metabolism and inducing cell dedifferentiation to an immature phenotype, denoted by the halted production of myelin proteins^{14,40,42}. Due to SC dysfunction, myelin damage such as morphological aberrations, demyelination and decompaction can arise^{14,43}. In this 2D *in vitro* model, our aim was to explore if ROFLU supplementation was sufficient to preserve the myelination phenotype of hyperglycemia-exposed SCs and if it could improve the redifferentiation of glucose-damaged cells. To quickly achieve a differentiated state, we cultured SCs with a membrane-permeable cAMP analog, which has been shown to have a fast and robust effect in promoting this phenotype transition^{10,31}. As a result, cAMP-treated SCs enlarged to 5-times the size of control cells and significantly increased the expression of MBP and Krox20, while exhibiting lower expression levels of cJUN (fig. 4A-D). However, at the protein level, we did not find significant differences between treated and control cells, likely due to the short differentiation period (3 days) being insufficient to allow protein synthesis (fig. 4E and 4F).

To mimic an acute hyperglycemic state we cultured the differentiated cells with medium containing glucose at 30 and 45 mM, which are supraphysiological concentrations routinely used in *in vitro* diabetic assays that aim to recapitulate blood sugar spikes^{14,17,44}. We observed that while cJUN expression was unaffected regardless of culture conditions, evidencing an absence of injury/repair response⁸, Krox20 expression was lower in high glucose conditions, suggesting de-differentiation⁴⁵. On the other hand, the myelin genes PLP and MBP, showed a similar or even higher expression in hyperglycemic conditions, with ROFLU potentiating MBP transcript levels (fig. 5A). This result was validated with protein expression analysis (fig. 5B), in which we noted again a significant MBP expression for ROFLU-treated cells at the highest glucose concentration. MAG, Krox20, O1 (SC differentiation marker¹⁰) and p75 (neurotrophin

receptor involved in remyelination⁴⁶) either showed similar or higher expression values than control.

Finally, we analysed whether ROFLU supplementation under normoglycemic conditions was effective in rescuing/inducing redifferentiation of SCs pre-exposed to high glucose levels. ROFLU-treated samples, pre-exposed to 45 mM glucose, showed a significantly higher cJUN expression. This suggests that the PDE4 inhibitor, by enhancing the cAMP levels, is able to potentiate the regenerative program in damaged cells. At the same time, ROFLU-treated samples exhibited lower Krox20 expression, but a higher (not significant) MBP and PLP expression (fig. 6A). In sum, this indicates that while directing SCs response to a regenerative phenotype, ROFLU-treated cells can simultaneously exhibit mature characteristics, even after glucose damage. At the protein level, all differentiation markers showed similar values to control, which evidences a recovery of a myelinating phenotype to basal levels (fig. 6B). Despite these promising finding, we noted that a similar outcome between DMSO and ROFLU conditions does not permit an unequivocal determination of the effectiveness of the PDE4 inhibitor.

In this work we have investigated for the first time, the influence of PDE4 inhibitors on the PN tissue, using *in vitro* models. We have demonstrated that PDE4 inhibitors may have a positive impact on the PN, stimulating and helping to maintain a mature myelinating phenotype of SCs, whether in a regenerative or diseased state. As exemplified, the use of *in vitro* models to quickly and easily study a compound's action on cells, cultured under controlled circumstances, can greatly aid the field of neurobiology and drug development on the pursuit of better therapies for PN-related problems.

Acknowledgments

We thank the Microscopy CORE Lab (M4I Maastricht University), especially Hans Duimel and Kevin Knoops for their help in TEM and confocal imaging. We also thank the province of Limburg for the project funding. This work was partly supported by the research programme VENI 2017 STW- project 15900 financed by the Dutch Research Council (NWO).

References

1. Tibbo, A. J., Tejada, G. S. & Baillie, G. S. Understanding PDE4's function in Alzheimer's disease; A target for novel therapeutic approaches. *Biochem. Soc. Trans.* **47**, 1557–1565 (2019).
2. Nikulina, E., Tidwell, J. L., Dai, H. N., Bregman, B. S. & Filbin, M. T. The phosphodiesterase inhibitor rolipram delivered after a spinal cord lesion promotes axonal regeneration and functional recovery. *Proc. Natl. Acad. Sci. U. S. A.* **101**, 8786–8790 (2004).
3. Ricciarelli, R. & Fedele, E. cAMP, cGMP and Amyloid β : Three Ideal Partners for Memory Formation. *Trends Neurosci.* **41**, 255–266 (2018).
4. Nabavi, S. M. *et al.* Phosphodiesterase inhibitors say NO to Alzheimer's disease. *Food Chem. Toxicol.* **134**, 110822 (2019).
5. Sanders, O. & Rajagopal, L. Phosphodiesterase Inhibitors for Alzheimer's Disease: A Systematic Review of Clinical Trials and Epidemiology with a Mechanistic Rationale. *J. Alzheimer's Dis. Reports* **4**, 185–215 (2020).
6. Syed, Y. A. *et al.* Inhibition of phosphodiesterase-4 promotes oligodendrocyte precursor cell differentiation and enhances CNS remyelination. *EMBO Mol. Med.* **5**, 1918–1934 (2013).
7. Walikonis, R. S. & Poduslo, J. F. Activity of cyclic AMP phosphodiesterases and adenylyl cyclase in peripheral nerve after crush and permanent transection injuries. *J. Biol. Chem.* **273**, 9070–9077 (1998).
8. Jessen, K. R. & Mirsky, R. The repair Schwann cell and its function in regenerating. *J. Physiol.* **13**, 3521–3531 (2016).
9. Knott, E. P., Assi, M. & Pearse, D. D. Cyclic AMP signaling: A molecular determinant of peripheral nerve regeneration. *Biomed Res. Int.* **2014**, (2014).
10. Bacallao, K. & Monje, P. V. Requirement of cAMP signaling for Schwann cell differentiation restricts the onset of myelination. *PLoS One* **10**, 1–31 (2015).
11. Morgan, L., Jessen, K. R. & Mirsky, R. The effects of cAMP on differentiation of cultured schwann cells: Progression from an early phenotype (04+) to a myelin phenotype (P₀+, GFAP-, N-CAM-, NGF-receptor-) depends on growth inhibition. *J. Cell Biol.* **112**, 457–467 (1991).
12. Udina, E. *et al.* Rolipram-induced elevation of cAMP or chondroitinase ABC breakdown of inhibitory proteoglycans in the extracellular matrix promotes peripheral nerve

- regeneration. *Exp. Neurol.* **223**, 143–152 (2010).
13. Reghina, A. D., Craciun, S. & Fica, S. Severe transient hyperglycemia in a prediabetic patient during mild acute pancreatitis. *Case Rep. Med.* **2015**, 3–5 (2015).
 14. Hao, W. *et al.* Hyperglycemia promotes Schwann cell de-differentiation and demyelination via sorbitol accumulation and Igf1 protein down-regulation. *J. Biol. Chem.* **290**, 17106–17115 (2015).
 15. Almhanna, K., Wilkins, P. L., Bavis, J. R. & Harwalkar, S. Hyperglycemia Triggers Abnormal Signaling and Proliferative Responses in Schwann Cells *. **27**, 1341–1347 (2002).
 16. Heckman, P. R. A., Wouters, C. & Prickaerts, J. Phosphodiesterase Inhibitors as a Target for Cognition Enhancement in Aging and Alzheimer's Disease: A Translational Overview. *Curr. Pharm. Des.* **21**, 317–331 (2014).
 17. Malheiro, A., Morgan, F., Baker, M., Moroni, L. & Wieringa, P. A three-dimensional biomimetic peripheral nerve model for drug testing and disease modelling. *Biomaterials* **257**, 120230 (2020).
 18. Kaewkhaw, R., Scutt, A. M. & Haycock, J. W. Integrated culture and purification of rat Schwann cells from freshly isolated adult tissue. *Nat Protoc* **7**, 1996–2004 (2012).
 19. Achiron, A. & Miron, S. Myelin associated antibodies: Myelin-associated glycoprotein autoantibodies, myelin basic protein autoantibodies and myelin proteolipid autoantibodies in neurologic diseases. *Autoantibodies* (Elsevier Inc., 2007).
 20. Anderson, T. J., Montague, P., Nadon, N., Nave, K. A. & Griffiths, I. R. Modification of Schwann cell phenotype with Plp transgenes: Evidence that the PLP and DM20 isoproteins are targeted to different cellular domains. *J. Neurosci. Res.* **50**, 13–22 (1997).
 21. Britsch, S. *et al.* The transcription factor Sox10 is a key regulator of peripheral glial development. *Genes Dev.* **15**, 66–78 (2001).
 22. Huang, L. *et al.* c-Jun gene-modified Schwann cells: upregulating multiple neurotrophic factors and promoting neurite outgrowth. *Tissue Eng. Part A* **21**, 1409–21 (2015).
 23. Tzifi, F. *et al.* The role of BCL2 family of apoptosis regulator proteins in acute and chronic leukemias. *Adv. Hematol.* **2012**, (2012).
 24. Liu, Z. *et al.* Specific marker expression and cell state of Schwann cells during culture in vitro. *PLoS One* **10**, e0123278 (2015).

25. Chen, M. *et al.* Serum starvation induced cell cycle synchronization facilitates human somatic cells reprogramming. *PLoS One* **7**, (2012).
26. Monje, P. V. *et al.* Non-antagonistic relationship between mitogenic factors and cAMP in adult Schwann cell re-differentiation. *Glia* **57**, 947–961 (2009).
27. Gonçalves, N. P. *et al.* Peripheral nerve regeneration is independent from Schwann cell p75NTR expression. *Front. Cell. Neurosci.* **13**, 1–14 (2019).
28. Li, H., Zuo, J. & Tang, W. Phosphodiesterase-4 inhibitors for the treatment of inflammatory diseases. *Front. Pharmacol.* **9**, 1–21 (2018).
29. Guttman-Yassky, E. *et al.* The role of phosphodiesterase 4 in the pathophysiology of atopic dermatitis and the perspective for its inhibition. *Exp. Dermatol.* **28**, 3–10 (2019).
30. Vignola, A. M. PDE4 inhibitors in COPD - A more selective approach to treatment. *Respir. Med.* **98**, 495–503 (2004).
31. Bacallao, K. & Monje, P. V. Opposing roles of pka and epac in the cAMP-dependent regulation of Schwann cell proliferation and differentiation. *PLoS One* **8**, 1–16 (2013).
32. Gambarotta, G., Fregnan, F., Gnani, S. & Perroteau, I. Neuregulin 1 role in schwann cell regulation and potential applications to promote peripheral nerve regeneration. *International Review of Neurobiology* vol. 108 (Elsevier Inc., 2013).
33. Arthur-Farraj, P. J. *et al.* c-Jun Reprograms Schwann Cells of Injured Nerves to Generate a Repair Cell Essential for Regeneration. *Neuron* **75**, 633–647 (2012).
34. Lee, H. J., Shin, Y. K. & Park, H. T. Mitogen Activated Protein Kinase Family Proteins and c-jun Signaling in Injury-induced Schwann Cell Plasticity. *Exp. Neurobiol.* **23**, 130–7 (2014).
35. Lavdas, A. A. & Matsas, R. Schwann Cell Morphology. *Encycl. Neurosci.* 475–484 (2009) doi:10.1016/B978-008045046-9.01749-6.
36. Hung, H. A., Sun, G., Keles, S. & Svaren, J. Dynamic regulation of Schwann cell enhancers after peripheral nerve injury. *J. Biol. Chem.* **290**, 6937–6950 (2015).
37. Knott, E. P., Assi, M. & Pearse, D. D. Cyclic AMP signaling: A molecular determinant of peripheral nerve regeneration. *Biomed Res. Int.* **2014**, (2014).
38. Stoll, G. & Müller, H. W. Nerve injury, axonal degeneration and neural regeneration: basic insights. *Brain Pathol.* **9**, 313–325 (1999).
39. Vægter, C. B. Peripheral Glial Cells in the Development of Diabetic neuropathy. *Front. Neurol.* **9**, 1–9 (2018).

40. Yagihashi, S., Mizukami, H. & Sugimoto, K. Mechanism of diabetic neuropathy: Where are we now and where to go? *J. Diabetes Investig.* **2**, 18–32 (2011).
41. Gonçalves, N. P. *et al.* Schwann cell interactions with axons and microvessels in diabetic neuropathy. *Nat. Rev. Neurol.* **13**, 135–147 (2017).
42. Cermenati, G. *et al.* Diabetes-induced myelin abnormalities are associated with an altered lipid pattern: Protective effects of LXR activation. *J. Lipid Res.* **53**, 300–310 (2012).
43. Daoud, A. K., Tayyar, M. A., Fouda, I. M. & Harfeil, N. A. Effects of diabetes mellitus vs. in vitro hyperglycemia on select immune cell functions Diabetes mellitus suppresses select immune cell functions Daoud *et al.* *J. Immunotoxicol.* **6**, 36–41 (2009).
44. Shin, Y. K. *et al.* The Neuregulin-Rac-MKK7 pathway regulates antagonistic c-jun/Krox20 expression in Schwann cell dedifferentiation. *Glia* **61**, 892–904 (2013).
45. Tomita, K. *et al.* The Neurotrophin Receptor p75 NTR in Schwann Cells is Implicated in Remyelination and Motor Recovery after Peripheral Nerve Injury. **1208**, 1199–1208 (2007).

Supplementary Information

Investigating the effect of phosphodiesterase-4 (PDE4) inhibitors on Schwann cells myelination in a 3D regeneration model and in a hyperglycemia model

Afonso Malheiro^{1*}, Melissa Scheppers^{2,3*}, Adrián Seijas Gamardo¹, Jos Prickaerts³, Lorenzo Moroni¹, Tim Vanmierlo^{2,3+}, Paul Wieringa¹⁺

4. MERLN Institute for Technology-Inspired Regenerative Medicine, Maastricht University
5. Department of Neuro-immunology, Biomedical Research Institute, Hasselt University, Hasselt 3500, Belgium.
6. Department Psychiatry and Neuropsychology, European Graduate School of Neuroscience, School for Mental Health and Neuroscience, Maastricht University, Maastricht 6200 MD, The Netherlands.

**these authors have contributed equally in this work*

+corresponding author

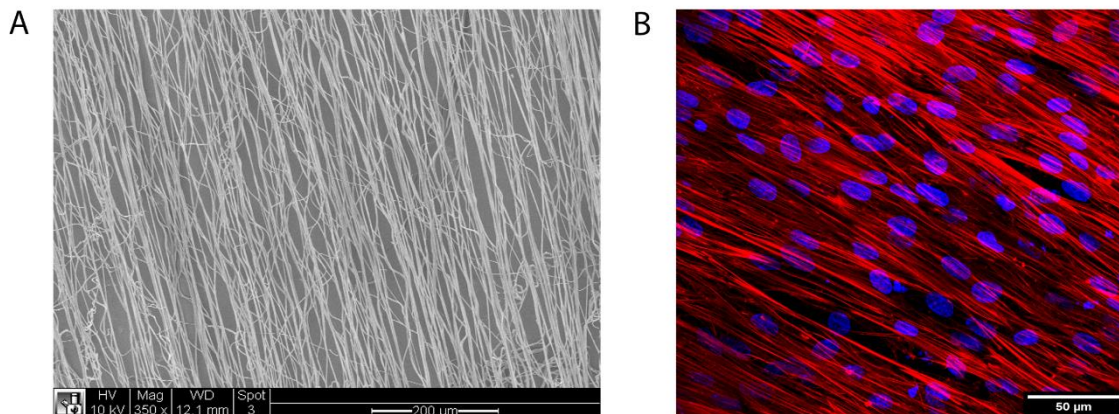


Figure S1. A) Scanning electron micrograph of the electrospun scaffold composed by aligned ultrathin PEOT/PBT fibers with $1.37 \pm 0.20 \mu\text{m}$. Scale bar is $200 \mu\text{m}$. B) Morphology of Schwann cells after 7 days of culture in the scaffold, with SC proliferation medium. Red is F-actin and blue is DAPI. Scale bar is $50 \mu\text{m}$.

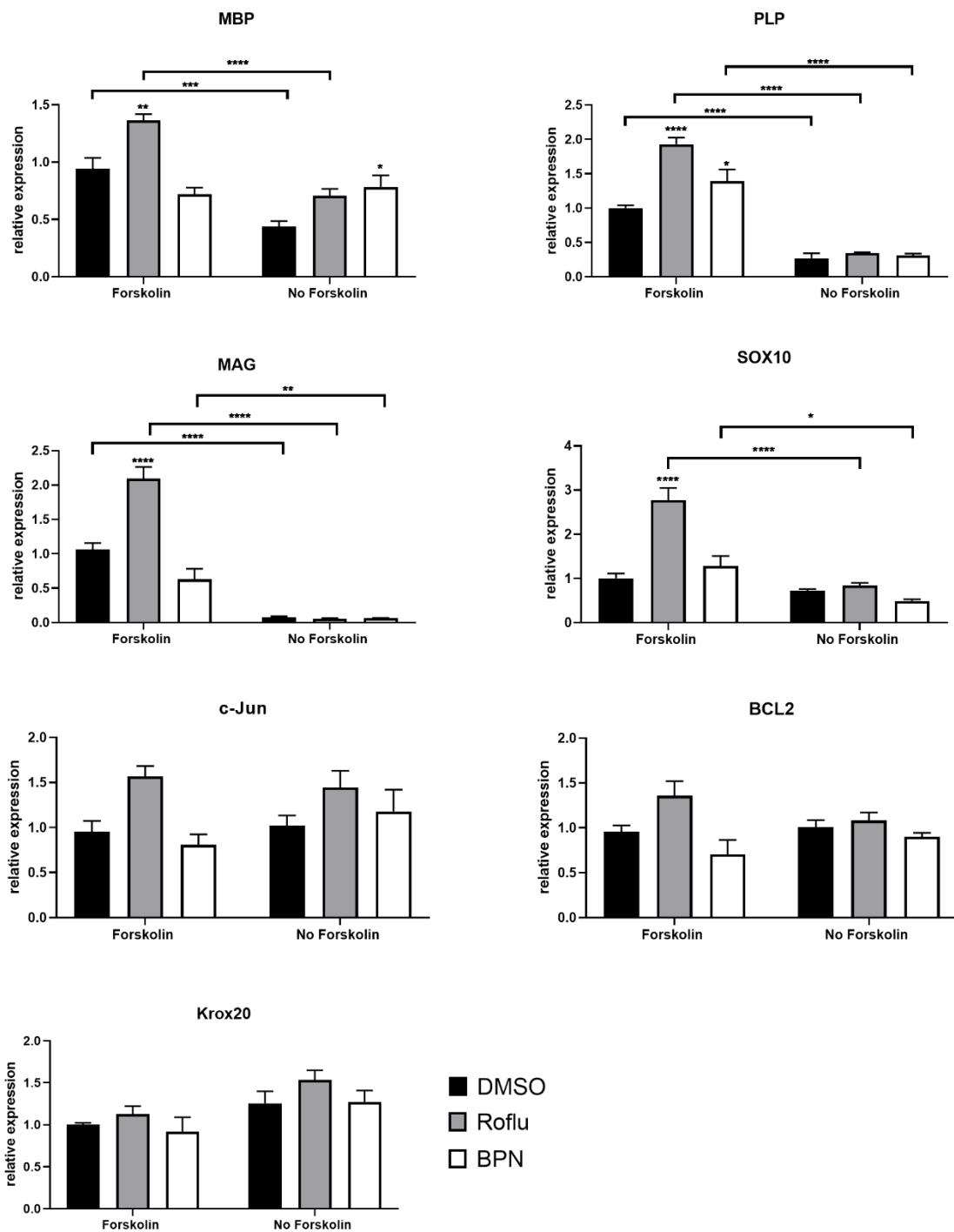


Figure S2. Gene expression, determined by qPCR, on the SCs bands after culture for 7 days in SC proliferation medium supplemented or not with forskolin and PDE4 inhibitors (ROFLU at 10 μ M or BPN at 5 μ M). DMSO was used as control. Transcript expression level was normalized to forskolin plus DMSO samples. This experiment was performed twice, using five replicates per condition. Bar graphs represent mean \pm SEM. Statistics were performed using

two-way ANOVA followed by Tukey's HSD post-hoc test where **** $p < 0.0001$, *** $p < 0.001$, ** $p < 0.01$ and * $p < 0.05$.

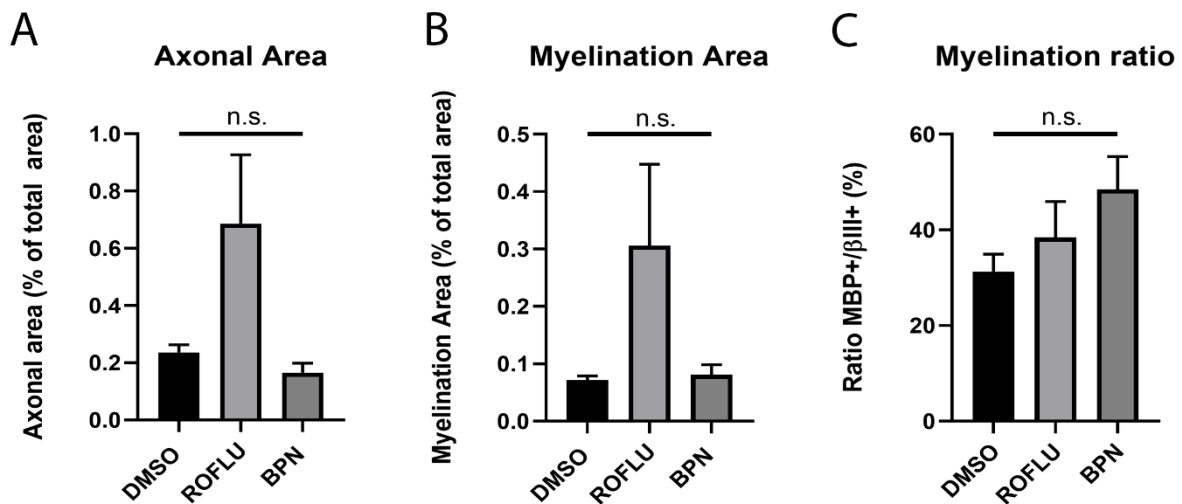


Figure S3. Quantification of the axonal area (A), myelination area (B) and myelination ratio (C) from iPSCs-derived neurons cultured with SCs for 14 days, after exposition to DMSO, ROFLU or BPN. Axonal area was determined by the ratio of β III-tubulin⁺ segment area (excluding cell body area) with the total scaffold area. Myelination area was determined by the ratio of MBP⁺ segment area (excluding cell body area) with the total scaffold area. Myelination ratio was calculated from the ratio of MBP⁺ segment with β III-tubulin⁺ segment on the same image. This experiment was performed twice and we used at least 5 replicates per condition. For the image analysis we took one image per sample, capturing the whole tissue. Statistics were done using one-way ANOVA followed by Tukey's post-hoc test. The note n.s. means not significant.

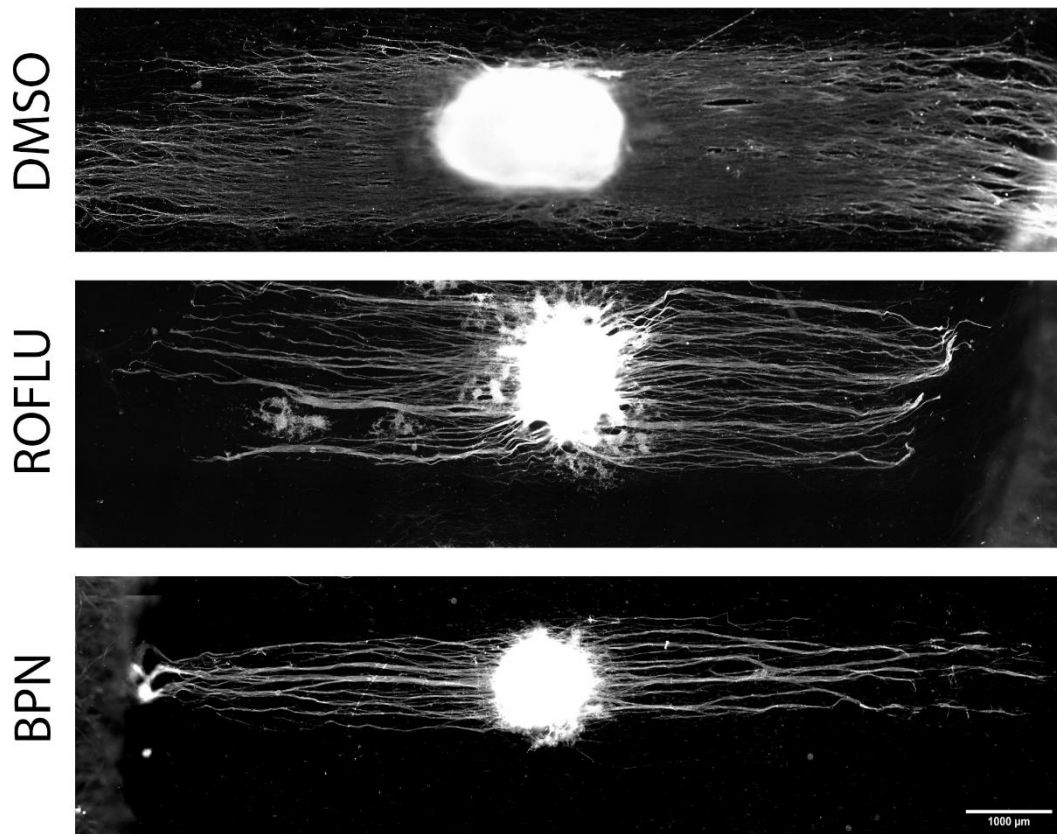


Figure S4. Overview of the myelin segments on the iPSCs/SCs 21 day co-cultures. The images were obtained from stitching of immunostaining micrographs to MBP⁺ structures. Prior to iPSCs-neuron seeding, SCs were cultures with SC proliferation medium containing DMSO (top image), ROFLU (10 μM; middle row) or BPN (5 μM; bottom image). Scale bar is 1000 μM.

Chapter 6

Development of a human model of innervated skin for *in vitro* testing

Afonso Malheiro¹, Maria Thon², Ana Filipa Lourenço¹, Adrián Seijas Gamardo¹, Sue Gibbs², Paul Wieringa¹, Lorenzo Moroni¹

¹MERLN Institute for Technology-Inspired Regenerative Medicine, Maastricht University

²Department of Molecular Cell Biology and Immunology, Amsterdam University Medical Center

Abstract

Sensory innervation of the skin is essential for its function, homeostasis and wound healing mechanisms. Thus, to adequately model the cellular microenvironment and function of native skin, *in vitro* human skin equivalents (hSE) containing a sensory neuron population began to be researched. In this work, we established a fully human three-dimensional (3D) platform of hSE innervated by induced pluripotent stem cell-derived nociceptors spheroids (hNSs), mimicking native innervation. Both the hSE and nociceptor population exhibited morphological and phenotypical characteristics resembling their native counterparts, such as epidermal and dermal layer formation and nociceptor marker exhibition, respectively. In the co-culture platform, neurites developed from the hNS and navigated in 3D to innervate the hSE from a distance. To probe both skin and nociceptor functionality, we applied a clinically available capsaicin patch (Qutenza™) directly over the hSE section and analyzed neuron reaction. Application of the patch caused an exposure time-dependent neurite regression and degeneration. In platforms absent of hSE, axonal degeneration was further increased, highlighting the role of the skin construct as a barrier. In sum, we established an *in vitro* tool of functional innervated skin with high interest for preclinical research.

Introduction

The skin is densely innervated by different sensory nerve fibers that equip individuals with the ability to sense touch, temperature and pain^{1,2}. This permits the recognition and avoidance of damaging stimuli, which is pivotal to maintain the physical integrity of skin (and other organs)³. For this, cutaneous nociceptor fibers play a major role, by detecting noxious stimuli, such as high temperature (>43°C), low pH substances (<6.0) and irritant chemicals (e.g. capsaicin), and conveying a signal to the central nervous system (CNS)⁴. Noxious stimuli detection is provided by sensor proteins, such as transient receptor potential vanilloid 1 (TRPV-1) channels, expressed within nociceptor fibers. Once activated, these channels open and induce neuron depolarization, triggering an action potential that is further propagated to the CNS, where a pain is perceived^{4,5}. Interestingly, the continuous targeting of TRPV-1 channels with a stable agonist, such as capsaicin, can induce nociceptor desensitization and nerve ending ablation, which results in a local analgesic effect instead⁴. In addition to providing sensorial ability, skin innervation is also necessary to maintain skin physiology and to promote re-epithelialization during wound healing^{2,6,7,8}. Thus, cutaneous nerves are not only essential for normal skin function, but also for restoring function after damage. Moreover, nerve defects due to pathological conditions, such as spinal cord injury or diabetic neuropathy, lead to impaired regeneration¹.

In recent years, the development of engineered human skin equivalents (hSE) has greatly evolved and several companies are now commercializing skin analogues composed of fibroblasts and keratinocytes that replicate the skin anatomy up to an extent³. Such models constitute a safe, inexpensive and quick alternative to animal testing and simultaneously provide a more translational research tool, due to their human source. Because of their defined cellular ecosystem, *in vitro* models also permit a simpler and more direct evaluation of specific cells and molecules contribution. Advanced hSE models containing other cellular components such as vasculature⁹, hair follicles¹⁰ and melanocytes¹¹ have been developed in order to better mimic the native microenvironment, to study specific interactions and to accurately model certain pathologies. Despite these advancements, innervated hSE platforms are still scarce, regardless of the importance of cutaneous nerves for skin function and wound regeneration mechanisms. The development of innervated hSE models would improve *in vitro* testing by providing more representative data and allowing a wider range of assays that probe neurons state and their influence on surrounding cells. This is of particular interest to screen compounds with potential neurotoxic effects and/or that may produce/mitigate pain¹², to design strategies for improved wound healing via nerve targeting⁷ or to investigate nerve relations with other cell types in health and pathological states (e.g. diabetic neuropathy)³. To show the influence of nerves on skin regeneration, Blais et al.⁶ constructed a skin model containing mouse sensory neurons, which upon implantation on a wounded mouse, led to faster wound regeneration (due

to substance P secretion) compared to control constructs (absent of neurons). However, due to the physiological differences between species, research using innervated skin models fully composed of human cells is needed. To this end, Muller et al.¹³ reported an innervated hSE model containing functional nociceptors obtained from induced pluripotent stem cells (iPSCs). Despite the successful integration of all cellular components, the reported strategy still presented some shortcomings such as disorganized and non-representative neuronal architecture, with neural cell bodies situated beneath the skin tissue; because of this configuration, sample sectioning is required to observe innervation pattern. Moreover, testing on this model remains to be demonstrated.

In this work, we show the development of an innervated hSE model with demonstrated applicability. The model is comprised of a fibrin/collagen hydrogel platform containing two separate compartments, one for a sensory neuron population and the other for a hSE construct. The sensory neurons, previously described in chapter 4, were differentiated from iPSCs, formed into a neurosphere, and exposed to nerve growth factor (NGF) to induce a mature nociceptor phenotype (TRPV-1⁺ and response to noxious stimuli) as well as electrical activity. The fabrication method of the hSE was also previously reported and the engineered tissue well-characterized^{14,15}. In this co-culture system, the neurospheres were able to develop extensive neurite projections throughout the gel platform, to innervate the hSE from a distance within 21 days. Co-cultures with primary neurons from a dorsal root ganglion (DRG) population instead, revealed similar neuron morphologies although innervating at a higher density. To validate the platform utility, we performed a topical application of a commercial capsaicin patch (Qutenza™) on the skin region and detected a time-dependent neural degradation of hNS and DRG neurons as a result. In sum, the work here described constitutes an advancement in the development of fully human and functional innervated hSE constructs that permit convenient testing and tissue analysis.

Materials and Methods

Agarose microwell platform fabrication

A 3% (w/v) sterile agarose (Thermo Fisher Scientific) solution was prepared in PBS. 8 ml of agarose solution were poured onto an in-house fabricated PDMS stamp with the negative template of 1580 microwells with 400 μm diameter. Centrifugation at 845 g was performed to remove air bubbles, followed by chilling for 45 min at 4 C for agarose solidification. When solid, the agarose blocks were removed, cut to fit in a 12 well-plate, washed with 70% ethanol, then washed twice in phosphate buffered saline (PBS) solution and left at 4°C until further use. The day before cell seeding, PBS was replaced with culture media containing Advanced RPMI

1640 supplemented with 1X glutamax (Thermo Fisher Scientific) and kept in the incubator at 37°C, 5% CO₂ overnight.

iPSCs culture

Human iPSC line LUMC0031iCTRL08 (Provided by the LUMC iPSC core facility) was cultured on Geltrex coated dishes at a density of 10×10^3 cells/cm² in mTESR1 medium (Stem Cell Technology). Cells were fed every alternate day with completely fresh medium and passaged weekly using Accutase (Stem Cell Technology). Upon splitting, cells were cultured in mTESR1 medium supplement with 10 µM of Y-27632 (Tocris) for 24 h and replaced with mTESR1 medium for further maintenance.

iPSCs differentiation into nociceptive neurons and neurosphere formation

In order to induce iPSCs differentiation into nociceptors, we adapted and modified the protocol published by Chambers et al.¹⁶. Nociceptor induction was initiated using single cell suspension of undifferentiated iPSCs detached with accutase, followed by seeding of 200 cells/microwell in mTESR1 medium supplemented with 10 µM of Y-27632 and 0.5% Geltrex (in solution) onto 400 µm agarose microwells. Cell suspension was forced to settle by centrifugation at 290 g for 2 min. Afterwards, cells were incubated for 24 h and were given a complete media change with mTESR1 medium. At this time, the cellular spheroid is formed and cell synchronization is initiated by the addition of mTESR1 medium supplemented with 1% dimethyl sulfoxide (DMSO). The cells were maintained for 72 h in the synchronization medium. Post synchronization cells were given a PBS wash and nociceptor induction was initiated by addition of dual SMAD inhibition media containing Advanced RPMI 1640 supplemented with Glutamax (both Thermo Fisher Scientific), 100 nM LDN-193189 (Tocris) and 10 µM SB431542 (Tocris). The spheres were maintained for 48 h in the dual SMAD inhibition media. Following this, neural crest commitment was induced via media containing Advanced RPMI 1640 supplemented with Glutamax, 3 µM CHIR99021 (Tocris) and 1 µM retinoic acid (Tocris). The spheres were maintained in the neural crest induction media for 5 days with media change every alternate day. Following this stage, the spheres were incubated in Notch inhibition media, consisting of Advanced RPMI supplemented with Glutamax, 10 µM SU5402 (Tocris) and 10 µM DAPT (Tocris), for 48 h.

Finally, the neurospheres, composed of trunk neural crest cells, were collected and seeded on coverslips or scaffolds. In these substrates, cells were cultured in neural maturation medium for at least 5 days to reach the nociceptor phenotype. The neural medium is composed of Neurobasal Medium, 0.5 mM Glutamax, 100 U/ml penicillin and 100 µg/ml streptomycin (all Thermo Fisher Scientific), 100 ng/ml human nerve growth factor (NGF), 50 µg/ml ascorbic acid

(all Sigma-Aldrich), 25 ng/ml human neuregulin-1 type III (NRG-1 SMDF) and N21 supplement (both from R&D systems).

Characterization of iPSCs-derived nociceptors phenotype

To characterize the formation of nociceptor neurons from iPSCs and compare their phenotype with DRG neurons, we seeded the neurospheres (at the end stage of differentiation) and DRGs on 12 mm laminin-coated coverslips (one sphere/DRG per coverslip). Laminin coating was performed the day before cell seeding, with 100 μ l of a solution containing 1 μ g/ml laminin-1 (R&D systems) and 2 μ g/ml poly-D-lysine (Sigma Aldrich) in PBS. The neurons were cultured for 7 days in neural medium composed of Neurobasal Medium, 0.5 mM Glutamax, 100 U/ml penicillin and 100 μ g/ml streptomycin (all Thermo Fisher Scientific), 100 ng/ml human nerve growth factor (NGF), 50 μ g/ml ascorbic acid (both Sigma-Aldrich) and N21 supplement (R&D systems). At day 7 of culture, the cells were fixed and immunostained as described below.

3D culture of DRGs and iPSCs neurospheres in a collagen/fibrin matrix

3D neuron cultures were performed by combining a neuron-seeded scaffold with a collagen/fibrin hydrogel. The scaffold was prepared by punching a 12 mm circular section from a nonwoven polyurethane mesh (6691 LL, Lantor B.V.). These sections were then sterilized by immersion in 70% ethanol for 1 h and transferred to sterile 24 well-plates. iPSCs neurospheres were collected from the agarose platforms and seeded on these scaffolds (one neurosphere per scaffold). The samples were cultured in neural medium and left to attach overnight, at 37°C, 5% CO₂. The same procedure was done for DRG cultures. To isolate DRGs, we dissected P7 Brown Norway rats, previously sacrificed by decapitation (following local and Dutch animal use guidelines). After collection, the DRG was carefully stripped from nerve roots and placed on the scaffold.

The day after, we prepared a sterile ice-cold solution of collagen type I (rat tail, Corning, 354249), fibrinogen (human, Enzyme Research Laboratories), thrombin (bovine, Sigma-Aldrich, T4648), NaOH (1N), PBS (10X) and deionized H₂O, to yield a final concentration of 4 mg/ml of collagen and 1 mg/ml of fibrin. 200 μ l of this solution was added on top of the cell-seeded scaffold and left to polymerise for 15 min at 37°C, 5% CO₂. The cells were cultured for 7 days with neural medium, at 37°C, 5% CO₂.

Human tissue and cell culture

Human juvenile foreskin was obtained after routine circumcisions from pediatric surgery. All skin samples were obtained in compliance with the “Code for Proper Secondary Use of Human Tissue” as formulated by the Dutch Federation of Medical Scientific Societies (www.federa.org) and approved by the institutional review board of the VU University medical center.

Keratinocytes and fibroblasts were isolated from foreskin and cultured essentially as previously described¹⁷. Keratinocytes were expanded in keratinocyte medium (KC medium) composed of Dulbecco's modified Eagle's medium (DMEM)/Ham's F12 (Corning) in a 3:1 ratio supplemented with 1% UltrosorG (BioSepra SA), 1 $\mu\text{mol/L}$ hydrocortisone (Sigma-Aldrich), 1 $\mu\text{mol/L}$ isoproterenol hydrochloride (Sigma-Aldrich), 0.1 $\mu\text{mol/L}$ insulin (Sigma-Aldrich), 2 ng/ml human keratinocyte growth factor (Sigma-Aldrich), 100 U/ml penicillin and 100 $\mu\text{g/ml}$ streptomycin (Corning). Fibroblasts were cultured in DMEM with 1% UltrosorG and 1% penicillin/ streptomycin. For all experiments, keratinocytes were used at passage 2 and fibroblasts at passage 2-3.

Formation of human skin equivalent (hSE)

hSE was constructed as previously described¹⁷. Fibroblasts (5×10^5 cells) were embedded in 350 μl of a 4 mg/mL collagen (rat tail; collagen type I; Corning) plus 1 mg/mL fibrin (human; Enzyme Research Laboratories) solution and this mixture pipetted into 24 mm transwell inserts (0.4 μm pore size; Corning). Hydrogels were cultured for 1-3 days submerged in KC medium. Keratinocytes (5×10^5 cells) were then seeded on top of the hydrogel and cultured submerged for 3-4 days in KC medium. Hereafter, hSE were further cultured at the air-liquid interface for another 10-14 days in skin medium composed of DMEM/Ham's F12 in a 3:1 ratio supplemented with 1% UltrosorG, 1 $\mu\text{mol/L}$ hydrocortisone, 1 $\mu\text{mol/L}$ isoproterenol hydrochloride, 0.1 $\mu\text{mol/L}$ insulin, 10 $\mu\text{mol/L}$ L-carnitine, 0.01 mol/L L-serine, 50 $\mu\text{g/mL}$ ascorbic acid (Sigma-Aldrich), and 1% penicillin/streptomycin.

Fabrication of a compartmentalized collagen/fibrin platform

The compartmentalized collagen/fibrin platforms were prepared as illustrated in fig. 3A. Briefly, we started by fabricating the polydimethylsiloxane (PDMS) mold units, which were made by pouring a PDMS solution (10:1 monomer:curing agent) (Farnell) on custom-made molds and curing for 2 h at 80°C. These custom-made molds (one to produce the reservoir and the other to produce the patterning unit) were created through milling (monoFAB SRM-20, Roland) of a poly(methyl methacrylate) (PMMA) slab (fig. S2). Afterwards, the PDMS units were cut from the mold and post-cured/sterilized for 4 h at 160°C and left in sterile conditions until use. To create the compartmentalized collagen/fibrin platforms, we first assembled the

PDMS units as demonstrated in fig. 3A, and then pipetted 150 μ l of a collagen/fibrin solution (4 mg/ml / 1mg/ml) inside the reservoir. After this, a scaffold composed of a sterile 8 mm circular cut of a nonwoven polyurethane mesh (6691 LL, Lantor B.V.) was added on top. The platforms were left to polymerize overnight at 37°C, 5% CO₂ and inside a petri dish filled with PBS to maintain humidity and prevent gel drying. The following day, these could be detached from the PDMS molds, by carefully picking the scaffold with a fine tip tweezers. The hydrogel platforms were left in neural medium until further use.

Development of an innervated skin model using the compartmentalized collagen/fibrin platform

The innervated skin model was constructed by sequential co-culture of iPSCs-derived nociceptor neurosphere with a hSE section, as illustrated in fig. 3D. Once differentiated, the neurospheres were picked from the mold and added into the neuron compartment of the collagen/fibrin platforms (previously dried up of medium). Immediately, the platforms were centrifuged at 50 g for 1 min, to promote cell settling. After this, 15 μ l of the same collagen/fibrin solution was added on top of the neurosphere to seal it. The solution was left to polymerize for 15 min by incubation at 37°C, 5% CO₂. After this, neural medium was added and the cells were cultured for 7 days in the same conditions, with medium refreshments every other day. At day 7, we retrieved the hSE cultures (at the mature stage) and made 3 mm circular sections using a sterile biopsy punch. These sections were then carefully placed on the skin compartment of the gel platform, previously filled with 15 μ l of collagen/fibrin solution, to promote the hSE immobilization. The gel platforms, containing the neurosphere and hSE section, were transferred to 24 well-plate inserts (VWR, BRND782807) and fitted into an adequate 24 well-plate (Thermo Fisher Scientific, 15503783). The medium composed of skin/neural medium at 1:1 was added without submerging the hSE sections, leaving them exposed to the air. The cells were cultured in this medium and conditions for additional 21 days, at 37°C, 5% CO₂.

Capsaicin patch testing on innervated skin platform

At day 46 of neurosphere culture (day 21 of skin/neuron co-culture) we performed the capsaicin patch test as illustrated in fig. 5A. For this, we made 3 mm circular cuts of a capsaicin patch (Qutenza™) using a sterile biopsy punch, and placed the cuts directly in contact with the skin section. The samples were incubated for 1 or 24 h, in neural/skin medium, at 37°C, 5% CO₂.

Immunostaining

Samples were fixed with 4% paraformaldehyde (PFA) for 25 min at room temperature (RT), rinsed thoroughly with PBS, and left in PBS until further use. Permeabilization and blocking was performed simultaneously with a solution of 1% triton X-100, 5% goat serum, 0.05% Tween20, and 1% bovine serum albumin (BSA) in PBS, for 24 h at 4°C, under mild agitation. Immediately, samples were incubated for 48 h at 4°C, under mild agitation, with primary antibody solutions containing 0.1% triton X-100, 5% goat serum, 0.05% Tween20, and 1% bovine serum albumin (BSA) in PBS. Following this, the samples were washed with a wash buffer composed of 0.05% Tween20 and 1% bovine serum albumin (BSA) in PBS, and left for 24 h at 4°C, under mild agitation, to remove unbound antibodies. Secondary antibody solutions were prepared in wash buffer and incubated for 48 h at 4°C, under mild agitation. Following this, we rinsed the samples with PBS, stained with DAPI (0.2 µg/ml) for 20 min at RT, and left them in PBS until imaging.

The used primary antibodies were the following: anti-βIII tubulin (Sigma-Aldrich, T8578, 1:500), anti-Substance P (Abcam, ab14184, 1:100), anti-CGRP (Abcam, ab22560, 1:500), anti-TRPV-1 (Alomone Labs, ACC-030, 1:100), and anti-involucrin (Abcam, ab181980, 1:100).

Finally, the used secondary antibodies were the following: goat anti-mouse conjugated with Alexa Fluor 488; goat anti-mouse conjugated with Alexa Fluor 568, goat anti-rabbit conjugated with Alexa Fluor 488 and donkey anti-sheep conjugated with Alexa Fluor 488 (all Thermo Fisher Scientific).

Microscopy and image analysis

Stereomicroscope images were acquired with a Nikon SMZ25 stereomicroscope. Fluorescent images were acquired with an inverted epifluorescence microscope (Nikon Eclipse Ti-e) or a confocal laser scanning microscope (Leica TCS SP8). 3D image reconstructions were processed with Amira (Thermo Fisher Scientific). All the other images were prepared and analyzed using Fiji software (<https://fiji.sc/>). To determine the axonal degeneration resultant from the capsaicin exposure experiment, we developed an algorithm that is able to detect associated morphological changes. The method is illustrated in fig. S7 and is based on the analysis of immunostaining images to βIII-tubulin. The original images are first converted to binary and then we use the analyze particle function in Fiji to segment objects that represent debris of degenerated axons. This function provides both the object counting and total object area. Additionally, we measure the total axonal area. Finally, we divide the object area by the total axonal area to determine the normalized degeneration area.

Statistical analysis

Boxplots are shown as data points from the minimum to maximum value. Bar graphs represent the mean + SD. Statistics were performed using an unpaired t-test or a one-way ANOVA followed by Tukey's HSD post-hoc test. The asterisks represent: *** $p < 0.001$; ** $p < 0.01$; * $p < 0.05$ and n.s. means $p > 0.05$.

Results

Fabrication of a human nociceptor 3D culture model

To generate human nociceptor spheroids (hNSs) we followed the protocol previously described in chapter 4 and illustrated in fig. 1A. At day 9 of differentiation, the mold contains a large collection of uniform, cohesive and round spheroids with an average diameter of $308.7 \pm 38.6 \mu\text{m}$ (fig. 1B). At this stage, the spheroids are harvested from the mold, transferred to the culture substrate and cultured for at least 7 days in NGF-supplemented neural medium to promote neurite outgrowth and nociceptor phenotype acquisition *in situ*. When cultured on laminin-coated ($1 \mu\text{g/ml}$) coverslips, the neurons are able to attach, survive and grow neurites. We show neurite outgrowth from an hNS cultured for 7 days in neural medium (fig. 1C), evidencing a dense and radial neurite projection ($\beta\text{III-tubulin}^+$ segments). To validate the acquisition of a nociceptor phenotype, we investigated the presence of characteristic nociceptor markers¹⁸, TRPV-1, calcitonin gene-related peptide (CGRP) and substance P, and compared it with primary sensory neurons, obtained from a rat DRG explant (fig. 1D). Both hNS neurons (fig. 1D, top row) and DRG neurons (fig. 1D, bottom row) revealed the presence of these markers, located throughout the axonal length. In chapter 4 we also validated the ability of these neurons to sense noxious stimuli by exposing them to resiniferatoxin (capsaicin analog and TRPV-1 ligand) and to elicit action potentials, thus validating neuronal functionality.

After phenotypical evaluation, we developed and analyzed a 3D culture model for hNS, using DRG cultures as a comparison. The model is composed of a 12-mm polyurethane scaffold supporting the hNS or DRG, which are cultured in neural medium. After overnight attachment, the cell-seeded scaffold was covered with a solution of collagen/fibrin (at 4 mg/ml and 1 mg/ml respectively), that quickly gelled and formed a stable hydrogel. As visible in fig. 1E, showing 7-day old models, both cell types could develop dense and extensive neurite projections throughout the gel. After this culture period the neurite length for hNSs and DRGs was not significantly different and exhibited a mean value of $488.6 \mu\text{m}$ for and $503.5 \mu\text{m}$, respectively (fig. S1).

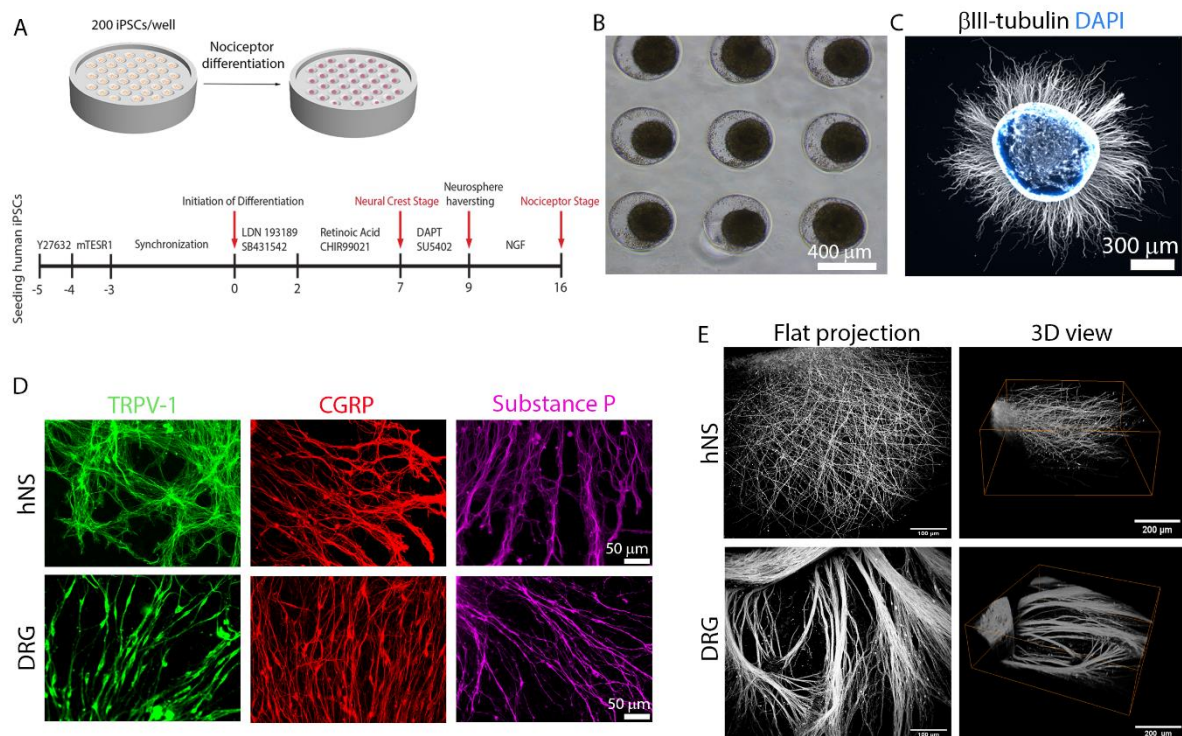


Figure 1. Development and characterization of iPSCs-derived nociceptors and 3D culture within fibrin/collagen hydrogels. A) Illustration of the process for iPSCs differentiation into nociceptors and spheroid formation. B) Brightfield micrograph of the agarose mold showing the formation of spherical, compact and uniform neuron clusters with an average diameter of $308.7 \pm 38.6 \mu\text{m}$. Scale bar is $400 \mu\text{m}$. C) Neurite outgrowth from the hNS after 7 days of culture on a laminin-coated coverslip. β III-tubulin is shown in white and DAPI in blue. Scale bar is $300 \mu\text{m}$. D) Characterization of the nociceptor phenotype from iPSCs-derived nociceptors (top row) and comparison with rat DRG neurons (bottom row). Both cell types were cultured for 7 days on laminin-coated coverslips and both show the expression of the characteristic nociceptor markers: TRPV-1 (green, left column), CGRP (red, middle column) and substance P (purple, right column). Scale bar is $50 \mu\text{m}$ for all images. E) 3D culture of hNSs (top row) and rat DRGs (bottom row) on a collagen/fibrin hydrogel for 7 days, demonstrating extensive neurite outgrowth throughout the gel, as visible through the flat projection (left column, scale bar is $100 \mu\text{m}$) and 3D view (right column, scale bar is $200 \mu\text{m}$).

Development of a human skin equivalent

To generate a human skin equivalent (hSE) we used a protocol previously established¹⁷ and illustrated in fig. 2A. After this culture period, the hSE construct appeared as a compact, opaque, elastic and circular tissue with an area of $159 \pm 7 \text{ mm}^2$, an approximate diameter of 14 mm and around 1 mm of thickness (fig. 2B). To analyze skin maturation, we performed histological and immunohistochemical analysis on the cross-sections (fig. 2C and 2D). As

visible from H&E staining (fig. 2C), the engineered tissue remarkably resembled the native structure¹⁹, evidencing the formation of a dermis and epidermis region. The dermis region denoted the presence of several elongated fibroblasts (in blue). The epidermis was characterized by a stratified cellular layer (in blue), culminating in a stratum corneum (in pink). Particularly, the hSE was characterized by the formation of a basal lamina in the dermal-epidermal transition, followed by a stratum basale (bottom zone; cuboidal keratinocytes), stratum spinosum (middle zone; slightly elongate keratinocytes) and stratum granulosum (top zone; very elongated keratinocytes) before the stratum corneum. In addition, the presence of keratin 10 (left image; in red) and loricrin (right image; in red) in the epidermal region of the hSE construct was detected (fig. 2D).

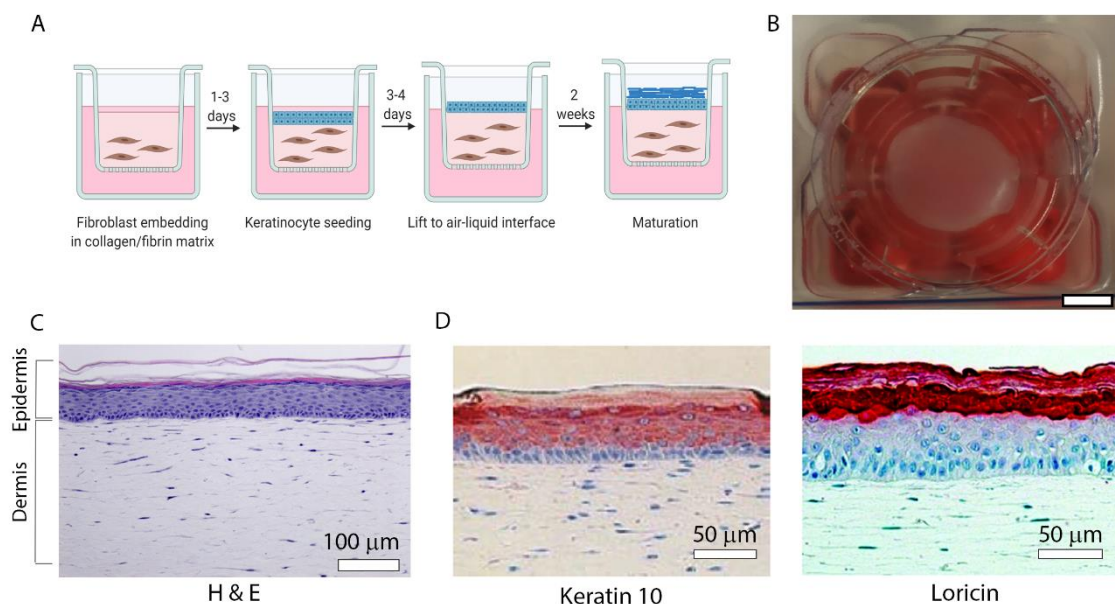


Figure 2. Development of a human skin equivalent composed of human fibroblasts and human keratinocytes on a collagen/fibrin matrix. A) Illustration of the followed protocol. In the first stage, fibroblasts are embedded in a collagen/fibrin matrix at a density of 5×10^5 cells/hydrogel (in 350 μ L) and cultured in submerged conditions for 1-3 days. Keratinocytes (5×10^5 cells) are then seeded on top of the gel and cultured in submerged conditions for 3-4 days. After this, the construct is lifted to an air-liquid interface to induce epidermal differentiation. The constructs are cultured for additional 2 weeks for further skin maturation. B) Photograph of the skin construct at the end stage of the protocol. Scale bar is 5mm. C) Hematoxylin and eosin (H&E) staining on a skin equivalent cross section showing the formation of dermis and epidermis, containing all characteristic layers. Scale bar is 100 μ m. D) Expression of keratin 10 (red, left image) and loricrin (red, right image) on skin equivalent layers. Samples were

counterstained with hematoxylin (blue). Scale bar is 50 μm . Illustration was made in biorender (<https://biorender.com/>).

Development of a skin innervation model in compartmentalized hydrogel platform

In order to fabricate a skin innervation model that is reproducible, biomimetic and permits a facile morphological assessment of both tissues, we developed a compartmentalized hydrogel platform. For this, we patterned two separate compartments within a collagen/fibrin hydrogel with 1.5 mm in height, measuring 1 mm and 3 mm in diameter, and intended for a neural population (hNS or DRG) and hSE section, respectively. To fabricate it, we followed the process illustrated in fig. 3A. A mesh support of nonwoven polyurethane is used to provide stable anchorage points to the hydrogel, facilitating the removal from the mold and future handling. After overnight polymerization, the patterned gels can be easily removed and maintained their structural stability, evidencing the presence of two separate compartments, separated by 1 mm (fig. 3B, 3C; a congo red dye was added to improve contrast).

For the preparation of the skin innervation model, we followed the timeline illustrated in fig. 3D, using either one hNS or DRG as neuron population. After implantation of the hSE section on the skin compartment, the platform was lifted to air and cultured for 21 days, with both tissues segregated but in proximity (fig. 3E). Following 21 days of co-culture we evaluated the neuronal outgrowth and the occurrence of innervation. hNSs developed a dense and radial neurite network with long neurite projections (marked by $\beta\text{III-tubulin}$) averaging 1786.6 μm in length (fig. 4A). Examining the border of the hSE section (marked by involucrin) at high magnification, it was possible to observe the occurrence of innervation, denoted by the presence of several neurites that grew into the skin region (fig. 4B and 4C). In DRG-containing platforms, we registered a similar neurite outgrowth pattern after the same culture period (fig. S3A). The mean neurite length was 2546.3 μm and extensive innervation was also detected (fig. S3B).

To quantify the innervation area in models composed of hNSs or DRGs, we acquired images of neurites present at the border of the hSE construct and penetrating into it. iPSCs-derived cells were able to generate a large innervation area (6.8×10^5 pixel area / mm^2), with DRGs producing an even higher number ($p < 0.05$) of innervating axons (1.7×10^6 pixel area / mm^2) (fig. S4).

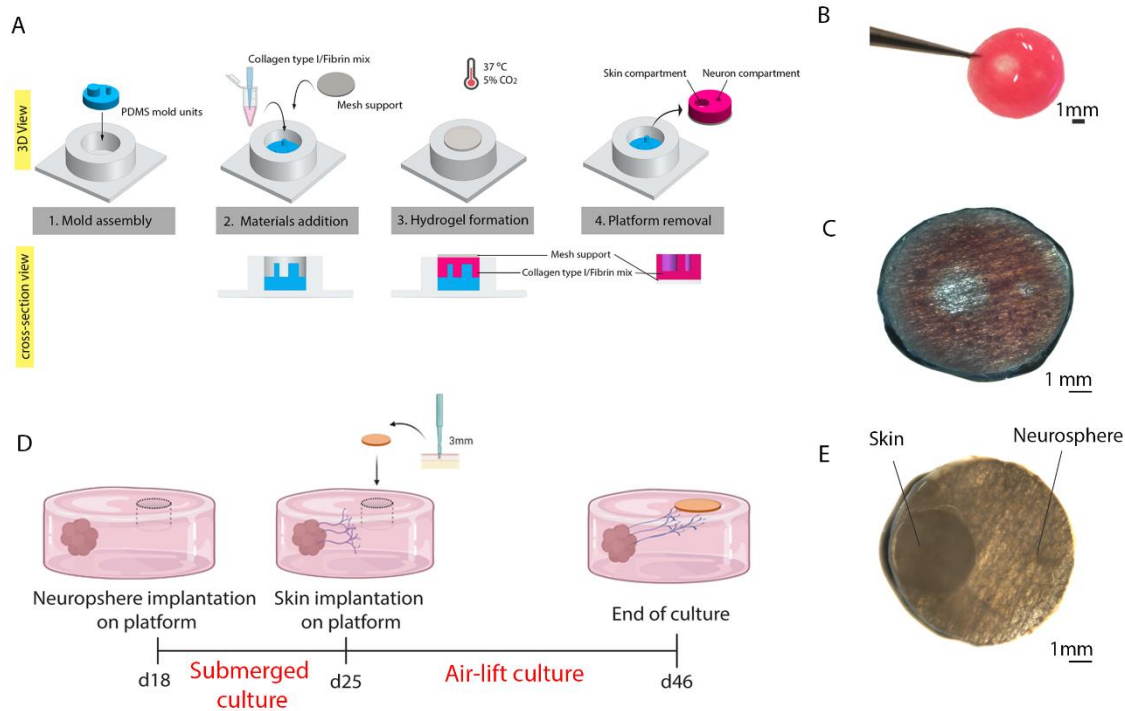


Figure 3. Fabrication of a collagen/fibrin platform with defined compartments for hSE and hNS. A) Illustration of the fabrication process. First, the PDMS mold units are assembled as demonstrated, with the pillars of the patterning unit facing up. Then, 150 μ l of a chilled collagen/fibrin mix solution is pipetted into the mold and a mesh support is placed on top. The gel is left to form overnight in the incubator at 37°C, 5% CO₂. The day after, the gel can be removed. B) Photograph of a gel evidencing the two wells for cell culture. The red color is from a red dye, added to improve visualization. Scale bar is 1 mm. C) Stereomicroscope micrograph showing in better detail the presence of compartments, for skin placement (3 mm; left compartment) and for neuron population seeding (1 mm; right compartment). D) Depiction of the followed protocol for the formation of an innervated skin platform. The timeline is relative to the beginning of the iPSCs culture protocol shown in fig. 1. Initially the hNS is implanted on the platform within the neural compartment. After 7 days of culture in submerged conditions with neural medium, the hSE section is added. For this, we take a 3mm biopsy from a larger hSE construct and carefully add it to the platform. A 10 μ l collagen/fibrin drop is added to bond it to the platform. The platforms are lifted to an air-liquid interface and cultured for 21 days with neural/skin medium at 1:1. E) Stereomicroscope micrograph showing the presence of a hSE section and a neurosphere in their defined compartments. Scale bar is 1 mm. Illustration (in D) was made in biorender (<https://biorender.com/>).

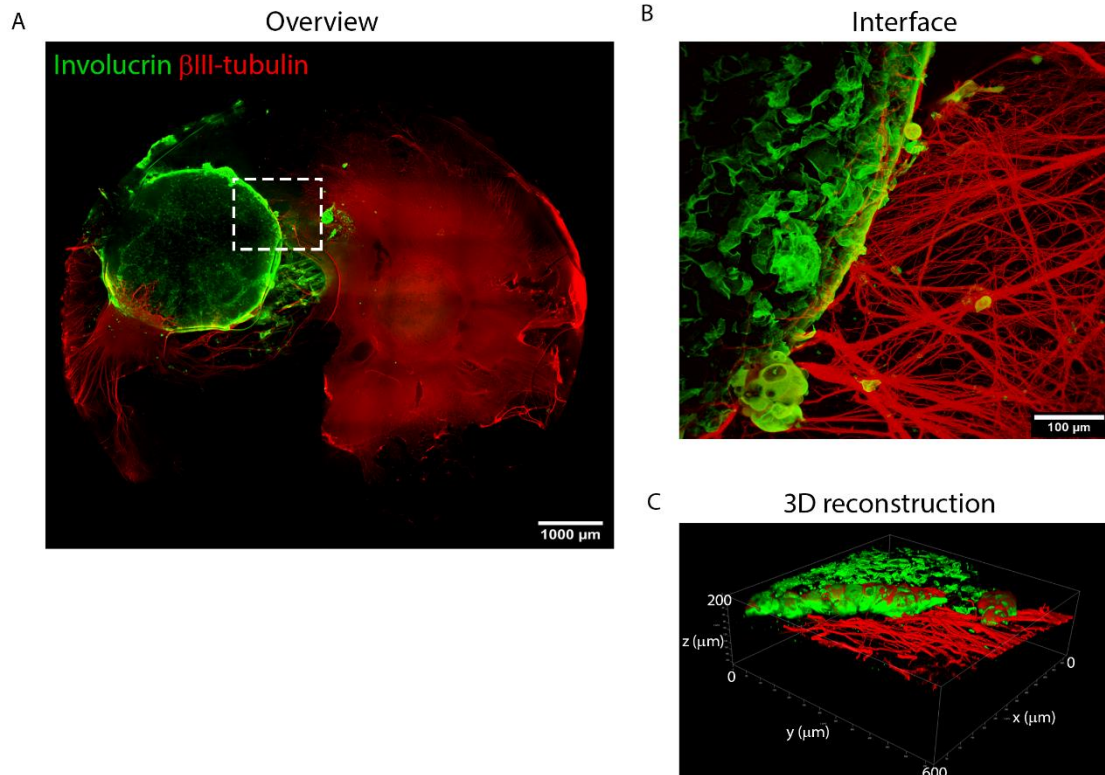


Figure 4. Remote innervation of a hSE section within the compartmentalized collagen/fibrin platform. A) Overview of the platform showing a vast neurite outgrowth (β III-tubulin, red) from the hNS towards the hSE compartment (involucrin, green). Scale bar is 1000 μ m. B) High magnification view of the white dashed rectangle marked in A). In the interface between the hSE section and the surrounding gel it is visible a large presence of neurites that penetrate into the hSE compartment. Scale bar is 100 μ m. C) 3D reconstruction of the interface view shown in B).

Innervated skin model function testing by capsaicin patch application

After characterization of a platform showing nociceptor innervation of a hSE construct, we performed an experiment that allowed simultaneous testing of the hSE and nociceptor function. For this, we applied a capsaicin patch topically (directly over the hSE section) for 1 or 24 h and measured the neural response (Fig. 5A). As a control, we used samples that were not exposed to the capsaicin patch. To dissect the influence of skin as an absorption barrier, we also tested platforms composed of hNS but lacking the hSE component. In these samples, the capsaicin patch was placed inside the void skin compartment. For comparison, we also realized this experiment on platforms composed of primary nociceptors from a rat DRG population (fig. S6).

The capsaicin patch was absorbed through the skin and delivered to the innervating neurites, causing subsequent degeneration. These morphological changes were evident when

comparing to control samples, in which normal neurite morphology was observed with no signs of injury (fig. 5B i). On the other hand, after 1 h of exposure (fig. 5B ii), neural degeneration (ND) was visible through the formation of blebs throughout the axonal network. If exposure to capsaicin was prolonged to 24 h, axonal degeneration was even more pronounced (fig. 5B iii). At this time point, bleb formation (BF) was ubiquitous and a loss of neurite alignment was observed (BF was 1318.0 ± 226.9). The appearance of blebs was significantly increased compared to control samples ($p < 0.001$; BF was 343.0 ± 110.3) and 1 h treated samples ($p < 0.05$; BF was 805.8 ± 464.9) (fig. 5C). Axonal degeneration measurements also revealed significantly more degraded neurites in 24 h-treated samples (ND was 0.04 ± 0.009) compared to those treated for 1 h ($p < 0.01$; ND was 0.021 ± 0.015) and control samples ($p < 0.001$; ND was 0.007 ± 0.002). In addition to degradation, we also observed signs of neurite retraction (pointed by white arrows in fig. 5B iii). We investigated neurite retraction in 2D hNS cultures (on laminin-coated coverslip) and saw that 24 h of capsaicin exposure (at $100 \mu\text{M}$) routinely formed wavefronts, resultant of pulled-back neurites (fig. S5). Moreover, we also saw that 24 h exposure could lead to the detachment of neural tissue in some areas (fig. S6B). Contrarily, control samples (fig. S6A) exhibited good neural tissue stability throughout the hydrogel. Innervation platforms composed of DRGs neurons showed a similar response as in hNS-containing platforms (fig. S8), with the capsaicin treatment leading to a time-dependent axonal degeneration with identical morphological changes. After 1 h of incubation degradation was still low (fig. S9; BC was 993.2 ± 402.4 ; ND was 0.039 ± 0.020), but after 24 h the neurites morphology exhibited clear signs of damage (fig. S9; BC was 2252.0 ± 507.3 ; ND was 0.1314 ± 0.04277) at a larger extent than hNS samples. In samples lacking a skin construct (fig. 5B bottom row), we could see that capsaicin diffusion was unhindered and thus neurite degeneration was even more pronounced. After 1h of exposure (fig. 5b v), a vast neurite degeneration and retraction was already observed (fig. S10; BC was 1929 ± 198.3 ; ND was 0.087 ± 0.042). Axonal degeneration was further increased when the exposure time was 24 h (fig. 5b vi), as most of the neurite network was destroyed or severely damaged (fig. S10; BC was 2610 ± 1815 ; ND was 0.15 ± 0.10).

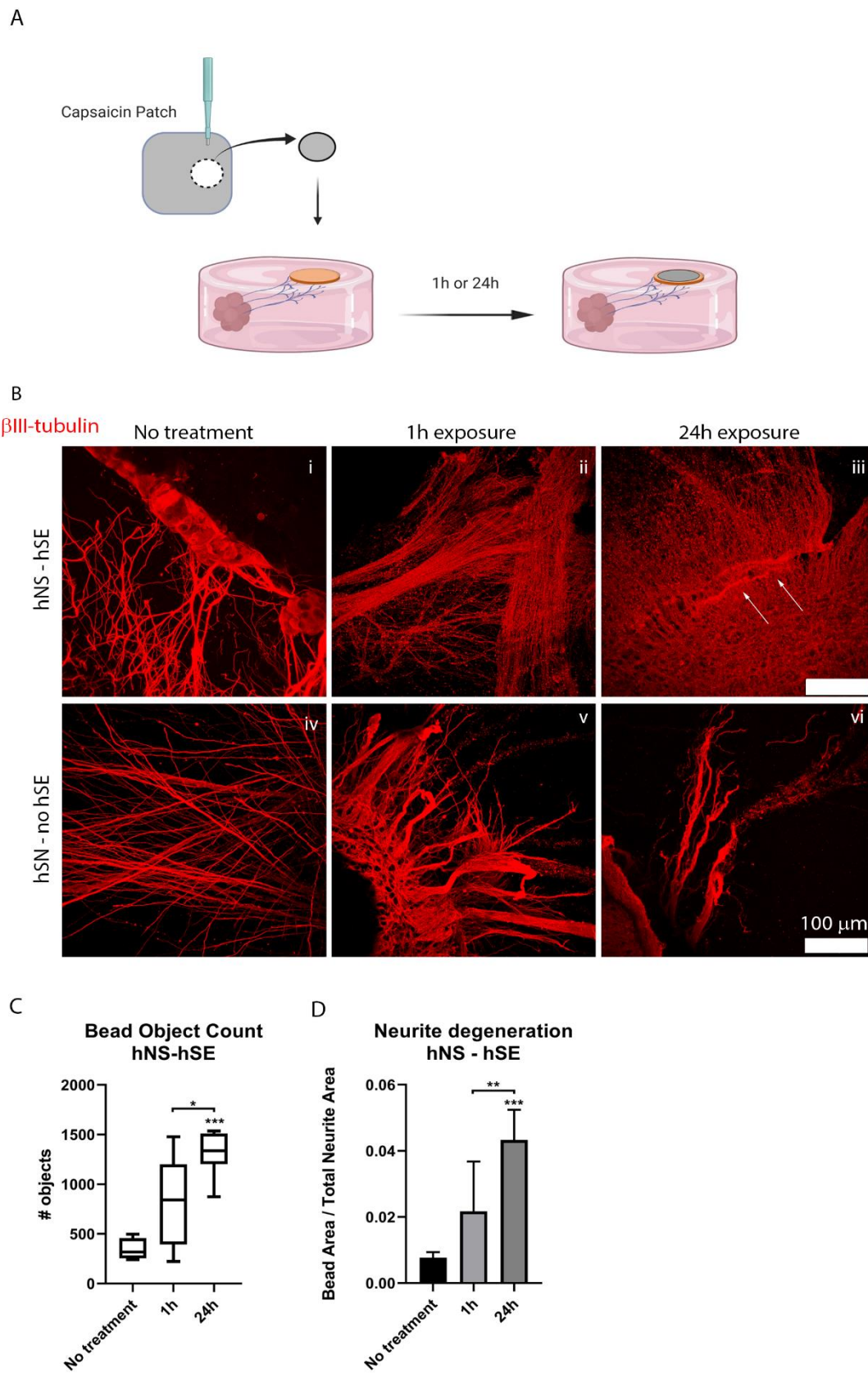


Figure 5. Nociceptor response to a capsaicin stimulus applied via a capsaicin patch, placed over the skin section. A) Illustration of the followed approach. A 3mm cut of a large capsaicin

patch was made with a biopsy punch and carefully placed over the skin. The samples were incubated for 1 h and 24 h and then analyzed. B) Immunostaining to β III-tubulin (in red) revealed that a capsaicin stimulus applied on the skin is absorbed and transmitted to the surrounding neurons, causing an exposure time-dependent degradation. After 1 h of exposure (top row, middle column) the signs of neurite degeneration are already evident. After 24 h of exposure (top row, right column) the amount of degenerated neurites increased and there were also signs of neurite retraction. In no treatment samples (top row, left column), the neurite morphology seemed normal, with no signs of injury. Samples with no added hSE (bottom row) showed that in the absence of a skin layer between the capsaicin patch and the gel platform, capsaicin diffusion was enhanced and consequently the effect over hNS at 1 h (middle image) or 24 h (right image) was even more pronounced. All scale bars are 100 μ m. C) and D) Quantification of the axonal degeneration observed in this experiment within the innervated hSE platform. C) Bead object count was performed by analyzing and counting circular objects in the images within a defined threshold. The boxplot shows data points from the minimum to maximum value. D) Neurite degeneration was obtained by dividing this value by the total neurite area. The bar graphs represent the mean + SD. Statistics were performed using one-way ANOVA followed by Tukey's HSD post-hoc test, where *** $p < 0.001$, ** $p < 0.01$ and * $p < 0.05$. Illustration was made in biorender (<https://biorender.com/>).

Discussion

Cutaneous sensory innervation is necessary to provide skin with its sensorial function and to promote efficient wound healing^{1,8}. Therefore, their presence within hSE is critical to better recapitulate the native skin structure/function, as well as to investigate pathologies involving cutaneous nerve fibers (e.g. diabetes)²⁰ and wound healing mechanisms/acceleration strategies^{6,21}. In particular, nociceptor fibers are essential to prevent organ damage, by mediating the pain sensing mechanisms that recognize noxious stimuli in direct (e.g. capsaicin) or indirect (e.g. high temperature) contact with the skin. In doing so, nociceptor fibers help avoiding them^{1,18,22}. Thus, *in vitro* hSE models incorporating nociceptors will also open the possibility to investigate the influence of compounds on skin and the underlying nerves (e.g. cosmetic, therapeutic creams, etc.)¹².

The goal of this work was to develop a 3D biomimetic model of human skin with innervating nociceptors. At the same time, we intended to design a platform that simplified *in vitro* testing, such as morphological evaluation of the innervating fibers. To achieve this, we fabricated a hydrogel platform containing two separate wells, for compartmentalized co-culture of a nociceptor population (hNS) and a skin equivalent (hSE) (fig. 3). The compartmentalization of tissues ensures reproducible and precise cell location, consistent nerve fiber length/innervation density and replicates the native mode of cutaneous innervation from a

distant DRG²³. Additionally, assessment of the innervating fibers can be done directly in whole-mount samples, thus avoiding the laborious and time-consuming process of sample sectioning. As a hydrogel material, we used a collagen/fibrin blend, which permits the simple and quick preparation of a patterned hydrogel with a stable shape. Moreover, these materials are permissive for both neural and skin cells growth and have been extensively used in skin and nerve tissue engineering approaches^{24,25}.

To prepare the hNS, we used the method reported in chapter 4, which yields a large number of self-aggregating and uniformly sized cell clusters (fig. 1A and 1B). When harvested, at the trunk neural crest stage, the cell clusters can be precisely placed on a chosen substrate, e.g. laminin-coated coverslip, where they exhibit neural outgrowth and attain a nociceptor phenotype (fig. 3C and 3D). Cultures of a collagen/fibrin hydrogel embedding a hNS-seeded scaffold resulted in a 3D, vast and fairly anisotropic neurite network (fig. 1E), with comparable densities to DRG cultures (fig. S1).

To fabricate a hSE model we used a well-established and reported method^{14,15} that generates a skin-like tissue with remarkable morphological resemblance to the native tissue²⁶, with clear formation of a dermis and stratified epidermis region (fig. 2B-D). To assemble the innervated skin model, we added the neural and skin tissues sequentially to the hydrogel platform, starting with the neural cell cluster, in order to prime neurite outgrowth within the hydrogel, before hSE implantation (fig. 3D). Co-cultures of 21 days resulted in a vast and radial 3D neurite outgrowth, reaching and innervating the hSE section (fig. 4). Comparative co-cultures with a primary DRG explant led to a similar neurite density, but with increased targeting towards the hSE that resulted in a larger innervation density compared to hNS-hSE models (fig. S3 and S4).

Once the skin innervation model was established, we devised an experimental setup to simultaneously evaluate the skin barrier function and nociceptor ability to detect noxious stimuli. To do this, we applied a commercially available capsaicin patch (Qutenza™) in contact with the hSE and directly measured the nociceptors' reaction, via fluorescent imaging of the whole sample (fig. 5A). Despite causing irritation and a burning sensation, capsaicin treatments are used in the clinic as a pain management solution; the molecule is able to selectively target and stimulate nociceptors, causing their reversible defunctionalization/ablation^{4,27}. In particular, the Qutenza™ patch delivers a high capsaicin concentration (80 mg capsaicin per gram of adhesive; 8%) and is shown to produce an effective pain relief for up to 12 weeks, after a single 60 min application⁴. Capsaicin activates TRPV-1 channels, promoting calcium influx and consequent mitochondrial dysfunction, inhibition of metabolism and loss of electrical excitability, leading to loss of function. Additionally, the maintenance of cellular membrane integrity may be compromised, resulting in the collapse/retraction of nerve endings^{4,28}. In our experiment with hNS-hSE platforms, we

observed that the capsaicin treatment led to the appearance of blebs within the neurite network, indicating neurite degeneration, in proportion to the patch application time (fig. 5B-D). This was evident when compared to the control samples, whose neurite networks appeared straight and with no beads. Because of these obvious morphological changes, we could quantify neurite degeneration, with an in-house developed imaging algorithm that tracked bead formation (fig. S7). We also observed neurite retraction as a consequence of capsaicin treatment in our 3D platform (fig. 5B) and in 2D cultures (fig. S5), indicating a similar behavior of these differentiated nociceptors compared to their native counterparts.

In the absence of a hSE construct, neurite damage was even more pronounced, exhibiting extensive degeneration already after 1 h of patch exposure and almost full neurite ablation after a 24 h treatment (fig. 5B bottom row and fig. S10). This finding underscores the ability of our skin construct to act as a barrier that slows the delivery of capsaicin to innervating fibers. In DRG containing platforms we also detected the same neurite regression and degeneration effect after capsaicin exposure (fig. S8), which indicates that our differentiated neurons replicate the primary neuron response to this noxious stimulus. However, the neurite damage was further accentuated in DRGs, compared to differentiated nociceptors (fig. 5C-D and fig. S9), probably due to a higher expression of TRPV-1 and thus increased sensitivity to capsaicin.

As demonstrated, this platform can support testing of compounds with potential effects on cutaneous nerves, applied via a method that mimics real topical applications. Particularly, substances that activate nociceptors and may trigger a painful sensation, as well as cause neurotoxicity, could be evaluated with this platform. Due to our platform design denoted by two horizontally separate compartments, testing on the platform is simplified by the ability to directly observe the innervating fibers without need for sample sectioning. This is an improvement from other hSE models¹³ where the stacked configuration of neurons and skin tissue requires sectioning to observe the innervating fibers. Our previous work (chapter 3) demonstrated that our iPSC-derived neurons could be stimulated to release CGRP and substance P, neuropeptides involved in nociceptive pain, after TRPV-1 stimulation with a capsaicin analog. Further quantification of these neuropeptide release would strengthen the experimental read-out, allowing to better determine the response of our model to noxious stimuli. Finally, the acquisition of histological and immunohistochemical cross-sectional images of the model after the co-culture period (and capsaicin exposure) would permit the evaluation of hSE quality as well as epidermal nerve fiber density/morphology. Regardless, we have shown here a method that combines two established tissue models to generate an innervated skin platform, with shown application in neuron testing.

Conclusion

We have developed a 3D platform containing nociceptor-innervated skin of human origin, recapitulating the native manner of innervation and that can be easily observed without sample sectioning. Using this platform, we demonstrated the potential to evaluate the effect of topical compounds on the innervating fibers. We believe that this pilot work contributes towards the pursuit of biomimetic and functional skin models for improved preliminary *in vitro* research that may enhance predictability of results in following animal and human trials.

Acknowledgements

We would like to thank the province of Limburg and VUMC for the project funding. This work was partly supported by the research program VENI 2017 STW- project 15900 financed by the Dutch Research Council (NWO).

References

1. Laverdet, B. *et al.* Skin innervation: Important roles during normal and pathological cutaneous repair. *Histol. Histopathol.* **30**, 875–892 (2015).
2. Emmerson, E. Efficient Healing Takes Some Nerve: Electrical Stimulation Enhances Innervation in Cutaneous Human Wounds. *J. Invest. Dermatol.* **137**, 543–545 (2016).
3. Randall, M. J., Jüngel, A., Rimann, M. & Wuertz-kozak, K. Advances in the Biofabrication of 3D Skin *in vitro*: Healthy and Pathological Models. *Front. Bioeng. Biotechnol.* **6**, (2018).
4. Anand, P. & Bley, K. Topical capsaicin for pain management: Therapeutic potential and mechanisms of action of the new high-concentration capsaicin 8 patch. *Br. J. Anaesth.* **107**, 490–502 (2011).
5. Barbara Frias, Merighi, A. Capsaicin, Nociception and Pain. *Molecules* **21**, (2016).
6. Blais, M. *et al.* Sensory Neurons Accelerate Skin Reepithelialization via Substance P in an Innervated Tissue-Engineered Wound Healing Model. *Tissue Eng. Part A* **20**, 2180–2188 (2014).
7. Parfejevs, V. *et al.* Injury-activated glial cells promote wound healing of the adult skin in mice. *Nat. Commun.* **9**, 1–16 (2018).
8. Emmerson, E. Efficient Healing Takes Some Nerve: Electrical Stimulation Enhances Innervation in Cutaneous Human Wounds. *J. Invest. Dermatol.* **137**, 543–545 (2017).
9. Miyazaki, H. *et al.* A novel strategy to engineer pre-vascularized 3-dimensional skin substitutes to achieve efficient, functional engraftment. *Sci. Rep.* **9**, 1–3 (2019).

10. Lee, J. *et al.* Hair-bearing human skin generated entirely from pluripotent stem cells. *Nature* (2020)
11. Ng, W. L., Qi, J. T. Z., Yeong, W. Y. & Naing, M. W. Proof-of-concept: 3D bioprinting of pigmented human skin constructs. *Biofabrication* **10**, (2018).
12. Pellevoisin, C., Bouez, C. & Cotovio, J. *Cosmetic industry requirements regarding skin models for cosmetic testing*. *Skin Tissue Models* Elsevier Inc. (2018).
13. Muller, Q. *et al.* Development of an Innervated Tissue-engineered Skin with Human Sensory Neurons and Schwann Cells Differentiated from iPS Cells. *Acta Biomater.* 1–9 (2018)
14. Vahav, I. *et al.* Reconstructed human skin shows epidermal invagination towards integrated neopapillae indicating early hair follicle formation in vitro. 761–773 (2020)
15. Kosten, I. J., Buskermolen, J. K., Spiekstra, S. W., De Gruijl, T. D. & Gibbs, S. Gingiva Equivalents Secrete Negligible Amounts of Key Chemokines Involved in Langerhans Cell Migration Compared to Skin Equivalents. *J. Immunol. Res.* **2015**, 13–17 (2015).
16. Chambers, S. M. *et al.* Combined small-molecule inhibition accelerates developmental timing and converts human pluripotent stem cells into nociceptors. *Nat. Biotechnol.* **30**, 715–720 (2012).
17. Ouwehand, K., Spiekstra, S. W., Waaijman, T. & Scheper, R. J. Langerhans cells derived from a human cell line in a full-thickness skin equivalent undergo allergen-induced maturation and migration. *J. Leukoc. Biol.* **90**, 1027–1033 (2011).
18. Dubin, A. E. & Patapoutian, A. Nociceptors: the sensors of the pain pathway. *J. Clin. Invest.* **120**, 3760–3772 (2010).
19. Mieremet, A. *et al.* Improved epidermal barrier formation in human skin models by chitosan modulated dermal matrices. *PLoS One* 1–20 (2017).
20. Yagihashi, S., Mizukami, H. & Sugimoto, K. Mechanism of diabetic neuropathy: Where are we now and where to go? *J. Diabetes Investig.* **2**, 18–32 (2011).
21. Weller, S. J. *et al.* Advances in Skin Regeneration Using Tissue Engineering. *J. Clin. Microbiol.* **36**, 1305–1317 (1998).
22. Smith, P. G. & Liu, M. Impaired cutaneous wound healing after sensory denervation in developing rats: Effects on cell proliferation and apoptosis. *Cell Tissue Res.* **307**, 281–291 (2002).
23. Roggenkamp, D. *et al.* Epidermal nerve fibers modulate keratinocyte growth via

- neuropeptide signaling in an innervated skin model. *J. Invest. Dermatol.* **133**, 1620–1628 (2013).
24. Chaudhari, A. A. *et al.* Future prospects for scaffolding methods and biomaterials in skin tissue engineering: A review. *Int. J. Mol. Sci.* **17**, (2016).
 25. Gu, X., Ding, F. & Williams, D. F. Neural tissue engineering options for peripheral nerve regeneration. *Biomaterials* **35**, 6143–6156 (2014).
 26. Vela-Romera, A. *et al.* Characterization of the human ridged and non-ridged skin: a comprehensive histological, histochemical and immunohistochemical analysis. *Histochem. Cell Biol.* **151**, 57–73 (2019).
 27. Peppin, J. F. & Pappagallo, M. Capsaicinoids in the treatment of neuropathic pain: A review. *Ther. Adv. Neurol. Disord.* **7**, 22–32 (2014).
 28. Chang, C., Jiang, B. & Chen, C. Ion Channels Involved in Substance P-Mediated Nociception and Antinociception. *Int. J. Mol. Sci.* **20**, 1–13 (2019).

Supplementary information

Development of a fully human model of innervated skin

Afonso Malheiro¹, Maria Thon², Ana Filipa Lourenço¹, Adrián Seijas Gamardo¹, Sue Gibbs², Paul Wieringa¹, Lorenzo Moroni¹

¹MERLN Institute for Technology-Inspired Regenerative Medicine, Maastricht University

²Department of Molecular Cell Biology and Immunology, Amsterdam University Medical Center

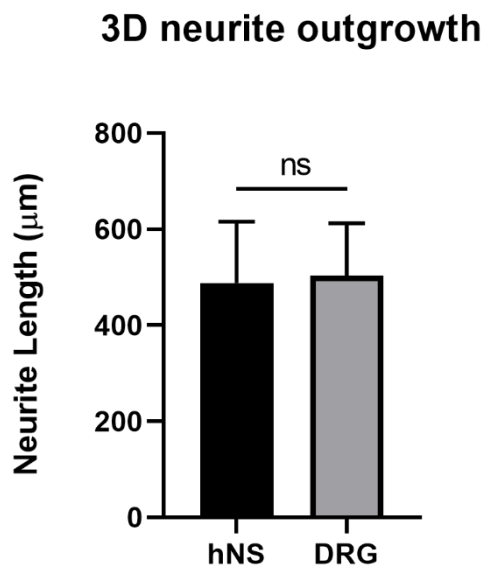


Figure S1. Neurite outgrowth from human nociceptor spheroids (hNS) (black bar) or rat DRGs (gray bar) in collagen/fibrin hydrogels. The bar graph represents the mean \pm SD obtained from neurite length measurements in images containing the full neurite length. At least 10 measurements were taken per image and 3 images were taken per sample ($n = 4$). Statistics were performed with an unpaired t-test and ns denotes $p > 0.05$.



Figure S2. Photograph of the PDMS units used to pattern the skin and neural compartments on the collagen/fibrin hydrogel. Scale bar is 10 mm.

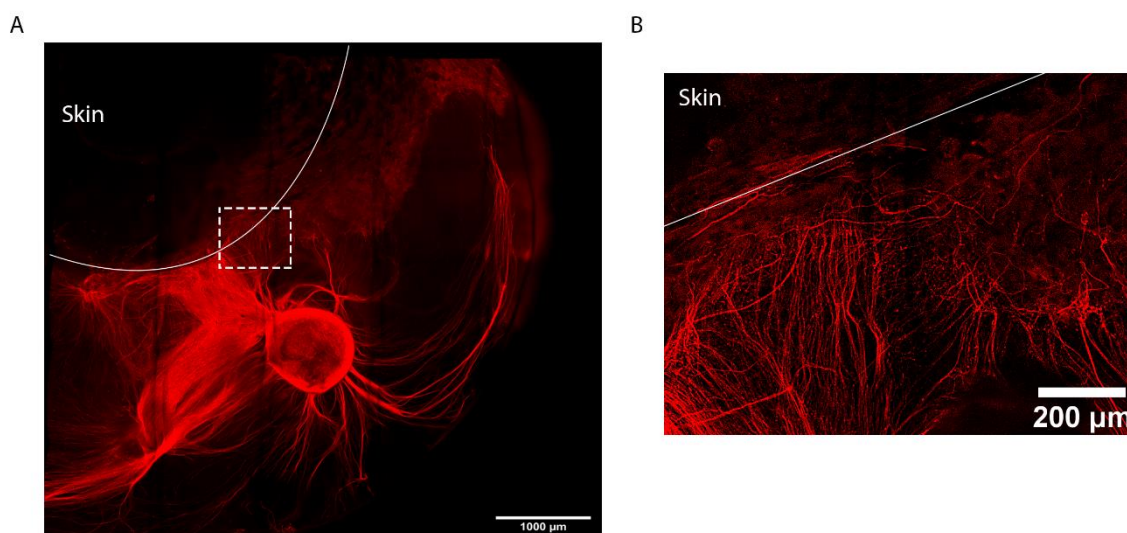


Figure S3. DRG remote innervation on the skin compartment. A) Overview of the whole platform showing the vast neurite outgrowth (immunostained by β III-tubulin in red) from the DRG cluster and into the compartment containing the skin section. This compartment is delineated with a white line. Scale bar is 1000 μ m. B) High magnification of the white dashed

box shown in A). This interface view illustrates well the extensive innervation of the cultured skin.

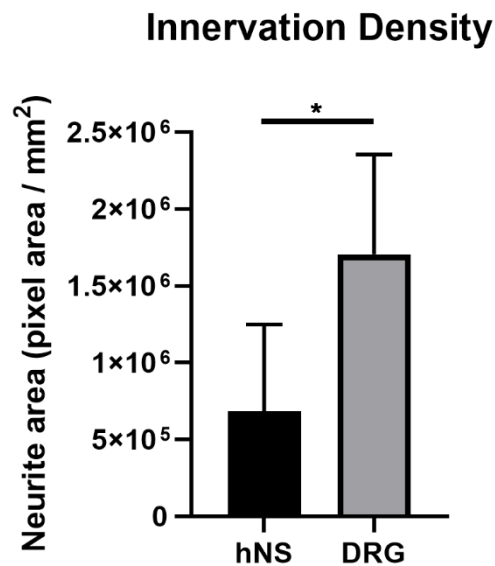


Figure S4. Innervation density measurement on innervated hSE models composed of hNS and DRG as nociceptor population. The measurements were obtained by selecting similar regions of interest (ROI) at the border of the hSE section that contained penetrating neurites. To quantify these, we measured the axonal area (β III-tubulin⁺ segments) and divided the results by the image area. For this we took 3 images per sample ($n = 3$). The bar graphs represent the mean \pm SD. Statistics were performed with an unpaired t-test, where * denotes $p < 0.05$.

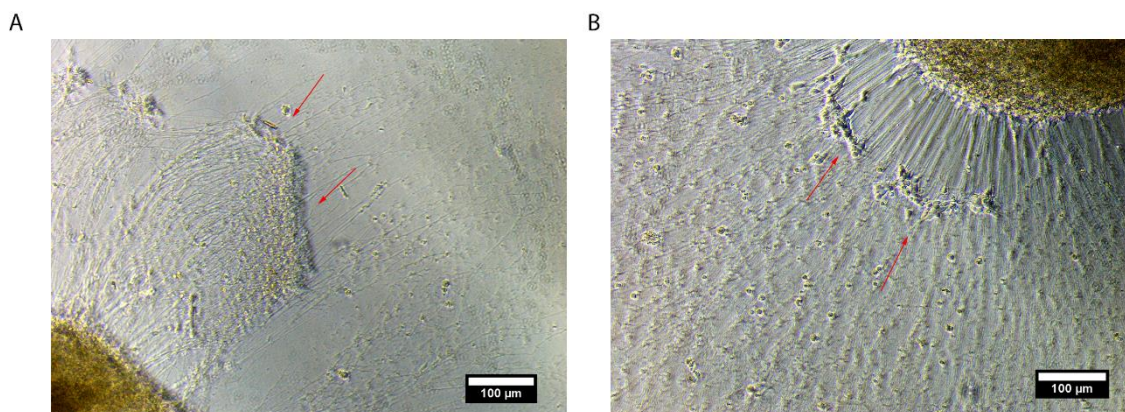


Figure S5. Capsaicin exposure effect on 7-day old hNS cultured on laminin-coated coverslips. After 24h of 100 μ M exposure, we detected the occurrence of neurite retraction in many regions, evidenced by the neurite front clustering pointed by the red arrows in A) and B). Neurite regrowth from those spots is also visible. Scale bars are 100 μ m.

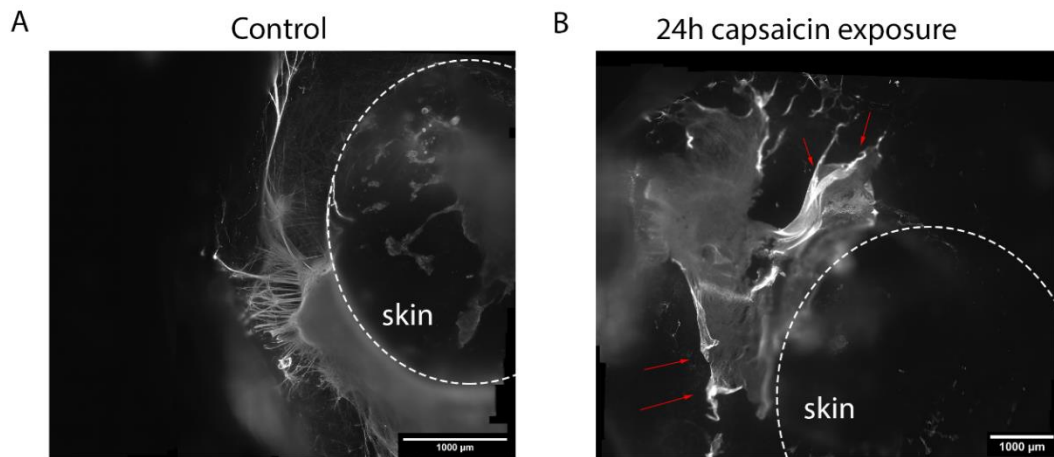


Figure S6. Capsaicin exposure effect on hNS cultured on the 3D compartmentalized platform. A) On control samples (left image), nociceptor neurites maintain a normal morphology (no blebbing or other signs of degradation) and remain innervating the hSE. B) Samples cultured with the capsaicin patch for 24 h, evidence a peeling aspect (red arrows), caused by extensive neurite regression. β III-tubulin is shown in white and the scale bars are 1000 μ m.

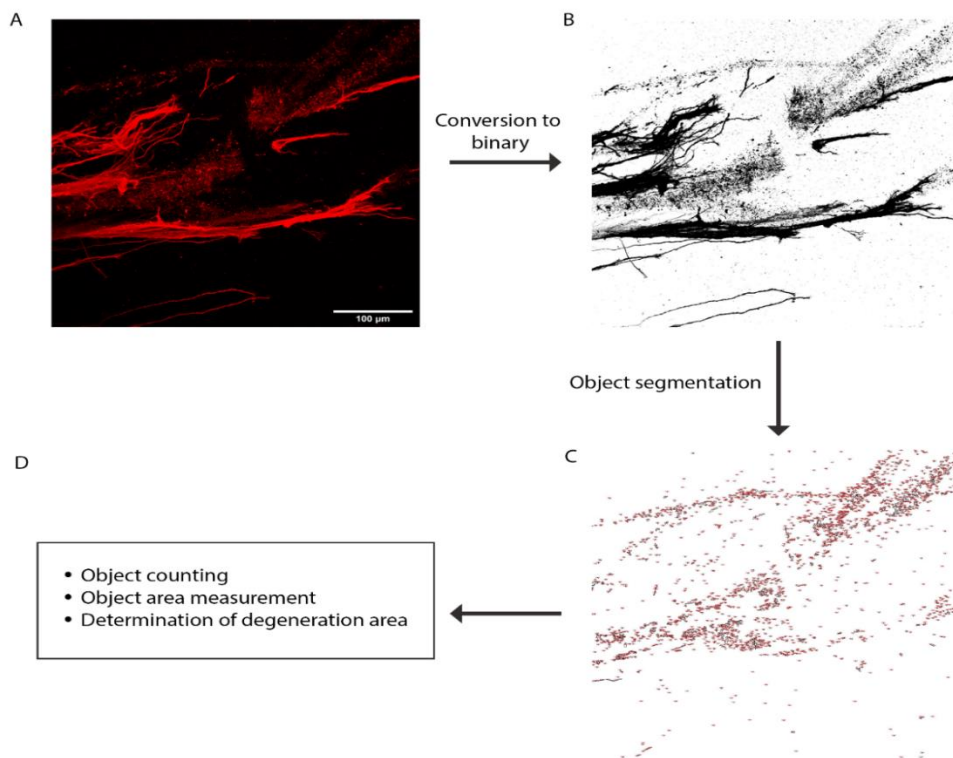


Figure S7. Algorithm for quantification of axonal degeneration. A) Original image from β III-tubulin⁺ segments. B) Binary image of A). C) Object segmentation with the Analyze particle function of imageJ. D) Object counting and area measurement.

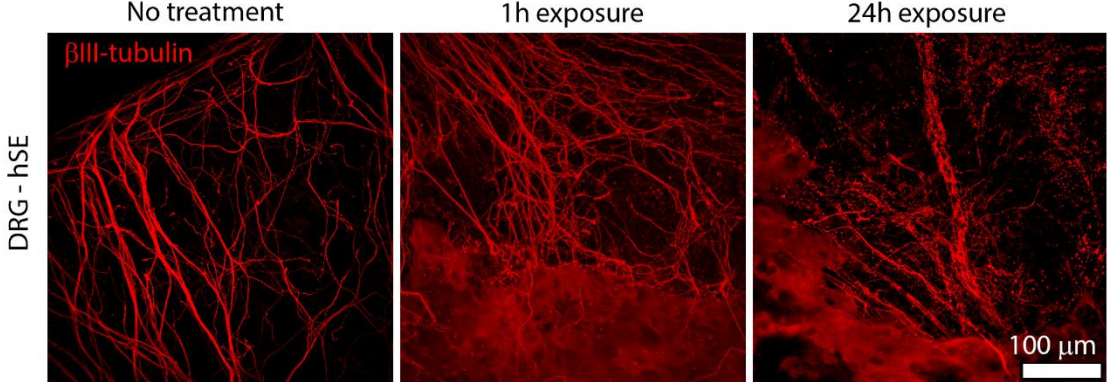


Figure S8. Capsaicin patch exposure test on DRG/hSE platforms. Samples were not treated (left image), exposed to the capsaicin patch for 1 h (middle image) or 24 h (right image). Control samples revealed normal neurite morphology, while capsaicin treated samples reveal some axonal damage, particularly visible in the 24 h condition. β III-tubulin is shown in red and the scale bar is 100 μ m.

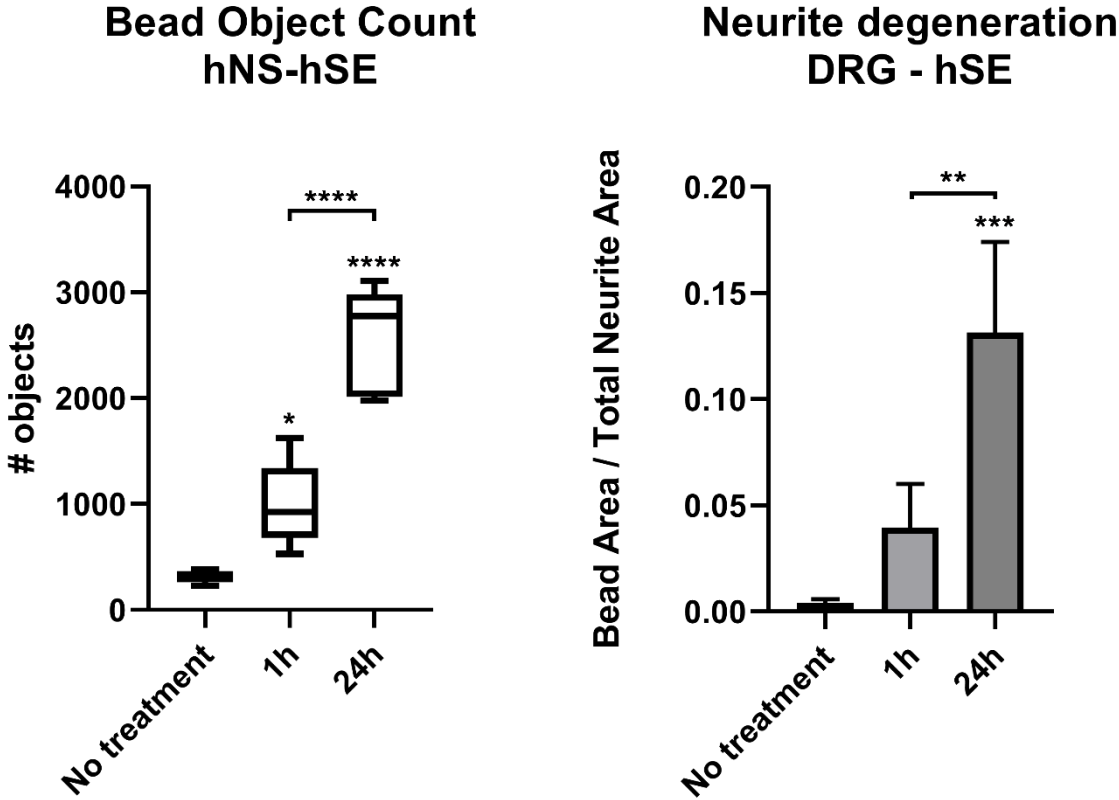


Figure S9. Quantification of the axonal degeneration in innervating platforms containing a DRG as neuron population. A) Bead object count was performed by analyzing and counting circular objects in the images within a defined threshold. The boxplot shows data points from the minimum to maximum value. B) Neurite degeneration was obtained by dividing this value by the total neurite area. Statistics were performed using one-way ANOVA followed by Tukey's HSD post-hoc test, where *** $p < 0.001$ and ** $p < 0.01$.

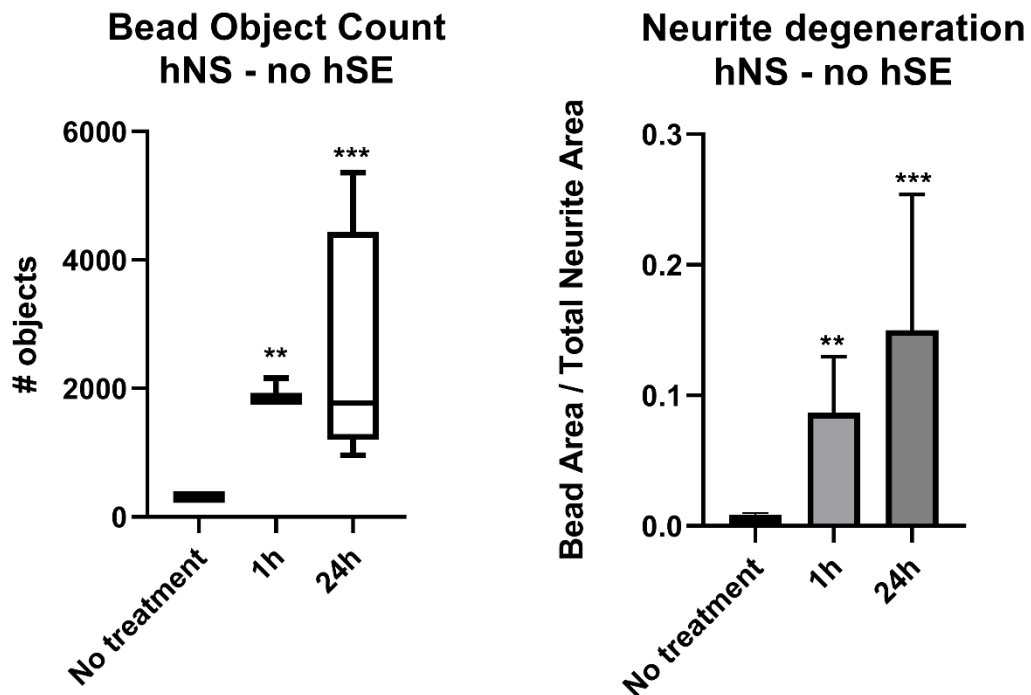


Figure S10. Quantification of the axonal degeneration in platforms devoid of a hSE section. A) Bead object count was performed by analyzing and counting circular objects in the images within a defined threshold. The boxplot shows data points from the minimum to maximum value. B) Neurite degeneration was obtained by dividing this value by the total neurite area. Statistics were performed using one-way ANOVA followed by Tukey's HSD post-hoc test, where *** $p < 0.001$ and ** $p < 0.01$.

Chapter 7

Exploring the neurovascular axis: neuron-glia-endothelial cell interactions within a biomimetic *in vitro* platform

Afonso Malheiro, Adrián Seijas Gamardo, Abhishek Harichandan, Carlos Mota, Paul Wieringa, Lorenzo Moroni

Complex Tissue Regeneration Department, MERLN Institute for Technology-Inspired Regenerative Medicine, Maastricht University

Abstract

Nerves and blood vessels are present in most organs and are indispensable for their function and homeostasis. Within these organs, neurovascular (NV) tissue forms congruent patterns and establishes vital interactions. Several pathologies, including diabetes type II, produce NV disruptions with serious consequences to patients that are complicated to study using animal models. Complex *in vitro* organ platforms, with neural and vascular supply, allow the investigation of such interactions, whether in normal or pathological context, in an affordable, simple and direct manner. To date, few *in vitro* models contain NV tissue, and most strategies report models with non-biomimetic representations of the native environment. To this end, we have established here a NV platform that contains mature vasculature and neural tissue, composed of human microvascular endothelial cells (HMVECs), induced pluripotent stem cell (iPSCs) derived sensory neurons, and primary rat Schwann cells (SCs) within a fibrin embedded polymeric scaffold. First, we show that SCs can induce the formation and stabilize vascular networks to the same degree as the traditional and more thoroughly studied human dermal fibroblasts (HDFs). We also show that through SC pre-patterning, we are able to control vessel orientation. Using our NV platform, we demonstrate the concomitant formation of three-dimensional neural and vascular tissue, and the influence of different medium formulations and cell types on the NV tissue outcome. Finally, we propose a protocol to form mature NV tissue, via integration of independent neural and vascular constituents. The platform described here provides a versatile and advanced model for *in vitro* research of the NV axis.

Introduction

Nerves and blood vessels (BVs) are commonly found in the same regions, forming overlapping arborized networks/patterns within tissues¹. This uncanny alignment is the result of intimately linked developmental pathways of these two systems, with each navigating side-by-side as tissues grow. This neurovascular (NV) alignment and codependency persists in mature tissues as both the neural and vascular tissues exhibit mutual requirements, where large nerves require vascularization to ensure nutrient and oxygen supply, and large BVs rely on innervation to regulate vasodilation and vasoconstriction^{2,3}. The underlying reason for this shared organization and distribution of nerves and BVs is similar: to provide sufficient coverage of a target tissue to ensure survival and function. Parallels also exist in terms of how these target tissues become innervated and vascularized; for both subunits of the NV axis, a tissue releases growth factors (GFs), in soluble or matrix-bound form, to attract and direct nerve and BV growth¹. For nerves, non-innervated target cells secrete GFs such as nerve growth factor (NGF) to attract neurons. For vessels, hypoxic tissues secrete vascular endothelial growth factor (VEGF) to trigger vascularization. In both cases, once the target tissue is stimulated by neuropeptides or sufficiently supplied with oxygen, the production of GFs by the target tissue subsides^{1,4}. To reach their targets, nerves and BVs make use of similar pathfinding mechanisms. The growth cone is a specialized tip of a growing neuron that has numerous filopodia that actively extend and retract in response to the environment, determining the direction of nerve growth. Similarly, sprouting BVs designate a specialized endothelial cell as “tip cell” to sense the milieu and pave the way, while trailing “stalk cells” proliferate and form capillary lumens^{1,3,5}. To promote development, survival and growth of nerve and vessel networks, there is a plethora of GFs and receptors which are common to both tissues^{5,6}. NGF, for instance, is a known neurotrophic factor but it can also exert a positive influence on endothelial cell (EC) proliferation, survival and migration. Similarly, the VEGF family is known to induce vasculogenesis and angiogenesis but can also promote neurogenesis⁵. Besides common molecular players, there is also mounting evidence of direct influence of nerves on vessels, and vice-versa, which results in the stereotyped NV alignment. For example, smooth muscle cells lining the vessels secrete artemin to induce sympathetic nerve fiber alignment^{6,7}. Conversely, within the skin, Schwann cells (SCs) associated with sensory nerves instruct vessel patterning via local VEGF secretion⁸. SCs and ECs interactions, in particular, have been more thoroughly investigated, with *in vitro* reports showing a promotion of ECs migration by SCs⁹ and *in vivo* reports showing that BVs direct the migration of SC cords during nerve regeneration¹⁰. However, there is scarce evidence regarding the vasculogenic/angiogenic potential of SCs. To better understand the NV axis, it is crucial to develop research platforms that allow the study of nerves and BVs in a normal or pathological state. While *in vivo* models provide the most complex representation in terms of tissue architecture and physiology, that

inherent complexity limits the ability to discern individual contributions of cells and molecules. Moreover, the various biological differences between humans and animal models diminish the clinical potential of the findings. A suitable *in vitro* model would not only improve the knowledge about native NV communication, but also accelerate translational research. For instance, in diabetes, a worldwide prevalent disease, microvascular damage is frequent, which in turn affects the function of peripheral nerves. It is known that hypoxia, resulting from microvessel alteration, leads to increase oxidative stress, inflammation and loss of trophic support for neurons and SCs¹¹. However, the current scarcity of *in vitro* NV models precludes the research and development of therapeutic drugs, which has to be presently conducted via diabetic (e.g. streptozotocin, STZ-induced, etc.) animal models. These models are sub-optimal, containing several limitations such as high variability, high cost, systemic damage (complicated to have a clear cause/effect understanding) and high incidence of secondary effects due to STZ treatment¹². To circumvent this, some models have been proposed, although most of them replicate the central nervous system NV unit^{13,14,15}. Peripheral nerve (PN) NV models include the work of Grasman et al.¹⁶, in which human umbilical vein ECs (HUVECs) stimulated axonal growth from a rat dorsal root ganglion population (DRG). However, this model has some drawbacks: first, HUVECs originate from a non-innervated tissue, the umbilical cord, thus limiting the model relevance; second, DRG extraction requires recurrent animal sacrifice, which poses ethical concerns and is an expensive procedure; lastly, the co-cultures were established on a glass coverslip, which does not provide the three-dimensional (3D) support required for the proper development and maturation of both tissues. Yuan et al.¹⁷ described a similar system, but containing human microvascular endothelial cells (HMVECs) as a vascular population instead. These cells originate from the skin, a richly innervated tissue, and thus constitute a more relevant cell source. The authors discovered that co-cultures of HMVECs and DRGs led to higher overall cell viability and higher expression of VEGF and NGF, compared to single cultures of each cell population. Yet, the use of a flat substrate in this culture system limits again the model biomimicry, particularly the vascular tissue, which cannot form luminized capillaries on a two-dimensional (2D) space. To improve upon this, Osaki et al.¹⁸ proposed an approach that uses embryonic stem cell-derived motor neurons (ESC-MNs) and induced pluripotent stem cell (iPSC)-derived ECs cultured on a collagen gel, to form a 3D NV unit within a microfluidic chip. The authors found out that the presence of ECs improved neurite length and function. Despite the shown technological advances, the depicted vascular networks do not present a mature vessel morphology and phenotype. Moreover, the absence of SCs excludes the possibility of forming myelinated axons and oversimplifies the model of a NV milieu, where the presence of different cell types is crucial for proper tissue function.

Here, we report the formation of a 3D NV platform, composed of human iPSCs-derived sensory (nociceptor) neurons, HMVECs and SCs. First, we describe the potential of SCs to

induce vasculogenesis of HMVECs in a fibrin hydrogel, with a similar outcome to the well-established human dermal fibroblasts (HDFs). We further conclude that SC-conditioned medium, despite enhancing tubule formation on matrigel-coated surfaces, is not sufficient to induce 3D vessel formation in fibrin hydrogels. We also demonstrate that, by pre-patterning of SCs with an aligned microfibrinous scaffold, we are able to direct vessel orientation. To fabricate a NV platform, we capitalize on the use of a neural model, developed by us and previously described in chapter 4. The model is composed by a 3D co-culture of functional human iPSCs-derived sensory neurons and SCs, seeded on a microfibrinous scaffold and embedded in a fibrin hydrogel. As a result we were able to obtain a vast anisotropic and myelinated neurite network. From this, we explored different strategies to include a vascular component and create a peripheral NV unit. Finally, we show that through initial segregation of neural and vascular cultures, followed by integration in a single unit, we are able to generate a mature NV model that show hallmarks of the native NV interactions, such as NV alignment.

We believe that the proposed model constitutes a significant advancement in the biofabrication of complex multicellular ecosystem that is the peripheral NV unit. The platform presented here can be utilized to tap into NV interactions and study NV associated pathologies in a simple, precise and affordable manner.

Materials and methods

Agarose microwell mold fabrication

A 3% (w/v) sterile agarose (Thermo Fisher Scientific) solution was prepared in PBS. 8 ml of agarose solution were poured onto an in-house fabricated PDMS stamp with the negative template of 1580 microwells with 400 μm diameter. Centrifugation at 845 g was performed to remove air bubbles, followed by chilling for 45 min at 4°C for agarose solidification. When solid, the agarose blocks were removed, cut to fit in a 12 well-plate, washed with 70% ethanol, then washed twice in phosphate buffered saline (PBS) solution and left at 4°C until further use. The day before cell seeding, PBS was replaced with culture media containing Advanced RPMI 1640 supplemented with 1X glutamax (Thermo Fisher Scientific) and kept in the incubator at 37°C, 5% CO₂ overnight.

Cell culture

Human iPSC line LUMC0031iCTRL08 (Provided by the LUMC iPSC core facility) was cultured on Geltrex coated dishes at a density of $10 \times 10^3/\text{cm}^2$ in mTESR1 medium (Stem Cell Technology). Cells were fed every alternate day with completely fresh medium and passaged weekly using Accutase (Stem Cell Technology). Upon splitting, cells were cultured in mTESR1 medium supplement with 10 μM of Y-27632 (Tocris) for 24 h and replaced with mTESR1 medium for further maintenance.

Adult human microvascular endothelial cells (HMVECs) were purchased from Lonza (CC-2543) and cultured on appropriate endothelial cell growth medium, which we refer here as vessel medium. The medium is composed of basal medium (CC-3156, Lonza) and supplements (CC-4147, Lonza), such as fetal bovine serum (FBS), hydrocortisone, human basic fibroblast growth factor (hFGF), vascular endothelial growth factor (VEGF), insulin-like growth factor (R3-IGF-1), ascorbic acid, human epidermal growth factor (hEGF), and gentamicin sulfate-amphotericin (GA-1000). The exact concentrations are undisclosed by the provider. Cells were expanded until passage 5 and used at that passage for 3D culture experiments with fibrin and for the angiogenesis assay on matrigel.

Normal adult human dermal fibroblasts (HDFs) were purchased from Lonza (CC-2511) and cultured with fibroblast growth medium composed of basal medium (CC-3131) and supplements (CC-4126), such as FBS, insulin, human fibroblast growth factor (hFGF) and gentamicin sulfate-amphotericin (GA-1000). Again, the exact concentrations are undisclosed by the provider. Cells were expanded until passage 6 and used for 3D culture experiments at that passage.

SCs isolation and purification

Primary rat Schwann cells (SCs) were harvested from the sciatic nerves of neonatal Wistar rat pups, following local and Dutch animal use guidelines. Nerve segments were extracted and digested, followed by cell isolation and purification as described by Kaewkhaw et al.¹⁹ Briefly, the collected nerves were sliced and digested in a 0.05% (wt/vol) collagenase solution for 60 min at 37°C, 5% CO₂. The cell suspension was filtered through a 40 µm cell strainer, centrifuged for 6 min at 400 g, followed by supernatant removal and cell pellet washing with DMEM containing 10% fetal bovine serum (FBS) and 100 U/ml penicillin and 100 µg/ml streptomycin. Cells were centrifuged again at 400 g for 6 min and the supernatant discarded. Finally, cells were re-suspended with 2 ml of Schwann cell proliferation and purification medium, composed of DMEM D-valine (Cell Culture Technologies), 2 mM L-glutamine, 10% (v/v) FBS, 1% (v/v) N2 supplement (R&D Systems), 20 µg/ml bovine pituitary extract, 5 µM forskolin, 100 U/ml penicillin and 100 µg/ml streptomycin, and 0.25 µg/ml amphotericin B (all Sigma-Aldrich), then plated on 35 mm petri dish pre-coated with 0.01% (v/v) poly-L-lysine (Sigma –Aldrich) and 1 µg/ml laminin (R&D systems) and incubated at 37°C, 5% CO₂. The use of D-valine in place of L-valine serves to inhibit fibroblast growth while permitting SCs survival and proliferation. 1 ml of fresh medium was added at day 7 of culture and subsequently the medium was changed every 2 days until confluency. Cells were used between passage number 3 and 6 (P3-P6).

iPSCs differentiation and neurosphere formation

In order to induce iPSCs differentiation into nociceptors, we adapted and modified the protocol published by Chambers et al.²⁰. Nociceptor induction was initiated using single cell suspension of undifferentiated iPSCs detached with accutase, followed by seeding of 200 cells/microwell in mTESR1 medium supplemented with 10 μM of Y-27632 and 0.5% Geltrex (in solution) onto 400 μm agarose microwells. Cell suspension was forced to settle by centrifugation at 290 g for 2 min. Afterwards, cells were incubated for 24 h and were given a complete media change with mTESR1 medium. At this time, the cellular spheroid is formed and cell synchronization is initiated by the addition of mTESR1 medium supplemented with 1% dimethyl sulfoxide (DMSO). The cells were maintained for 72 h in the synchronization medium. Post synchronization cells were given a PBS wash and nociceptor induction was initiated by addition of dual SMAD inhibition media containing Advanced RPMI 1640 supplemented with Glutamax (both Thermo Fisher Scientific), 100 nM LDN-193189 (Tocris) and 10 μM SB431542 (Tocris). The spheres were maintained for 48 h in the dual SMAD inhibition media. Following this, neural crest commitment was induced via media containing Advanced RPMI 1640 supplemented with Glutamax, 3 μM CHIR99021 (Tocris) and 1 μM retinoic acid (Tocris). The spheres were maintained in the neural crest induction media for 5 days with media change every alternate day. Following this stage, the spheres were incubated in notch inhibition media, consisting of Advanced RPMI supplemented with Glutamax, 10 μM SU5402 (Tocris) and 10 μM DAPT (Tocris), for 48 h.

Finally, the neurospheres, composed of trunk neural crest cells, were collected and seeded on coverslips or scaffolds. In these substrates, cells were cultured in neural maturation medium for at least 5 days to reach the nociceptor phenotype. The neural medium is composed of Neurobasal Medium, 0.5 mM Glutamax, 100 U/ml penicillin and 100 $\mu\text{g}/\text{ml}$ streptomycin (all Thermo Fisher Scientific), 100 ng/ml human nerve growth factor (NGF), 50 $\mu\text{g}/\text{ml}$ ascorbic acid (all Sigma-Aldrich), 25 ng/ml human neuregulin-1 type III (NRG-1 SMDF) and N21 supplement (both from R&D systems).

Scaffold fabrication and sterilization

The scaffolds were fabricated via a two-step electrospinning (ESP) process with a custom-built apparatus. The first step was the production of a release layer by electrospaying a solution of 50% polyethyleneoxide (PEO, Mn = 3350, Sigma-Aldrich) in Milli-Q onto aluminum foil. For this, the solution flowed through a 0.8 mm inner diameter stainless steel needle (Unimed S.A.) at 2 ml/h, while subjected to 20 kV and at a distance of 10 cm from a 60 mm diameter mandrel rotating at 5000 rpm. Afterwards, a nonwoven polyurethane mesh (6691 LL (40 g/m²), a kind gift from Lantor B.V., The Netherlands) was prepared by punching an array of 12 mm circular holes and placed on the mandrel, covering the PEO sprayed-foil. We then

produced the scaffolds by ESP of 300PEOT55PBT45 (PolyVation) in 75:25 Chloroform/1,1,3,3-hexafluoroisopropanol solution onto the mesh support structure. For this process, the solution flowed through a 0.5 mm inner diameter stainless steel needle (Unimed S.A.) at 0.75 ml/h, while applying a voltage of 12 kV and at a distance of 10 cm from a rotating mandrel (at 5000 rpm). During both processes, the humidity remained at 35-40% and the temperature at 22-24°C. Finally, we generated individual scaffolds from the polyurethane mesh by punching 15 mm-outer diameter sections concentric to the 12 mm holes, resulting in a thin ESP membrane supported by a polyurethane mesh ring. To detach the scaffolds, these were dipped in deionized water and left in phosphate buffered saline (PBS) until further use. When required for cell seeding, the scaffolds were transferred to a 24 well plate and immersed in 70% ethanol for 1h for sterilization, followed by repeated PBS washes and air-drying. These were then maintained in sterile PBS until needed.

Fabrication of a 3D biomimetic PN platform

To fabricate our PN platform we followed the process illustrated in Fig. 1A. While the iPSCs differentiated and formed neurospheres as described above, we simultaneously seeded the scaffolds with 100×10^3 primary SCs and cultured these for 7 days with SC medium. During this time, cells were allowed to populate the scaffold and align with its fibers to form highly anisotropic SCs bands. After 7 days, when SCs bands were fully formed, we added one neurosphere per scaffold. For this, we simply retrieved the neurospheres from the agarose mold into an Eppendorf, and carefully pipetted one neurosphere onto each scaffold containing 125-150 μ l of neural medium. After this, we let the neurospheres adhere to the substrate for at least 6 hours, before adding neural medium. This medium was composed of Neurobasal Medium, 0.5 mM Glutamax, 100 U/ml penicillin and 100 μ g/ml streptomycin (all Thermo Fisher Scientific), 100 ng/ml human nerve growth factor (NGF), 50 μ g/ml ascorbic acid (all Sigma-Aldrich), 25 ng/ml human neuregulin-1 type III (NRG-1 SMDF) and N21 supplement (both from R&D systems). The following day we added 300 μ l of fibrin, composed of 3.5 mg/ml human fibrinogen (Enzyme Research Laboratories), 5 U/ml thrombin (Sigma-Aldrich) and 2.5 mM CaCl_2 . After full gel formation (~15 min), neural medium containing 100 μ g/ml aprotinin was added. The cultures were maintained for 7 or 21 days at 37°C, 5% CO_2 and the medium refreshed every other day.

Fabrication of a 3D vascularized fibrin platform

The 3D vascularized platforms were fabricated through the co-culture of HMVECs with either HDFs or SCs, in a fibrin hydrogel. Briefly, cells were counted and added to a tube at a density of 1.5 M cells/ml for HMVECs and 0.3 M cells/ml for HDFs or SCs. After this, cells were resuspended in 150 μ l of 10 mg/ml human fibrinogen plasminogen depleted (Enzyme

Research Laboratories) and the suspension was added to either a 24 well-plate or scaffold. Following this, 150 μ l of thrombin at 20 U/ml and containing 5 mM CaCl_2 was added to induce fibrin polymerization. The gels were allowed to form for about 15 min and then vessel medium (formulation above) was added. The samples were cultured for 10 days, with daily medium changes and at 37°C, 5% CO_2 .

Fabrication of a NV platform

To assemble a NV platform, we followed two distinct strategies. The first strategy was used to assess the influence of different culture conditions, namely cells and medium type, on the development of neural and vascular tissue. For this, we either coated the scaffold with laminin by adding 100 μ l of 1 μ g/ml laminin-1 (R&D systems) and 2 μ g/ml poly-D-lysine (Sigma Aldrich), or seeded it with SCs (100×10^3 cells/scaffold). The scaffolds were maintained in SC proliferation medium, for 7 days. After this, a neurosphere was placed at the center of both laminin and SC-seeded scaffolds, and the co-cultures maintained in neural medium for 7 days. At day 14, we added either 300 μ l of blank fibrin or fibrin containing HMVECs (1.5 M/ml). The platforms were cultured for additional 10 days, in either neural medium or a 1:1 mix of neural/vessel medium. For the second strategy, we aimed to build a mature NV platform by merging a previously formed vascular model and nerve model. The vascular model was composed of a HMVECs/SCs co-culture and formed as described in the section before. The vascular cultures were maintained for 11 days in vessel medium. The nerve model was formed as described in the 3D nerve model fabrication section, and the iPSCs/SCs co-cultures maintained for 4 days in neural medium. To make a single NV unit, we picked up the vascular model, which was formed over a polyurethane mesh ring that facilitated handling, and transferred it over the nerve model. Both components were bound together by dispersing 150 μ l of fibrin over them and leaving it to polymerize for about 15 min. After that, the cultures were supplemented with neural/vessel medium at 1:1 and kept for 10 days. All cultures were kept at 37°C, 5% CO_2 , and the medium changed every other day.

Collection of SCs or HDFs conditioned medium

SCs or HDFs were seeded at 10×10^3 cells/cm² on 6 well-plates in 1 ml of normal vessel medium. The day after, the medium was removed and 2 ml of fresh medium was added. The cells were cultured for 5 days and 1 ml of medium was collected every day and stored at -80°C.

Tube formation assay on matrigel

For matrigel coating, we dispensed 150 μ l of ice-cold matrigel (CB-40234A, Thermo Fisher Scientific) into the wells of a 48 well-plate. The plate was incubated at RT for 10 min,

followed by incubation at 37°C for 30 min. After this, HMVECs were collected in normal vessel medium or SCs-conditioned vessel medium and 250 µl of cell seeding solution was added into each well, at a density of 75×10^3 cells/cm². The cells were cultured for 48 h at 37°C, 5% CO₂.

Cytokine array

The detection of cytokines present within normal vessel medium, SCs-conditioned medium and HDFs-conditioned medium was performed with a cytokine array kit (AAR-CYT-2-2, Ray Biotech). The protocol was performed as indicated by the manufacturer and the membranes were imaged with a chemiluminescence imaging system (Chemidoc, Bio-rad) at an appropriate charge-couple device (CCD) exposure.

Immunostaining

Samples were fixed with 4% paraformaldehyde (PFA) for 25 min at room temperature (RT), rinsed thoroughly with PBS, and left in PBS until further use. Permeabilization and blocking was performed simultaneously with a solution of 1% triton X-100, 5% goat serum, 0.05% Tween20, and 1% bovine serum albumin (BSA) in PBS, for 24 h at 4°C, under mild agitation. Samples were then incubated for 48 h at 4°C, under mild agitation, with primary antibody solutions containing 0.1% triton X-100, 5% goat serum, 0.05% Tween20, and 1% bovine serum albumin (BSA) in PBS. Following this, the samples were washed with a wash buffer composed of 0.05% Tween20 and 1% bovine serum albumin (BSA) in PBS, and left for 24 h at 4°C, under mild agitation, to remove unbound antibodies. Secondary antibody solutions were prepared in wash buffer and incubated for 48 h at 4°C, under mild agitation. Following this, we rinsed the samples with PBS, stained with DAPI (0.2 µg/ml) for 20 min at RT, and left them in PBS until imaging. For F-actin staining we used Alexa Fluor 488- or Alexa Fluor 568-phalloidin (Thermo Fisher Scientific) at 1:75 dilution in PBS for 1 hr at RT.

The used primary antibodies were the following: anti-βIII tubulin (Sigma-Aldrich, T8578, 1:500), anti-S100 (Sigma-Aldrich, S2644, 1:100), anti-Myelin Basic Protein, MBP (Thermo Fisher, PA1-46447, 1:50), anti-CD31 (Agilent, M082329-2, 1:100), anti-CD31 (Abcam, ab32457, 1:100) anti-laminin (Bio-connect, LS-C384320, 1:100), anti-collagen IV (Nordic MUBio, MUB0338S, 1:100), anti-von Willebrand Factor (Abcam, ab194405, 1:100), anti-VE-cadherin (Cell Signalling Technology, D87F2, 1:100) and anti-alpha smooth muscle actin (Thermo Fisher Scientific, PA5-19465, 1:100).

Finally, the used secondary antibodies were the following: goat anti-mouse conjugated with Alexa Fluor 488; goat anti-mouse conjugated with Alexa Fluor 568, goat anti-rabbit conjugated with Alexa Fluor 488 and goat anti-rabbit conjugated with Alexa Fluor 568 (all Thermo Fisher Scientific).

Imaging

Brighfield images were acquired with an inverted microscope (Nikon Eclipse Ti-e). Fluorescent images were acquired with an inverted microscope (Nikon Eclipse Ti-e) or a confocal laser scanning microscope (Leica TCS SP8). For scanning electron microscopy (SEM), the samples were mounted on sample stubs with carbon tape and gold-sputtered for 40 s at 30 mA (Cressington Sputter Coater 108 auto). SEM Imaging was conducted with a SEM (FEI/Philips XL-30 ESEM) at $V= 10$ kV.

TEM imaging

Samples were prepared by fixation in 4% PFA in PBS, followed by washing with 0.1 M Cacodylate (3x for 15 min). Cells were fixed again with 2.5% glutaraldehyde in Cacodylate 0.1 M overnight (minimum of 1 h), followed by washing with 0.1 M Cacodylate (3x 15 min), postfixed with 1% Osmiumteroxide + 1.5% potassium hexacyanoferrate (II) trihydrate in Cacodylate 0.1 M, then washed again with 0.1 M Cacodylate 3x for 15 min. Then we proceeded to a dehydration series (70% for 30 min, 90% for 30 min and 2x 100% for 30 min), followed by propylenoxide 2x 30 min and Propylenoxide:Epon LX112 (1:1) overnight with stirring. Samples were covered with fresh epon LX112 7 h with stirring and embedded in beemcapsules with fresh epon 3 days at 60°C. 60 nm sections were then cut with a diamond knife, stained with uranyl acetate and lead citrate and imaged with a TEM (FEI Tecnai G2 Spirit BioTWIN iCorr).

Image analysis

3D images and videos of neurons and vascular channels were processed with Amira (Thermo Fisher Scientific) or Leica Application Suit (LAS X, Leica Microsystems) software. 2D images were processed and analyzed with Fiji software (<https://fiji.sc/>). To quantify neural morphological parameters, we captured images that contained the whole tissue sample. Neurite length was obtained with Simple Neurite Tracer plugin²¹, by measuring the distance between cell bodies and the edge of the respective axons. Neurite area was obtained by first converting images of β III tubulin⁺ cells to binary images and measuring the pixel area occupied by the neurites, excluding cell bodies. Then, we divided this value by the total area of the scaffold. To measure the orientation degree of HMVECs we used the OrientationJ plugin²² and applied the Measure function over identical circular ROIs to obtain the coherence values (where 0 is full isotropy and 1 is full anisotropy). For this experiment, we took at least 10 measurements per sample. Vascular channel network analysis of 3D fibrin cultures was performed after acquisition of at least 5 images per sample. Vascular tubes analysis of 2D matrigel cultures was performed after acquiring images capturing the whole well where cells were cultured. Vessel/tube length was determined manually by measuring the length of an individual vessel until the next bifurcation. Vessel/tube branching density was determined by

manually counting the number of branching points within an image and dividing this value by the image area. Vessel/tube density was determined by manually counting the number of vessels within an image and dividing this value by the image area. Vessel area was obtained by converting images to binary and measuring the occupied area of CD31⁺ structures. This value was then divided by the total area of the image. Finally, to quantify the amount of detected cytokines in the membrane array images, we measured the integrated pixel density within identical circular ROIs manually positioned over the membrane spots. The final values were obtained by first correcting the samples signal through background subtraction. Then, we normalized the values on the conditioned medium samples by multiplying the spots value (individual cytokines) with the ratio between the positive control of the reference membrane (normal medium) and the sample membrane (conditioned mediums). This sample cytokine value was then divided by the corresponding reference cytokine value to obtain the final relative secretion value. Those values were then used to build a heat map, with different color codes according to the relative secretion value.

Statistics

We have built the graphs and analyzed the data using the software GraphPad Prism. Bar graphs are shown as mean \pm SD and boxplots represent data point between the minimal and maximal value. Statistical significances were determined employing an unpaired t-test or two-way analysis of variance (ANOVA) followed by a Tukey's honestly significant difference (HSD) post-hoc test (*p < 0.05, ** p < 0.01, ***p < 0.005, ****p < 0.0001 and ns is p > 0.05). The comparisons on the graphs from Fig. 6 are done relatively to the laminin samples.

Results

Formation of a 3D biomimetic PN platform

In order to create a NV unit, we first sought out to develop a platform that would allow neural tissue to grow in a manner that replicates the native PN environment. For this, we used the protocol established in chapter 4, which makes use of iPSCs-derived neurons, in form of spheroids (neurospheres), and primary SCs, co-cultured in an aligned microfibrous scaffold with fibrin embedding. The biofabrication protocol is illustrated in fig. 1A, where we show the two process phases: 1) Neurosphere formation and SC seeding on scaffolds. For this, we seeded iPSCs on an agarose mold with 400 μ m microwells (200 cells per well) and applied a spheroid formation/nociceptor differentiation protocol over the course of 18 days. At the same time, we expanded primary SCs and seeded them on aligned microfibrous scaffolds (100 x 10³ cells / scaffold) at day 11. The SCs are cultured in proliferation medium for 7 days, in order to

populate the scaffold and form aligned cell bands, reminiscent of bands of Büngner. After this period, the neurospheres were collected and added to the scaffold (one neurosphere per scaffold). After attachment, a fibrin hydrogel was added to the top of the construct. The hydrogel provides the 3D support, necessary for cells to grow beyond the substrate. Additionally, it allows the inclusion of other tissues, in this case, vascular tissue. The co-cultures were maintained up to 21 days to allow proper tissue maturation, i.e. axon myelination. The first checkpoint was at day 7 of culture, where we could see that the neurite development was already vast, well aligned and assumed a 3D conformation (fig. 1B). When cells were allowed to further grow for 21 days, we could observe an increase in the neurite volume and the formation of surrounding myelin (fig. 1C). When analyzing the construct cross-section via TEM, we could clearly visualize the presence of compacted and abundant myelin layers, with an average thickness of 89.1 ± 17.6 nm.

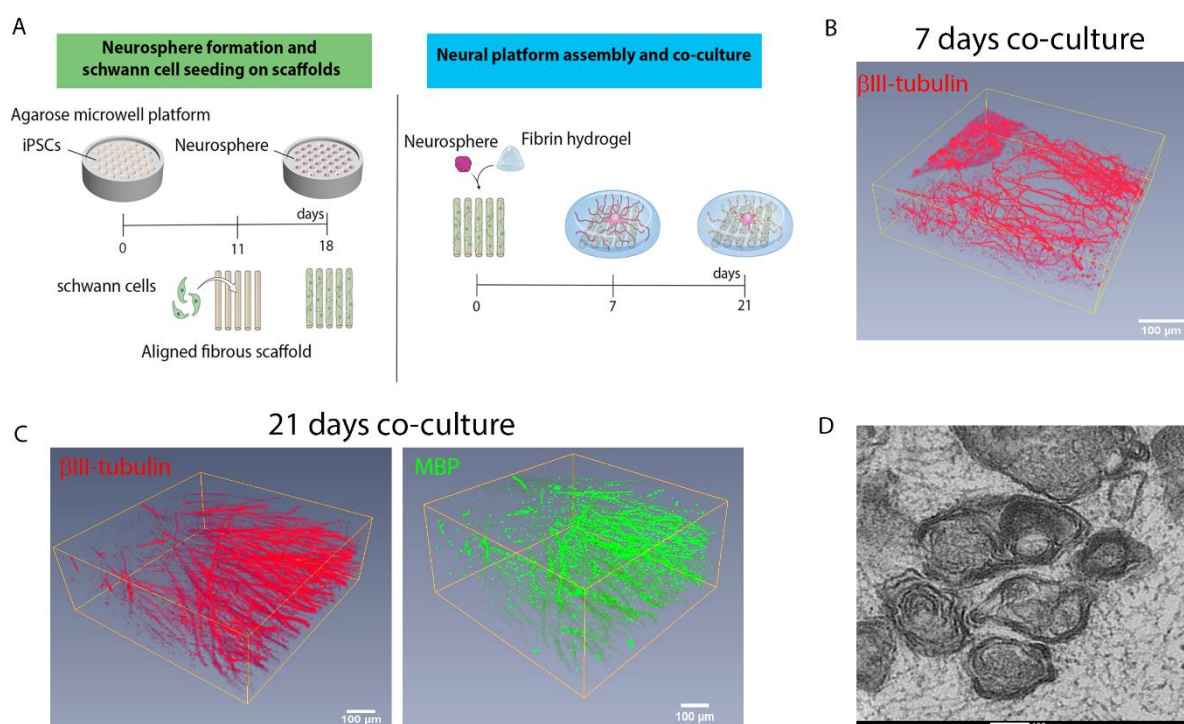


Figure 1. Development of a 3D biomimetic PN platform. A) Illustration of the biofabrication process, depicting its two main phases. The first phase is the formation of nociceptor neurospheres via iPSCs differentiation within an agarose mold containing 400 μ m microwells. The whole process takes 18 days from the day cells are seeded (at a density of 200 cells per well) until the spheres are ready to be harvested. The differentiation process itself takes only 14 days. At day 11, primary SCs are seeded and cultured on an aligned microfibrinous scaffold (at a density of 100×10^3 cells per scaffold). In the second phase, the neurospheres are harvested and placed on the SC-seeded scaffold (one neurosphere per scaffold). A fibrin

hydrogel embedding is also added, following neurosphere attachment. The co-culture is maintained for up to 21 days to allow compact myelination to occur. B) At 7 days of co-culture, there is already a vast, 3D and aligned neurite outgrowth, as illustrated by the 3D reconstruction of a micrograph showing immunostaining to β III-tubulin (in red). C) At 21 days of co-culture, neurites maintain their anisotropy and show signals of myelination as evidenced by the 3D reconstruction of a micrograph, correlating β III-tubulin⁺ (in red) with MBP⁺ segments (in green). For C) and D) the scale bar is 100 μ m. D) TEM micrograph of the platform cross-section showing the presence of multiple, compact myelin rings surrounding the neurites (average thickness is 89.1 ± 17.6 nm). The scale bar is 100 nm.

Formation of a 3D vascularized platform with HMVECs and HDFs

To form a hydrogel platform containing vascular channels we used a protocol adapted from literature^{23,24,25}. As a hydrogel, we chose again the same fibrin formulation used to fabricate the PN platform. This ensured that the material would be permissive for the growth of both tissues, and thus facilitated integration at a later stage. In our approach, we combined HMVECs and HDFs, at a concentration of 1.5×10^6 and 3×10^5 cells/ml respectively (5:1 ratio), randomly dispersed within a fibrin hydrogel. The cells were cultured for 10 days in vessel medium to allow vessel formation and maturation (fig. 2A). In fig. 2B, we show that the presence of HDFs is critical for proper vessel development; As shown elsewhere, HDFs produce angiogenic factors that stimulate vessel formation and directly associate with the vessels to stabilize them^{23,24,26}. As depicted here, in cultures lacking HDFs (fig. 2B, left image) the resulting vessels are poorly formed and not well interconnected. In contrast, the inclusion of HDFs results in vessels that are better formed and display good interconnectivity (fig. 2B, right image). We also characterized these newly formed vessels according to traditional phenotypical markers present in native vasculature (fig. 2C). VE-cadherin, a major component of the adherens junctions and essential for the endothelial barrier²⁷, is visibly present at the border between cells (fig. 2C top left). Von Willebrand factor (vWF), a blood glycoprotein that mediates platelet adhesion to damage sites, essential for hemostasis and characteristic of mature vessels²⁷, was also present along the vessel wall (fig. 2C bottom left). We also evaluated the expression of laminin and collagen type IV, two extracellular matrix (ECM) molecules that are part of the endothelium basal lamina and also indicate vessel maturation^{28,29}. As shown in fig. 2C (right column), these markers are present and located adjacently to the vessel wall, forming the basement membrane. Finally, in fig. 2D, we show that the formed vessels are 3D and open inside, with an average lumen diameter of 5.9 μ m, which is slightly smaller than typically reported values³⁰, but within the range for capillaries (5 to 10 μ m)³¹.

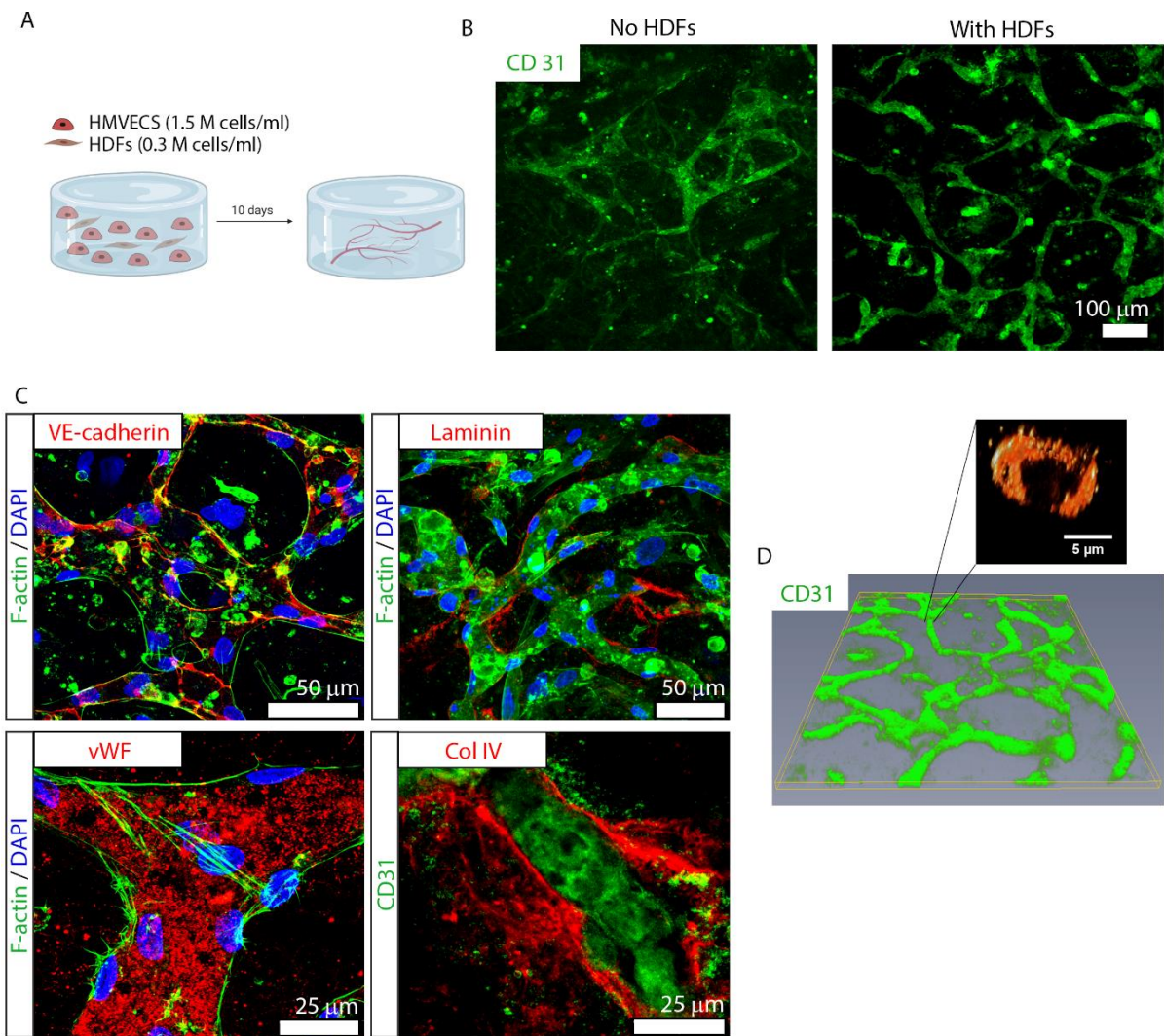


Figure 2. Formation and characterization of a 3D vascular channel network composed of HMVECs and HDFs. A) Illustration of the biofabrication process. Each 3D culture is composed of 300 μl of human fibrin containing HMVECs, at 1.5×10^6 cells/ml and HDFs, at 0.3×10^5 cells/ml, forming a ratio of 5:1. The culture is maintained for at least 10 days. B) The presence of HDFs within the culture is essential for the formation and maintenance of well-defined vessels. The micrograph on left side shows poor vessel formation in the absence of HDFs. On the other hand, when present, HDFs promote the development of well-defined and interconnected vascular channels (right micrograph). The vascular channel formation is denoted by CD31 immunostaining (in green) and the scale bar is 100 μm . C) Characterization of the vessels phenotype with the traditional vascular markers: VE-cadherin (in red; top left tile), laminin (in red; top right tile), von Willebrand factor (vWF, in red; bottom left tile) and collagen type IV (col IV; in red; bottom right tile). F-actin is shown in (green) and DAPI (in blue) (top tiles and bottom left). For the bottom right tile, CD31 is shown in green. The scale bar in

the top tiles is 50 μm and in the bottom tiles is 25 μm . D) 3D reconstruction of a micrograph depicting a vascular network, evidenced by CD31 immunostaining (in green). As exemplified, the vascular network is 3D, well interconnected and shows the presence of lumens with an average diameter of 5.9 μm . Illustration made with biorender (<https://biorender.com/>).

Formation of a 3D vascularized platform with HMVECs and SCs

After establishing a vascular model composed of HMVECs and HDFs, we were also interested in assessing the potential of SCs as vasculogenesis promoters and mural cells. Since SCs are known to secrete VEGF and are used in our PN model to achieve myelination, the substitution of HDFs with SCs would simplify the construction of a neurovascular model. However, we first evaluated the feasibility of using rat SCs with human cells by investigating the ability of rat VEGF (VEGF-165) in binding and activating the VEGF receptor (vascular endothelial receptor 2; VEGFR2) on HMVECs. As demonstrated in fig. S1, both human (middle image) and rat VEGF (right image) at 5 ng/ml were sufficient to induce the receptor phosphorylation. Conversely, when using control medium (basal medium plus 5% FBS and depleted of VEGF), the receptor was not activated. Once we confirmed the ability of rat-derived VEGF to communicate with HMVECs, we also tested the purity of our SC population. When extracting these cells from sciatic nerves, the isolated cell population contains contaminating fibroblasts, but these can be removed to obtain pure SCs cultures, as evidenced by the ubiquitous S100⁺ cells (SC marker) and the absence of CD90⁺ cells (fibroblast marker) (fig. S2).

Next, we co-cultured HMVECs with either HDFs or SCs in a fibrin hydrogel, as depicted in Fig. 2A, and evaluated the resulting vessel network after 10 days (fig. 3). As expected, co-cultures with HDFs promoted an extensive interconnected and stable vessel network (fig. 3A, right image). Remarkably, when co-cultured with SCs, the resulting network was also well-formed, interlinked and seemingly steady (fig. 3A, middle image), similarly to HDFs/HMVEC co-cultures. In contrast, single cultures of HMVECs did not produce any vessels (fig. 3A, left image). Through image analysis, we quantified the vessel morphology obtained in the co-culture systems (Fig. 3B). There were no significant differences vessel density, i.e. number of vessels per area, between the two cell types (44.6 ± 22.4 in HDFs versus 55.9 ± 17.7 in SCs). HDFs promoted a higher ($p < 0.05$) vessel area than SCs ($20.2 \pm 4.3\%$ versus $17.2 \pm 4.3\%$, respectively), but a shorter vessel length ($p < 0.001$) ($155.7 \pm 66.1 \mu\text{m}$ versus $199.2 \pm 85.9 \mu\text{m}$, respectively). Finally, branching density analysis, i.e. number of branching points per area, revealed a higher number ($p < 0.05$) in SCs cultures (47.5 ± 17.6) compared to cultures containing HDFs (34.7 ± 15.3).

After the surprising finding that SCs are suitable to promote vessel development to a similar extent as HDFs, we decided to further characterize this new co-culture system. In fig.

3C, we show that SCs (S100⁺; in green) were dispersed through the gel but also directly associated with the vessel wall (CD31⁺; in red). Interestingly, SCs adjacent to the vessel wall expressed alpha smooth muscle actin (α SMA), a cell marker indicative of mural cell differentiation³² and vessel maturation (fig. 3D). Using the same set of markers as described above for HDFs, we further characterized the vessel phenotype. As seen in fig. 3E, VE-cadherin (top left), vWF (bottom left), laminin (top right) and col-IV (bottom right) were also present and located in the same regions. Finally, we show in fig. 3F that the HMVECs/SCs 10-day co-cultures in fibrin resulted in vast 3D vascular channel network with lumens of 4.6 μ m in diameter. To emphasize that lumen formation was homogenous and not sporadic, we show a moving cross-section of the vessel network in supplementary movie 1, where it is visible that all vessels are open throughout.

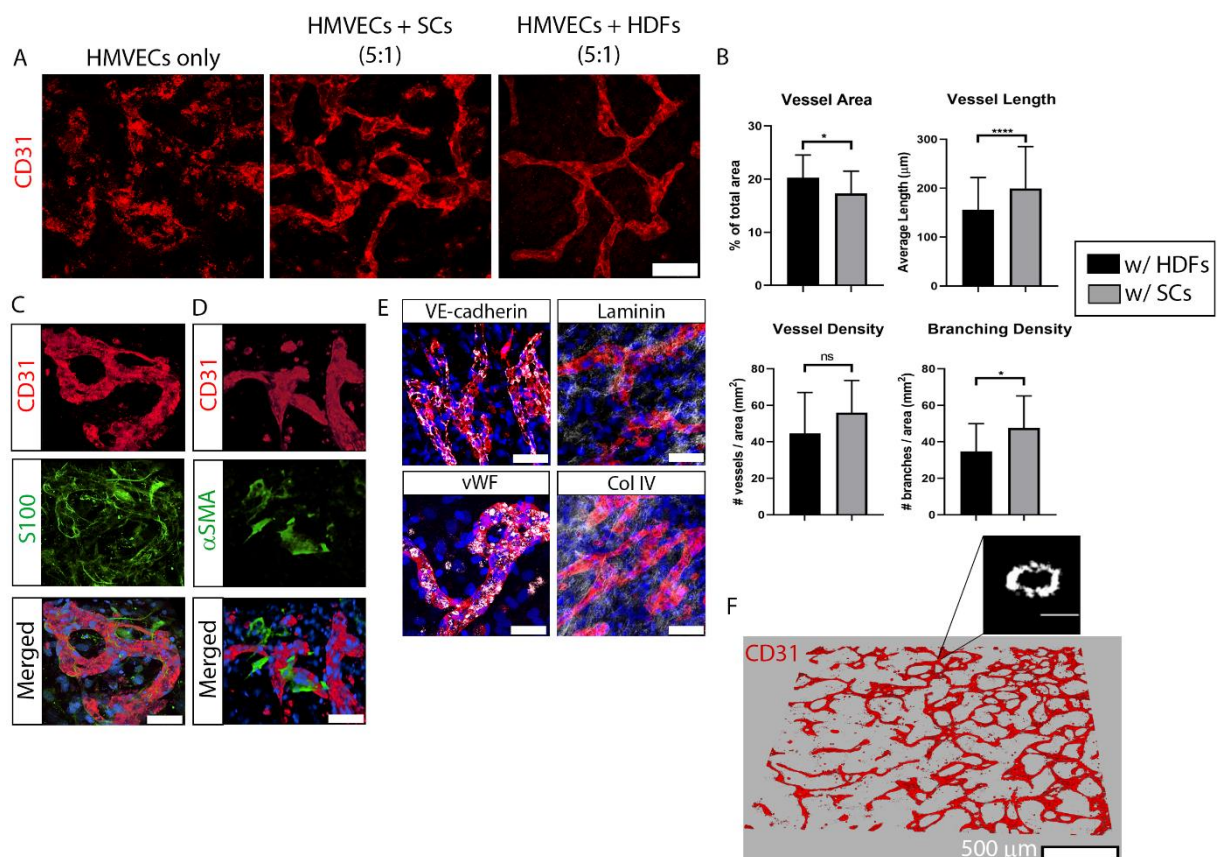


Figure 3. Formation and characterization of a 3D vascular channel network composed of HMVECs and SCs. A) Comparison of vascular networks after 10 days of culture, composed by HMVECs only (left tile), HMVECs plus HDFs at 5:1 ratio (middle tile) and HMVECs plus SCs at 5:1 ratio (right tile). CD31 is shown in red and the scale bar is 100 μ m. B) Quantification and comparison of networks formed with SCs (black bars) or HDFs (gray bars) through the parameters: vessel area (top left), vessel length (top right), vessel density (bottom left) and branching density (bottom right). The bar graphs represent the mean \pm SD. Vessel area was determined as the ratio of CD31⁺ area per total image area. The vessel length was determined

as the total length of an individual vessel until the next bifurcation. Vessel density was determined as the ratio of number of vessels contained in an image per image area. Branching density was determined as the ratio of vessel branching points contained in an image per image area. This experiment was performed twice and we used at least four replicates per condition. For the image analysis, we took at least five images per sample. Statistics were performed using an unpaired t-test, where **** $p < 0.0001$, * $p < 0.05$ and ns denotes $p > 0.05$. C) 3D reconstruction of a micrograph depicting an intimate association of SCs (S100; green) and vessels (CD31; red). D) 3D reconstruction showing that SCs when associated with vessels (CD31; red) also express alpha smooth muscle actin (α SMA; green). E) Vascular vessels characterization resulting from the co-culture of HMVECs and SCs via the traditional markers: VE-cadherin (white; top left tile), laminin (white; top right tile), vWF (white; bottom left tile) and col IV (white; bottom right tile). CD31 is shown in red and DAPI in blue. For C), D) and E) the scale bar is 50 μm . F) 3D reconstruction of a vascular network showing the formation of well-defined, 3D interconnected vessels with lumens (average diameter of 4.6 μm). CD31 is shown in red and the scale bar is 500 μm for the network overview image and 5 μm for the lumen detail image.

SC-conditioned medium analysis and influence on vasculogenesis

To further investigate the role of SCs in vessel formation we also analyzed its secretome and assessed if SCs-conditioned medium is sufficient to induce vessel formation. First, we performed a classical angiogenesis assay on a Matrigel layer to compare vascular tube formation in normal vessel medium or vessel medium pre-conditioned by SCs (fig. 4A). As demonstrated in fig. 4B, when cultured for 48 h with SCs-conditioned medium, HMVEC tubule formation is more extensive and widespread than with normal vessel medium. For improved visualization, we traced the tubules with a purple line (original brightfield images shown in fig. S3). HMVECs cultured with conditioned medium produced significantly longer ($583.6 \pm 239.8 \mu\text{m}$ versus $513.3 \pm 224.2 \mu\text{m}$; $p < 0.001$), more numerous tubules (77.1 ± 24.2 versus 53.3 ± 10.6 tubes/ mm^2 ; $p < 0.05$), and also a more branched network (66.3 ± 20.0 versus 48.0 ± 9.6 branching points/ mm^2 ; $p < 0.05$) compared to HMVECs in normal vessel medium (fig. 4C).

Once established that SC-conditioned medium has a positive influence on tubule formation, we wanted to compare which specific growth factors were being released by HDFs and SCs. The secretome profile of both cell types was similar, particularly for wound healing and immunomodulatory cytokines, with exception of IFN-gamma and CD86, which were substantially higher for SCs compared to HDFs (fig. 4D). As expected, due to their role *in vivo*, SCs also released a larger concentration of neuromodulatory cytokines, including beta-NGF, CNTF and agrin. With regard to pro-angiogenic cytokines, VEGF-A was released in similar

amounts by both cell types, but PDGF-AA was more actively secreted by SCs. The original cytokine array membrane images can be found in fig. S4.

Finally, we assessed if SCs-conditioned medium had the same angiogenic potential in a fibrin-based 3D culture with HMVECs and, thus, if the presence of SCs is entirely necessary. In cultures with conditioned medium but lacking SCs, there was a massive HMVEC proliferation throughout the gel and the formation of monolayer on top of the gel, but no apparent vessel formation (fig. 4E, left image). In contrast, the presence of SCs led to the formation of a vast interconnected network of well-delineated vessels (fig. 4E, right image).

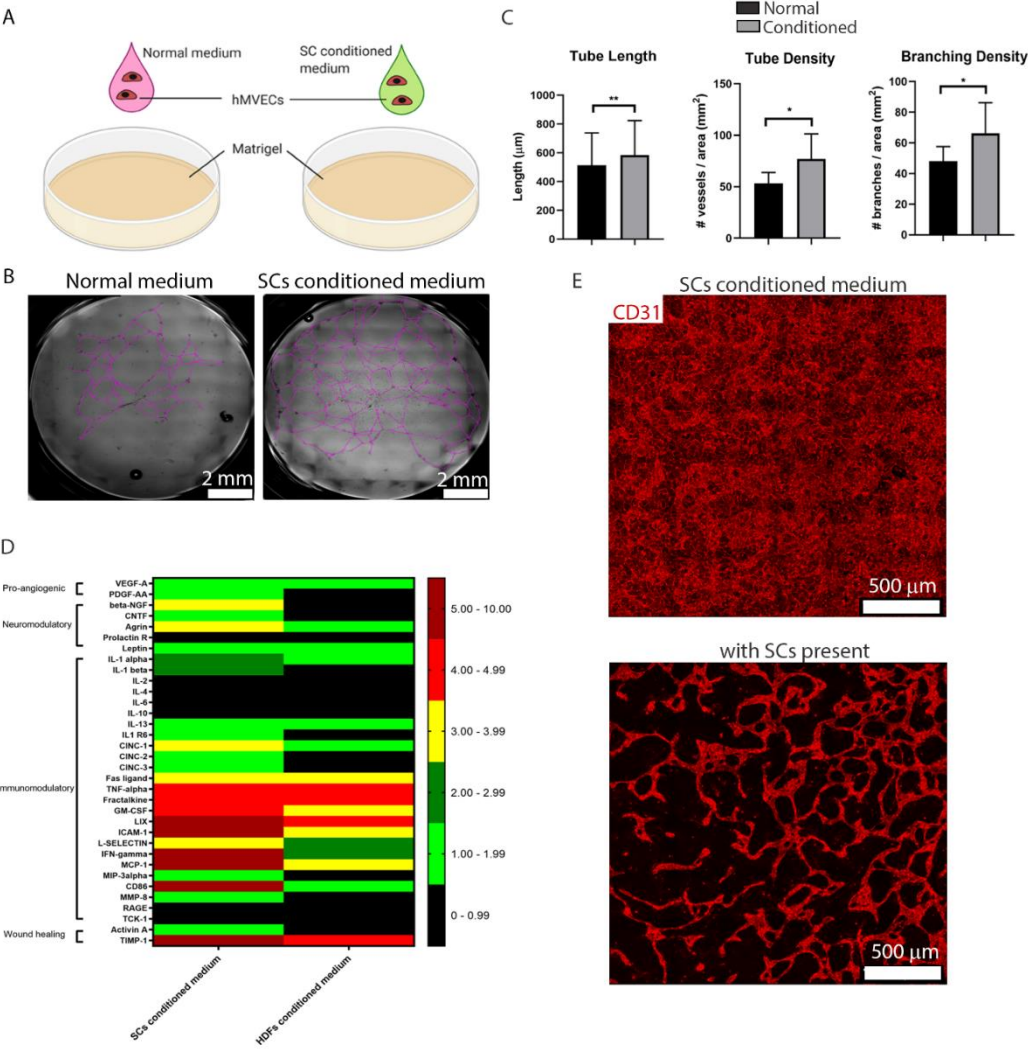


Figure 4. Exploring the influence of SCs and its secretome on the formation of vascular networks with hMEVCs. A) Illustration of the experiment where HMVECs were seeded in either normal or SCs-conditioned medium, onto matrigel coated wells at 75×10^3 cells/cm² and the resulting network was evaluated after 48 hr. B) Brightfield micrographs taken 48 hr after cell seeding showing the differences in tube formation between normal (left image) and SCs-conditioned medium (right image). Purple traces were drawn on top of the tubes for better

visualization. The scale bar is 2 mm. C) Characterization and comparison of hMEVC tube formation on matrigel samples when cultured with normal (black bars) or SCs-conditioned medium (gray bars) using the parameters: vessel length (left graph), vessel density (middle graph) and branching density (right graph). The bar graphs represent the mean \pm SD. This experiment was performed twice and we used 3 replicates per condition. The whole well was imaged in order to determine the measured parameters. To quantify the length of the tubes, we measure the length of each individual tube until the next bifurcation. The tube density was determined as the total number of tubes divided by the total well area. The branching density was calculated as the total number of branches divided by the total well area. Statistics were performed using an unpaired t-test, where $**p < 0.01$ and $*p < 0.05$. D) Determination and comparison of an array of cytokines present in SCs- (left column) versus HDFs-conditioned medium (right column). The secreted amount of each cytokine was normalized to a control medium (normal medium). The value of the ratio between conditioned and normal medium for each cytokine was translated to a color code, denoting 0 to 0.99 (black), 1.00 to 1.99 (light green), 2.00 to 2.99 (dark green), 3.00 to 3.99 (yellow), 4.00 to 4.99 (red) and 5.00 to 10.00 (dark red). Cytokines were organized in categories representing their most prominent function, such as pro-angiogenic, neuromodulatory, immunomodulatory or wound healing. E) Micrographs of 10-day cultures of hMEVCs only (in SCs-conditioned medium; left image) or HMVECs plus SCs (in normal medium; right image) showing immunostaining to CD31 (red). As visible, SCs-conditioned medium is not sufficient to promote vessel formation. The presence of SCs within the culture is required for vessel formation and maintenance. Scale bars are 500 μm .

Directing vessel orientation through SCs patterning

After identifying a direct role of SCs in aiding vessel formation, we questioned if these were able to induce vessel patterning. To assess this, we generated an experimental set up using SCs seeded on aligned microfibrillar scaffolds to pattern SC bands. Afterwards, HMVECs were seeded in a fibrin hydrogel on top of the construct, and vessel formation was evaluated after 10 days of co-culture (fig. 5A). The scaffolds used were identical to those in the PN platform and were composed of PEOT/PBT aligned micro-fibers of $1.37 \pm 0.20 \mu\text{m}$ (Fig. 5B).

SCs, seeded at 100×10^3 SCs, adhered, proliferated and aligned with the scaffold after 7 days of culture, as visible by F-actin staining (fig. 5C). After addition of a 300 μl fibrin gel containing HMVECs (1.5×10^6 cells/ml), the formed vessels acquired an overall orientation that followed the one of the underlying scaffold fibers (fig. 5D, right image). The average length of these vessels was $550.9 \pm 265.3 \mu\text{m}$. In control cultures, with scaffolds devoid of SCs, vessel formation was minimal and most HMVECs organized in a branched monolayer (fig. 5D, left

image). In the latter situation, HMVECs orientation was isotropic, and thus cell alignment measurements showed a low coherence value of 0.02 ± 0.01 (fig. 5F). In contrast, SCs scaffolds promoted a significantly larger ($p < 0.0001$) HMVEC anisotropy, with a coherence value of 0.11 ± 0.04 . Lastly, we also evaluated the aligned vessel morphology and interaction between both cell types in more depth. As shown in fig. 5E, the patterned microvessels were 3D and maintained open channels throughout their structure, as visible in the orthogonal projections of CD31⁺ cells from both viewing planes. In supplementary movie 2, we show a moving cross-section of the vessels to exemplify that the lumens are steadily maintained through the aligned vascular network. SCs, marked by S100, were present along the vessels border, maintaining an aligned morphology (fig. 5E). In supplementary movie 3, we show that these SCs were present throughout the whole construct and were able to migrate from the scaffold layer where the alignment was maintained, to the upper layers where cell orientation became random.

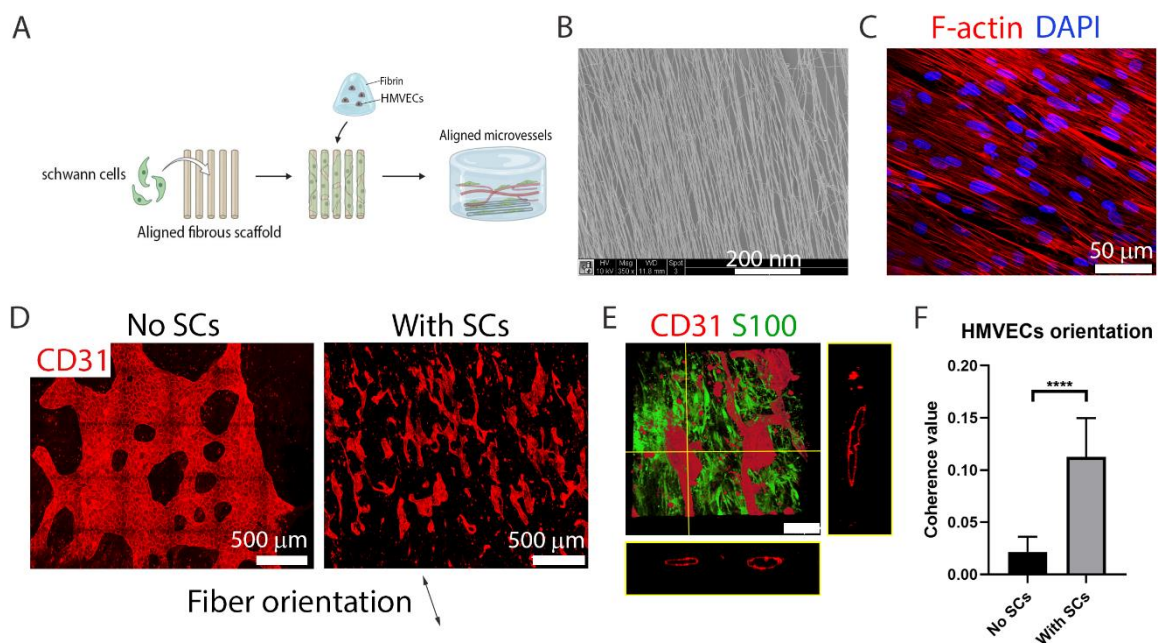


Figure 5. Pre-aligned SCs can influence hMEVCs to form an oriented vessel network following the same direction. A) Illustration of the followed strategy. In the first phase, 100×10^3 SCs are seeded on an aligned fibrous scaffold and cultured in SCs proliferation medium for 7 days in order to form aligned cell bands. In the second phase, the scaffold is covered with $300 \mu\text{l}$ of fibrin containing 1.5×10^6 HMVECs/ml. The co-culture is maintained for additional 10 days in normal vessel medium. B) SEM micrograph of the scaffold denoting the presence of aligned micro-sized polymeric fibers composed of PEOT/PBT. The scale bar is 200 nm. C) Morphological appearance of SCs after 7 days of culture in the scaffold. As visible, the cells are highly aligned at this timepoint. F-actin is shown in red and DAPI in blue. The scale bar is 50 μm . D) The presence of pre-aligned SCs promotes the formation of vessels (CD31, in red)

that follow an overall fiber/SCs direction (right image). The length of these vessels is $550.9 \pm 265.3 \mu\text{m}$. In the absence of SCs within the scaffold/fibrin platform, HMVECs do not form vessels or follow any overall direction (left image). E) SCs immunostained by S100 (in green) exhibit an overall alignment at the z-plane of the vessels (CD31, red) and are intimately associated with them. The vascular channels also display wide lumens as seen by the CD31 orthogonal projections of the xz- and yz-plane. F) Quantification of hMVECs orientation via coherence measurement on equally sized ROIs from CD31 micrographs (where 0 is full isotropy and 1 is full anisotropy). As visible, the presence of SCs promotes a statistical significant increase ($p < 0.0001$) in cell alignment. The bar graphs represent the mean \pm SD. All experiments were performed once and we used five replicates per condition. Ten measurements were taken per sample. Statistics were performed using an unpaired t-test, where **** $p < 0.0001$. Illustration made with biorender (<https://biorender.com/>).

Development of a neurovascular platform

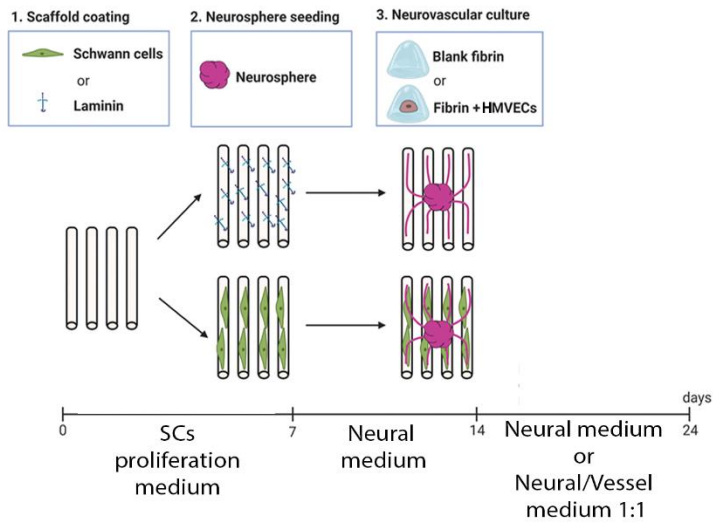
Neural tissue assessment

Following the development of a 3D neural platform and a 3D microvascular model, we set out to combine both biofabrication approaches to create a 3D neurovascular platform (fig. 6A). We compared the neural growth in platforms with different compositions, such as the scaffold coating (laminin or SCs) and fibrin content (blank or with HMVECs), and cultured with different media. In this way, we could dissect the influence of individual parameters and determine the best conditions for optimal neural growth. As depicted in fig. 6A, the scaffolds were either coated with laminin ($1 \mu\text{g/ml}$) or seeded with SCs (100×10^3 cells per scaffold). After 7 days of culture in SCs proliferation medium, we added one neurosphere in the center of the scaffolds and cultured the platforms for extra 7 days in neural medium to promote neurite outgrowth. At day 14, a blank fibrin hydrogel or an HMVEC-laden fibrin gel (1.5×10^6 cells/ml) was added on top of the construct. The platforms were cultured for additional 10 days in pure neural medium (NM) or neural/vessel medium in equal proportions (1:1 medium). In all conditions, the neurons attached and survived the culture period. The resulting morphology was however quite different among conditions. In general, neurons cultured with NM developed longer and more aligned neurites than in the mixed medium condition (fig. 6C). When quantifying the neurite length (fig. 6C), we detected the same trend in both media with respect to culture substrates. SCs-seeded scaffolds with blank fibrin promoted the highest neurite length, with a mean value of $2522.4 \pm 564.2 \mu\text{m}$ in NM and $868.3 \pm 294.5 \mu\text{m}$ in 1:1 medium. Laminin-coated scaffolds with blank fibrin promoted a mean length of $1784.0 \pm 491.4 \mu\text{m}$ when cultured with NM, and $624.2 \pm 207.8 \mu\text{m}$ when cultured in 1:1 medium. Interestingly, the addition of HMVECs impaired neurite outgrowth with these cultures showing a dramatic reduction ($p < 0.0001$) in the NM group for both laminin-coated ($775.3 \pm 203.7 \mu\text{m}$) and SC-

seeded scaffolds ($651.9 \pm 184.1 \mu\text{m}$). When culturing with 1:1 medium instead, the neurite length in platforms with HMVEC-loaded fibrin was similar to those with blank fibrin, and only inferior ($p < 0.0001$) to SCs scaffolds with blank fibrin.

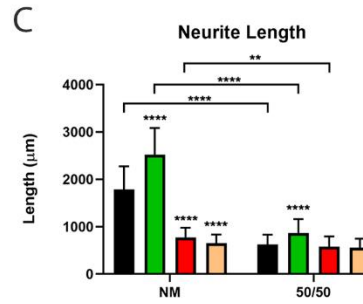
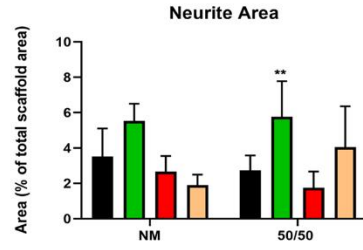
Regarding neurite area, we registered a similar trend in both medium groups. Samples composed of SCs-seeded scaffolds with blank fibrin ranked the highest again, displaying a neurite area (shown as % of total scaffold area) of $5.5 \pm 0.9\%$ for NM and $5.8 \pm 2.0\%$ for 50/50 medium. In the NM group, laminin-coated scaffolds with blank fibrin displayed the second highest neurite area with $3.5 \pm 1.6\%$. When HMVECs were added with fibrin, the neurite area decreased to $2.7 \pm 0.9\%$ in laminin-coated scaffolds and to $1.9 \pm 0.6\%$ in SCs-seeded scaffolds. Finally, for the 1:1 medium group, the condition with both SCs and HMVECs led to an area of $4.11 \pm 2.3\%$. Laminin-coated scaffolds with blank fibrin followed, occupying $2.7 \pm 0.9\%$ of the scaffold area. Finally, laminin-coated scaffolds with HMVEC-laden fibrin promoted a neurite area of only $1.9 \pm 0.9\%$. Despite the reduction in neurite length and area in HMVEC-containing scaffolds, we could see that the neurite density, i.e. number of fibers emanating from the cluster, was higher than in other conditions, which is probably a result of increased neuron proliferation. However, due to cell crowding and size of the features of interest, it is hard to distinguish neurites from cell bodies, and thus precise quantification is impaired in this case.

A



B

■ Laminin
 ■ SCs
 ■ HMVECs
 ■ SCs + HMVECs
 NM - neural medium
 50/50 - neural/vessel medium at 1:1



D

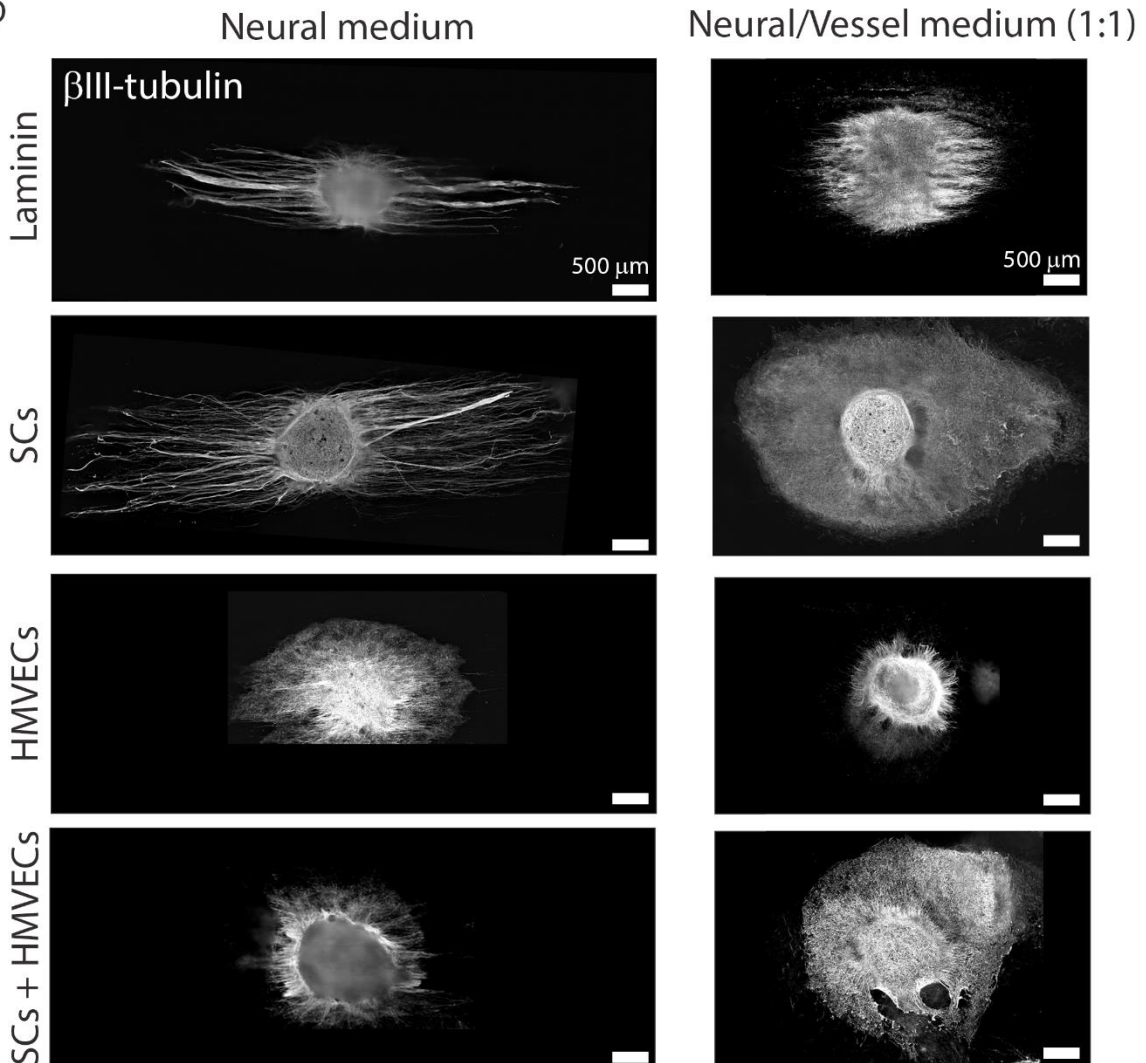


Figure 6. Development of a neurovascular platform and neural tissue assessment. A) Illustration of the followed strategy. In the first phase, the aligned microfibrinous scaffold was coated with laminin (1 $\mu\text{g/ml}$) or seeded with SCs (100×10^3 cells per scaffold). The cultures were maintained for 7 days in SC proliferation medium to allow SCs to populate the scaffold. In the second phase, one neurosphere was placed on the center of a laminin-coated or a SCs-seeded scaffold. The culture medium was then switched to neural medium and the culture maintained for 7 days to induce neurite outgrowth. After this period, 300 μl of blank fibrin or fibrin containing 1.5×10^6 HMVECs/ml was added to both types of scaffold. The cultures were maintained for extra 10 days in either full neural medium or a mixed medium composed of neural medium and vessel medium at 1:1 ratio. Quantification and comparison of the B) neurite area (top graph) and C) neurite length (bottom graph) between samples of laminin-coated scaffolds plus blank fibrin (black bars); SCs-seeded scaffolds plus blank fibrin (green bars); laminin coated scaffolds plus HMVEC-laden fibrin (red) or SCs-seeded scaffolds plus HMVEC-laden fibrin (light orange bars). Left column bars represent samples cultured in neural medium and the right column represent samples in neural/vessel medium at 1:1 ratio. D) Overview of the neurite morphology of the abovementioned platform conditions, via immunostaining to β III-tubulin (white). Scale bar is 500 μm . The bar graphs represent the mean \pm SD. This experiment was performed twice and we use at least five replicates per condition. The whole sample was measured in order to quantify the neurite area and neurite length. Neurite area was determined by the β III-tubulin⁺ area, excluding the cell bodies, divided by the total scaffold area. Neurite length was determined by the length spanning from the tip of an axon until the point where it emanates from the cell body. At least 20 measurements were taken per sample. Statistics were performed via two-way ANOVA followed by Tukey's multiple comparison test, where ****p < 0.0001 and ** p < 0.01. Comparisons were done relative to laminin samples. Illustration made with biorender (<https://biorender.com/>).

Vascular tissue assessment

We also assessed vascular tissue formation in the conditions that contained HMVEC-laden fibrin. As demonstrated in fig. 7A, HMVECs (marked by CD31) were attracted to the neurospheres (β III-tubulin⁺) in platforms cultured with both mediums and regardless of SCs presence. When zooming in close to the neurosphere (fig. 7A right column), in NM medium HMVECs were unable to form vessels, organizing instead into a monolayer. On the other hand, in mixed medium, HMVECs were able to arrange in an interconnected vessel network that is circumscribed to the neurosphere area. When inspecting this network in higher detail (fig. 7A right column), it was visible that neurites and vessels followed a parallel direction, indicative of neurovascular alignment.

In fig. 7B, we show examples of the vessel network formed in platforms that were cultured in 1:1 medium and with (right image) or without (left image) SCs seeded on the scaffold. As depicted, both conditions permitted vessel formation on top of the neuron clusters, and the presence of SCs did not seem to enhance vascularization dramatically. To verify this, we quantified the developed vascular network (fig. 7C). Both conditions yielded a similar area ($0.3 \pm 0.1\%$ for no SCs and $0.3 \pm 0.1\%$ with SCs) and similar vessel density (2.5 ± 0.4 vessels/ mm^2 for no SCs and 2.0 ± 0.2 vessels/ mm^2 with SCs). Regarding vessel length, however, we noted a significant difference ($p < 0.0001$) in platforms containing SCs ($363.8 \pm 82.2 \mu\text{m}$) compared to those absent of glial cells ($190.4 \pm 86.5 \mu\text{m}$).

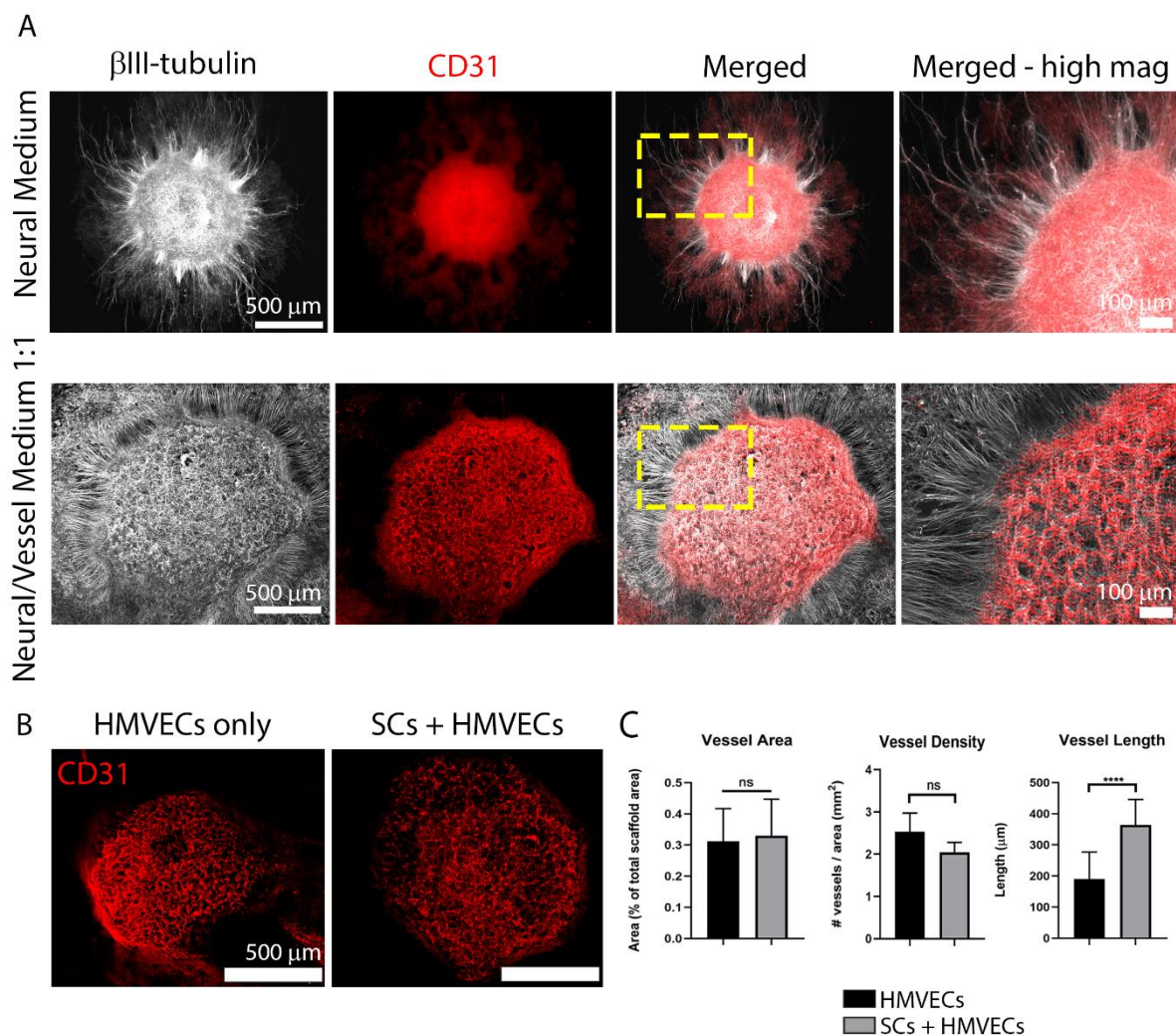


Figure 7. Vascular tissue development on the fabricated neurovascular platform. A) Comparison of the neural and vascular tissue formation on platforms composed of SC-seeded scaffolds and hMVECs-laden fibrin cultured on neural medium (top row) or neural/vessel medium at 1:1 (bottom row). Full neural medium promoted neurite outgrowth but was not sufficient to induce vessel formation. Neural/Vessel medium at 1:1 promoted simultaneous neuron proliferation, neurite outgrowth and vessel formation, which was mostly circumscribed

to the top of the neurosphere. β III-tubulin is shown in white and CD31 in red. The right most column depicts a high magnification view of the yellow-dashed box marked in the merged column. For the low magnification images, the scale bar is 500 μ m, while for the high magnification it is 100 μ m. B) Vessel formation on platforms composed of laminin-coated scaffolds with HMVECs-laden fibrin (left image) or SCs-seeded scaffolds and HMVECs-laden fibrin (right image). Vascular development (marked by CD31 in red) was similar in platforms with and without SCs present. The scale bar is 500 μ m. C) Quantification and comparison of the vascular network on platforms with SCs (gray bars) and without (black bars) using the parameters: vessel area (left graph), vessel density (middle graph) and vessel length (right graph). The bar graphs represent mean \pm SD. Vessel area was determined as the ratio of CD31⁺ area per total image area. Vessel density was determined as the ratio of number of vessels contained in an image per image area. The vessel length was determined as the total length of an individual vessel until the next bifurcation. This experiment was performed twice and we use at least five replicates per condition. Statistics were performed using an unpaired t-test, where ****p < 0.0001 ns denotes not significant.

Development of mature vessel innervation platform

In an effort to improve the fabrication of a neurovascular platform we developed a new assembly strategy (fig. 8A), in which both vascular and nerve model are first formed separately to provide the optimal conditions for the development of each tissue, and then bonded into a single and compact NV unit. The vascular component contained a co-culture of HMVEC/SCs, built as described in fig. 3, and cultured for 11 days. The nerve component was prepared as described in fig. 1 and the iPSCs/SCs co-culture maintained for 4 days. At the point where both models were merged, the vascular unit displayed an interconnected vessel network, and the nerve model showed vast neurite outgrowth from the cluster.

To bond both structures, we added fibrin gel, which is a common material between both models, and thus promoted a facile integration. After 21 days of culture we investigated the developed vasculature/neuronal morphology and resulting NV interactions. To compare the progression of vascular development in platforms pre- and post-integration with the neural scaffolds (fig. 8A), we assessed vascular morphology at 11-day (pre-integration; vascular component) and 21-day cultures (post-integration; NV platform). The 11-day co-cultures showed well-formed vessels, reminiscent of a vascular plexus, with a large diameter, short length and a tortuous/meandering pattern. In 21-day co-cultures, the vessels continued to develop and the resulting structures resembled mature microvessels, with a thinner diameter, larger length and more strongly oriented. We quantified both vessel networks and compared the outcome in fig. S5. The mean vessel diameter decreased from $31.1 \pm 9.5 \mu$ m to $9.2 \pm 2.3 \mu$ m overtime (fig. S5A; p < 0.0001), while the mean vessel length increased from 199.2 ± 85.8

μm to $279.5 \pm 140.6 \mu\text{m}$ (fig. S5B; $p < 0.001$). Regarding vessel area (fig. S5C) and branching density (fig. S5E) there was no difference between timepoints. However, there was a higher number of vessels per area (fig. S5D) present at day 21 (111.9 ± 27.4 vessels/ mm^2) compared to day 11 (56.0 ± 17.8 vessels/ mm^2). In fig. 8C and 8D, we exposed different examples of NV interactions that we observed in our platform. In fig. 8C, we show the resulting interactions in the region comprised by the neurosphere. In this region, we noticed a large presence of HMVECs, which denotes an attraction of these cells towards the neuron cluster. The cells that migrated and came in direct contact with the neurosphere (top images), tended to cover its whole surface, forming a monolayer. In a different manner, HMVECs that were attracted to this region, but remained over $200 \mu\text{m}$ from the neurosphere surface were able to form vascular structures. These structures, resembling a vascular plexus, appeared to be newly formed, due to their morphology that is visibly less mature than the 21-day old microvessels (fig. 8B). Finally, in fig. 8D we show neurovascular interactions in regions distant from the neurosphere. Here, we observed a large presence of mature vessels and no indication of new vessel formation or endothelial cell migration. Neurites that extended over large distances into these remote regions were observed to surround the microvessels located there. In several cases, we noticed both signs of NV alignment and possible vessel innervation.

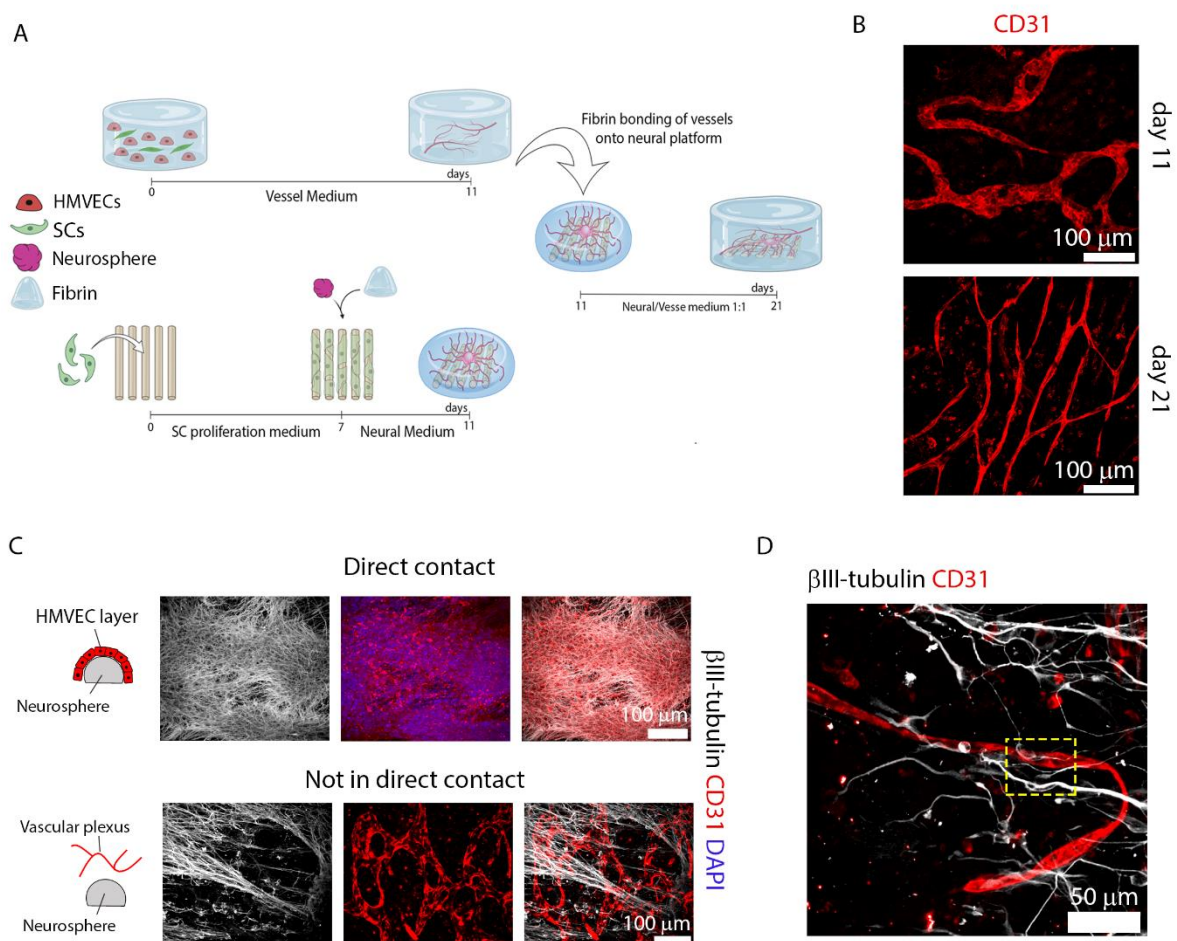


Figure 8. Development and characterization of a platform for mature vessel innervation. A) Illustration of the platform, which is composed of two separate components: a 3D vessel network platform (top part) and a 3D neural tissue platform (bottom part). The vessel network platform was composed of a 300 μl fibrin hydrogel loaded with HMVECs (1.5×10^6 cells/ml) and SCs (0.3×10^5 cells/ml). To improve stabilization and ease of handling, the cell-laden fibrin hydrogel was cross-linked over a polyurethane mesh ring. After seeding, the cultures were maintained for 10 days in vessel medium. At the same time, the 3D neural tissue platform was prepared by first seeding the aligned scaffold with SCs (100×10^3 cells/scaffold), which is cultured for 7 days in SCs proliferation medium, and then adding a neurosphere and a fibrin hydrogel embedding (150 μl). This co-culture was maintained for 4 days in neural medium to promote neurite outgrowth. For the creation of the vessel innervation platform, the component containing the vascular channels was transferred on top of the neural tissue component, and these are bonded with 150 μl of fibrin hydrogel. This platform was then cultured for 10 days in neural/vessel medium at 1:1 (middle part). B) Vessel morphology (shown by CD31 in red) at d21 (bottom image) shows further maturation denoted by thinning, less branching and a straighter pattern compared to vessels at d11 (top image). C) HMVECs are attracted towards the neurosphere and form either a monolayer, when in direct contact (top row), or a vascular plexus, when not in direct contact (bottom row). Scale bar is 100 μm . D) Vessel innervation occurred primarily on regions farther away from the neurosphere cluster, where vessels maintained their morphology and neurites could innervate it and align with the vessels as highlighted in the yellow-dashed box. For C) and D) β III-tubulin is shown in white and CD31 in red. Scale bar is 100 μm for C) and 50 μm for D). Illustration made with biorender (<https://biorender.com/>).

Discussion

Due to the dependence of most organs on innervation and vascular supply, the development of *in vitro* models containing functional and biomimetic NV tissue is critical to generate complex and more representative organ platforms. Interactions within the NV axis are also common, starting during the developmental phase and persisting in adult life. Additionally, several pathologies, such as diabetes type 2, produce NV dysfunctions and aberrations^{33,34,35}. In this regard, *in vitro* NV models can accelerate research by providing a simple and inexpensive tool that permits a better understanding of NV interactions, pathophysiology mechanisms and its specific biological players. To this end, recent efforts have been carried to reconstruct the NV multicellular ecosystem, although with limitations regarding the relevance of cell sources and level of biomimicry^{16,17,18,36}. To tackle this, we have developed a NV platform that takes into consideration the crucial biological and physical

requirements of the neural and vascular components, by merging an optimized 3D nerve model with an optimized 3D vascular network model, in a single cohesive unit.

The nerve model was previously established in chapter 4 and consists of a 3D co-culture of human iPSCs-derived sensory nociceptors with primary rat SCs. SCs are obtained in high yield from rat sciatic nerves, purified and formed into aligned cell bands, to replicate their native morphology³⁷ and induce axonal anisotropy. iPSCs are differentiated into nociceptors and formed into a cell cluster (neurosphere), morphologically similar to a DRG, which permits precise control over the cell number and cell positioning on the platform³⁸. This approach constitutes a better alternative to animal-sourced DRGs (e.g. from rats); despite showing interaction with human endothelial cells *in vitro*^{17,36}, DRG use in NV models carries several drawbacks. DRG isolation is a high cost, laborious procedure that needs recurrent animal sacrifice. Moreover, DRGs are not a pure neuron population, containing other cells types such as SCs and macrophages^{39,40}, which limit the formation of a clear model of cell-cell communication. For this reason, *in vitro* models of the PN⁴¹ and peripheral NV unit¹⁸ have employed stem cell-derived neurons to provide a continuous and reproducible cell source with distinct phenotypes (e.g. sensory⁴² or motor neurons⁴³).

To assemble our 3D nerve model, a neurosphere is combined with the SC-seeded scaffold and the construct embedded in fibrin hydrogel (fig. 1A). The hydrogel intertwines with scaffold fibers and forms a stable and easy-to-handle culture platform when polymerized. Fibrin was selected due to its low-cost and accessibility, as well as being permissive for neuron growth and remodeling. Moreover, fibrin fibers are naturally formed during nerve regeneration, to allow axonal regrowth⁴⁴. After 7 days of co-culture, the neurite outgrowth is vast, 3D and well oriented (fig. 1B). After 21 days of culture, the neuronal development continues, and by this point there is an evident formation of aligned and myelinated segments (fig. 1C) with compacted myelin rings (fig. 1D), denoting a mature and biomimetic nerve construct.

To produce a 3D vascular model we based our method on previous reports that combined ECs at high density and a support cell type, within a hydrogel²⁶ (fig. 2A). The high EC density aids in vessel formation by replicating the initial stages of vasculogenesis, where blood islands form and then fuse to give rise to the primary vascular plexus^{45,46}. As an EC population, we opted for primary HMVECs, which have been previously shown to generate morphologically mature vessels²⁶. These cells are obtained from skin microvessels, which form interactions with nerves in their native environment^{47,48}, thus making this model more clinically relevant than HUVECs¹⁶ that originate from a non-innervated source (the umbilical cord). In addition, HMVECs can be directly harvested from patients, via simple skin biopsies, which also allows the fabrication of patient-specific models for personalized medicine⁴⁹. Alternatively, stem-cell derived ECs are a possible option, but the current protocols necessitate further optimization to yield phenotypically mature vessels at the same level as primary ECs⁵⁰. To

provide trophic support and physically stabilize the vessels at a later stage of development, support cell types such as mesenchymal stem cells³², pericytes⁵¹ and fibroblasts²⁶ have been widely used. We opted for fibroblasts (dermal origin, HDFs), because these cells are present within native skin and nerves, thus representing a suitable partner for HMVECs and neurons. Fibroblasts secrete a myriad of soluble angiogenic factors such as VEGF and FGF⁵² and several reports have shown that they are suitable partners for ECs to generate mature vasculature^{26,24,53,54}. As a material to support both cells, we opted again for fibrin, since it has been shown to be a suitable matrix for vessel formation *in vitro*⁵⁵ and *in vivo*⁵⁶, and it is the same material used within our nerve model, thus ensuring a facile integration of both models into a single NV unit. Fibrin supports the attachment and proliferation of both HMVECs and HDFs, which can remodel the matrix to form open vascular channels, while depositing ECM. In our study, we confirmed that the presence of HDFs essential for the generation of stable and interconnected vascular channels (fig. 2B) and found that a 1:5 ratio of HDFs to HMVECs within fibrin was a sustainable culture condition. When inspecting the vessel phenotype, we found markers characteristic of BVs, such as vessel wall sealing (VE-cadherin), vessel wall maturation (vWF) and ECM deposition (laminin and collagen IV) (fig. 2C). In addition to this, the formed networks were vast and displayed open lumens with a diameter in the range of native capillaries (fig. 2D), evidencing proper vessel development^{31,57}.

After establishing the vascular model with HDFs, we were interested in evaluating the impact of SCs on vessel formation. Reports about SC-ECs interactions are scarce, but previous work⁹ has shown that SCs improve human EC migration. Mukoyama et al.⁸ have also shown that SCs within PNs are responsible for vasculature patterning in skin. To assess SC influence on BV formation, we replicated the vascular model optimized for HDFs (fig. 2A), using SCs that were pre-checked for fibroblast contamination (fig. S2). To our surprise, co-cultures with SCs not only had a clear influence on endothelial cells but resulted in well-formed, stable and interconnected vessels, morphologically similar to HDFs co-cultures (fig. 3A). HDFs co-cultures produced slightly wider vessels, occupying a larger area and with larger lumens, while SCs co-cultures formed longer and more branched vascular networks (fig. 3B), also expressing several phenotypical maturation markers (fig. 3E). The networks formed by HMVECs in partnership with SCs were extensive, interlinked and with open channels, slightly smaller than HDFs co-cultures (fig. 3F).

To date, there are no reports regarding the vasculogenic potential of SCs in 3D cultures with ECs. We clearly show, for the first time, that SCs act as proper mural cells by directly associating with the vessels to provide a physical support (fig. 3C). More interestingly, these SCs in intimate contact with the vessel wall, and only these, express α SMA (fig. 3D), a mural cell marker (expressed by pericytes and smooth muscle cells) responsible to regulate contractility in capillaries⁵⁸. This finding highlights that SCs, notorious for their plasticity,^{59,60}

may also act as pericytes, physically and chemically supporting vascular channels. Furthermore, the construction of our NV platform could be further simplified by only necessitating three different cell types rather than four, minimizing the required culture steps and materials to simultaneously obtain mature neurons and BVs. Yet, the exact molecular players and signaling pathways responsible for the phenotypic change remain to be elucidated. In sum, we concluded here that SCs can induce vessel formation and stabilization and therefore can replace HDFs within the NV platform.

To further investigate the influence of SCs on HMVECs, we tested the angiogenic potential of SCs-conditioned medium using a matrigel assay, the gold standard for evaluating the pro-angiogenic influence of compounds^{61,62} (fig. 4A). SCs-conditioned medium resulted in longer tubules and formed a tubule network that was denser and more branched compared to control cultures (normal vessel medium) (fig. 4B and fig. 4C). With this experiment we could infer that the SCs secretome contains promoters of angiogenesis. Conversely, Huang et al.⁶³ described that human SCs-conditioned medium inhibits angiogenesis, which is probably mediated by TIMP-2, a member of the TIMP family (tissue inhibitors of metalloproteinases) with known *in vivo* and *in vitro* anti-angiogenic properties^{64,65}. When analyzing the composition of SCs-conditioned medium in comparison to HDF-conditioned and control medium, indeed we found in both conditioned media a large presence of TIMP-1, another potent angiogenic inhibitor^{66,67}. We also found the presence of VEGF-A, a major pro-angiogenic factor, in both conditioned media (fig. 4D). This confirms that a balanced production of pro- and anti-angiogenic proteins is necessary for the orchestration of vascular networks, and that the presence of secreted inhibitors in this case does not negate the angiogenic potential of neither HDFs nor SCs. Discrepancies between our results and previous reports can be attributed to differences in experimental conditions, which may have altered the secretome, such as the cell source and culture parameters (e.g. FBS concentration). Additionally, we observed that SCs-conditioned medium possessed a richer composition than the one obtained with HDFs, particularly higher quantities of neuromodulatory and immunomodulatory cytokines. This finding highlights the versatility of SCs in performing supportive roles to both neurons and ECs. Finally, we also tested if SCs-conditioned medium was sufficient to drive vessel formation in 3D cultures in fibrin, or if SCs presence was required. As illustrated in fig. 3E, the presence of SCs is essential to attain a proper vessel morphology, probably due to increased and local secretion of cytokines, as well as physical interaction with HMVECs, to shape and stabilize vessels in this 3D environment.

As a next step, we wanted to see if our patterning of aligned SCs into Bands of Bungers structures would induce orientation of the BVs within 3D cultures (fig. 5A). *In vivo* reports show that BVs align with nerves, mimicking their pattern, in a VEGF-mediated process and that SCs are, together with neurons, the producers of this VEGF source^{8,68}. As previously shown, rat

VEGF is able to stimulate HMVECs (fig. S1) and SCs are able to induce randomly oriented vessels within fibrin hydrogels (fig. 3). HMVECs were attracted to the anisotropic SCs substrate, migrating down the gel and concentrating in the scaffold region to form vessels that followed the SCs/fiber overall direction (fig. 5D). SCs anisotropic pattern, in particular, seems to be the main cause of this vessel alignment, maintaining their orientation while surrounding the vessels (fig. 5E). SCs also further proliferated and navigated through the gel, but the aligned cell layer could be maintained and was sufficient to enable vessel co-orientation (supplementary movie 3). Additionally, the formed vessels were morphologically mature, displaying open channels throughout their entire volume. In contrast, in the absence of SCs there was no vessel formation or preferred HMVEC orientation, ruling out that the embedded scaffold alone is sufficient to induce anisotropy (fig. 5D and fig. 5F). We could conclude that SCs have the ability to pattern BVs and that our Bands of Büngner structures can induce aligned vasculature. Compared to randomly dispersed SCs/HMVECs fibrin cultures, the vasculogenic potential is almost identical, since the EC density is the same and there are only minor differences regarding SCs seeding density (90×10^3 cells in random cultures and 100×10^3 cells/scaffold). However, morphological differences are vast, with the pre-patterned SCs scaffold promoting longer ($\sim 550.9 \mu\text{m}$) and more aligned vessels, but with lower interconnectivity.

Having optimized the angiogenic interactions between SCs and ECs within our 3D culture environment, we expanded to build a complete NV platform that contains iPSCs-derived sensory neurons, HMVECs as the EC population and SCs as both glial and mural cells. To systematically integrate these different elements, we needed to understand the individual contribution of these cells to neural development and to determine which medium composition would be appropriate for simultaneous neural and vessel network formation. To test this, we followed the protocol described in fig. 6A, where we sequentially added the different cellular components and cultured the whole platform in either pure neural medium (NM) or a mix of neural and vessel medium at 1:1 (50/50). As expected, NM led to a higher neurite length for all scaffold conditions compared to 50/50 medium (fig. 6C and 6D). However, in terms of neurite area, both media had a similar effect. Visual inspection suggests that the 50/50 medium may have promoted neuron proliferation (fig. 6D), as the samples contained a larger neuron population but with smaller fibers compared to NM, which approximates the overall neurite area.

This increased neuron proliferation can be explained by the growth factors present exclusively in the 50/50 medium, which have been shown to induce neural stem cell proliferation. This includes epidermal growth factor⁶⁹, fibroblast growth factor⁷⁰, hydrocortisone⁷¹, insulin-growth factor^{72,73} and VEGF⁷⁴. Additionally, SCs also produce endogenous VEGF (as also demonstrated earlier) and this in combination with the exogenous source, may synergistically

induce neuron proliferation and/or migration⁷⁵. Surprisingly, the addition of an EC population in our platform did not significantly enhance neurite length and area. This could be a result of EC attraction to the neurosphere, which may have hindered neurite outgrowth in favor of EC-neuron interactions. Conversely, in the setup reported by Grasman et al.¹⁶ in 2D co-cultures of DRGs and HUVECs, and by Osaki et al.¹⁸ in 3D co-cultures of ESC-MNs and iPSCs-ECs, the presence of ECs enhanced neurite outgrowth. We hypothesize that differences in the timing of EC addition, neurosphere size and dimensionality of the construct (2D vs 3D and platform dimensions) may all contribute to these disparities.

Within NV platforms, we detected that NM alone was not sufficient to drive vasculogenesis. Instead, HMVECs formed a monolayer over the neurosphere. On the other hand, mixed medium led to the formation of a linked and extensive vessel network, again with a strong spatial correlation to the neuron cluster (fig. 7A). This finding highlights the necessity to provide a specific and balanced chemical milieu to be able to simultaneously generate neural and vascular networks. Regarding HMVEC agglomeration within the neurosphere, we hypothesize that this is the result of a gradient of angiogenic GFs, produced by the neurons, as a consequence of hypoxia. In the region of the cluster and especially in its core oxygen concentration is presumably lower due to cell crowding. It is well described that hypoxic conditions activate hypoxia inducible factor-1 (HIF-1) and lead to VEGF upregulation^{6,76}. Thus, we believe that a higher VEGF concentration in the cluster region caused HMVEC attraction. This hypothesis also explains why HMVEC-only platforms could form vessels at a similar extent than those containing HMVECs and SCs, with exception for the vessel length (fig. 7B and 7C). We assume that neuron-derived VEGF production was probably enough to promote vessel formation, rendering SCs redundant for this process.

In this NV platform, the vessel morphology was clearly more immature than those formed in the 3D vascular model (fig. 3). In most vascular tissue engineering approaches, and ours in particular, vessel formation happens via a vasculogenesis-like process that entails EC agglomeration followed by primitive vessel network formation, remodeling and maturation⁷⁷. The success of this intricate process is largely dependent on the culture conditions, such as medium composition, cell density, cell types and available growth space. While we could provide the optimal conditions in the vascular model, the NV platform was sub-optimal for vessel formation due to the necessity to accommodate also neuronal growth. As an example, in the NV platform, early NV interactions can hinder EC agglomeration and limit the vasculogenic process. With this in mind, we developed a different biofabrication sequence (fig. 8A), where the neural and vascular component were formed separately under optimal conditions to allow proper tissue development and maturation. Then, at a later stage, both components were integrated into a single NV unit, mimicking more accurately the

developmental process in which the capillary plexus is first formed from coalescent BVs and then peripheral axon innervation occurs to drive consequent NV alignment⁷⁸.

In this integrated NV platform, the developed BVs were thinner, longer and forming a less branched pattern than the BVs from the vascular component (fig. 8B). This signifies that after NV platform integration and switch from vessel to mixed medium, the vasculature continued to remodel and acquired a configuration typical of a stable/mature network⁵⁷ clearly distinct from the primitive plexus of day 11 cultures. Compared to the vasculature in our previous NV platform (fig 7), this new assembly method resulted in a more biomimetic and mature vascular tissue, even despite the shorter culture period. This evidences that the initial stages of vasculogenesis are largely dependent on optimal culture conditions. However, after a period of primitive plexus formation, the vascular network can further develop in combination with neurons and in a medium that suits both tissues.

In this NV model, we could observe different NV interactions, depending on the region of the platform. Once again, a large concentration of HMVECs were found over the neurosphere, further evidencing that the neuron cluster promotes EC attraction and probably proliferation, even from an already established vascular network. These attracted HMVECs formed a monolayer when in direct contact with the neurosphere, or a primitive plexus when above the neurosphere but not in direct contact with it (fig. 8C). We hypothesize that due to lack of space and early association/interaction with neurons, the HMEVCs in direct contact with the neurosphere failed to form new vessels. On the other hand, those HMVECs above the neurosphere had the conditions to agglomerate and form a vascular plexus of primitive morphology. This finding suggests that the pre-established vascular network is dynamic and can engage in angiogenic processes⁵⁷, expanding and colonizing the platform, particularly in the regions with higher oxygen/nutrient demand. In the periphery of the cluster, most BVs had a mature morphology, probably resultant from remodeling of the pre-established vascular network. In their vicinity, we could find long neurite projections farther away from the cluster, which followed the same direction as the BVs to navigate side-by-side (fig. 8D). Besides NV alignment, we also found instances of juxtaposed neurons and BVs, indicating possible innervation. This finding suggests that the BV network is also exerting its influence on the neural tissue, recruiting neurites and forming a mutual arborized pattern in the process. The tissue landscape that we could naturally achieve here is reminiscent of native NV units found within organs, such as the ear skin⁴⁸ or gut mesentery⁷⁹. While these intricate NV patterns can be observed and studied with high detail and fidelity using animal tissue specimens and advanced sample preparation procedures, the model here proposed aims to provide the same level of biological complexity, but in an *in vitro* setting. However, to fabricate this model, there is no need for recurrent animal sacrifice, and observations can be made in a simple, direct and affordable manner. Because the cellular environment is defined precisely, NV interactions

concerning developmental and adult stages can be dissected, and the specific biological players investigated. Moreover, the control over the chemical milieu permits the simulation of pathological conditions (e.g. hyperglycemia, hypoxia, dyslipidemia) that produce NV disruptions, as well as to experiment therapeutic drug candidates. Finally, this platform can serve as delivery method of neural and vascular supply to a target tissue in order to engineer complex organ models.

In sum, we propose here a method to fabricate mature, dynamic and mutually interactive NV tissue. Particularly for the vascular component, we have also shown the ability of SCs to function as mural cells, to form, direct and support mature vasculature. We believe that the platform here described offers an advanced, versatile and useful tool for development and research of NV tissue.

Acknowledgments

We thank the Microscopy CORE Lab (M4I Maastricht University), especially Hans Duimel and Kevin Knoop for their help in TEM and confocal imaging. We also thank the province of Limburg for the project funding. This work is part of the research programme Veni 2017 STW-project 15900, which is (partly) financed by the Dutch Research Council (NWO).

References

1. Carmeliet, P. & Tessier-Lavigne, M. Common mechanisms of nerve and blood vessel wiring. *Nature* **436**, 193–200 (2005).
2. Morotti, M., Vincent, K., Brawn, J., Zondervan, K. T. & Becker, C. M. Peripheral changes in endometriosis-associated pain. *Hum. Reprod. Update* **20**, 717–736 (2014).
3. Eichmann, A. & Thomas, J. L. Molecular parallels between neural and vascular development. *Cold Spring Harb. Perspect. Med.* **3**, 1–16 (2013).
4. Eichmann, A., Makinen, T. & Alitalo, K. Neural guidance molecules regulate vascular remodeling and vessel navigation. *Genes Dev.* **19**, 1013–1021 (2005).
5. Raab, S. & Plate, K. H. Different networks, common growth factors: Shared growth factors and receptors of the vascular and the nervous system. *Acta Neuropathol.* **113**, 607–626 (2007).
6. Carmeliet, P. Blood vessels and nerves: common signals, pathways and diseases. *Nat. Rev. Genet.* **4**, 710–720 (2003).

7. Andreone B, Lacoste B, G. C. Neuronal and Vascular Interactions. *Annu Rev Neurosci* **38**, 25–46 (2015).
8. Mukoyama, Y. S., Shin, D., Britsch, S., Taniguchi, M. & Anderson, D. J. Sensory nerves determine the pattern of arterial differentiation and blood vessel branching in the skin. *Cell* **109**, 693–705 (2002).
9. Ramos, T., Ahmed, M., Wieringa, P. & Moroni, L. Schwann cells promote endothelial cell migration. *Cell Adh. Migr.* **9**, 441–451 (2015).
10. Cattin, A. L. *et al.* Macrophage-Induced Blood Vessels Guide Schwann Cell-Mediated Regeneration of Peripheral Nerves. *Cell* **162**, 1127–1139 (2015).
11. Gonçalves, N. P. *et al.* Schwann cell interactions with axons and microvessels in diabetic neuropathy. *Nat. Rev. Neurol.* **13**, 135–147 (2017).
12. Wang-Fischer, Y. & Garyantes, T. Improving the reliability and utility of streptozotocin-induced rat diabetic model. *J. Diabetes Res.* **2018**, (2018).
13. Achyuta, A. K. H. *et al.* A modular approach to create a neurovascular unit-on-a-chip. *Lab Chip* 542–553 (2013)
14. Adriani, G. *et al.* A 3D neurovascular microfluidic model consisting of neurons, astrocytes and cerebral endothelial cells as a blood–brain barrier. *Lab Chip* **12**, 169–182 (2017).
15. Chou, C.-H., Sinden, J. D., Couraud, P.-O. & Mado, M. In Vitro Modeling of the Neurovascular Environment by Coculturing Adult Human Brain Endothelial Cells with Human Neural Stem Cells. *PLoS One* **9**, e106346 (2014).
16. Grasman, J. M. & Kaplan, D. L. Human endothelial cells secrete neurotropic factors to direct axonal growth of peripheral nerves. *Sci. Rep.* **7**, 1–12 (2017).
17. Yuan, Q., Li, J. J., An, C. H. & Sun, L. Biological characteristics of rat dorsal root ganglion cell and human vascular endothelial cell in mono- and co-culture. *Mol. Biol. Rep.* **41**, 6949–6956 (2014).
18. Osaki, T., Sivathanu, V. & Kamm, R. D. Engineered 3D vascular and neuronal networks in a microfluidic platform. *Sci. Rep.* **8**, 1–13 (2018).
19. Kaewkhaw, R., Scutt, A. M. & Haycock, J. W. Integrated culture and purification of rat Schwann cells from freshly isolated adult tissue. *Nat Protoc* **7**, 1996–2004 (2012).
20. Chambers, S. M. *et al.* Combined small-molecule inhibition accelerates developmental timing and converts human pluripotent stem cells into nociceptors. *Nat. Biotechnol.* **30**,

- 715–720 (2012).
21. Longair, M. H., Baker, D. A. & Armstrong, J. D. Simple neurite tracer: Open source software for reconstruction, visualization and analysis of neuronal processes. *Bioinformatics* **27**, 2453–2454 (2011).
 22. Püspöki, Z., Storath, M., Sage, D. & Unser, M. Transforms and Operators for Directional Bioimage Analysis: A Survey. *Focus Bio-Image Informatics* 69–93 (2016)
 23. Velazquez, O. C., Snyder, R., Liu, Z. J., Fairman, R. M. & Herlyn, M. Fibroblast-dependent differentiation of human microvascular endothelial cells into capillary-like 3-dimensional networks. *FASEB J.* **16**, 1316–1318 (2002).
 24. Kunz-Schughart, L. A. *et al.* Potential of fibroblasts to regulate the formation of three-dimensional vessel-like structures from endothelial cells in vitro. *Am. J. Physiol. Cell Physiol.* **290**, C1385-98 (2006).
 25. Chen, X. F. *et al.* Rapid Anastomosis of Endothelial Progenitor Cell-Derived Vessels with Host Vasculature Is Promoted by a High Density of Cotransplanted Fibroblasts. *Tissue Eng. Part A* **16**, 585–594 (2010).
 26. Eckermann, C. W., Lehle, K., Schmid, S. A., Wheatley, D. N. & Kunz-Schughart, L. A. Characterization and modulation of fibroblast/endothelial cell co-cultures for the in vitro preformation of three-dimensional tubular networks. *Cell Biol. Int.* **35**, 1097–1110 (2011).
 27. Review, I. The secretion of von Willebrand factor from endothelial cells ; an increasingly complicated story. **11**, 192–201 (2014).
 28. Barreto-Ortiz, S. F. *et al.* Fabrication of 3-dimensional multicellular microvascular structures. *FASEB J.* **29**, 3302–3314 (2015).
 29. Peterson, A. W. *et al.* Vasculogenesis and angiogenesis in modular collagen-fibrin microtissues. *Biomater. Sci.* **2**, 1497–1508 (2014).
 30. Liu, H., Kitano, S., Irie, S., Levato, R. & Matsusaki, M. Collagen Microfibers Induce Blood Capillary Orientation and Open Vascular Lumen. *Adv. Biosyst.* **4**, 1–8 (2020).
 31. Axnick, J. & Lammert, E. Vascular lumen formation. *Curr. Opin. Hematol.* **19**, 192–198 (2012).
 32. Jeon, J. S. *et al.* Generation of 3D functional microvascular networks with human mesenchymal stem cells in microfluidic systems. *Integr. Biol.* **6**, 555–563 (2014).
 33. John R.Giudicessi, BA.Michael J.Ackerman., 2013. Neurovascular injury in acute

- hyperglycemia and diabetes: A comparative analysis in experimental stroke. *Bone* **23**, 1–7 (2008).
34. Vinik, A. I. *et al.* Dermal neurovascular dysfunction in type 2 diabetes. *Diabetes Care* **24**, 1468–1475 (2001).
 35. Yagihashi, S., Mizukami, H. & Sugimoto, K. Mechanism of diabetic neuropathy: Where are we now and where to go? *J. Diabetes Investig.* **2**, 18–32 (2011).
 36. Yuan, Q., Sun, L., Yu, H. & An, C. Human microvascular endothelial cell promotes the development of dorsal root ganglion neurons via BDNF pathway in a co-culture system. *Biosci. Biotechnol. Biochem.* **81**, 1335–1342 (2017).
 37. Lavdas, A. A. & Matsas, R. Schwann Cell Morphology. *Encycl. Neurosci.* 475–484 (2009)
 38. Haberberger, R. V., Barry, C., Dominguez, N. & Matusica, D. Human dorsal root ganglia. *Front. Cell. Neurosci.* **13**, 1–17 (2019).
 39. L. Sheng, M. Christopher, A. M. Rapid Isolation of Dorsal Root Ganglion Macrophages. *Physiol. Behav.* **176**, 100–106 (2016).
 40. Spiegel, I. & Peles, E. A novel method for isolating schwann cells using the extracellular domain of Necl1. *J. Neurosci. Res.* **87**, 3288–3296 (2009).
 41. Sharma, A. D. *et al.* Engineering a 3D functional human peripheral nerve in vitro using the Nerve-on-a-Chip platform. *Sci. Rep.* **9**, 1–12 (2019).
 42. Clark, A. J. *et al.* Co-cultures with stem cell-derived human sensory neurons reveal regulators of peripheral myelination. *Brain* **140**, 898–913 (2017).
 43. Hyung, S. *et al.* Coculture of Primary Motor Neurons and Schwann Cells as a Model for In Vitro Myelination. *Sci. Rep.* 1–11 (2015)
 44. Wieringa, P. A., Gonçalves de Pinho, A. R., Micera, S., van Wezel, R. J. A. & Moroni, L. Biomimetic Architectures for Peripheral Nerve Repair: A Review of Biofabrication Strategies. *Adv. Healthc. Mater.* **1701164**, 1–19 (2018).
 45. Patan, S. Vasculogenesis and angiogenesis as mechanisms of vascular network formation, growth and remodeling. *J. Neurooncol.* **50**, 1–15 (2000).
 46. Risau, W. Mechanisms of angiogenesis. *Nature* **386**, 671–674 (1997).
 47. Li, W. *et al.* Peripheral nerve-derived CXCL12 and VEGF-A regulate the patterning of arterial vessel branching in developing limb skin. *Dev. Cell* **24**, 359–371 (2013).

48. Yamazaki, T. *et al.* Whole-Mount Adult Ear Skin Imaging Reveals Defective Neuro-Vascular Branching Morphogenesis in Obese and Type 2 Diabetic Mouse Models. *Sci. Rep.* **8**, 1–11 (2018).
49. Edhayan, G. *et al.* Inflammatory properties of inhibitor of DNA binding 1 secreted by synovial fibroblasts in rheumatoid arthritis. *Arthritis Res. Ther.* **18**, 1–12 (2016).
50. Bezenah, J. R., Kong, Y. P. & Putnam, A. J. Evaluating the potential of endothelial cells derived from human induced pluripotent stem cells to form microvascular networks in 3D cultures. *Sci. Rep.* 1–14 (2018)
51. Osaki, T., Sivathanu, V. & Kamm, R. D. Vascularized microfluidic organ-chips for drug screening, disease models and tissue engineering. *Curr. Opin. Biotechnol.* **52**, 116–123 (2018).
52. Newman, C., Nakatsu, M. N., Chou, W., Gershon, P. D. & Hughes, C. C. W. The requirement for fibroblasts in angiogenesis: fibroblast-derived matrix proteins are essential for endothelial cell lumen formation. *Mol. Biol. Cell* **22**, 3791–3800 (2011).
53. Nakatsu, M. N. *et al.* Angiogenic sprouting and capillary lumen formation modeled by human umbilical vein endothelial cells (HUVEC) in fibrin gels: The role of fibroblasts and Angiopoietin-1. *Microvasc. Res.* **66**, 102–112 (2003).
54. Costa-Almeida, R. *et al.* Fibroblast-Endothelial Partners for Vascularization Strategies in Tissue Engineering. *Tissue Eng. Part A* **21**, 1055–1065 (2014).
55. Knezevic, L. *et al.* Engineering Blood and Lymphatic Microvascular Networks in Fibrin Matrices. *Front. Bioeng. Biotechnol.* **5**, 1–12 (2017).
56. White, S. M. *et al.* Longitudinal *In Vivo* Imaging to Assess Blood Flow and Oxygenation in Implantable Engineered Tissues. *Tissue Eng. Part C Methods* **18**, 697–709 (2012).
57. Potente, M., Gerhardt, H. & Carmeliet, P. Basic and therapeutic aspects of angiogenesis. *Cell* **146**, 873–887 (2011).
58. Alarcon-Martinez, L. *et al.* Capillary pericytes express α -smooth muscle actin, which requires prevention of filamentous-actin depolymerization for detection. *Elife* **7**, 1–17 (2018).
59. Lee, H. J., Shin, Y. K. & Park, H. T. Mitogen Activated Protein Kinase Family Proteins and c-jun Signaling in Injury-induced Schwann Cell Plasticity. *Exp. Neurobiol.* **23**, 130–7 (2014).
60. Stierli, S., Imperatore, V. & Lloyd, A. C. Schwann cell plasticity-roles in tissue

- homeostasis, regeneration, and disease. *Glia* **67**, 2203–2215 (2019).
61. Ponce, M. L. In vivo matrigel migration assay protocol. *Angiogenesis* **467**, 183–188 (2009).
 62. Mousseau, Y. *et al.* In vitro 3D angiogenesis assay in egg white matrix: Comparison to Matrigel, compatibility to various species, and suitability for drug testing. *Lab. Investig.* **94**, 340–349 (2014).
 63. Huang, D. *et al.* Schwann cell-conditioned medium inhibits angiogenesis. *Cancer Res.* **60**, 5966–5971 (2000).
 64. Keith Brewa and Hideaki Nagaseb. The tissue inhibitors of metalloproteinases (TIMPs): An ancient family with structural and functional diversity. *Biochim Biophys Acta* **1803**, 55–71 (2010).
 65. Dong-Wan Seo, H. L., Liliana Guedez, Paul T. Wingfield, T. D. & Rita Salloum, Bei-yang Wei, and W. G. S.-S. TIMP-2 Mediated Inhibition of Angiogenesis: An MMP-Independent Mechanism. *Expert Opin. Biol. Ther.* **5**, 359–368 (2005).
 66. Reed, M. J., Koike, T., Sadoun, E., Sage, E. H. & Puolakkainen, P. Inhibition of TIMP1 enhances angiogenesis in vivo and cell migration in vitro. *Microvasc. Res.* **65**, 9–17 (2003).
 67. Ikenaka, Y. *et al.* Tissue inhibitor of metalloproteinases-1 (TIMP-1) inhibits tumor growth and angiogenesis in the TIMP-1 transgenic mouse model. *Int. J. Cancer* **105**, 340–346 (2003).
 68. Mukouyama, Y.-S., Gerber, H.-P., Ferrara, N., Gu, C. & Anderson, D. J. Peripheral nerve-derived VEGF promotes arterial differentiation via neuropilin 1-mediated positive feedback. *Development* **132**, 941–52 (2005).
 69. Egawa, E. Y., Kato, K., Hiraoka, M., Nakaji-Hirabayashi, T. & Iwata, H. Enhanced proliferation of neural stem cells in a collagen hydrogel incorporating engineered epidermal growth factor. *Biomaterials* **32**, 4737–4743 (2011).
 70. Murphy, M., Drago, J. & Bartlett, P. F. Fibroblast growth factor stimulates the proliferation and differentiation of neural precursor cells in vitro. *J. Neurosci. Res.* **25**, 463–475 (1990).
 71. Ninomiya, E. *et al.* Glucocorticoids promote neural progenitor cell proliferation derived from human induced pluripotent stem cells. *Springerplus* **3**, 1–8 (2014).
 72. Qi, Z. *et al.* Enhancement of neural stem cell survival, proliferation and differentiation by

- IGF-1 delivery in graphene oxide-incorporated PLGA electrospun nanofibrous mats. *RSC Adv.* **9**, 8315–8325 (2019).
73. Nieto-Estévez, V., Defterali, Ç. & Vicario-Abejón, C. IGF-I: A key growth factor that regulates neurogenesis and synaptogenesis from embryonic to adult stages of the brain. *Front. Neurosci.* **10**, 1–9 (2016).
 74. Sun, J., Zhou, W., Ma, D. & Yang, Y. Endothelial cells promote neural stem cell proliferation and differentiation associated with VEGF activated Notch and Pten signaling. *Dev. Dyn.* **239**, 2345–2353 (2010).
 75. Mackenzie, F. & Ruhrberg, C. Diverse roles for VEGF-A in the nervous system. *Development* **139**, 1371–1380 (2012).
 76. Marrella, A. *et al.* Engineering vascularized and innervated bone biomaterials for improved skeletal tissue regeneration. *Mater. Today* **21**, 362–376 (2018).
 77. Rouwkema, J. & Khademhosseini, A. Vascularization and Angiogenesis in Tissue Engineering: Beyond Creating Static Networks. *Trends in Biotechnology* vol. 34 (2016).
 78. James, J. M. & Mukoyama, Y. suke. Neuronal action on the developing blood vessel pattern. *Semin. Cell Dev. Biol.* **22**, 1019–1027 (2011).
 79. Neckel, P. H., Mattheus, U., Hirt, B., Just, L. & Mack, A. F. Large-scale tissue clearing (PACT): Technical evaluation and new perspectives in immunofluorescence, histology, and ultrastructure. *Sci. Rep.* **6**, 1–13 (2016).

Supplementary information

Exploring the neurovascular axis: neuron-glia-endothelial cell interactions within a biomimetic *in vitro* platform

Afonso Malheiro, Adrián Seijas Gamardo, Abhishek Harichandan, Carlos Mota, Paul Wieringa, Lorenzo Moroni

MERLN Institute for Technology-Inspired Regenerative Medicine, Maastricht University

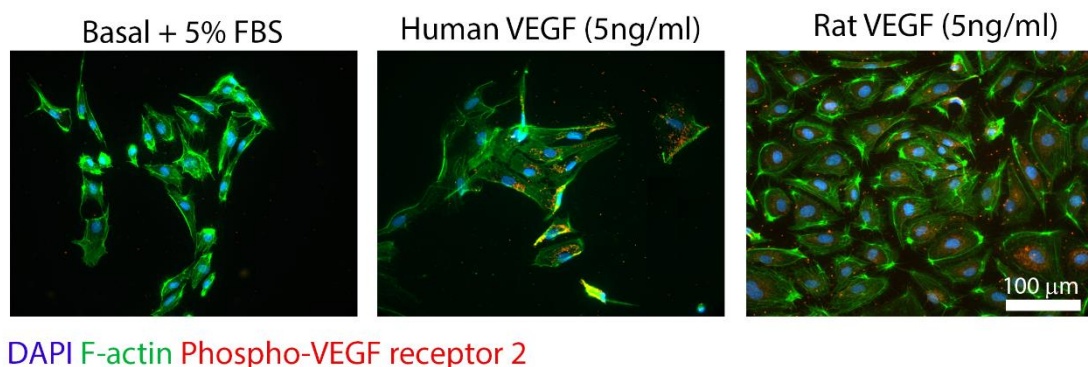


Figure S1. Both human and rat VEGF-165 can bind to the VEGF receptor-2 of HMVECs and induce its phosphorylation, as shown by phospho-VEGR2 immunostaining (in red). All samples were cultured in basal medium plus 5% FBS with either human VEGF (5ng/ml, middle image), rat VEGF (5ng/ml, right image) or no added VEGF (left image) for 24 h. F-actin is shown in green and DAPI in blue. Scale bar is 100 μ m.

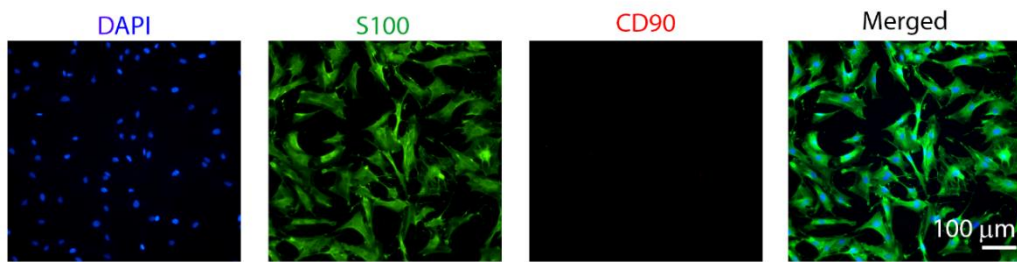


Figure S2. Characterization of the primary SCs isolated and purified from a rat sciatic nerve. All cells express S100 (green) and there were no signs of fibroblast contamination (CD90, red). DAPI is shown in blue and the scale bar is 100 μm .

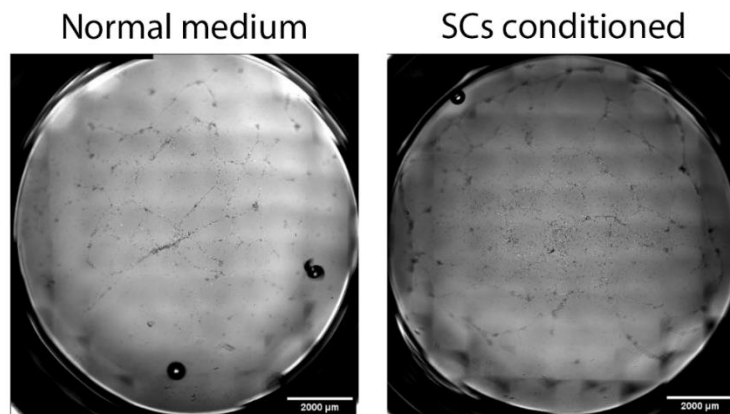


Figure S3. Brightfield micrograph showing tube formation from HMVECs, seeded onto matrigel-coated wells and cultured with normal vessel medium (left image) or SCs conditioned vessel medium (right image) for 48 h. Scale bar is 2000 μm .

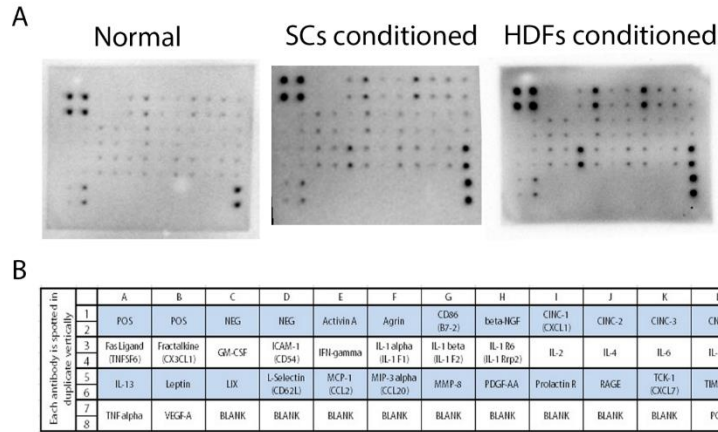


Figure S4. A) Images of the cytokine array membrane after incubation with normal vessel medium (left image), SCs conditioned vessel medium (middle image) or HDFs conditioned vessel medium (right image). B) Manufacturer table of the detectable cytokines within the membrane. POS means positive control and NEG means negative control. BLANK refers to empty spots in the membrane.

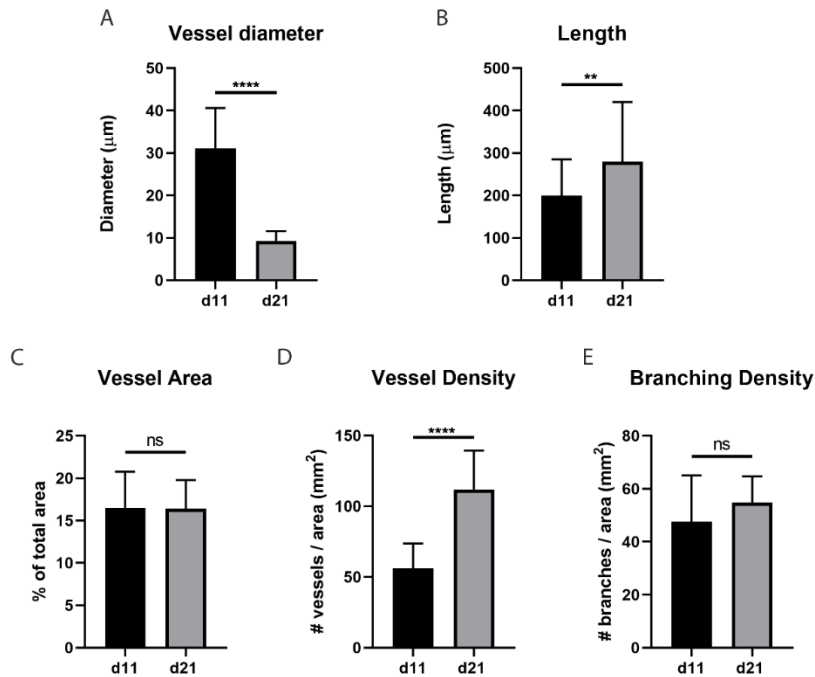


Figure S5. Characterization and comparison of formed vessel networks at 11 days (vasculature only platform) or 21 days of culture (neurovascular platform). 11 day cultures refer to the vessels in the vasculature only platform (prior to transfer to the neural platform), and are composed of solely HMVECs and SCs at 5:1, cultured in vessel medium. 21 days cultures refer to the vessels formed in the neurovascular platform. This is composed of 11 day vessel cultures that are transferred to a neural platform and cultured for additional 10 days in mixed

medium (neural/vessel medium at 1:1), to form the neurovascular model. A) Vessel diameter, obtained from measuring the diameter of individual vessels. B) Vessel length, determined as the total length of an individual vessel until the next bifurcation. C) Vessel area was determined as the ratio of CD31⁺ area per total image area. D) Vessel density, determined as the ratio of number of vessels contained in an image per image area. E) Branching density, determined as the ratio of vessel branching points contained in an image per image area. All graphs represent the mean \pm SD. For the image analysis, we took at least five images per sample (n = 4). Statistics were performed using an unpaired t-test, where ****p < 0.0001, **p < 0.01 and ns denotes p > 0.05.

Chapter 8

General Discussion

The work here described fits within the field of tissue engineering/organ modelling for *in vitro* research purposes. Particularly, the overarching goal of this project was to develop an *in vitro* model of peripheral neurovascular tissue. The main motivation for this was the need to develop support tissue for organ models, which currently lack the required complexity to act as true replicas. To approach this problem, we simplified the task by dividing the neurovascular unit into a nerve and a vascular component. These components were developed individually and then finally combined once both models were fully established, showing proper tissue replication. Due to the biological and technological challenges and the lack of prior knowledge within the field, we have given more emphasis to the development of the nerve component. Its fabrication method is described in chapter 3, and a further improved version followed in chapter 4. Capitalizing on the acquired knowledge and established model, we used the platform to conduct drug tests and biochemical assays for a specific application (chapter 5). In chapter 6, we adapted some of the techniques developed in previous chapters and established a new platform for innervation of a skin construct. Finally, in chapter 7 we added vascularization to a previously established nerve platform, thus reaching the goal of creating a neurovascular model.

In this chapter, we start by discussing animal models as the pillar for fundamental research, addressing their benefits and disadvantages. Following this, we discuss how the shift to *in vitro* models enhanced research capabilities. We highlight the opportunities offered by the use of *in vitro* models, as well as the challenges faced in the field. Finally, we discuss the recent technological developments and contextualize/summarize our findings.

Animal models

Fundamental research has heavily relied on the use of animals to better understand the biology and physiology governing developmental and adult stage processes, whether in a normal or pathological context. Animal research has also been performed to evaluate the efficiency and safety of regenerative medicine therapies based on chemical compounds, cells, biomaterials, or a combination of these within an implantable tissue engineered construct. The greatest advantage of animal models is that even in those of small-scale, there is a high level of biological complexity and cross-talk, which allows researchers to perform tests in a more holistic manner rather than in isolated parts¹. For instance, in a single experiment one can investigate the efficiency of a drug delivery method, the efficacy of that drug, and the potential

side effects. The system interconnectivity, however, can also constitute a hurdle, if the objective is to dissect and isolate components and assess specific interactions or mechanisms unequivocally. Translating animal research findings has also been a subject of debate, with external validity aspects being thoroughly discussed². First and foremost, the differences between species, regarding genome but also physiological parameters, are commonly regarded as the culprit for the failure in result translation to humans. In addition to this, a mismatch of experimental conditions with the real-life setting, such as subject health, diet, and age can also account for inaccurate pathology modelling. To use animals within research involves the breeding and sacrificing of a large number of subjects, in order to explore all the research variables and attain statistical validity. This has two costs — monetary and ethical — and both of them contribute to an increased burden, be it financial, ethical or even time-related. To prevent misuse of animals, guidelines for animal protection and welfare are in place, which can be summarized as the 3Rs: replacement, reduction and refinement¹. The first rule, replacement, states that animals must not be used whenever other, non-animal-based, experimental approaches are available, with similar relevance and reliability¹. This has propelled the development and use of *in vitro* models for preclinical research, which will be addressed in the following section.

***In vitro* models: the early days**

Early *in vitro* research goes back to 1950s when scientists began understanding and possessed the means to conduct preliminary investigations in a dish prior to animal testing. The primary concern was to evaluate the toxicity of a chemical compound or biomaterial, which can be manifested as general cytotoxicity, genotoxicity, mutagenesis and carcinogenesis³. While *in vitro* models have not fully replaced the animal models, the potential to conduct a pre-evaluation regarding the efficacy and safety of a therapy has greatly improved *in vivo* research success and reduced the overall research costs. Another major focus of *in vitro* research has been in understanding the fundamentals of human diseases in order to develop new and better methods of diagnosis, prevention and intervention⁴. However, a conundrum arises, because humans cannot be used as test beds in early research, while animals are intrinsically distinct from humans. This variation between humans and other animal species limits the ability to use animal models to mimic human diseases, and especially those that do not find an exact correlation in the animal kingdom. For this reason, *in vitro* humanized models have emerged, providing a more representative and clinically relevant tool. However, to build a human disease model that provides accurate and reliable data is no minor feat. Human pathologies are a complex phenomenon, often involving multiple organs systems such as the immune, vascular or neural systems, and greatly depend on various personal parameters. Despite this, it is possible to deconstruct the problem and start to gradually recapitulate the final complexity of

the body in a dish, which will contribute to greater understanding and ultimately finding a solution. For this, investigators started by building simple tissue models and progressively add more features that are critical for the disease etiology and progression⁴. The building blocks for these models are obviously the cells, and thus, it is critical to obtain a source that is relevant, sustainable and reproducible. Primary cells provide the direct functional units of a tissue, but due to their limited proliferation and difficulty or even impossibility (e.g. brain) to be harvested, their potential is limited. Alternatively, cell lines have been widely used and have become a valuable tool, by providing a cost effective, well-defined and simple to use option with almost unlimited supply⁵. However, the differences compared to their primary counterparts can be vast, and thus the conclusions withdrawn from studies employing cell lines must be handled with care. As helpful as they may be, the strength of cell lines lies in preliminary testing, yet control experiments with more representative cells should be subsequently performed to validate the findings⁵. In this regard, the emergence of stem cell technologies, and particularly induced pluripotent stem cells (iPSCs), constitutes a great development for modern research. iPSCs can be generated from fibroblasts after treatment with a specific cocktail of growth factors, which circumvents ethical issues associated with other pluripotent cells of embryonic origin. Cells can be harvested directly from a patient, induced to a pluripotent state and re-differentiated to a desired lineage. After overcoming technical hurdles related to reprogramming protocols, iPSCs lines could be routinely generated and because the cells can self-renew unlimited times, it is now easy to maintain a large stock available^{6,7}. In the past years several research groups have worked towards developing and refining differentiation protocols of iPSCs into virtually any cell type. Additionally, gene mutations have also been introduced to iPSCs to produce disease models⁸. To make better organ representations, these protocols have been adapted for three-dimensional (3D) culture, and organoids of various kind, such as brain, intestine, liver or kidney, have been formed. Organoid formation mimics human development as cells self-organize towards an organ replica, which in some cases can be histologically indistinguishable from actual human organs⁷. However, organoid models still possess many limitations. These include a generalized lack of organ complexity, such as vasculature and innervation presence; lack of inter-organ communication; absence of physiological conditions, such as shear stress, and difficulty in tissue accessibility, important for tasks such as tissue perfusion⁷. Because of this, scientists began to adopt engineering principles to improve their replica strategies, creating a new generation of organ models.

Towards advanced *in vitro* models

In the past decades the field of tissue engineering (TE) has emerged from the combination of engineering techniques and natural sciences, such as biology and chemistry. In TE, the aim is to build a tissue substitute for regenerative medicine (RM) or a tissue analogue for research purposes, such as drug screening and disease modelling. This can be achieved via the combination of a biomaterial-based scaffold with cells and biomolecules, followed by *in vitro* maturation⁹. The scaffold can act on many levels by providing structural support, mechanical integrity, topographical guidance and chemical content. It can be composed of solid polymers but also hydrogels, of natural or synthetic origin, with fine-tuned properties designed for the tissue in question. While some scaffolds are intended as temporary support, others, such as supramolecular hydrogels, aim at mimicking the extracellular matrix (ECM) interactions by introducing dynamic bonds within the construct¹⁰. Cells from the parenchyma, stroma or supportive networks (e.g. vasculature, neuronal and lymphatic networks) can be introduced in the scaffold and further matured to native-like tissues via the supplementation of specific biomolecules. However, to harmoniously combine several tissues within a functional and biomimetic cohesive unit is an intricate challenge that increases proportionally with increasing organ complexity. This hurdle has limited the development of integrated and functional multi-tissue platforms, and at the same time has propelled the development and application of biofabrication technologies, such as bioprinting. By providing the ability to precisely and automatically have spatial (and temporal) control over cells and biomaterials, these technologies offer promising advances towards functional organ replicas¹¹. In **chapter 2**, we discuss in length the opportunities that biofabrication technologies can present to progress the complexity within organ models/substitutes, with particular emphasis in vasculature patterning¹². Besides bioprinting, there are several other technologies available, such as fused deposition modelling and electrospinning, which have been extremely useful in providing a tissue framework. In particular, electrospinning offers a very simple and cost-effective technique to generate ECM-like fibers with controlled architecture¹¹. This technique was used extensively in this thesis work to provide a scaffold that houses and directs the morphology of Schwann cells (SCs) and neurons (**chapters 3, 4, 5 and 7**).

While biofabrication approaches have progressed immensely to produce excellent tissue representations, some challenges still remain within organ models, particularly in the control of physical and chemical parameters, which include physiological settings such as oxygen tension or pH gradients, but also drug concentration gradients. Moreover, current tissue analysis methods are invasive, disruptive and cumbersome, whereas automated non-invasive capability is highly desired for reproducible and long-term monitoring¹³. To this end, microfluidic technologies that allow a precise environmental control and in-line detection have been combined with TE models to produce organ-on-a-chip devices, which can even be further

linked to create multi-organ platforms^{13,14}. These are distinct from early microfluidic platforms with planar non-representative cell cultures, which do not provide a valid method for drug testing. Instead, by combining tissue analogues with high-end technological platforms, *in vitro* models will be greatly enhanced to the benefit of preclinical research.

Wiring up the system: our efforts

Within the human body, most tissues are densely innervated by various types of fibers that confer them functionality. That is the case of skeletal muscles, which require motor fiber innervation for volitional control, or the case of skin that needs sensory fibers for its sensitization ability. The peripheral nerve (PN) system is also highly prone to damage, which can occur from trauma or due to a systemic disorder. Therefore, *in vitro* models of the PN and tissue innervation models are highly desired to provide drug testing and disease modelling platforms. The PN system however is a complicated tissue to model, due to its multicellular composition and its intricate hierarchical architecture denoted by anisotropic bundles of fibers. The difficulties derive from the lack of access to viable human primary cell sources and the technological challenges that are necessary to overcome to fabricate such structures using adequate biomaterials. For this reason, early models were commonly composed of animal tissue explants, most notably dorsal root ganglions (DRGs) from rat or chicken origin, in flat or isotropic 3D substrates. Despite their success in generating mature nerve-like tissue, DRGs contain a mixed cell population with SCs and other cell types and their use demands recurrent animal sacrifice¹⁵. For this reason, cell lines such as PC12 cells, which provide a cheap and abundant source of neurons with defined phenotypes, started to be adopted in neuronal models.

In **chapter 3**, we show the creation of a 3D biomimetic PN model constructed from PC12 cells (with a neuronal priming treatment) and primary rat SCs. We compared the morphology of this model with the one composed by DRGs instead and show that our cell line model generates tissue with similar architecture and maturation levels. To show applications of this model, we demonstrated the ability to influence neurite outgrowth via protein inhibition, we performed toxicity tests with a known neurotoxin (suramin), and we modelled diabetes-induced hyperglycemia while screening the therapeutic effects of an aldose reductase inhibitor (epalrestat) that showed benefits in mitigating myelin damage. The developed platform contained some unique features, such as scaffold and hydrogel combination to generate three-dimensional anisotropic neural tissues mimicking both the physical and hydrated properties of the native ECM. The achieved level of biomimicry and neural maturation with a low-cost and easy-to-culture cell line makes it a very attractive and useful *in vitro* model to conduct preliminary investigations. However, because PC12 cells are a limited representation of actual neurons, we worked towards obtaining a replacement that could take this PN model a step

further. After optimization, we established an iPSCs-derived nociceptor protocol that yields a large number of even-sized spheroids composed of functional nociceptors (**chapter 4**). We show that these neurons are electrically active and able to detect and react to noxious stimuli (capsaicin and resiniferatoxin). Furthermore, we used these neurospheres to establish a 3D model similar to that built from PC12 cells, demonstrating a large improvement in terms of neuronal length, area, alignment and stability compared to conventional glass substrates. With this humanized model, we evidenced again the possibility to model hyperglycemia-induced myelin damage and to conduct therapeutic drug screenings. Finally, we used this 3D model as an innervation platform by incorporating pancreatic pseudoislets or endometrial organoids and co-culturing them with the neurons until they become innervated. The developed platform constitutes an improvement in terms of tissue functionality, tissue architecture and range of applications compared to existing literature approaches^{16,17,18} and thus we expect to have provided a useful contribution towards better *in vitro* models. However, this model is not absent of limitations. The first challenge is to achieve a fully human tissue model, by substituting the current rat-origin SCs with human stem cell-derived SCs, which would need protocol establishment and evaluation. Secondly, the current seeding method could benefit from an automated process in order to reproducibly generate similar tissue architectures. Alternatively, we could develop an encasing structure that compartmentalizes cell populations. Regarding neural electrical activity, the current protocol demands that cells are cultured for at least 40 days in order to be sufficiently polarized, which is a longer period than other reported works¹⁹. Furthermore, the electrophysiology measurements are difficult to conduct in the 3D model. The simplest solution would be to employ imaging methods such as calcium imaging, but even this would require extensive testing and validation when translating from 2D to 3D measurements. Finally, the innervation models shown here are still too preliminary and no evidence is shown regarding multi-tissue interactions. These examinations were beyond our primary scope but in the future, further investigation would be necessary to validate the applicability of these innervation models.

In **chapter 5** we selected some elements established in the previous chapters, to conduct investigations with a class of drugs, termed phosphodiesterase-4 inhibitors. Particularly, we investigated the influence of two compounds, roflumilast and BPN17440, on SCs myelinating phenotype, whether in a regeneration or hyperglycemia setting. We found that both compounds can enhance the SCs myelinating phenotype in terms of gene and protein expression. Additionally, SCs are still able to engage in iPSCs-derived neuron myelination (although without clear differences to control cultures). In our disease model, we detected an apparent benefit of roflumilast supplementation to prevent SC dedifferentiation in high glucose conditions, and improve redifferentiation after high glucose exposure. However, we would need to conduct further testing to unequivocally determine a benefit of PDE4 inhibitor

supplementation to prevent glucose damage. Despite the preliminary findings, the work displayed in this chapter demonstrates the potential of the developed *in vitro* tools in serving as a research platform to screen drugs and model pathologies with great ease and reduced costs.

In **chapter 6**, we developed a fully human innervated skin model by combining our iPSCs nociceptor tool with an established skin construct. We were able to show 3D remote innervation of the skin that can be conveniently assessed without sample sectioning. Additionally, we show an application/functionality of this platform by placing a capsaicin patch on the skin section and measuring consequential neuronal damage, thus evidencing both skin function as absorptive barrier and nociceptors function as noxious-stimuli detectors. Still, the lack of cross-section imaging means we were unable to demonstrate nerve fiber penetration in the dermal region, which is needed to strengthen this model validity. Despite this, the work described here contains a valuable and useful contribution for the skin research field, by providing new testing tools.

Finally, in **chapter 7**, we built the peripheral neurovascular *in vitro* model by adding vascularization to the nerve platform described in **chapter 4**. In the single vascular model, we were able to show, for the first time, a role of SCs as mural cells to promote the formation of 3D morphologically mature vascular networks with vast area and high interconnectivity. The nerve and vascular component were merged into a single cohesive unit and we could demonstrate neurovascular interactions such as neuronal attraction of vascularization and neurovascular alignment. By generating neuronal and vascular tissue within a platform, we created the basic units necessary to support a wide range of target tissues. This model is a significant enhancement in terms of bioarchitecture mimicry and tissue maturation compared to existing neurovascular models^{20,21,22}. Thus, we believe that the work described here constitutes a stepping-stone towards achieving increased complexity within organ models for better and more reliable *in vitro* research.

Where do we go from here?

The future of PN and innervation models lies, as already mentioned, in the combination of tissue engineering and microfabrication technologies to achieve PN-on-chip/innervation-on-chip devices that will greatly streamline the testing phase. By using platforms that permit spatial arrangement and model biomimetic tissue development, multiple tissues can be precisely positioned and matured *in situ*, to form reproducible and complex tissue analogues. For this, the establishment of representative cell models of a normal or pathological setting, as well as representative ECM materials is a necessity. The triggering of neuron electrical activity on demand via non-invasive and non-destructive methods, for instance via optogenetic control^{23,24}, will permit a regulated interaction between nerves and the target tissue, thus

providing an extra and clear insight regarding the innervation role. Besides this, in-line detection methods will be required to improve the observational capabilities and to exert a tight regulation over physical and chemical parameters that are paramount to determine the weight of all variables. The addition of micro/macrophuidic channels within the platform will permit a regulated perfusion of the system to imitate physiological conditions in embryonic and adult stages and to deliver of biomolecules (e.g. drugs) in precise quantities and to defined regions. Finally, the standardization of testing and analysis methods will increase the robustness and external reproducibility of the experiments.

References

1. Barré-Sinoussi, F. & Montagutelli, X. Animal models are essential to biological research: Issues and perspectives. *Futur. Sci. OA* **1**, 4–6 (2015).
2. Pound, P. & Ritskes-Hoitinga, M. Is it possible to overcome issues of external validity in preclinical animal research? Why most animal models are bound to fail. *J. Transl. Med.* **16**, 1–8 (2018).
3. Xiong, Z. Y. and H.-R. In vitro, Tissue-Based Models as a Replacement for Animal Models in Testing of Drugs at the Preclinical Stages. *Intech* 13 (2016).
4. Benam, K. H. *et al.* Engineered In Vitro Disease Models. *Annu. Rev. Pathol. Mech. Dis.* **10**, 195–262 (2015).
5. Kaur, G. & Dufour, J. M. Cell lines: Valuable tools or useless artifacts. *Spermatogenesis* **2**, 1–5 (2012).
6. Abu-Dawud, R., Graffmann, N., Ferber, S., Wruck, W. & Adjaye, J. Pluripotent stem cells: Induction and self-renewal. *Philos. Trans. R. Soc. B Biol. Sci.* **373**, 61–63 (2018).
7. Kim, J., Koo, B. K. & Knoblich, J. A. Human organoids: model systems for human biology and medicine. *Nat. Rev. Mol. Cell Biol.* **21**, 571–584 (2020).
8. Rowe, R. G. & Daley, G. Q. Induced pluripotent stem cells in disease modelling and drug discovery. *Nat. Rev. Genet.* **20**, 377–388 (2019).
9. Groll, J. *et al.* Biofabrication: reappraising the definition of an evolving field. *Biofabrication* **8**, 013001 (2016).
10. Geckil, H., Xu, F., Zhang, X., Moon, S. & Demirci, U. Engineering hydrogels as extracellular matrix mimics. *Nanomedicine (Lond)*. **5**, 469–84 (2010).
11. Moroni, L. *et al.* Biofabrication strategies for 3D in vitro models and regenerative medicine. *Nat. Rev. Mater.* (2018)

12. Malheiro, A., Wieringa, P., Mota, C., Baker, M. & Moroni, L. Patterning Vasculature: The Role of Biofabrication to Achieve an Integrated Multicellular Ecosystem. (2016)
13. Zhang, Y. S. *et al.* Multisensor-integrated organs-on-chips platform for automated and continual in situ monitoring of organoid behaviors. *Proc. Natl. Acad. Sci. U. S. A.* **114**, E2293–E2302 (2017).
14. Low, L. A., Mummery, C., Berridge, B. R., Austin, C. P. & Tagle, D. A. Organs-on-chips: into the next decade. *Nat. Rev. Drug Discov.* (2020)
15. Malheiro, A., Morgan, F., Baker, M., Moroni, L. & Wieringa, P. A three-dimensional biomimetic peripheral nerve model for drug testing and disease modelling. *Biomaterials* **257**, 120230 (2020).
16. Clark, A. J. *et al.* Co-cultures with stem cell-derived human sensory neurons reveal regulators of peripheral myelination. *Brain* **140**, 898–913 (2017).
17. Wainger, B. J. *et al.* Modeling pain in vitro using nociceptor neurons reprogrammed from fibroblasts. *Nat Neurosci* **18**, 17–24 (2015).
18. Sharma, A. D. *et al.* Engineering a 3D functional human peripheral nerve in vitro using the Nerve-on-a-Chip platform. *Sci. Rep.* **9**, 1–12 (2019).
19. Osaki, T., Sivathanu, V. & Kamm, R. D. Engineered 3D vascular and neuronal networks in a microfluidic platform. *Sci. Rep.* **8**, 1–13 (2018).
20. Yuan, Q., Sun, L., Yu, H. & An, C. Human microvascular endothelial cell promotes the development of dorsal root ganglion neurons via BDNF pathway in a co-culture system. *Biosci. Biotechnol. Biochem.* **81**, 1335–1342 (2017).
21. Grasman, J. M. & Kaplan, D. L. Human endothelial cells secrete neurotropic factors to direct axonal growth of peripheral nerves. *Sci. Rep.* **7**, 1–12 (2017).
22. Osaki, T., Uzel, S. G. M. & Kamm, R. D. Microphysiological 3D model of amyotrophic lateral sclerosis (ALS) from human iPS-derived muscle cells and optogenetic motor neurons. *Sci. Adv.* **4**, 1–16 (2018).
23. Uzel, S. G. M. *et al.* Microfluidic device for the formation of optically excitable, three-dimensional, compartmentalized motor units. *Sci. Adv.* **2**, (2016).

Chapter 9

Valorization

When it comes to research, conflicting thoughts come to my mind. On one side, I firmly believe that research should focus on real world problems and work collaboratively to find efficient solutions in an economical and sustainable manner. This entails working from day one towards a goal to minimize tangential tasks that often arise when the direction is unclear. On the other hand, I also believe that uncompromised fundamental research is needed to expand the base knowledge. Oftentimes, in the quest for nothing, a serendipitous outcome results in an extraordinary and impactful finding. Thus, it seems to me that a balance between translational and innovative research is necessary to achieve an optimal valorization path. The research shown here commenced with a mildly defined goal/concept and it took some trial-and-error and some tangential exploratory work to finally arrive at the present stage.

In this chapter, the valorization potential of the research described in this thesis is discussed, specifically how it fits within societal needs and how it can be commercially explored.

The need for organ models

The drug development process is a long and expensive path that lasts, on average, 10 to 12 years and uses hundreds of millions of dollars to generate a single clinically applicable product¹. Most of the budget is spent during the clinical trial phase, and a large fraction of it is wasted since several drug candidates prove to be inefficient or unsafe^{1,2}. To reduce the time and costs, it is imperative to improve the predictive power of the pre-clinical phase, which means eliminating ineffective drug candidates as soon as possible and detecting compounds with potential benefits early on. To this end, 3D *in vitro* organ models can provide a tremendous help and revolutionize the pharmaceutical industry, with organ-on-a-chip technologies representing the lion's share of this emerging field. By combining tissue engineering strategies with microfluidic/microfabrication technologies, miniaturized versions of an organ functional element can be fabricated and analyzed in a convenient manner. The goal is to provide a better testing system than current *in vitro* culture models, which do not recapitulate several aspects of native organs and thus produce unreliable data. Compared to animal models, these devices would also provide a superior testing platform, by permitting a direct, real-time and more focused analysis with overall reduced costs³. However, to produce a true replica of an organ

that presents identical characteristics in terms of gene expression, protein production, and physiological activity is an immense task, and validation studies will be required to define what are the benchmarks. Furthermore, it will be necessary to evaluate the pharmacokinetic behavior within the organ model and compare it with the ADME-TOX (adsorption, delivery, metabolism, excretion/toxicity) database¹.

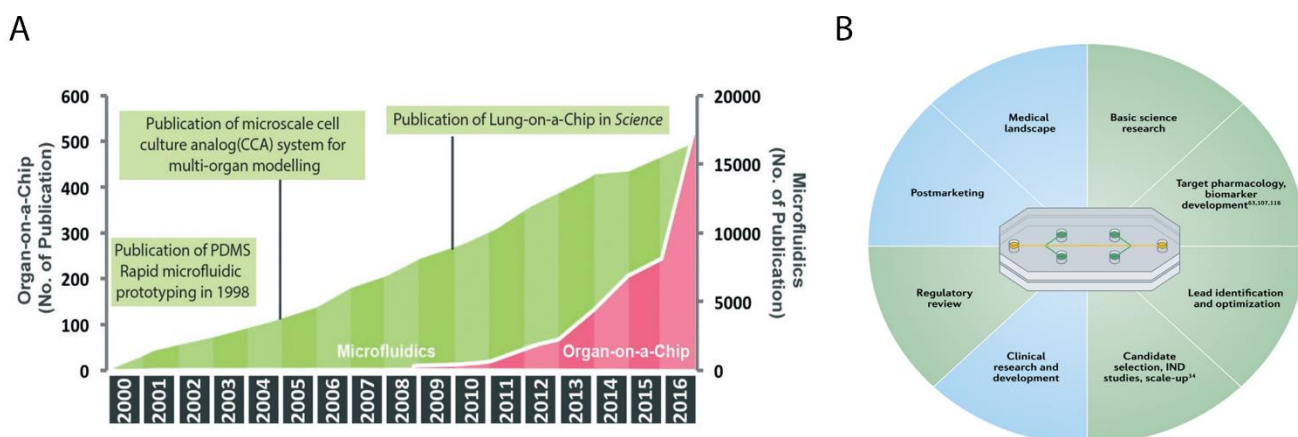


Figure 1. Organ models in research. A) Rise in publications in the organ-on-a-chip space from 2000 to 2016. Data extracted from Zhang et al., *Organ-on-a-chip devices advance to market* (2016)¹. B) Utility of organs-on-a-chip on drug development phases. Green components represent the current or shortly predicted use of devices and blue components represent possible and predictable utility. Diagram extracted from Low et al., *Organs-on-chips: into the next decade* (2020)⁴.

The market of organ models

Due to the long developmental road ahead, it will still take some years until organ-on-a-chip platforms become standard within the drug development pipeline. Despite this, several companies have already emerged in the scene and are commercializing organ models. In some cases, the commercial product is behind the biotechnological state-of-the-art, but the creation of these companies allow them to be pioneers and colonize the marketplace¹. The type of product depends obviously on the type of tissue/organ in question, but also in the type of function analysis that is of interest. Currently, organ models can be categorized in:

- **Interface models** – example: lung-on-a-chip, gut-on-a-chip, kidney-on-a-chip (from Emulate, Inc)
- **Multi-organ models** – example: Human-on-a-chip (TissUse GmbH), Multi-organ chip (Hesperos, Inc)

- **Parenchymal tissue models** – example: AngioChip (TARA Biosystems, Inc), 3D cardiac systems (Myriamed GmbH)

To date, most devices only manage to model a single or a small-range of tissue functions, and the device in itself is often a simplistic representation, far from representing the biological anatomy, of the complex and hierarchical organ microenvironment. Thus, the current market is still developing and pursuing the creation of improved *in vitro* organ models that also replicate anatomical functionality.

Neural models: the existing competition

With peripheral nerve (PN) models in mind, there are a few companies commercializing compartmentalized microfluidic devices for neural cultures, such as Xona Microfluidics® (selling the XonaChips®) and ANANDA Devices (selling the Neuro-HTS™). Such devices permit a simple segregation of soma and axons, which is convenient to analyze axonal damage resultant from injury or disease-related imbalances and to screen therapeutic drug candidates. However, these platforms are composed of two-dimensional (2D) simplistic nerve tissue replicas that are very different from actual PNs. The only existing company that has a realistic PN model and whose product is closely related to this research is AxoSim, Inc that sells the NerveSim™ platform. This platform is composed of a plastic mold with a key hole-like design where a hydrogel (Matrigel) and cells are placed. Prior to implantation in the platform, human induced pluripotent stem cells (iPSCs)-derived neurons and human primary Schwann cells are formed into a spheroid. The cells are cultured in the platform up to 4 weeks to produce long anisotropic and myelinated neurites that can be probed for electrical activity. Beyond this, the platform has no other validated applications, as also described in their reference paper⁵.

Applicability of this research

In this research, we describe the development of *in vitro* PN and tissue innervation platforms. Due to the high worldwide incidence of PN damage caused by traumatic injuries, such as motor vehicle accidents or sports injuries, or because of a pathophysiology, such as diabetes-related hyperglycemia, it is imperative to have PN *in vitro* models for preclinical research. The innervation of tissues is also critical for their function and homeostasis, and thus for an accurate *in vitro* modelling, it is necessary to include a neural component. Nerve presence can also have nefarious consequences such as propagating cancer⁶ and transmitting high levels of pain in patients with endometriosis⁷. Therefore, this research falls upon a broad range of clinical needs that are highly relevant for the medical and pharmaceutical industry.

1) Peripheral nerve models

In chapter 3, we developed our first version of a PN model, based on a scaffold/hydrogel hybrid platform and using a cell line (PC12) as neuron population. The scaffold/hydrogel system constitutes a novel approach towards forming three-dimensional (3D) and anisotropic neural tissue in a simple and affordable manner. Using low technological and cheap culture methods, we were able to generate PN tissue with high-level of maturity and high-level of versatility regarding its contents (protein composition and cellular presence). We demonstrate the use of this model in neurotoxicity, drug screening and disease modelling studies, all of which are highly relevant within the neurobiology field. Despite its discrepancies from actual human neurons, PC12 cells constitute an important and useful tool because of their low-cost/low-maintenance requirements and wide range of applications, such as in neurotransmitter release tests. Therefore, we envision the use this method across labs for a “do-it-yourself” PN model fabrication, via full protocol replication or customized adaptation. Additionally, the major model components such as the scaffold and silicone platform could be commercially explored to facilitate the assembly tasks of potential clients.

In chapter 4, we developed an improved version of the PN platform, by substituting the PC12 cell line with human induced pluripotent stem cells (iPSCs)-derived nociceptors. These neurons are of human origin and we demonstrated that they behave as actual nociceptors, exhibiting electrical activity and reacting to noxious stimuli. These characteristics makes them suitable to construct an *in vitro* pain model that can be used to assess the safety and potential painful effects of a certain drug. In literature there are already a few *in vitro* nociceptor models such as the work of Wainger et al.⁸ and Jones et al.⁹ However, none of these models achieved the level of PN biomimicry and maturation that we attained which makes our model the most representative sensory PN model. Additionally, we developed a method that generates thousands of nociceptor spheroids, with uniform sizes, and in a short time frame. This confers a higher level of reproducibility and robustness to our method in comparison to existing models. When co-culturing the nociceptor spheroid with Schwann cells (SCs) in the scaffold/fibrin hydrogel system, we were able to generate 3D, long, anisotropic and stable myelinated tissue. Compared to the NerveSim™, our platform is larger (in fact the largest ever shown), thus showing a better approximation to the actual human dimensions. Rather than using Matrigel, our model is built from a less expensive and more defined hydrogel material (fibrin gel). Additionally, we show the ability to conduct disease modelling and drug screening experiments. In sum, due to the large range of applications and low competition, this platform is endowed with high commercial appeal. We contemplate the establishment of the 3D platform as a product that can be purchased ready-made, in order for laboratories to conduct their own investigations. Alternatively, the model components such as the agarose mold and scaffold could be sold individually or in a package, to allow researchers to assemble the platform

themselves. Finally, a testing service could be set up to provide, upon client (e.g. pharmaceutical companies) request, a detailed assessment of a compound's action on nerves (and nociceptors in particular). We demonstrate an example of the latter in chapter 5, where we investigate the action of phosphodiesterase-4 (PDE4) inhibitors on SCs and neurons. PDE4 inhibitors are a family of compounds with high research interest within neurobiology/neurosciences, due to their various proved benefits. New formulations of these drugs were synthesized by a collaborator based in Maastricht and Hasselt University, and were tested in our facilities using our system.

2) Innervation models

As previously mentioned, innervation models are highly desired within biomedical research, and besides some literature reports (using motor rather than sensory neurons^{10,11}), there are no products in the market yet. In chapter 4, we demonstrate that our platform is also suitable to innervate target tissues, showing examples with pancreatic and endometrial tissue models. Both of these tissues are associated with neural pathologies, and thus the existence of innervation models will provide a very useful and needed research tool to investigate pathophysiological mechanisms and screen therapeutic drug candidates. In chapter 7, we maintained the same platform components, but altered its assembly process to include vasculature and generate a neurovascular model. The simultaneous presence of a vascular and neural network constitutes a step forward to achieve higher organ modelling complexity, necessary to improve the current state of organ-on-a-chip platforms. Therefore, this model can work as supporting unit for target tissues that require both vascular and neural supply.

Lastly, in chapter 6 we described the formation of a human innervated skin model. Advanced skin models are coveted within the biomedical field due to the large incidence of skin-related conditions. Additionally, because of the European Commission ban on the use of animals for cosmetic testing, there has been an increased interest by cosmetic companies, such as L'Oreal, in developing their own skin models. Currently, several companies, such as Phenion, LabSkin and Episkin, already commercialize skin equivalents. However, none of these products contains the innervation component that is critical for skin function and regeneration. Furthermore, the presence of nociceptors within a skin equivalent will provide the ability to detect if topically applied products can produce an adverse/unwanted reaction, such as irritation or burning sensation. Therefore, we envision that this model has a high commercial appeal, particularly for the pharmaceutical and cosmetic industry.

Future improvements

Despite the mentioned achievements, we recognize that in order to succeed in extracting the most valorization of this research, a number of improvements are still required. These improvements fall upon a number of parameters that due to the nature of this fundamental research do not yet meet the necessary criteria for commercialization. The suggested modifications are:

- 1) **Automated and clean fabrication** – The current scaffold production and assembly method is heavily reliant on manual labor. Automation would reduce the fabrication time and improve reproducibility. This could be achieved using an industrial setting electrospinning apparatus with precise control of all parameters for scaffold production, followed by an automated scaffold-cutting tool. These operations would be undertaken in a cleanroom facility to minimize contamination.
- 2) **Inclusion of microfluidic channels** – The addition of a perfusion system would greatly enhance the platform potential, by permitting a regulated perfusion of the vascular network or controlled drug delivery. This could be achieved with the microfabrication of an encasing structure made from a non-leachable/non-cytotoxic material (e.g. glass) that would permit to template channels (via removable rods, ambient-responsive materials, etc.). The platform could then be coupled to a perfusion pump for delivery of medium at a physiological shear stress value.
- 3) **Physical/Chemical parameter modelling** – Computational models (using for instance the COMSOL Multiphysics software) backed up by “real-life” experiments to describe some relevant physical and chemical parameters, such as oxygen concentration, which have an influence in several biological processes (e.g. angiogenesis).
- 4) **Precise cell positioning** – Automated methods for cell seeding to improve the reproducibility of the tissue-engineered constructs. This could be achieved using robotic spheroid dispensing techniques. Alternatively, formation of cell compartments within microfluidic platforms, where cells can be immobilized.
- 5) **In-line sensing devices** – Development of sensors that could be incorporated within the platform to acquire parameter information (pH, oxygen level, neuron activity, etc. in real-time and non-destructively).

References

1. Zhang, B. & Radisic, M. Organ-on-a-chip devices advance to market. 2395–2420 (2017).
2. Paul, S. M. *et al.* How to improve RD productivity: The pharmaceutical industry's grand challenge. *Nat. Rev. Drug Discov.* **9**, 203–214 (2010).
3. Wu, Q. *et al.* Organ-on-a-chip: Recent breakthroughs and future prospects. *Biomed. Eng. Online* **19**, 1–19 (2020).
4. Low, L. A., Mummery, C., Berridge, B. R., Austin, C. P. & Tagle, D. A. Organs-on-chips: into the next decade. *Nat. Rev. Drug Discov.* (2020).
5. Sharma, A. D. *et al.* Engineering a 3D functional human peripheral nerve in vitro using the Nerve-on-a-Chip platform. *Sci. Rep.* **9**, 1–12 (2019).
6. Boilly, B., Faulkner, S., Jobling, P. & Hondermarck, H. Nerve Dependence: From Regeneration to Cancer. *Cancer Cell* **31**, 342–354 (2017).
7. Morotti, M., Vincent, K. & Becker, C. M. Mechanisms of pain in endometriosis. *Eur. J. Obstet. Gynecol.* **209**, 8–13 (2017).
8. Wainger, B. J. *et al.* Modeling pain in vitro using nociceptor neurons reprogrammed from fibroblasts. *Nat Neurosci* **18**, 17–24 (2015).
9. Jones, I. *et al.* Development and validation of an in vitro model system to study peripheral sensory neuron development and injury. *Sci. Rep.* **8**, 1–15 (2018).
10. Osaki, T., Uzel, S. G. M. & Kamm, R. D. Microphysiological 3D model of amyotrophic lateral sclerosis (ALS) from human iPS-derived muscle cells and optogenetic motor neurons. *Sci. Adv.* **4**, 1–16 (2018).
11. Uzel, S. G. M. *et al.* Microfluidic device for the formation of optically excitable, three-dimensional, compartmentalized motor units. *Sci. Adv.* **2**, (2016).

Summary

The development of organ models with increased tissue complexity is needed to improve the validity of *in vitro* preclinical research. For this, the generation of neuronal and vascular networks within organ models is of utmost importance to provide tissues with electrical and oxygen/nutrient support, required for their long-term survival and functionality. The work described in this thesis fits within this purpose, as our overarching goal was to develop a humanized neurovascular platform for *in vitro* applications. In **chapter 1**, we provide an overview of the neurovascular (NV) system, exposing their parallels and interactions during developmental, adult and regenerative stages, as well as NV disruptions in a pathological context. We highlight the NV coupling as an integral part of the human body and consequently as a requirement for proper organ modelling. In **chapter 2**, we review and discuss the potential of biofabrication approaches to increase complexity within engineered tissues. Particularly, we focus on vasculature and existing techniques to pattern it, such as material-induced, structure-induced and direct cell patterning strategies. We propose that a combination of these strategies will be required to achieve multi-scale networks that mimic native hierarchical structures. In **chapter 3**, we demonstrate the creation of a 3D biomimetic *in vitro* peripheral nerve (PN) model built from PC12 cells and primary rat Schwann cells (SCs), and compare the tissue morphology to a similar model built from animal tissue explants (rat dorsal root ganglia). Using the PC12-based platform, we showed a range of applications such as toxicity screening, axonal growth modelling, diabetes modelling and drug screening. In **chapter 4**, we improve the PN platform by substituting PC12 cells with induced pluripotent stem cells (iPSCs)-derived nociceptors, which we characterize in terms of functionality. We perform a side-by-side comparison of our 3D platform with conventional glass coverslips, making the case that our system is largely superior to standard culture methods. Again, we use our PN platform to model a diabetic-like state and conduct therapeutic drug tests. Finally, we demonstrate the potential to include target tissues for the creation of innervation models. In **chapter 5**, we apply our 3D platform and SC model as a drug testing platform. We focus on the effect of phosphodiesterase-4 (PDE4) inhibitors on the SC myelinating phenotype, when SCs are in a nerve-regenerating setting or when exposed to a diabetic-like environment. In **chapter 6**, we develop a fully human skin innervation platform through the combination of our iPSCs-nociceptor neurospheres with an established skin model. Using this platform, we show the ability to conduct drug tests. In **chapter 7**, we display the fabrication of a NV platform through the combination of a 3D vascular and 3D neural model. In this NV model, we exhibit the establishment of several NV interactions. In **chapter 8**, a historical and critical perspective of preclinical research with regards to animal and *in vitro* models is given. The research themes are fitted within this context and a future

outlook about general *in vitro* models and particularly innervation models is provided. Finally, in **chapter 9**, we explore the utility and commercial appeal of this research.

Samenvatting

De ontwikkeling van orgaanmodellen met verhoogde weefselcomplexiteit is nodig om de validiteit van *in vitro* preklinisch onderzoek te verbeteren. Hiervoor is het genereren van neuronale en vasculaire netwerken binnen orgaanmodellen van het grootste belang om weefsels te voorzien van elektrische stimulatie en zuurstof/voedingsondersteuning, vereist voor overleving en functionaliteit op de lange termijn. Het werk beschreven in dit proefschrift past binnen deze context, aangezien ons overkoepelende doel was om een gehumaniseerd neurovasculair platform te ontwikkelen voor *in vitro* toepassingen. In **hoofdstuk 1** geven we een overzicht van het neurovasculaire (NV) systeem, waarbij we overeenkomsten en interacties illustreren gedurende de verschillende stadia van ontwikkeling, volwassenheid en regeneratie, evenals NV-verstoringen in een pathologische context. We lichten de NV-koppeling uit als een integraal onderdeel van het menselijk lichaam en daardoor als een vereiste voor een goede orgaanmodellering. In **hoofdstuk 2** bespreken we en vatten we de potentie van biofabricage-benaderingen samen om de complexiteit van gemanipuleerde weefsels te vergroten. In het bijzonder richten we ons op het vaatstelsel en bestaande technieken om patronen te maken, zoals materiaal-geïnduceerde, structuur-geïnduceerde en directe celpatroonstrategieën. We stellen voor dat een combinatie van deze strategieën nodig zal zijn om netwerken met verschillende niveaus te creëren die natuurlijke hiërarchische structuren nabootsen. In **hoofdstuk 3** demonstreren we de creatie van een 3D biomimetisch *in vitro* perifere zenuwmodel (PZ) opgebouwd uit PC12-cellen en primaire Schwann-cellen van ratten (SC's). Daarin vergelijken we de weefselmorfologie met een soortgelijk model dat is opgebouwd uit explants van dierlijk weefsel (dorsale wortel ganglia van ratten).. Met behulp van het PC12-gebaseerde platform lieten we een reeks toepassingen zien, zoals toxiciteit screening, axonale groei-modellering, diabetes modellering en medicijnscreening. In **hoofdstuk 4** verbeteren we het PZ-platform door PC12-cellen te vervangen door nociceptoren gedifferentieerd vanuit geïnduceerde pluripotente stamcellen (iPSCs), die we karakteriseren op basis van functionaliteit. We vergelijken ons 3D-platform met conventionele dekglasma's, waardoor we aantonen dat ons systeem grotendeels superieur is ten opzichte van standaard kweekmethoden. We gebruiken ons PZ-platform nogmaals om een diabetische toestand te modelleren en therapeutische medicatie te testen. Ten slotte demonstreren we de potentie om doelweefsels op te nemen om innervatie-modellen te creëren. In **hoofdstuk 5** passen we ons 3D-platform en SC-model toe als platform om medicatie te testen. We concentreren ons op

het effect van fosfodiësterase-4 (PDE4) -remmers op het SC-myeliniserende fenotype, wanneer SCs zich in een zenuw-regenererende omgeving bevinden of wanneer ze worden blootgesteld aan een diabetische omgeving. In **hoofdstuk 6** ontwikkelen we een volledig menselijk huidinnervatie platform door onze iPSC-nociceptor-neurosferen te combineren met een beproefd huidmodel. Met behulp van dit platform laten we zien dat we medicatie kunnen testen. In **hoofdstuk 7** laten we de fabricage van een NV-platform zien door de combinatie van een 3D vasculair en 3D neuraal model. In dit NV-model tonen we de totstandkoming van verschillende NV-interacties aan. In **hoofdstuk 8** wordt een historisch en kritisch perspectief gegeven op preklinisch onderzoek met betrekking tot dier- en *in vitro* modellen. De onderzoeksthema's passen in deze context en er wordt een toekomstperspectief gegeven over algemene *in vitro* modellen en, in het bijzonder, innervatie modellen. Ten slotte onderzoeken we in **hoofdstuk 9** het nut en de commerciële aantrekkingskracht van dit onderzoek

Acknowledgments

This part is by no doubt the one I was most looking forward to write. Not only because this signals the end of this endeavor, but also because I can genuinely take time to thank the people that made all of this possible. First and foremost, and there is no other way I could start this, I need to acknowledge the role that my parents had. The education they provided me and the one they gave me access to, was key to stimulate me as a curious person with appreciation for knowledge. Their moral and financial support together with their guidance in decisive moments was also crucial to bring where I am today. And of course, the love they gave me. Here, would also like to thank my sister Mariana and my extended family, which provided me with many enjoyable and relaxing moments throughout my life.

To Lorenzo, the person that accepted me as a young master student and then had the courage (madness?) to hire me as a PhD student, I am owing you a big thank you. You were the best boss I could ever had (really mean it) and you are definitely putting the bar quite high for my next jobs. Your human side really shines and contrasts with the often robotization of academia. I wish you the best of success and hope that a time to relax comes at some point, because you will deserve it. To my other boss, Paul, I also have to thank the nice scientific discussions and constant challenge to reach higher. I think you are a brilliant scientist with a passion for education and great achievements await you.

Zarina, you were the person that stuck right by my side during a sizable part of my PhD. I think that without your support and peace of mind that you offered me, this could have been quite a different journey, and I am thankful that it was made with you. Your kindness and love taught me a lot.

In Maastricht, I was able to find amazing people and some of them I am lucky to call friends. The boys group, *conmary*, composed by Nello, Daniel, Shivesh, Pere and Tristan, definitely provided me some of the best moments during my PhD time. In particular, I will remember our incredible dinners and parties, which I hope that we can re-enact for the following years, despite our distance. In this group, I would need to include an honorary member and best housemate one could expect, Tate. A lot of good times, in and out of the house, were spent with you, so thank you for those. I lived with several people during my stay in Maastricht, but definitely will be remembering the times with Jenni, who is probably the best listener and kindest person around, and Lukas, the man responsible to recruit me into Praaglaan, the finest house in Maastricht, and dare to say, the Netherlands.

In our famous dinners, we were lucky to be joined by lovely ladies who I can also call friends: Filipa, Einav, Claudia and Mariona, thank you for putting up with us. Outside of work, I met wonderful people and some of them, I found after joining the Love Foundation. In the preparation and during the events, I had the chance to do things I would never expect to do as

PhD student in a scientific field. It was definitely a breath of fresh air and a lot of fun. I would particularly recognize Philippe, Lukas, David and Neal, whom I foresee as the greatest social entrepreneur of Limburg.

When I moved to Maastricht, I was lucky to immediately find a little Portugal at my workspace. Some of the first people I met, the 3D's composed by Daniel, Danielle and David, plus Victor (not Portuguese but almost) made me feel at home and eased the transition to this foreign country, where sandwiches are considered lunch. Thank you for the lovely dinners, especially during the Christmas period.

In MERLN, I was incredibly lucky to belong to a place with simultaneously ultra-high tech lab spaces but also with very down to earth, friendly people. Even the bosses were nice, and I would need to acknowledge Matt, Pamela, Carlos and Aurélie for being friendly and not looking down on us peasants, while being incredibly competent in their job. As for younger people there are a lot of names I would need to call. My good friend and paronymph, Chloe, thank you for the amazing conversations, far away trips and your overall presence ☺. To Jasia, Stacy, Kwasi, Josh, Shazad, Sami (turns into a superman in Ramadan), Carlos, Omar, Fiona, Jip, Denny, Dennis, Eduardo, Rabeil, Pascal, Ivo, Clarissa, Adrian, Francesca, Ravi, Erik, Giot, Gabriella, Yousra, Tony & Louis (I will remember you everytime it's Halloween) thank you for being part of my journey. I am also extremely thankful to join different football groups to get my weekly dose of ball kicking, extremely needed for my well-being.

Outside of MERLN, I also need to acknowledge other people, especially Hugo, Rita and Cho, whom I had and still have amazing, thoughtful conversations that truly make my day.

I could not write this without mentioning my friends in Portugal, part of the B3K group, whom I have maintained a strong connection throughout this time, and hope that persists for many years: In particular Peixe (thank you for the amazing cover art), Mário, António, Brito I&II, Queirós, Nogueira, Chitas, Inês, Neskk, Rudra, Lino, Madeira I&II, Chico, Frogz, Martins, Tintim, Félix, Venâncio and Chaves.

Thank you all for being there for me and constantly helping me to improve.

Ubuntu.

Biography

Afonso Malheiro was born on 28th November 1990 in Lisbon, Portugal. Early on he developed an interest for science, geography, history and architecture, particularly football stadium design. However, his clear inaptitude for artistic expression and the lack of employment in human sciences, directed his study choices towards classic scientific subjects. After completing high school, he pursued a bachelor degree in Biomedical Engineering, attracted by the field novelty and its highly interesting topics. He completed his degree in the School of Engineering of the Catholic University of Portugal in February 2012. After that, not disappointed with what he had learned, he decided to further his knowledge in the field and pursue a master's degree in Biomedical Engineering. For that, he moved to the Netherlands to enroll in the University of Twente, where he followed a track in Molecular, Cellular and Tissue Engineering. In his 2nd year, he performed an internship in the Wake Forest Institute for Regenerative Medicine, where he worked on a research project regarding 3D printing of polymeric/ceramic scaffolds for bone tissue engineering. Back in the Netherlands, he initiated a master thesis project, supervised by Prof. Lorenzo Moroni, where he developed a new biofabrication technique based in direct writing electrospinning. Using this technique, he showed an application for scaffold fabrication of articular cartilage constructs. This project was completed in December 2014, and shortly after in March 2015, he started a PhD program in the MERLN Institute, Maastricht University. Again, under the wings of Prof. Lorenzo Moroni, and also Dr. Paul Wieringa, he developed several *in vitro* platforms of nerve tissue to model the peripheral nerve, innervate target tissues and build neurovascular constructs. The aim of this work was to develop new *in vitro* tools that represent the native tissues and can be applied for research purposes, such as disease modelling and drug testing. Beyond science, he maintains a keen curiosity for everything else and a clear aptitude to enjoy life.



Publication record and scientific communications related to this thesis

- Afonso Malheiro, Paul Wieringa, Carlos Mota, Matthew Baker, and Lorenzo Moroni. Patterning Vasculature: The Role of Biofabrication to Achieve an Integrated Multicellular Ecosystem. *ACS Biomater. Sci. Eng.* (2016)
- Afonso Malheiro, Francis Morgan, Matthew Baker, Lorenzo Moroni, Paul Wieringa, A three-dimensional biomimetic peripheral nerve model for drug testing and disease modelling. *Biomaterials* (2020)
- Afonso Malheiro, Abhishek Harichandan, Joyce Bernardi, Adrián Seijas Gamardo, Gonda F. Konings, Paul Volders, Andrea Romano, Carlos Mota, Paul Wieringa, Lorenzo Moroni. 3D culture platform of human iPSCs-derived nociceptors for peripheral nerve modelling and tissue innervation (submitted, under revision)
- Afonso Malheiro, Paul Wieringa, Lorenzo Moroni. The peripheral neurovascular link: an overview of interactions and in vitro models (submitted, under revision)